UNIVERSIDADE DE LISBOA
INSTITUTO SUPERIOR TÉCNICO

UNIVERSITAT POLITÈCNICA DE CATALUNYA
DEPARTMENT OF CHEMICAL ENGINEERING

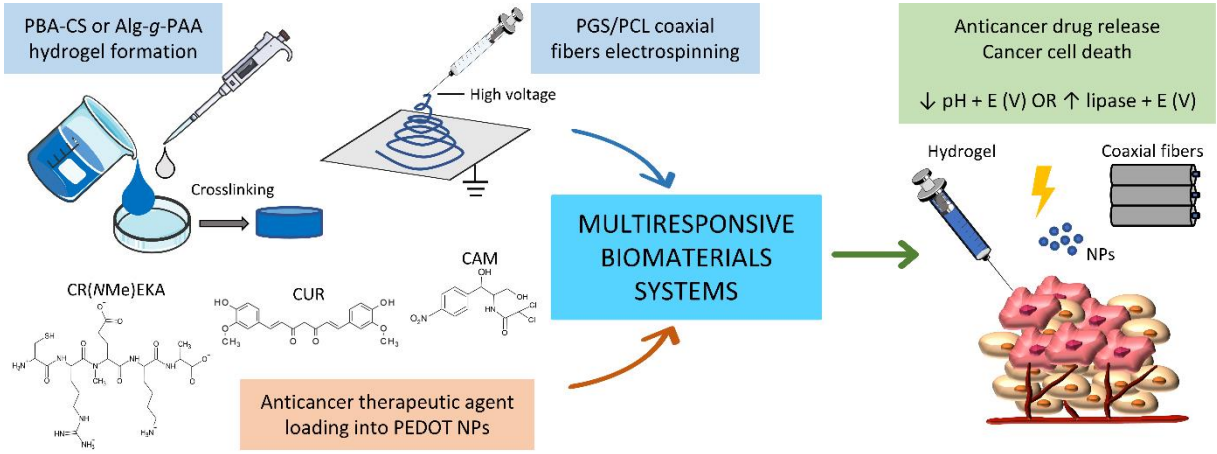

New multiresponsive materials platforms for cancer treatment: Smart electroconductive nanoparticles and transdermal devices

Maria Leonor Matos Resina

Supervisor: Doctor Frederico Alves Castelo Ferreira
Supervisor: Doctor Carlos Enrique Alemán Llansó
Co-supervisor: Doctor Teresa Sofia Araújo Esteves

Thesis approved in public session to obtain the PhD Degree in Bioengineering

Jury final classification: Pass with Distinction and Honour

2024

UNIVERSIDADE DE LISBOA
INSTITUTO SUPERIOR TÉCNICO

UNIVERSITAT POLITÈCNICA DE CATALUNYA
DEPARTMENT OF CHEMICAL ENGINEERING

New multiresponsive materials platforms for cancer treatment: Smart electroconductive nanoparticles and transdermal devices

Maria Leonor Matos Resina

Supervisor: Doctor Frederico Alves Castelo Ferreira
Supervisor: Doctor Carlos Enrique Alemán Llansó
Co-supervisor: Doctor Teresa Sofia Araújo Esteves

Thesis approved in public session to obtain the PhD Degree in Bioengineering

Jury final classification: Pass with Distinction and Honour

Jury

Chairperson: Doctor João Pedro Estrela Rodrigues Conde, Instituto Superior Técnico, Universidade de Lisboa.
Members of the Committee:
Doctor Maria Luisa Gelmi, Department of Pharmaceutical Science, Università degli Studi di Milano Statale, Itália
Doctor Jorge Manuel Ferreira Morgado, Instituto Superior Técnico, Universidade de Lisboa
Doctor Antonella Accardo, Department of Pharmacy, University of Naples Federico II, Itália
Doctor Henrique Martiniano Vazão de Almeida, CENIMAT - Centro de Investigação de Materiais - CENIMAT|i3N Faculdade de Ciências e Tecnologia da Universidade Nova de Lisboa

Funding Institution
FCT: Fundação para a Ciência e a Tecnologia

2024

Abstract

Cancer remains the leading cause of death in many developed countries. Despite significant progress in cancer treatment many challenges persist, such as severe side effects, damage to healthy tissues due to non-specific drug distribution and high systemic toxicity.

Multiresponsive biomaterials systems have emerged as powerful tools for biomedical applications, especially in cancer treatment. This research aims to advance materials approaches to cancer therapy through the development of new electro-responsive materials platforms, incorporating smart nanoparticles (NPs) and transdermal or implantable devices. For example, NPs were used for controlled drug delivery triggered by electrical stimulation, while the devices also responded to secondary stimuli such as acidic pH or to the presence of tumor biomarkers. This combination of external and endogenous stimuli provides enhanced spatiotemporal control over drug delivery.

Several therapeutic agents were tested, including an anticancer pentapeptide (CR(*N*Me)EKA), or drugs like curcumin, and chloramphenicol. The therapeutic agents were loaded into poly(3,4-ethylenedioxythiophene) NPs (PEDOT NPs), which provided the electrical stimuli response. These drug-loaded PEDOT NPs were then incorporated into various biomaterials scaffolds, such as pH-responsive hydrogels and bio-responsive fibers, creating multiresponsive devices. For instance, to achieve a multiresponsive injectable carrier for controlled delivery of the anticancer peptide CR(*N*Me)EKA, a biocompatible and pH-responsive hydrogel, formed by phenylboronic acid grafted with chitosan, was synthesized and loaded with PEDOT NPs. An electro-chemo responsive hydrogel for chloramphenicol release was prepared by grafting polyacrylic acid onto sodium alginate and encapsulating PEDOT NPs *in situ*. Additionally, a wireless biomaterials-based electrostimulation system was developed to enable controlled and on-demand release of anticancer drugs, promoting *in vitro* human prostate cancer cell death. This system utilized curcumin-loaded PEDOT NPs encapsulated in coaxial poly(glycerol sebacate)/poly(caprolactone) electrospun fibers.

Overall, this work lays the foundation for designing and developing smarter, more effective biomaterial-based delivery systems for anticancer therapy.

Keywords: cancer therapy; controlled drug delivery; electroresponsive nanoparticles; multiresponsive biomaterials; targeting cancer cells.

Resumo

O cancro continua a ser a principal causa de morte em muitos países desenvolvidos. Apesar do progresso significativo no tratamento do cancro muitos desafios persistem, incluindo efeitos secundários graves, danos aos tecidos saudáveis e alta toxicidade sistémica.

Os sistemas de biomateriais multi-responsivos emergiram como ferramentas poderosas para aplicações biomédicas, especialmente no tratamento do cancro. Esta investigação visa avançar nas abordagens de novos materiais para a terapia do cancro através do desenvolvimento de novas plataformas de materiais electro-responsivos, incorporando nanopartículas (NPs) inteligentes e dispositivos transdérmicos ou implantáveis. Por exemplo, NPs foram usadas para a libertação controlada de medicamentos desencadeada por estimulação elétrica, enquanto os dispositivos também respondiam a estímulos secundários, como pH ácido ou à presença de biomarcadores tumorais. Esta combinação de estímulos externos e endógenos proporciona maior controlo espácio-temporal sobre a libertação de medicamentos.

Vários agentes terapêuticos foram carregados em nanopartículas de poli(3,4-etilenedioxitiofeno) (PEDOT NPs), que forneceram a resposta ao estímulo elétrico. Estas PEDOT NPs foram então incorporadas em vários biomateriais, como hidrogéis sensíveis ao pH e fibras bio-responsivas, criando dispositivos multi-responsivos. Por exemplo, para alcançar um sistema injetável multi-responsivo para a libertação controlada do peptídeo CR(*N*Me)EKA, foi sintetizado um hidrogel sensível ao pH, formado por ácido fenilborónico enxertado com quitosano, e carregado com PEDOT NPs. Um hidrogel electro-quimo-responsivo para libertação de cloranfenicol foi preparado pela enxertia de ácido poli(acrílico) em alginato de sódio e encapsulação de PEDOT NPs. Além disso, foi desenvolvido um sistema de electroestimulação sem fios baseado em PEDOT NPs carregadas com curcumina encapsuladas em fibras coaxiais de poli(glicerol sebacato)/poli(caprolactona) para permitir a libertação controlada de curcumina, promovendo a morte de células cancerígenas humanas de próstata *in vitro*.

No geral, este trabalho lança as bases para o design e desenvolvimento de sistemas de libertação mais inteligentes e eficazes baseados em biomateriais para a terapia anticancerígena.

Palavras-chave: terapia anticancerígena; entrega controlada de medicamentos; nanopartículas electro-responsivas; biomateriais multi-responsivos; terapia direcionada a cancro.

Resumen

El cáncer sigue siendo la principal causa de muerte en muchos países desarrollados. A pesar del significativo progreso en el tratamiento del cáncer persisten muchos desafíos, incluyendo efectos secundarios graves, daño a los tejidos sanos y alta toxicidad sistémica.

Los sistemas de biomateriales multi-responsivos han surgido como herramientas poderosas para aplicaciones biomédicas, especialmente en el tratamiento del cáncer. Esta investigación tiene como objetivo avanzar en la terapia del cáncer mediante el desarrollo de nuevas plataformas de materiales electro-responsivos, incorporando nanopartículas (NPs) inteligentes y dispositivos transdérmicos o implantables. Por ejemplo, se usaron NPs para la liberación controlada de fármacos desencadenada por estimulación eléctrica, mientras que los dispositivos respondieron a estímulos como el pH ácido o biomarcadores tumorales. Esta combinación de estímulos externos y endógenos proporciona un mayor control espaciotemporal sobre la liberación de fármacos.

Se probaron varios agentes terapéuticos, que se cargaron en NPs de poli(3,4-etilendioxitiofeno) (PEDOT NPs), que proporcionaron la respuesta al estímulo eléctrico. Estas PEDOT NPs se incorporaron en varios biomateriales, como hidrogeles sensibles al pH y fibras bio-responsivas, creando dispositivos multi-responsivos. Para lograr un sistema inyectable multi-responsivo para la liberación controlada del péptido CR(*N*Me)EKA, se sintetizó un hidrogel sensible al pH, formado por ácido fenilborónico injertado con quitosano, y se cargó con PEDOT NPs. Se preparó un hidrogel electro-quimio sensible para la liberación de cloranfenicol mediante la injertación de ácido poliacrílico en alginato de sodio y la encapsulación de PEDOT NPs. Además, se desarrolló un sistema de electroestimulación inalámbrico basado en PEDOT NPs cargadas con curcumina encapsuladas en fibras coaxiales de poli(sebacato de glicerol)/poli(caprolactona) para la liberación controlada de curcumina, promoviendo la muerte de células cancerosas humanas *in vitro*.

En general, este trabajo sienta las bases para el diseño y desarrollo de sistemas de liberación más inteligentes y efectivos basados en biomateriales para la terapia anticancerígena.

Palabras clave: terapia anticancerígena; entrega controlada de medicamentos; nanopartículas electro-responsivas; biomateriales multi-responsivos; terapia direccionada al cáncer.

Acknowledgments

Borrowing the words of many PhD students that sat (figuratively) where I am now, this Thesis would not be possible without the contributions, both direct and indirect, of many people.

First, I would like to thank Professor Joaquim Cabral for accepting me in the PhD Program in Bioengineering – Cell Therapies and Regenerative Medicine, and also for the constant availability and support in paperwork and general problem solving regarding all aspects of the PhD Program.

Second, I would like to thank FCT - Fundação para a Ciência e a Tecnologia, I.P., for the PhD scholarship (SFRH/BD/145057/2019).

Third, I would like to thank my supervisors for all the support and guidance.

I'm deeply grateful to Professor Frederico Ferreira for turning what I thought was a research assistant interview into a pseudo PhD interview. Professor Frederico, thank you for the opportunity, for all the support and for constantly challenging me in scientific pursuits. When I took your entrepreneurship classes, I never thought I would end up as your PhD student, but even then, your scientific enthusiasm was visible and kind of contagious, in a good sense of course. Thank you for believing in me and teaching me how to do science.

Teresa Esteves, thank you for all the knowledge you have passed to me in the lab, and thank you for trying to convert Frederico's scientific enthusiasm to lab day-to-day experiments. I'm also grateful for all the support and time you spent with me, from teaching moments to companionship moments. Thank you for trying to calm me, especially at the beginning, when I felt a bit overwhelmed with the PhD.

I'm also very thankful to Professor Carlos Alemán for accepting me in the Polymers and Biopolymers PhD Program, and for welcoming me in the IMEM group at UPC. Thank you for suggesting doing this Thesis as a co-tutelle and for finding the funding for UPC tuition. Carlos, thank you for showing me new perspectives on doing science. I come out of this experience very enriched as a scientist, having experienced different types of supervision and different lab environments.

I also want to thank Mar Pérez Madrigal for the informal supervision during my stay at UPC, for always being available for me (to answer questions and discuss science) and for involving me in fostering collaborations outside UPC. Also, I would like to thank all the Professors and PosDocs in the group who helped, trained and taught me new things.

Next, I want to thank the people who strengthened my resolve to pursue a PhD. Fábio Garrudo, Ana Carina Manjua, João Silva, and Flávio Ferreira. You guys taught me so much, thank you! A special thanks goes to Fábio who taught me a lot of the techniques used in this Thesis. Fábio, your participation enriched this work so much more! And thank you for the brainstorming sessions and for

the support and friendship outside the lab. Also, a thank you note for Paola Sanjuan Alberte for the bipolar electrochemistry tips, they were very valuable.

A special thank you to Karima El Hauadi, not quite but at the same time yes, my first MSc student. Without you the making of Chapter III and Chapter IV would've taken much longer and wouldn't have been as fun to do! Also, thank you to Pili Casale and Pau Caballero, respectively my first unofficial and official BSc students. Although you haven't contributed to this Thesis directly, thanks to you I have started to learn how to teach, which is also a great part of the scientists' way.

A great thank you to all my iBB friends, 7th and 8th floor included. Sara, Miguel, Cris and Jorge thank you for all the support and for the friendship in the bad and good moments, while we navigated this PhD adventure together!

Another great thank you to all my IMEM-PSEP friends. We are so many, it's impossible to name everyone, but thank you David, Júlia, Matteo, MariCarmen, Marc, Merve, Lola, Tanaz, Jillian, Hussain, Hamidreza, Davit, Metsino, Adrián, Samuele, Jordi… To the "older" ones, thank you for welcoming me in Barcelona, for showing me the ways of the PhD student (2nd floor office is still the best), and for making me "come out of my shell". Thank you for the brainstorming sessions and for sharing knowledge, the different backgrounds of everyone really enriched me as a scientist and as a person! Also, thank you all for sharing all the non-sense and for the fun moments we spent together! I have met great people in Barcelona, made friends from different parts of the world, but I will keep you all in my heart forever. Creo que llevo amigos para la vida. Obrigada. Gracias. Graciès. Grazie. Salamat. Teşekkürler. با تشکر. நன்றி. მადლობა. I hope I got everything right!

David, Júlia y MariCarmen, gracias por estar en las buenas y las malas. Donde sea que el futuro nos lleve, espero lograr mantenerlos en mi vida.

To my friends from "before the PhD" (Lisa, Iza, João, Manel, Sara…), thank you for being so understanding and supportive. Thank you for not being mad because I missed so many of your special occasions (birthdays, weddings, birth of my "nieces" and "nephews") because I was far away and busy. Thank you for being the kind of friends that can go months without talking (reels and memes don't count) and pick it up right where we left off. Special thanks to you Lisssaaa, for visiting me every year.

Finally, and most important of all, I want to thank my family from the bottom of my heart. Thank you for accompanying me in this journey and for the constant care and support, even in moments of disaggrement. Without you this wouldn't have been possible.

Mãe, sem ti não teria chegado até aqui. Obrigada pela força que me transmites todos os dias.

Pai, obrigada por estares sempre presente mesmo à distância.

E aos que já partiram, gosto de pensar que se sentem orgulhosos de mim.

Ainda que seja simbólico, dedico-vos esta Tese.

Table of contents

List of figures

Chapter II

Chapter III

Chapter IV

Chapter V

Chapter VI

Chapter VII

Chapter VIII

List of tables

Abbreviations

5-FU	5-Fluorouracil
AAc	Acrylic acid
AAm	Acrylamide
AC	Alternating current
AIBN	Azo-bis isobutyronitrile
Alg	Alginate
Alg-*g*-PAA	Alginate-*grafted*-poly(acrylic acid)
ANI	Aniline
APMA	*N*-(3-aminopropyl) methacrylamide
APS	Ammonium persulfate
BSA	Bovine serum albumin
CA	Chronoamperometry
CAM	Chloramphenicol
CD	Circular dichroism
CIS	Cisplatin
co-PMMA	Poly(methyl methacrylate-co-methacrylic acid)
CP	Conducting polymer
CR(*N*Me)EKA	Cys-Arg-(*N*-methyl)Glu-Lys-Ala
CREKA	Cys-Arg-Glu-Lys-Ala
CS	Chitosan
CS-PBA	Chitosan-phenyl boronic acid
CUR	Curcumin
CV	Cyclic voltammetry
DBSA	Dodecylbenzene sulfonic acid
DC	Direct current
DLS	Dynamic light scattering
DMAEM	2-(Dimethylamino)ethyl methacrylate
DMAPMA	*N*-(3-(dimethylamino)propyl)methacrylamide
DMEM	Dubelcco's Modified Essential Medium
DOTAP	1,2-Dioleoyl-3-trimethylammonium-propane chloride
DOX	Doxorubicin
DPPG	1,2-Dipalmitoyl-sn-glycero-3-phospho-rac-glycerol sodium

DSC	Differential scanning calorimetry
DTX	Docetaxel
EBA	*N,N'*-ethylenebis(acrylamide);
ECM	Extracellular matrix
EDOT	3,4-Ethylenedioxythiophene
EGDMA	Ethylene glycol dimethylacrylate
EGFR	Epidermal growth factor receptor
EGM-2	Endothelial growth medium-2
EWC	Equilibrium water content
FBS	Fetal bovine sérum
FTIR	Fourier-transform infrared spectroscopy
Gel	Gelatin
GelMA	Gelatin methacryloyl
GF	Gel fraction
HAp	Hydroxyapatite
HFP	1,1,1,3,3,3-Hexafluoropropanol
HPLC	High performance liquid chromatography
HRP	Horse radish peroxidase
HSA	Human serum albumin
HUVECs	Human umbilical vein endothelial cells (HUVECs)
ItAc	Itaconic acid
LC	Loading capacity
Lipoid-S75	Soybean phosphatidylcholine
LVE	Linear viscoelastic
MBA	*N,N'*-methylenebisacrylamide
MD	Molecular dynamics
MEM	Minimum Essential Medium
MIPs	Molecularly imprinted polymers
MRI	Magnetic resonance imaging
MTT	3-(4,5-Dimethylthiazol-2-yl)-2,5-diphenyltetrazolium bromide
NIPAM	*N*-isopropylacrylamide
NIPs	Non-imprinted polymers
NPs	Nanoparticles
NIR	Near infrared

NTs	Nanotubes
PAA	Poly(acrylic acid)
PANI	Poly(aniline)
PBA	Phenyl boronic acid
PBS	Phosphate buffered saline
PCL	Poly(caprolactone)
PDA	1,4-Bis(acryloyl)piperazine
PEDOT	Poly(3,4-ethylenedioxythiophene)
PEDOT:PSS	Poly(3,4-ethylenedioxythiophene):poly(styrene sulfonate)
PEGDMA	Poly(ethylene glycol)dimethacrylate
PFA	Paraformaldehyde
PGS	Poly(glycerol sebacate)
PNIPAM	Poly(*N*-isopropylacrylamide)
PPy	Polypyrrole
PSMA	Prostate specific membrane antigen
QCM	Quartz crystal microbalance
RF	Riboflavin
RPMI	Roswell Park Memorial Institute
SDBS	Sodium dodecylbenzene sulfonate
SDS	Sodium dodecyl sulfate
SEM	Scanning electron microscopy
SR	Swelling ratio
TBAm	*N*-tert-butylacrylamide
TEM	Transmission electron microscopy
TEMED	*N,N,N',N'*-Tetramethylethylenediamine
TFE	2,2,2-Trifluoroethanol
TME	Tumor microenvironment
UV	Ultraviolet
UV-Vis	Ultraviolet-Visible
VEGF	Vascular endothelial growth factor

Chapter I – Research concept

I - 1. Motivation

Cancer is the leading cause of death in many developed countries, with an estimated 19.3 million new cancer cases and 10.0 million cancer deaths worldwide in 2020 with a growing tendency.[1] Breast cancer was the most diagnosed cancer in the world in 2020, with prostate cancer reaching fourth position.[1] In the United States, in 2023, breast cancer accounted for 31% of cancer diagnostics for women of all ages, while prostate cancer was the most diagnosed in men accounting for 29% of new cases.[2] It is interesting to note that although cervical cancer is one of the most preventable types of cancer it is the top leading cause of cancer death among females between 20 and 39 years of age in the United States.[2] Furthermore, although sometimes effective, conventional chemotherapy has many challenges, namely the harsh side effects, such as damage to healthy tissue, due to drugs' nonspecific distribution in the body and high systemic toxicity.

This project aims to contribute to materials approaches to treat cancer, namely through the development of new electro-responsive materials platforms comprising (i) smart nanoparticles (NPs) and (ii) transdermal or implantable devices.

The suggested platforms explore a dual mode of action on cancer treatment in which multi-responsive systems are proposed. For instance, NPs will be used for controlled drug delivery upon electrical stimulation, and the device will add on a second stimuli response like changes in pH or the presence of tumor markers (*e.g.* overexpression of proteins or enzymes). The use of both external (or exogenous) and endogenous stimuli confers a higher degree of spatiotemporal control over drug delivery. Therefore, this thesis will include the following steps:

1) Develop smart NPs, responsive to an external stimulus, such as an electrical field or potential range, to trigger the following responses:

    a. Drug delivery of anticancer peptides and anti-cancer drugs (inhibition of cell growth or inductor of cell apoptosis) or anti-angiogenic drugs that will suppress further tumor blood vessels formation;

    b. Drug delivery of antibiotics to prevent bacterial infections upon tumor resection surgery.

2) Develop a set of materials for application in a transdermal device, that will function as a reservoir of NPs, assemble polymer constructs (hydrogels and fibers), and characterize them. The full construct should have elastic properties for optimum skin compatibility. Additionally, the device should have specific properties necessary to achieve the release function of the construct while being biocompatible, namely:

    a. pH-response to acidic tumor microenvironment (TME);

b. Response to tumor markers, such as peptides or overexpressed proteins or enzymes.

3) Set up an appropriate testing platform using various human cancer and normal cell lines to validate the systems, which allows a quick translation of results from bench to bedside.

Furthermore, this thesis will also contemplate tissue engineering platforms to promote tissue regeneration after tumor resection surgery using electroconductive hydrogels to promote faster skin regeneration while avoiding scarring.

I - 2. Research questions and research strategy

For the accomplishment of the objectives of this thesis, a research framework was elaborated to answer relevant research questions.

Self-assembly of anticancer peptides

A strategy that has shown great promise in treating heterogeneous cancer types is the targeting of tumor vasculature by clogging the existing blood vessels to promote tumor necrosis.[3] This approach has garnered positive results by exploring a tumor-homing peptide derivative with the sequence Cys-Arg-Glu-Lys-Ala (CREKA).[4] This pentapeptide recognizes fibrin and fibronectin complexes, therefore binding to clotted plasma proteins in tumor vasculature.[4] Using engineered CREKA analogs, by exchanging Arg, Glu, or Lys by the respective N-methyl derivatives, biological activity and proteolytic resistance of the CREKA tumor-homing pentapeptide improved significantly.[5]

Considering the anticancer peptide CREKA, we identified an interesting gap in the literature concerning the possible self-assembly of this peptide into supramolecular structures. We further hypothesized that the methylation of the Glu residue in CREKA would lead to changes in the peptide's secondary structure, possibly interfering with peptide self-assembly processes and anticancer activity. Therefore, we posed the relevant questions:

1) Can CREKA and its methylated derivative (CR(*N*Me)EKA) peptide form self-assembled structures of interest? If formed, how will these self-assembly processes be affected by experimental conditions, namely, by peptide concentration and by the pH of the medium?

The answers to these questions are proposed in Chapter III.

Electroconductive polymers to design NPs

In this work we used poly(3,4-ethylenedioxythiophene) (PEDOT), which is an electroconductive biocompatible polymer previously used to promote neural stem cell differentiation under electrical stimulation,[6] and to make NPs.[7] We proposed the synthesis of the PEDOT NPs to be performed by

emulsion polymerization in water at 40 ℃ using 3,4-ethylenedioxythiophene (EDOT) monomer, sodium dodecylbenzene sulfonate (SDBS) as a stabilizer and doping agent simultaneously, and ammonium persulfate (APS) as the oxidizing agent. Considering this straightforward reaction and the NP stability in aqueous medium, we question the following:

1) Can PEDOT NPs be successfully loaded with different types of anticancer drugs during polymerization? Can these NPs also be loaded with larger molecules, like anticancer peptides, in the same way?
2) Can the release of such molecules be promoted with the same type of electrical stimuli or different stimuli are necessary depending on molecule type?

The answers to these questions are proposed in Chapters IV to VI.

Controlled delivery of anticancer peptides and anticancer drugs from NPs

The use of NPs or nanoworms, coated with CREKA, has been shown to induce further blood clotting in tumor vasculature, consequently creating additional binding sites for the CREKA sequence. This results in a self-amplifying homing system that induces tumor necrosis by suppressing blood flow.[4] CREKA or its derivatives are charged peptides, which means that it could be used as a dopant agent in electroactive conducting polymers (ECPs), such as PEDOT, to manufacture electroresponsive NPs.[8,9] Another strategy is to include in the core of the NPs a drug presenting the capacity to be oxidized or reduced (e.g. curcumin, chloramphenicol). In this way, it will be possible to induce its release by an electrochemical stimulus and induce a signal to be measured *in vitro*. Following this later feature, successful drug release systems have been previously demonstrated with vitamin K3 and dopamine.[10,11]

We hypothesize that anticancer peptides and anticancer drugs can be delivered in a controlled way by electrostimulation of PEDOT NPs, therefore, we question:

1) Can we promote the delivery of CR(*N*Me)EKA peptide to cancer cells in a controlled manner using PEDOT NPs? Will the anticancer activity of the CR(*N*Me)EKA peptide be maintained after electrostimulation and its release?
2) Further, can we deliver anticancer drugs, such as curcumin (CUR) and chloramphenicol (CAM), using electroresponsive NPs? Will anticancer activity be maintained after electrostimulation and release of each drug?
3) Can PEDOT NPs be loaded into different kinds of polymers and biopolymers? Is the presence of PEDOT NPs enough to make a hydrogel electroresponsive? Can these NPs be used to build multiresponsive systems? For example, can we further fine-tune these

delivery systems by increasing complexity, adding a hydrogel or fiber layer, to make it responsive to the TME (e.g. pH changes or biomarkers)?

We propose answers to these questions in Chapters IV to VI.

Molecularly imprinted polymers (MIPs) for cancer cell targeting

Overexpressed tumor-specific receptors provide a specific cancer cell targeting that can be explored with the use of biomarkers. Such biomarkers can be recognized by affinity elements, such as proteins,[12] antibodies, oligonucleotide aptamers,[13] and peptides.[14–16] Molecularly imprinted polymers (MIPs) have been developed to recognize small molecules,[17] but lately also to recognize larger molecules, such as DNA fragments and peptides.[18] Furthermore, MIPs for different tumor biomarkers have also been successfully developed, namely for prostate cancer diagnosis.[19,20] Therefore, we question:

1) Can we formulate a MIP capable of discriminating human breast cancer cells from healthy cells?
2) Can we formulate a dual imprinting MIP, that can target breast cancer cells and deliver an anticancer drug, in a controlled way, upon external electrical stimulation?

An innovative strategy that is proposed here is the replacement of the usual affinity elements for tumor targeting (e.g. antibody) with a MIP. The rationale behind this is that they are tailor-made for specific recognition of a molecular target that can be applied to biomolecules, including tumor markers.[21]

MIPs will be prepared to have complementary pockets to specific peptide sequences recognized by tumor cells. The templates used will be the oligonucleotide sequences or the native or derived peptide sequences that will be targeted. The functional monomers and cross-linkers will be chosen according to the chemical functionalities present in the target molecules. Also, an initiator will be appropriately chosen.

We propose some answers to these questions in Chapter VII.

Tissue regeneration platforms

Although this thesis is centered on developing new electroresponsive materials platforms for cancer treatment, we also identified a gap in research concerning tissue regeneration post-cancer treatment. After cancer treatment, wound healing in excision sites is impaired due to the harsh impact of such treatment on the patient's body. Soft materials, such as hydrogels, have been studied for wound healing applications.[22,23] Moreover, electrostimulation has also been shown to induce

fibroblast and keratinocyte growth and migration in wound healing processes.[24,25] Therefore, we question:

1) Can an electroresponsive hydrogel based on a conducting polymer and a biopolymer be produced to support wound healing?
2) Can the mechanical properties of such material be improved by crosslinking under UV light avoiding the addition of chemical additives? Can we make it resistant to wear and tear?
3) Can such a hydrogel withstand electrostimulation and promote cell growth and migration at the same time?

We propose answers to these questions in Chapter VIII.

Cellular testing platforms

Drug delivery models must be validated, before being translated to clinical applications. The most straightforward research strategy is the use of *in vitro* two-dimensional (2D) cell cultures as an initial approach to validate the effects of small drugs and peptides, but also to evaluate cell response to electrostimulation. Assays can include biocompatibility, cytotoxicity, and cell morphology evaluation. Cell assays are used in Chapters IV to VIII to validate the results regarding biomedical and potential clinical application.

I - 3. Objectives

The results of this Thesis have been organized in six different Chapters (III, IV, V, VI, VII and VIII). Chapter III and VI are connected by CR(*N*Me)EKA [Cys-Arg-(*N*Me)Glu-Lys-Ala, where (*N*Me)Glu refers to *N*-methyl-Glu], a peptide that was reported to induce prostate tumor necrosis and significant reduction in tumor growth, albeit both the general and specific objectives of each Chapter are very different. More specifically, while Chapter III is focused on the tendency of the peptide to aggregate, which may affect its physical stability, toxicity and immunogenicity, Chapter IV is devoted to engineer a carrier to load the peptide and facilitate its controlled delivery.

In Chapter III we aimed to investigate, for the first time, the self-assembly of CR(*N*Me)EKA anticancer peptide and, by extension, of its parent peptide, CREKA (Cys-Arg-Glu-Lys-Ala), as a function of the pH and concentration. The specific objectives of Chapter III are:

1) Study the secondary structures preferred by CR(*N*Me)EKA and CREKA in solution and in the solid state using circular dichroism (CD) and Fourier-transform infrared spectroscopy (FTIR).

2) Compare the experimental results derived from the studies proposed in 1) with those achieved using atomistic molecular dynamics (MD) computer simulations to provide understandable molecular models.
3) Study the morphology of the aggregates formed by CR(*N*Me)EKA and CREKA using SEM and hypothesize a self-assembly mechanism.

In Chapter IV, we have designed a polymeric platform as a carrier for the controlled delivery of short and highly hydrophilic anticancer peptides, which are challenging because of both their small size and high affinity towards water. The specific objectives of Chapter IV are:

4) Engineer and characterize a multi-component, multi-responsive, injectable and biocompatible carrier for the controlled delivery of CR(*N*Me)EKA considering both the acidic pH of tumoral tissues (endogenous stimulus) and the experience of the research group in electrical stimulation for controlled release (exogenous stimulus). This carrier has been designed combining two components: a soft hydrogel able to respond as a chemoactuator to pH changes and electro-responsive NPs.
5) Evaluate and optimize the response of each component of the carrier according to the required functions. Thus, the type and strength of the electrical stimuli used to release the peptide form the electro-responsive NPs, as well as the chemo-response of the hydrogel to improve the targeted diffusion of peptide delivered from NPs, have been iteratively analyzed and modified to achieve the most effective platform for controlled and targeted delivery.

The common link between Chapter V and the previous one (Chapter IV) is the design, preparation and characterization of a multi-responsive carrier for the loading and controlled release of an anticancer drug. However, in this case CAM, which is an antibiotic with anticancer properties, has been used instead of a peptide. The main difference between CAM and the peptide used in Chapter IV is that the former is hydrophobic while CR(*N*Me)EKA is hydrophilic. The two specific objectives of Chapter V are:

6) Design and characterize a multi-component, multi-responsive and biocompatible carrier for the controlled delivery of CAM considering both endogenous chemical stimuli and exogenous electrical stimuli. The carrier has been engineered combining the electrical response of conducting polymer NPs and a soft hydrogel that responds to changes in pH, even though the latter is completely different from that used in Chapter IV.
7) Evaluate and optimize the release of CAM from dual-responsive carrier using electrical stimuli at different pHs, as well as demonstrate that the released drug is biologically active and,

therefore, the great potential of this smart material to fight against bacterial infections and to provide local cancer treatment.

Chapter VI is focused on the development of a wireless electrostimulated system for the treatment of breast and prostate cancer. For this purpose, a multi-component carrier made of (a) conducting polymer NPs similar to those used in Chapters IV and V, which have been loaded with CUR, a drug with promising anticarcinogenic properties, and (b) biodegradable fibers, have been engineered. In detail, the specific objectives of Chapter VI are:

8) Engineer, prepare and characterize an electroresponsive carrier based on conducting polymer NPs loaded with anticancer drug, which are in turn encapsulated into biodegradable polyester fibers. The main criterion used for the choice of the materials employed for the fibrous matrix was the control of the systemic release of conducting polymer NPs, which was achieved by considering a response to endogenous enzymatic activity at tumor sites.
9) Evaluate the delivery of CUR-loaded conducting polymer NPs from the polyester fibers by enzymatic degradation and the release of CUR from the delivered conducting polymer NPs by applying external electrical stimuli. More specifically, in this work, wireless electrostimulation has been employed as a new alternative to electro-regulate the release of CUR.
10) Demonstrate the biocompatibility of the carrier and its components, as well as the biological activity of released drug, proving the potential of the developed system as transdermal device for long-term release of nanocarriers for therapeutic action.

Chapters VII and VIII aim to explore the possibilities of new avenues of research for the near future. On the one hand, we have explored the potential of MIPs as materials for preventive detection and effective treatment of cancer, while on the other hand, we have developed a self-healing, stretchable and electroresponsive hydrogel for skin tissue engineering applications with electrical stimulation. The specific objective of Chapter VII has been set as follows:

11) Prospect the synergistic potential of MIPs to target CD44, a transmembrane glycoprotein that is overexpressed in many cancer types (in particular breast cancer). For this purpose, the peptide that constitutes the epitope of such cancer cell marker has been identified as a molecular footprint and has been imprinted onto polymer matrices to engineer MIPs. Then, the specificity and affinity of the developed MIPs towards breast cancer cells has been evaluated.

The two specific objectives of Chapter VIII are:

12) Propose the utilization of electrical stimuli for skin regeneration using electroresponsive hydrogels. For this purpose, a new conducting polymer-based hydrogel has been engineered according to the skin characteristics, prepared and, subsequently, characterized. More specifically, the hydrogel consisted on a mixture of PEDOT:PSS and gelatin, which has been crosslinked by UV light using riboflavin.
13) Test the biocompatibility of the hydrogel using fibroblast cells and examine their response to electrical stimulation in terms of cell migration and cell proliferation.

I - 4. References

(1) Sung, H.; Ferlay, J.; Siegel, R. L.; Laversanne, M.; Soerjomataram, I.; Jemal, A.; Bray, F. Global Cancer Statistics 2020: GLOBOCAN Estimates of Incidence and Mortality Worldwide for 36 Cancers in 185 Countries. *CA Cancer J Clin* **2021**, *71* (3), 209–249. https://doi.org/10.3322/CAAC.21660.

(2) Siegel, R. L.; Miller, K. D.; Wagle, N. S.; Jemal, A. Cancer Statistics, 2023. *CA Cancer J Clin* **2023**, *73* (1), 17–48. https://doi.org/10.3322/CAAC.21763.

(3) Agemy, L.; Sugahara, K. N.; Kotamraju, V. R.; Gujraty, K.; Girard, O. M.; Kono, Y.; Mattrey, R. F.; Park, J. H.; Sailor, M. J.; Jimenez, A. I.; Cativiela, C.; Zanuy, D.; Sayago, F. J.; Aleman, C.; Nussinov, R.; Ruoslahti, E. Nanoparticle-Induced Vascular Blockade in Human Prostate Cancer. *Blood* **2010**, *116* (15), 2847–2856. https://doi.org/10.1182/BLOOD-2010-03-274258.

(4) Simberg, D.; Duza, T.; Park, J. H.; Essler, M.; Pilch, J.; Zhang, L.; Derfus, A. M.; Yang, M.; Hoffman, R. M.; Bhatia, S.; Sailor, M. J.; Ruoslahti, E. Biomimetic Amplification of Nanoparticle Homing to Tumors. *Proc Natl Acad Sci U S A* **2007**, *104* (3), 932–936. https://doi.org/10.1073/PNAS.0610298104/SUPPL_FILE/10298FIG9.JPG.

(5) Zanuy, D.; Sayago, F. J.; Revilla-López, G.; Ballano, G.; Kotamraju, V. R.; Jiménez, A. I.; Cativiela, C.; Nussinov, R.; Sawvel, A. M. Engineering Strategy to Improve Peptide Analogs: From Structure-Based Computational Design to Tumor Homing. *J Comput Aided Mol Des* **2013**, *27* (1), 31–43. https://doi.org/10.1007/s10822-012-9623-5.

(6) Pires, F.; Ferreira, Q.; Rodrigues, C. A. V.; Morgado, J.; Ferreira, F. C. Neural Stem Cell Differentiation by Electrical Stimulation Using a Cross-Linked PEDOT Substrate: Expanding the Use of Biocompatible Conjugated Conductive Polymers for Neural Tissue Engineering. *Biochimica et Biophysica Acta (BBA) - General Subjects* **2015**, *1850* (6), 1158–1168. https://doi.org/10.1016/J.BBAGEN.2015.01.020.

(7) Puiggalí-Jou, A.; Cejudo, A.; Del Valle, L. J.; Alemán, C. Smart Drug Delivery from Electrospun Fibers through Electroresponsive Polymeric Nanoparticles. *ACS Appl Bio Mater* **2018**, *1* (5), 1594–1605. https://doi.org/10.1021/ACSABM.8B00459/SUPPL_FILE/MT8B00459_SI_001.PDF.

(8) Puiggalí-Jou, A.; del Valle, L. J.; Alemán, C. Cell Responses to Electrical Pulse Stimulation for Anticancer Drug Release. *Materials* **2019**, *12* (16), 1–15. https://doi.org/10.3390/ma12162633.

(9) Puiggalí-Jou, A.; Micheletti, P.; Estrany, F.; del Valle, L. J.; Alemán, C. Electrostimulated Release of Neutral Drugs from Polythiophene Nanoparticles: Smart Regulation of Drug–Polymer Interactions. *Adv Healthc Mater* **2017**, *6* (18), 1–11. https://doi.org/10.1002/adhm.201700453.

(10) Molina, B. G.; Domínguez, E.; Armelin, E.; Alemán, C. Assembly of Conducting Polymer and Biohydrogel for the Release and Real-Time Monitoring of Vitamin K3. *Gels 2018, Vol. 4, Page 86* **2018**, *4* (4), 86. https://doi.org/10.3390/GELS4040086.

(11) Fabregat, G.; Giménez, A.; Díaz, A.; Puiggalí, J.; Alemán, C.; Fabregat, G.; Giménez, A.; Díaz, A.; Puiggalí, J.; Alemán, C. Dual-Functionalization Device for Therapy through Dopamine Release and Monitoring. *Macromol Biosci* **2018**, *18* (5), 1800014. https://doi.org/10.1002/MABI.201800014.

(12) Majumder, P. Integrin-Mediated Delivery of Drugs and Nucleic Acids for Anti-Angiogenic Cancer Therapy: Current Landscape and Remaining Challenges. *Bioengineering 2018, Vol. 5, Page 76* **2018**, *5* (4), 76. https://doi.org/10.3390/BIOENGINEERING5040076.

(13) Chen, C.; Zhou, S.; Cai, Y.; Tang, F. Nucleic Acid Aptamer Application in Diagnosis and Therapy of Colorectal Cancer Based on Cell-SELEX Technology. *npj Precision Oncology 2017 1:1* **2017**, *1* (1), 1–7. https://doi.org/10.1038/s41698-017-0041-y.

(14) Le Joncour, V.; Laakkonen, P. Seek & Destroy, Use of Targeting Peptides for Cancer Detection and Drug Delivery. *Bioorg Med Chem* **2018**, *26* (10), 2797–2806. https://doi.org/10.1016/J.BMC.2017.08.052.

(15) Gao, W.; Xiang, B.; Meng, T. T.; Liu, F.; Qi, X. R. Chemotherapeutic Drug Delivery to Cancer Cells Using a Combination of Folate Targeting and Tumor Microenvironment-Sensitive Polypeptides. *Biomaterials* **2013**, *34* (16), 4137–4149. https://doi.org/10.1016/J.BIOMATERIALS.2013.02.014.

(16) Pérez-Herrero, E.; Fernández-Medarde, A. Advanced Targeted Therapies in Cancer: Drug Nanocarriers, the Future of Chemotherapy. *European Journal of Pharmaceutics and Biopharmaceutics* **2015**, *93*, 52–79. https://doi.org/10.1016/J.EJPB.2015.03.018.

(17) Esteves, T.; Viveiros, R.; Bandarra, J.; Heggie, W.; Casimiro, T.; Ferreira, F. C. Molecularly Imprinted Polymer Strategies for Removal of a Genotoxic Impurity, 4-Dimethylaminopyridine, from an Active Pharmaceutical Ingredient Post-Reaction Stream. *Sep Purif Technol* **2016**, *163*, 206–214. https://doi.org/10.1016/J.SEPPUR.2016.01.053.

(18) You, M.; Yang, S.; Tang, W.; Zhang, F.; He, P. Molecularly Imprinted Polymers-Based Electrochemical DNA Biosensor for the Determination of BRCA-1 Amplified by SiO2@Ag. *Biosens Bioelectron* **2018**, *112*, 72–78. https://doi.org/10.1016/J.BIOS.2018.04.038.

(19) Tang, P.; Wang, Y.; Huo, J.; Lin, X. Love Wave Sensor for Prostate-Specific Membrane Antigen Detection Based on Hydrophilic Molecularly-Imprinted Polymer. *Polymers (Basel)* **2018**, *10* (5). https://doi.org/10.3390/polym10050563.

(20) Pilvenyte, G.; Ratautaite, V.; Boguzaite, R.; Ramanavicius, A.; Viter, R.; Ramanavicius, S. Molecularly Imprinted Polymers for the Determination of Cancer Biomarkers. *Int J Mol Sci* **2023**, *24* (4). https://doi.org/10.3390/ijms24044105.

(21) Miyata, T.; Jige, M.; Nakaminami, T.; Uragami, T. Tumor Marker-Responsive Behavior of Gels Prepared by Biomolecular Imprinting. **2006**.

(22) Soleimanpour, M.; Mirhaji, S. S.; Jafari, S.; Derakhshankhah, H.; Mamashli, F.; Nedaei, H.; Karimi, M. R.; Motasadizadeh, H.; Fatahi, Y.; Ghasemi, A.; Nezamtaheri, M. S.; Khajezade, M.; Teimouri, M.; Goliaei, B.; Delattre, C.; Saboury, A. A. Designing a New Alginate-Fibrinogen Biomaterial Composite Hydrogel for Wound Healing. *Sci Rep* **2022**, *12* (1), 1–17. https://doi.org/10.1038/s41598-022-11282-w.

(23) George, B.; Bhatia, N.; Kumar, A.; Gnanamani, A.; Thilagam, R.; Shanuja, S. K.; Vadakkadath Meethal, K.; Shiji, T. M.; T. V, S. Bioinspired Gelatin Based Sticky Hydrogel for Diverse Surfaces in Burn Wound Care. *Sci Rep* **2022**, *12* (1), 1–19. https://doi.org/10.1038/s41598-022-17054-w.

(24) Kloth, L. C. Electrical Stimulation Technologies for Wound Healing. *Adv Wound Care (New Rochelle)* **2014**, *3* (2), 81–90. https://doi.org/10.1089/wound.2013.0459.

(25) Tai, G.; Tai, M.; Zhao, M. Electrically Stimulated Cell Migration and Its Contribution to Wound Healing. *Burns Trauma* **2018**, *6*, 1–7. https://doi.org/10.1186/s41038-018-0123-2.

Chapter II – State of the art

II - 1. Cancer

Cancer is the leading cause of death in many developed countries, with an estimated 19.3 million new cancer cases and 10.0 million cancer deaths worldwide in 2020 with a growing tendency.[1] Breast cancer was the most diagnosed with 11.7% of cases in the world in 2020, with prostate cancer reaching fourth position with 7.3%.[1] In the United States, in 2023, breast cancer accounted for 31% of cancer diagnostics for women of all ages, while prostate cancer was the most diagnosed in men accounting for 29% of new cases.[2] It is interesting to note that although cervical cancer is one of the most preventable types of cancer (e.g. by vaccination against human papillomavirus (HPV)), it is the top leading cause of cancer death among females between 20 and 39 years of age in the United States.[2]

The overall success rate for oncology drugs in clinical trials, from 835 drug developers, from 2003 to 2011, was only 6.7%.[3] If the time interval is extended to the period of 2000-2015, this value drops to 3.4% for 5764 companies. Nevertheless, considering only the last 10 years of this same period, the probability of a well-succeeded trial of a potential drug for oncological treatment was as low as 2.1%. On the other hand, if only trials that use cancer biomarkers in patient stratification are considered, then the probability of success rises to 10.7%,[4] thus showing the importance of improving the initial testing platforms to include cancer biomarkers.

Before initiating clinical trials, drugs usually undergo high-throughput screening using two-dimensional (2D) culture systems, and those showing therapeutic potential are approved for pre-clinical animal testing.[5,6] The low success rates, long duration, and high costs associated with drug development and subsequent clinical trials, evidence the need for more effective testing tools and platforms for predicting the clinical efficacy of anticancer drugs.

Overall, the rising numbers of cancer incidence and the increasing burden of cancer in healthcare, accompanied by the low success rates of clinical trials for anticancer drugs show the need for new biomaterials platforms to be developed. These platforms would aim to aid in drug development and testing by building appropriate platforms that are important in advancing cancer treatment, but also to develop new drug delivery platforms that circumvent anticancer drugs' undesirable characteristics, therefore boosting the success rate of clinical trials for cancer treatment.

II - 1.1. Tumor physiology and microenvironment

The physiology of tumors and their microenvironment has been extensively studied, leaving us with a set of distinctive features of those abnormal tissues that are now the basis for non-surgical anticancer therapy. Two of the most recognizable differences between normal and cancer tissues are the rate of cell proliferation and vascularization since they are inherently related, with the innermost cells being less proliferative than those in the periphery of the tumor (the latter are closer to blood

vessels and, therefore, have more nutrients available).[7,8] Additionally, tumor vasculature has also been shown to be abnormal, with the establishment of new microvessels in the niche (leaky and tortuous vessels with irregular blood flow, Fig. II - 1) and excessive amount of angiogenic activity by the overexpression of proangiogenic factors, like vascular endothelial growth factor (VEGF).[7,9,10] Those characteristics affect the oxygenation of the cells, as the ones in the inner part of the tumor site will receive less oxygen, thus being in a state of hypoxia.[11] Another consequence of the distance to blood vessels is low extracellular pH, which is related to deficient elimination of metabolic wastes due to difficult transportation to the vasculature,[8] and to the acidity of metabolic products (carbonic and lactic acid) as hypoxia pushes the cell metabolism towards glycolysis.[11] Unfortunately, the inherent properties of cancer physiology and TME have direct consequences on therapeutic approaches, as hypoxia is known to impede the effectiveness of radiotherapy,[7] and low pH interferes with cellular uptake of weak bases, such as doxorubicin, a drug often used in chemotherapy.[8]

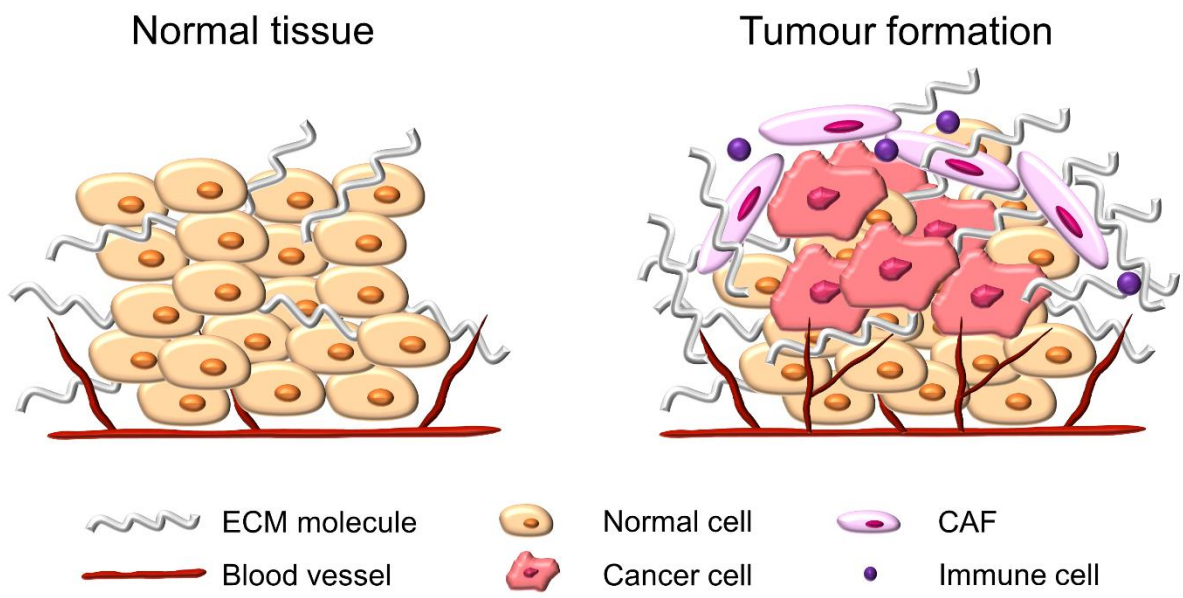

Fig. II - 1. Schematic representation of tumor formation compared to normal tissue, including cancer cells, abnormal vascularization, stiffer ECM, recruitment of immune cells, and cancer-associated fibroblasts (CAFs).

A key component of the TME is the ECM (Fig. II - 1). In normal tissue, the ECM is a network composed of macromolecules, including collagen, fibronectin, fibrin, laminin, various proteoglycans, and hyaluronan, playing a role as biomechanical support (e.g. blocking or facilitating cell migration, regulating stiffness or porosity of the niche and conferring structural tissue integrity).[12,13] The extracellular macromolecules of the ECM are also responsible for certain biochemical properties that

influence cell proliferation and differentiation, also concerning signaling for interaction with the environment and other cells, the binding of growth factors, and the initiation of signaling cascades.[9,13]

On one hand, ECM deregulation is influenced by the aberrant behavior of cancer-corrupted stromal cells (e.g. fibroblasts, endothelial cells, adipocytes, infiltrating immune cells), and on the other hand, deregulation of the ECM affects the local cells, perpetuating abnormal cell behavior in cancer. Abnormal ECM biochemical properties include excessive ECM component production and higher tissue rigidity, as is often seen in breast cancer. Cancer-associated fibroblasts (CAFs) are usually induced to transdifferentiate into myofibroblasts due to tumor site inflammation, which consequently leads to the production of large amounts of collagen. In turn, the excessive collagen is overly cross-linked by enzymes, which contributes to cancer progression by providing the mechanical support that cancer cells need (Fig. II - 1).[9,13,14]

II - 1.1.1. Tumor surfaceome biomarkers

As any kind of tissue, cancer cells express distinct biomarkers, either intracellular or proteins expressed on the cell surface. The latter have been considered as potential targets for diagnosis or therapy by directly blocking pathways related to their expression, and even for targeted delivery of anticancer drugs. The cell surface proteome, or surfaceome, has recently been assessed to establish a link between the proteins expressed on the cell surface of certain types and subtypes of cancer and diagnosis. Surfaceome analysis could be a powerful tool, as an *in silico* study of the human surfaceome has revealed that, of the 2331 cell surface proteins present in the 610 cancer cell lines assessed, 231 are expressed in all of them, while 529 are only expressed in one or very few specific cancer cell lines.[15] These findings agree with the existence of biomarkers that are common to many tumor types as is the case of CD44, a family of transmembrane glycoproteins whose different isoforms are expressed in different cancers (e.g. pancreatic, gastric, breast, and prostate).[16,17] The folate receptor alpha is another example of a protein widely overexpressed in various cancer types, such as endometrial adenocarcinoma, ovary, breast, and non-small cell lung cancer.[18,19]

Studies targeting only tumor surfaceomes have revealed new potential tumor markers. For instance, three surfaceome-encoding genes (WNT5A, CNGA2, and IGSF9B) were identified in breast cancer and these were correlated with poorer survival outcomes in patients with this type of cancer.[20] In a study, systemically profiling prostate cancer surfaceome, the authors were able to identify surface proteins to distinguish between subtypes of prostate cancer: adenocarcinoma specifically expressed STEAP1, FXYD3, and prostate specific membrane antigen (PSMA), while neuroendocrine prostate cancer specifically expressed NCAM1, SNAP25, and CEACAM5.[21] Interestingly, the expression of PSMA,

which is generally used as a prostate cancer biomarker, was validated in adenocarcinoma but not in neuroendocrine prostate cancer.[22]

II - 1.2. Examples of cancer types

In this work, three main cancer types have been selected for the *in vitro* cell assays to validate the developed materials' platforms. As such, brief descriptions of healthy vs tumor tissue will be discussed for breast, prostate, and cervical tissues.

II - 1.2.1. Breast cancer

Healthy breast tissue is a highly organized structure composed of a central lumen of epithelial cells tightly attached to an outer layer of myoepithelial cells by cadherins. Those cells are in turn separated from stromal cells (mostly adipocytes and fibroblasts) and ECM by the basement membrane. Cancer cells show rapid proliferation and differentiation, reduced cell adhesion in addition to secreting growth factors, like VEGF, that induce vascularization, and cytokines that alter ECM and stromal cells. For example, adipocytes secrete hormones and growth factors that stimulate the growth of the tumor, and macrophages are recruited. Then, the highly organized mammary gland ruptures, and the basement membrane is lost due to the secretion of soluble factors that degrade it. Thus, rapidly proliferating epithelial cells come in direct contact with ECM and stromal cells, which in turn are affected. Consequently, cell density in the tumor site is higher and more collagen is produced, leading to a stiffer and denser ECM.[23]

II - 1.2.2. Prostate cancer

Normal prostate tissue is composed of a duct-forming epithelial compartment and stromal cells that include a high number of smooth muscle cells and a smaller number of fibroblasts, endothelial, and nerve cells. Normal tissue homeostasis is maintained by stromal-epithelial interaction, where smooth muscle cells regulate the migration of epithelial cells and these in turn regulate the differentiation of smooth muscle cells. During cancer progression, there is a deregulation of organ homeostasis with stromal fibroblasts playing a central role. By differentiating into myofibroblasts, those cells participate in promoting changes in the ECM and aid in tumorigenic immune tolerance. In addition, they enhance tumor cell proliferation and modify the response to androgens by altering the expression of androgens receptors. Additionally, VEGF is expressed in tumor cells and integrin expression is altered, thus modulating cell survival during angiogenesis.[24,25]

II - 1.2.3. Cervical cancer

The cervix is constituted mostly by fibromuscular tissue connecting the body of the uterus to the vagina. It is lined with columnar and squamous epithelium in the endocervix and ectocervix, respectively. The stroma of the cervix is dense, while the columnar epithelium is composed of a single layer of tall glandular cells and the squamous epithelium is composed of uniform, stratified, and non-keratinized squamous cells.[26] Infection with HPV leads to the integration of viral DNA into the genome of epithelial cells of the cervix, thus leading to the persistence of the E6 and E7 oncogenes. These viral genes lead to changes in the proteins encoded by the p53 and pRb genes, which generates a deregulation and increase in cell proliferation, and an impairment in cell apoptosis. Additionally, the E5 oncogene affects the synthesis of host cell DNA, also altering the differentiation of keratinocytes.[27,28] Further alterations include deregulation of immune microenvironment and overexpression of metalloproteinase (MMP) proteins, particularly MMP-2 and MMP-9, which are responsible for the degradation of ECM. Overexpression of such proteins allows cancer cells to penetrate the ECM, allowing the spreading of cancer cells.[29–31]

II - 2. Smart materials for cancer treatment

Smart materials have emerged in the field of biomedical research, in particular in cancer treatment research, as these are materials with adjustable functional or structural properties in response to a stimulus or changes in the surrounding environment.[32] Such characteristics make smart materials very interesting to be applied in drug delivery systems for cancer treatment since the many physiological and chemical cues in the TME could be used to trigger the delivery of an anticancer drug due to the change in the material's properties.

In general, smart materials could be designed to respond to several different stimuli, such as chemical, biological, or mechanical.[32] Considering cancer treatment, materials' responses to cancer-endogenous stimuli, such as changes in the pH of the TME,[33] higher glutathione levels,[34] or hypoxia have been explored.[35,36] Alternatively, the application of external stimuli, like ultrasounds, has also been studied to trigger a response in materials leading to anticancer drug delivery.[37]

Stimuli-responsive materials systems can be designed in different scales and morphologies, such as NPs, fibers, or hydrogels, depending on the potential treatment approach. NPs and other nanocarriers are the most suitable for intracellular drug delivery as they are materials in the nanoscale range and can be designed to cross the cell membrane, for example for targeting the mitochondria.[38,39] On the other hand, microscale materials, like fibers and certain hydrogels, are often designed as transdermal patches or implantable/injectable scaffolds that will then release the therapeutic agent. Logically, multiple-component systems can also be designed by incorporating nanocarriers within fiber meshes or hydrogels. Furthermore, one can also include multiple stimuli responses within the same system by attributing different stimuli responses to each of the components of the system, or by including sequential drug discharge in response to the same type of stimuli.

Here, we discuss the recent advances in smart materials platforms designed for cancer treatment, covering the types of stimuli used in such systems, focusing on pH and electrically responsive systems, but also on the design and synthesis of the materials themselves from NPs, fibers, and hydrogels to combinations of these, and the applicability of the delivery methods.

II - 2.1. Exploring stimuli-responsive materials in cancer treatment

Smart materials can be designed to respond to various kinds of stimuli. These can be based on TME characteristics (Fig. II - 2), like acidic pH or hypoxia, so that the response, that is the release of the therapeutic agent, can be triggered upon reaching the right location in the body of the patient. This type of stimuli can be defined as endogenous stimuli, as the material will respond to the conditions it encounters in the TME. Other types of stimuli that are not intrinsically associated with

the conditions found in the TME, such as response to temperature or electrostimulation, can be designated as exogenous stimuli.

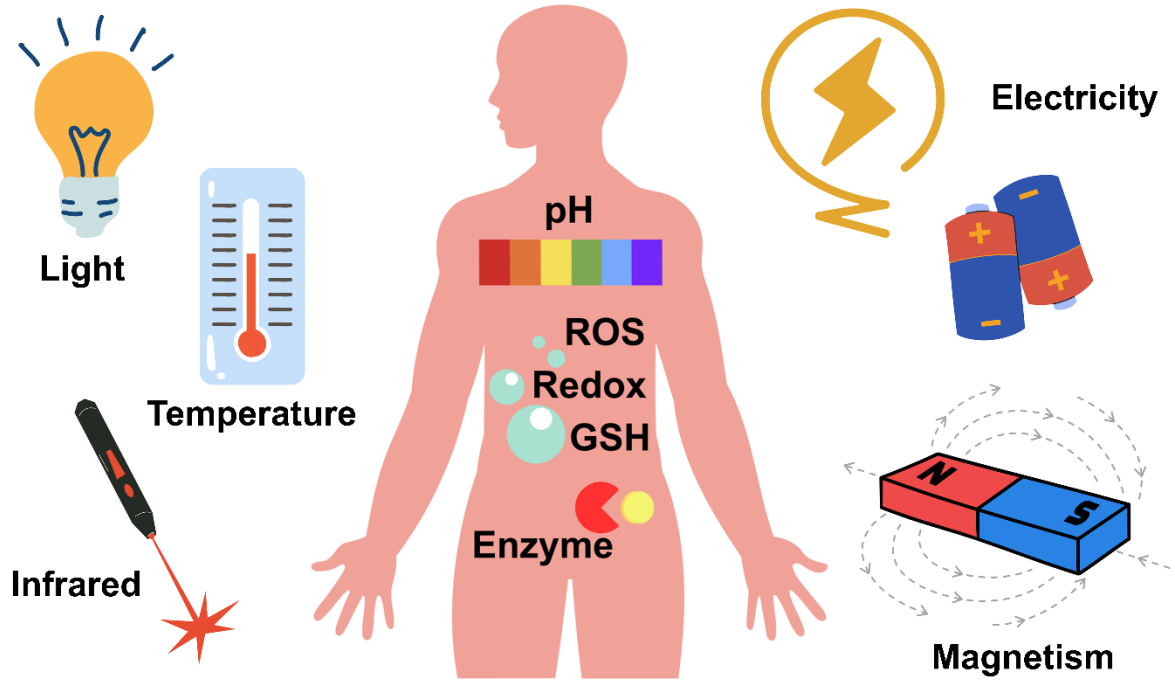

Fig. II - 2. Schematic representation of different types of stimuli that can be used to inspire the design of stimuli-responsive materials for cancer treatment: endogenous (pH, redox, GSH, ROS and enzyme) and exogenous (electricity, magnetism, infrared, light, and temperature) stimuli. GSH – glutathione, ROS – reactive oxygen species.

II - 2.1.1. Endogenous stimuli

The selection of which endogenous stimulus a smart material should respond to in cancer treatment applications is often based on TME characteristics. The most recognizable differences between normal tissues and tumors are the increased cell proliferation and vascularization.[7,8] Additionally, tumor vasculature has also been shown to be abnormal, with the establishment of new leaky and tortuous vessels with irregular blood flow in the TME.[7,9,10] Those characteristics affect the oxygen levels being delivered to cells, thus being in a state of hypoxia.[11,40,41] Another consequence is low extracellular pH, which is related to deficient elimination of metabolic wastes,[8] and to the acidity of metabolic products (carbonic and lactic acid).[11,40] Closely related to hypoxia and low pH is the increased production of reactive oxygen species (ROS) and an increased expression of glutathione (GSH), which is an intracellular antioxidant and regulator of cellular redox state, thus protecting cells from damage caused by ROS.[42–46] It is also worth mentioning that there is also overexpression of some enzymes in cancer progression, such as esterase,[47–49] and lipase.[50–52] Considering that alterations in pH and redox-related alterations are the most relevant in the TME, some of the most reported

endogenous stimuli used for designing smart materials for cancer treatment are pH, GSH, and changes in redox state.

II - 2.1.1.1. pH-responsive materials

pH-responsive materials have become a promising tool for precision medicine in the field of oncology. These materials can react to the acidic pH environment commonly present within tumors. This lower pH setting offers the potential for selectively targeting cancer cells, enabling precise drug delivery to cancer cells while reducing systemic side effects. Materials designed to respond to pH changes have been carefully constructed with various mechanisms, structures, and characteristics.

Drug delivery systems that respond to pH levels are engineered to release the therapeutic agent they carry by alterations in the material's solubility or the cleavage of chemical bonds at a lower pH, leading to targeted drug release near cancer cells. Many pH-responsive polymer-based drug delivery systems rely on the stability of these polymers at the neutral pH of the blood but are disrupted in acidic environments, which can trigger the release of the drug, due to the presence of acid-sensitive bonds that are cleaved in acidic conditions.

Typical pH-sensitive systems utilize NPs and hydrogels as drug carriers for cancer treatment.[53–58] NPs can be made from materials that degrade or change their properties at certain pH levels, thus affecting the NPs' interaction with cancer cells, and enhancing drug delivery and uptake by the cells.[59–65]

Smart hydrogels, that swell or contract in response to pH changes, are being explored as injectable drug carriers that can release drugs upon encountering the acidic TME. The benefits of using hydrogels include high water content, biocompatibility, minimal invasiveness, and the capacity to effectively transport various therapeutic agents such as small molecule drugs, proteins, and nucleic acids.

pH-responsive hydrogels usually contain functional groups that undergo ionization in reaction to pH variations. This ionization may lead to the swelling or shrinking of the hydrogel, depending on its crosslinking degree and polymer composition, consequently influencing the release rate of the encapsulated drug. The ability of the hydrogel to swell or shrink in response to changes in pH enables precise and on-demand drug delivery. In a neutral pH environment such as healthy tissue, the hydrogel maintains its structure, limiting significant drug release. Conversely, within an acidic TME, the hydrogel could expand and release the encapsulated drug.[66,67] Furthermore, hydrogels can be loaded with anticancer agents through various methods, including physical entrapment or chemical bonding. As such, drugs can be released by diffusion as the polymer matrix swells, or by the degradation of the gel matrix in response to the acidic pH.[68,69]

The choice of hydrogel matrix is crucial in determining the properties and performance of pH-responsive drug delivery systems (Table II - 1). Several studies employ a variety of biopolymers and crosslinkers, tailored to achieve desired properties such as biocompatibility, mechanical strength, and pH responsiveness. For example, chitosan (CS)-based hydrogels offer excellent biocompatibility and mucoadhesive properties, while carboxymethyl cellulose (CMC) provides high water retention and swelling capacity.

Table II - 1. Examples of pH-responsive hydrogels for cancer treatment applications. Summary of studies published between 2015 and 2024 using the keywords "cancer", "drug delivery", "pH-responsive", and "hydrogel".

Hydrogel matrix	Other hydrogel components	Drug	Delivery pH	Ref
CS	Poly(acrylamide-maleic acid)	DOX	4.5	[70]
	HNT, graphitic-carbon nitride	QC	5.4	[71]
	Poly(NIPAM-co-itaconic acid)	DOX	5.5	[72]
	PNIPAM, Au NPs	CUR	5.5	[73]
	PNIPAM, folic acid-conjugated GO	DOX	5.5	[74]
CMCS	Reduced GO/aldehyde functionalized PEG	DOX	6.5	[75]
CECS	4armPEG-benzaldehyde	DOX	5.6	[76]
GEL	Aldehyde-functionalized PEG, laponite	DOX	5.0	[77]
	Citric acid-based graphene quantum dots (GQDs)	DOX	4.5	[78]
CMC	$CoFe_2O_4$/GO	CUR	5.6	[79]
	PEG, HNT	5-FU	5.5	[80]
	Hydroxyethyl cellulose-acrylonitrile-linseed oil polyol (CHAP), Na-montmorillonite	CIS	4.0	[81]
	Poly(acrylic acid), HNT	CUR	5.4	[82]
	PVP, graphitic carbon nitride	QC	5.4	[83]
Peptide	Peptide (KKFKFEFEF)	MTX	6.5	[84]
	Peptide (FER-8)	PTX	5.5	[85]
Starch	Tyramine, tannic acid, phenolated Fe_3O_4 NPs	DOX	4.0	[86]
Agarose	PVP, hydroxyapatite	QC	5.4	[87]
P(HEMA)	PEG diacrylate	MTX	5.0	[88]
	Methacrylic acid	DOX	6.5	[89]
PEG	Poly(propylene fumarate), citric acid, glycine	DOX	5.5	[90]
PNIPAM	Fe_3O_4, poly(acrylic acid), PEG methacrylate	HER	5.4	[91]
	Acrylamide	CUR	5.5	[92]

Abbreviations: 5-FU: 5-Fluorouracil; CIS: cisplatin; CMC: carboxymethyl cellulose; CS: chitosan; CUR: curcumin; DOX: doxorubicin; GEL: gelatin; GO: graphene oxide; GQDs: graphene quantum dots; HER: herceptin; HNT: halloysite nanotubes; MTX: methotrexate; NIPAM: N-isopropylacrylamide; P(HEMA): poly(2-hydroxyethyl methacrylate); PEG: poly(ethyleneglycol); PNIPAM: poly(N-isopropylacrylamide); PTX: paclitaxel; PVP: polyvinylpyrrolidone; QC: quercetin.

CS has been explored for its ability to fight microorganisms and prevent the formation of bacterial biofilms, and its potential to generate hydrogels for the delivery of drugs, due to its compatibility with living tissues and the ability to respond to changes in pH, making it doubly advantageous in cancer

therapy.[93] The use of CS as a pH-responsive hydrogel for anticancer drug delivery has been recurrently reported, being used together with other polymers such as N-isopropylacrylamide (NIPAM),[72–74] and acrylamide,[70] to deliver doxorubicin (DOX), CUR, and quercetin (QC), while being responsive in a pH range from 4.5 to 5.5.[70–74] Carboxymethyl CS (CMCS) and N-carboxyethyl CS (CECS) have also been shown to respond to changes in pH and promote the delivery of DOX for cancer treatment applications.[75,76]

Other biopolymers often employed to design pH-responsive systems are gelatin (GEL),[77,78] and CMC, being used to deliver CUR, QC, cisplatin (CIS), and 5-fluorouracil (5-FU) in the acidic pH range of 4.0-5.6.[79–83] The delivery of the anticancer drugs methotrexate (MTX) and paclitaxel (PTX) has also been accomplished through the use of peptide-based hydrogels at pH of 5.5 and 6.5, respectively.[84,85] Other examples of bio-based hydrogels, like agarose and starch, have also been reported as viable options for the same type of systems and application.[86,87] Alternatively, hydrogels based only on synthetic polymers, such as poly(2-hydroxyethyl methacrylate) (P(HEMA)),[88,89] PEG,[90] or poly(N-isopropylacrylamide) (PNIPAM),[91,92] have also been used in the pH range of 5.4-6.5 to successfully deliver CUR, DOX, and herceptin (HER) for cancer treatment applications, showing to be biocompatible.

Overall, these studies demonstrate the versatility of pH-responsive hydrogels in drug delivery applications, encompassing a wide range of biopolymer matrices, crosslinking strategies, drug payloads, and pH-responsive behaviors tailored for cancer treatment. The selection of drugs and pH delivery conditions are carefully considered to optimize the therapeutic efficacy and minimize off-target effects. By incorporating pH-responsive moieties or adjusting the formulation, these hydrogels can selectively release drugs in response to the acidic TME, enhancing drug accumulation at the target site while reducing systemic toxicity. This approach holds great promise for improving the efficacy of chemotherapy and overcoming drug resistance in cancer treatment.

II - 2.1.1.2. Redox and GSH-responsive materials

Redox-responsive materials undergo structural or functional alterations in reaction to changes in the redox state of the surrounding environment. Redox reactions involve electron transfer between chemical species, and such reactions can be used for various purposes, including drug delivery, sensing, and stimuli-responsive materials.

An important characteristic of redox-responsive materials is their capacity to undergo reversible modifications as a result of shifts in the redox environment. These modifications can be activated by factors like pH, temperature, ROS, or the presence of specific molecules active in redox processes.[94,95] GSH, a tripeptide thiol (γ-glutamyl-cysteinyl-glycine), plays a vital role in cellular redox balance and

serves as an important indicator of cellular oxidative stress.[96] Many designed redox-responsive materials react to changes in GSH levels enabling their use for targeted drug delivery and biosensing within cellular environments.[97] Materials sensitive to GSH concentration can release drugs or other substances based on variations in GSH level, with this responsiveness allowing controlled drug delivery triggered by elevated levels seen with certain medical conditions, such as cancer.[98–101] Moreover, by incorporating GSH-responsive elements into sensor platforms, it is possible to develop highly sensitive biosensors as selective detection methods for GSH and related biomolecules.[102–105]

Overall, redox-sensitive materials, particularly those that respond to GSH, show great potential for various biomedical and biotechnological uses because of their capacity to react to specific cellular redox signals. This makes them valuable for drug delivery, biosensing, and other biomedical applications.

II - 2.1.2. Exogenous stimuli

Although there are many endogenous stimuli to take advantage of when designing smart materials for cancer treatment applications, one can also investigate other types of stimuli that are not associated with cancer intrinsic characteristics. Exogenous stimuli (Fig. II - 2) are often useful to increase the range of stimuli-responsive materials available, thus increasing the chances of designing useful platforms for controlled anticancer drug delivery. Examples of actuation modes to exogenous stimuli are responses to ultrasounds, magnetic stimulation, electrostimulation, infrared irradiation, or temperature changes. Furthermore, one can potentially improve the responsiveness of the materials or introduce different types of stimulus-response in the same material platform, for example by associating pH and electrical response in the same material system.

The exploration of external electrical stimuli, resorting to electroresponsive materials, presents a promising avenue for non-invasive therapeutic interventions. By leveraging on these external stimuli, such materials can be engineered to modulate biological processes, facilitate drug delivery, and interact with physiological systems in a controlled manner. This non-invasive approach holds potential for targeted interventions with reduced side effects, enhanced patient comfort, and improved therapeutic outcomes. Through interdisciplinary research, efforts integrating material science, biotechnology, biomedical engineering, development and optimization of stimuli-responsive materials for therapeutic purposes, continues to advance, paving the way for innovative strategies in healthcare.

II - 2.1.2.1. NIR-responsive materials

Near-infrared (NIR) responsive materials represent a category of novel materials engineered to be sensitive to NIR light, which can penetrate biological tissues without causing harm up to a specific depth. The capacity of these materials to react to NIR light renders them particularly valuable in the context of cancer treatment, with recent advancements including applications in photothermal therapy, controlled drug release, and diagnostics.[67,106] Certain materials can transform NIR light into thermal energy upon exposure, leading to the targeted destruction of cancer cells through localized heating (photothermal therapy).[107,108] An example is the use of carbon nanotubes (NTs) in conjunction with therapeutic agents such as siRNAs, enabling a combination of photothermal and gene therapy.[109,110]

Multifunctional NPs can carry drugs and deliver them specifically to cancer cells, using NIR light to regulate or activate the drug release from the NPs, enabling targeted therapy directly at the cancer site, thereby enhancing treatment efficacy while minimizing adverse effects on healthy tissues.[111] Examples include temperature-sensitive liposomes and other polymeric nanomaterials that release their drug payloads, such as immunostimulatory agents, in response to localized heating triggered by NIR irradiation.[110,112]

II - 2.1.2.2. Magnetism-responsive materials

Materials that are sensitive to magnetism are currently under development for a range of cancer treatment purposes, leveraging their distinctive characteristics to enhance focused drug administration, imaging, and therapy. Superparamagnetic iron oxide NPs are widely employed because they can be directed to the tumor location through external magnetic fields. This capability allows accurate targeting of drug delivery, potentially improving efficiency while reducing medication dosage and minimizing side effects.[110] The superparamagnetic properties of magnetic NPs can also be used for hyperthermia treatment, where the application of an alternating magnetic field leads to heat generation.[110]

Magnetism-responsive nanomaterials can also be used for cancer immunotherapy by guiding functionalized magnetic NPs for the clustering of T-cells around the tumor.[113] In diagnostic and therapeutic combination approaches, magnetic NPs can be used combined with magnetic resonance imaging (MRI) or luminescent materials, allowing for MRI or luminescence-guided chemotherapy through real-time monitoring.[114,115]

II - 2.1.2.3. Electroresponsive materials

Materials that respond to electricity can alter their characteristics, such as shape or conductivity, when exposed to an electric stimulus. This ability can be utilized for various medical approaches in treating cancer, including precision drug delivery and interference with cancer cell communication.[116,117]

One method entails using electric fields as a therapeutic intervention referred to as electrochemotherapy. Brief, yet intense, electric pulses are administered at the tumor location to enhance the permeability of cancer cell membranes, facilitating more efficient absorption of chemotherapy medications. Additionally, electrostimulation may also impact cancer cells directly by disrupting their growth and division without causing harm to normal cells through certain low-frequency electric fields—a technique known as "tumor-treating fields".[116,118,119] These electric fields interfere with cancer cell division, impairing their ability to proliferate and survive. Moreover, the use of electrically responsive materials in combination with other treatment modalities, such as phototherapy or immunotherapy, holds promise for synergistic therapeutic outcomes in cancer treatment.

Another approach involves employing polymers that are sensitive to electricity in drug release systems. These polymers can encapsulate drugs and dispense them upon the application of an electric stimulus. When placed near a tumor through implantation or injection, an external electrical signal prompts the polymer to discharge the therapeutic agent directly at the tumor site, enhancing effectiveness while minimizing side effects compared to systemic chemotherapy. This precise and regulated drug release mechanism has the potential to reduce harm to healthy tissues and maximize treatment efficacy.[120]

In fact, most electroresponsive materials developed for cancer treatment are designed to be used as drug delivery systems, with examples presented in Table II - 2. Many of these systems are based simply on conducting polymers (CP), particularly synthesized in the form of nanocarriers, envisioning the transport of such nanocarriers to the tumor site and subsequent localized delivery of the drug through electrostimulation.

Table II - 2. Electroresponsive materials systems to promote drug delivery for anticancer treatment applications. Summary of studies published between 2015 and 2024 using the keywords “cancer”, “drug delivery”, and “electroresponsive”.

System	Materials	Stimulation regime	Drug	Potential application	Ref
Nanowires	PPy	−1 V (vs Ag|AgCl)	DOX	Oral and breast cancer	[121]
Hydrogel	PEDOT:PSS and GelMA	DC electric field at 1.5 V	5-FU	Skin cancer	[122]
NPs	HAp	0-2 V (vs Ag|AgCl)	DOX	Colon and ovarian cancer	[123]
	PEDOT	−1.25 V (vs Ag|AgCl)	CUR	Breast and prostate cancer	[124]
	PEDOT	−0.4 V to 0.8 V (vs Ag|AgCl) at 100 mV/s	CREKA peptide	Prostate cancer	[125]
Liposomes	DOTAP, Lipoid-S75 and DPPG	0.5 mA/cm^2 constant current	CIS and DTX	Oral cancer	[126]
Films	*co*-PMMA	Pulses applying fixed potential −1.5 V or current 300 µA	CUR	Cancer (general)	[127]
Microfibers/NPs	PCL and PEDOT	1 V (vs Ag|AgCl)	CUR	Breast cancer	[128]
Hydrogel/NPs	Alg-*g*-PAA and PEDOT	Alternating −0.6 V, 0.0 V and 0.6 V (vs Ag|AgCl)	CAM	Cancer (general)	[66]
Nanofibers/NPs	PGS/PCL and PEDOT	AC square wave between -10 V and 0 V	CUR	Breast and prostate cancer	[129]
Hydrogel/NPs	PBA-CS and PEDOT	Alternating −0.5 V and 0.0 V (vs Ag|AgCl)	CR(*N*Me)EKA peptide	Prostate cancer	[130]

Abbreviations: 5-FU: 5-fluorouracil; Alg-*g*-PAA: alginate-*grafted*-poly(acrylic acid); CAM: chloramphenicol; CIS: cisplatin; CUR: curcumin; DOTAP: 1,2-dioleoyl-3-trimethylammonium-propane chloride; DOX: doxorubicin; DPPG: 1,2-Dipalmitoyl-sn-glycero-3-phospho-rac-glycerol sodium; DTX: docetaxel; GelMA: gelatin methacryloyl; HAp: hydroxyapatite; Lipoid-S75: soybean phosphatidylcholine; PBA-CS: chitosan-phenyl boronic acid; PCL: polycaprolactone; PEDOT: poly(3,4-ethylenedioxythiophene); PGS: polyglycerol sebacate; *co*-PMMA: poly(methyl methacrylate-*co*-methacrylic acid); PPy: polypyrrole; PSS: poly(styrenesulfonate).

PEDOT is a conducting polymer that is frequently used in such applications, due to its high conductivity, high biocompatibility, and good colloidal stability when synthesized as NPs. From 2015 to the present year, many works have reported the use of PEDOT NPs as a drug delivery system for

potential anticancer drugs, including CUR for the treatment of breast and prostate cancer,[129–132] CAM for targeting the mitochondria in cervical cancer,[66] and anticancer peptides like CREKA and CR(*N*Me)EKA directed at prostate cancer therapy.[133] Examples like PEDOT NPs demonstrate the potential of CPs in facilitating controlled drug delivery for various cancers, showcasing the versatility and effectiveness of electroresponsive materials in oncology. Polypyrrole (PPy) is another CP used to synthesize nanocarriers in the form of nanowires, loaded with the anticancer drug DOX, which was later released upon electrostimulation of the nanowires, to target oral squamous carcinoma and breast cancer while applying photothermal therapy simultaneously.[121] Other types of materials, such as polymers (e.g., poly(caprolactone), methacrylate-based), ceramics, and liposomes, have also been reported for controlled drug delivery using electrical stimuli to release anticancer drugs such as CUR, DOX, CIS, and docetaxel (DTX).[123,126,127] One can conclude that electrostimulation is a strong candidate for exogenous stimulation, as a common characteristic in the studies presented in Table II - 2 is the use of safe low voltages to the body to achieve drug release.

Overall, the integration of electrically responsive materials into cancer treatment strategies represents a promising avenue for improving therapeutic outcomes. Moreover, polymers sensitive to electricity enable precise control over drug release, allowing for localized delivery directly to tumor sites while minimizing systemic side effects.

II - 2.1.3. Multiresponsive materials systems

In the context of stimuli-responsive materials systems, the creation of composite materials composed of different elements that are sensitive to different stimuli has been a significant development. Particularly in the context of cancer treatment, the most significant combination of stimuli response includes endogenous sensitivity to changes in pH, with the response to an exogenous stimulus combining an intrinsic characteristic of the disease (acidic pH), and an external stimulation that can add layers of control to drug delivery for instance. Electrostimulation is a strong candidate for exogenous stimulation, as it provides a highly controlled delivery method for anticancer therapeutic agents using safe low voltages to the body.

II - 2.1.3.1. pH and electroresponsive materials systems

Combining both pH and electric stimulus responsiveness in materials for drug delivery systems offers an advanced approach to regulating the release of anticancer drugs in the body, ensuring precise timing and location. This combined reactivity has the potential to improve the targeting and effectiveness of cancer treatments while reducing adverse effects.

In terms of mechanism, the acidic conditions found in the TME could trigger the initial release of the drug from the material, while an external electric field could then be used to further regulate this release. This would provide a two-part control system that can be adjusted for optimal therapeutic results. For example, a NP could be engineered to release its anticancer agent upon encountering the acidic environment of a tumor (pH-sensitive) and then be additionally controlled or activated by an external electric field (electroresponsive). A common strategy involves using polymer or NP-based systems with functional groups that respond to changes in pH and electric fields. These materials may include CPs like polyaniline (PANI) or PPy, as well as polymethacrylates or polycaprolactones with pH-responsive properties.

However, designing materials that are responsive to both pH and electrical stimuli involves challenges such as stability of the system in the bloodstream, specificity for cancer cells, and ensuring that the electrical stimulus is not harmful to healthy tissues.

Using NPs that respond to electrical stimuli in combination with hydrogels sensitive to changes in pH for the delivery of anticancer drugs, represents an innovative approach that capitalizes on multiple environmental signals to achieve targeted and regulated drug release. The system would involve incorporating drug-loaded electroresponsive NPs within a pH-responsive hydrogel matrix, potentially utilizing materials such as PPy or PEDOT for the NPs, and CS, CMC or alginate for the hydrogel, for example. Upon administration, the hydrogel would first react to the acidic pH of the TME, leading to swelling or degradation and enabling the release of the embedded NPs near cancer cells. Subsequently, applying an external electric stimulus could further modulate drug release from the NPs by triggering changes in their structure or charge distribution.[66] Alternatively, simultaneous stimulation by applying a potential, as the hydrogel/NP system reaches the tumor site, could lead to a drug release highly controlled by two factors.[66] This dual sensitivity not only takes advantage of tumor acidity for precise localization but also allows secondary control over drug release via electric fields, facilitating enhanced specificity in drug delivery while minimizing systemic exposure. However, integrating these two responsive elements presents challenges related to maintaining individual component functionality within a combined structure, requiring careful design considerations such as biodegradability of the hydrogel and stability of NPs until the desired time point, alongside overall biocompatibility of the system within complex biological environments.

While this strategy holds great promise conceptually and offers numerous potential benefits, it is important to acknowledge that much research is still at the experimental and preclinical stages. Successful advancement will necessitate addressing technical hurdles like optimizing the safe application of electrical stimulation without causing harm to surrounding tissues; ensuring consistent and predictable drug release rates; and establishing device safety overall. Nevertheless, potentially

achieving such a high degree of spatial and temporal control in cancer therapy makes this a very promising and innovative area of research.

II - 3. Biomolecular targeting

The concept of biomolecular targeting using bioimprinted MIPs represents a promising strategy for conferring selectivity towards tumor cells while minimizing adverse effects on healthy tissues during drug delivery. This feature delves into the utilization of bioimprinted MIPs as a means to achieve a highly targeted drug delivery, that can be complemented by a controlling mechanism to preserve healthy tissues. Moreover, this introduction sets the stage for future research directions, envisioning the integration of imprinting technology for selective recognition with electroresponsive controlled drug release achieved through PEDOT-based systems, for example. Through this exploration, the potential synergies between selective recognition and stimuli-responsive materials for controlled release mechanisms pave the way for innovative approaches in precision medicine and targeted therapeutics.

II - 3.1. Bioimprinted MIPs

The interest in molecular imprinting technology, studied since the 1970s, has grown exponentially between the 1970s and mid-2010s,[134] with applications ranging from separation and purification, as selective adsorbers or membranes, to sensors.[135,136]

MIPs are synthetic polymers that are tailor-made for specific recognition. As antibodies and enzymes, their three-dimensional structure and functional groups, with a specific orientation, are orchestrated to allow a selective molecular binding. Functional monomers interact with the template, or printed molecule, forming a template-monomer complex. Polymerization takes then place, in the presence of the template, by reaction of a cross-linker and an initiator. After the polymer is formed, the template molecule is removed, leaving the MIP with empty cavities, that act as specific binding sites,[137,138] as represented in a simplified scheme in Fig. II - 3. This cavity will preferentially bind the template, as it matches the template's geometry, and has affinity for its complementary functional groups. MIPs can be synthesized using virtually any molecule as a template, ranging from drugs, small molecules, amino acids, chiral enantiomers, DNA, peptides, proteins and even whole cells,[139–146] thus translating into a target molecule size range from a few Da (*e.g.* 126 Da melamine[147]) to several kDa (*e.g* 66.5 kDa bovine serum albumin (BSA)[148] and 180 kDa spike glycoprotein of SARS-CoV-2[149,150]).

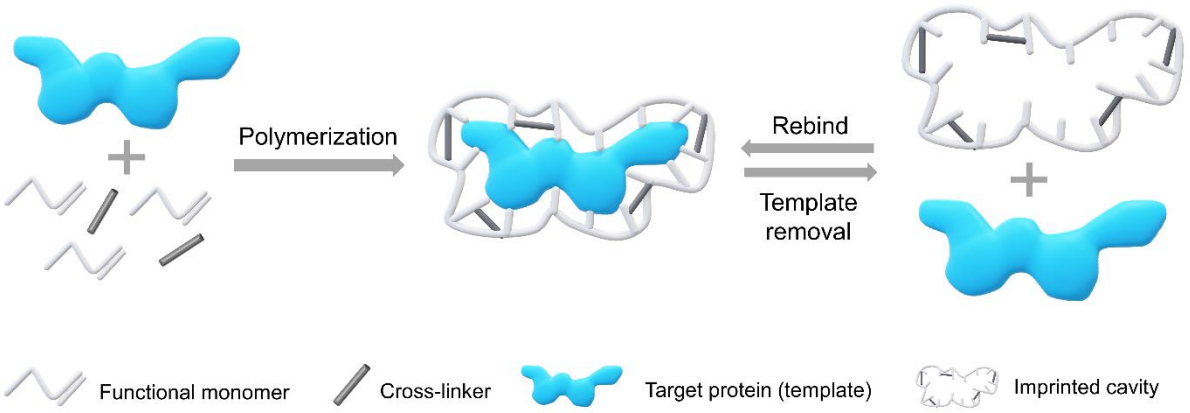

Fig. II - 3. Schematic representation of protein MIP synthesis.

Biomolecules such as antibodies, some receptors, and enzymes are the gold standard for affinity tools, since their target recognition capacity is highly selective and sensitive. However, the use of natural biomolecules presents disadvantages, including: limited working conditions, such as mild temperature, narrow pH range and low stability in organic solvents. Antibody production in mammalian cells has been optimized over last decades, still the associate production costs are high. Recombinant expression in bacterial or yeast systems still presents limitations like endotoxin production.[151–156] Therefore, given that MIPs are usually cheap, easy to synthesize in a reproducible way, and have shown robust performances in a variety of solvents,[138,157] bioimprinted MIPs, using biomolecules as templates, have been considered as suitable alternatives for medical diagnosis and theragnostics in the biomedicine field and as replacement of enzymes in catalytic processes or even used as bioelectrodes for energy harvesting based on microbial fuel cells in more advanced MIP applications.[158]

Due to their functional similarity to their natural counterparts, MIPs designed for biomolecules have been referred to as “plastic antibodies” or “artificial receptors”. Research developed on MIPs selective for biomacromolecules, like proteins or peptides, is particularly important, since these have the potential to contribute towards biomedical applications aiming at biosensors, toxic analyte sequestration, or drug delivery systems, among others.[138,144,159,160]

Molecularly imprinted technology has significantly contributed on the development of novel biosensors for disease detection. Namely, several cancer diagnostics sensors based on MIPs have been developed, using prostate, breast, ovarian and hepatic cancer biomarkers as target molecules.[161] Polypyrrole-based electrochemical MIP sensors were developed targeting the CA-125 marker for epithelial ovarian cancer,[162] the CA15-3 marker for breast cancer,[163] and the PSA protein marker for prostate cancer.[164] In the latter study, the sensor presented a limit of detection (LOD) as low as 2.0

pg/mL, which is below the threshold "risk" values of 4.0-10.0 ng/mL of PSA concentration in blood, thus showing the potential competitiveness of this assay. Biomarkers for neurodegenerative diseases is another relevant focus area of MIP-based biosensors with recent advances in the development of MIP-based electrochemical sensors for Alzheimer's and Parkinson's diseases.[165] For instance, a very competitive Alzheimer's disease MIP biosensor was designed for an amyloid-β peptide using a combination of polypyrrole and carbon nanotubes, reaching a LOD as low as 0.3 fg/mL.[166] A MIP-based biosensor was similarly developed for α-synuclein peptides with a LOD of 10 fg/mL, for Parkinson's disease.[167] Overall, such studies suggest a growing tendency to develop MIP-based biosensors to enable high detection sensitivities.[168–170]

The following sections are focused on clarifying the concept of bioimprinted MIPs, elucidating their synthesis process and elucidating their significance in contemporary biomedical research, and also providing typical reagents, imprinting techniques, and polymerization approaches available for bioimprinted MIP fabrication, underscoring their diversity and potential applications. Importantly, a comprehensive analysis of the specific imprinting technique (epitope-based solid phase synthesis) employed in this thesis will be provided, including the rationale behind template selection, and outline the anticipated outcomes to further elucidate its potential contributions to biomedical research in the context of cancer therapy.

II - 3.2. Protein-imprinted polymers

Proteins are biomacromolecules of significant interest in research, with special focus on their detection and quantification, since they are often biomarkers of important human diseases, including viral infections,[171–175] hormonal and DNA regulation processes,[176,177] and many cancer types.[159,178–180] However, the detection and quantification of proteins require labour and cost-intensive separation methods, often based on immunoassays.

Table II - 3 shows a short overview of the common functional monomers, initiators, cross-linkers, and solvents used for the preparation of protein-imprinted MIPs. Apart from the polymerization method chosen, the reagents employed appear to be quite similar among reported studies, in terms of functional monomers, initiators, and cross-linkers.[181,182]

Table II - 3. Overview of polymerization reagents (monomers, cross-linkers, initiators) and solvents used inprotein imprinting technology.

Template	Monomers	Cross-linker	Initiator	Solvent	Ref
Cytochrome c	AAm	MBA EBA PDA PEGDMA	APS TEMED	Water Tris-buffered saline	[183]
	AAm	MBA	APS	PBS	[184]
Haemoglobin	Dopamine	N/A	APS	PBS	[185]
	AAm	MBA	APS	PBS	[184]
BSA	DMAEM	MBA PEGDMA	Irgacure® 2959	Potassium phosphate buffer and ethanol	[186]
Albumin	AAm	MBA	APS	PBS	[184]
DNAzyme complex	AAm NIPAm DMAPMA	MBA	APS TEMED	Aqueous buffer solution	[177]
Prostate-specific membrane antigen (PSMA)	AAm DMAEM	EGDMA	AIBN	Methanol/water mixture	[178]
Epidermal growth factor receptor (EGFR)	NIPAm TBAm Acrylic acid APMA	MBA	APS TEMED	PBS	[159]
Ribonuclease A	AAm	MBA	APS	PBS	[184]
Human serum albumin (HSA)	3-(methacryloxy) propyltrimethoxysilane	-	-	PBS Tween 20 solution	[187]

Abbreviations: AAm: acrylamide; AIBN: azo-bis isobutyronitrile; APMA: N-(3-aminopropyl) methacrylamide; APS: ammonium persulfate; DMAEM: 2-(dimethylamino)ethyl methacrylate; DMAPMA: N-(3-(dimethylamino)propyl)methacrylamide; EBA: N,N'-ethylenebis(acrylamide); EGDMA: ethylene glycol dimethylacrylate; MBA: N,N'-methylenebisacrylamide; N/A: not available; NIPAm: N-isopropylacrylamide; PBS: phosphate buffered saline; PDA: 1,4-bis(acryloyl)piperazine; PEGDMA: poly(ethylene glycol)dimethacrylate; SDS: sodium dodecyl sulphate; TBAm: N-tert-butylacrylamide; TEMED: N,N,N',N'-Tetramethylethylenediamine.

To obtain MIPs for biomacromolecules, two main protein imprinting strategies have been developed: protein imprinting, including i) non-oriented surface imprinting and ii) oriented surface imprinting, where the entire protein works as a template; and epitope imprinting, where the template

will be a part of the structure of the target protein. Examples can be found of protein and epitope imprinting strategies discussed in this section are represented in Fig. II - 4.

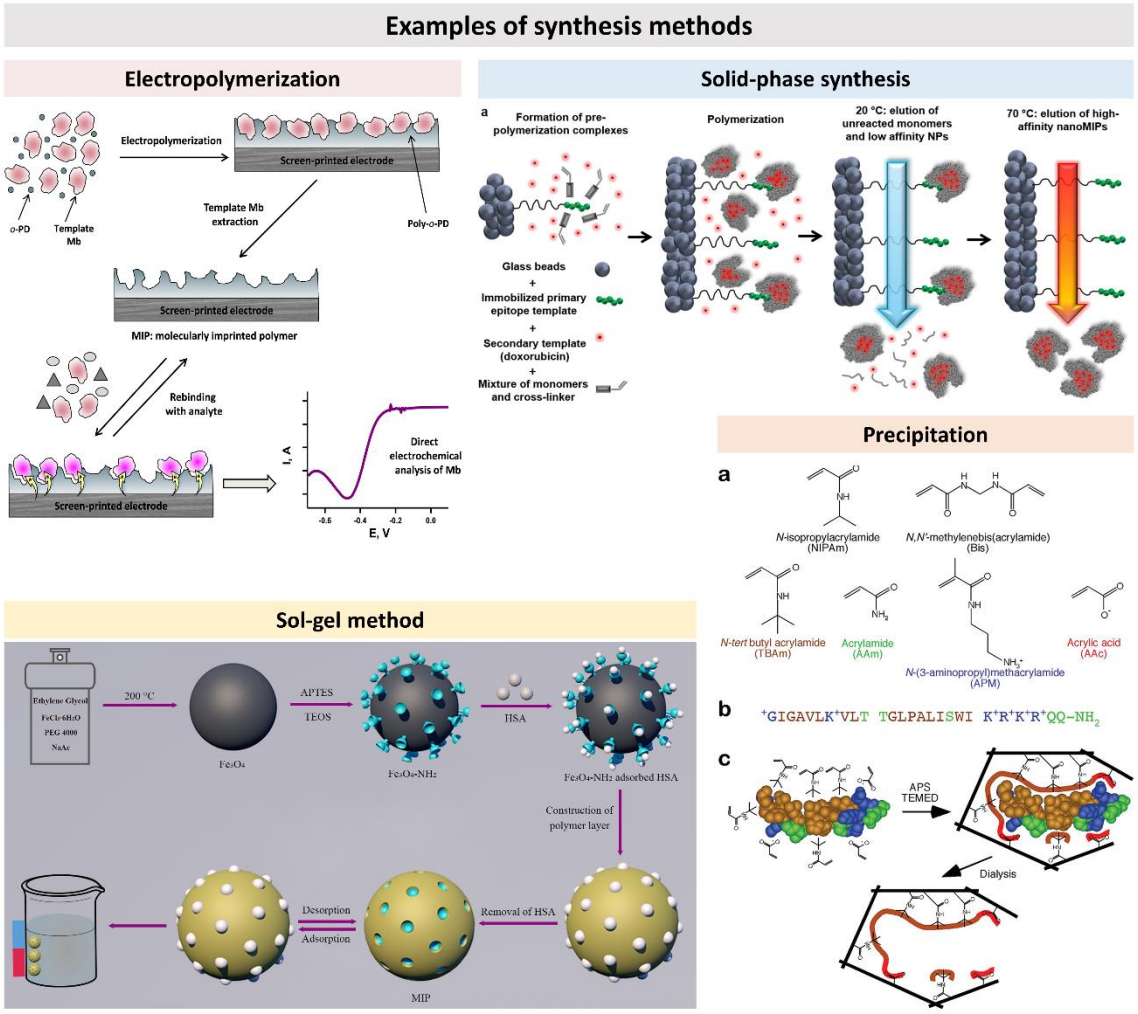

Fig. II - 4. Molecular bioimprinting synthesis methods: non-oriented surface imprinting – electropolymerization (reprinted from [188], Copyright 2023, with permission from Elsevier) and precipitation (reprinted with permission from [189], Copyright 2023 American Chemical Society); oriented surface imprinting – sol-gel (reprinted from [187], Copyright 2023, with permission from Elsevier); epitope imprinting: solid-phase synthesis (reprinted with permission from [159], Copyright 2023 American Chemical Society).

II - 3.2.1. Protein imprinting

In the protein imprinting approach, the whole protein is used as the template. Such strategy, following the traditional MIP concept, could be argued as the most appropriate biomimetic approach in terms of binding affinity, since it would retain the tertiary structure of the target protein, as well as, affinity groups for weak protein interactions, such as hydrogen bonds, electrostatic and van der Waals

interactions.[190] However, epitope imprinting, may provide a recognition mechanism more similar to natural receptors. Depending on the application, it may be useful to have a binding site corresponding to a specific peptide motif of the entire biomolecule. This is particularly relevant for cell membrane proteins, when considering specific biological variants detection, or to promote cost-effective MIP development and manufacture strategies. The literature reports MIPs targeting common proteins, such as BSA, albumin, ribonuclease A, horseradish peroxidase (HRP), or cytochrome c, using molecular imprinting methods based on different strategies for the immobilization of the target, and varied functional monomers (Table II - 4).[184,186,191] After MIP preparatiom, template removal techniques include protein denaturation steps, so that the template changes its conformation and will be released from the imprinted cavity, followed by washing steps to promote the elution of the denatured template. A drawback of these methods is that they do not allow the recovery of the template molecule for reuse. Another methodology is based solely in washing with mild solvents, like aqueous solutions, thus relying on disruption of weak interactions, such as electrostatic and hydrogen bonds, and the slow diffusion of the protein through the polymer network. Additionally, the use of thermo-responsive monomers (e.g. N-isopropylacrylamide) in the structure of the MIP allows the release of the protein simply by increasing the temperature of the washing solution above the lower critical solution temperature (LCST), which leads to increase space between polymer chains, allowing the protein to be released from the MIP's cavity.

Table II - 4. Examples of templates used in the protein imprinting approach with template removal procedures.

Template	Template removal	Ref
Cytochrome c	Digestion with trypsin and washing with SDS solution	[183]
	Washing with ethanol, NaOH, and acetic acid with SDS solutions	[184]
Haemoglobin	Washing with SDS solution	[185]
	Washing with ethanol, NaOH, acetic acid with SDS solutions	[184]
BSA	Washing with potassium phosphate buffer	[186]
Albumin	Washing with ethanol, NaOH, and acetic acid with SDS solutions	[184]
DNAzyme complex	Washing with water	[177]
Prostate-specific membrane antigen (PSMA)	Soaking in $^{aqueous}\ NH_3$/methanol, followed by washing with water and methanol	[178]
Epidermal growth factor receptor (EGFR)	Washing with water in solid phase extraction and centrifugal dialysis	[159]
Ribonuclease A	Washing with ethanol, NaOH, acetic acid with SDS	[184]
Listeria monocytogenes	Acetic acid and trypsin	[146]

Some studies report the development of MIPs for the whole tertiary protein structure in solution, by addition of the target biomolecule to the reaction mixture,[192,193] or even the use of whole cells, like bacteria, to develop MIP-based sensors reaching relevant LOD values. A MIP-based electrochemical sensor developed for *Listeria monocytogenes* presented a LOD of 70 CFU/mL.[146] However, the most common approach resorts to solid phase synthesis (which will be explored in this thesis) in which the template protein is first immobilized in a solid support such as silica beads,[168,194] glass surfaces,[183,186] and other silica molds,[184,195] and an affinity chromatography step is used for the synthesis and purification of the molecularly imprinted NPs (MIP-NPs) (Fig. II - 4 and Fig. II - 5). Immobilization of the protein on the solid support can be achieved using an affinity ligand of the protein,[196] or by chemical functionalization of the surface of the solid support.[168] The use of an affinity ligand enables the orientation of the immobilized protein, meaning that all binding sites are constructed with similar orientation, thus improving binding site homogeneity.

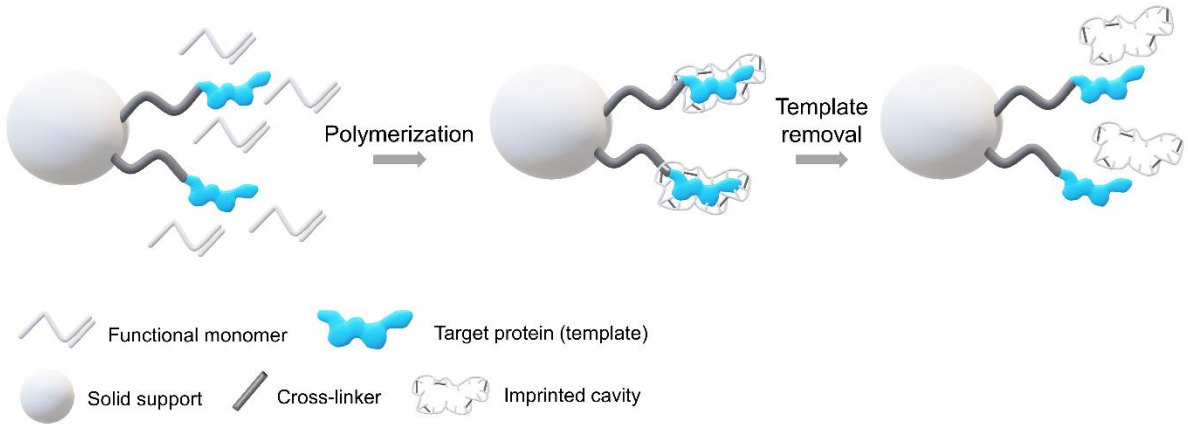

Fig. II - 5. Schematic representation of protein imprinting with the target protein immobilized on the surface of a silica bead.

Ambrosini and co-workers reported the use of solid-phase synthesis of MIP-NPs for protein recognition using the model protein trypsin (23 kDa),[196] adapting the solid-phase synthesis method previously developed for synthesis of a MIP for melamine, a small molecule (<1 kDa).[147] Trypsin was immobilized on the surface of glass beads, and the beads were then packed into a column, where the functional monomers (NIPAM and EBA) were added, and the reaction took place. Finally, several washing steps were performed for purification of the MIPs. Despite the difference in size of the target molecules, the immobilization on the solid support appears to depend mostly on the functional groups present in the target molecule, thus rendering solid-phase synthesis a versatile method for MIP synthesis. Still, one has to consider that large biomolecules are more complex and they often have similar reactive groups (e.g. amines or carboxylic acids) on different locations, which makes more challenging to obtain specificity on immobilization of the template biomolecule with uniform orientations. One advantage of the solid-phase synthesis strategy is the decrease of the cost of the process due to the solid phase being reused for MIP synthesis, thereby saving template molecules. One study reported the maintenance of the size and dissociation constant (K_D) of MIPs for over 30 batches of template reuse,[147] with that value being inferior to the standard protein A chromatography performance for antibody production, which can be reused for 100 cycles. However, stability of proteins under reaction conditions for several cycles should be assessed, as literature is scarce concerning this information and there is a severe lack of studies presenting a process design and model along with realistic economic analyses.

To selectively separate lysozyme from a mixture of proteins in aqueous solution, acrylamide and acryloyl-β-cyclodextrin were used as functional monomers.[194] Here, the target protein was immobilized on the surface of silica beads and the polymerization reaction took place around the immobilized lysozyme. After removal of the template and consequent detachment from the beads,

the MIPs were packed in a column. A successful high performance liquid chromatography (HPLC) separation was achieved, with lysozyme selectively separated from cytochrome c, BSA and avidin, with a maximum adsorption capacity for lysozyme of 44.6 mg/g, being 4 times higher than for the remaining proteins.[194] Overall, these studies highlight the high values of maximum adsorption capacities achieved through solid-phase synthesis of MIPs for proteins, thus suggesting that immobilization and consequent orientation of the template molecule might contribute to higher selectivity of the MIPs.

A different approach that also does not require the immobilization of the template is MIP electrosynthesis, where cyclic voltammetry (CV) is used for electropolymerisation of the MIP. Here, a pre-polymerization mixture of template protein and monomer is prepared, which is then deposited onto an electrode surface by applying cyclic potential sweeps. A study on the electrochemical quantification of troponin T (37 kDa), a biomarker of myocardial injury, used o-phenylenediamine as a monomer and a gold electrode for deposition of the MIP to build a biosensor based on a redox probe.[197] A similar study for recognition and electrochemical detection of myoglobin (18 kDa) used screen-printed electrodes where the pre-polymerisation mixture of myoglobin and o-phenylenediamine was electrodeposited.[188] Even so, it is necessary to consider the difficulty to scale-up electrosynthesis processes due to potential difficulties to increase the electrode active area and electronic transport in the bulk of the reaction mixture. Furthermore, recyclability of the template is not considered, thus limiting the applicability of this method to less expensive targets, or resulting in processes with prohibitive costs.

Only one molecular imprinting methodology was reported with the objective to synthesizing a replica of the protein, which is based on a two-step imprinting process. The strategy follows the approach to: i) firstly, obtain a molecular cast of the target antibody, synthesized as a MIP particle, and then ii) perform the second imprinting stage, analogous to a stamping method, in which polymerization occurs by compression of the pre-synthetized MIP particles onto a pre-polymerized layer placed on the surface of a quartz crystal microbalance (QCM) electrode. Therefore, the polymer layer will be covered with molecularly imprinted antibody replicas after removing the stamp.[198–201] This methodology limits the range of applications to those that are usually based on immobilized antibodies on surfaces, such as biosensors or immunoassays that are often performed on chips. However, it is difficult to gather if the production of such immunoassay platforms could be improved with this strategy instead of using actual antibodies. Again, literature is found lacking in an actual economic analysis of the cost of production.

Although direct imprinting for detection and separation of proteins seems to be fairly well explored in the literature, there is still a call for designing MIPs for other challenging proteins with biomedical interest, particularly disease biomarkers, like surface membrane proteins expressed in

cancer, for example, the biomarker expressed on breast cancer cells CD44 that will be explored as the template for the bioimprinted MIP in this thesis.

One point of concern is the fact that cross-selectivity between similar proteins may impair MIP performance, resulting on false positives, as several studies look at the selectivity of the MIPs against proteins that are not the target, but share similar structural characteristics. Indeed, in a competitive assay, using the previously mentioned lysozyme MIPs, no statistical difference was found in the adsorption capacity for lysozyme, trypsin, and cytochrome c, three proteins of high isoelectric point. While such MIP bound preferentially to lysozyme, the maximum adsorption capacity was close to 800 mg/g for the three proteins.[202] This result raises concern over the fact that imprinting alone may not account for the selectivity of certain classes of proteins.

II - 3.2.2. Epitope imprinting

When entire proteins are used as templates for MIP preparation, their efficient removal after polymerization is impaired, due to difficult diffusion through the MIP network. Additionally, proteins' tertiary conformations, which depend on conditions, such as pH, solvent, and temperature,[203] are unstable, contributing to the lack of MIPs selectivity. To overcome such drawbacks, using only a part of the protein as the template has been proposed as an imprinting strategy. Indeed, in the epitope imprinting approach, short linear peptides are used as the target molecules for the MIP, as will be the case for the CD44 template explored in this thesis. Therefore, in this case, the selective recognition neglects the protein 3D conformational specificity and relies on amino acid recognition, since imprinting is based only on the amino acid sequence, the primary structure of the peptide, instead of secondary and tertiary structures of proteins. Epitope design and selection strategies have been extensively discussed,[204] covering computational tools for selection of appropriate amino acids sequences and peptide length to maximize affinity of the MIP developed.

A possible strategy for proteins that have their C- or N-terminus exposed is to use such extremity as the site around which the MIP will be formed and the protein selectively captured. Nonapeptides as target molecules, peptides with a nine amino acid sequence length, have been selected to be large enough to allow the unique identification of a particular protein.[205] Such strategy was used for the development of MIPs for cytochrome c, BSA and alcohol dehydrogenase (ADH), in which nine amino acid sequence peptides of the C-terminus of these proteins were successfully used as templates in the synthesis of molecular imprinted films.[205] In these examples, the authors also used solid phase synthesis to facilitate the polymerization reaction around the template peptides.

MIP-NPs were also synthesized for an exposed C-terminus peptide of green fluorescent protein (GFP) by inverse microemulsion polymerization, using AAm and *N,N'*-methylenebisacrylamide (MBA)

as monomers, and APS and *N,N,N',N'*-Tetramethylethylenediamine (TEMED) as initiators.[206] Surfactants were also added so that polymerization occurred in inverse microemulsion, where the peptide was correctly oriented at the interface of water and oil domains, without the need for previous template surface immobilization. In another study, an exposed antigenic domain of Lpp20, an outer membrane lipoprotein antigen specifically expressed by all the *H. pylori* strains, was used as a template in inverse mini-emulsion polymerization, using AAm as functional monomer. The obtained MIP was successfully assessed to capture the bacteria *H. pylori*.[207] While examples of epitope imprinting by inverse emulsion polymerization are still scarcely reported, possibly due to poor stability of epitopes on the water/oil interface, this is an innovative and apparent simple method for MIP preparation, as it skips the steps of template immobilization required on solid phase synthesis, *i.e.* avoids the steps of activation and functionalization of the solid support, immobilization of template and several washing steps.

It is worth noting that most studies overviewed use acrylate-based functional monomers, without discussing further progress in the literature in the selection and use of alternative types of monomers. Similarly, MBA and APS are the recurrent choices for cross-linker and initiator, respectively. Such selection has several advantages in terms of polymerization techniques' efficiency and obtained MIP performance. However, considering concerns on promoting the development of sustainable and greener processes in MIP design,[208] alternative reagents could be procured, such as, for example, itaconic acid obtained from fermentation of Aspergillus species.

Overall, epitope imprinting has the advantage of relying only on the use of short peptides as templates instead of the whole protein, which are potentially easy to synthesize, and thus more available than their protein counterparts. As such, concerning the bioimprinted MIPs to be developed for the CD44 epitope for breast cancer targeting, the solid phase synthesis will be explored, and the functional monomers will include acrylate-based monomers, such as acrylic acid, but also itaconic acid will be explored as an alternative in Chapter VII of this thesis.

II - 3.2.2.1. Conformational epitope imprinting

Epitope imprinting based on the primary structure of an exposed peptide sequence, although efficient, is limited, as not all proteins meet the required criteria, such as the target protein to include an exposed C-terminus or an amino acid sequence both specific and short enough. A possible solution for these limitations is the use of conformational epitope imprinting. This approach uses as template the primary, secondary and tertiary structure of the selected epitope, thus, incorporating the recognition of the specific 3D conformation of the epitope into the MIP.

This strategy was applied in the design of a MIP for the p32 protein, by inverse microemulsion polymerization.[179] p32, a membrane protein that is overexpressed on the surface of varied tumor cell types, has the potential to target and mediate drug delivery and thus the developed MIP has the potential to actively target tumors. This protein has an N-terminal α-helix in the extracellular domain, which was set as the target site for the MIP. The peptide apamin mimics the extracellular domain of p32, as it has a sequence of seven aa residues identical to the one present on this domain, and it was successfully used as the imprinting template.[179]

II - 3.2.2.2. Peptide imprinting

Peptide imprinting has not only been used for protein recognition, but also for recognition of the peptides themselves. In this strategy, a short peptide sequence is again used as template. Synthesis of peptide-selective MIPs has been reported for varied peptides. A MIP for the recognition of the hormone oxytocin was synthetized by bulk polymerization, using as template a tetrapeptide with the same three amino-acid C-terminal section of the structure of oxytocin, and using methacrylic acid (MAA) as functional monomer and ethylene glycol dimethacrylate (EGDMA) as crosslinker.[176]

A MIP for the recognition of the hormone angiotensin II, with a detection limit of 8 pM, was achieved by free radical polymerization using as functional monomer sodium acrylate, and as cross-linker poly(ethylene glycol) diacrylate. In this case, the whole peptide was used as template since the it has a short eight aa sequence.[209]

The synthesis of MIP-NPs for the specific binding of melittin, which is a bee venom biotoxin, was achieved by precipitation polymerization.[189] Melittin has 26 amino acids, of which 6 are positively charged, 6 residues at the C-terminus are hydrophilic, and the remainder is mostly composed of non-polar amino acid residues. In this study, the authors established a rationale for monomer selection considering the overall polarity of the peptide and the individual charge of each amino acid residue of the peptide sequence. Hence, the optimum monomer combination should comprise a mix of hydrophobic and negatively charged monomers to bind to the opposing charges of the residues of the target peptide. The two most successful monomer combinations contain 40% of hydrophobic monomers (*N*-tert-butylacrylamide, TBAm) and 5% of negatively charged functional monomers (acrylic acid, AAc), or 5% hydrogen bonding monomer (AAm), 5% negatively charged monomers (AAc) and 40% of hydrophobic monomers (TBAm). K_D obtained by nonlinear fitting of Langmuir isotherms for these MIPs were in the range of 7.3-25 pM, which are comparable to the K_D of a natural antibody (10 pM to 5 nM),[210–212] thus suggesting that the same affinities can be achieved for the MIP as the natural counterpart, showing the importance of functional monomer selection for successful biomacromolecule MIP synthesis. These strategies illustrate a more holistic approach where the global

charge and hydrophobic/hydrophilic balance of molecules are considered on MIP design, to potentiate more probable success in tailoring host site formation to template-specific structural properties.

II - 3.3. Applications

MIPs for biomacromolecules have the potential for numerous applications, from bioseparation and purification processes in biotechnology and pharmaceutical industries to biomedical applications. Many of the studies described in this section target selective recognition of proteins aiming at the potential application of MIPs in the separation and purification of proteins within pharma or food industry processes. In this context, the use of MIPs has been explored in affinity chromatography as it has been demonstrated for lysozyme, BSA, haemoglobin, and cytochrome c.[184,185,191,192,194]

The biomedical field covers a broad spectrum of potential applications for biomacromolecule MIPs, spanning from biosensors and targeted drug delivery. MIP-based biosensors have been extensively explored in the literature, with protein quantification method being the prime target for MIP application, as the current technology relies on expensive immunoassays. An especially motivating application of MIP biosensors is their use as diagnostic tools. Fig. II - 6 and Table II - 5 resume some examples of recent studies using MIPs for proteins, coupled to varied sensing units, as biosensor diagnostic tests with clinical relevance. As previously mentioned, MIP-based biosensors for detection of biomarkers of cancer and neurodegenerative diseases, often using electrochemical detection, have been a focus of recent research. Nevertheless, MIP-based electrochemical biosensors have also been developed for other clinically relevant biomarkers such as troponin T,[197] or myoglobin in cardiac disease.[188] Several studies have also explored MIPs for detection of viral detection systems, for example for poliovirus,[213] bovine leukaemia virus,[214] and dengue virus.[171]

Of particular relevance in recent years are MIP-based sensors for detection of SARS-CoV-2, for instance using a disposable electrochemical chip with high sensitivity,[175] or a surface plasmon resonance optical sensor,[172] capable of detecting SARS-CoV-2 in nasopharyngeal swab samples of COVID-19 positive patients (Fig. II - 6). Further works using MIP-based electrochemical sensors for SARS-CoV-2 have been developed using electroconductive polymers, namely polypyrrole, with significant sensitivity of detection with calibration curves with protein concentrations ranging 0-25 µg/mL.[149,150] A study worth noting is the design of an electrochemical sensor using two alkane thiols (11-mercaptoundecanoic acid and 6-mercapto-1-hexanol) to form a self-assembled monolayer MIP for the spike protein of SARS-CoV-2 with a reported LOD as low as 0.34 nM and a limit of quantification around 1 nM.[215] Overall, electrochemical detection coupled to MIP for proteins appears to be a promising method to reach low LODs for relevant clinical targets.

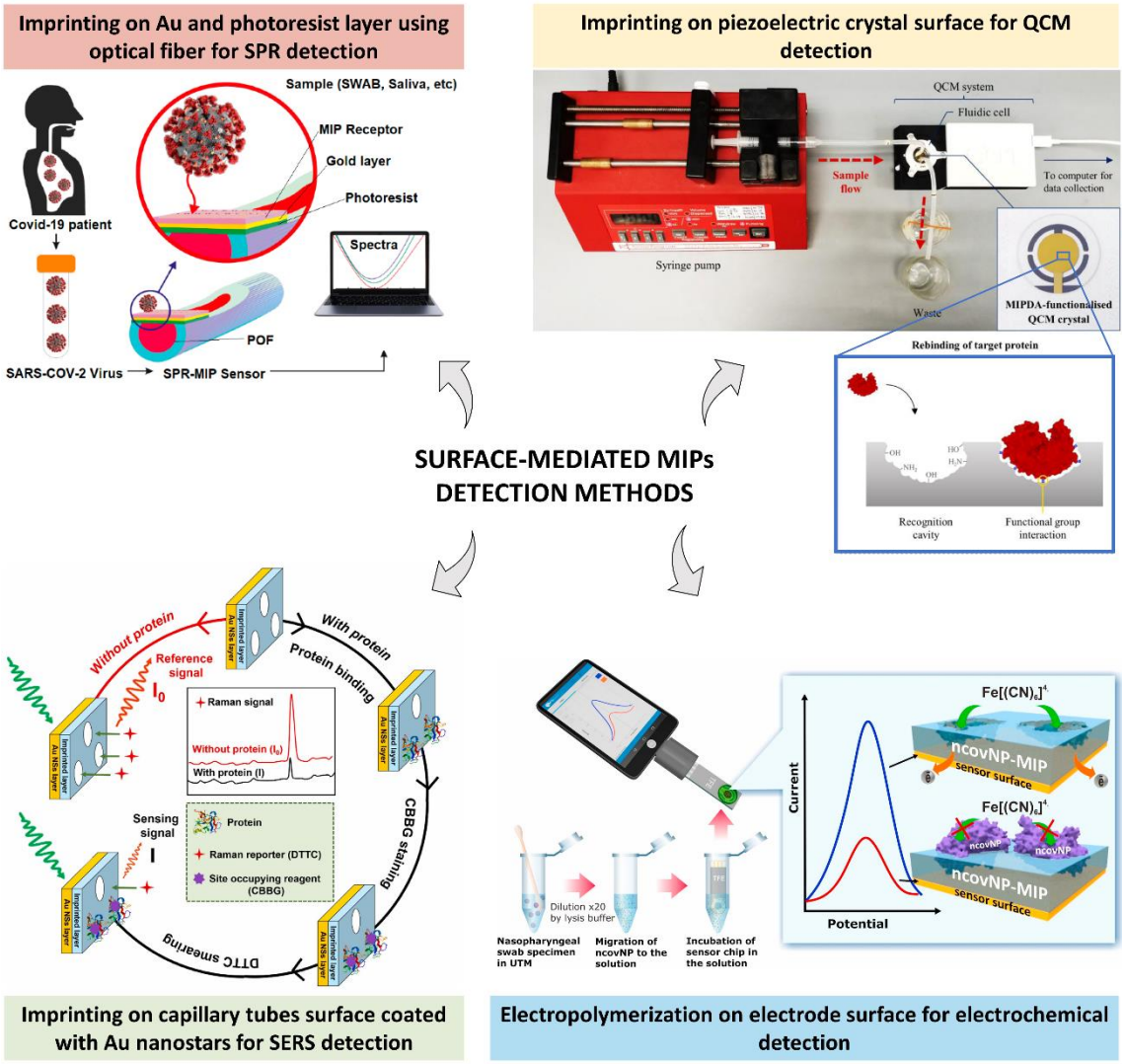

Fig. II - 6. Representative surface mediated MIPs detection methods, including surface plasmon resonance (SPR) using a plastic optical fiber (POF) (reprinted with permission from [172] under Creative Commons License – Attribution 4.0 International – CC BY 4.0 – https://creativecommons.org/licenses/by/4.0/legalcode), QCM (reprinted from [216], Copyright 2023, with permission from Elsevier), surface-enhanced Raman scattering (SERS) (reprinted from [148], Copyright 2023, with permission from Elsevier), and an electrochemical method (reprinted from [175], Copyright 2023, with permission from Elsevier).

Table II - 5. MIPs for proteins with clinical relevance and detection units as biosensor diagnostic tools.

Target protein	Clinical relevance	Detection	Ref
Troponin T	Cardiac biomarker for early cardiac disease diagnosis	Electrochemical	[197]
Myoglobin	Very early cardiac biomarker of acute myocardial infarction	Square wave and differential pulse voltammetry	[188]
Albumin	Indicator of kidney or liver disfunction	QCM	[217]
Butyrylcholinesterase	Acute and chronic liver damage indicator; prognostic indicator in cancer	Electrochemical	[218]
Human chorionic gonadotropin	Marker of ectopic pregnancy or trophoblastic tumors; screen for fetal congenital abnormalities	Chemosensing by extended-gate field-effect transistors and capacitive impedimetry	[195]
PSMA	Prostate cancer biomarker	Love wave sensor	[178]
Carcinoembryonic antigen (CEA) and poliovirus	CEA: Colon cancer biomarker; Poliovirus: causative agent of poliomyelitis	Potentiometry	[213]
Bovine leukaemia virus glycoprotein	Bovine leukaemia diagnostic	Electrochemical	[214]
Dengue virus NS1 protein	Indicator of dengue virus infection	QCM	[171]
Human interleukin-1	Indicator of varied inflammatory diseases	Luminescence	[219]
SARS-CoV-2 nucleoprotein	COVID-19 diagnostic	Electrochemical	[175]
Subunit 1 of the SARS-CoV-2 Spike protein	COVID-19 diagnostic	Surface plasmon resonance	[172]
SARS-CoV-2 Spike protein	COVID-19 diagnostic	Electrochemical	[149,150,215]

MIPs may also be explored as targeting agents, for example, of a tumor, by binding to the membrane surface protein of the tumor cells, namely of a protein that is overexpressed on the surface of cancer cells. In this line of work, MIP-NPs have been developed to target the extracellular α-helix domain of the p32 protein in *in vitro* and *in vivo* models.[179] Such type of MIPs, loaded with a fluorescent probe (IR-783 dye), were assessed for tumor imaging in mice, and when encapsulating a

photosensitizer compound, such as methylene blue, that was used for photodynamic treatment of tumors. The encapsulation process took place during polymerization by simply adding the desired compounds (IR-783 and methylene blue) to the aqueous phase before initiating the inverse microemulsion polymerization, where AAm and MBA were used, respectively, as functional monomer and cross-linker.[179] This study demonstrated that MIP-NPs can simultaneously function as targeting tools and nanocarriers for drugs.

In another study, the C-terminal linear peptide of EGFR (amino acids 418−435: SLNITSLGLRSLKEISDG), an overexpressed receptor on the cell surface of many tumors, was used as the template for production of MIP-NPs by solid phase synthesis. This MIP was assessed for targeted drug delivery to MDA-MB-468 breast cancer cells.[159] In this case, a dual imprinting strategy was followed, in which the chosen drug (doxorubicin) was used as a secondary template present in solution with the monomers (NIPAm, TBAm and *N*-(3-aminopropyl) methacrylamide (APMA)) and the cross-linker (MBA),[159] as represented in Fig. II - 7. After binding of the MIP to the EGFR receptor, the anticancer drug was released by diffusion and accumulate around cancer cells, promoting cancer cell death. This study illustrates a strategy where the MIP presents binding sites for the drug and for the membrane receptor, demonstrating that MIP-NPs can selectively deliver a drug, by response to the TME, to specific cell targets.

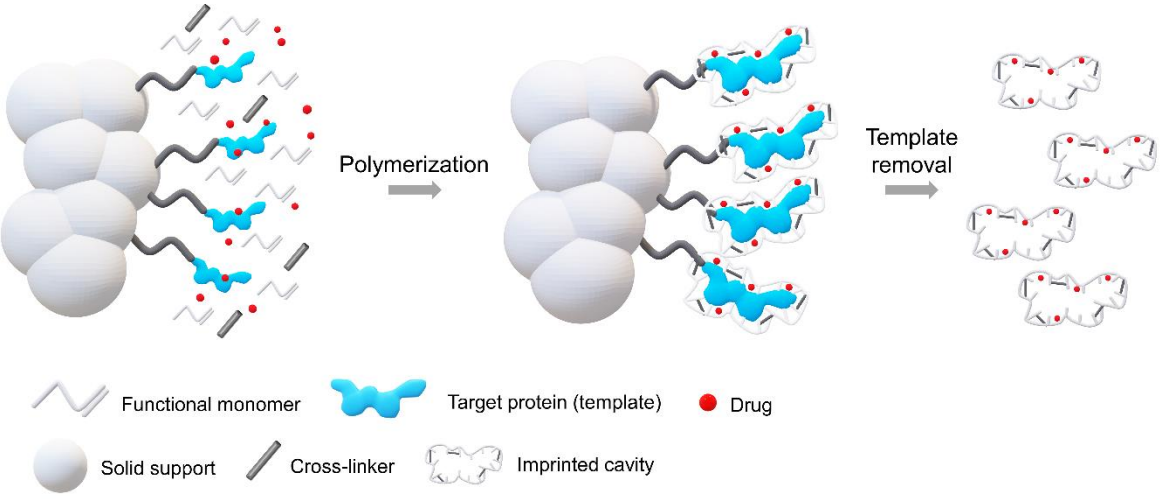

Fig. II - 7. Schematic representation of dual imprinting strategy using solid-phase synthesis.

The potential of using MIPs for therapies in humans is an extremely important feature that need to be addressed. Some studies have demonstrated efficacy in cell culture and some have used *in vivo* models, such as mice. For instance, a MIP targeting the folate receptor in cancer cells have been tested

in mice bearing cervical cancer (HeLa) tumors, showing both the safety of using the MIPs in an organism, while showing the effectiveness of the targeting of the tumor and drug delivery.[220]

An important feature in clinical applications is the successful detection of a therapeutic targeting agent by imaging techniques. A synergistic chemo- and photo-dynamic cancer therapy with a dual imaging agent relying on dual-template MIP-NPs was recently demonstrated in *in vitro* and *in vivo* models. In this study, the MIPs were synthetized for the CD59 epitope, as this protein is overexpressed in solid tumors, and the secondary template was doxorubicin as the chemotherapy agent. For the dual fluorescent/magnetic resonance imaging, gadolinium-doped silicon quantum dots were first prepared and used as the core of the MIP-NPs, and photosensitizer chlorin e6, the photo-dynamic cancer therapeutic, was embedded in the silica core. The polymerization took place on the surface using NIPAm, Aam and TBAm as functional monomers and MBA as cross-linker.[221] The synthesis process complexity increases the number of variables to be considered over the synthesis, *i.e.* functional monomers that will match functional groups in both peptide and drug templates, cross-linkers, initiators and solvents compatible for both molecules. This work successfully showed that the already evidenced targeting ability of MIPs for biomarkers can be further explored to comprise several therapeutic options. Furthermore, it also evidences the potential of protein MIP-NPs to be coupled to imaging tools, allowing a more precise guided cancer treatment.

II - 4. Summary

In the field of cancer treatment, the development and utilization of smart responsive materials, particularly those responsive to pH and electrostimulation, mark a significant step towards personalized and effective therapies. The multifaceted challenges posed by cancer demand innovative solutions that can adapt to the dynamic microenvironments within the body. pH-responsive materials offer a tailored approach, capitalizing on the acidic nature of the TME to selectively deliver therapeutic payloads to cancer tissues while sparing healthy cells. This targeted delivery minimizes off-target effects and enhances the efficacy of cancer therapies, reducing systemic toxicity and improving patient outcomes.

Moreover, the integration of electroresponsive materials introduces a new dimension of control and precision in cancer treatment, offering unique advantages such as controlled and on-demand drug delivery. By harnessing external stimuli such as electrical signals, these materials enable real-time modulation of drug release kinetics and cellular interactions. This dynamic responsiveness empowers clinicians to fine-tune therapeutic interventions according to individual patient needs, optimizing treatment efficacy and minimizing the adverse effects of traditional chemotherapy. Additionally, electroresponsive materials hold promise for synergistic approaches, facilitating combination therapies and overcoming multidrug resistance mechanisms prevalent in many cancers.

The versatility and adaptability of smart responsive materials underscore their potential as a cornerstone of future cancer therapeutics. As research advances, further refinement of these materials will likely enhance their biocompatibility, specificity, and functionality, unlocking new avenues for precision medicine. Collaborative efforts across disciplines, from materials science to oncology, will be essential in driving forward this transformative field. By harnessing the power of smart responsive materials, we can envision a future where cancer treatment is not only more effective but also more personalized, offering hope to patients and caregivers alike in the fight against this devastating disease.

The field of molecular imprinting of biomacromolecules has seen significant growth over the past decade despite the inherent challenges, such as the need for their synthesis to be compatible with the use of aqueous media and allow for the immobilization of the target molecule, to ensure that proteins and peptides maintain their native conformations during polymerization.

In light of the advantages of MIPs, such as being cheap, easy to synthesize in a reproducible way, and showing robust performances in a variety of solvents, it is not surprising that MIPs for biomolecules have been considered suitable for medical diagnosis and therapeutics, but also as replacements of enzymes in catalytic processes or even used as bioelectrodes for energy harvesting.

Concerning the template molecule, most proof-of-concept studies used as template readily available and “low-cost” proteins, such as BSA or cytochrome c. This could be somewhat expected as more interesting protein targets are expensive, as is the case of human disease biomarkers, such as receptors that are overexpressed on the surface of tumor cells. However, the impact of using MIPs, instead of antibodies, is based on the cost-effectiveness of the process to obtain MIPs, therefore it is important to maintain low costs when expensive templates are used. A possible strategy could be the reuse of the template in several polymerization reactions, when it is immobilized on a solid surface, similar to what is seen for catalytic enzymes in bioprocesses, that are reused throughout batches until they lose enzymatic activity. Unfortunately, the literature is severely lacking on studies reporting for how many batches, can the templates be reused in MIPs synthesis, with only one available study reporting the maintenance of the MIPs properties (size and K_D) for over 30 batches.[147]

Epitope imprinting appears to be a promising approach for the near future as it not only minimizes the complications of dealing with very large and condition-sensitive templates during polymerization, but also decreases the difficulty in template removal after syntheses, due to diffusion constraints in the polymer network. This strategy could contribute to decrease the cost associated with the template as well. However, this also comes with limitations as these epitopes need to comply with certain characteristics, namely an appropriate length to ensure a specific recognition mechanism, and loss of the tertiary structure contributions to recognition specificity.

In terms of applications, the potential of using MIPs as biosensors seems to be a consensus in the literature, with most studies focusing on diagnostics, ranging from cardiovascular and neurodegenerative diseases to cancer. There is a continuous call for new MIP development as new pathogens are identified, and more reliable disease biomarkers are being assessed in biology and medicine. The targeting potential for directed drug delivery has also been reported showing that MIPs for biomarkers can target tumors and function as drug carriers, for example. However, it was not until recently that MIPs with dual affinity sites (biomarker and drug) were synthetized and tested in *in vitro* and *in vivo* models. Indeed, this adds complexity to the synthesis process and possible cross interference in binding site formation for the protein should be further assessed. So far, studies have relied on MIP-NP endocytosis by the cells for drug delivery or laser incidence for photodynamic therapy. Thus, it would be interesting to assess the incorporation of stimuli responsive characteristics on MIPs, such as pH-responsive or electro-responsive, for enhanced controlled targeted drug delivery.

Furthermore, it is extremely important to ensure the safety of use of MIPs in human patients. However, very few studies have been performed using animal models in pre-clinical settings, to show the safety and efficacy of MIPs for therapeutic applications.

Overall, moving forward to clinical approval and commercialization of MIPs for proteins and peptides for biomedical applications, it would be interesting to see further studies reporting biocompatibility, safety, and immunogenic responses using *in vivo* models to ease the bench-to-bedside transition. Additionally, for studies claiming the reusability of the template and the downsizing of production costs, it will be important to have experimental data and economic analysis supporting claims that would ease the path to commercial success of MIPs.

II - 5. References

(1) Sung, H.; Ferlay, J.; Siegel, R. L.; Laversanne, M.; Soerjomataram, I.; Jemal, A.; Bray, F. Global Cancer Statistics 2020: GLOBOCAN Estimates of Incidence and Mortality Worldwide for 36 Cancers in 185 Countries. *CA Cancer J Clin* **2021**, *71* (3), 209–249. https://doi.org/10.3322/CAAC.21660.

(2) Siegel, R. L.; Miller, K. D.; Wagle, N. S.; Jemal, A. Cancer Statistics, 2023. *CA Cancer J Clin* **2023**, *73* (1), 17–48. https://doi.org/10.3322/CAAC.21763.

(3) Hay, M.; Thomas, D. W.; Craighead, J. L.; Economides, C.; Rosenthal, J. Clinical Development Success Rates for Investigational Drugs. *Nat Biotechnol* **2014**, *32* (1), 40–51.

(4) Wong, C. H.; Siah, K. W.; Lo, A. W. Estimation of Clinical Trial Success Rates and Related Parameters. *Biostatistics* **2019**, *20* (2), 273–286. https://doi.org/10.1093/biostatistics/kxx069.

(5) Kunz-Schughart, L. A.; Freyer, J. P.; Hofstaedter, F.; Ebner, R. The Use of 3-D Cultures for High-Throughput Screening: The Multicellular Spheroid Model. *J Biomol Screen* **2004**, *9* (4), 273–285. https://doi.org/10.1177/1087057104265040.

(6) Van Den Brand, D.; Massuger, L. F.; Brock, R.; Verdurmen, W. P. R. Mimicking Tumors: Toward More Predictive in Vitro Models for Peptide- and Protein-Conjugated Drugs. *Bioconjug Chem* **2017**, *28* (3), 846–856. https://doi.org/10.1021/acs.bioconjchem.6b00699.

(7) Brown, J. M.; Giaccia, A. J. The Unique Physiology of Solid Tumors: Opportunities (and Problems) for Cancer Therapy. *Cancer Res* **1998**, *58*, 1408–1416.

(8) Tannock, I. F. Tumor Physiology and Drug Resistance. *Cancer and Metastasis Reviews* **2001**, *20*, 123–132.

(9) Bray, L. J.; Hutmacher, D. W.; Bock, N. Addressing Patient Specificity in the Engineering of Tumor Models. *Front Bioeng Biotechnol* **2019**, *7* (September), 1–36. https://doi.org/10.3389/fbioe.2019.00217.

(10) Jain, R. K. Normalizing Tumor Microenvironment to Treat Cancer: Bench to Bedside to Biomarkers. *Journal of Clinical Oncology* **2013**, *31* (17), 2205–2218. https://doi.org/10.1200/JCO.2012.46.3653.

(11) Parks, S. K.; Cormerais, Y.; Pouysségur, J. Hypoxia and Cellular Metabolism in Tumour Pathophysiology. *J Physiol* **2017**, *595* (8), 2439–2450. https://doi.org/10.1113/JP273309.

(12) Dvorak, H. F.; Weaver, V. M.; Tlsty, T. D.; Bergers, G. Tumor Microenvironment and Progression. *J Surg Oncol* **2011**, *103* (6), 468–474. https://doi.org/10.1002/jso.21709.

(13) Lu, P.; Weaver, V. M.; Werb, Z. The Extracellular Matrix: A Dynamic Niche in Cancer Progression. *Journal of Cell Biology* **2012**, *196* (4), 395–406. https://doi.org/10.1083/jcb.201102147.

(14) Fong, E. L. S.; Harrington, D. A.; Farach-Carson, M. C.; Yu, H. Heralding a New Paradigm in 3D Tumor Modeling. *Biomaterials* **2016**, *108*, 197–213. https://doi.org/10.1016/j.biomaterials.2016.08.052.

(15) Bausch-Fluck, D.; Goldmann, U.; Müller, S.; van Oostrum, M.; Müller, M.; Schubert, O. T.; Wollscheid, B. The in Silico Human Surfaceome. *Proc Natl Acad Sci U S A* **2018**, *115* (46), E10988–E10997. https://doi.org/10.1073/pnas.1808790115.

(16) Li, W.; Qian, L.; Lin, J.; Huang, G.; Hao, N.; Wei, X.; Wang, W.; Liang, J. CD44 Regulates Prostate Cancer Proliferation, Invasion and Migration via PDK1 and PFKFB4. *Oncotarget* **2017**, *8* (39), 65143–65151. https://doi.org/10.18632/oncotarget.17821.

(17) Chen, C.; Zhao, S.; Karnad, A.; Freeman, J. W. The Biology and Role of CD44 in Cancer Progression: Therapeutic Implications. *J Hematol Oncol* **2018**, *11* (1), 1–23. https://doi.org/10.1186/s13045-018-0605-5.

(18) Necela, B. M.; Crozier, J. A.; Andorfer, C. A.; Lewis-Tuffin, L.; Kachergus, J. M.; Geiger, X. J.; Kalari, K. R.; Serie, D. J.; Sun, Z.; Aspita, A. M.; O'Shannessy, D. J.; Maltzman, J. D.; McCullough, A. E.; Pockaj, B. A.; Cunliffe, H. E.; Ballman, K. V.; Thompson, E. A.; Perez, E. A. Folate Receptor-α (FOLR1) Expression and Function in Triple Negative Tumors. *PLoS One* **2015**, *10* (3), e0122209. https://doi.org/10.1371/journal.pone.0122209.

(19) Xing, L.; Xu, Y.; Sun, K.; Wang, H.; Zhang, F.; Zhou, Z.; Zhang, J.; Zhang, F.; Caliskan, B.; Qiu, Z.; Wang, M. Identification of a Peptide for Folate Receptor Alpha by Phage Display and Its Tumor Targeting Activity in Ovary Cancer Xenograft. *Sci Rep* **2018**, *8* (1), 1–13. https://doi.org/10.1038/s41598-018-26683-z.

(20) Fonseca, A. L.; Da Silva, V. L.; Da Fonsêca, M. M.; Meira, I. T. J.; Da Silva, T. E.; Kroll, J. E.; Ribeiro-Dos-Santos, A. M.; Freitas, C. R.; Furtado, R.; De Souza, J. E.; Stransky, B.; De Souza, S. J. Bioinformatics Analysis of the Human Surfaceome Reveals New Targets for a Variety of Tumor Types. *Int J Genomics* **2016**, *2016*. https://doi.org/10.1155/2016/8346198.

(21) Lee, J. K.; Bangayan, N. J.; Chai, T.; Smith, B. A.; Pariva, T. E.; Yun, S.; Vashisht, A.; Zhang, Q.; Park, J. W.; Corey, E.; Huang, J.; Graeber, T. G.; Wohlschlegel, J.; Witte, O. N. Systemic Surfaceome Profiling Identifies Target Antigens for Immune-Based Therapy in Subtypes of Advanced Prostate Cancer. *Proc Natl Acad Sci U S A* **2018**, *115* (19), E4473–E4482. https://doi.org/10.1073/pnas.1802354115.

(22) Chang, S. S. Overview of Prostate-Specific Membrane Antigen. *Rev Urol* **2004**, *6* (Suppl 10), S13–S18.

(23) Levental, K. R.; Yu, H.; Kass, L.; Lakins, J. N.; Egeblad, M.; Erler, J. T.; Fong, S. F. T.; Csiszar, K.; Giaccia, A.; Weninger, W.; Yamauchi, M.; Gasser, D. L.; Weaver, V. M. Matrix Crosslinking Forces

Tumor Progression by Enhancing Integrin Signaling. *Cell* **2009**, *139* (5), 891–906. https://doi.org/10.1016/j.cell.2009.10.027.

(24) Härmä, V.; Virtanen, J.; Mäkelä, R.; Happonen, A.; Mpindi, J. P.; Knuuttila, M.; Kohonen, P.; Lötjönen, J.; Kallioniemi, O.; Nees, M. A Comprehensive Panel of Three-Dimensional Models for Studies of Prostate Cancer Growth, Invasion and Drug Responses. *PLoS One* **2010**, *5* (5). https://doi.org/10.1371/journal.pone.0010431.

(25) Eder, T.; Weber, A.; Neuwirt, H.; Grünbacher, G.; Ploner, C.; Klocker, H.; Sampson, N.; Eder, I. E. Cancer-Associated Fibroblasts Modify the Response of Prostate Cancer Cells to Androgen and Anti-Androgens in Three-Dimensional Spheroid Culture. *Int J Mol Sci* **2016**, *17* (9), 1–15. https://doi.org/10.3390/ijms17091458.

(26) Prendiville, W.; Sankaranarayanan, R. *Colposcopy and Treatment of Cervical Precancer*; International Agency for Research on Cancer, Ed.; World Health Organization: Geneva, 2017; Vol. 45.

(27) Volkova, L. V.; Pashov, A. I.; Omelchuk, N. N. Cervical Carcinoma: Oncobiology and Biomarkers. *International Journal of Molecular Sciences*. MDPI November 1, 2021. https://doi.org/10.3390/ijms222212571.

(28) James, C. D.; Morgan, I. M.; Bristol, M. L. The Relationship between Estrogen-Related Signaling and Human Papillomavirus Positive Cancers. *Pathogens*. MDPI AG May 1, 2020. https://doi.org/10.3390/pathogens9050403.

(29) Yao, S.; Zhao, L.; Chen, S.; Wang, H.; Gao, Y.; Shao, N. Y.; Dai, M.; Cai, H. Cervical Cancer Immune Infiltration Microenvironment Identification, Construction of Immune Scores, Assisting Patient Prognosis and Immunotherapy. *Front Immunol* **2023**, *14*. https://doi.org/10.3389/fimmu.2023.1135657.

(30) Li, J.; Wan, C.; Li, X.; Quan, C.; Li, X.; Wu, X. Characterization of Tumor Microenvironment and Tumor Immunology Based on the Double-Stranded RNA-Binding Protein Related Genes in Cervical Cancer. *J Transl Med* **2023**, *21* (1). https://doi.org/10.1186/s12967-023-04505-9.

(31) Zhao, Y.; Yao, R.; Ouyang, L.; Ding, H.; Zhang, T.; Zhang, K.; Cheng, S.; Sun, W. Three-Dimensional Printing of Hela Cells for Cervical Tumor Model in Vitro. *Biofabrication* **2014**, *6* (3). https://doi.org/10.1088/1758-5082/6/3/035001.

(32) Greco, F.; Mattoli, V. Introduction to Active Smart Materials for Biomedical Applications. In *Piezoelectric Nanomaterials for Biomedical Applications. Nanomedicine and Nanotoxicology.*; Ciofani, G., Menciassi, A., Eds.; Springer: Berlin, Heidelberg, 2012; pp 1–27. https://doi.org/10.1007/978-3-642-28044-3_1.

(33) Bhattacharya, S.; Prajapati, B. G.; Singh, S. A Critical Review on the Dissemination of PH and Stimuli-Responsive Polymeric Nanoparticular Systems to Improve Drug Delivery in Cancer Therapy. *Crit Rev Oncol Hematol* **2023**, *185* (103961). https://doi.org/10.1016/J.CRITREVONC.2023.103961.

(34) Kennedy, L.; Sandhu, J. K.; Harper, M. E.; Cuperlovic-culf, M. Role of Glutathione in Cancer: From Mechanisms to Therapies. *Biomolecules* **2020**, *10* (10), 1–27. https://doi.org/10.3390/BIOM10101429.

(35) Kumari, R.; Sunil, D.; Ningthoujam, R. S. Hypoxia-Responsive Nanoparticle Based Drug Delivery Systems in Cancer Therapy: An up-to-Date Review. *Journal of Controlled Release* **2020**, *319*, 135–156. https://doi.org/10.1016/J.JCONREL.2019.12.041.

(36) Qin, F.; Zhou, H.; Li, J.; Liu, J.; Wang, Y.; Bai, R.; Liu, S.; Ma, M.; Liu, T.; Gao, F.; Du, P.; Lu, X.; Chen, C. Hypoxia and PH Co-Triggered Oxidative Stress Amplifier for Tumor Therapy. *Eur J Pharmacol* **2021**, *905* (174187). https://doi.org/10.1016/j.ejphar.2021.174187.

(37) Moradi Kashkooli, F.; Jakhmola, A.; Hornsby, T. K.; Tavakkoli, J. (Jahan); Kolios, M. C. Ultrasound-Mediated Nano Drug Delivery for Treating Cancer: Fundamental Physics to Future Directions. *Journal of Controlled Release* **2023**, *355*, 552–578. https://doi.org/10.1016/J.JCONREL.2023.02.009.

(38) Fogal, V.; Zhang, L.; Krajewski, S.; Ruoslahti, E. Mitochondrial/Cell-Surface Protein P32/GC1qR as a Molecular Target in Tumor Cells and Tumor Stroma. *Cancer Res* **2008**, *68* (17), 7210–7218. https://doi.org/10.1158/0008-5472.CAN-07-6752.

(39) Liu, S.; Tian, H.; Ming, H.; Zhang, T.; Gao, Y.; Liu, R.; Chen, L.; Yang, C.; Nice, E. C.; Huang, C.; Bao, J.; Gao, W.; Shi, Z. Mitochondrial-Targeted CS@KET/P780 Nanoplatform for Site-Specific Delivery and High-Efficiency Cancer Immunotherapy in Hepatocellular Carcinoma. *Advanced Science* **2024**, *2308027*, 1–17. https://doi.org/10.1002/advs.202308027.

(40) Emami Nejad, A.; Najafgholian, S.; Rostami, A.; Sistani, A.; Shojaeifar, S.; Esparvarinha, M.; Nedaeinia, R.; Haghjooy Javanmard, S.; Taherian, M.; Ahmadlou, M.; Salehi, R.; Sadeghi, B.; Manian, M. The Role of Hypoxia in the Tumor Microenvironment and Development of Cancer Stem Cell: A Novel Approach to Developing Treatment. *Cancer Cell Int* **2021**, *21* (62), 1–26. https://doi.org/10.1186/S12935-020-01719-5.

(41) Chen, Z.; Han, F.; Du, Y.; Shi, H.; Zhou, W. Hypoxic Microenvironment in Cancer: Molecular Mechanisms and Therapeutic Interventions. *Signal Transduct Target Ther* **2023**, *8* (70). https://doi.org/10.1038/s41392-023-01332-8.

(42) Niu, B.; Liao, K.; Zhou, Y.; Wen, T.; Quan, G.; Pan, X.; Wu, C. Application of Glutathione Depletion in Cancer Therapy: Enhanced ROS-Based Therapy, Ferroptosis, and Chemotherapy. *Biomaterials* **2021**, *277*, 121110. https://doi.org/10.1016/J.BIOMATERIALS.2021.121110.

(43) Marini, H. R.; Facchini, B. A.; di Francia, R.; Freni, J.; Puzzolo, D.; Montella, L.; Facchini, G.; Ottaiano, A.; Berretta, M.; Minutoli, L. Glutathione: Lights and Shadows in Cancer Patients. *Biomedicines 2023, Vol. 11, Page 2226* **2023**, *11* (8), 2226. https://doi.org/10.3390/BIOMEDICINES11082226.

(44) Valenti, G. E.; Tasso, B.; Traverso, N.; Domenicotti, C.; Marengo, B. Glutathione in Cancer Progression and Chemoresistance: An Update. *Redox Experimental Medicine* **2023**, *2023* (1). https://doi.org/10.1530/REM-22-0023.

(45) Kennedy, L.; Sandhu, J. K.; Harper, M. E.; Cuperlovic-culf, M. Role of Glutathione in Cancer: From Mechanisms to Therapies. *Biomolecules* **2020**, *10* (10), 1–27. https://doi.org/10.3390/BIOM10101429.

(46) Schauenburg, A. D.; Gao, B.; Rochet, L. N. C. Macrocyclic Dual-Locked "Turn-On" Drug for Selective and Traceless Release in Cancer Cells. *Angewandte Chemie - International Edition* **2024**, No. e202314143. https://doi.org/10.1002/anie.202314143.

(47) Fang, T.; Ye, Z.; Chen, X.; Wang, Y.; Wan, J.; Wang, H. Repurposing of Camptothecin: An Esterase-Activatable Prodrug Delivered by a Self-Emulsifying Formulation That Improves Efficacy in Colorectal Cancer. *Int J Pharm* **2021**, *599*, 120399. https://doi.org/10.1016/J.IJPHARM.2021.120399.

(48) Kumari, R.; Majumder, M. M.; Lievonen, J.; Silvennoinen, R.; Anttila, P.; Nupponen, N. N.; Lehmann, F.; Heckman, C. A. Prognostic Significance of Esterase Gene Expression in Multiple Myeloma. *British Journal of Cancer 2021 124:8* **2021**, *124* (8), 1428–1436. https://doi.org/10.1038/s41416-020-01237-1.

(49) McGoldrick, C. A.; Jiang, Y. L.; Paromov, V.; Brannon, M.; Krishnan, K.; Stone, W. L. Identification of Oxidized Protein Hydrolase as a Potential Prodrug Target in Prostate Cancer. *BMC Cancer* **2014**, *14* (1), 1–14. https://doi.org/10.1186/1471-2407-14-77/FIGURES/9.

(50) Kuemmerle, N. B.; Rysman, E.; Lombardo, P. S.; Alison, J.; Lipe, B. C.; Wells, W. A.; Pettus, J. R.; Froehlich, H. M.; Memoli, V. A.; Morganelli, P. M.; Swinnen, J. V; Luika, A.; Chaychi, L.; Fricano, C. J.; Eisenberg, B. L.; William, B.; Kinlaw, W. B. Lipoprotein Lipase Links Dietary Fat to Solid Tumor Cell Proliferation. *Molecular Cancer Theranostics* **2011**, *10* (3), 427–436. https://doi.org/10.1158/1535-7163.MCT-10-0802.Lipoprotein.

(51) Nomura, D. K.; Lombardi, D. P.; Chang, J. W.; Niessen, S.; Anna, M.; Long, J. Z.; Hoover, H. H.; Cravatt, B. F. Monoacylglycerol Lipase Exerts Dual Control over Endocannabinoid and Fatty Acid

Pathways to Support Prostate Cancer. *Chem Biol* **2012**, *18* (7), 846–856. https://doi.org/10.1016/j.chembiol.2011.05.009.Monoacylglycerol.

(52) Cui, Y.; Jiao, Y.; Wang, K.; He, M.; Yang, Z. A New Prognostic Factor of Breast Cancer: High Carboxyl Ester Lipase Expression Related to Poor Survival. *Cancer Genet* **2019**, *239*, 54–61. https://doi.org/10.1016/j.cancergen.2019.09.005.

(53) Gao, F.; Wu, J.; Niu, S.; Sun, T.; Li, F.; Bai, Y.; Jin, L.; Lin, L.; Shi, Q.; Zhu, L. M.; Du, L. Biodegradable, Ph-Sensitive Hollow Mesoporous Organosilica Nanoparticle (HMON) with Controlled Release of Pirfenidone and Ultrasound-Target-Microbubble-Destruction (UTMD) for Pancreatic Cancer Treatment. *Theranostics* **2019**, *9* (20), 6002–6018. https://doi.org/10.7150/thno.36135.

(54) Bakhshi, V.; Poursadegh, H.; Amini-Fazl, M. S.; Salari, D.; Javanbakht, S. Synthesis and Characterization of Bio-Nanocomposite Hydrogel Beads Based on Magnetic Hydroxyapatite and Chitosan: A PH-Sensitive Drug Delivery System for Potential Implantable Anticancer Platform. *Polymer Bulletin* **2023**. https://doi.org/10.1007/s00289-023-05072-1.

(55) Bhattacharya, S.; Prajapati, B. G.; Singh, S. A Critical Review on the Dissemination of PH and Stimuli-Responsive Polymeric Nanoparticular Systems to Improve Drug Delivery in Cancer Therapy. *Crit Rev Oncol Hematol* **2023**, *185* (103961). https://doi.org/10.1016/j.critrevonc.2023.103961.

(56) Liu, X.; Zhou, H.; Veisi, H.; Karmakar, B.; Liu, C. Imatinib-Loaded Pectin-Modified Magnetic Nanoparticles as a Smart PH-Responsive Therapeutic System against Proliferation of Gastric Cancer Cell Line. *Inorg Chem Commun* **2024**, *161* (112022). https://doi.org/10.1016/j.inoche.2024.112022.

(57) Fan, W.; Chen, M.; Raza, F.; Zafar, H.; Jahan, F.; Chen, Y.; Ge, L.; Yang, M.; Wu, Y. PH-Sensitive Peptide Hydrogel Encapsulating the Anti-Angiogenesis Drug Conbercept and Chemotherapeutic Drug Dox as a Combination Therapy for Retinoblastoma. *Mater Adv* **2024**. https://doi.org/10.1039/d3ma01028g.

(58) Akbari, P.; Taebpour, M.; Akhlaghi, M.; Hasan, S. H.; Shahriyari, S.; Parsaeian, M.; Haghirosadat, B. F.; Rahdar, A.; Pandey, S. Regulation of the P53 Tumor Suppressor Gene and the Mcl-2 Oncogene Expression by an Active Herbal Component Delivered through a Smart Thermo-PH-Sensitive PLGA Carrier to Improve Osteosarcoma Treatment. *Medical Oncology* **2024**, *41* (68), 1–16. https://doi.org/10.1007/s12032-023-02291-4.

(59) Pourmadadi, M.; Tajiki, A.; Abdouss, M.; Beig Mohammadi, A.; Kharaba, Z.; Rahdar, A.; Díez-Pascual, A. M. Novel Carbon Quantum Dots Incorporated Polyacrylic Acid/Polyethylene Glycol PH-Sensitive Nanoplatform for Drug Delivery. *Inorg Chem Commun* **2024**, *159* (111814). https://doi.org/10.1016/j.inoche.2023.111814.

(60) Rahimi, S.; Khoee, S.; Ghandi, M. Preparation and Characterization of Rod-like Chitosan–Quinoline Nanoparticles as PH-Responsive Nanocarriers for Quercetin Delivery. *Int J Biol Macromol* **2019**, *128*, 279–289. https://doi.org/10.1016/j.ijbiomac.2019.01.137.

(61) Guan, J.; Zhou, Z. Q.; Chen, M. H.; Li, H. Y.; Tong, D. N.; Yang, J.; Yao, J.; Zhang, Z. Y. Folate-Conjugated and PH-Responsive Polymeric Micelles for Target-Cell-Specific Anticancer Drug Delivery. *Acta Biomater* **2017**, *60*, 244–255. https://doi.org/10.1016/j.actbio.2017.07.018.

(62) Soltani, M.; Souri, M.; Moradi Kashkooli, F. Effects of Hypoxia and Nanocarrier Size on PH-Responsive Nano-Delivery System to Solid Tumors. *Sci Rep* **2021**, *11* (19350), 1–12. https://doi.org/10.1038/s41598-021-98638-w.

(63) Zhao, Y.; Luo, Z.; Li, M.; Qu, Q.; Ma, X.; Yu, S. H.; Zhao, Y. A Preloaded Amorphous Calcium Carbonate/Doxorubicin@silica Nanoreactor for PH-Responsive Delivery of an Anticancer Drug. *Angewandte Chemie - International Edition* **2015**, *54*, 919–922. https://doi.org/10.1002/anie.201408510.

(64) Liu, X.; Zhang, P.; Song, H.; Tang, X.; Hao, Y.; Guan, Y.; Chong, T.; Hussain, S.; Gao, R. Unveiling a PH-Responsive Dual-Androgen-Blocking Magnetic Molecularly Imprinted Polymer for Enhanced Synergistic Therapy of Prostate Cancer. *ACS Appl Mater Interfaces* **2024**, *16*, 4348–4360. https://doi.org/10.1021/acsami.3c13732.

(65) Liang, J.; Huang, Q.; Hua, C.; Hu, J.; Chen, B.; Wan, J.; Hu, Z.; Wang, B. PH-Responsive Nanoparticles Loaded with Graphene Quantum Dots and Doxorubicin for Intracellular Imaging, Drug Delivery and Efficient Cancer Therapy. *ChemistrySelect* **2019**, *4*, 6004–6012. https://doi.org/10.1002/slct.201803807.

(66) Resina, L.; El Hauadi, K.; Sans, J.; Esteves, T.; Ferreira, F. C.; Pérez-Madrigal, M. M.; Alemán, C. Electroresponsive and PH-Sensitive Hydrogel as Carrier for Controlled Chloramphenicol Release. *Biomacromolecules* **2023**, *24* (3), 1432–1444. https://doi.org/10.1021/acs.biomac.2c01442.

(67) Gautam, R.; Matai, I.; Soni, S. Photothermally Modulated Drug Release Kinetics for PH and Thermo-Responsive Hydrogel System. *J Mater Res* **2023**, *39* (3), 398–411. https://doi.org/10.1557/s43578-023-01233-0.

(68) de Oliveira Pedro, R.; Goycoolea, F. M.; Pereira, S.; Schmitt, C. C.; Neumann, M. G. Synergistic Effect of Quercetin and PH-Responsive DEAE-Chitosan Carriers as Drug Delivery System for Breast Cancer Treatment. *Int J Biol Macromol* **2018**, *106*, 579–586. https://doi.org/10.1016/j.ijbiomac.2017.08.056.

(69) Xu, L.; Qiu, L.; Sheng, Y.; Sun, Y.; Deng, L.; Li, X.; Bradley, M.; Zhang, R. Biodegradable PH-Responsive Hydrogels for Controlled Dual-Drug Release. *J Mater Chem B* **2018**, *6* (3), 510–517. https://doi.org/10.1039/C7TB01851G.

(70) Akkaya, B.; Akkaya, R.; Celikkaya, S. I.; Sarıaydin, N.; Raheem, K. Y. Doxorubucin Loaded PH-Responsive Chitosan-Poly(Acrylamide-Maleic Acid) Composite Hydrogel for Anticancer Targeting. *J Mol Struct* **2023**, *1274*, 134536. https://doi.org/10.1016/J.MOLSTRUC.2022.134536.

(71) Sabzini, M.; Pourmadadi, M.; Yazdian, F.; Khadiv-Parsi, P.; Rashedi, H. Development of Chitosan/Halloysite/Graphitic-carbon Nitride Nanovehicle for Targeted Delivery of Quercetin to Enhance Its Limitation in Cancer Therapy: An in Vitro Cytotoxicity against MCF-7 Cells. *Int J Biol Macromol* **2023**, *226*, 159–171. https://doi.org/10.1016/J.IJBIOMAC.2022.11.189.

(72) Fathi, M.; Alami-Milani, M.; Geranmayeh, M. H.; Barar, J.; Erfan-Niya, H.; Omidi, Y. Dual Thermo- and PH-Sensitive Injectable Hydrogels of Chitosan/(Poly(N-Isopropylacrylamide-Co-Itaconic Acid)) for Doxorubicin Delivery in Breast Cancer. *Int J Biol Macromol* **2019**, *128*, 957–964. https://doi.org/10.1016/J.IJBIOMAC.2019.01.122.

(73) Howaili, F.; Özliseli, E.; Küçüktürkmen, B.; Razavi, S. M.; Sadeghizadeh, M.; Rosenholm, J. M. Stimuli-Responsive, Plasmonic Nanogel for Dual Delivery of Curcumin and Photothermal Therapy for Cancer Treatment. *Front Chem* **2021**, *8*, 602941. https://doi.org/10.3389/FCHEM.2020.602941/BIBTEX.

(74) Fong, Y. T.; Chen, C. H.; Chen, J. P. Intratumoral Delivery of Doxorubicin on Folate-Conjugated Graphene Oxide by In-Situ Forming Thermo-Sensitive Hydrogel for Breast Cancer Therapy. *Nanomaterials 2017, Vol. 7, Page 388* **2017**, *7* (11), 388. https://doi.org/10.3390/NANO7110388.

(75) Liu, W.; Zhang, X.; Zhou, L.; Shang, L.; Su, Z. Reduced Graphene Oxide (RGO) Hybridized Hydrogel as a near-Infrared (NIR)/PH Dual-Responsive Platform for Combined Chemo-Photothermal Therapy. *J Colloid Interface Sci* **2019**, *536*, 160–170. https://doi.org/10.1016/J.JCIS.2018.10.050.

(76) Zhan, J.; Wu, Y.; Wang, H.; Liu, J.; Ma, Q.; Xiao, K.; Li, Z.; Li, J.; Luo, F.; Tan, H. An Injectable Hydrogel with PH-Sensitive and Self-Healing Properties Based on 4armPEGDA and N-Carboxyethyl Chitosan for Local Treatment of Hepatocellular Carcinoma. *Int J Biol Macromol* **2020**, *163*, 1208–1222. https://doi.org/10.1016/J.IJBIOMAC.2020.07.008.

(77) Cimen, Z.; Babadag, S.; Odabas, S.; Altuntas, S.; Demirel, G.; Demirel, G. B. Injectable and Self-Healable PH-Responsive Gelatin-PEG/Laponite Hybrid Hydrogels as Long-Acting Implants for Local Cancer Treatment. *ACS Appl Polym Mater* **2021**, *3* (7), 3504–3518. https://doi.org/10.1021/ACSAPM.1C00419/SUPPL_FILE/AP1C00419_SI_005.MP4.

(78) Javanbakht, S.; Nabi, M.; Shaabani, A. Graphene Quantum Dots-Crosslinked Gelatin via the Efficient Ugi Four-Component Reaction: Safe Photoluminescent Implantable Carriers for the PH-Responsive Delivery of Doxorubicin. *Materialia (Oxf)* **2021**, *20*, 101233. https://doi.org/10.1016/J.MTLA.2021.101233.

(79) Daneshmoghanlou, E.; Miralinaghi, M.; Moniri, E.; Sadjady, S. K. Fabrication of a PH-Responsive Magnetic Nanocarrier Based on Carboxymethyl Cellulose-Aminated Graphene Oxide for Loading and In-Vitro Release of Curcumin. *J Polym Environ* **2022**, *30* (9), 3718–3736. https://doi.org/10.1007/S10924-022-02467-5/METRICS.

(80) Ghasemizadeh, H.; Pourmadadi, M.; Yazdian, F.; Rashedi, H.; Navaei-Nigjeh, M.; Rahdar, A.; Díez-Pascual, A. M. Novel Carboxymethyl Cellulose-Halloysite-Polyethylene Glycol Nanocomposite for Improved 5-FU Delivery. *Int J Biol Macromol* **2023**, *232*, 123437. https://doi.org/10.1016/J.IJBIOMAC.2023.123437.

(81) Kouser, R.; Vashist, A.; Zafaryab, M.; Rizvi, M. A.; Ahmad, S. Na-Montmorillonite-Dispersed Sustainable Polymer Nanocomposite Hydrogel Films for Anticancer Drug Delivery. *ACS Omega* **2018**, *3* (11), 15809–15820. https://doi.org/10.1021/ACSOMEGA.8B01691/ASSET/IMAGES/MEDIUM/AO-2018-01691Q_M005.GIF.

(82) Pourmadadi, M.; Darvishan, S.; Abdouss, M.; Yazdian, F.; Rahdar, A.; Díez-Pascual, A. M. PH-Responsive Polyacrylic Acid (PAA)-Carboxymethyl Cellulose (CMC) Hydrogel Incorporating Halloysite Nanotubes (HNT) for Controlled Curcumin Delivery. *Ind Crops Prod* **2023**, *197*, 116654. https://doi.org/10.1016/J.INDCROP.2023.116654.

(83) Salehi, M.; Pourmadadi, M.; Abdouss, M.; Rahdar, A.; Díez-Pascual, A. M. Novel Carboxymethyl Cellulose/Polyvinyl Pyrrolidone Hydrogel Incorporating Graphitic Carbon Nitride for Quercetin Delivery. *Inorg Chem Commun* **2024**, *160*, 111932. https://doi.org/10.1016/J.INOCHE.2023.111932.

(84) Zhang, J.; Lin, W.; Yang, L.; Zhang, A.; Zhang, Y.; Liu, J.; Liu, J. Injectable and PH-Responsive Self-Assembled Peptide Hydrogel for Promoted Tumor Cell Uptake and Enhanced Cancer Chemotherapy. *Biomater Sci* **2022**, *10* (3), 854–862. https://doi.org/10.1039/D1BM01788H.

(85) Raza, F.; Zhu, Y.; Chen, L.; You, X.; Zhang, J.; Khan, A.; Khan, M. W.; Hasnat, M.; Zafar, H.; Wu, J.; Ge, L. Paclitaxel-Loaded PH Responsive Hydrogel Based on Self-Assembled Peptides for Tumor Targeting. *Biomater Sci* **2019**, *7* (5), 2023–2036. https://doi.org/10.1039/C9BM00139E.

(86) Eskandani, M.; Derakhshankhah, H.; Zare, S.; Jahanban-Esfahlan, R.; Jaymand, M. Enzymatically Crosslinked Magnetic Starch-Grafted Poly(Tannic Acid) Hydrogel for “Smart” Cancer Treatment:

An in Vitro Chemo/Hyperthermia Therapy Study. *Int J Biol Macromol* **2023**, *253*, 127214. https://doi.org/10.1016/J.IJBIOMAC.2023.127214.

(87) Samadi, A.; Pourmadadi, M.; Yazdian, F.; Rashedi, H.; Navaei-Nigjeh, M.; Eufrasio-da-silva, T. Ameliorating Quercetin Constraints in Cancer Therapy with PH-Responsive Agarose-Polyvinylpyrrolidone -Hydroxyapatite Nanocomposite Encapsulated in Double Nanoemulsion. *Int J Biol Macromol* **2021**, *182*, 11–25. https://doi.org/10.1016/J.IJBIOMAC.2021.03.146.

(88) Farzanfar, J.; Farjadian, F.; Roointan, A.; Mohammadi-Samani, S.; Tayebi, L. Assessment of PH Responsive Delivery of Methotrexate Based on PHEMA-St-PEG-DA Nanohydrogels. *Macromol Res* **2021**, *29* (1), 54–61. https://doi.org/10.1007/S13233-021-9007-6/METRICS.

(89) Comert Onder, F.; Kalin, S.; Onder, A.; Ozay, H.; Ozay, O. Assessment of Release and Anticancer Effect of Innovative PH-Responsive and Antioxidant-Biodegradable Hydrogel by Using Parthenocissus Quinquefolia L. Extract as a Crosslinker. *J Drug Deliv Sci Technol* **2023**, *90*, 105113. https://doi.org/10.1016/J.JDDST.2023.105113.

(90) Vijayan, V. M.; Shenoy, S. J.; Victor, S. P.; Muthu, J. Stimulus Responsive Nanogel with Innate near IR Fluorescent Capability for Drug Delivery and Bioimaging. *Colloids Surf B Biointerfaces* **2016**, *146*, 84–96. https://doi.org/10.1016/J.COLSURFB.2016.05.059.

(91) Zhang, X.; Wei, P.; Wang, Z.; Zhao, Y.; Xiao, W.; Bian, Y.; Liang, D.; Lin, Q.; Song, W.; Jiang, W.; Wang, H. Herceptin-Conjugated DOX-Fe3O4/P(NIPAM-AA-MAPEG) Nanogel System for HER2-Targeted Breast Cancer Treatment and Magnetic Resonance Imaging. *ACS Appl Mater Interfaces* **2022**, *14* (14), 15956–15969. https://doi.org/10.1021/ACSAMI.1C24770/SUPPL_FILE/AM1C24770_SI_001.PDF.

(92) Santhamoorthy, M.; Vy Phan, T. T.; Ramkumar, V.; Raorane, C. J.; Thirupathi, K.; Kim, S. C. Thermo-Sensitive Poly (N-Isopropylacrylamide-Co-Polyacrylamide) Hydrogel for PH-Responsive Therapeutic Delivery. *Polymers 2022, Vol. 14, Page 4128* **2022**, *14* (19), 4128. https://doi.org/10.3390/POLYM14194128.

(93) Laganà, A.; Facciolà, A.; Iannazzo, D.; Celesti, C.; Polimeni, E.; Biondo, C.; Di Pietro, A.; Visalli, G. Promising Materials in the Fight against Healthcare-Associated Infections: Antibacterial Properties of Chitosan-Polyhedral Oligomeric Silsesquioxanes Hybrid Hydrogels. *J Funct Biomater* **2023**, *14* (428), 1–15. https://doi.org/10.3390/jfb14080428.

(94) Chen, J.; Wang, S.; Zhang, H.; Li, H.; Wang, F.; Wang, Y.; Zhao, Q. Temperature/Redox Dual-Responsive Self-Assembled Nanogels for Targeting Delivery of Curcumol to Enhance Anti-Tumor and Anti-Metastasis Activities against Breast Cancer. *J Drug Deliv Sci Technol* **2024**, *92* (105389). https://doi.org/10.1016/j.jddst.2024.105389.

(95) Tian, Y.; Wang, Y.; Shen, S.; Jiang, X.; Wang, Y.; Yang, W. Temperature and Redox Dual-Responsive Biodegradable Nanogels for Optimizing Antitumor Drug Delivery. *Particle and Particle Systems Characterization* **2015**, *32*, 1092–1101. https://doi.org/10.1002/ppsc.201500153.

(96) Qin, F.; Zhou, H.; Li, J.; Liu, J.; Wang, Y.; Bai, R.; Liu, S.; Ma, M.; Liu, T.; Gao, F.; Du, P.; Lu, X.; Chen, C. Hypoxia and PH Co-Triggered Oxidative Stress Amplifier for Tumor Therapy. *Eur J Pharmacol* **2021**, *905* (174187). https://doi.org/10.1016/j.ejphar.2021.174187.

(97) Shi, J.; Wang, Y.; Wu, Y.; Li, J.; Fu, C.; Li, Y.; Xie, X.; Fan, X.; Hu, Y.; Hu, C.; Zhang, J. Tumor Microenvironment ROS / PH Cascade-Responsive Supramolecular Nanoplatform with ROS Regeneration Property for Enhanced Hepatocellular Carcinoma Therapy. *ACS Appl Mater Interfaces* **2024**. https://doi.org/10.1021/acsami.3c16022.

(98) Fang, Y.; Jiang, Y.; Zou, Y.; Meng, F.; Zhang, J.; Deng, C.; Sun, H.; Zhong, Z. Targeted Glioma Chemotherapy by Cyclic RGD Peptide-Functionalized Reversibly Core-Crosslinked Multifunctional Poly(Ethylene Glycol)-b-Poly(ε-Caprolactone) Micelles. *Acta Biomater* **2017**, *50*, 396–406. https://doi.org/10.1016/j.actbio.2017.01.007.

(99) Lili, Y.; Ruihua, M.; Li, L.; Fei, L.; Lin, Y.; Li, S. Intracellular Doxorubicin Delivery of a Core Cross-Linked, Redox-Responsive Polymeric Micelles. *Int J Pharm* **2016**, *498*, 195–204. https://doi.org/10.1016/j.ijpharm.2015.12.042.

(100) Fu, H.; Shi, K.; Hu, G.; Yang, Y.; Kuang, Q.; Lu, L.; Zhang, L.; Chen, W.; Dong, M.; Chen, Y.; He, Q. Tumor-Targeted Paclitaxel Delivery and Enhanced Penetration Using TAT-Decorated Liposomes Comprising Redox-Responsive Poly(Ethylene Glycol). *J Pharm Sci* **2015**, *103*, 1160–1173. https://doi.org/10.1002/jps.24291.

(101) Wang, X.; Li, L.; Wang, D.; Zuo, S.; Liu, T.; Dong, F.; Zhang, X.; He, Z.; Sun, B.; Sun, J. Minor Change in the Length of Carbon Chain Has a Great Influence on the Antitumor Effect of Paclitaxel-Fatty Alcohol Prodrug Nanoassemblies: Small Roles, Big Impacts. *Nano Res* **2022**, *15* (4), 3367–3375. https://doi.org/10.1007/s12274-021-3895-9.

(102) Zheng, J.; Wu, Y.; Xing, D.; Zhang, T. Synchronous Detection of Glutathione/Hydrogen Peroxide for Monitoring Redox Status in Vivo with a Ratiometric Upconverting Nanoprobe. *Nano Res* **2019**, *12* (4), 931–938. https://doi.org/10.1007/S12274-019-2327-6/METRICS.

(103) Krouskop, T. A.; Wheeler, T. M.; Kallel, F.; Garra, B. S.; Hall, T. Elastic Moduli of Breast and Prostate Tissues under Compression. *Ultrason Imaging* **1998**, *20* (4), 260–274. https://doi.org/10.1177/016173469802000403.

(104) Subba, S. H.; Park, S. Y. In Situ Cancer-Cell-Triggered Visible Changes in Mechanical Properties, Electroconductivity, and Adhesiveness of a MnO2@PD-Based Mineralized Hydrogel. *ACS Appl*

Mater Interfaces **2023**, *15* (32), 38357–38366. https://doi.org/10.1021/ACSAMI.3C08501/ASSET/IMAGES/LARGE/AM3C08501_0005.JPEG.

(105) Wang, Q.; Wang, C.; Wang, X.; Zhang, Y.; Wu, Y.; Dong, C.; Shuang, S. Construction of CPs@MnO2–AgNPs as a Multifunctional Nanosensor for Glutathione Sensing and Cancer Theranostics. *Nanoscale* **2019**, *11* (40), 18845–18853. https://doi.org/10.1039/C9NR06443E.

(106) Qin, X.; Wang, Z.; Guo, C.; Jin, Y. Multi-Responsive Drug Delivery Nanoplatform for Tumor-Targeted Synergistic Photothermal/Dynamic Therapy and Chemotherapy. *New J. Chem* **2020**, *44*, 3593. https://doi.org/10.1039/c9nj05650e.

(107) Duan, Q.; Gao, J.; Zhang, Q.; Wang, X.; Li, H.; Guo, X.; Han, D.; Wang, X.; Xi, Y.; Guo, L.; Li, P.; Xue, J.; Sang, S. Photothermal Effects of Supra-CNDs@GelMA Composite Hydrogels under near-Infrared Stimulation. *Colloids Surf A Physicochem Eng Asp* **2024**, *682* (132862). https://doi.org/10.1016/j.colsurfa.2023.132862.

(108) Yang, W.; Wang, L.; Fan, L.; Li, W.; Zhao, Y.; Shang, L.; Jiang, M. Photothermal Responsive Microcarriers Encapsulated With Cangrelor and 5-Fu for Colorectal Cancer Treatment. *Small Methods* **2023**, *2301002*, 1–12. https://doi.org/10.1002/smtd.202301002.

(109) Zhao, Y.; Zhao, T.; Cao, Y.; Sun, J.; Zhou, Q.; Chen, H.; Guo, S.; Wang, Y.; Zhen, Y.; Liang, X. J.; Zhang, S. Temperature-Sensitive Lipid-Coated Carbon Nanotubes for Synergistic Photothermal Therapy and Gene Therapy. *ACS Nano* **2021**, *15*, 6517–6529. https://doi.org/10.1021/acsnano.0c08790.

(110) Yang, G.; Liu, Y.; Chen, J.; Ding, J.; Chen, X. Self-Adaptive Nanomaterials for Rational Drug Delivery in Cancer Therapy. *Acc Mater Res* **2022**, *3*, 1232–1247. https://doi.org/10.1021/accountsmr.2c00147.

(111) Dadwal, A.; Baldi, A.; Kumar Narang, R. Nanoparticles as Carriers for Drug Delivery in Cancer. *Artif Cells Nanomed Biotechnol* **2018**, *46* (S2), 295–305. https://doi.org/10.1080/21691401.2018.1457039.

(112) Zhang, Y.; Li, J.; Pu, K. Recent Advances in Dual- and Multi-Responsive Nanomedicines for Precision Cancer Therapy. *Biomaterials* **2022**, *291*, 121906. https://doi.org/10.1016/J.BIOMATERIALS.2022.121906.

(113) Kosmides, A. K.; Necochea, K.; Hickey, J. W.; Schneck, J. P. Separating T Cell Targeting Components onto Magnetically Clustered Nanoparticles Boosts Activation. *Nano Lett* **2018**, *18* (3), 1916–1924. https://doi.org/10.1021/acs.nanolett.7b05284.

(114) Thirunavukkarasu, G. K.; Cherukula, K.; Lee, H.; Jeong, Y. Y.; Park, I. K.; Lee, J. Y. Magnetic Field-Inducible Drug-Eluting Nanoparticles for Image-Guided Thermo-Chemotherapy. *Biomaterials* **2018**, *180*, 240–252. https://doi.org/10.1016/j.biomaterials.2018.07.028.

(115) Ghazimoradi, M.; Tarlani, A.; Alemi, A.; Ghorbani, M.; Hamishehkar, H.; Varma, R. S. Design and Synthesis of Novel Trifunctional Drug Carrier Comprising Luminescent-Magnetic Nanocomposite Adorned with a PH-Sensitive Copolymer as a Controlled Switch for Dual Drug Delivery. *J Alloys Compd* **2024**, *980* (173451). https://doi.org/10.1016/j.jallcom.2024.173451.

(116) Carvalho, J. A Bioelectric Model of Carcinogenesis, Including Propagation of Cell Membrane Depolarization and Reversal Therapies. *Sci Rep* **2021**, *11* (13607), 1–11. https://doi.org/10.1038/s41598-021-92951-0.

(117) Jain, A.; Jobson, I.; Griffin, M.; Rahman, R.; Smith, S.; Rawson, F. J. Electric Field Responsive Nanotransducers for Glioblastoma. *Bioelectron Med* **2022**, *8* (1), 1–9. https://doi.org/10.1186/S42234-022-00099-7/FIGURES/3.

(118) Berkelmann, L.; Bader, A.; Meshksar, S.; Dierks, A.; Hatipoglu Majernik, G.; Krauss, J. K.; Schwabe, K.; Manteuffel, D.; Ngezahayo, A. Tumour-Treating Fields (TTFields): Investigations on the Mechanism of Action by Electromagnetic Exposure of Cells in Telophase/Cytokinesis. *Sci Rep* **2019**, *9* (7362), 1–11. https://doi.org/10.1038/s41598-019-43621-9.

(119) Hsieh, C. H.; Lu, C. H.; Chen, W. T.; Ma, B. L.; Chao, C. Y. Application of Non-Invasive Low Strength Pulsed Electric Field to EGCG Treatment Synergistically Enhanced the Inhibition Effect on PANC-1 Cells. *PLoS One* **2017**, *12* (11), 1–17. https://doi.org/10.1371/journal.pone.0188885.

(120) Radu, E. R.; Semenescu, A.; Voicu, S. I. Recent Advances in Stimuli-Responsive Doxorubicin Delivery Systems for Liver Cancer Therapy. *Polymers 2022, Vol. 14, Page 5249* **2022**, *14* (23), 5249. https://doi.org/10.3390/POLYM14235249.

(121) Lee, H.; Hong, W.; Jeon, S.; Choi, Y.; Cho, Y. Electroactive Polypyrrole Nanowire Arrays: Synergistic Effect of Cancer Treatment by on-Demand Drug Release and Photothermal Therapy. *Langmuir* **2015**, *31* (14), 4264–4269. https://doi.org/https://doi.org/10.1021/acs.langmuir.5b00534.

(122) Oktay, S.; Alemdar, N. Electrically Controlled Release of 5-Fluorouracil from Conductive Gelatin Methacryloyl-Based Hydrogels. *J Appl Polym Sci* **2019**, *46914*, 1–8. https://doi.org/10.1002/app.46914.

(123) Geuli, O.; Miller, M.; Leader, A.; He, L.; Melamed-Book, N.; Tshuva, E. Y.; Reches, M.; Mandler, D. Electrochemical Triggered Dissolution of Hydroxyapatite/Doxorubicin Nanocarriers. *ACS Appl Bio Mater* **2019**, *2* (5), 1956–1966. https://doi.org/10.1021/acsabm.9b00011.

(124) Puiggalí-Jou, A.; Micheletti, P.; Estrany, F.; del Valle, L. J.; Alemán, C. Electrostimulated Release of Neutral Drugs from Polythiophene Nanoparticles: Smart Regulation of Drug–Polymer Interactions. *Adv Healthc Mater* **2017**, *6* (18), 1–11. https://doi.org/10.1002/adhm.201700453.

(125) Puiggalí-Jou, A.; Del Valle, L. J.; Alemán, C. Encapsulation and Storage of Therapeutic Fibrin-Homing Peptides Using Conducting Polymer Nanoparticles for Programmed Release by Electrical Stimulation. *ACS Biomater Sci Eng* **2020**, *6* (4), 2135–2145. https://doi.org/10.1021/acsbiomaterials.9b01794.

(126) Sonaje, K.; Tyagi, V.; Chen, Y.; Kalia, Y. N. Iontosomes: Electroresponsive Liposomes for Topical Iontophoretic Delivery of Chemotherapeutics to the Buccal Mucosa. *Pharmaceutics* **2021**, *13* (1), 1–19. https://doi.org/10.3390/pharmaceutics13010088.

(127) Neumann, S. E.; Chamberlayne, C. F.; Zare, R. N. Electrically Controlled Drug Release Using PH-Sensitive Polymer Films. *Nanoscale* **2018**, *10* (21), 10087–10093. https://doi.org/10.1039/c8nr02602e.

(128) Puiggalí-Jou, A.; Cejudo, A.; Del Valle, L. J.; Alemán, C. Smart Drug Delivery from Electrospun Fibers through Electroresponsive Polymeric Nanoparticles. *ACS Appl Bio Mater* **2018**, *1* (5), 1594–1605. https://doi.org/10.1021/acsabm.8b00459.

(129) Resina, L.; Garrudo, F. F. F.; Alemán, C.; Esteves, T.; Ferreira, F. C. Wireless Electrostimulation for Cancer Treatment: An Integrated Nanoparticle/Coaxial Fiber Mesh Platform. *Biomaterials Advances* **2024**, 213830. https://doi.org/10.1016/J.BIOADV.2024.213830.

(130) Resina, L.; Esteves, T.; Pérez-Rafael, S.; García, J. I. H.; Ferreira, F. C.; Tzanov, T.; Bonardd, S.; Díaz, D. D.; Pérez-Madrigal, M. M.; Alemán, C. Dual electro-/pH-responsive nanoparticle/hydrogel system for controlled delivery of anticancer peptide. *Biomaterials Advances* **2024**, 213925. https://doi.org/10.1016/j.bioadv.2024.213925.

(131) Puiggalí-Jou, A.; Cejudo, A.; Del Valle, L. J.; Alemán, C. Smart Drug Delivery from Electrospun Fibers through Electroresponsive Polymeric Nanoparticles. *ACS Appl Bio Mater* **2018**, *1* (5), 1594–1605. https://doi.org/10.1021/ACSABM.8B00459/SUPPL_FILE/MT8B00459_SI_001.PDF.

(132) Puiggalí-Jou, A.; del Valle, L. J.; Alemán, C. Cell Responses to Electrical Pulse Stimulation for Anticancer Drug Release. *Materials* **2019**, *12* (16), 1–15. https://doi.org/10.3390/ma12162633.

(133) Puiggalí-Jou, A.; Del Valle, L. J.; Alemán, C. Encapsulation and Storage of Therapeutic Fibrin-Homing Peptides Using Conducting Polymer Nanoparticles for Programmed Release by Electrical Stimulation. *ACS Biomater Sci Eng* **2020**, *6* (4), 2135–2145. https://doi.org/10.1021/acsbiomaterials.9b01794.

(134) Ansari, S.; Masoum, S. Molecularly Imprinted Polymers for Capturing and Sensing Proteins: Current Progress and Future Implications. *Trends in Analytical Chemistry* **2019**, *114*, 29–47. https://doi.org/10.1016/j.trac.2019.02.008.

(135) Alexander, C.; Andersson, H. S.; Andersson, L. I.; Ansell, R. J.; Kirsch, N.; Nicholls, I. A.; O'Mahony, J.; Whitcombe, M. J. Molecular Imprinting Science and Technology: A Survey of the Literature

for the Years up to and Including 2003. *Journal of Molecular Recognition* **2006**, *19* (2), 106–180. https://doi.org/10.1002/jmr.760.

(136) Whitcombe, M. J.; Kirsch, N.; Nicholls, I. A. Molecular Imprinting Science and Technology: A Survey of the Literature for the Years 2004-2011. *Journal of Molecular Recognition* **2014**, *27* (6), 297–401. https://doi.org/10.1002/jmr.2347.

(137) Scriba, G. K. E. Chiral Recognition in Separation Science – an Update. *J Chromatogr A* **2016**, *1467*, 56–78. https://doi.org/10.1016/j.chroma.2016.05.061.

(138) Hui Lee, S.; Doong, R. A. Design of Size-Tunable Molecularly Imprinted Polymer for Selective Adsorption of Pharmaceuticals and Biomolecules. *J Biosens Bioelectron* **2016**, *07* (04). https://doi.org/10.4172/2155-6210.1000228.

(139) Ping Li; Fei Rong; Yibing Xie; Van Hu; Chunwei Yuan. Study on the Binding Characteristic of S-Naproxen Imprinted Polymer and the Interactions between Templates and Monomers. *Zhurnal Analiticheskoj Khimii* **2004**, *59* (10), 1043–1048.

(140) Hammam, M. A.; Wagdy, H. A.; El Nashar, R. M. Moxifloxacin Hydrochloride Electrochemical Detection Based on Newly Designed Molecularly Imprinted Polymer. *Sens Actuators B Chem* **2018**, *275* (August), 127–136. https://doi.org/10.1016/j.snb.2018.08.041.

(141) Lin, J. M.; Nakagama, T.; Uchiyama, K.; Hobo, T. Capillary Electrochromatographic Separation of Amino Acid Enantiomers Using On-Column Prepared Molecularly Imprinted Polymer. *J Pharm Biomed Anal* **1997**, *15* (9–10), 1351–1358. https://doi.org/10.1016/S0731-7085(96)02013-4.

(142) Mohajeri, S. A.; Ebrahimi, S. A. Preparation and Characterization of a Lamotrigine Imprinted Polymer and Its Application for Drug Assay in Human Serum. *J Sep Sci* **2008**, *31* (20), 3595–3602. https://doi.org/10.1002/jssc.200800377.

(143) Haginaka, J.; Sakai, Y. Uniform-Sized Molecularly Imprinted Polymer Material for (S)-Propranolol. *J Pharm Biomed Anal* **2000**, *22* (6), 899–907. https://doi.org/10.1016/S0731-7085(00)00293-4.

(144) Suedee, R.; Srichana, T.; Rattananont, T. Enantioselective Release of Controlled Delivery Granules Based on Molecularly Imprinted Polymers. *Drug Delivery: Journal of Delivery and Targeting of Therapeutic Agents* **2002**, *9* (1), 19–30. https://doi.org/10.1080/107175402753413145.

(145) Trinh, T.; Liao, C.; Toader, V.; Barlóg, M.; Bazzi, H. S.; Li, J.; Sleiman, H. F. DNA-Imprinted Polymer Nanoparticles with Monodispersity and Prescribed DNA-Strand Patterns. *Nat Chem* **2018**, *10* (2), 184–192. https://doi.org/10.1038/NCHEM.2893.

(146) Liustrovaite, V.; Pogorielov, M.; Boguzaite, R.; Ratautaite, V.; Ramanaviciene, A.; Pilvenyte, G.; Holubnycha, V.; Korniienko, V.; Diedkova, K.; Viter, R.; Ramanavicius, A. Towards

Electrochemical Sensor Based on Molecularly Imprinted Polypyrrole for the Detection of Bacteria—Listeria Monocytogenes. *Polymers (Basel)* **2023**, *15* (1597). https://doi.org/10.3390/polym15071597.

(147) Poma, A.; Guerreiro, A.; Whitcombe, M. J.; Elena, V. Solid-Phase Synthesis of Molecularly Imprinted Polymer Nanoparticles with a Reusable Template – " Plastic Antibodies ." *Adv Funct Mater* **2013**, *23* (22), 2821–2827. https://doi.org/10.1002/adfm.201202397.

(148) Arabi, M.; Ostovan, A.; Zhang, Z.; Wang, Y.; Mei, R.; Fu, L.; Wang, X.; Ma, J.; Chen, L. Label-Free SERS Detection of Raman-Inactive Protein Biomarkers by Raman Reporter Indicator: Toward Ultrasensitivity and Universality. *Biosens Bioelectron* **2021**, *174*, 112825. https://doi.org/10.1016/J.BIOS.2020.112825.

(149) Ratautaite, V.; Boguzaite, R.; Brazys, E.; Plausinaitis, D.; Ramanavicius, S.; Samukaite-Bubniene, U.; Bechelany, M.; Ramanavicius, A. Evaluation of the Interaction between SARS-CoV-2 Spike Glycoproteins and the Molecularly Imprinted Polypyrrole. *Talanta* **2023**, *253* (123981).

(150) Ratautaite, V.; Boguzaite, R.; Brazys, E.; Ramanaviciene, A.; Ciplys, E.; Juozapaitis, M.; Slibinskas, R.; Bechelany, M.; Ramanavicius, A. Molecularly Imprinted Polypyrrole Based Sensor for the Detection of SARS-CoV-2 Spike Glycoprotein. *Electrochim Acta* **2022**, *403* (139581). https://doi.org/10.1016/j.electacta.2021.139581.

(151) Arbabi-Ghahroudi, M. Camelid Single-Domain Antibodies: Promises and Challenges as Lifesaving Treatments. *Int J Mol Sci* **2022**, *23* (5009). https://doi.org/10.3390/ijms23095009.

(152) Asaadi, Y.; Jouneghani, F. F.; Janani, S.; Rahbarizadeh, F. A Comprehensive Comparison between Camelid Nanobodies and Single Chain Variable Fragments. *Biomark Res* **2021**, *9* (87). https://doi.org/10.1186/s40364-021-00332-6.

(153) Liu, Y.; Huang, H. Expression of Single-Domain Antibody in Different Systems. *Appl Microbiol Biotechnol* **2018**, *102* (2), 539–551. https://doi.org/10.1007/s00253-017-8644-3.

(154) Malaquias, A. D. M.; Marques, L. E. C.; Pereira, S. S.; de Freitas Fernandes, C.; Maranhão, A. Q.; Stabeli, R. G.; Florean, E. O. P. T.; Guedes, M. I. F.; Fernandes, C. F. C. A Review of Plant-Based Expression Systems as a Platform for Single-Domain Recombinant Antibody Production. *Int J Biol Macromol* **2021**, *193*, 1130–1137. https://doi.org/10.1016/j.ijbiomac.2021.10.126.

(155) Mark, J. K. K.; Lim, C. S. Y.; Nordin, F.; Tye, G. J. Expression of Mammalian Proteins for Diagnostics and Therapeutics: A Review. *Mol Biol Rep* **2022**, *49* (11), 10593–10608. https://doi.org/10.1007/s11033-022-07651-3.

(156) Thompson, M. K.; Fridy, P. C.; Keegan, S.; Chait, B. T.; Fenyö, D.; Rout, M. P. Optimizing Selection of Large Animals for Antibody Production by Screening Immune Response to Standard Vaccines. *J Immunol Methods* **2016**, *430*, 56–60. https://doi.org/10.1016/j.jim.2016.01.006.

(157) Wackerlig, J.; Schirhagl, R. Applications of Molecularly Imprinted Polymer Nanoparticles and Their Advances toward Industrial Use: A Review. *Anal Chem* **2016**, *88* (1), 250–261. https://doi.org/10.1021/acs.analchem.5b03804.

(158) Ostovan, A.; Arabi, M.; Wang, Y.; Li, J.; Li, B.; Wang, X.; Chen, L. Greenificated Molecularly Imprinted Materials for Advanced Applications. *Advanced Materials* **2022**, *34* (42). https://doi.org/10.1002/adma.202203154.

(159) Canfarotta, F.; Lezina, L.; Guerreiro, A.; Czulak, J.; Petukhov, A.; Daks, A.; Smolinska-Kempisty, K.; Poma, A.; Piletsky, S.; Barlev, N. A. Specific Drug Delivery to Cancer Cells with Double-Imprinted Nanoparticles against Epidermal Growth Factor Receptor. *Nano Lett* **2018**, *18* (8), 4641–4646. https://doi.org/10.1021/acs.nanolett.7b03206.

(160) Chen, W.; Meng, Z.; Xue, M.; Shea, K. J. Molecular Imprinted Photonic Crystal for Sensing of Biomolecules. *Molecular Imprinting* **2016**, *4* (1), 1–12. https://doi.org/10.1515/molim-2016-0001.

(161) Pilvenyte, G.; Ratautaite, V.; Boguzaite, R.; Ramanavicius, A.; Viter, R.; Ramanavicius, S. Molecularly Imprinted Polymers for the Determination of Cancer Biomarkers. *Int J Mol Sci* **2023**, *24* (4). https://doi.org/10.3390/ijms24044105.

(162) Rebelo, T. S. C. R.; Costa, R.; Brandão, A. T. S. C.; Silva, A. F.; Sales, M. G. F.; Pereira, C. M. Molecularly Imprinted Polymer SPE Sensor for Analysis of CA-125 on Serum. *Anal Chim Acta* **2019**, *1082*, 126–135. https://doi.org/10.1016/j.aca.2019.07.050.

(163) Santos, A. R. T.; Moreira, F. T. C.; Helguero, L. A.; Sales, M. G. F. Antibody Biomimetic Material Made of Pyrrole for CA 15-3 and Its Application as Sensing Material in Ion-Selective Electrodes for Potentiometric Detection. *Biosensors (Basel)* **2018**, *8* (8). https://doi.org/10.3390/bios8010008.

(164) Yazdani, Z.; Yadegari, H.; Heli, H. A Molecularly Imprinted Electrochemical Nanobiosensor for Prostate Specific Antigen Determination. *Anal Biochem* **2019**, *566*, 116–125.

(165) Pilvenyte, G.; Ratautaite, V.; Boguzaite, R.; Plausinaitis, D.; Ramanaviciene, A.; Bechelany, M.; Ramanavicius, A. Molecularly Imprinted Polymers for the Recognition of Biomarkers for Some Neurodegenerative Diseases. *J Pharm Biomed Anal* **2023**, *228* (115343).

(166) Özcan, N.; Medetalibeyoglu, H.; Akyildirim, O.; Atar, N.; Yola, M. L. Electrochemical Detection of Amyloid-Beta Protein by Delaminated Titanium Carbide MXene/Multi-Walled Carbon Nanotubes Composite with Molecularly Imprinted Polymer. *Mater Today Commun* **2020**, *23* (101097).

(167) Lee, M.-H.; Thomas, J. L.; Su, Z.-L.; Yeh, W.-K.; Monzel, A. S.; Bolognin, S.; Schwamborn, J. C.; Yang, C.-H.; Lin, H.-Y. Epitope Imprinting of Alpha-Synuclein for Sensing in Parkinson's Brain Organoid Culture Medium. *Biosens Bioelectron* **2021**, *175* (112852).

(168) Canfarotta, F.; Poma, A.; Guerreiro, A.; Piletsky, S. Solid-Phase Synthesis of Molecularly Imprinted Nanoparticles. *Nat Protoc* **2016**, *11* (3), 443–455. https://doi.org/10.1038/nprot.2016.030.

(169) Ramanavicius, S.; Samukaite-Bubniene, U.; Ratautaite, V.; Bechelany, M.; Ramanavicius, A. Electrochemical Molecularly Imprinted Polymer Based Sensors for Pharmaceutical and Biomedical Applications (Review). *J Pharm Biomed Anal* **2022**, *215* (114739). https://doi.org/10.1016/j.jpba.2022.114739.

(170) Ramanavicius, S.; Ramanavicius, A. Development of Molecularly Imprinted Polymer Based Phase Boundaries for Sensors Design (Review). *Adv Colloid Interface Sci* **2022**, *305* (102693). https://doi.org/10.1016/j.cis.2022.102693.

(171) Tai, D. F.; Lin, C. Y.; Wu, T. Z.; Chen, L. K. Recognition of Dengue Virus Protein Using Epitope-Mediated Molecularly Imprinted Film. *Anal Chem* **2005**, *77* (16), 5140–5143. https://doi.org/10.1021/ac0504060.

(172) Cennamo, N.; D'agostino, G.; Perri, C.; Arcadio, F.; Chiaretti, G.; Parisio, E. M.; Camarlinghi, G.; Vettori, C.; Di Marzo, F.; Cennamo, R.; Porto, G.; Zeni, L. Proof of Concept for a Quick and Highly Sensitive On-Site Detection of Sars-Cov-2 by Plasmonic Optical Fibers and Molecularly Imprinted Polymers. *Sensors* **2021**, *21* (5), 1–17. https://doi.org/10.3390/s21051681.

(173) Liv, L.; Çoban, G.; Nakiboğlu, N.; Kocagöz, T. A Rapid, Ultrasensitive Voltammetric Biosensor for Determining SARS-CoV-2 Spike Protein in Real Samples. *Biosens Bioelectron* **2021**, *192* (January). https://doi.org/10.1016/j.bios.2021.113497.

(174) Sukjee, W.; Thitithanyanont, A.; Manopwisedjaroen, S.; Seetaha, S.; Thepparit, C.; Sangma, C. Virus MIP-Composites for SARS-CoV-2 Detection in the Aquatic Environment. *Mater Lett* **2022**, *315* (February), 131973. https://doi.org/10.1016/j.matlet.2022.131973.

(175) Raziq, A.; Kidakova, A.; Boroznjak, R.; Reut, J.; Öpik, A.; Syritski, V. Development of a Portable MIP-Based Electrochemical Sensor for Detection of SARS-CoV-2 Antigen. *Biosens Bioelectron* **2021**, *178* (November 2020). https://doi.org/10.1016/j.bios.2021.113029.

(176) Rachkov, A.; Minoura, N. Recognition of Oxytocin and Oxytocin-Related Peptides in Aqueous Media Using a Molecularly Imprinted Polymer Synthesized by the Epitope Approach. *J Chromatogr A* **2000**, *889* (1–2), 111–118. https://doi.org/10.1016/S0021-9673(00)00568-9.

(177) Zhang, Z.; Liu, J. Intracellular Delivery of a Molecularly Imprinted Peroxidase Mimicking DNAzyme for Selective Oxidation. *Mater Horiz* **2018**, *5* (4), 738–744. https://doi.org/10.1039/c8mh00453f.

(178) Tang, P.; Wang, Y.; Huo, J.; Lin, X. Love Wave Sensor for Prostate-Specific Membrane Antigen Detection Based on Hydrophilic Molecularly-Imprinted Polymer. *Polymers (Basel)* **2018**, *10* (5). https://doi.org/10.3390/polym10050563.

(179) Zhang, Y.; Deng, C.; Liu, S.; Wu, J.; Chen, Z.; Li, C.; Lu, W. Active Targeting of Tumors through Conformational Epitope Imprinting. *Angewandte Chemie - International Edition* **2015**, *54* (17), 5157–5160. https://doi.org/10.1002/anie.201412114.

(180) Han, S.; Su, L.; Zhai, M.; Ma, L.; Liu, S.; Teng, Y. A Molecularly Imprinted Composite Based on Graphene Oxide for Targeted Drug Delivery to Tumor Cells. *J Mater Sci* **2019**, *54* (4), 3331–3341. https://doi.org/10.1007/s10853-018-3023-8.

(181) Teixeira, S. P. B.; Reis, R. L.; Peppas, N. A.; Gomes, M. E.; A Domingues, R. M. Epitope-Imprinted Polymers: Design Principles of Synthetic Binding Partners for Natural Biomacromolecules. *Sci Adv* **2021**, *7* (eabi9884).

(182) Yang, K.; Li, S.; Liu, L.; Chen, Y.; Zhou, W.; Pei, J.; Liang, Z.; Zhang, L.; Zhang, Y. Epitope Imprinting Technology: Progress, Applications, and Perspectives toward Artificial Antibodies. *Advanced Materials* **2019**, *31* (50). https://doi.org/10.1002/adma.201902048.

(183) El Kirat, K.; Bartkowski, M.; Haupt, K. Probing the Recognition Specificity of a Protein Molecularly Imprinted Polymer Using Force Spectroscopy. *Biosens Bioelectron* **2009**, *24* (8), 2618–2624. https://doi.org/10.1016/j.bios.2009.01.018.

(184) Li, Y.; Yang, H. H.; You, Q. H.; Zhuang, Z. X.; Wang, X. R. Protein Recognition via Surface Molecularly Imprinted Polymer Nanowires. *Anal Chem* **2006**, *78* (1), 317–320. https://doi.org/10.1021/ac050802i.

(185) Ouyang, R.; Lei, J.; Ju, H. Artificial Receptor-Functionalized Nanoshell: Facile Preparation, Fast Separation and Specific Protein Recognition. *Nanotechnology* **2010**, *21* (18). https://doi.org/10.1088/0957-4484/21/18/185502.

(186) Kryscio, D. R.; Peppas, N. A. Surface Imprinted Thin Polymer Film Systems with Selective Recognition for Bovine Serum Albumin. *Anal Chim Acta* **2012**, *718*, 109–115. https://doi.org/10.1016/j.aca.2012.01.006.

(187) Guoning, C.; Hua, S.; Wang, L.; Qianqian, H.; Xia, C.; Hongge, Z.; Zhimin, L.; Chun, C.; Qiang, F. A Surfactant-Mediated Sol-Gel Method for the Preparation of Molecularly Imprinted Polymers and Its Application in a Biomimetic Immunoassay for the Detection of Protein. *J Pharm Biomed Anal* **2020**, *190*, 113511. https://doi.org/10.1016/J.JPBA.2020.113511.

(188) Shumyantseva, V. V.; Bulko, T. V.; Sigolaeva, L. V.; Kuzikov, A. V.; Archakov, A. I. Electrosynthesis and Binding Properties of Molecularly Imprinted Poly-o-Phenylenediamine for Selective Recognition and Direct Electrochemical Detection of Myoglobin. *Biosens Bioelectron* **2016**, *86*, 330–336. https://doi.org/10.1016/j.bios.2016.05.101.

(189) Hoshino, Y.; Kodama, T.; Okahata, Y.; Shea, K. J. Peptide Imprinted Polymer Nanoparticles: A Plastic Antibody. *J Am Chem Soc* **2008**, *130* (46), 15242–15243. https://doi.org/10.1021/ja8062875.

(190) Boysen, R. I. Advances in the Development of Molecularly Imprinted Polymers for the Separation and Analysis of Proteins with Liquid Chromatography. *J Sep Sci* **2019**, *42* (1), 51–71. https://doi.org/10.1002/jssc.201800945.

(191) Wang, P.; Zhu, H.; Liu, J.; Ma, Y.; Yao, J.; Dai, X.; Pan, J. Double Affinity Integrated MIPs Nanoparticles for Specific Separation of Glycoproteins: A Combination of Synergistic Multiple Bindings and Imprinting Effect. *Chemical Engineering Journal* **2019**, *358* (August 2018), 143–152. https://doi.org/10.1016/j.cej.2018.09.168.

(192) Wang, X.; Dong, S.; Bai, Q. Preparation of Lysozyme Molecularly Imprinted Polymers and Purification of Lysozyme from Egg White. *Biomedical Chromatography* **2014**, *28* (6), 907–912. https://doi.org/10.1002/bmc.3207.

(193) Yang, M.; Dong, Q.; Guan, Y.; Zhang, Y. Molecularly Imprinted Polymers with Shape-Memorable Imprint Cavities for Efficient Separation of Hemoglobin from Blood. *Biomacromolecules* **2023**. https://doi.org/10.1021/acs.biomac.2c01285.

(194) Zhang, W.; Qin, L.; He, X.-W.; Li, W.-Y.; Zhang, Y.-K. Novel Surface Modified Molecularly Imprinted Polymer Using Acrylol-Beta-Cyclodextrin and Acrylamide as Monomers for Selective Recognition of Lysozyme in Aqueous Solution. *J Chromatogr A* **2009**, *1216*, 4560–4567.

(195) Dabrowski, M.; Zimińska, A.; Kalecki, J.; Cieplak, M.; Lisowski, W.; Maksym, R.; Shao, S.; D'Souza, F.; Kuhn, A.; Sharma, P. S. Facile Fabrication of Surface-Imprinted Macroporous Films for Chemosensing of Human Chorionic Gonadotropin Hormone. *ACS Appl Mater Interfaces* **2019**, *11* (9), 9265–9276. https://doi.org/10.1021/acsami.8b17951.

(196) Ambrosini, S.; Beyazit, S.; Haupt, K.; Tse Sum Bui, B. Solid-Phase Synthesis of Molecularly Imprinted Nanoparticles for Protein Recognition. *Chemical Communications* **2013**, *49* (60), 6746–6748. https://doi.org/10.1039/c3cc41701h.

(197) Karimian, N.; Turner, A. P. F.; Tiwari, A. Electrochemical Evaluation of Troponin T Imprinted Polymer Receptor. *Biosens Bioelectron* **2014**, *59*, 160–165. https://doi.org/10.1016/j.bios.2014.03.013.

(198) Hussain, M.; Wackerlig, J.; Lieberzeit, P. A. Biomimetic Strategies for Sensing Biological Species. *Biosensors (Basel)* **2013**, *3* (1), 89–107. https://doi.org/10.3390/bios3010089.

(199) Jenik, M.; Schirhagl, R.; Schirk, C.; Hayden, O.; Lieberzeit, P.; Blaas, D.; Paul, G.; Dickert, F. L. Sensing Picornaviruses Using Molecular Imprinting Techniques on a Quartz Crystal Microbalance. *Anal Chem* **2009**, *81* (13), 5320–5326. https://doi.org/10.1021/ac8019569.

(200) Latif, U.; Qian, J.; Can, S.; Dickert, F. L. Biomimetic Receptors for Bioanalyte Detection by Quartz Crystal Microbalances — from Molecules to Cells. *Sensors (Switzerland)* **2014**, *14* (12), 23419–23438. https://doi.org/10.3390/s141223419.

(201) Schirhagl, R.; Lieberzeit, P. A.; Dickert, F. L. Chemosensors for Viruses Based on Artificial Immunoglobulin Copies. *Advanced Materials* **2010**, *22* (18), 2078–2081. https://doi.org/10.1002/adma.200903517.

(202) Culver, H. R.; Steichen, S. D.; Peppas, N. A. A Closer Look at the Impact of Molecular Imprinting on Adsorption Capacity and Selectivity for Protein Templates. *Biomacromolecules* **2016**, *17* (12), 4045–4053. https://doi.org/10.1021/acs.biomac.6b01482.

(203) Kryscio, D. R.; Fleming, M. Q.; Peppas, N. A. Conformational Studies of Common Protein Templates in Macromolecularly Imprinted Polymers. *Biomed Microdevices* **2012**, *14* (4), 679–687. https://doi.org/10.1007/s10544-012-9648-5.

(204) Tse Sum Bui, B.; Mier, A.; Haupt, K. Molecularly Imprinted Polymers as Synthetic Antibodies for Protein Recognition: The Next Generation. *Small* **2023**, *19* (2206453). https://doi.org/10.1002/smll.202206453.

(205) Nishino, H.; Huang, C. S.; Shea, K. J. Selective Protein Capture by Epitope Imprinting. *Angewandte Chemie - International Edition* **2006**, *45* (15), 2393–2396. https://doi.org/10.1002/anie.200503760.

(206) Zeng, Z.; Hoshino, Y.; Rodriguez, A.; Yoo, H.; Shea, K. J. Synthetic Polymer Nanoparticles with Antibody-Like Affinity for a Hydrophilic Peptide. *ACS Nano* **2011**, *4(1)* (199), 1–12. https://doi.org/doi:10.1021/nn901256s.

(207) Han, J.; Sun, Y.; Hou, J.; Wang, Y.; Liu, Y.; Xie, C.; Lu, W.; Pan, J. Preliminary Investigations into Surface Molecularly Imprinted Nanoparticles for Helicobacter Pylori Eradication. *Acta Pharm Sin B* **2015**, *5* (6), 577–582. https://doi.org/10.1016/j.apsb.2015.09.003.

(208) Arabi, M.; Ostovan, A.; Li, J.; Wang, X.; Zhang, Z.; Choo, J.; Chen, L. Molecular Imprinting: Green Perspectives and Strategies. *Advanced Materials* **2021**, *33* (2100543). https://doi.org/10.1002/adma.202100543.

(209) Rachkov, A.; Hu, M.; Bulgarevich, E.; Matsumoto, T.; Minoura, N. Molecularly Imprinted Polymers Prepared in Aqueous Solution Selective for [Sar1,Ala8]Angiotensin II. *Anal Chim Acta* **2004**, *504* (1), 191–197. https://doi.org/10.1016/S0003-2670(03)00764-5.

(210) Friguet, B.; Chaffotte, A. F.; Djavadi-Ohaniance, L.; Goldberg, M. E. Measurements of the True Affinity Constant in Solution of Antigen-Antibody Complexes by Enzyme-Linked Immunosorbent Assay. *J Immunol Methods* **1985**, *77* (2), 305–319. https://doi.org/10.1016/0022-1759(85)90044-4.

(211) Landry, J. P.; Ke, Y.; Yu, G. L.; Zhu, X. D. Measuring Affinity Constants of 1,450 Monoclonal Antibodies to Peptide Targets with a Microarray-Based Label-Free Assay Platform. *J Immunol Methods* **2015**, *417*, 86. https://doi.org/10.1016/J.JIM.2014.12.011.

(212) Pan, Y.; Sackmann, E. K.; Wypisniak, K.; Hornsby, M.; Datwani, S. S.; Herr, A. E. Determination of Equilibrium Dissociation Constants for Recombinant Antibodies by High-Throughput Affinity Electrophoresis. *Scientific Reports 2016 6:1* **2016**, *6* (1), 1–11. https://doi.org/10.1038/srep39774.

(213) Wang, Y.; Zhang, Z.; Jain, V.; Yi, J.; Mueller, S.; Sokolov, J.; Liu, Z.; Levon, K.; Rigas, B.; Rafailovich, M. H. Potentiometric Sensors Based on Surface Molecular Imprinting: Detection of Cancer Biomarkers and Viruses. *Sens Actuators B Chem* **2010**, *146* (1), 381–387. https://doi.org/10.1016/j.snb.2010.02.032.

(214) Ramanaviciene, A.; Ramanavicius, A. Molecularly Imprinted Polypyrrole-Based Synthetic Receptor for Direct Detection of Bovine Leukemia Virus Glycoproteins. *Biosens Bioelectron* **2004**, *20*, 1076–1082. https://doi.org/10.1016/j.bios.2004.05.014.

(215) Zukauskas, S.; Rucinskiene, A.; Ratautaite, V.; Ramanaviciene, A.; Pilvenyte, G.; Bechelany, M.; Ramanavicius, A. Electrochemical Biosensor for the Determination of Specific Antibodies against SARS-CoV-2 Spike Protein. *Int J Mol Sci* **2023**, *24* (1). https://doi.org/10.3390/ijms24010718.

(216) Lim, H. J.; Saha, T.; Tey, B. T.; Lal, S. K.; Ooi, C. W. Quartz Crystal Microbalance-Based Biosensing of Proteins Using Molecularly Imprinted Polydopamine Sensing Films: Interplay between Protein Characteristics and Molecular Imprinting Effect. *Surfaces and Interfaces* **2023**, *39*, 102904. https://doi.org/10.1016/J.SURFIN.2023.102904.

(217) Lin, T.-Y.; Hu, C. H.; Chou, T. C. Determination of Albumin Concentration by MIP-QCM Sensor. *Biosens Bioelectron* **2004**, *20* (1), 75–81. https://doi.org/10.1016/j.bios.2004.01.028.

(218) Ozcelikay, G.; Kurbanoglu, S.; Zhang, X.; Soz, C. K.; Wollenberger, U.; Ozkan, S. A.; Yarman, A.; Scheller, F. W. Electrochemical MIP Sensor for Butyrylcholinesterase. *Polymers (Basel)* **2019**, *11* (12), 1–11. https://doi.org/10.3390/polym11121970.

(219) Tao, Z.; Tehan, E. C.; Bukowski, R. M.; Tang, Y.; Shughart, E. L.; Holthoff, W. G.; Cartwright, A. N.; Titus, A. H.; Bright, F. V. Templated Xerogels as Platforms for Biomolecule-Less Biomolecule Sensors. *Anal Chim Acta* **2006**, *564* (1), 59–65. https://doi.org/10.1016/j.aca.2006.01.076.

(220) Liu, S.; Bi, Q.; Long, Y.; Li, Z.; Bhattacharyya, S.; Li, C. Inducible Epitope Imprinting: "Generating" the Required Binding Site in Membrane Receptors for Targeted Drug Delivery. *Nanoscale* **2017**, *9* (17), 5394–5397. https://doi.org/10.1039/c6nr09449j.

(221) Peng, H.; Qin, Y.-T.; He, X.-W.; Li, W.-Y.; Zhang, Y. Epitope Molecularly Imprinted Polymer Nanoparticles for Chemo-/Photodynamic Synergistic Cancer Therapy Guided by Targeted Fluorescence Imaging. *ACS Appl Mater Interfaces* **2020**. https://doi.org/10.1021/acsami.0c00468.

Chapter III – Dendritic self-assembled structures from therapeutic charged pentapeptides

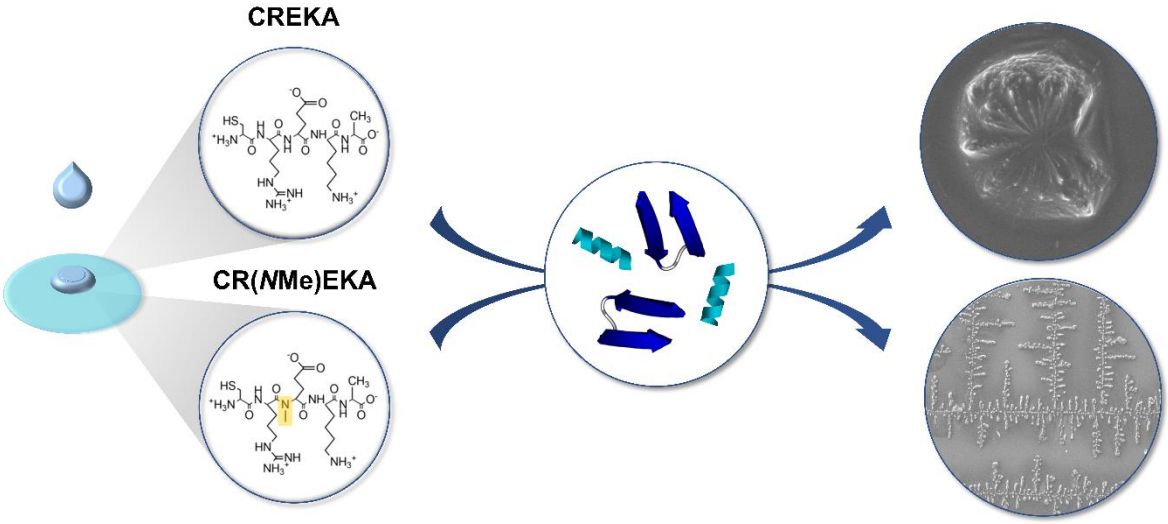

III - 1. Introduction

Cancer is the leading cause of death worldwide, being responsible for nearly 10 million deaths in 2020 (nearly one in six deaths).[1] Although over the last few years, significant progress has been made in cancer treatment, which involves chemotherapy, biological and hormonal therapy, surgery and/or radiation, the two main problems still persist: current cancer treatment has a high cost and, what is worst, it still causes adverse side effects. The latter are of particular concern when chemotherapeutic agents are used. For example, doxorubicin, which is a conventional and still widely used chemotherapeutic agent, causes oxidative stress-mediated injury to the brain, kidney, and heart.[2-4] Furthermore, cancer cells can develop resistance to chemotherapeutic drugs, which results in higher mortality rates.[5-6]

In recent years, therapeutic peptides have become a novel and promising approach for the development of anti-cancer agents with less potential side effects.[7-12] Anti-cancer peptides (ACPs) exhibit several advantages over chemistry-based chemotherapeutic agents, such as high specificity and low toxicity to normal cells. They also display some disadvantages, such as cell membrane impermeability and poor *in vivo* stability.[13] However, such drawbacks can be partially or, even, totally overcome by designing suitable peptide modifications.

Among ACPs, CR(*N*Me)EKA [Cys-Arg-(*N*Me)Glu-Lys-Ala, where (*N*Me)Glu refers to *N*-methyl-Glu], was found to be particularly attractive for prostate cancer on account of its small size (*i.e.* five residues only).[14] This ACP, which induces prostate tumor necrosis and significant reduction in tumor growth, was inspired by CREKA (Cys-Arg-Glu-Lys-Ala) (Scheme III - 1), a pentapeptide discovered by *in vivo* phage display technique[15] that has been extensively utilized for the image diagnosis of tumors[16-19] and to inhibit tumor cell migration and invasion.[14,20] Furthermore, CREKA and CR(*N*Me)EKA have been loaded into intrinsically conducting polymers films and NPs to promote their specificity towards fibrin-fibronectin complexes[21,22] and to regulate their delivery by electro-stimulation,[23] respectively. Besides, CREKA has been extensively used for therapeutic applications,[24-29] including cancer treatment.[24,28,29] Not only did the substitution of Glu in CREKA by (*N*Me)Glu in CR(*N*Me)EKA over-stabilize the peptide bioactive conformation, but also significantly increased its resistance to endogenous proteases.[30]

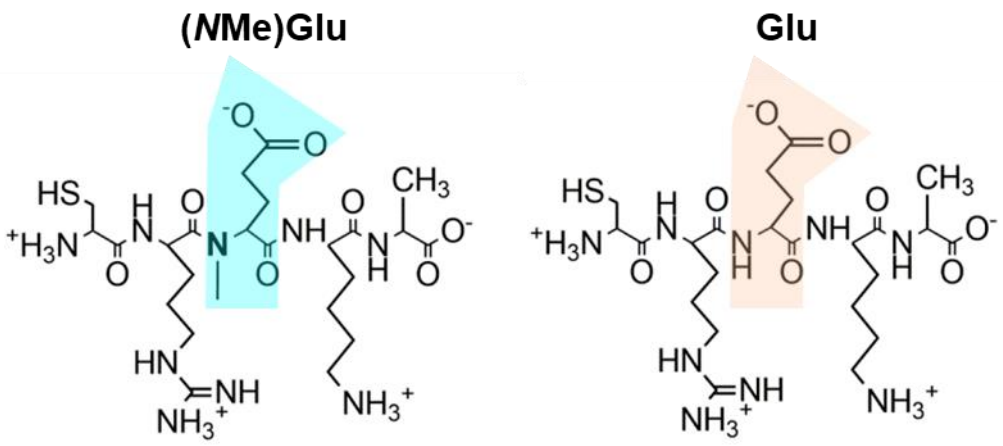

Scheme III - 1. Chemical structure of CR(*N*Me)EKA (left) and CREKA (right). The (*N*Me)Glu and Glu residues are highlighted.

Recently, both CR(*N*Me)EKA and CREKA were reported to tend to rapidly form aggregates, which increased in size, from the nanometric to the submicrometric scale, with peptide concentration,[31] with this behavior being more pronounced for CR(*N*Me)EKA than for CREKA. Indeed, the diameter of CR(*N*Me)EKA aggregates, as measured by dynamic light scattering (DLS), increased from 59 ± 21 nm to 470 ± 172 nm when the peptide concentration varied from 0.5 to 5 mg/mL, while the aggregates of CREKA increased from 255 ± 55 nm to 589 ± 93 nm. However, many aspects of CREKA and CR(*N*Me)EKA aggregates, including their morphologies, remain unstudied.

Peptide aggregates are usually formed by the self-assembly of individual molecules, which under controlled conditions form supramolecular structures through well-defined non-covalent interactions.[32] For a given peptide, not only does the peptide concentration define the self-assembly process, but also the properties of the environment (*i.e.* polarity and volatility), and, in some cases, the substrate, as well.[33] In order to understand the driving forces that dominate peptide self-assembly and assembly mechanisms, this process has been carefully studied lately for model peptides, including polar,[34-36] amphiphilic,[37-39] and highly hydrophobic compounds.[40-42] Regarding therapeutic peptides, their self-assembly in amorphous or highly ordered aggregates may reduce the physical stability of the peptides in question, not only leading to a loss in activity, but also other critical problems, such as toxicity and immunogenicity.[43] Therefore, within this context, it is worth noting that complete knowledge and understanding of the aggregation tendency of ACPs is of fundamental importance for their clinical usage.

In this chapter, we aim to investigate, for the first time, the self-assembly of CR(*N*Me)EKA ACP and, by extension, of its parent peptide, CREKA. Initially, we provide experimental evidence of the secondary structures preferred by both peptides as a function of peptide concentration and pH, which have been identified in solution, as well as in the aggregate (solid) state using circular dichroism (CD)

and FTIR spectroscopy, respectively. Spectroscopic results have been supported by Molecular Dynamics (MD) computer simulations based on atomistic models. Finally, the experimental conditions that give rise to well-defined self-assembled aggregates have been examined, and the shape of such aggregates has been characterized by SEM. A self-assembly mechanism is proposed to explain the formation of CR(*N*Me)EKA dendritic microstructures with fractal geometry.

III - 2. Materials and methods

III - 2.1. Materials

CREKA and CR(*N*Me)EKA peptides with > 98% of HPLC purity were purchased from Biomatik (Toronto, ON). Ultrapure milli-Q water was used to prepare all the aqueous solutions.

III - 2.2. Samples preparation

Initial stock solutions of CREKA and CR(*N*Me)EKA peptides were prepared at 5 mg/mL concentration in milli-Q water. The desired peptide concentration solutions were prepared by dilution of the stock solutions with milli-Q water. Phosphate buffered saline (PBS) solutions at three pH values (4, 7 and 10) were considered, with acid and basic pHs being adjusted using concentrated HCl and NaOH solutions, respectively.

III - 2.3. Spectroscopic studies

Circular dichroism (CD) spectra) were recorded between 200 and 250 nm at room temperature using a Chirascan plus qCD equipment, a 10 mm cell path and 700 µL of aqueous peptide solutions at different concentrations and pHs. Spectra, which were acquired at a scan speed of 60 $nm \cdot min^{-1}$ with a 1 nm step using a 1 nm band-with and a time-per-point of 1 s, were averaged after three accumulations and corrected by subtraction of the background spectrum.

FTIR spectra of solid peptides were recorded on a FTIR Jasco 4100 spectrophotometer equipped with an attenuated total reflection (ATR) accessory (Top-plate) and a diamond crystal (Specac model MKII Golden Gate Heated Single Reflection Diamond ATR). Samples, which were evaluated using the spectra manager software, were prepared by dropping 20 µL of aqueous peptide solution on aluminum foil and left at 4 ^{o}C until complete solvent evaporation. For each sample, 32 scans were recorded between 4000 and 600 cm^{-1} with a resolution of 4 cm^{-1}.

III - 2.4. Computer simulations

All bonding and non-bonding parameters for standard amino acids were obtained from Amber03 force field.[44] The parameters of the non-coded (*N*Me)Glu residue had previously been computed and fitted into Amber03.[44].

Two different systems, one for each studied peptide, were built by randomly placing 15 identical molecules in a simulation box with an intermolecular average distance of about 1.8 nm (*i.e.* molecules were mostly non-interacting among each other, according to the "*minimum-bias*" approach). At the simulated conditions (neutral pH), each studied peptide molecule presented a positive net charge, which was neutralized by adding a chloride ion per strand, for a total of 15 anions per studied model. Finally, each simulation box (9.5 × 8.5 × 9.0 nm^3) was filled with approximately 23000 TIP3P water molecules,[45] with overlapping water molecules being removed.

Molecular dynamics (MD) series were performed with NAMD 2.10 software package.[46] The time step was set at 2 fs, and the distances of all bonds involving hydrogen atoms were kept at their equilibrium values with the RATLLE algorithm.[47] Atom pair distance cut-offs were applied at 1.4 nm to compute all van der Waals interactions. To avoid discontinuities in this energy component, the van der Waals energy term was forced to slowly converge to zero by applying a smoothing factor from 1.0 nm. Electrostatic interactions were extensively computed by means of Ewald summations. The real space term was defined by the van der Waals cut-off (1.4 nm), while the reciprocal space was computed by interpolation of the effective charge into a charge mesh with a grid thickness of 1 point per $Å^3$ (particle mesh Ewald).[48] In all MD simulations, both temperature and pressure were controlled by the weak coupling method, the Berendsen thermo-barostat,[49] and a time constant of 1 ps was applied for heat bath coupling and pressure relaxation.

Equilibration was achieved by applying the following steps: 1) the energy of each system was relaxed by 10^4 steps of energy minimization using Newton Raphson method; 2) then, the solvent was equilibrated using a 1 ns long trajectory with NVT conditions at 500 K while the peptides were kept frozen; 3) the temperature was set at 298 K and another 1 ns NVT trajectory was run, unfreezing the peptide chains for thermal equilibration; and 4) 1 ns in NPT conditions, pressure set at 1.034 bar, and keeping the former temperature in order to relax the density of the solution. This later step is the beginning of the production runs of each trajectory series, keeping identical simulation conditions to those of the NPT equilibration cycle.

III - 2.5. Morphological studies

20 μL aliquots of the peptide solutions at different concentrations and pH values were placed on glass coverslips and kept inside a cold chamber (4 ^oC) until dryness (~15 days). Scanning electron

microscopy (SEM) studies were performed in a Focussed Ion Beam Zeiss Neon 40 scanning electron microscope operating at 5 kV and equipped with an EDX spectroscopy system. Samples were mounted on a double-side adhesive carbon disc and sputter-coated with a thin layer of carbon to prevent sample charging problems.

III - 3. Results and discussion

III - 3.1. Secondary structure in solution and solid state

Firstly, the conformation of CREKA and CR(*N*Me)EKA was examined in solution by circular dichroism (CD) considering not only different peptide concentrations (from 0.01 to 1 mg/mL), but also diverse pH values (4, 7 and 10). Indeed, their secondary structure, as well as the tendency to self-assemble into ordered structures, was expected to be drastically affected by the ionization state of the charged residues: Arg, Glu / (*N*Me)Glu and Lys residues (Scheme 1). The pKa of Glu, Arg and Lys side groups is 4.2, 12.5 and 10.5, respectively; while the pKa of the ionizable amino and carboxylate groups of the N- and C-terminus is ~8 and ~3, respectively.[50] Accordingly, the Glu / (*N*Me)Glu side group will be predominantly neutral at pH 4, while the Arg and Lys side groups and the two backbone terminal groups will remain ionized (total molecular charge: +2). Instead, all such residues and backbone terminal groups will be predominantly ionized at pH 7 (total molecular charge: +1), while at pH 10 the amino terminal group will be de-ionized (total charge: +0). Hence, the pH will govern ionization and, thus, the intra and intermolecular electrostatic interactions that control the secondary structure of CREKA and CR(*N*Me)EKA.

The CD spectra recorded for different peptide solutions at neutral pH are displayed in Fig. III - 1. For concentrations $\leq$ 0.1 mg/mL, CREKA exhibits a negative band at around 200 nm, which shifts to a higher wavelength with increasing peptide concentration (208 nm at 0.1 mg/mL), and a positive band at 222 nm (Fig. III - 1a). This profile, which is maintained at pH 4 and 10 (Fig. III - 2a), is fully consistent with a random structure. The shape of the spectrum changes when CREKA concentration is $\geq$ 0.25 mg/mL. In such cases, a single positive band (*i.e.* the negative band disappears) is detected, and the position of the maximum increasing with peptide concentration (from 225 nm for 0.25 mg/mL to 232 nm for 1.0 mg/mL). These spectra, which are typically associated with a β-turn,[51-53] are in good agreement with the bioactive conformation proposed for CREKA, which consisted of a turn conformation with the charged side chains pointing outwards to facilitate the formation of intermolecular interactions.[54] The slight shift in wavelength of the peaks could be correlated with the increasing contribution of arginine with increasing concentration of peptide, as high arginine content has been shown to make more difficult the detection of protein signal in CD spectra.[55]

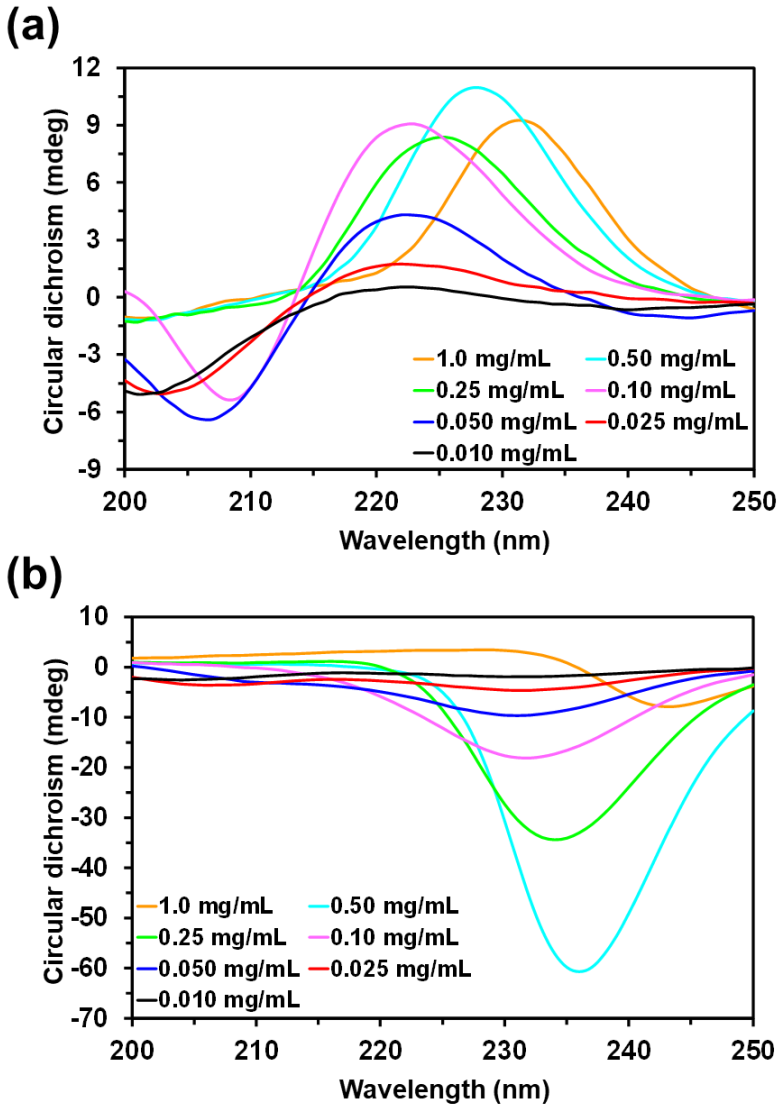

Fig. III - 1. CD spectra for (a) CREKA and (b) CR(NMe)EKA in aqueous solution and pH 7 at different peptide concentrations.

The spectra obtained for CR(*N*Me)EKA were completely different from those recorded for CREKA. CR(*N*Me)EKA exhibits a single negative band that shifts from 231 nm at low concentrations to 243 nm at 1.0 mg/mL (Fig. III - 1b). This profile has been related to a β-sheet structure and the shift observed at increasing peptide concentrations, which is practically independent of the pH (Fig. III - 2b), suggests the enhancement of the β-sheet structure.[56,57] Thus, the change from positive peak to negative peak in the same region translates into a change in conformation from β-turn to β-sheet with the methylation of the peptide. Accordingly, it is hypothesized that intermolecular CR(*N*Me)EKA···CR(*N*Me)EKA interactions favor a more extended structure, which should promote self-

assembly aggregation processes. Our hypothesis is supported by the conformational restrictions imposed by the (*N*Me)Glu residue, which stabilize elongated conformations.[30]

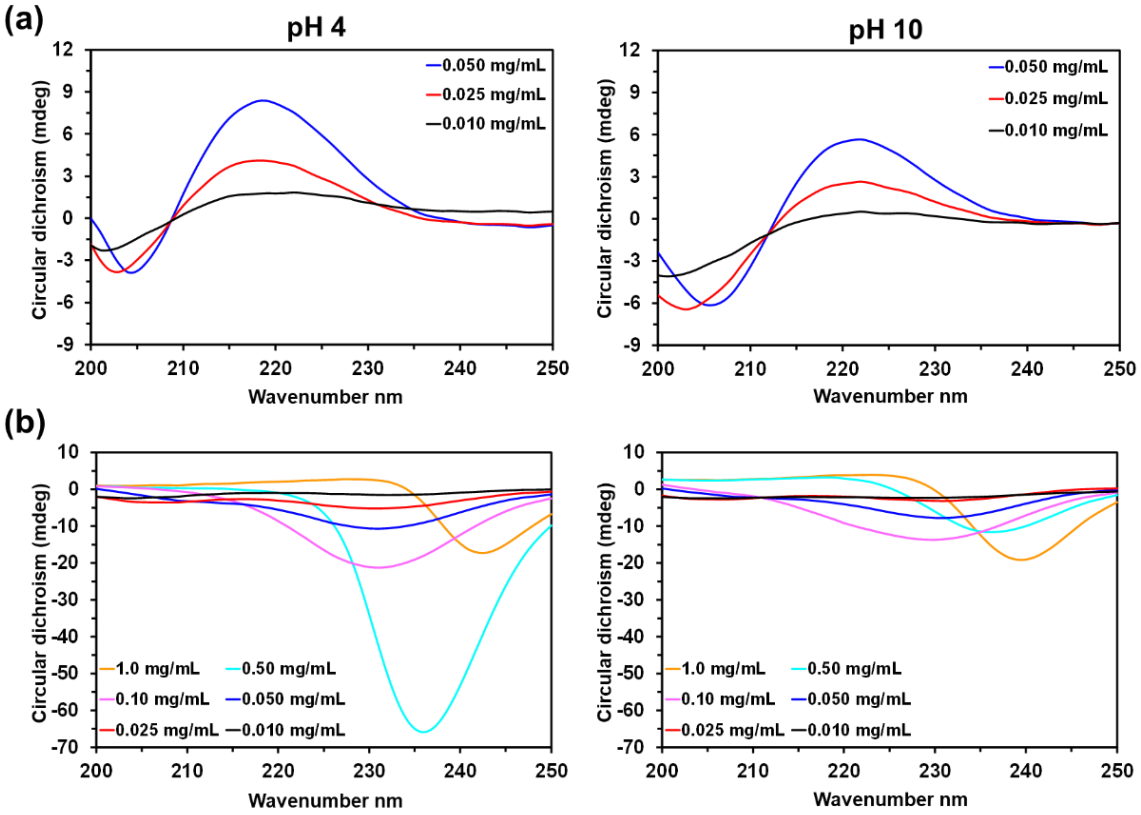

Fig. III - 2. CD spectra for (a) CREKA and (b) CR(*N*Me)EKA in aqueous solution and pH 4 (left) and pH 10 (right) at different peptide concentrations.

The secondary structure of CREKA and CR(*N*Me)EKA in the aggregate state was studied as a function of the ionization state and peptide concentration of the feeding solution using FTIR spectroscopy. For this purpose, 20 μL of peptide aqueous solutions at 0.01, 0.1, 1.0, 2.0 and 5.0 mg/mL concentrations and at pH 4, 7 and 10 were dropped on aluminum substrate and left at 4 ^{o}C until complete solvent evaporation. Fig. III - 3 displays the recorded spectra in the region of the amide I (1600–1800 cm^{-1}) and amide II (1470–1570 cm^{-1}), which are the most prominent and sensitive bands of the peptide backbone and are related to peptide secondary structural components.

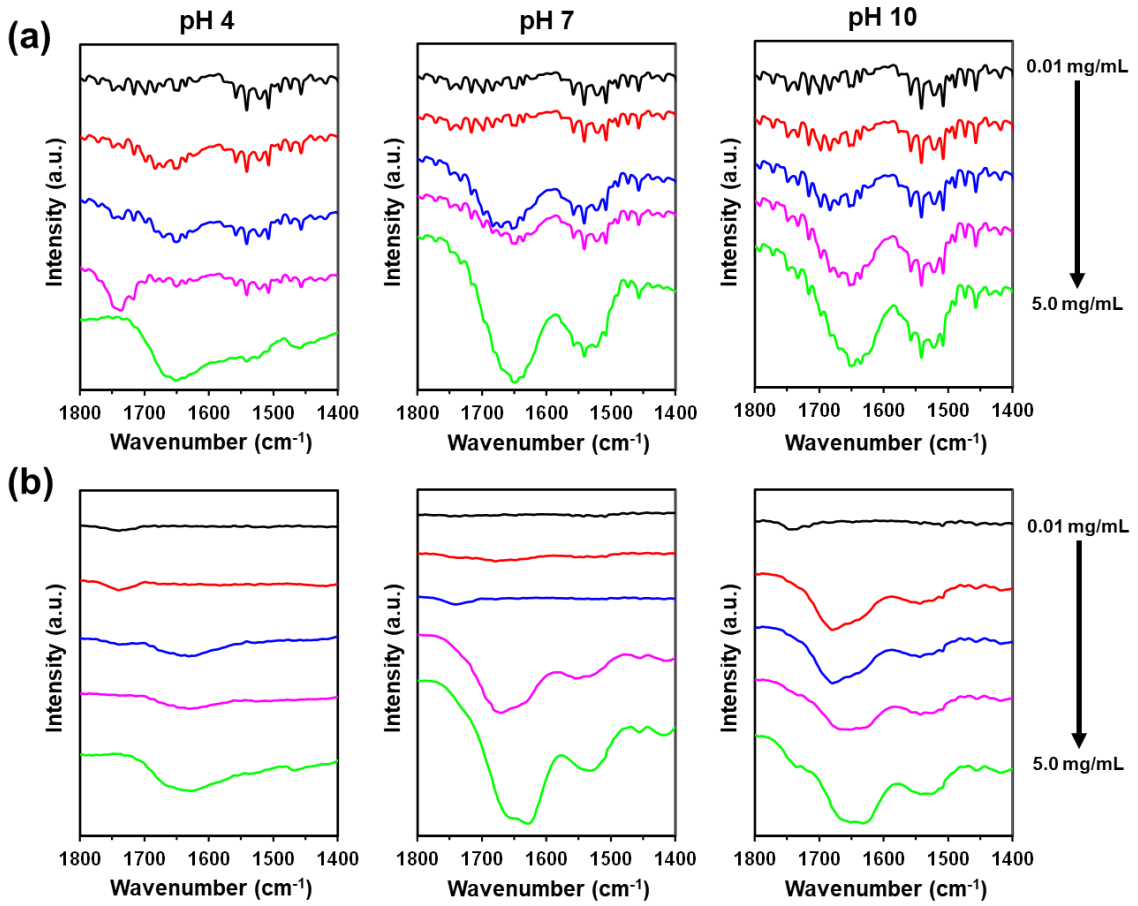

Fig. III - 3. FTIR spectra in the amide I and II regions for (a) CREKA and (b) CR(*N*Me)EKA peptides. Spectra were recorded after evaporation of the solvent at 4 ^{o}C. For this purpose, peptide aqueous solutions at 0.01, 0.1, 1.0, 2.0 and 5.0 mg/mL concentrations and at pH 4, 7 and 10 were dropped on aluminum substrate.

For both peptides, the spectra recorded at neutral and basic pH are better defined than those at acid pH, which suggests that electrostatic interactions play a crucial role in the aggregation process. CREKA shows a predominant broad absorption band centered at 1650 cm^{-1}, which increases with peptide concentration (Fig. III - 3a). Although this has been assigned to a random coil conformation, the small peaks in the range of 1600-1700 cm^{-1} suggest that other secondary structural motifs have a minor contribution (*e.g.* β-sheet, 3_{10}-helix and β-turn at 1620, 1669 and 1683 cm^{-1}). This feature is fully consistent with the fact that small peptides present more than one conformation since subtle conformational rearrangements allow the interconversion between different secondary structures. Conversely, small peaks are not detected in the CR(*N*Me)EKA spectra, which only show a pronounced broad band centered at 1620-1660 cm^{-1} interval (Fig. III - 3b). At the higher concentrations and pH 7 and 10, this band splits into two peaks centered at 1628 and 1658 cm^{-1}, which are consistent with pseudo-extended and turn or random coil structures, respectively. In CR(*N*Me)EKA, the

conformational variability of CREKA is expected to be restricted by the constrictions imposed by the substitution of Glu by (*N*Me)Glu. Besides, the amide II peak, which corresponds to the N–H bending vibration and the C–N stretching vibration (amide II), experiences a redshift from 1550 to 1534 cm^{-1} with increasing peptide concentration, which is consistent with the formation of intermolecular hydrogen bonds in the aggregates.

Computer MD simulations on CREKA and CR(*N*Me)EKA atomistic models were performed considering 15 independent peptide molecules, which were initially non-interacting, in a simulation box filled with water molecules (see Methods section). After 70 ns of production trajectories, the preferred hydrogen bond patterns were analyzed as a function of how the peptide chains are organized (*i.e.* isolated or part of an aggregate). The geometric criteria used to account for hydrogen bonds were: (1) distances H···O shorter than 0.3 nm; and (2) angles ∠N-H···O higher than 120.0°. Fig. III - 4 shows the distribution of preferred hydrogen bonding patterns as function of the number of chains present in an aggregate for the production trajectory (being the number of chains 1 when a peptide is not part of an aggregate). As can be seen, the results confirmed the previously presented observations.

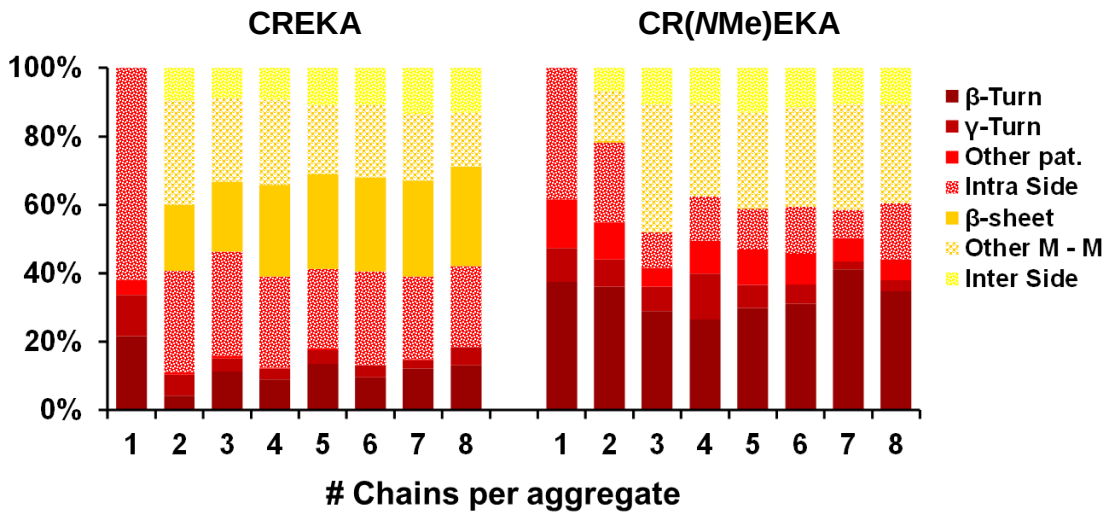

Fig. III - 4. Percentage of types of hydrogen bond patterns as a function of the aggregate size after 70 ns of simulation. Aggregates of 1 chain refer to chains that are not part of any assembly. The legend refers to: β-turn and γ-turn: hydrogen bond pattern proper to those conformations; Other pat.: other intramolecular hydrogen bonds pattern between amide groups; Intra Side: intramolecular hydrogen bonds in which side chain groups are involved; β-sheet: intermolecular hydrogen bonds between main chain amide groups in chains adopting β-strand conformations; M-M: intermolecular hydrogen bonds between main chain amide groups in strands with not defined conformation; Inter side: intermolecular hydrogen bonds in which side chain groups are involved.

When CREKA chains are not part of an aggregate, they majorly adopt undefined conformations, with a predominance of structures that are stabilized by hydrogen bonds involving polar and charged groups from the side chains, whereas CR(*N*Me)EKA peptides predominantly present hydrogen bond patterns compatible with defined turn conformations. The behavior of both peptides when aggregating is also differential. Hydrogen bonds in CREKA aggregates are predominantly between main chain amide groups with a clear tendency to form β-sheet patterns, especially when the size of the aggregate (in the number of interacting chains) increases. On the other hand, CR(*N*Me)EKA aggregates present a strong tendency to not interact via main chain amide groups and, thus, strongly retain the intramolecular hydrogen patterns that were predominant when not being part of an aggregate. While CREKA clusters of chain tend to form hydrogen bond organizations compatible with β-sheet structures, CR(*N*Me)EKA clusters tend to organize via other interactions (generally by salt bridges) while preserving the conformational features that they presented before aggregating. Overall, results derived from atomistic modeling using MD simulations are in good agreement with CD and FTIR observations in terms of interactions.

On the other hand, several interesting structural differences can be observed between both studied peptides. CREKA chains, as statistical analysis had already shown, have an acute tendency to laterally assemble via its amide groups, forming chain pairs. This pattern, which is present in all detected aggregates, corresponds to arrangements compatible with β-sheet motif, in several degrees of formation. Fig. III - 5 depicts the final snapshot of the simulation, demonstrating that there are 10 chains out of 15 participating in aggregated structures. Eight of these chains form either full-fletched sheets or structures reminiscent of such organization. Among the five detected clusters, two of them are almost canonic β-sheets (cluster 01 and cluster 05 in Fig. III - 5b) whereas the remaining present assemblies can be understood as distorted sheets or not fully formed structures.

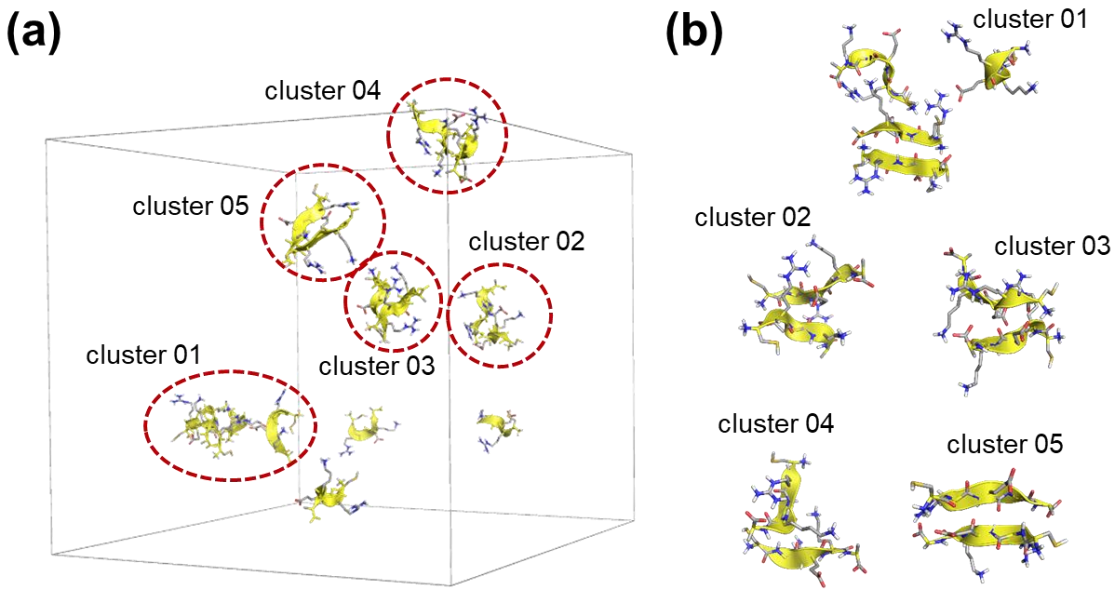

Fig. III - 5. Molecular representation of the last snapshot of the simulated CREKA system: (a) The complete simulation box, including non-associated chains and (b) the enlarged detail images of each detected molecular assembly. Atom colours follow the CPK convention. Hydrophobic hydrogen atoms have been removed for clarity. Main chain α-carbons and backbone have been remarked in yellow.

Two other remarkable features can be observed. Firstly, only one aggregate (cluster 01, Fig. III - 5b) presents one chain whose assembly is not directly driven by the interaction between main chain amide groups. The four chains assembly shows a two stranded sheet interacting with two extra chains via both salt bridges and dipole-charge interactions. This feature becomes relevant when compared with the aggregation features of CR(*N*Me)EKA system (see below). The second noteworthy aspect is the strands orientation within sheets. Of five two-stranded assemblies, 3 of them are antiparallel and 2 are parallel. This structural diversity has been observed in many amyloid-like structures fibers derived from small peptides,[58] when the final outcome of the fully formed fiber does not only depend

on the inner stability of the sheets themselves but on the ability to favor both intra-sheet long distance interactions and the possibility of enhancing inter-sheet lateral interactions.

In contrast, CR(*N*Me)EKA shows significant differences in the assembly outcome compared to the unmodified peptide (Fig. III - 6). Despite presenting similar ratio of assembled chains versus free strands, the aggregation pattern is quite dissimilar. In CR(*N*Me)EKA the presence of sheet-like structures is reduced to a single cluster (cluster 02 in Fig. III - 6b) even though this structure is not an ideal β-sheet, because the presence of a methylated amide group per strands hampers the formation of more than a single inter-chain hydrogen bond. Moreover, even in this case, a recurrent new structural pattern can be observed, which will be repeated in the other observed assemblies. The most favored interaction pattern consists of polar and charged driven interactions between the peptides side chains, which favours the formation of 2D assemblies as a core organization rather than a single rotation axis observed in fibers based on stacking of β-strands. Within this context, cluster 03 becomes exemplary, in which 4 strands mainly associate via side chain driven interactions and the core of the aggregate is made up of two strands preserving a turn conformation, which is the predominant arrangement when chains are not part of an aggregate. This crossed-like organization hints a possible growth path compatible with the formation of the fractal flat spikes observed by electronic microscopy. When this new structural trait is combined with previous analysis, in which most CR(*N*Me)EKA free chains in the simulation consistently adopted turn conformations, it is possible to infer a potential mechanism of assembly based on lateral association of pre-conformed chains via polar/charge interactions of their respective sidechains.

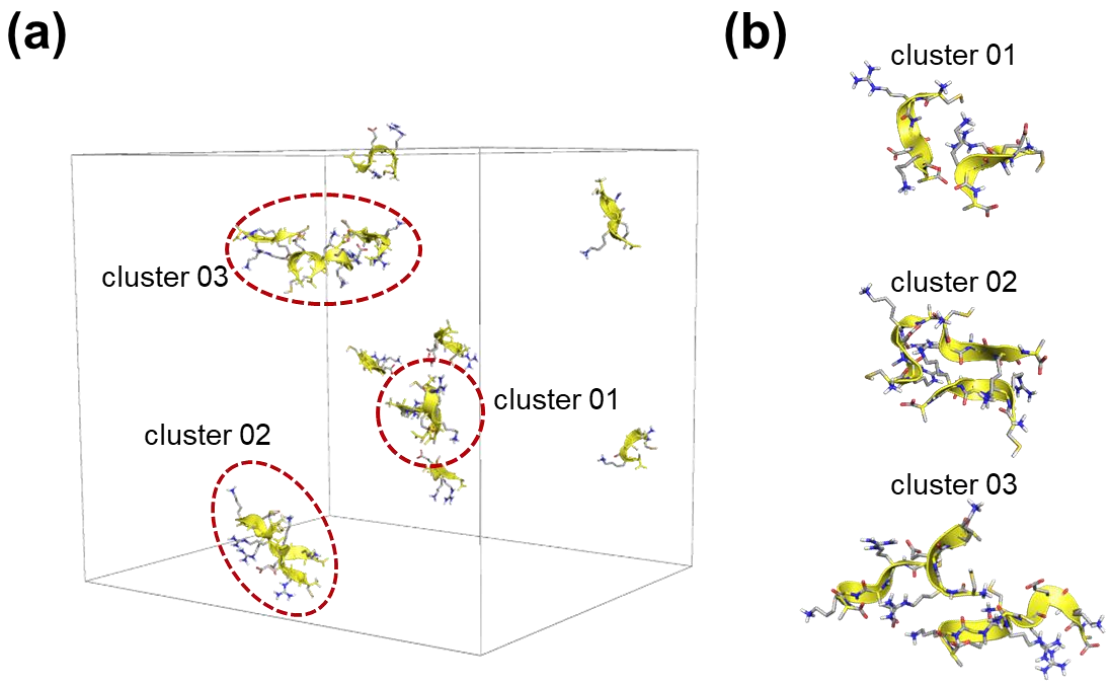

Fig. III - 6. Molecular representation of the last snapshot of the simulated CR(*N*Me)EKA system: (a) The complete simulation box, including non-associated chains and (b) the enlarged detail images of each detected molecular assemblies. Atom colors follow the CPK convention. Hydrophobic hydrogen atoms have been removed for clarity. Main chain α-carbons and backbone have been remarked in yellow.

III - 3.2. Morphology of self-assemblies

The morphology of the self-assemblies formed by CREKA and CR(*N*Me)EKA was investigated using SEM and considering different peptides solutions, which were prepared varying both the concentration (from 0.01 to 5.0 mg/mL) and the pH (4, 7 and 10). For this purpose, a drop of 20 µL of peptides solution was placed on a clean glass cover slip and dried at 4 ^{o}C until complete desiccation. SEM micrographs displayed in the figures correspond to reproducible and abundant morphologies.

The tendency of CREKA to form self-assemblies with well-defined and reproducible morphologies was extremely poor. In fact, pseudo-regular aggregates were only systematically formed using low and moderate peptide concentrations at acid pH, or using low peptide concentrations at neutral pH. In addition, as is illustrated by representative SEM micrographs (Fig. III - 7), the morphologies obtained under such conditions, which predominantly consist of fibers of micrometric thickness, were poorly defined. The absence of reproducible self-assembled nano- and microstructures with well-defined morphology is fully consistent with the large conformational variability observed for CREKA by CD (Fig. III - 1 and Fig. III - 2), FTIR spectroscopy (Fig. III - 3) and MD simulations (Fig. III - 4). This conformational variability, together with the fact that intermolecular interactions among CREKA molecules are

dominated by strong repulsive and attractive electrostatic interactions, result in a self-assembly process controlled by kinetics instead of thermodynamics: the rapid formation of aggregates stabilized by unspecific interactions prevent the formation of well-defined morphologies. Such behavior opposes that observed for highly aromatic small peptides, which tend to form micro- and nanostructures with ultra-well-defined morphologies stabilized by specific intermolecular interactions (*e.g.* π-π stacking).[33,40,41] Hence, those interactions, which are much weaker than electrostatic ones, favor the thermodynamics control over the kinetics control in the self-assembly process.

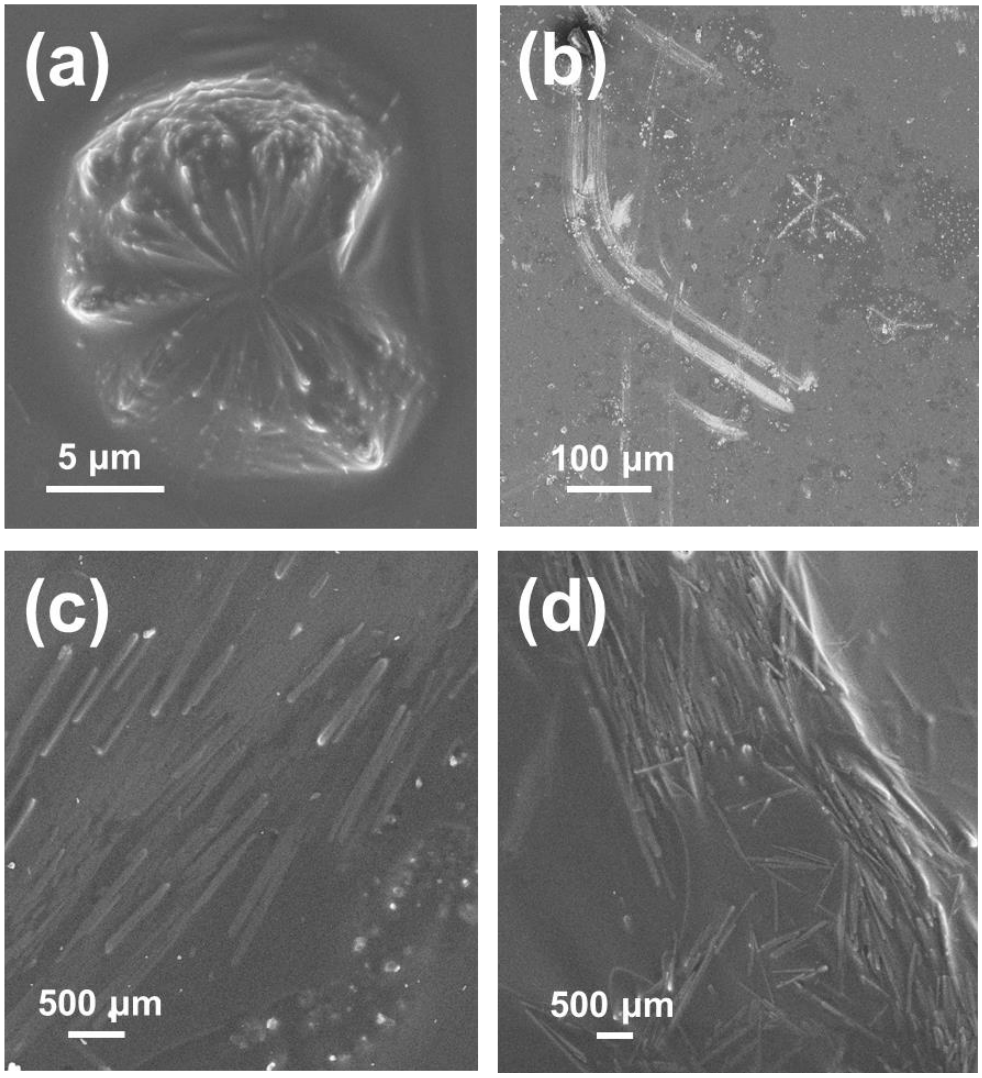

Fig. III - 7. SEM micrographs of poorly defined microstructures formed from CREKA solutions at 4 ^{o}C using the following conditions: (a) 0.01, (b) 0.1 and (c) 1 mg/mL peptide concentration at pH 4, and (d) 0.1 mg/mL peptide concentration at pH 7.

In contrast, CR(*N*Me)EKA showed a significant tendency to form ordered microstructures when the peptide concentration was low or, even, moderate (≤ 2 mg/mL). At low peptide concentrations,

CR(*N*Me)EKA spontaneously formed stable branched dendritic structures with micrometric branches growing from elongated primary frameworks of millimeter length (Fig. III - 8). Such kind of structures, which exhibit fractal characteristics, were found to be very abundant and repetitive at 0.01 mg/mL at pH 4 (Fig. III - 8a) and 0.1 mg/mL at pH 7 (Fig. III - 8b). Similar self-assemblies were also reported for human amylin,[59] a small (37 residues) and intrinsically disordered protein, short amphiphilic peptides (*e.g.* Fmoc-phenylalanine-tyrosine-phosphate),[60] and highly aromatic peptides (*e.g.* phenylalanine-oligomers capped with fluorenylmethoxycarbonyl and fluorenylmethyl esters at the N-terminus and C-terminus, respectively),[41] among others.

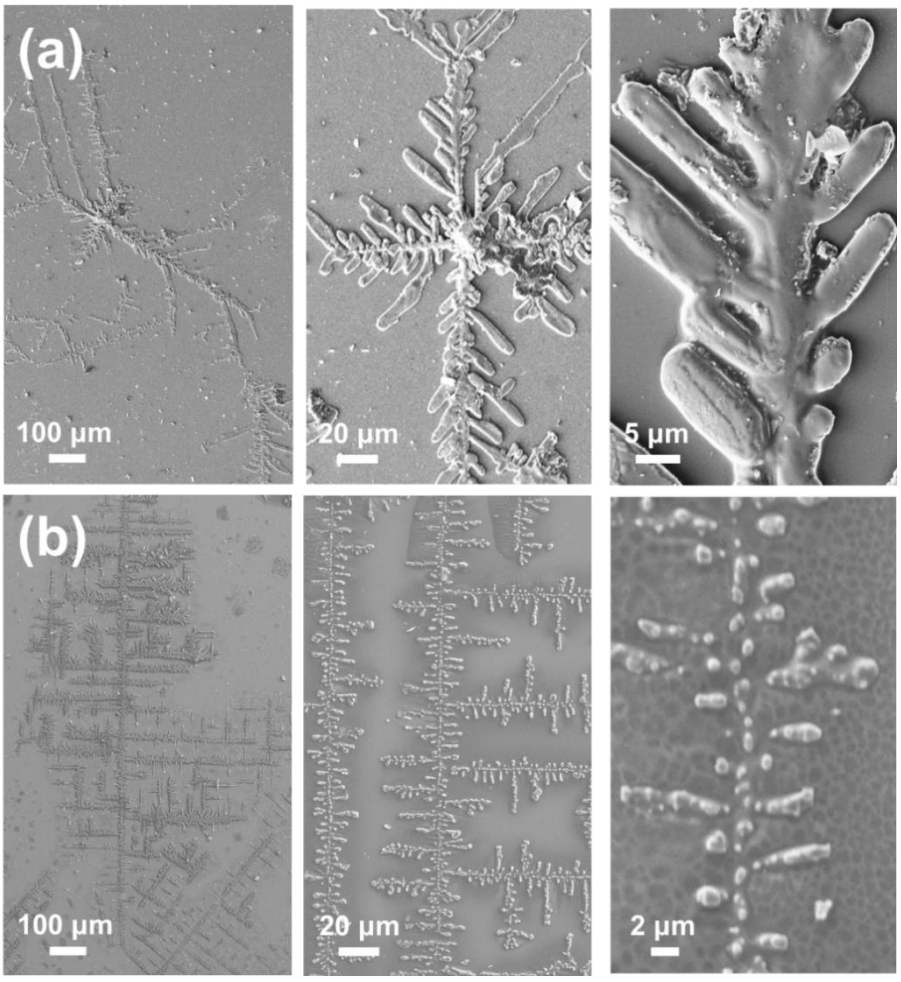

Fig. III - 8. SEM micrographs of dendritic microstructures formed from CR(*N*Me)EKA solutions at 4 ^{o}C using the following conditions: (a) 0.01 mg/mL at pH 4, and (b) 0.1 mg/mL at pH 7.

In the case of CR(*N*Me)EKA, it should be emphasized that the formation of fractal-like structures is pH- and concentration-dependent and only occurred when the net charge of the peptide molecule is the highest or very high and, simultaneously, the peptide concentration is low. As discussed above, the neutral state of the side carboxylate group of the (*N*Me)Glu at pH 4 contributes to a net peptide

charge of +2, while the net charge decreases to +1 at pH 7. At such conditions, repulsive intermolecular interactions result in a fractal self-assembly through a diffusion-limited aggregation process when the peptide concentration is low enough. The diffusion-limited kinetics is supported by the conformational restrictions induced by (*N*Me)Glu residues, which drastically reduce the degree of freedom of CR(*N*Me)EKA in comparison to CREKA.[30] Instead, no dendritic-like or any other ordered assembly was detected when the peptide charge is null at pH 10. Besides, low peptide concentrations allow attractive peptide···peptide interactions to dominate the aggregation process, facilitating the orderly self-assembly of molecules. On the contrary, when the peptide concentration is excessively high (> 1 mg/mL), the intermolecular separation between functional groups with charges of the same sign is too short and the influence of repulsive peptide···peptide interactions predominates, governing the self-assembly process and leading the molecules to aggregate disorderly.

Additional experiments were performed by interrupting the growth of the branched dendritic structures and observing their morphology before the slow evaporation of the solvent ended. Representative SEM micrographs are reported in Fig. III - 9a.

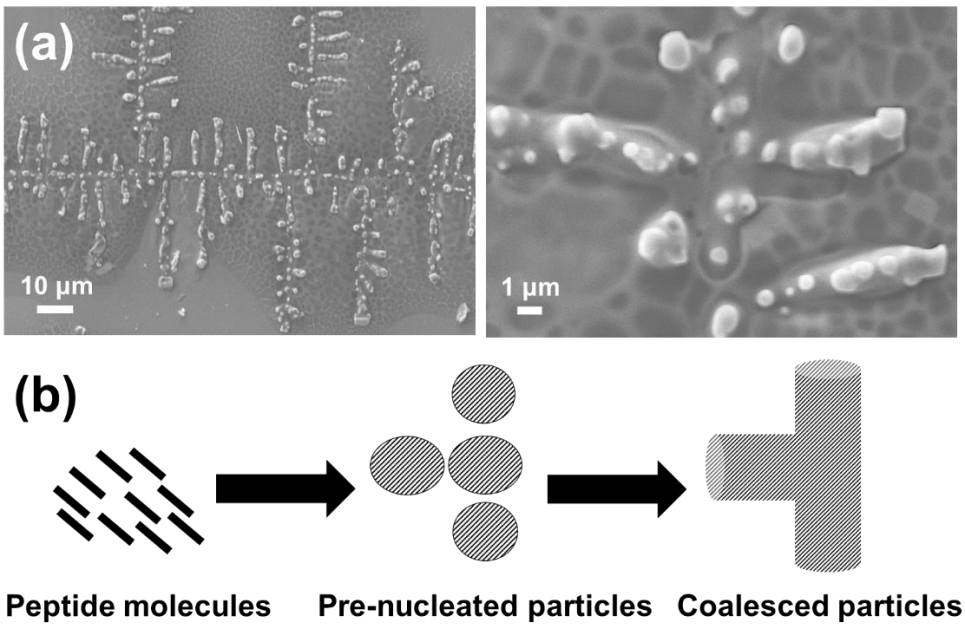

Fig. III - 9. (a) SEM micrographs of dendritic microstructures pre-formed from 0.1 mg/mL CR(*N*Me)EKA solutions at pH 7 and 4 ^{o}C. Micrographs were recorded when only half of the solvent had slowly evaporated in the cold room. (b) Sketch of the mechanism proposed for the formation of the dendritic structures.

As it can be seen, the structures displayed in Fig. III - 8 and Fig. III - 9a are consistent with a two-step self-assembly mechanism, which is sketched in Fig. III - 9b. Firstly, pseudo-spherical particles are

pre-nucleated through a diffusion-limited self-assembly process. This step gives place to an interrupted structure with dendritic geometry. After that, the interactions between the solvent accessible surface of such pre-nucleated structures and the charged/polar groups moieties of peptide molecules in the solution cause more aggregation and the coalescence of pre-nucleated particles (Fig. III - 9b). Therefore, the interrupted dendritic structure transforms into a continuous structure.

Details of how the coalescence of neighboring particles occurs are shown in Fig. III - 10, which displays SEM micrographs of structures formed before the solvent was completely evaporated. The space between the particles was filled through the self-assembly of more peptide molecules, which caused the pre-formed particles to grow until they came into contact and merged. The directional growing of the coalescent inter-particle assemblies and, consequently, the formation of a continuous fractal geometry, have been attributed to the loss of conformational freedom induced by the (*N*Me)Glu residue.

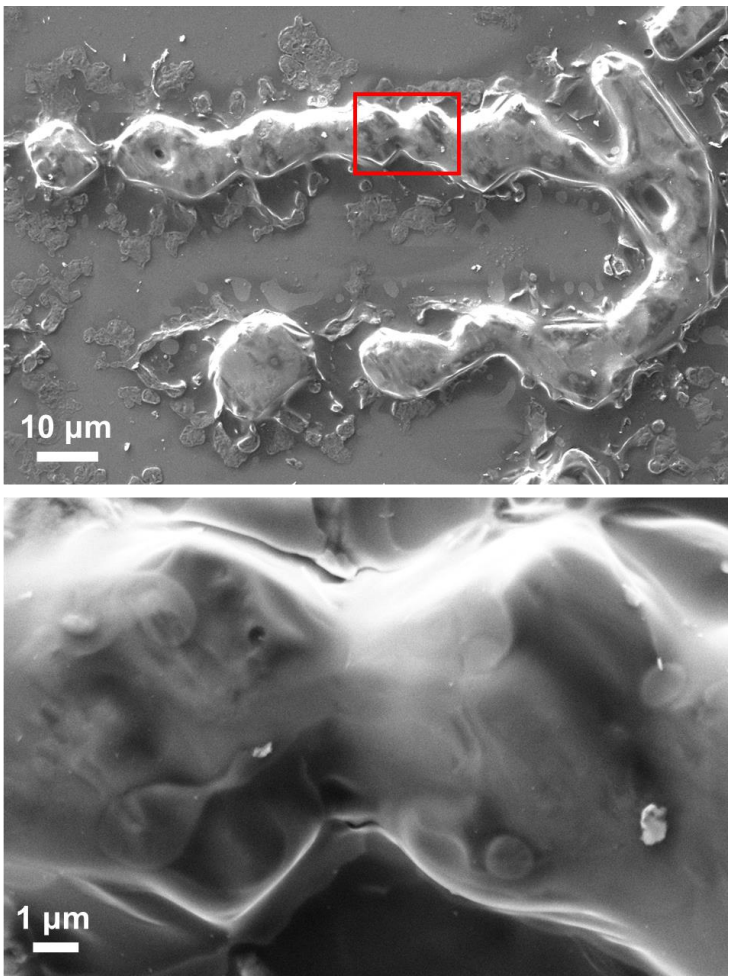

Fig. III - 10. SEM micrographs of structures derived from 0.1 mg/mL CR(*N*Me)EKA solutions at pH 7 and 4 ^{o}C, recorded when the solvent had not been completely evaporated, showing the contact and merging of preformed particles.

Unfortunately, no additional morphological information could be obtained from the MD simulations. This is due to the limitations of the MD simulations, which, on the one hand, only contain 15 peptide molecules (hundreds, if not thousands, would be needed to establish a correlation with the experimentally observed morphology), and on the other hand, the time scale of the simulations being too short. Although nowadays it is possible to carry out simulations of a few micro-seconds, the observed self-assembly process is not controlled kinetically but thermodynamically, and therefore occurs at much higher time scales. Finally, it should be mentioned that, as the self-assembly occurs at the same time as the evaporation of the solvent, the incorporation of this last process to the simulation would increase its complexity.

Because of their unusualness, no practical application has been developed yet for peptide-based self-assembled dendritic microstructures with fractal patterns. However, the exploitation of such hierarchical architectures in applications requiring multiple-length scale is expected to be valuable in the near future. The unique properties of fractal dendritic structures, as for example the large surface area and the self-similarity, combined with the advantages of peptides as biomaterials, are beneficial for potential applications in advanced biosensors, microprinting, biocatalysis and, in general, in the biomedical field. In the case of the studied ACP, CR(*N*Me)EKA, it is not yet known whether the dendritic assembled structures that we have observed *in vitro* are stable *in vivo*, in which the surrounding conditions are much less controlled. However, the exploitation of the fractal geometry to increase the efficacy of the ACP by adjusting a sustained dosage deserves consideration, as it would reduce the adverse side effects. Therefore, future studies will focus on examining the stability of CR(*N*Me)EKA assemblies in physiological conditions and in controlling their disassembly process.

Another interesting feature consisted in the formation of micrometric (~15×20 μm^2) rhombohedrum crystals (6 faces) that were sporadically detected in the dendritic microstructures pre-formed from 0.1 mg/mL CR(*N*Me)EKA solutions at neutral pH (Fig. III - 11). However, although these structures were clearly identified when the self-assembly process was interrupted, they were never detected when the inter-particle space was filled by the peptide at the end of the self-assembly process. These results evidence that the conformational restrictions imposed in CR(*N*Me)EKA contribute to a crystallization process, even though crystals were not abundant enough and were too small for crystal structure determination using X-ray diffraction.

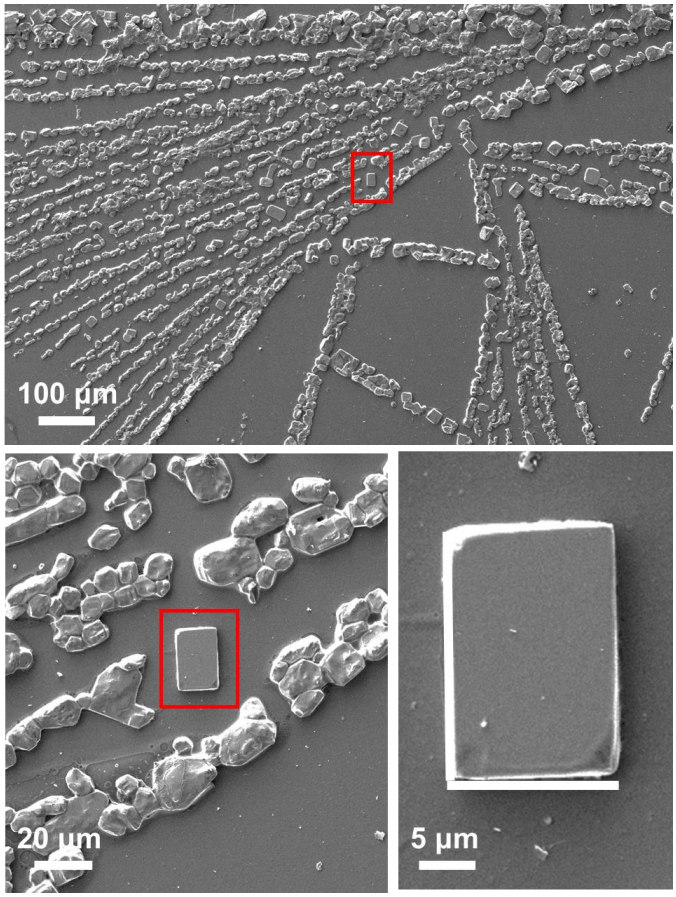

Fig. III - 11. SEM micrographs of rhombohedrum crystals pre-formed from 0.1 mg/mL CR(*N*Me)EKA solutions at pH 7 and 4 ^{o}C, recorded when only half of the solvent had evaporated.

Finally, at higher peptide concentrations, CR(*N*Me)EKA self-assembled into irregular microparticles that consisted of densely packed nanoplates or nanofibers (*i.e.* plates of micrometric length and nanometric thickness). These structures, which are illustrated in Fig. III - 12 for the 1.0 mg/mL peptide solution at pH 7, suggest a change in the self-assembly mechanism, which is hypothesized as the growth of abundant nanostructures around a nucleation site. However, the thickness of such nanostructure is apparently limited by peptide-peptide electrostatic interactions, which are expected to have a marked role than in solutions with lower peptide concentrations.

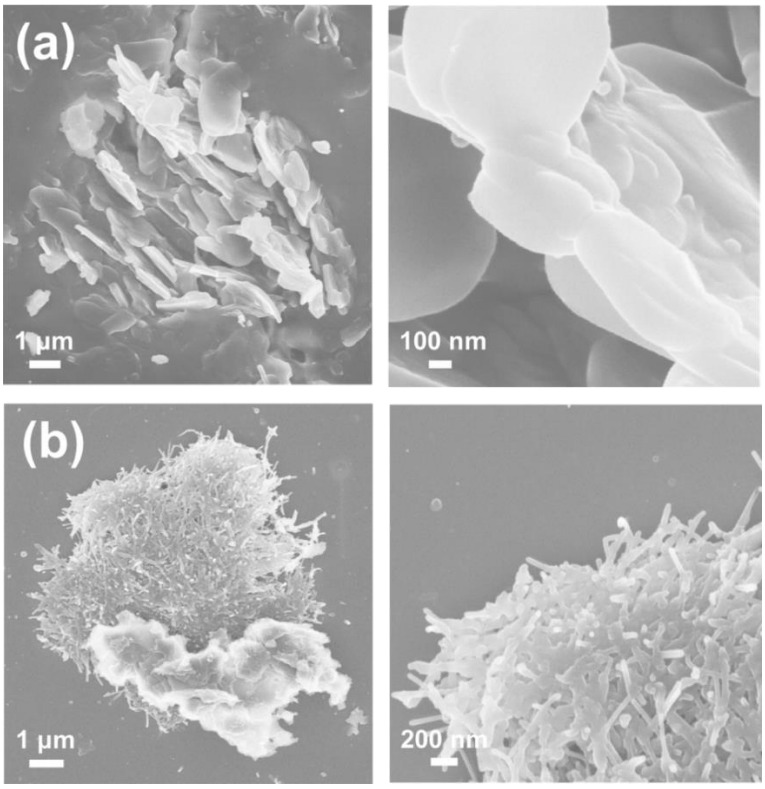

Fig. III - 12. SEM micrographs of irregular particles made of (a) nanoplates and (b) nanofibers obtained for 1.0 mg/mL CR(*N*Me)EKA solutions at pH 7.

Similar assemblies, especially those of clustered nanofibers, were also observed for 2.0 mg/mL peptide solutions (Fig. III - 13). However, although the size and density of nanofibers were similar to those observed for 1.0 mg/mL peptide solutions, the global size of the irregular particles was slightly higher. Instead, no regular self-assembly was detected for 5 mg/mL CR(*N*Me)EKA solutions, regardless of pH value. At such high peptide concentration, repulsive interactions clearly govern the dynamics of the CR(*N*Me)EKA molecules in solution and, therefore, the evaporation of the solvent resulted in the deposition of irregular peptide layers on the glass substrate.

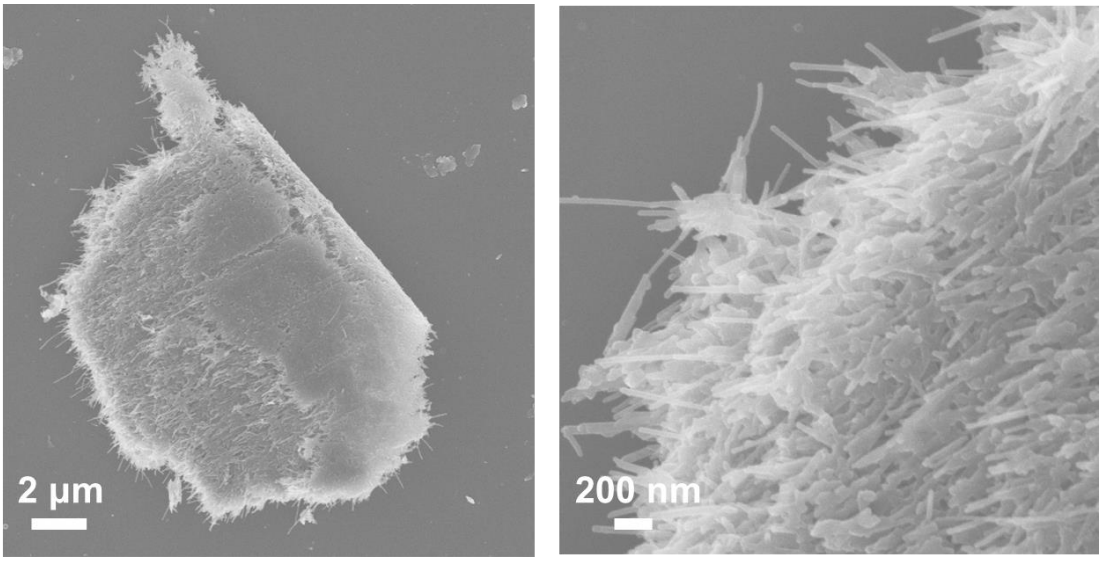

Fig. III - 13. SEM micrographs of irregular particles made of nanofibers obtained for 2.0 mg/mL CR(*N*Me)EKA solutions at pH 7.

In summary, results suggest that the aggregation of the two studied peptides is due to intermolecular electrostatic interactions among their ionized groups. Such aggregation phenomena are observed for both CREKA and CR(*N*Me)EKA, which is consistent with the fact that both bear the same ionizable side chains. On the other hand, the conformational restriction introduced in CR(*N*Me)EKA seems to play a major role in the organization of the peptide molecules during the aggregation process. While CREKA have a poor tendency to form aggregates with well-defined morphologies, the conformational restriction imposed in CR(*N*Me)EKA is consistent with the formation of microstructures with well-defined shapes. In particular, the formation of dendritic microstructures with fractal geometry, which are observed for diluted CR(*N*Me)EKA solutions at acid and neutral pH, is consistent with the regular nucleation process (*i.e.* the lateral association of pre-conformed chains) identified by MD simulations.

III - 4. Conclusions

Harnessing the self-assembly of ACPs for a more efficient release is a significant challenge to improve the efficacy of cancer treatments and eliminate toxicity in healthy tissues. In this chapter, we have reported the self-assembly tendencies of CR(*N*Me)EKA, an ACP with proved efficacy, and its parent compound, CREKA. Conformational studies in solution and in the aggregated states have been conducted using CD, FTIR spectroscopy and MD simulations, which revealed that the restrictions imposed by the (*N*Me)Glu residue drastically reduce the flexibility of CR(*N*Me)EKA in comparison to CREKA. Apparently, this feature is crucial to explain the significant differences found between the self-assembly behavior of the two peptides. Also, the net molecular charge, which is controlled through

the pH, is key for the formation of aggregates with well-defined, regular, and reproducible morphologies.

CREKA, which rarely self-assembles into aggregates with well-defined morphologies, tends to form non-shaped structures with no regular organization. Instead, CR(*N*Me)EKA forms abundant and reproducible dendritic microstructures with fractal geometry when the following conditions are fulfilled: 1) the net charge of the peptide is +2 or +1 (acid and neutral pH), which in conjunction with the conformational restrictions, favor ordered self-assembly; and 2) the peptide concentration in the solution is low enough to avoid that peptide-peptide repulsive interactions dominate the dynamics of the solution. Furthermore, we have observed that dendritic microstructures grow in a two-step process: 1) formation of pre-nucleated pseudo-spherical particles and, even, rhombohedral crystals; and 2) filling of the inter-particle space following a directional self-assembly process. We hope that this groundwork facilitates further research regarding the therapeutic utilization of ACPs, for example, the encapsulation of CR(*N*Me)EKA in nanocarriers for controlled targeted delivery, which is presented in the next chapter of this thesis.

III - 5. References

(1) Sung, H.; Ferlay, J.; Siegel, R. L.; Laversanne, M.; Soerjomataram, I.; Jemal, A.; Bray, F. Global Cancer Statistics 2020: GLOBOCAN Estimates of Incidence and Mortality Worldwide for 36 Cancers in 185 Countries. *CA Cancer J Clin* **2021**, *71* (3), 209–249. https://doi.org/10.3322/CAAC.21660.

(2) Joshi, G.; Sultana, R.; Tangpong, J.; Cole, M. P.; St Clair, D. K.; Vore, M.; Estis, S.; Butterfield, D. A. Free Radical Mediated Oxidative Stress and Toxic Side Effects in Brain Induced by the Anti Cancer Drug Adriamycin: Insight Into Chemobrain. *Free Radical Res.* **2005**, *39*, 1147–1154.

(3) Zhou, S.; Palmeira, C. M.; Wallace, K. B. Doxorubicin-Induced Persistent Oxidative Stress to Cardiac Myocytes. *Toxicol. Lett.* **2001**, *121*, 151–157.

(4) Ponnusamy, L.; Mahalingaiah, P. K.; Singh, K. P. Chronic Oxidative Stress Increases Resistance to Doxorubicin-Induced Cytotoxicity in Renal Carcinoma Cells Potentially Through Epigenetic Mechanism. *Mol. Pharmacol.* **2016**, *89*, 27–41.

(5) Zahreddine, H.; Borden, K. L. Mechanisms and Insights into Drug Resistance in Cancer. *Front. Pharmacol.* **2013**, *4*, 28.

(6) Li, X.; Lewis, M. T.; Huang, J.; Gutierrez, C.; Osborne, C. K.; Wu, M. F.; Hilsenbeck, S. G.; Paylick, A.; Zhang, X.; Chamness, G. C.; Wong, H.; Rosen, J.; Chang, J. C. Intrinsic Resistance of Tumorigenic Breast Cancer Cells to Chemotherapy. *J. Natl. Cancer Inst.* **2008**, *100*, 672–679.

(7) Wang, L.; Wang, N.; Zhang, W.; Cheng, X.; Yan, Z.; Shao, G.; Wang, X.; Wang, R.; Fu, C. Therapeutic Peptides: Current Applications and Future Directions. *Sig. Transduct. Target Ther.* **2022**, *7*, 48.

(8) Chiangjong, W.; Chutipongtanate, S.; Hongeng, S. Anticancer Peptide: Physicochemical Property, Functional Aspect and Trend in Clinical Application. *Int. J. Oncol.* **2020**, *57*, 678-696.

(9) Peyressatre, M.; Prevel, C.; Pellerano, M.; Morris, M. C. Targeting Cyclin-Dependent Kinases in Human Cancers: From Small Molecules to Peptide Inhibitors. *Cancers* 2015, *7*, 179-237.

(10) Kang, H. K.; Choi, M.-C.; Seo, C. H.; Park, Y. Therapeutic Properties and Biological Benefits of Marine-Derived Anticancer Peptides. *Int. J. Mol. Sci.* **2018**, *19*, 919.

(11) Xu, Y.; Sun, L.; Feng, S.; Chen, J.; Gao, Y.; Guo, L.; An, X.; Nie, Y.; Zhang, Y.; Liu, X.; Ning, X. Smart pH-Sensitive Nanogels for Enhancing Synergistic Anticancer Effects of Integrin αvβ3 Specific Apoptotic Peptide and Therapeutic Nitric Oxide. *ACS Appl. Mater. Interfaces* **2019**, *11*, 34663-34675.

(12) Bezu, L.; Keep, O.; Cerrato, G.; Pol, J.; Fucikova, J.; Spisek, R.; Zitvogel, L.; Kroemer, G.; Galluzzi, L. Trial Watch: Peptide-Based Vaccines in Anticancer Therapy. *Oncoimmunology* **2018**, *7*, e1511506.

(13) Fosgerau, K.; Hoffmann, T. Peptide Therapeutics: Current Status and Future Directions. *Drug Disco. Today* **2015**, *20*, 122-128.

(14) Agemy, L.; Sugahara, K. N.; Kotamraju, V. R.; Gujraty, K.; Girard, O. M.; Kono, Y.; Mattrey, R. F.; Park, J.-H.; Sailor, M. J.; Jimenez, A. I.; Cativiela, C.; Zanuy, D.; Sayago, F. J.; Alemán, C.; Nussinov, R.; Ruoslahti, E. Nanoparticle-Induced Vascular Blockade in Human Prostate Cancer. *Blood* **2010**, *116*, 2847-2856.

(15) Simberg, D.; Duza, T.; Park, J. H.; Essler, M.; Pilch, J.; Zhang, L.; Derfus, A. M.; Yang, M.; Hoffman, R. M.; Bhatia, S.; Sailor, M. J.; Ruoslahti, E. Biomimetic Amplification of Nanoparticle Homing to Tumors. *Proc. Natl. Acad. Sci. U. S. A.* **2007**, *104*, 932-936.

(16) Song, Y.; Huang, Z.; Xu, J.; Ren, D.; Wang, Y.; Zheng, X.; Shen, Y.; Wang, L.; Gao, H.; Hou, J.; Pang, Z.; Qian, J.; Ge, J. Multimodal SPION-CREKA Peptide Based Agents for Molecular Imaging of Microthrombus in a Rat Myocardial Ischemia-Reperfusion Model. *Biomaterials* **2014**, *35*, 2961-2970.

(17) Zeng, Z.; Chen, Z.; Tang, L.; Yang, H.; Liu, N.; Zhou, H.; Li, Y.; Wu, J.; Deng, Z.; Deng, H.; Hong, X.; Xiao, Y. A Novel Near-Infrared Fluorescent Light-Up Probe for Tumor Imaging and Drug-Induced Liver Injury Detection. *Chem. Commun.* **2019**, *55*, 2541-2544.

(18) Wang, L.-J.; Li, H.-S.; Wang, Q.-S.; Wu, H.-B.; Han, Y.-J.; Zhou, W.-J.; Wang, M.; Huang, S. Construction and Evaluation of the Tumor-Targeting, Cell-Penetrating Multifunctional Molecular Probe iCREKA. *Contrast Media Mol. Imaging* **2018**, *2018*, 7929617.

(19) Zhou, Z. X.; Qutaish, M.; Han, Z.; Schur, R. M.; Liu, Y. Q.; Wilson, D. L.; Lu, Z. R. MRI Detection of Breast Cancer Micrometastases with a Fibronectin-Targeting Contrast Agent. *Natur. Commun.* **2015**, *6*, 7984.

(20) Jiang, K.; Song, X.; Yang, L.; Li, L.; Wan, Z.; Sun, X.; Gong, T.; Lin, Q.; Zhang, Z. Enhanced Antitumor and Anti-Metastasis Efficacy Against Aggressive Breast Cancer with a Fibronectin-Targeting Liposomal Doxorubicin. *J. Control. Release* **2018**, *271*, 21-30.

(21) Fabregat, G.; Teixeira-Dias, B.; del Valle, L. J.; Armelin, E.; Estrany, F.; Alemán, C. Incorporation of a Clot-Binding Peptide into Polythiophene: Properties of Composites for Biomedical Applications. *ACS Appl. Mater. Interfaces* 2014, *6*, 11940-11954.

(22) Puiggalí-Jou, A.; del Valle, L. J.; Armelin, E.; Alemán, C. Fibrin Association at Hybrid Biointerfaces Made of Clot-Binding Peptides and Polythiophene. *Macromol. Biosci.* **2016**, *16*, 1461−1474.

(23) Puiggalí-Jou, A.; del Valle, L. J.; Alemán, C. Encapsulation and Storage of Therapeutic Fibrin-Homing Peptides Using Conducting Polymer Nanoparticles for Programmed Release by Electrical Stimulation. *ACS Biomater. Sci. Eng.* ***2020****, 6,* 2135-2145.

(24) Ferreira, T. H.; de Oliveira Freitas, L. B.; Fernandes, R. S.; dos Santos, V. M.; Resende, J. M.; Cardoso, V. N.; de Barros, A. L. B.; de Sousa, E. M. B. Boron Nitride Nanotube-CREKA Peptide As an Effective Target System to Metastatic Breast Cancer. *J. Pharm. Investig.* **2020**, *50*, 469-480.

(25) Chen, J.; Song, Y. N.; Huang, Z. Y. Modification with CREKA Improves Cell Retention of Myocardial Ischemia Reperfusion. *Eur. Heart J.* **2019**, *40*, 3268-3268.

(26) Chen, J.; Song, Y.; Huang, Z.; Zhang, N.; Xie, X.; Liu, X.; Yang, H.; Wang, Q.; Li, M.; Li, Q.; Gong, H.; Qian, J.; Pang, Z.; Ge, J. Modification with CREKA Improves Cell Retention in a Rat Model of Myocardial Ischemia Reperfusion. *Stem Cells* **2019**, *37*, 663-676.

(27) Huang, Z. Y.; Song, Y. N.; Ge, J. B.; Huang, Z.; Song, Y.; Pang, Z.; Zhang, B.; Yang, H.; Shi, H.; Chen, J.; Gong, H.; Qian, J.; Ge, J. Targeted Delivery of Thymosin beta 4 to the Injured Myocardium Using CREKA-Conjugated Nanoparticles. *Int. J. Nanomed.* **2017**, *12*, 3023-3036.

(28) Okur, A. C.; Erkoc, P.; Kizilel, S. Targeting Cancer Cells Via Tumor-Homing Peptide CREKA Functional PEG Nanoparticles. *Colloids Surf. B* **2016**, *147*, 191-200.

(29) Zhang, B.; Wang, H.; Shen, S.; She, X.; Shi, W.; Chen, J.; Zhang, Q.; Hu, Y.; Pang, Z.; Jiang, X. Fibrin-Targeting Peptide CREKA-Conjugated Multi-Walled Carbon Nanotubes for Self-Amplified Photothermal Therapy of Tumor. *Biomaterials* **2016**, *79*, 46-55.

(30) Zanuy, D.; Sayago, F. J.; Revilla-López, G.; Ballano, G.; Agemy, L.; Kotamraju, V. R.; Jiménez, A. I.; Cativiela, C.; Nussinov, R.; Sawvel, A. M.; Stucky, G.; Ruoslahti, E.; Alemán, C. Engineering Strategy to Improve Peptide Analogs: From Structure-Based Computational Design to Tumor Homing. *J. Comput. Aided Mol.* **2013**, *27*, 31-43.

(31) Zanuy, D.; Puiggalí-Jou, A.; Conflitti, P.; Bocchinfuso, G.; Palleschi, A.; Alemán, C. Aggregation Propensity of Therapeutic Fibrin-Homing Pentapeptides: Insights from Experiments and Molecular Dynamics Simulations. *Soft Matter* **2020**, *16*, 10169-10179.

(32) Whitesides, G. M.; Mathias, J. P.; Seto, C. T. Molecular Self-Assembly and Nanochemistry: A Chemical Strategy for the Synthesis of Nanostructures. *Science* **1991**, *254*, 1312-1319.

(33) Mayans, E.; Alemán, C. Revisiting the Self-assembly of Highly Aromatic Phenylalanine Homopeptides. *Molecules* **2020**, *25*, 6037.

(34) Wang, M.; Wang, J.; Zhou, P.; Deng, J.; Zhao, Y.; Sun, Y.; Yang, W.; Wang, D.; Li, Z.; Hu, X.; King, S. M.; Rogers, S. E.; Cox, H.; Waigh, T. A.; Yang, J.; Lu, J. R.; Xu, H. Nanoribbons Self-Assembled from Short Peptides Demonstrate the Formation of Polar Zippers between β-Sheets. *Nat. Commun.* **2018**, *9*, 5118.

(35) Díaz-Caballero, M.; Navarro, S.; Fuentes, I.; Teixidor, F.; Ventura, S. Minimalist Prion-Inspired Polar Self-Assembling Peptides. *ACS Nano* **2018**, *12*, 5394-5407.

(36) Hu, X.; Liao, M.; Gong, H.; Zhang, L.; Cox, H.; Waigh, T. A.; Lu, J. R. Recent Advances in Short Peptide Self-Assembly: From Rational Design to Novel Applications. *Curr. Opin. Colloid Interface Sci.* **2020**, *45*, 1.

(37) Li, X.; Cao, C.; Wei, P.; Xu, M.; Liu, Z.; Liu, L.; Zhong, Y.; Li, R.; Zhou, Y.; Yi, T. Self-Assembly of Amphiphilic Peptides for Recognizing High Furin-Expressing Cancer Cells. *ACS Appl. Mater. Interfaces* **2019**, *11*, 12327-12334.

(38) Qiu, F.; Chen, Y.; Tang, C.; Zhao, X. Amphiphilic Peptides as Novel Nanomaterials: Design, Self-Assembly and Application. *Int. J. Nanomedicine* **2018**, *13*, 5003-5022.

(39) Zhao, Y.; Yang, W.; Chen, C.; Wang, J.; Zhang, L.; Xu, H. Rational Design and Self-Assembly of Short Amphiphilic Peptides and Applications. *Curr. Opin. Colloid Interface Sci.* **2018**, *35*, 112-123.

(40) Mayans, E.; Ballano, G.; Casanovas, J.; Díaz, A.; Pérez-Madrigal, M. M.; Estrany, F.; Puiggalí, J.; Cativiela, C.; Alemán, C. Self-Assembly of Tetraphenylalanine Peptides. *Chem. Eur. J.* **2015**, *21*, 16895-16905

(41) Mayans, E.; Ballano, G.; Casanovas, J.; del Valle, L. J.; Pérez-Madrigal, M. M.; Estrany, F.; Jiménez, A. I.; Puiggalí, J.; Cativiela, C.; Alemán, C. Hierarchical Self-Assembly of Di-, Tri- and Tetraphenylalanine Peptides Capped with Two Fluorenyl Functionalities: From Polymorphs to Dendrites. ***Soft Matter*** **2016**, *12*, 5475-5488.

(42) Pérez-Madrigal, M. M.; Gil, A. M.; Casanovas, J.; Jiménez, A. I.; Macor, L. P.; Alemán, C. Self-Assembly Pathways in a Triphenylalanine Peptide Capped with Aromatic groups. *Colloids Surf. B* **2022**, *216*, 112522.

(43) Zapadka, K. L.; Becher, F. J.; Gomes dos Santos, A. L.; Jackson, S. E. Factors Affecting the Physical Stability (Aggregation) of Peptide Therapeutics. *Interface Focus* **2017**, *7*, 20170030.

(44) Duan, Y.; Wu., C.; Chowdhury, S.; Lee, M. C.; Xiong, G.; Zhang, W.; Yang, R.; Cieplak, P.; Luo, R.; Lee, T.; Caldwell, J.; Wang, J.; Kollman, P. A. A point-Charge Force Field for Molecular Mechanics Simulations of Proteins Based on Condensed-Phase Quantum Mechanical Calculations. *J. Comput. Chem.* **2003**, *24*, 1999-2012.

(45) Jorgensen, W. L.; Chandrasekhar, J.; Madura, J. D.; Impey, R. W.; Klein, M. L. Comparison of Simple Potential Functions for Simulating Liquid Water. *J. Chem. Phys.* **1983**, *70*, 926-935.

(46) Phillips, J. C.; Braun, R.; Wang, W.; Gumbart, J.; Tajkhorshid, E.; Villa, E.; Chipot, C.; Skeel, R. D.; Kale, L.; Schulten, K. Scalable Molecular Dynamics with NAMD. *J. Comput. Chem.* **2005**, *26*, 1781-1802.

(47) Andersen, H. C. Rattle: A "Velocity" Version of the Shake Algorithm for Molecular Dynamics Calculations. *J. Comput. Phys.* **1993**, *52*, 24-34.

(48) Toukmaji, A.; Sagui, C.; Board, J.; Darden, T. Efficient Particle-Mesh Ewald Based Approach to Fixed and Induced Dipolar Interactions. *J. Chem. Phys.* **2000**, *113*, 10913–10927.

(49) Berendsen, H. J. C.; Postma, J. P. M.; van Gunsteren, W. F.; DiNola, A.; Haak, J. R. Molecular Dynamics with Coupling to An External Bath. *J. Chem. Phys.* **1984**, *81*, 3684–3690.

(50) Grimsley, G. R.; Scholtz, J. M.; Pace, C. N. A Summary of the Measured pK Values of the Ionizable Groups in Folded Proteins. *Protein Sci.* **2009**, *18*, 247-251.

(51) Juban, M. M.; Javadpour, M. M.; Barkley, M. D. Circular Dichroism Studies of Secondary Structure of Peptides. In: Shafer W.M. (Eds) Antibacterial Peptide Protocols. Methods In Molecular Biology™ 1997, vol 78, Humana Press.

(52) Iyer, A.; Roeter, S. J.; Kogan, V.; Woutersen, S.; Claessens, M. M. A. E.; Subramaniamm, V. C-Terminal Truncated α-Synuclein Fibrils Contain Strongly Twisted β-sheets. *J. Am. Chem. Soc.* **2017**, *139*, 15392–15400.

(53) Kornmueller, K.; Letofsky-Papst, I.; Gradauer, K.; Mikl, C.; Cacho-Nerin, F.; Leypold, M.; Keller, W.; Leitinger, G.; Amenitsch, H.; Prassl, R. Tracking Morphologies at the Nanoscale: Self-Assembly of An Amphiphilic Designer Peptide into a Double Helix Superstructure. *Nano Res.* **2015**, *8*, 1822–1833.

(54) Zanuy, D.; Flores-Ortega, A.; Casanovas, J.; Curcó, D.; Nussinov, R.; Alemán, C. The Energy Landscape of a Selective Tumor-Homing Pentapeptide. *J. Phys. Chem. B* **2008**, *112*, 8692–8700.

(55) Chakraborty, J.; Halder, U. C. Promotion and Suppression of Thermal Aggregation of β-Lactoglobulin by Arginine: A Concentration Dependent Mechanism. *CS & IT* **2013**, 445-459.

(56) Pashuck, E. T.; Cui, H.; Stupp, S. I. Tuning Supramolecular Rigidity of Peptide Fibers Through Molecular Structure. *J. Am. Chem. Soc.* **2010**, *132*, 6041–6046.

(57) Acar, H.; White, A. D.; Hamsici, S. Peptide Framework for Screening the Effects of Amino Acids on Assembly. *Sci. Adv.* **2022**, *8*, eabj0305.

(58) Gallardo, R.; Ranson, N. A.; Radford, S. E. Amyloid Structures: Much More than Just a Cross-β-Fold. *Curr. Opin. Struct. Biol.* **2017**, *60*, 7–16.

(59) Khatun, S.; Singh, A.; Maji, S.; Maiti, T. K.; Pawar, N.; Gupta, A. N. Fractal Self-Assembly and Aggregation of Human Amylin. *Soft Matter* **2020**, *16*, 3143–3153.

(60) Wang, W.; Chau, Y. Self-Assembled Peptide Nanorods as Building Blocks of Fractal Patterns. *Soft Matter* **2009**, *5*, 4893–4898.

Chapter IV – Dual electro-/pH-responsive nanoparticle/hydrogel system for controlled delivery of anticancer peptide

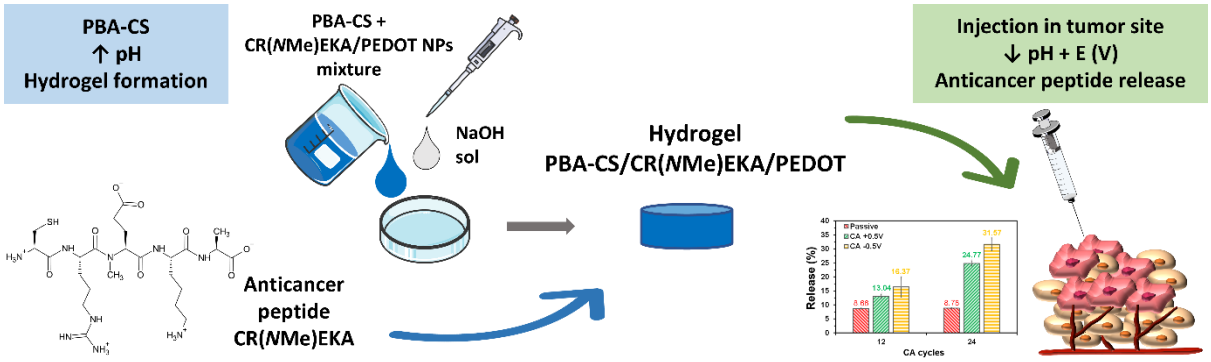

IV - 1. Introduction

Therapeutic peptides are bioactive agents with a well-defined primary structure and usually small size (*i.e.* < 50 amino acids with molecular weights comprised between 500 and 5000 Da).[1-5] The therapeutic effect of such compounds is mainly ascribed to their high activity, specificity, and affinity. Another advantage of therapeutic peptides is that they do not accumulate in specific organs, which minimizes the risk of toxic side effects. As a result of such distinct characteristics and therapeutic potential, approximately 60 peptides have reached the market and around 250 are being tested in humans, while more than 400 are in non-clinical investigations.[6]

Although the field of therapeutic peptides started with natural human hormones,[7] it is currently recognized that naturally occurring peptides are often not directly transferable to therapeutics because of their limitations (*e.g.* low chemical and physical stability, which refer to degradation and aggregation, respectively, and short circulating plasma half-life due to the presence of numerous peptidases).[8-13] Additional restrictions for therapeutic peptides are both the proteolytic activity of digestive enzymes and the complex biological barriers in the gastrointestinal tract, affecting their oral bioavailability.[11-14] Two strategies can be combined to overcome such drawbacks. First, the chemical and physical stability of therapeutic natural peptides can be improved through rational design, replacing specific amino acids by synthetic amino acids.[15-18] Through efficient substitutions, this approach produces peptide analogs with resistance against enzymatic degradation, enhanced stability of the bioactive conformation, and a reduced tendency towards aggregation. Second, specific carriers for therapeutic peptides can be developed to improve their bioavailability and medicinal effectiveness.[19-22]

In this chapter, a polymeric platform is presented, that was specifically designed as a carrier, for the controlled delivery of short and highly hydrophilic therapeutic peptides, which are the most challenging not only because of their small size, but also due to their high affinity towards water. For this purpose, we used a highly hydrophilic pentapeptide, CR(*N*Me)EKA (Cys-Arg-*N*-methyl-Glu-Lys-Ala; Scheme IV - 1a) as a benchmark case. CR(*N*Me)EKA is a peptide analog that was engineered to improve the stability of CREKA (Cyst-Arg-Glu-Lys-Ala; Scheme IV - 1b),[23] a peptide that interacts with fibrin clots and possesses favorable targeting ability to fibrin-fibronectin complexes in animal models with different pathologies (*e.g.* neoplasia, atherosclerosis and myocardial ischemia-reperfusion).[24-26] Of particular interest is the capacity of CREKA nanoworms to accumulate in tumor periphery, as evidenced by the presence of fibrin(ogen)-containing deposits in the vessel lumens.[23] This capacity was used to mediate glioblastoma-homing and prolong the retention of therapeutic NPs at the tumor site.[27] However, CREKA, which was conjugated with synthetic and natural materials (*e.g.* polymer NPs,[27-29] polymer-metal hybrid NPs,[30,31] polymer films,[32,33] and liposomes[34]) for imaging of tumor cells

and cancer therapies, showed very poor resistance to proteolysis. Such disadvantage was overcome by engineering the CR(*N*Me)EKA analog, featuring resistance against endogenous proteases,[23,35] over-stabilized bioactive conformation,[23] and lower tendency to aggregation.[36,37] Indeed, CR(*N*Me)EKA displayed important anti-cancer properties, inducing prostate tumor necrosis and significant reduction in tumor growth.[23] This was attributed to the blocking effect of tumor blood flow due to coverage of prostate cancer vessels, which was much higher for CR(*N*Me)EKA than for CREKA.

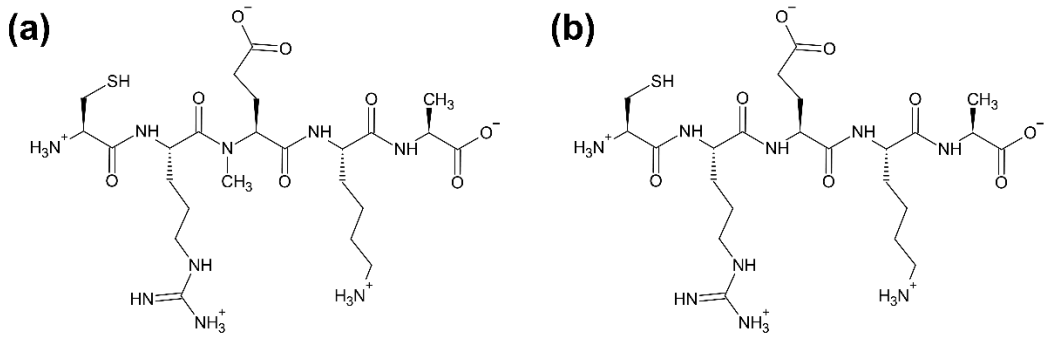

Scheme IV - 1. Chemical structure of (a) CR(*N*Me)EKA and (b) CREKA peptides.

To obtain a multi-responsive injectable carrier for the controlled delivery of CR(*N*Me)EKA, a biocompatible and pH-responsive hydrogel (named PBA-CS),[38,39] which is formed by phenylboronic acid (PBA) grafted with chitosan (CS), has been made conductive by incorporating biocompatible and electro-responsive peptide-loaded PEDOT NPs.[40,41] In this way, the release of the peptide from CR(*N*Me)EKA/PEDOT NPs is promoted by applying electrical stimuli, while the hydrogel vehicle responds as a chemoactuator to the chemical environment (pH), enhancing the release rate. After characterization of the PBA-CS hydrogel, PEDOT and CR(*N*Me)EKA/PEDOT NPs, and the conductive hydrogels obtained thereof (PBA-CS/PEDOT and PBA-CS/CR(*N*Me)EKA/PEDOT), the peptide release from CR(*N*Me)EKA/PEDOT NPs and PBA-CS/CR(*N*Me)EKA/PEDOT have been assessed upon different types of electrical stimuli.

IV - 2. Materials and methods

IV - 2.1. Materials

Chitosan (CS) medium molecular weight (DS: 63.2%), *N*-(3-dimethylaminopropyl)-*N'*-ethylcarbodiimide hydrochloride (EDC·HCl), *N*-hydroxysuccinimide (NHS), EDOT monomer, sodium dodecylbenzene sulfonate (SDBS), APS and MTT [3-(4,5-dimethylthiazol-2-yl)-2,5-diphenyltetrazolium bromide] were purchased from Sigma-Aldrich, whereas 3-carboxyphenyl boronic acid (PBA) was purchased from TCI. Glacial acetic acid (USP, BP, Ph. Eur.; pure, pharma grade) was purchased from

Pharma Eur. The CR(*N*Me)EKA peptide with > 98% HPLC purity was purchased from Biomatik (Toronto, ON). Ultrapure Milli-Q water was used to prepare all the aqueous solutions. Methanol (99.8%), acetonitrile (99.9%) and trifluoroacetic acid (99%) of HPLC grade were purchased from Fisher Scientific. High glucose Dulbecco's modified Eagle medium (DMEM), Ham's F-12K (Kaighn's) medium, Roswell Park Memorial Institute (RPMI) medium, fetal bovine serum (FBS), penicillin (100 units/mL), streptomycin (100 µg/mL), and amphotericin (25 µg/mL), 0.25% trypsin/EDTA solution, and LIVE/DEAD kit, Alexa Fluor 488 and Hoechst dye were purchased from Gibco™ by Thermo Fisher Scientific. All reagents were used as received without further purification.

IV - 2.2. Synthesis of PBA-CS hydrogel

PBA was grafted to CS (190-310 kDa) using a previously reported procedure (Scheme IV - 2).[38,39] Briefly, CS (1 g) was dissolved in 0.3 wt% acetic acid solution (120 mL) in a 250 mL flask. PBA (0.795 g, 4.32 mmol) and NHS (493 mg, 4.28 mmol) were dissolved in methanol (40 mL) and stirred at room temperature for 30 min. EDC·HCl (665 mg, 3.47 mmol) was added and stirred to form a uniform solution. Then, the mixed solution of PBA/NHS/EDC·HCl was added to the CS in acetic acid solution. After stirring for 24 h, the mixture was transferred to a dialysis tube with a molecular weight cut-off of 3.5 kDa and dialyzed against distilled water with one change every 4 h for three days. The dialysate was freeze-dried to yield a white powder product. The grafting ratio of PBA was determined to be 63% by 1H-NMR comparing the carbon/nitrogen (C/N) molar ratio. Then, PBA-CS (50 mg) was dissolved in a 2% (v/v) acetic acid aqueous solution (5 mL). After introducing 200 µL of the resulting solution in a mold, the hydrogel was formed by adjusting the pH to 8 by adding 20 µL of 1 M NaOH solution. The gelation took approximately 30 min and was confirmed by the vial-tilt test.

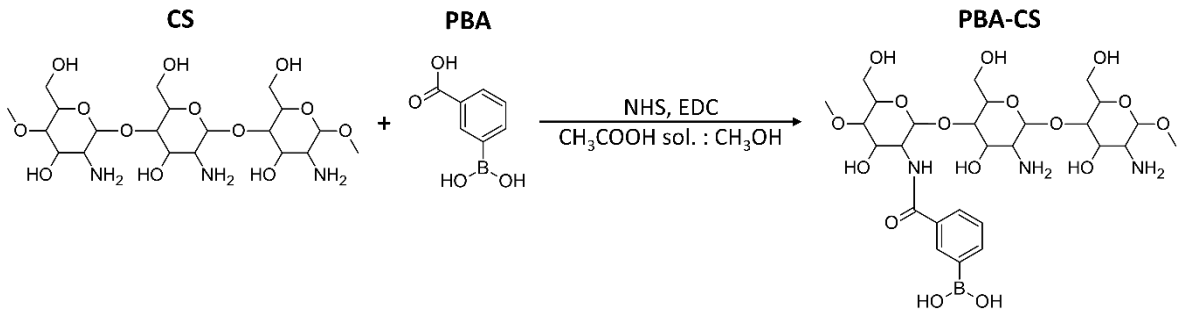

Scheme IV - 2. Synthesis of PBA-CS.

IV - 2.3. Synthesis of PEDOT NPs

PEDOT NPs were prepared by emulsion polymerization (Scheme IV - 3a). For this purpose, a SDBS surfactant solution (0.0163 g to 4.5 mL Milli-Q water, 9.3 mM) was prepared and kept at 40 °C and

750 rpm for 1 h. This was followed by the addition of 17.8 µL of EDOT monomer (32.2 mM) and, again, was stirred for 1 h at 750 rpm at 40 °C. Finally, an APS aqueous solution (0.0192 g to 0.5 mL Milli-Q water, 0.8 M) was added, and the reaction was kept for 16 h at 40 °C and 750 rpm, protected from light with aluminum foil. No sedimentation was observed after the reaction, which indicates good colloidal stability. The side products and unreacted chemicals were removed by a sequence of three centrifugations at 11000 rpm for 40 min at 4 °C alternating with 20 min of sonication, using milli-Q water for washing steps. The final product was then kept at 40 °C in an oven for 3 days until complete dryness (*i.e.* a constant weight value was observed). Then, the PEDOT NPs were re-dispersed in Milli-Q water by using a vortex and sonication bath, to obtain a dispersion of 5 mg/mL.

The synthetic procedure used to obtain CR(*N*Me)EKA/PEDOT NPs was identical to that described for PEDOT NPs with the exception of the step involving the addition of the EDOT monomer. In that case, 0.5 mL of a peptide solution (10 mg/mL in ultra-pure H_2O) was added in addition to the EDOT monomer.

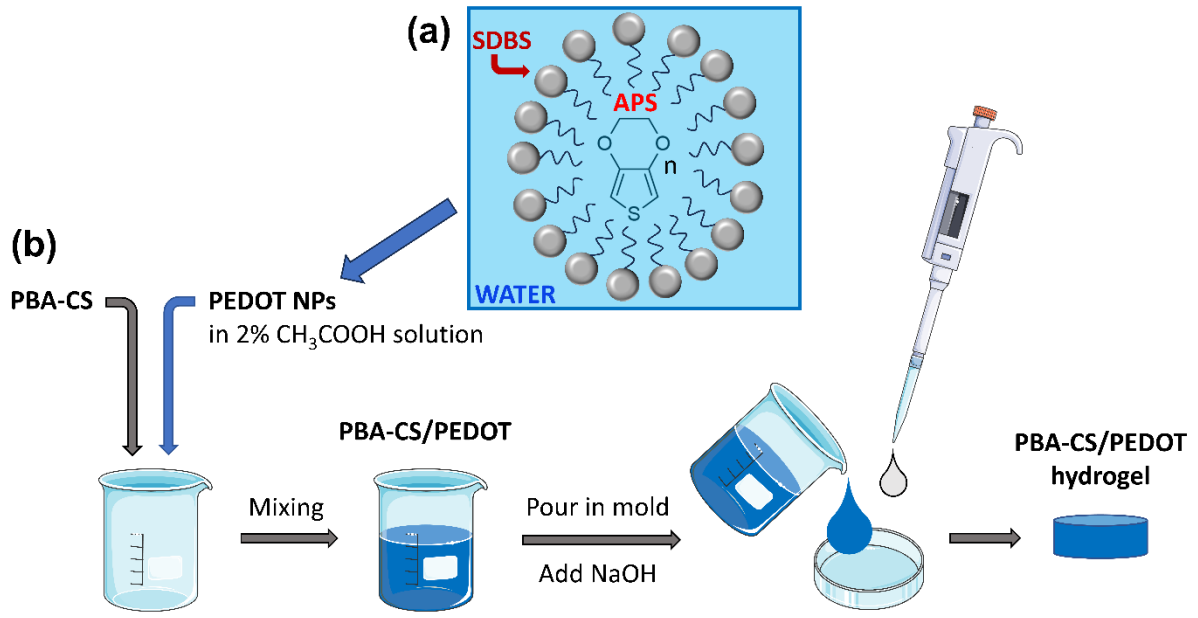

Scheme IV - 3. (a) Schematic representation of the chemical synthesis of PEDOT NPs and (b) process used to load PEDOT NPs in the PBA-CS hydrogel.

IV - 2.4. Preparation of PBA-CS hydrogel containing PEDOT NPs

PEDOT and CR(*N*Me)EKA/PEDOT NPs were loaded *in situ* during the gelling of the PBA-CS hydrogel. For this purpose, 1 mg of the corresponding NPs was added to the acetic acid aqueous solution used to dissolve the PBA-CS. Then, the resulting mixture (200 µL) was incorporated into a mold, and the pH was adjusted to 8 using a 1 M NaOH solution (20 µL), as for the PBA-CS hydrogel. The gelled systems,

which were formed in around 30 min, were denoted PBA-CS/PEDOT and PBA-CS/CR(*N*Me)EKA/PEDOT. The process is sketched for the PBA-CS/PEDOT hydrogel in Scheme IV - 3b.

IV - 2.5. Quantification of CR(*N*Me)EKA loading and release

CR(*N*Me)EKA was quantified using a Hitachi LaChrom HPLC system at room temperature with UV detection at 220 nm, using a reverse-phase Nucleosil C18 120 Å column (5 µm, 250 mm × 4 mm, Macherey-Nagel). The HPLC method was isocratic for 25 min at 0.5 mL/min with the mobile phase consisting of 10% acetonitrile, 10% methanol and 80% water, modified with 0.1% trifluoroacetic acid, and a 20 µL injection volume. CR(*N*Me)EKA samples obtained from the supernatants of NPs centrifugation steps after synthesis, and from the release medium during passive and electrostimulation release assays were centrifuged once more for 20 min at 12500 rpm in a Z233M-2 (Hermle) centrifuge. Afterwards, the supernatant was filtered with nylon syringe filters (13 mm diameter and 0.22 µm pore size, Tecnocroma), and analyzed by HPLC.

IV - 2.6. Fourier-transform infrared (FTIR) spectroscopy

FTIR transmittance spectra were recorded on an FTIR Jasco 4100 spectrophotometer. Samples were deposited on an attenuated total reflection accessory (Top-plate) with a diamond crystal (Specac model MKII Golden Gate Heated Single Reflection Diamond ATR). For each sample, 64 scans were performed between 4000 and 600 cm^{-1} with a resolution of 4 cm^{-1}.

IV - 2.7. Scanning electronic microscopy (SEM)

SEM micrographs were obtained using a Focussed Ion Beam Zeiss Neon 40 scanning electron microscope operating at 5 kV. Samples were mounted on a double-sided adhesive carbon disc and sputter-coated with a thin layer of carbon to prevent sample charging problems. For the estimation of NPs size distributions, n = 100 was considered. To record SEM micrographs of the hydrogels, lyophilized samples were considered. For lyophilization, samples were first hydrated for 3 h, after which they were frozen for 10 min using liquid nitrogen. Then, the hydrogels were broken into two pieces (for the pores to be observed at the rupture zone) and lyophilized for 3 days.

IV - 2.8. Dynamic light scattering (DLS) and zeta-potential

DLS studies were performed using a NanoBrook Omni Zeta Potential Analyzer from Brookheaven Instruments. Measurement consisted of 3 runs of 120 s duration each, which were averaged to obtain the effective size. Samples were analyzed at 25 °C using a scattering angle of 90°. To determine the Z-

potential, particles were re-suspended in a 0.01 M phosphate buffer saline (PBS) solution, and 30 consecutive measurements were taken of each sample.

IV - 2.9. Rheological characterization of the hydrogels

Rheological measurements of the as-prepared PBA-CS and PBA-CS/PEDOT hydrogels were performed using a modular compact rheometer, MCR302 (Anton Paar, Austria), equipped with electrically heated plates using a 25 mm parallel sandblasted plate test geometry and a solvent trap to prevent dehydration during testing. All samples were subjected to testing at 25 °C with n = 4. Frequency sweep measurements were performed at 1% strain in the range between 0.1 and 1000 rad/s. Oscillatory strain amplitude sweep measurements were carried out at a constant frequency (1 rad/s) and in a range of increasing strains (from 0.01 to 1000%). Besides, with the aim of exploring their self-healing properties, hydrogels were subjected to cyclic strain time sweep measurements with an alternating strain (5% and 1000%). The upper shear strain value corresponds to a value out of the linear viscoelastic region according to the strain sweep test results. Additionally, continuous flow of the hydrogels was examined by monitoring the change in hydrogel viscosity as a function of the increasing shear rate (0.01 – 100 s^{-1}).

IV - 2.10. Macroscopic characterization of the hydrogels

The gel fraction (GF), equilibrium water content (EWC), and hydration ratio (HR) of the PBA-CS hydrogel system, with or without PEDOT NPs, were evaluated in triplicate at pH 5, 7 and 9. First, to determine the GF, the as-prepared hydrogels were lyophilized, and their weights (m_{1L}) were recorded. The hydrogels were washed in 0.01 M PBS at different pH values for 24 h, with frequent changes in water to remove the remaining soluble fraction, and lyophilized again (m_{2L}). The GF was expressed as

$$\mathrm{GF}\ (\%) = \frac{m_{2\mathrm{L}}}{m_{1\mathrm{L}}} \times 100 \qquad \text{(IV - 1)}$$

The temporal evolution of the mass of the gel fraction (MGF) with respect to the mass of the as-synthesized hydrogel (m_{1L}) was also evaluated at pH 5 considering five lyophilization/re-hydration cycles distributed over two weeks. Thus, the MGF of cycle *i* (MGF^i) was defined as

$$\mathrm{MGF}^i\ (\%) = \frac{m_{\mathrm{i}}}{m_{1\mathrm{L}}} \times 100 \qquad \text{(IV - 2)}$$

where m_{i} is the mass of the hydrogel after *i* lyophilization/re-hydration cycles.

To determine the equilibrium water content (EWC), the prepared hydrogels were allowed to swell in 0.01 M phosphate buffer saline (PBS) solution at pH 5, 7 or 9 for 2 days, so that swelling could reach equilibrium. The surface water was then removed with soft tissue paper, and the weights were recorded (m_{2d}). The hydrogels were then lyophilized, and the weights were recorded (m_l). Hence, the EWC was determined using the following expression:

$$\text{EWC}\ (\%) = \frac{m_{2d} - m_l}{m_{2d}} \times 100 \qquad \text{(IV - 3)}$$

Additionally, the temporal evolution of the hydration ratio (HR) was examined as a function of the pH. The HR at time *t* was evaluated considering the mass of the hydrogel hydrated in 0.01 PBS for *t* hours (m_t) with respect to the mass of the as-synthesized samples (m_0):

$$\text{HR}\ (\%) = \frac{m_t}{m_0} \times 100 \qquad \text{(IV - 4)}$$

Electrochemical characterization was carried out by CV using an Autolab PGSTAT302N. Experiments were conducted in a 0.1 M PBS solution (pH 5, 7 or 9 adjusted with HCl and NaOH) at room temperature. The initial and final potentials were −0.8 V, the reversal potential was +0.8 V and the scan rate, 100 mV/s. In order to stabilize the samples before the CV measurements, they were incubated in the corresponding pH solution for 5 min. All experiments were performed at least 3 times using independent samples.

IV - 2.11. Peptide release from CR(*N*Me)EKA/PEDOT NPs

For passive release studies, 20 µL of CR(*N*Me)EKA/PEDOT NPs (5 mg/mL) were deposited on the surface of stainless steel (0.5 cm x 0.5 cm) and left to dry overnight. Then, the electrodes were immersed in 7 mL of 0.01 M PBS solution (pH 5) and kept in a shaker at 37 °C at 80 rpm for 2 h. The released peptide was quantified by HPLC, as described above. Passive release experiments were repeated three times and the averages were plotted.

For electrostimulated release studies, 20 µL of CR(*N*Me)EKA/PEDOT NPs (5 mg/mL) were deposited on the surface of stainless steel (0.5 cm × 0.5 cm) and left to dry overnight. A three-electrode configuration was used: the stainless steel-CR(*N*Me)EKA/PEDOT was the working electrode, a platinum wire was the counter electrode, and Ag|AgCl was the reference electrode. 7 mL of 0.1 M PBS (pH 5) was used as the electrolytic medium. For hydrogel stimulation, the hydrogel was placed between stainless steel and a Transwell insert membrane (Falcon ®, Corning Inc., USA), and the same conditions were used (Scheme IV - 4). The voltage was applied by: 1) CV using a potential window from –0.50 V to +0.80 V during 60, 100 and 150 consecutive cycles at a scan rate of 100 mV/s; and 2) chronoamperometry (CA) using a voltage of +0.50 V or –0.50 V. A total of 1, 3, 6, 12 and 24 CA cycles were applied, and each cycle consisted of: a) the application of the potential (+0.50 V or –0.50 V) for 240 s (4 min); and b) interruption of the voltage for 300 s (5 min). All measurements were repeated at least three times, and the average with the standard deviation was plotted on the graphs.

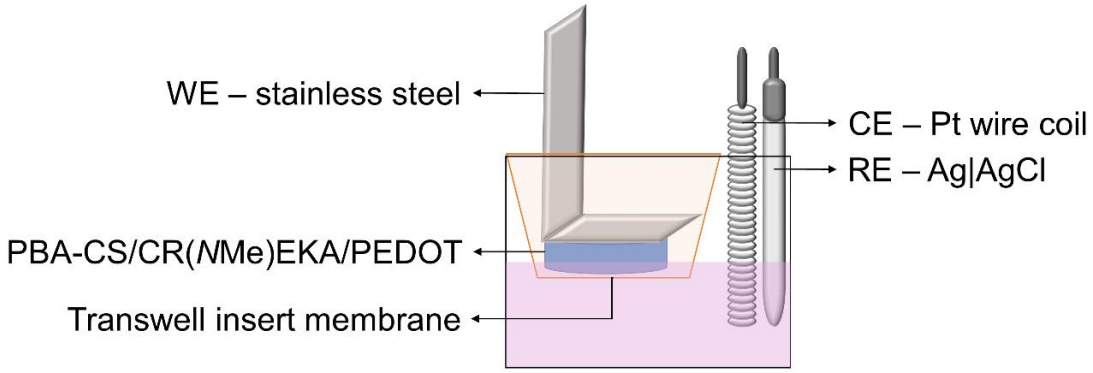

Scheme IV - 4. Setup used for electrostimulation of the hydrogels. WE – working electrode, RE – reference electrode, CE – counter electrode.

IV - 2.12. Cellular assays

Cellular assays were performed using MG-63 (osteoblast cell line with fibroblast morphology), and COS-1 (fibroblast-like isolated from the kidney of African green monkey), which were cultured in high glucose DMEM, and also in PC-3 (human prostate cancer) and PNT-2 (normal human prostate epithelium immortalized with SV40) cells, which were cultured in Kaighn's medium and RPMI medium, respectively, both supplemented with 10% FBS, and 1% of penicillin (100 units/mL), streptomycin (100 µg/mL), and amphotericin (25 µg/mL). Cultures were maintained in a humidified incubator with an atmosphere of 5% CO_2 and 95% O_2 at 37 °C. Culture media were changed every two days. When the cells reached 80-90% confluence, they were detached using 2 mL of trypsin (0.25% trypsin/EDTA) for 5 min at 37 °C. Finally, cells were re-suspended in 5 mL of fresh medium and their concentration was determined by counting with a Neubauer camera using 0.4% trypan blue.

The tested hydrogel systems (PBA-CS and PBA-CS/PEDOT) were placed in 24-well plates and sterilized using UV irradiation for 15 min in a laminar flux cabinet. Controls were simultaneously performed by culturing MG-63 cells directly on the surface of tissue culture polystyrene (TCPS) wells. For adhesion and proliferation assays, 2×10^4 and 5×10^4 cells, respectively, were deposited on the surface of each well, and contact with the sample was promoted through Transwell inserts. The latter, which consists in a holder that is placed inside a well with a membrane on the bottom, allows the transfer of molecules between the hydrogel sample and the cells that are on the bottom of the well. Then, attachment of cells to the surface was promoted by incubating under culture conditions for 30 min. Finally, 2 mL of the culture medium were added to each well. After periods of 24 h and 7 days, all cells on the surface of the samples were detached and quantified as previously described to evaluate cell viability at different stages of the culture.

PC-3, PNT-2 and COS-1 cells were seeded at a density of 2×10^4 cells/well in 96-well plates for viability assays, and after 24 h, they were further cultured in medium supplemented with 1.25 mg/mL of CR(*N*Me)EKA, and the supernatant from PBA-CS/CR(*N*Me)EKA/PEDOT after CA electrostimulation using –0.5 V and 24 cycles (dilution from 1:1 to 1:8) for 24 h. Cell viability was evaluated by the colorimetric MTT assay, while cells were imaged by confocal microscopy.

IV - 2.12.1. MTT assay

Cell viability was evaluated by the colorimetric MTT assay. Specifically, 1 mL or 100 µL of MTT solution (5 mg/mL in PBS) were added to each well in 24-well containing MG-63 cells or 96-well plates containing PC-3, PNT-2 and COS-1 cells, respectively. After 3 h of incubation, the samples were washed twice with PBS. To dissolve formazan crystals, 1 mL or 100 µL of DMSO was added to each well in 24-well or 96-well plates, respectively. Finally, the absorbance was measured in a plate reader at 570 mm. The viability results correspond to the average of three independent replicas (n = 3) for each system. The results were normalized with respect to the control for relative percentages. Statistical analyses were performed with a confidence level of 95% ($p < 0.05$) using Student's T-test.

IV - 2.12.2. Confocal microscopy

For the LIVE/DEAD viability assay, after 24 h or 7 days of incubation, cells were washed 3 times, 5 min each with 0.01 M PBS, stained with 0.5 µL/mL calcein stock solution (green for live cells) and 2 µL/mL ethidium bromide stock solution (red for dead cells) for 30 min, and washed again 3 times for 5 min each with 0.01 M PBS. Samples were protected from light and kept at 4 °C before imaging, which was performed using a10X objective of an Axio Observer 7 (Confocal laser microscope Carl ZEISS LSM 800). Imaging processing was completed with ZEN and ImageJ software. Confocal microscopy images of PC-3 and COS-1 cells after release of the CR(*N*Me)EKA peptide were acquired to visualize the actin cytoskeleton with green-fluorescent Alexa Fluor 488 phalloidin and nuclei with blue Hoechst dyes.

IV - 3. Results and discussion

IV - 3.1. Chemical and morphological characterization

The successful grafting of PBA to CS was confirmed by FTIR spectroscopy (Fig. IV - 1a). The higher intensity of the peaks at 1544 and 1376 cm^{-1} for PBA-CS than for CS was attributed to the contributions of the benzene ring vibration and the B–O deformation and stretching from PBA, respectively.[42]

Comparison of the FTIR spectra recorded for PEDOT NPs and for the CR(*N*Me)EKA peptide with that recorded for CR(*N*Me)EKA/PEDOT NPs (Fig. IV - 1b) confirmed the successful loading of the peptide.

In addition to the typical bands of PEDOT, CR(*N*Me)EKA/PEDOT NPs showed the characteristic amide I (1645 cm^{-1}) and amide II (1530 cm^{-1}) bands of the peptide, as well as peaks at 1179 and 1128 cm^{-1}, which were associated with the side groups of Arg ($–N^+H_3$) and (*N*Me)Glu (C–O).[43] On the other hand, the FTIR spectrum of the PBA-CS/PEDOT hydrogel (Fig. IV - 1a) showed the characteristic fingerprints of PEDOT NPs (Fig. IV - 1b) and the PBA-CS hydrogel (Fig. IV - 1a).

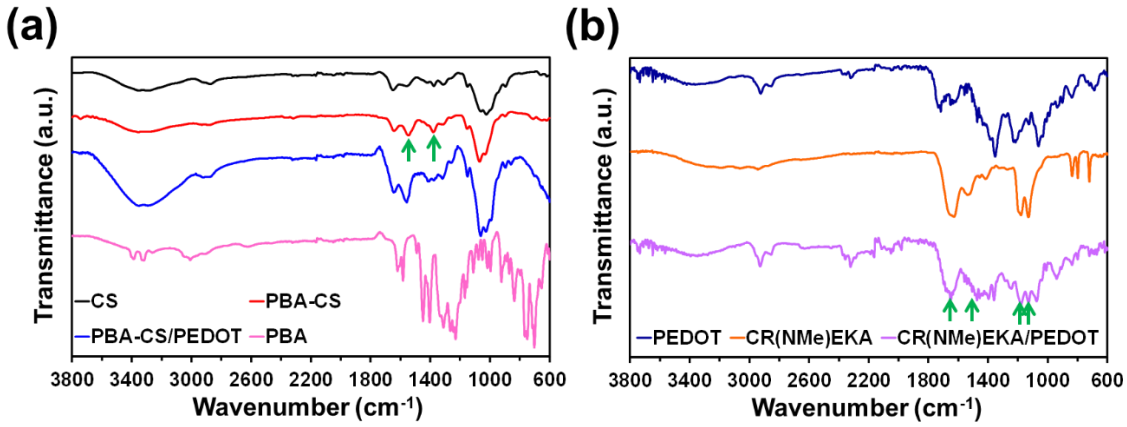

Fig. IV - 1. FTIR spectra of (a) CS, PBA-CS, PBA-CS/PEDOT and PBA, and (b) PEDOT NPs, CR(*N*Me)EKA peptide and CR(*N*Me)EKA/PEDOT NPs. Green arrows: C–C of the thiophene ring around 1300 cm^{-1}, C=C stretching band and C=C stretching vibration around 1500-1600 cm^{-1}, C=O stretching bands around 1600 cm^{-1}.

SEM images of PEDOT and CR(*N*Me)EKA/PEDOT NPs (Fig. IV - 2a-b) revealed a well-defined spherical shape of PEDOT NPs, whereas the loading of the charged peptide altered this shape to slightly irregular ovaloid aggregates. Additionally, the size of the PEDOT NPs (118 ± 14 nm) increased by a factor of approximately 1.8, to 210 ± 75 nm, when the peptide was loaded (Fig. IV - 2c-d). The average size of PEDOT and CR(*N*Me)EKA/PEDOT NPs was also determined by DLS, and the results obtained were consistent with those obtained by SEM. Indeed, the average size of CR(*N*Me)EKA/PEDOT NPs was higher than that of PEDOT NPs by a factor of 1.8 (*i.e.* 235 ± 78 nm *vs* 146 ± 23 nm) and showed higher polydispersity. Quantitative differences between SEM and DLS size estimations were associated mainly to the methods attributes as: 1) size values derived from SEM micrographs correspond to the polymeric core of the NPs, which result from both the drying process and the high vacuum inside the SEM chamber, while DLS provides a hydrodynamic diameter in suspension; and 2) in DLS, the presence of bigger particles contributes to an increase in light scattering, thus shifting the measured particle size towards higher values.[44]

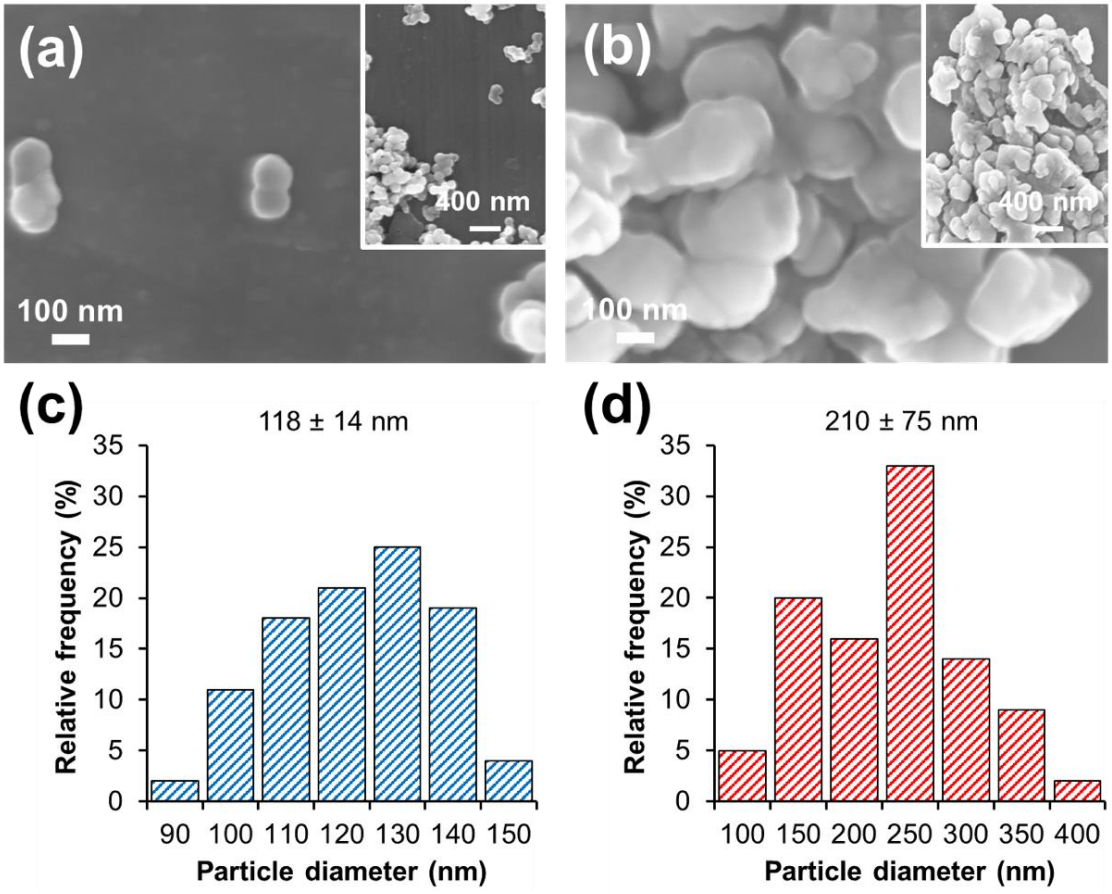

Fig. IV - 2. SEM images of (a) PEDOT and (b) CR(*N*Me)EKA/PEDOT NPs. Size histograms (n = 100) for (c) PEDOT and (d) CR(*N*Me)EKA/PEDOT NPs.

The Z-potential defines the electrostatic repulsion or attraction between NPs in a dispersion, and thus their colloidal stability. For our system, the Z-potential values determined for CR(*N*Me)EKA/PEDOT and PEDOT NPs, which were -34 ± 2 and -29 ± 2 mV, respectively, imply that the NPs' charge prevents them from aggregating due to electric repulsion.[45,46] On the other hand, the negative values of the Z-potential have been attributed to the negatively charged SBDS dopant agent, which surrounds the NPs and interact electrostatically with the oxidized PEDOT chains and the positively charged peptide molecules. Indeed, the same feature has been observed for PEDOT NPs prepared by emulsion polymerization using other dopant agents.[40]

In order to evaluate the loading efficiency (LE) for CR(*N*Me)EKA/PEDOT NPs, HPLC-UV was used to quantify the peptide remaining in the supernatant after NP synthesis (calibration curve shown in Fig. IV - 3), which was subtracted from the initial peptide amount. The LE was found to be as high as 80 ± 4 %. The high amount of peptide loaded in the NPs is consistent with the larger size and higher Z-potential (in absolute value) of the CR(*N*Me)EKA/PEDOT NPs with respect to the PEDOT NPs. It is worth noting that positively charged CR(*N*Me)EKA peptide molecules were bound to the NPs through

attractive electrostatic interactions with the dopant $SDBS^-$ counter-anions rather than with oxidized PEDOT chains that were also positively charged.

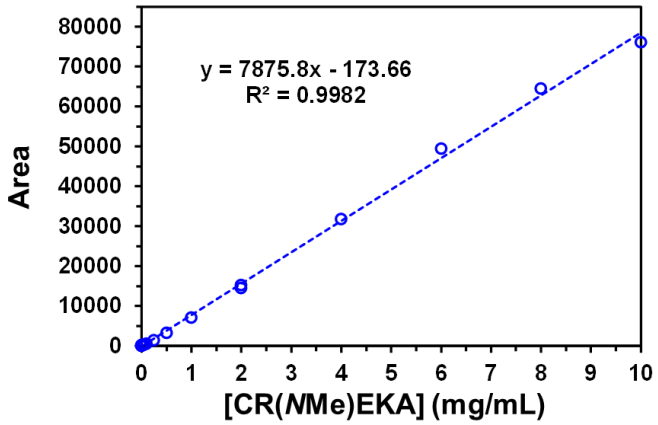

Fig. IV - 3. Calibration curve used to quantify the peptide loading efficiency and the peptide release by HPLC.

SEM micrographs of PBA-CS showed a continuous and interconnected porous 3D structure in which thin hydrogel layers were arranged without any clear preferential orientation (Fig. IV - 4a). Although the incorporation of PEDOT NPs did not alter the 3D structure, the PBA-CS/PEDOT samples exhibited ultra-thin fibers, not only crossing the pores, but also coating the surface of PBA-CS layers (Fig. IV - 4b). Such fibers were attributed to the PEDOT NPs, which aggregated and coalesced, thus giving rise to a percolated 3D network of conducting fibers.

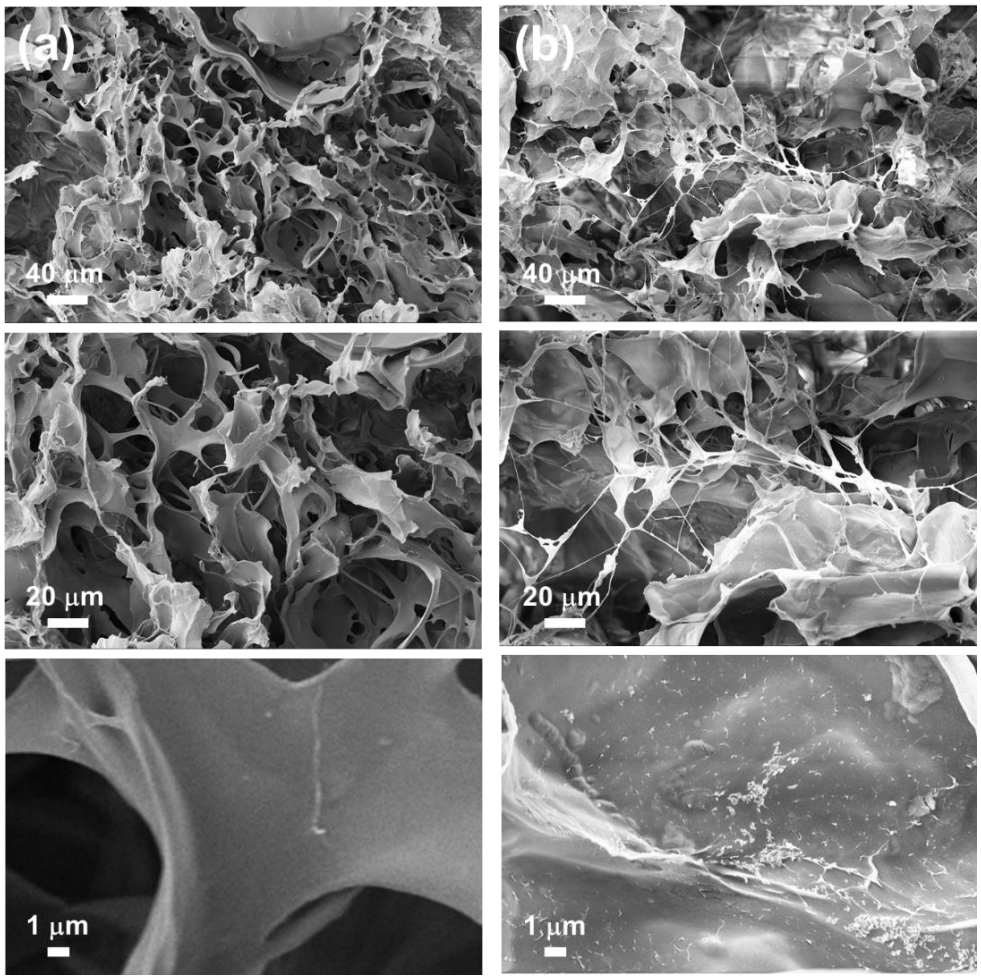

Fig. IV - 4. Cross-section SEM images of (a) PBA-CS and (b) PBA-CS/PEDOT at different magnifications.

IV - 3.2. Stability and swelling capacity of the hydrogels

To examine the stability of the PBA-CS hydrogel with and without loaded NPs, the GF was determined at acidic, neutral and basic pH values (*i.e.* pH 5, 7 and 9, respectively). The results (Table IV - 1.) indicated that the GF of PBA-CS was approximately 30%, regardless of the pH. For PBA-CS/PEDOT, this value decreased to 10-15%, especially at neutral and basic pH, which indicated that the cross-linking efficiency decreased in the presence of NPs. Since the boronate bonds between polymer chains are known to dissociate at acidic pH,[47,48] the temporal stability of the hydrogels was studied considering MGF^{i} for five cycles (i = 5) distributed over two weeks. After a rapid reduction in the first cycle, the mass of the gel fraction stabilized for both PBA-CS and PBA-CS/PEDOT and lasted for at least two weeks, thus validating their stability for biomedical applications at acidic pHs, such as the one found in the TME (Fig. IV - 5).

Table IV - 1. GF and EWC of PBA-CS and PBA-CS/PEDOT hydrogels at acidic, neutral and basic pH.

Hydrogel	pH	GF (%)	EWC (%)
PBA-CS	5	25 ± 7	81 ± 5
	7	36 ± 8	86 ± 2
	9	25 ± 4	76 ± 6
PBA-CS/PEDOT	5	24 ± 2	80 ± 3
	7	15 ± 3	86 ± 1
	9	9 ± 3	86 ± 3

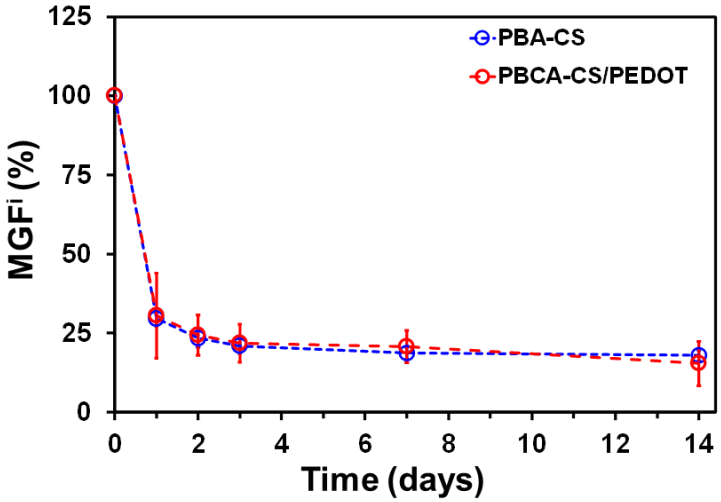

Fig. IV - 5. Temporal evolution of the MGF^i at pH 5 considering five cycles (i = 5) distributed over two weeks for PBA-CS and PBA-CS/PEDOT hydrogels.

Although boronate bonds are hydrolyzed very rapidly at pH < 5.0,[47,48] considering the biological application presented in this study, we did not consider pH values lower than 5. However, results displayed in Fig. IV - 5 and Table IV - 1. indicate that the behavior of boronate bonds is altered by other factors, making difficult the prediction of the GF and MGF^i. Some of these factors could be: 1) the microenvironments created by the complex 3D structure of hydrogels, which could play a role similar to that played by the microenvironments in large structured proteins (*i.e.* the pKa of acid / basic residues buried inside such macromolecules is drastically altered[49,50]); and 2) the presence of unreacted charged / polar groups in chitosan and, especially, the oxidized PEDOT NPs alter the conditions at which boronate ester bonds are stable, as suggest the results for PBA-CS/PEDOT (Table IV - 1.).

On the other hand, the EWC, which measures the percentage of water that the hydrogels retain at equilibrium, was close to 80-85% for both PBA-CS and PBA-CS/PEDOT, independently of the pH (Table IV - 1.). To obtain more precise information on the swelling capacity of hydrogels and its dependence

on pH, the HR of PBA-CS and PBA-CS/PEDOT was assessed as a function of time and pH, introducing the samples into PBS solutions at pH 5, 7 and 9. Increasing the incubation time, the HR of PBA-CS (Fig. IV - 6a) rapidly decreased at acidic pH, was almost preserved at neutral pH, and rapidly increased at basic pH. Such behavior can be explained by the dynamic nature of the boronate ester bond and the pH responsiveness of PBA-CS.[47,48] The hydrogel, obtained under basic conditions, collapsed at acidic pH owing to the dissociation of the boronate bonds between the polymer chains. Instead, the HR was stable at neutral pH, while the structure was reinforced at basic pH by forming additional bonds. For PBA-CS/PEDOT, the temporal evolution of the HR followed the same behavior (Fig. IV - 6b), even though changes at basic pH were moderate in comparison to PBA-CS. This was attributed to the steric effect of PEDOT NPs, which was found to decrease the boronate bonds stability (Table IV - 1.).

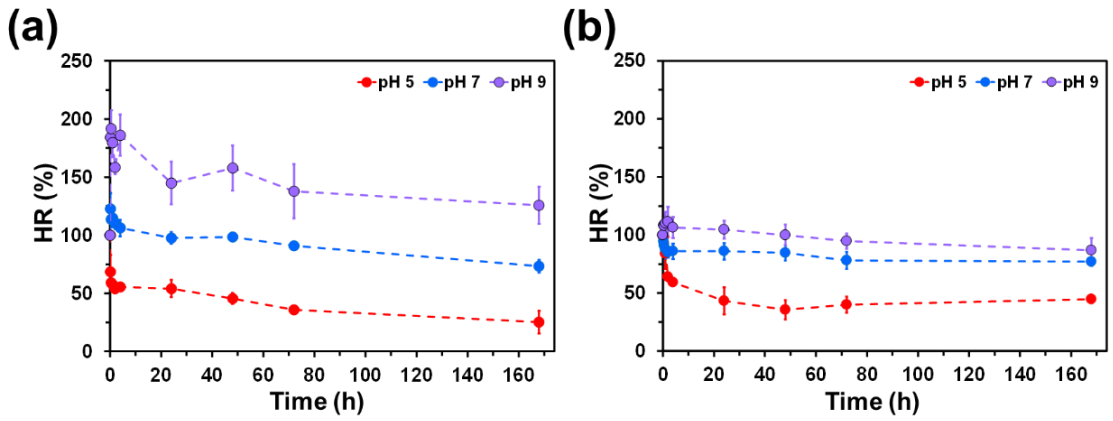

Fig. IV - 6. Temporal evolution of HR for (a) PBA-CS and (b) PBA-CS/PEDOT hydrogels at pH 5, 7 and 9.

All hydrogels displayed good injectability and shape-recovery properties, illustrated for PBA-CS/PEDOT in Fig. IV - 7a. When the hydrogel was introduced into a syringe and re-injected, the resulting cylindrical shape quickly adopted the initial bulk geometry. In addition to the shape restoration capacity of the post-injected hydrogels, both the PBA-CS and PBA-CS/PEDOT hydrogels displayed a self-healing response. After cutting the hydrogels into halves, pieces of different types of hydrogels were put in contact and switched from room (25 °C) to physiological temperatures (37 °C). The samples perfectly healed after 30 min (Fig. IV - 7b).

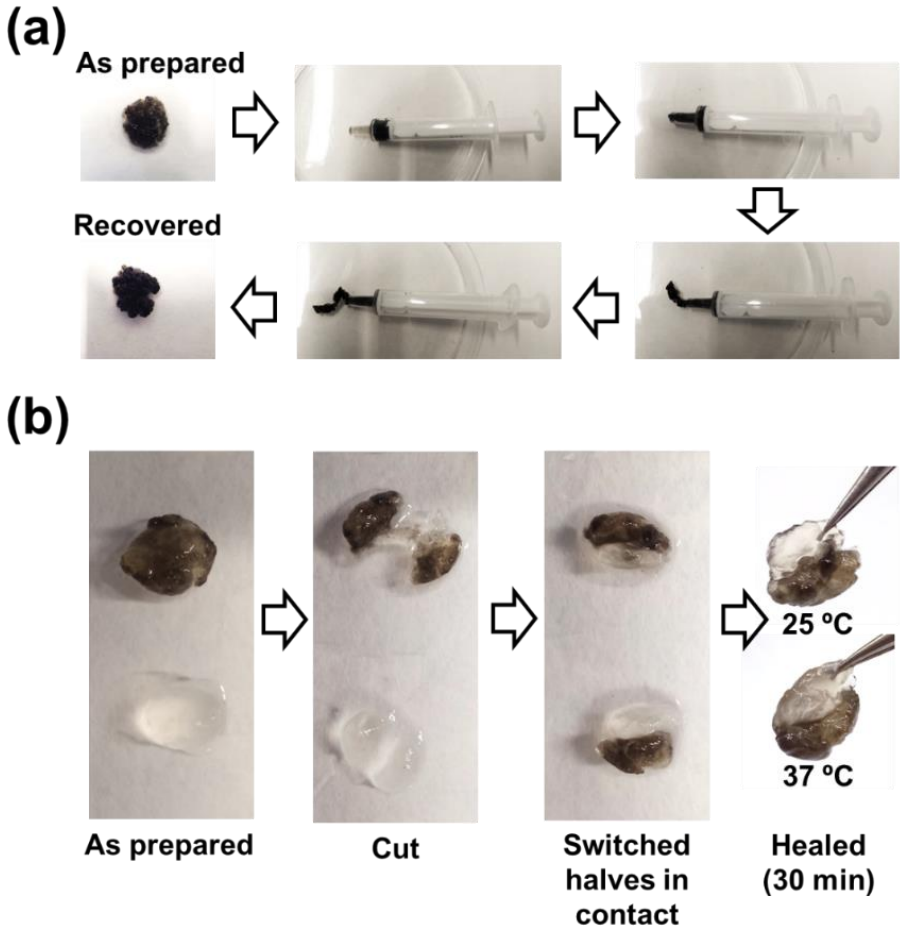

Fig. IV - 7. (a) Digital photographs showing the shape of PBA-CS/PEDOT as-prepared, the re-injection of the hydrogels and their shape restoration. (b) Digital photographs showing the self-healing property of the PBA-CS and PBA-CS/PEDOT hydrogels (colorless and dark, respectively).

The viscoelastic properties of the PBA-CS and PBA-CS/PEDOT hydrogels were explored (Fig. IV - 8, Fig. IV - 9 and Fig. IV - 10). First, frequency sweep testing was carried out to quantify the overall viscoelastic response, with the storage modulus (*G*') accounting for the ability of the material to store energy elastically under shear and the loss modulus (*G*'') representing the viscous component (Fig. IV - 8). For both systems, gel-like behavior was observed, as the elastic component *G'* was higher than the viscous value *G''*, and the values were constant for almost all the tested shear frequency ranges. Specifically, the *G'* modulus (determined at 1 rad/s and 1% strain in frequency sweeps) was found to be 3.5 ± 0.5 kPa and 3.8 ± 0.5 kPa for PBA-CSA and PBA-CSA/PEDOT, respectively, which indicates that both systems display similar stiffness regardless of the presence of PEDOT NPs.

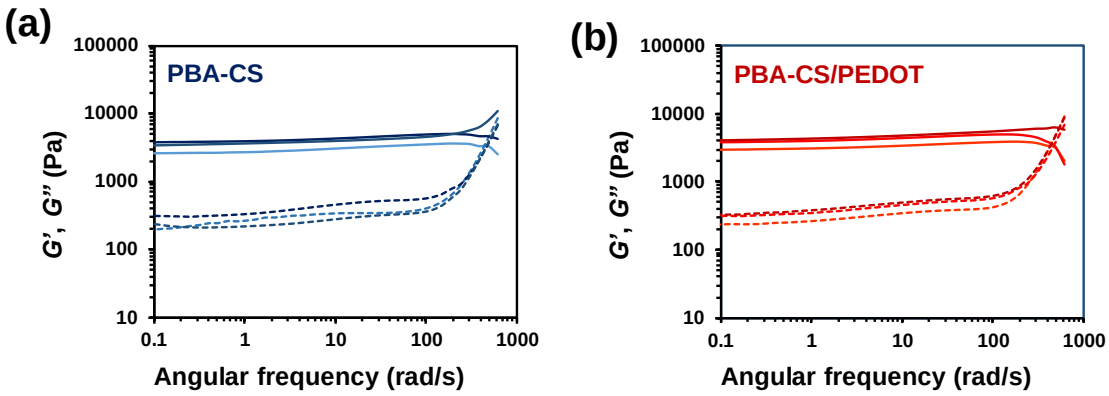

Fig. IV - 8. Representative curves of storage (*G*' - solid line) and loss (*G*'' - dashed line) modulus as a function of frequency for (a) PBA-CS and (b) PBA-CS/PEDOT hydrogels (n = 3) at 25 °C.

The mechanical properties of both hydrogel formulations were also explored by monitoring the change of *G*' and *G*'' in a range of increasing strains (Fig. IV - 9a). Strain sweep test confirmed the gel-like state of the materials and revealed a broad linear viscoelastic (LVE) region. The LVE region for each hydrogel corresponds to the region where the G' values are independent of the applied deformation. Structural changes of the hydrogels were considered when deviation from the linear behavior was observed.

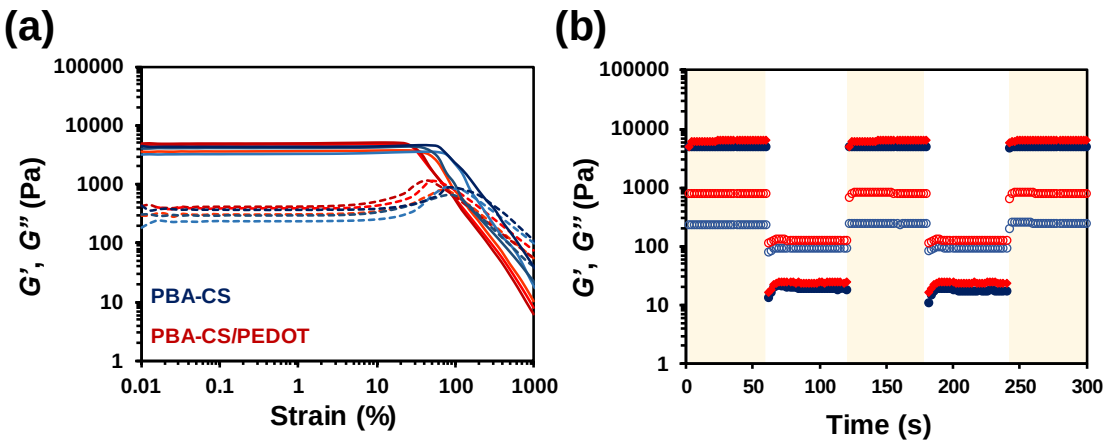

Fig. IV - 9. (a) Rheological strain sweep testing: curves of storage (*G*' - solid line) and loss (*G*'' - dashed line) moduli as a function of strain for PBA-CS (blue) and PBA-CS/PEDOT (red) hydrogels at 25 °C (n = 3); (b) Cyclic strain time sweep measurements with an alternating strain at 5% (yellow background where *G*' (solid circles) > *G*'' (empty circles)) and 1000% (white background - *G*'<*G*'') for both PBA-CS (blue) and PBA-CS/PEDOT (red) hydrogels.

When submitted to amplitude sweep tests (Fig. IV - 9a), the hydrogels' viscoelastic performance remained stable for almost the entire amplitude range, only yielding at strain values higher than 35%.

As before, comparison of the strain sweep curves recorded for the control hydrogel (PBA-CS hydrogel) with those obtained for the system containing PEDOT NPs evidenced no significant differences in their viscoelasticity. After adding PEDOT NPs, the mechanical strength of the samples, evaluated by comparing their *G'* values in the LVE region, did not vary significantly with respect to the control system. Accordingly, the PBA-CS/PEDOT hydrogel strength was not affected by the dispersion of PEDOT NPs, indicating that the gelation was mainly governed by boronate ester bonding. However, at very high strain values, minor differences at the gel-sol transition (*i.e.* flow point indicated by the crossover between *G'* and *G''* curves) were observed between systems, which indicated a potential interaction between PEDOT NPs and PBA-CS polymer chains. Despite this, the hydrogels maintain their shape after gelation and resist deformation under mild stress, which makes them suitable for the intended biomedical applications and shows that PEDOT NPs have no negative impact on their mechanical integrity and stiffness.

Second, cyclic strain time sweep measurements were recorded to determine *G'* and *G''* values of PBA-CSA and PBA-CSA/PEDOT hydrogels (Fig. IV - 9b). Two cycles were performed alternating different strain values, 5% or 1000%, and the results were indicative of a thixotropic response. The hydrogels were reversibly deformed under the applied stress (*G''* > *G'*), but recovered their original state almost immediately (*G'* > *G''*) when the stress was removed, independently of the presence of PEDOT NPs. Hence, the hydrogels possess high recoverability of their initial viscoelastic properties when subjected to repetitive strain beyond the yield point. Similarly, by means of flow curves recorded at 25 °C (Fig. IV - 10), their shear-thinning response was quantified as viscosity decreased under increased shear, thus allowing the material to flow more easily.

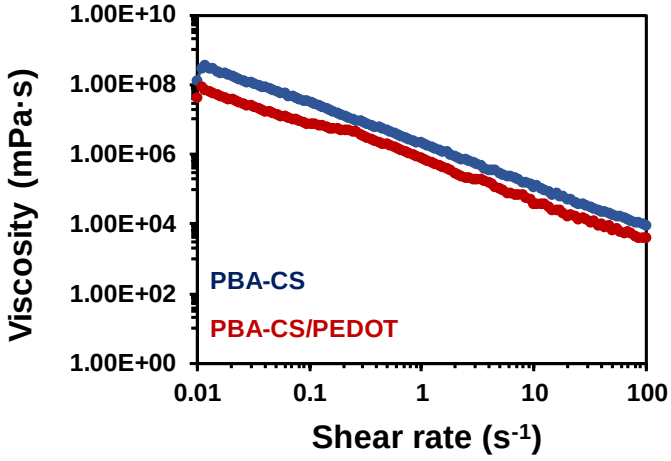

Fig. IV - 10. Flow curve for PBA-CS (blue) and PBA-CS/PEDOT hydrogels (red) at 25 °C.

Overall, such shear-thinning response and, in turn, injectability of PBA-CS/PEDOT hydrogels, is advantageous in that they can be easily and precisely administered to a specific location in the body by minimally invasive delivery systems. Furthermore, PBA-CS/PEDOT hydrogels can conform to irregular shapes or cavities within the body, properly covering the targeted area and, consequently, maximizing their therapeutic effect when loaded with functional cargo. This property, which is particularly crucial for hydrogels intended for targeted drug delivery, ensures optimal interfacial contact with the targeted tissue.

IV - 3.3. Electrically controlled peptide release from CR(*N*Me)EKA/PEDOT NPs and PBA-CS/CR(*N*Me)EKA/PEDOT hydrogel

The utilization of electric voltage to stimulate and control the release of drugs is an important field in biomedical engineering.[51-53] However, as a prior step to the electro-regulated release assays, it has been confirmed that the hydrogel loaded with NPs maintains the electrochemical activity previously observed for PEDOT NPs alone.[29,40,54] The response of the prepared systems is illustrated in Fig. IV - 11, which compares the cyclic voltammograms of PBA-CS and PBA-CS/PEDOT hydrogels at pH 5, 7 and 9.

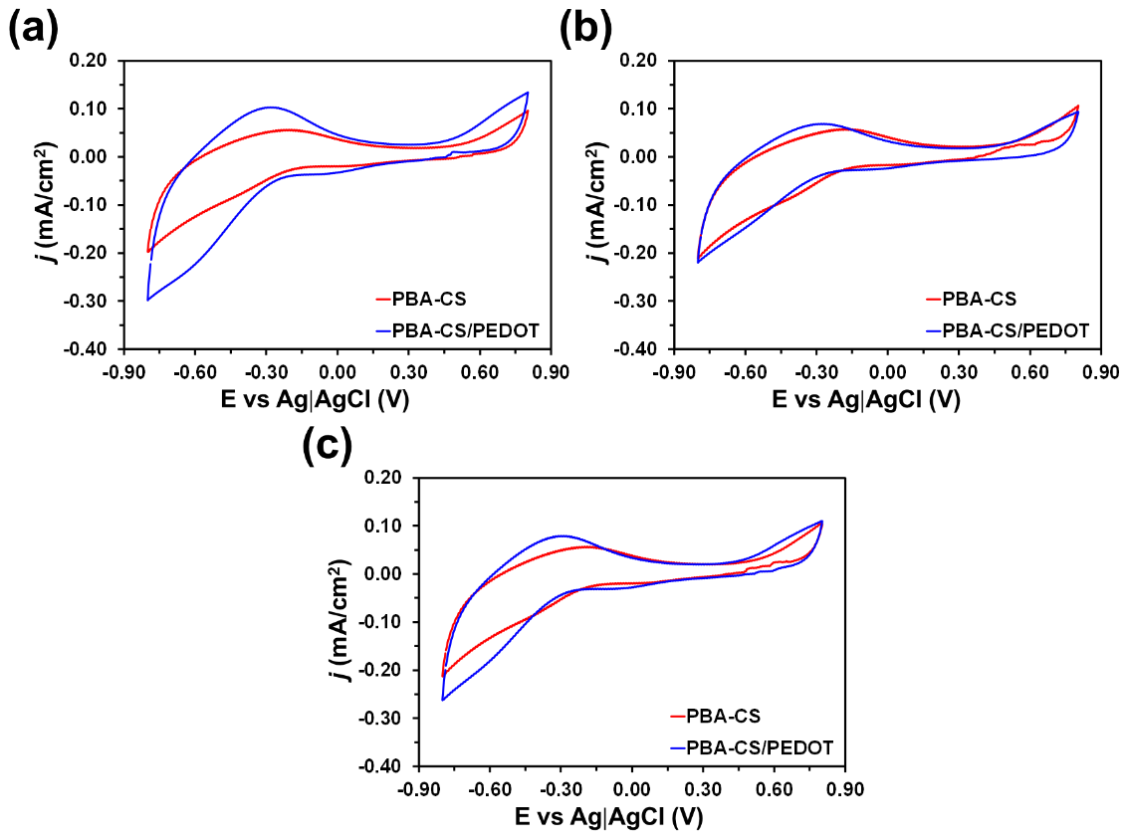

Fig. IV - 11. Cyclic voltammograms recorded for PBA-CS and PBA-CS/PEDOT hydrogels in PBS at (a) pH 5, (b) pH 7 and (c) pH 9.

As it was expected, the PBA-CS hydrogel behaved as an electro-responsive system due to the charged groups and the corresponding counterions (*i.e.* ionic contribution to the electrochemical response). After the incorporation of PEDOT NPs, the electrochemical activity increased slightly, which is reflected by the fact that the area of the voltammogram was higher for PBS-CS/PEDOT than for PBA-CS hydrogel at the three studied pH values. This small enhancement in the electrochemical response was due to the activation of PEDOT NPs through the ionic transport. However, PEDOT NPs did not produce a significant increment of electroactivity since electronic conducting paths were not created (*i.e.* the amount of PEDOT NPs was not enough to produce percolation). Although the difference between the two systems showed a relatively small pH dependence, the area of the voltammograms obtained for PBA-CS/PEDOT hydrogel at pH 5 was larger than those at pH 9 and pH 7 (Fig. IV - 12b). This was attributed to the role of H_3O^+ ions that interact with the dopant anions of PEDOT NPs, altering the oxidation degree of PEDOT chains. Overall, PBA-CS/PEDOT system is electroactive mainly due the ionic contribution from PBA-CS, which is expected to facilitate the release of the peptide through the activation of the loaded NPs. As the differences induced by the pH are relatively small, this chemical factor is not expected to significantly affect the activation of peptide-loaded NPs.

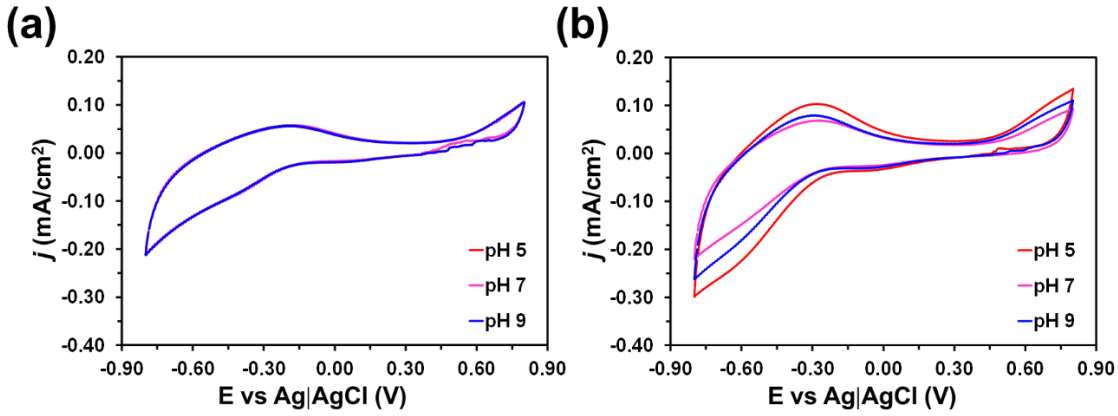

Fig. IV - 12. Representative cyclic voltammograms recorded in PBS at pH 5, 7 and 9 for (a) PBA-CS and (b) PBA-CS/PEDOT hydrogels.

In this work, the electrically controlled release of CR(*N*Me)EKA molecules was investigated using an acidic medium instead of a neutral medium (*i.e.* healthy prostate cell's exhibit a pH of 7.3[55,56]) due to: 1) the acidic microenvironment (pH 5 to 6.8) found in tumors;[57-59] and 2) the reported dissociation of boronate bonds in Alg–$B(OH)_2$ at acidic pH,[47,48] leading to hydrogel collapse (Fig. IV - 6), promoting the peptide release. From the mechanistic point of view, the release of CR(*N*Me)EKA from CR(*N*Me)EKA/PEDOT NPs was studied using the redox properties of PEDOT to alter peptide···polymer

interactions. Thereafter, the peptide release from PBA-CS/CR(*N*Me)EKA/PEDOT system was assessed to study the pH responsive behavior of the boronate bonds.

In the prepared CR(*N*Me)EKA/PEDOT NPs, the polymer chains are in the oxidized state with positive charges along the backbone. The previously discussed Z-potential values showed that PEDOT is strongly associated with anionic SDBS molecules, which in turn are strongly associated with cationic CR(*N*Me)EKA through electrostatic interactions, thus retaining the peptide in the NPs. Passive release studies by diffusion during 2 h of incubation of CR(*N*Me)EKA/PEDOT NPs, showed only 1.68% ± 0.09% release. When such NPs are electrochemically reduced, the polymer chains gain electrons and become neutral or negatively charged, which defines weak or repulsive interactions, respectively, with SDBS and CR(*N*Me)EKA. The effect of the electrochemical reduction on the peptide release was investigated by CV and CA.

In CV, the applied potential increases or decreases linearly as a function of time. The potential was scanned at a constant rate of 100 mV/s starting at –0.50 V (initial potential) and reversing the sweep direction when it reaches +0.80 V (reversal potential) to come back to the value of –0.50 V (final potential). Thus, the time used for each CV cycle was 26 s. Fig. IV - 13a shows the cumulative peptide release profile for CR(*N*Me)EKA/PEDOT NPs after 60, 100 and 150 consecutive CV scans (*i.e.* 26 min, ~43 min and 65 min of electrical stimulation). It is worth noting that the release remained constant (around 1.7%) through the whole process, which is practically identical to the value obtained considering 2 h of passive diffusion.

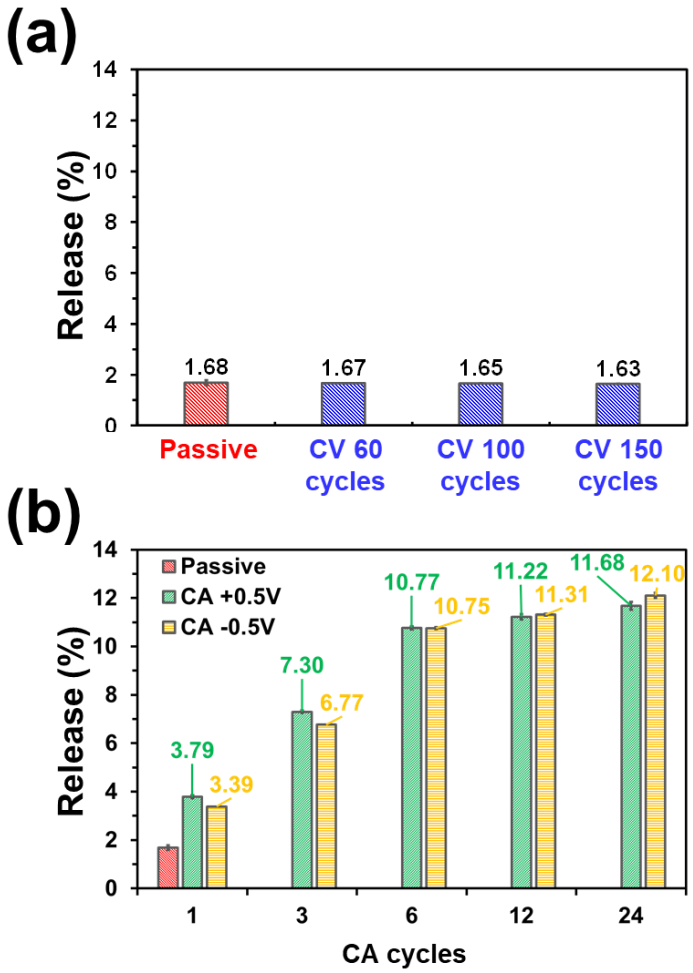

Fig. IV - 13. Peptide release profiles for CR(*N*Me)EKA/PEDOT NPs as a function of the number of (a) CV and (b) CA cycles. The results from passive diffusive release (2 h, red) are displayed in both graphics.

In contrast, each CA cycle consisted in the application of a constant voltage of +0.50 V or –0.50 V for 4 min followed by a period of 5 min without any potential. The resulting release profile (Fig. IV - 13b) shows that, after only one CA cycle (9 min), the percentage of peptide delivered practically doubled the passive release observed after 2 h, independently of the potential sign (*i.e.* 3.79% ± 0.06% and 3.39% ± 0.01% for +0.50 V and –0.50 V, respectively, *vs*. 1.68% ± 0.09%). Furthermore, the amount of released peptide increased rapidly with the number of cycles until reaching a threshold value of 6 cycles, after which the increment was delayed. The CR(*N*Me)EKA released after 6 CA cycles (around 10.8%) augmented by only 10% (*i.e.* to around 12.0%) when applying 24 cycles. This observation suggests that only peptide molecules located on or close to the surface of the NPs were delivered when exposed to CA electro-stimulation.

The release mechanism was based on altering the electrostatic interactions between the positively charged peptide and the negatively charged dopant SDBS molecules, which also interact with the oxidized PEDOT chains, as was evidenced by Z-potential measures on PEDOT and CR(*N*Me)EKA/PEDOT

NPs. By applying a voltage of –0.50 V, the PEDOT chains were reduced and, consequently, the dopant SDBS anions were partially expelled from the NPs, dragging CR(*N*Me)EKA molecules to the solution (Scheme IV - 5a). However, it is worth mentioning that a significant part of the SBDS···CR(*N*Me)EKA complexes remained in the NPs due to their neutrality, which explains why the release progressed very slowly after applying 6 CA cycles. Instead, when a voltage of +0.50 V is applied, the oxidation level of the PEDOT chains increases. Therefore, the fraction of SDBS counter-anions that have to interact with such re-oxidized polymer chains to achieve charge neutralization also increases, resulting in the cleavage of part of the SBDS···CR(*N*Me)EKA complexes and, consequently, the spontaneous release of CR(*N*Me)EKA molecules from the matrix (Scheme IV - 5a).

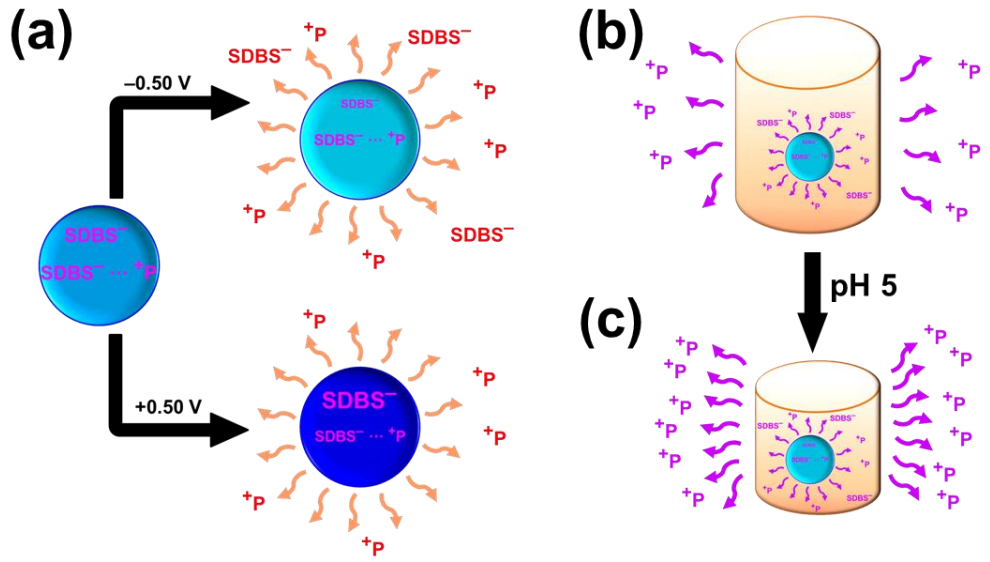

Scheme IV - 5. Proposed peptide (⁺P) release mechanisms for (a) CR(*N*Me)EKA/PEDOT NPs, as a function of the sign applied potential, and (b, c) PBA-CS/CR(*N*Me)EKA/PEDOT hydrogel, considering (b) the local microenvironments inside the hydrogel and (c) the hydrogel collapse under acidic conditions. The size of the letters inside the NPs increases or decreases with the amount of $SDBS^-$ counter-anion neutralizing oxidized PEDOT chains and the amount of $SDBS^-\cdots{}^+P$ complexes.

It should be mentioned that the release of CR(*N*Me)EKA was preliminary evaluated using very small PEDOT NPs (47 ± 9 nm) prepared using a different synthetic protocol with a surfactant as dopant agent, compared to this work (210 ± 75 nm).[29] Because of the different nature of the NPs, the electro-regulated release profiles were completely different from those displayed in Fig. IV - 13. More specifically, the release after 100 CV cycles using the same potential window and scan rate was of 37.8% ± 6.3% (*vs* 1.65 % ± 0.02% in this work), suggesting that the sweep from a negative potential to a positive potential (+0.80 V) largely affected the oxidation state of the PEDOT chains inducing the swelling of such small NPs.[29] There are reports on the combination of PEDOT, doped with polystyrene

sulfonate (PEDOT:PSS), with alginate (Alg) to create semi-interpenetrated conductive hydrogels (PEDOT/Alg), which were loaded with neutral drugs.[60] Those hydrogels were obtained through the replacement of PSS by Alg, while Alg chains were physically crosslinked by adding $CaCl_2$. Although a controlled release was achieved, in a 5 % wt. $CaCl_2$ aqueous solution, by applying electrical stimuli, PEDOT/Alg was found to present some serious drawbacks. Although PEDOT/Alg semi-interpenetrated hydrogels were very stable in Ca^{2+}-containing media, they were completely unstable in, for example, PBS due to the substitution of Ca^{2+} ions by monovalent cations, leading to an immediate and complete release of the drug.

Taking into account the release profiles in Fig. IV - 13, the peptide release from the PBA-CS/CR(*N*Me)EKA/PEDOT system was assessed considering electrostimulation by CA alone. Fig. IV - 14 compares the release profiles obtained after 12 and 24 CA cycles with that obtained by passive diffusion after 108 and 216 min (*i.e.* the times equivalent to 12 and 24 CA cycles, respectively). The passive release was almost constant with time (~8.7%) and much lower than the ones obtained by electrostimulation, with the latter being around 2 and 3.5-fold higher for 12 and 24 cycles, respectively. The highest CR(*N*Me)EKA release was obtained for a voltage of –0.50 V, which indicates that the mechanism controlled through the reduction of PEDOT favors the delivery process with respect to that obtained by increasing the oxidation level (+0.50 V).

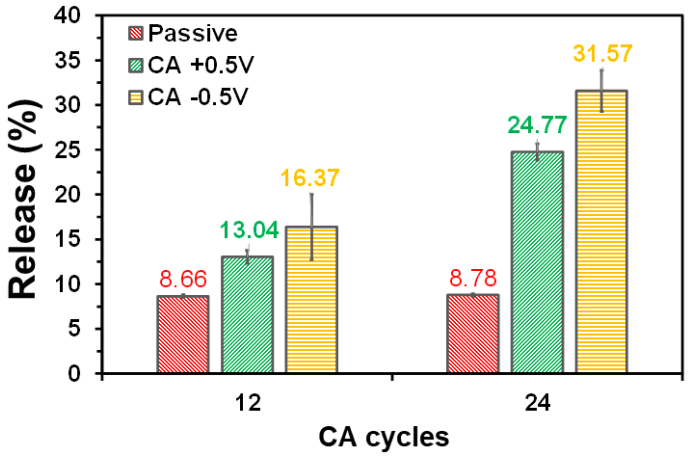

Fig. IV - 14. Peptide release profiles for PBA-CS/CR(*N*Me)EKA/PEDOT hydrogel as a function of the number of CA cycles. The results from passive release (108 and 216 min for 12 and 24 CA cycles, respectively) are displayed for comparison.

Another interesting feature is that, in all cases, the amounts of peptide released from PBA-CS/CR(*N*Me)EKA/PEDOT system were much higher than those delivered from CR(*N*Me)EKA/PEDOT NPs (*i.e.* without the PBA-CS hydrogel). This observation was attributed to the combination of two coexisting factors: 1) the microenvironment created inside the hydrogel; and 2) the dynamic nature

of the boronate ester bond. The local microenvironment, which favored the peptide release by the concentration gradient (Scheme IV - 5b), also explained why the passive release was much higher for PBA-CS/CR(*N*Me)EKA/PEDOT hydrogel than for CR(*N*Me)EKA/PEDOT NPs. Moreover, this phenomenon was enhanced by the collapse of the hydrogel at pH 5 due to dissociation of the boronate bonds between the polymer chains (see Fig. IV - 6). The disruption of such bonds resulted in smaller microenvironments, which promoted a concentration gradient peptide release (Scheme IV - 5c).

IV - 3.4. Cell assays

The toxicity of PBA was reported to be very low (*i.e.* 900 mg/kg of body weight[61]) and, therefore, has not been re-investigated in this work. The biocompatibility of peptide-free systems was examined using MG-63 cells, which is often used in viability assays to show biocompatibility. The anticancer activity of peptide-loaded systems was examined using COS-1 and PNT-2 as normal cell lines used as control, and PC-3 cells. The latter is a classical prostate cancer cell line that exhibits high metastatic potential compared to other prostate cancer cell line models,[62] making it especially appropriate to assess if the bioactivity and, therefore, anticancer effect of CR(*N*Me)EKA for prostate cancer is maintained after electrostimulation.

The biocompatibility of the PBA-CS matrix, the peptide-unloaded PBA-CS/PEDOT hydrogel, and the electrostimulated PBA-CS/PEDOT hydrogel was investigated assessing MG-63 cells viability at 24 h and 7 days of cell culture. Results are presented in Fig. IV - 15a, including those obtained for the TCPS control. The number of adhered cells in contact with PBA-CS, non-electrostimulated PBA-CS/PEDOT and electrostimulated PBA-CS/PEDOT is very similar to that of TCPS control, which is a well-known biocompatible material. This behavior, which is maintained after 7 days (or improved in the case of the electrostimulated hydrogel), indicates that those synthetic materials do not have any impact in cell metabolism or on their surface attachment.

After 24 h, the number and morphology of MG-63 cells cultured on the control was similar to that of cells cultured in the presence of PBA-CS, PBA-CS/PEDOT and electrostimulated PBA-CS/PEDOT platforms (Fig. IV - 15b). After 7 days, the number of MG-63 cells increased rapidly in all cases. However, in the case of non-electrostimulated PBA-CS/PEDOT, large cohesive rafts of cells were formed, which were not present in the control of TCPS, PBA-CS and electrostimulated PBA-CS/PEDOT hydrogel. This feature revealed that PBA-CS/PEDOT hydrogel promoted cell proliferation. Overall, the results supported the biocompatibility of the assembled platforms.

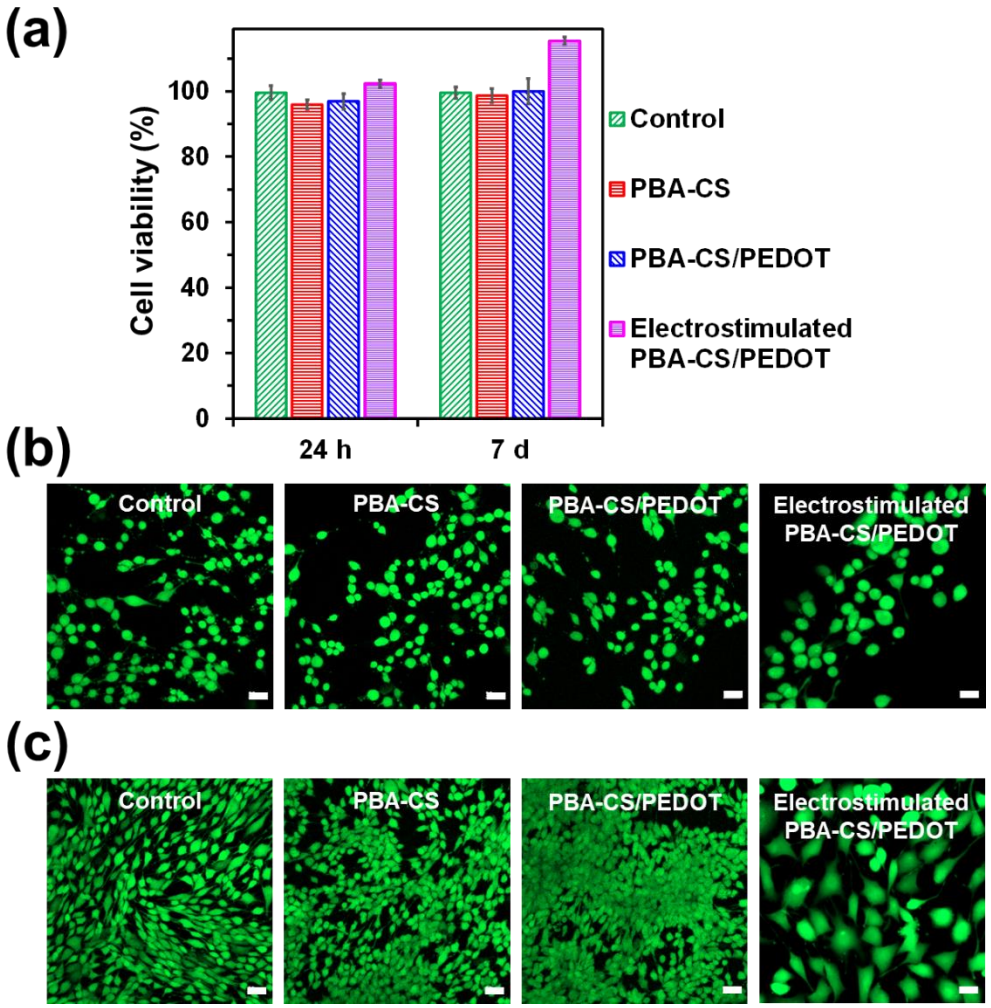

Fig. IV - 15. (a) Cell viability values for the MG-63 cell line after exposure for 24 h and 7 days to PBA-CS, PBA-CS/PEDOT and electrostimulated PBA-CS/PEDOT hydrogels. Error bars indicate the standard deviation (*n* = 3). (b, c) Confocal microscopy images of MG-63 cells after being exposed for (b) 24 h and (c) 7 days to PBA-CS, PBA-CS/PEDOT and electrostimulated PBA-CS/PEDOT hydrogels. Cells were stained with calcein (green - live cells) and ethidium bromide (red - dead cells). In all cases, the control was TCPS.

In vitro studies were also conducted to prove that the delivered anticancer peptide preserves its bioactivity against prostate cancer cells. For this purpose, the anticancer activity of the peptide molecules released by electrostimulation from the PBA-CS/CR(*N*Me)EKA/PEDOT system was evaluated by studying the viability of PC-3, PNT-2 and COS-1 (control) cells cultured for 24 h in culture medium containing the released peptide. Four cases were considered for each cell type: 1) cells cultured in a culture medium without CR(*N*Me)EKA (blank assays); 2) cells cultured in a medium with an initial CR(*N*Me)EKA concentration of 1.25 mg/mL (control peptide assays); 3) cells cultured in the cultured medium containing the released peptide after chronoamperometric stimulation of PBA-CS/CR(*N*Me)EKA/PEDOT hydrogel using –0.5 V and 24 cycles (with a peptide concentration of 0.083 ±

0.005 mg/mL); and 4) cells cultured in a medium with a CR(*N*Me)EKA concentration identical to that released in the assays described in 3) (peptide equivalent to that released in the supernatant). In order to consider the effect of the peptide concentration, different dilutions (from 1:1 to 1:8) of the initial peptide solution and the release peptide supernatant solution were considered for 2) and 3), respectively.

As expected, the cell viability of PC-3 cells decreased with both the control peptide and the CA supernatant, even though such reduction depended on the CR(*N*Me)EKA concentration (Fig. IV - 16a). In fact, the peptide was found to be cytotoxic also for COS-1 and PC-3 cells when its concentration was very high (1.25 mg/mL), but less than for PNT-2 cells. For both cell lines, the viability increased when the peptide solution was diluted (*i.e.* with decreasing peptide concentration). After the 1:2 dilution (0.625 mg/mL), the cell viability was maintained at around 85%, 80% and 60% for COS-1, PNT-2 and PC-3 cells, respectively, until the concentration of CR(*N*Me)EKA was so low (0.001 mg/mL) that no significant detrimental effect was observed.

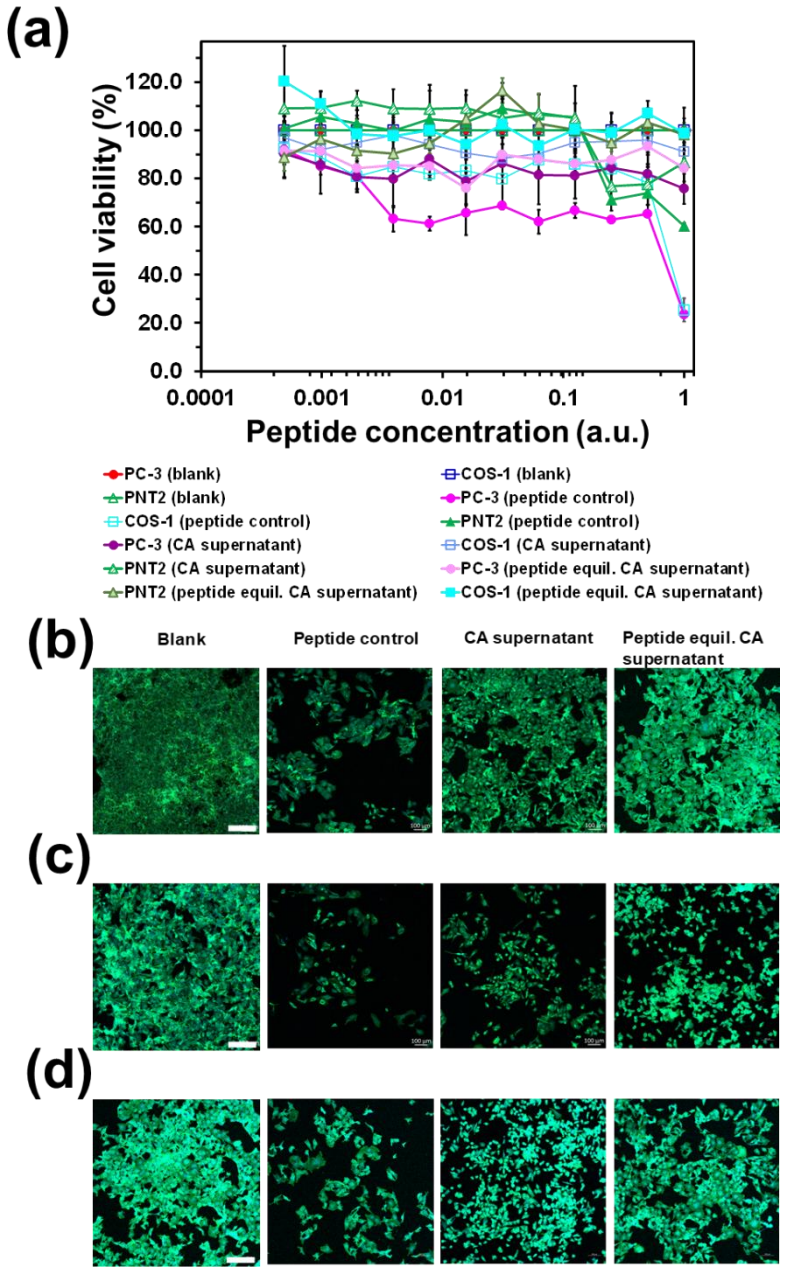

Fig. IV - 16. (a) Cell viability values for COS-1, PC-3 and PNT-2 cell lines after being exposed for 24 h to culture medium (blank), a CR(*N*Me)EKA solution (peptide control), the peptide-containing supernatant after chronoamperometric stimulation of PBA-CS/CR(*N*Me)EKA/PEDOT hydrogel applying –0.5 V and 24 cycles, and a peptide solution with a concentration equivalent to that obtained by electrical stimulation of PBA-CS/CR(*N*Me)EKA/PEDOT hydrogel. The effect of the concentration was examined by diluting the initial peptide solution (1.25 mg/mL) and peptide-containing supernatant (0.083 ± 0.005 mg/mL) from 1:1 to 1:8. Error bars indicate the standard deviation (n = 3). (b-d) Confocal microscopy images of (b) COS-1, (c) PC-3 and (d) PNT-2 cells after being exposed for 24 h to the culture medium (blank), the peptide solution, the supernatant after CA and a peptide solution with a concentration equivalent to that obtained in the supernatant after CA. Cells were stained with Alexa Fluor 488 dye (green - cell cytoplasm) and Hoechst dye (blue - cell nuclei).

Apparently, the impact of the supernatant from chronoamperometric electrostimulation on the cell viability was lower than that of the control solution, which was attributed to the fact that the peptide concentration was significantly lower in the former than in the latter. However, this behavior was qualitatively similar to that described above, although the survival of COS-1 and PNT-2 cells was approximately 15% and 19%, respectively, higher than that of PC-3 cells (Fig. IV - 16a). These results agreed with those obtained using peptide solutions with a peptide concentration equivalent to that released in the supernatant by electrostimulation. The confocal microscopy images were consistent with the obtained viability profiles, as is reflected in the representative micrographs displayed for COS-1 (Fig. IV - 16b), PC-3 (Fig. IV - 16c), and PNT-2 (Fig. IV - 16d) cells. Overall, these results demonstrated that the peptide in the supernatant preserved its anticancer activity.

IV - 4. Conclusions

In this chapter, a previously engineered anticancer pentapeptide, CR(*N*Me)EKA, was loaded into PEDOT NPs, which in turn were incorporated into a PBA-CS hydrogel to evaluate the controlled release. The assembled PBA-CS/PEDOT carrier combines multiple functions, such as: i) on-demand controlled release of the anticancer peptide using external electric fields; ii) self-regulated pH-controlled delivery in the acidic microenvironment of tumoral tissues; iii) peptide protection to maintain its antitumoral activity; and iv) mechanical stability and injectability. Although the release kinetics and dosage were controlled through electro-responsive NPs, the dynamic behavior of boronate ester bonds in the hydrogel additionally enhanced the peptide release, thereby reducing the number of electro-stimulation cycles. The viscoelastic behavior of the PBA-CS hydrogel was determined by rheological studies, while the bioactivity of released CR(*N*Me)EKA was validated *in vitro*. Overall, the encapsulation of CR(*N*Me)EKA/PEDOT NPs, capable of on-demand peptide release, in a pH-responsive CS-PBA hydrogel with injectable properties, will allow the controlled delivery of the anticancer peptide near tumor cells in the human body. The carrier developed in this study has the ability to provide controlled release patterns for small hydrophilic anticancer peptides and shows potential for uses in customized peptide therapeutics.

IV - 5. References

(1) L. Wang, N. Wang, W. Zhang, X. Cheng, Z. Yan, G. Shao, X. Wang, R. Wang, C. Fu. Therapeutic peptides: current applications and future directions. *Sig. Transduct. Target Ther.* **2022**, 7(48).

(2) M. Xu, X. Liu, P. Li, Y. Yang, W. Zhang, S. Zhao, Y. Zeng, X. Zhou, L.-h. Zeng, G. Yang, Modified natriuretic peptides and their potential roles in cancer treatment, *Biomed. J*. **2022**, 45, 118-131.

(3) B. M. Cooper, J. Iegre, D. H. O'Donnovan, M. Ö. Halvarsson, D. R. Spring, Peptides as a platform for targeted therapeutics for cancer: peptide–drug conjugates (PDCs). *Chem. Soc. Rev*. **2021**, 50, 1480-1494.

(4) M. Mahlapuu, C. Björn, J. Ekblom, Antimicrobial peptides as therapeutic agents: opportunities and challenges. *Crit. Rev. Biotechnol*. **2020**, 40, 978-992.

(5) A. C. Lee, J. L. Harris, K. K. Khanna, J. H. A. Hong, Comprehensive review on current advances in peptide drug development and design, *Int. J. Mol. Sci*. 2019, 20, 2383.

(6) S. Rastogi, S. Shukla, M. Kalaivani, G. N. Singh, Peptide-based therapeutics: Quality specifications, regulatory considerations, and prospects. *Drug Discov. Today* **2019**, 24, 148-162.

(7) D. J. Craik, D. P. Fairlie, S. Liras, D. Price, The future of peptide-based drugs. *Chem. Biol. Drug Des*. **2013**, 81, 136-147.

(8) R. Böttger, R. Hoffmann, D. Knappe, Differential stability of therapeutic peptides with different proteolytic cleavage sites in blood, plasma and serum. *PLoS One*. **2017**, 12, e0178943.

(9) T. Kremsmayr, A. Aljnabi, J. B. Blanco-Canosa, H. N. T. Tran, N. B. Emidio, and M. Muttenthaler, On the utility of chemical strategies to improve peptide gut stability. *J. Med. Chem*. **2022**, 65, 6191-6206.

(10) Z. Antosova, M. Mackova, V. Kral, T. Macek, Therapeutic application of peptides and proteins: parenteral forever?. *Trends Biotechnol*. **2009**, 27, 628-635.

(11) K. Fosgerau, T. Hoffmann, Peptide therapeutics: current status and future directions. *Drug Discov. Today* **2015**, 20, 122-128.

(12) K. L. Zapadka, F. J. Becher, A. L. Gomes Dos Santos, S. E. Jackson, Factors affecting the physical stability (aggregation) of peptide therapeutics. *Interface Focus* **2017**, 17, 20170030.

(13) M. Werle, A. Bernkop-Schnürch, Strategies to improve plasma half life time of peptide and protein drugs. *Amino Acids* 2006, 30, 351-367.

(14) J. L. Lau, M. K. Dunn, Therapeutic peptides: Historical perspectives, current development trends, and future directions. *Bioorg. Med. Chem*. **2018**, 26, 2700-2707.

(15) E. Lenci, A. Trabocchi, Peptidomimetic toolbox for drug discovery. *Chem. Soc. Rev*. **2020**, 49, 3262-3277.

(16) M. Muttenthaler, G. F. King, D. J. Adams, P. F. Alewood, Trends in peptide drug discovery. *Nat. Rev. Drug Discov*. **2021**, 20, 309-325.

(17) W. Li, F. Separovic, N. M. O'Brien-Simpson, J. D. Wade, Chemically modified and conjugated antimicrobial peptides against superbugs. *Chem. Soc. Rev***. 2021**, 50, 4932-4973.

(18) C. J. Tsai, J. Zheng, C. Alemán, R. Nussinov, Structure by design: from single proteins and their building blocks to nanostructures. *Trends Biotechnol*. **2006**, 24, 449-454.

(19) S. Haddadzadegan, F. Dorkoosh, A. Bernkop-Schnürch, Oral delivery of therapeutic peptides and proteins: Technology landscape of lipid-based nanocarriers, *Adv. Drug Deliv.y Rev*. **2022**, 182, 114097.

(20) E. Y. Jiang, S. T. Desroches, A. G. Mikos, Particle carriers for controlled release of peptides. *J. Control. Release* **2023**, 306, 953-968.

(21) S. Lv, M. Sylvestre, A. N. Prossnitz, L. F. Yang, S. H. Pun, Design of polymeric carriers for intracellular peptide delivery in oncology applications. *Chem. Rev.* **2021**, 121, 11653-11698.

(22) J. Wu, J. K. Sahoo, Y. Li, Q. Xu, D. L. Kaplan, Challenges in delivering therapeutic peptides and proteins: A silk-based solution. *J. Control. Release* **2022**, 345, 176-189.

(23) L. Agemy, K. N. Sugahara, V. R. Kotamraju, K. Gujraty, O. M. Girard, Y. Kono, R. F. Mattrey, J.-H. Park, M. J. Sailor, A. I. Jimenez, C. Cativiela, D. Zanuy, F. J. Sayago, C. Alemán, R. Nussinov, E. Ruoslahti, Nanoparticle-induced vascular blockade in human prostate cancer. *Blood* **2010**, 116, 2847-2856.

(24) B. Zhang, H. Wang, S. Shen, X. She, W. Shi, J. Chen, Q. Zhang, Y. Hu, Z. Pang, X. Jiang, Fibrin-targeting peptide CREKA-conjugated multi-walled carbon nanotubes for self-amplified photothermal therapy of tumor. *Biomaterials* **2016**, 79, 46-55.

(25) E. J. Chung, Y. Cheng, R. Morshed, K. Nord, Y. Han, M. L. Wegscheid, B. Auffinger, D. A. Wainwright, M. S. Lesniak, M. V. Tirrell, Fibrin-binding, peptide amphiphile micelles for targeting glioblastoma. *Biomaterials* **2014**, 35, 1249-1256.

(26) A. Puiggalí-Jou, L. J. del Valle, E. Armelin, C. Alemán, Fibrin association at hybrid biointerfaces made of clot-binding peptides and polythiophene. *Macromol. Biosci*. **2016**, 16, 1461-1474.

(27) J. Wu, J. Zhao, B. Zhang, Y. Qian, H. Gao, Y. Yu, Y. Wei, Z. Yang, X. Jiang, Z. Pang, Polyethylene glycol–polylactic acid nanoparticles modified with cysteine–arginine–glutamic acid–lysine–alanine fibrin-homing peptide for glioblastoma therapy by enhanced retention effect. *Int. J. Nanomedicine* **2014**, 9, 5261-5271.

(28) J. Zhao, B. Zhang, S. Shen, J. Chen, Q. Zhang, X. Jiang, Z. Pang, CREKA peptide-conjugated dendrimer nanoparticles for glioblastoma multiforme delivery. *J. Colloid Interf. Sci*. **2015**, 450, 396-403.

(29) A. Puiggalí-Jou, L. J. del Valle, C. Alemán, Encapsulation and storage of therapeutic fibrin-homing peptides using conducting polymer nanoparticles for programmed release by electrical stimulation. *ACS Biomater. Sci. Eng.* **2020**, 6, 2135-2145.

(30) Y. Zhong, Y. Zhang, J. Xie, J. Zhou, J. Liu, M. Ye, L. Zhang, B. Qiao, Z. g. Wang, H.-t. Ran, D. Guo, Low-intensity focused ultrasound-responsive phase-transitional nanoparticles for thrombolysis without vascular damage: A synergistic nonpharmaceutical strategy. *ACS Nano* **2019**, 13, 3387-3403.

(31) V. S. Perera, G. Covarrubias, M. Lorkowski, P. Atukorale, A. Rao, S. Raghunathan, R. Gopalakrishnan, B. O. Erokwu, Y. Liu, D. Dixit, S. M. Brady-Kalnay, D. Wilson, C. Flask, J. Rich, P. M. Peiris, E. Karathanasis, E. One-pot synthesis of nanochain particles for targeting brain tumors. *Nanoscale* **2017**, 9, 9659-9667.

(32) G. Fabregat, B. Teixeira-Dias, L. J. del Valle, E. Armelin, F. Estrany, C. Alemán, Incorporation of a clot-binding peptide into polythiophene: Properties of composites for biomedical applications. *ACS Appl. Mater. Interfaces* **2014**, 6, 11940-11954.

(33) A. Puiggalí, L. J. del Valle, E. Armelin, C. Alemán, Fibrin association at hybrid biointerfaces made of clot-binding peptides and polythiophene. *Macromol. Biosci*. **2016**, 16, 1461-1474.

(34) K. Jiang, X. Song, L. Yang, L. Li, Z. Wan, X. Sun, T. Gong, Q. Lin, Z. Zhang, Enhanced antitumor and anti-metastasis efficacy against aggressive breast cancer with a fibronectin-targeting liposomal doxorubicin *J. Control. Release* **2018**, 271, 21-30.

(35) D. Zanuy, F. J. Sayago, G. Revilla-López, G. Ballano, L. Agemy, V. R. Kotamraju, A. I. Jiménez, C. Cativiela, R. Nussinov, A. M. Sawvel, G. Stucky, E. Ruoslahti, C. Alemán, Engineering strategy to improve peptide analogs: from structure-based computational design to tumor homing. *J. Comput. Aided Mol*. **2013**, 27, 31-43.

(36) D. Zanuy, A. Puiggalí-Jou, P. Conflitti, G. Bocchinfuso, A. Palleschi, C. Alemán, Aggregation propensity of therapeutic fibrin-homing pentapeptides: insights from experiments and molecular dynamics simulations. *Soft Matter* **2020**, 16, 10169-10179.

(37) K. El Hauadi, L. Resina, D. Zanuy, T. Esteves, F. Castelo Ferreira, M. M. Pérez-Madrigal, C. Alemán. Dendritic self-assembled structures from therapeutic charged pentapeptides. *Langmuir* **2022**, 38, 12905-12914.

(38) Z. Wu, S. Zhang, X. Zhang, S. Shu, T. Chu, D. Yu, Phenylboronic acid grafted chitosan as a glucose-sensitive vehicle for controlled insulin release. *J. Pharm. Sci*. **2011**, 100, 2278–2286.

(39) J. Li, W. Hu, Y. Zhang, H. Tan, X. Yan, L. Zhao, H. Liang, pH and glucose dually responsive injectable hydrogel prepared by *in situ* crosslinking of phenylboronic modified chitosan and oxidized dextran. *J. Polym. Sci. Part A: Polym. Chem*. **2015**, 53, 1235-1244.

(40) A. Puiggalí-Jou, P. Micheletti, F. Estrany, L. J. del Valle, C. Alemán, Electrostimulated release of neutral drugs from polythiophene nanoparticles: smart regulation of drug–polymer interactions. *Adv. Healthcare Mater*. **2017**, 6, 1700453.

(41) H, Ensahei, A. Puiggalí-Jou, N. Saperas, C. Alemán, Conducting polymer nanoparticles for a voltage-controlled release of pharmacological chaperones. *Soft Matter* **2021**, 17, 3314-3321.

(42) J. Wang, Y. Wang, M. Gao, X. Zhang, P. Yang, multilayer hydrophilic poly(phenol-formaldehyde resin)-coated magnetic graphene for boronic acid immobilization as a novel matrix for glycoproteome analysis. *ACS Appl. Mater. Interfaces* **2015***,* 7, 16011-16017.

(43) A. Barth, The infrared absorption of amino acid side chains. *Prog. Biophys. Mol. Biol*. **2000**, 74, 141-173.

(44) H. Fissan, S. Ristig, H. Kaminski, C. Asbach, M. Epple. Comparison of different characterization methods for nanoparticle dispersions before and after aerosolization. *Anal. Methods* **2014**, 6, 7324-7334.

(45) S. A. Wissinga, O. Kayserb, R. H. Muller, solid lipid nanoparticles for parenteral drug delivery. *Adv. Drug Deliver. Rev*. **2004**, 56, 1257–1272.

(46) C. Jacobs, O. Kayser, R. H. Müller, Nanosuspensions as a new approach for the formulation for the poorly soluble drug tarazepide*. Int. J. Pharm*. **2000**, 196, 161-164.

(47) E. Aeridou, D. Díaz Díaz, C. Alemán, M. M. Pérez-Madrigal. Advanced functional hydrogel biomaterials based on dynamic b–o bonds and polysaccharide building blocks. *Biomacromolecules* **2020**, 21, 3984-3996.

(48) A. Pettignano, S. Grijalvo, M. Häring, R. Eritja, N. Tanchoux, F. Quignard, D. Díaz-Díaz. Boronic acid-modified alginate enables direct formation of injectable, self-healing and multistimuli-responsive hydrogels. *Chem. Commun*. **2017**, 53, 3350-3353.

(49) M. J. Harms, C. A. Castañeda, J. L. Schlessman, G. R. Sue, D. G. Isom, B. R. Cannon, E. B. García-Moreno, The pK(a) values of acidic and basic residues buried at the same internal location in a protein are governed by different factors. *J. Mol. Biol*. **2009**, 389, 34-47.

(50) E. L. Mehler, M. Fuxreiter, I. Simon, E. B. Garcia-Moreno, The role of hydrophobic microenvironments in modulating pKa shifts in proteins. *Proteins* **2002**, 48, 283-92.

(51) A. *Puiggalí-Jou*, L. J. Del Valle, C. *Alemán*. Drug delivery systems based on intrinsically conducting polymers. *J. Control. Release* **2019**, 309, 244-264.

(52) G. Xu, Y. Lu, C. Cheng, X. Li, J. Xu, Z. Liu, J. Liu, G. Liu, Z. Shi, Z. Chen, F. Zhang, Y. Jia, D. Xu, W. Yuan, Z. Cui, S. S. Low, Q. Liu, Battery-free and wireless smart wound dressing for wound infection monitoring and electrically controlled on-demand drug delivery. *Adv. Funct. Mater*. **2021**, 31, 2100852.

(53) H. Muñoz-Galán, B. G. Molina, O. Bertran, M. M. Pérez-Madrigal, C. Alemán, Combining rapid and sustained insulin release from conducting hydrogels for glycemic control. *Eur. Polym. J.* **2022**, 181, 111670.

(54) H. Enshaei, A. Puiggalí-Jou, L. J. del Valle, P. Turon, N. Saperas, C. Alemán, C., Nanotheranostic interface based on antibiotic-loaded conducting polymer nanoparticles for real-time monitoring of bacterial growth inhibition. *Adv. Healthcare Mater*. **2021**, 10, 2001636.

(55) A. R. Lima, A. M. Araújo, J. Pinto, C. Jerónimo, R. Henrique, M. L. Bastos, M. Carvalho, P. Guedes de Pinho, Discrimination between the human prostate normal and cancer cell exometabolome by GC-MS. *Sci. Rep*. **2018**, 8, 5539.

(56) W. R. Fair, J. J. Cordonnier, The pH of prostatic fluid: a reappraisal and therapeutic implications. *J. Urol*. **1978**, 120, 695-698.

(57) R. A. Gatenby, R. J. Gillies, Why do cancers have high aerobic glycolysis? *Nat. Rev. Cancer* **2004**, 4, 891-899.

(58) E. Boedtkjer, S. F. Pedersen, The acidic tumor microenvironment as a driver of cancer. *Annu. Rev. Physiol*. **2020**, 82, 103-126.

(59) L. Feng, Z. Dong, D. Tai, Y. Zhang, Z. Liu, The acidic tumor microenvironment: a target for smart cancer nano-theranostics, *Natl. Sci. Rev.* **2018**, 5, 269-286.

(60) A. Puiggalí-Jou, E. Cazorla, G. Ruano, I. Babeli, M. P. Ginebra, J. García-Torres, C. Alemán, Electroresponsive alginate-based hydrogels for controlled release of hydrophobic drugs. *ACS Biomat. Sci. Eng.* **2020**, *6*, 6228-6240.

(61) M. A. Soriano-Ursúa, E. D. Farfán-García, Y. López-Cabrera, E. Querejeta, J. G. Trujillo-Ferrara, Boron-containing acids: Preliminary evaluation of acute toxicity and access to the brain determined by Raman scattering spectroscopy, *NeuroToxicology* **2014**, 40, 8-15.

(62) I.-P. Huang, S.-P. Sun, S.-H Cheng, C.-H. Lee, C.-Y. Wu, C.-S. Yang, L.-W. Lo, Y.-K. Lai, Enhanced chemotherapy of cancer using pH-sensitive mesoporous silica nanoparticles to antagonize P-glycoprotein–mediated drug resistance. *Mol Cancer Ther.* **2011**, 10, 761-769.

Chapter V – Electro-responsive and pH-sensitive hydrogel as carrier for controlled chloramphenicol release

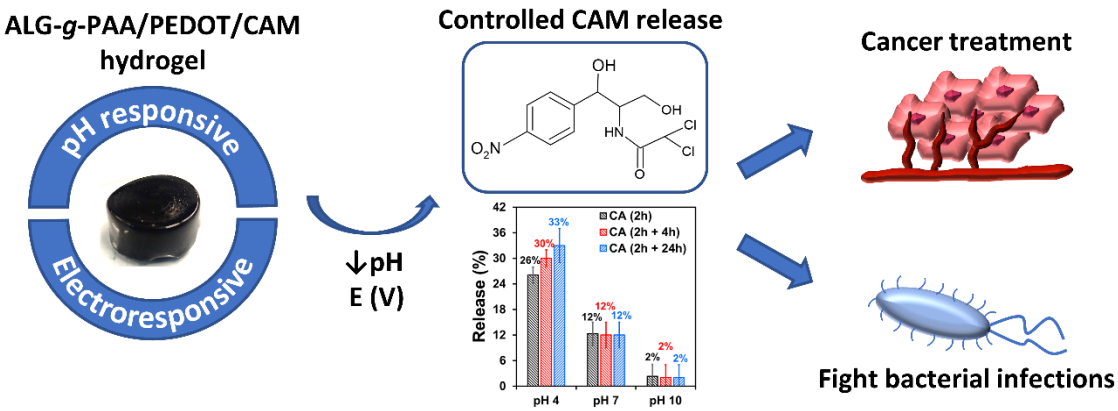

V - 1. Introduction

Recent advances in the field of drug delivery systems have shown the capability of releasing accurate amounts of therapeutic agents, or other bioactive substances at a specific location.[1-3] This is particularly important for antibiotics since such drugs suffer several limitations that cannot be ignored, as for example low accumulation and penetration in diseased cells/tissues, limited bioavailability of the drugs, and off-target toxicity.[4] Furthermore, antibiotic overexposure predisposes to antibiotic resistance, which is a global public health problem.[5-6] To avoid many of such problems, efforts have been focused on the development of smart systems for the release of antibiotics to the site of infection. These mainly consist of stimuli-responsive antibiotic delivery bioplatforms, which can release antibiotics in a controlled and timely fashion. These stimuli can either be exogenous (light,[7,8] magnetism,[9,10] ultrasound,[11,12] and electrical[13,14]) or endogenous (pH,[15,16] redox reactions,[17] and enzymatic[18,19]).

Various types of antimicrobial release devices, such as hydrogels,[20,21] NPs,[22,23] micro/nano-fibers,[24,25] and film-based reservoir devices,[26,27] have been proposed. Among them, pulsatile antibiotic delivery systems using external electrical stimulation signals have drawn attention, as they allow repeatable and reliable drug release flux for therapeutic needs, thereby allowing remote control of local drug administration. Within this context, conducting polymers (CPs), which are organic materials with characteristics similar to those encountered in metals (*i.e.* good electrical, and optical properties) and with the outstanding properties of conventional polymers (*i.e.* flexibility in processing, lightness of weight, and easiness in synthesis), play a major role.[13] Among CPs, PEDOT exhibits superior capacitive performance, high electrical conductivity, stability in aqueous media and biocompatibility.[28-31]

PEDOT has been extensively used to load different types of drugs for subsequent controlled release through the application of different kinds of electrical stimuli.[14,32-36] For example, anti-inflammatory dexamethasone was successfully released from loaded PEDOT films by applying CV scans between –0.3 V and 0.45 V,[32] while anticancer botulin was delivered applying a constant potential of −0.5 V for 10 min.[33] CUR, which displays a wide spectrum of medicinal properties, including anti-bacterial,[37] was released from loaded PEDOT NPs using a constant potential at 0.50, −0.50, −1.00 or −1.25 V for 3 min.[34] Instead, the release of CAM from loaded PEDOT NPs was very slow, independently of the kind of electrical stimuli.[14] Despite of such slowness, released CAM, which is a broad spectrum antibiotic that is effective against a variety of susceptible and serious bacterial infections,[38] inhibited bacterial growth.[14] A constant electrical potential was also successfully employed to release the antibiotic ciprofloxacin from loaded PEDOT fibers[35] and CUR from loaded PEDOT hydrogels.[36]

Noteworthy, and most interestingly, CAM, which has been reported to inhibit mitochondrial functions of eukaryotic cells,[39-41] is also being considered as a potential option for cancer treatment.[42,43] The metabolism of cancer cells, especially of cancer stem cells, is fundamentally regulated by an abundance of mitochondria compared to normal cells, including normal stem cells.[44] Thus, in cancer cells, the low energy efficiency of the anaerobic metabolism is compensated by the presence of more mitochondria than in normal cells, which exhibit an aerobic metabolism. Accordingly, as part of anticancer therapy, the utilization of CAM and other antibiotics that target cancer metabolisms reached great repercussions for its implications in clinical oncology.[44-47] Indeed, in a recent study, Lamb *et al.*[44] proved that CAM inhibits the formation of tumor stem cells, which are responsible for metastasis by giving growth to new tumors.[48]

In this Chapter, we go one step further, generating an electro-chemo responsive system for the controlled release of CAM bearing in mind its dual biofunctionality. To engineer this multiresponsive system, we have harnessed the ability of PEDOT NPs to respond to electrical stimuli and assembled them into a hydrogel that responds to changes in pH. Although the extracellular pH at the end of the stationary phase of bacterial cell growth was found to be specific for each type of bacteria,[49,50] most bacterial organisms grow around pH values of 6.0–7.5, with some thriving in more acidic or alkaline conditions.[51] Indeed, a pH range exists for which bacteria grow best, which comprises minimum and maximum pH values to ensure growth, as well as an optimum pH. For instance, *Lactobacillus acidophilus*,[52] *Escherichia coli*[53] or *Staphylococcus aureus*[54] can survive in environments with pH as low as 4. On the other hand, tumors present a locally acidic environment that is now recognized as a tumor phenotype that drives cancer progression, causing tumor cells to become more invasive and lead to metastasis.[55]

Bearing the importance of the pH in mind, polyacrylic acid (PAA) hydrogels are known to exhibit reversible coil-to-globule conformational transitions at around pH 5, which are driven by the state of ionization of the carboxylic group. At low pH, PAA adopts a compact (but not fully collapsed) globular conformation (contracted hydrogel). Conversely, as the pH increases, ionization occurs and the polymer expands into a fully solvated open coil conformation (expanded hydrogel).[56,57] Herein, the abrupt contracted-to-expanded transition of PAA has been tuned by grafting PAA to sodium alginate (Alg) using MBA as cross-linker, with the resulting hydrogel being denoted Alg-*g*-PAA. Though, the ionization of the carboxylic groups with increasing pH has been employed to regulate the electrically-induced release of CAM from loaded PEDOT NPs, the release decreased drastically with increasing pH. It is worth noting that, although Alg hydrogels bear carboxylic acid groups, their direct use as a drug carrier and release system was avoided due to the fact that they do not experience volume changes associated with conformational transitions.[58]

V - 2. Materials and methods

V - 2.1. Materials

EDOT monomer (97%), SDBS (technical grade), APS (98 %), CAM (98%), ethanol (99%, HPLC grade), PBS, sodium alginate (Alg, low viscosity alginic acid sodium salt from brown algae), AAc (≥ 99%), potassium persulfate (KPS, 99%), MBA (99%), and MTT were purchased from Sigma-Aldrich (USA). High glucose Dulbecco's modified Eagle medium (DMEM), Roswell Park Memorial Institute (RPMI) medium, fetal bovine serum (FBS), penicillin (100 units/mL), streptomycin (100 µg/mL), and amphotericin (25 µg/mL), 0.25% trypsin/EDTA solution, and LIVE/DEAD kit, Alexa Fluor 488 and Hoechst dye were purchased from Gibco™ by Thermo Fisher Scientific (USA). All reagents were used as received without further purification.

V - 2.2. Synthesis of PEDOT and PEDOT/CAM NPs

PEDOT NPs were prepared by emulsion polymerization. Firstly, an SDBS surfactant solution (0.0815 g to 20 mL milli-Q water, 9.3 mM) was prepared and kept at 40 °C and 750 rpm for 1 h. Then, EDOT monomer (88.8 µL, 32.2 mM) was added to the micellar solution. At the same time, 2.5 mL of water or 10 mg/mL of CAM solution in ethanol (0.025 g to 2.5 mL ethanol) were added to the solution for the synthesis of PEDOT or PEDOT/CAM NPs, respectively. The mixtures were kept at 40 °C and 750 rpm for 1 h and, subsequently, an aqueous solution of the initiator APS (0.456 g to 2.5 mL milli-Q water, 0.8 M) was added. The reaction was kept at 40 °C and 750 rpm, protected from light, for 18 h. Purification of NPs and removal of unreacted reagents was achieved by three cycles of 40 min centrifugation at 4 °C and 11000 rpm, alternating with 20 min of sonication. The final product was then kept at 40 °C in an oven for 3 days until complete dryness. Afterwards, the NPs were re-dispersed in milli-Q water by using a vortex and a sonication bath, to obtain 5 mg/mL solutions of each NP category.

V - 2.3. Synthesis of Alg-*g*-PAA, Alg-*g*-PAA/PEDOT, and Alg-*g*-PAA/PEDOT/CAM hydrogels

Alg-*g*-PAA hydrogel was prepared by adapting the procedure reported by Thakur and Arotiba.[59] For this purpose, Alg (0.5 g) was homogeneously dissolved at 50 ^{o}C in milli-Q water (19 mL). Then, 1.657 g of AAc co-monomer (1.21 M) and 0.025 g of MBA cross-linker (8.5 mM) were added to the Alg solution.

The same protocol was followed for preparing Alg-*g*-PAA hydrogel loaded with PEDOT NPs (Alg-*g*-PAA/PEDOT) or PEDOT/CAM NPs (Alg-*g*-PAA/PEDOT/CAM). The only difference was the addition of a

mass of the corresponding NPs equal to 20% of the mass of Alg to the mixture containing Alg, AA and MBA. This was followed by the incorporation of 0.026 g of KPS (5 mM) under stirring. The reaction mixtures were maintained at 70 °C for 1.5 h to complete the polymerization reaction. Afterward, the hydrogel was washed with acetone to remove unreacted reagents and stored at 4 °C until further use.

V - 2.4. Spectroscopic studies

FTIR spectra were recorded on a FTIR Jasco 4100 spectrophotometer equipped with an attenuated total reflection accessory (Top-plate) and a diamond crystal (Specac model MKII Golden Gate Heated Single Reflection Diamond ATR) connected to a computer with spectra manager software. For each sample, 32 scans were recorded between 4000 and 600 cm^{-1} with a resolution of 4 cm^{-1}. To record the spectra of the NPs, 20 µL of PEDOT or PEDOT/CAM NPs aqueous dispersions (10 mg/mL) were dropped on aluminum foil and left overnight for solvent drying. FTIR spectra of Alg and AA co-monomer were recorded using directly the reagent powder, while the Alg-*g*-PAA hydrogel was lyophilized for 3 days before analysis. UV spectra were recorded using a Cary100 UV–vis spectrophotometer controlled by the UVProbe 2.31 software.

V - 2.5. Microscopic studies

SEM studies were performed in a Focused Ion Beam Zeiss Neon 40 scanning electron microscope operating at 5 kV. For visualization of NPs, samples were prepared by dropping 10 µL of PEDOT NPs (0.01 mg/mL) or PEDOT/CAM NPs (0.01 mg/mL) in suspension on aluminum foil. After left overnight for solvent evaporation, the piece of foil was mounted on a double-sided adhesive carbon disc and coated with a thin carbon layer. For the estimation of NPs size distributions, n = 100 was considered. In order to record SEM micrographs of Alg-*g*-PAA and Alg-*g*-PAA/PEDOT hydrogels, samples were firstly hydrated during 3 h, after which they were frozen for 10 min using liquid nitrogen. Then, the hydrogels were broken in two pieces (for the pores to be observed at the rupture zone) and lyophilized for 3 days. The resulting samples were then placed on a double-sided adhesive carbon disc and coated with a thin carbon layer. The size distribution of the pores was estimated considering n = 100.

High resolution Transmission Electron Microscopy (TEM) was performed in a JEOL 2010F microscope equipped with a field emission electron source and operated at an accelerating voltage of 200 kV. The point-to-point resolution was 0.19 nm, and the resolution between lines was 0.14 nm. Samples were dispersed in an aqueous suspension using an ultrasonic bath, and a drop of the suspension was placed over a grid with holey-carbon film. Images were not filtered or treated by means of digital processing and they correspond to raw data.

V - 2.6. Dynamic light scattering (DLS) and zeta-potential

DLS and z-potential studies were performed using NanoBrook 90 Plus Zeta Potential Analyzer (Brookheaven Instruments Co., Blue Point Road Holtsville, NY, USA). Samples were re-suspended in milli-Q water at a concentration of 0.01 mg/mL and placed into a cuvette of polystyrene with light pass of 1 cm to be analyzed at 25 ^{o}C using a scattering angle of 90^{o}. The z-potential of PEDOT and PEDOT/CAM NPs was determined at pH 7.

V - 2.7. Hydrogels' characterization

The swelling response of the prepared hydrogels was studied as a function of the pH. For this purpose, Alg-*g*-PAA, Alg-*g*-PAA/PEDOT and Alg-*g*-PAA/PEDOT/CAM lyophilized samples were cut in small pieces and immersed in 5 mL of 0.01 M PBS at pH 4 (adjusted using a hydrochloric acid solution), 7 and 10 (adjusted using a sodium hydroxide solution), under agitation at 80 rpm and 37 ^{o}C. The weight of the wet (*i.e.* swollen) hydrogels was measured at different times (0, 0.5, 1, 2, 4, 6, 24, 48, and 72 h) to calculate the swelling ratio (SR) after the surface moisture of the hydrogel was removed:

$$\text{SR}\ (\%) = \frac{m_t - m_0}{m_0} \times 100 \qquad \text{(V - 1)}$$

where m_t is the mass of the swollen sample at time *t* (hydrated in 0.01 M PBS at pH 4, 7 or 10 for *t* h) and m_0 is the mass of the samples at time 0 h (*i.e.* as synthesized). All experiments were conducted considering three repetitions (*n* = 3).

The equilibrium water content (EWC) was calculated using Eq. V - 2:

$$\text{EWC}\ (\%) = \frac{m_{48h} - m_0}{m_{48h}} \times 100 \qquad \text{(V - 2)}$$

where m_{48h} refers to the mass of the wet hydrogel (hydrated in 0.01 M PBS at pH 4, 7 or 10 for 48 h) after the surface moisture was removed. Finally, the gel fraction (GF) was defined as:

$$\text{GF}\ (\%) = \frac{m_{\text{LIO}-2}}{m_{\text{LIO}-1}} \times 100 \qquad \text{(V - 3)}$$

where $m_{\text{LIO}-1}$ is the mass after lyophilizing the hydrogel one time (*i.e.* $m_{\text{LIO}-1} = m_0$) and $m_{\text{LIO}-2}$ is the mass of the hydrogel after lyophilizing, re-hydrating for 24 h in 0.01 M PBS to remove the remaining soluble fraction, and lyophilizing again (*n* = 3).

V - 2.8. Rheological properties

All rheology studies were performed on an Anton Parr MCR 302 rheometer fitted with a parallel plate configuration (diameter of 20 mm) at 25 °C and using a solvent trap. Hydrogels were prepared and submitted to the condition tested (either 24 h in PBS at pH 4, 7 or 10; or 2 h under the CA electrical stimuli at pH 4 followed by 24 h in PBS at pH 4), after which samples were cut with dimensions of 2 cm in diameter and 0.5 cm in thickness. Before testing, the upper plate was carefully lowered to a plate separation of 1 mm, the hydrogel was trimmed, and the measurement was started. Frequency

sweeps were carried out applying a constant strain of 1%, while the frequency was ramped logarithmically from 0.1 to 100 rad/s. Meanwhile, amplitude sweeps were conducted applying a constant frequency of 1 Hz (6.28 rad/s), while the strain was ramped logarithmically from 0.1% to 5000%. All measurements were repeated in triplicate, and representative/averaged charts are shown.

V - 2.9. Loading capacity (LC)

Firstly, the absorbance *vs* CAM solution concentration in ethanol at 278 nm was plotted (Fig. V - 2). For the quantification of the loading capacity (LC, in %), Eq. V – 4 was used where m_{loaded} corresponds to the mass of CAM initially incorporated to the solution used for the synthesis of PEDOT/CAM (0.025 g) minus the mass of CAM remaining free in the solution after the synthesis of PEDOT/CAM. To determine this last fraction, 10, 20 and 50 µL of PEDOT/CAM NPs solutions at a concentration of 5 mg/mL were incubated in absolute ethanol to a total of 1 mL and left at 4 ^{o}C for 2 weeks to promote the full unstimulated release of CAM from the NPs. The solutions were centrifuged at 11000 rpm and the supernatants were analyzed by UV-visible spectroscopy.

$$LC = \frac{m_{loaded}}{m_{NPs}} \times 100 \qquad \text{(V - 4)}$$

V - 2.10. CAM release from PEDOT/CAM NPs

To trigger the release of CAM from PEDOT/CAM NPs, two different electric stimuli, CV and CA, were evaluated. CV and CA cycles were applied using an Autolab PGSTAT302N and NOVA software. For CV cycles, the initial and final potential were −0.50 V, and the reversal potential was +0.80 V, while the scan rate was 0.1 V/s. Each CA cycle consisted of the application of a potential of 0.60 V for 100 s, followed by an interruption (*i.e.* 0.00 V) for 5 min, and, subsequently, the application of a potential of −0.6 V for 100 s, followed by another interruption for 5 min. The CA cycles were repeatedly applied for 2 h.

A drop of 20 µL of PEDOT (control) or PEDOT/CAM NPs, at 5 mg/mL in suspension, was deposited on the surface of a screen-printed carbon electrode (SPCE) and left to dry. Then, the coated SPCE was immersed in a cell containing 3 mL solution of 0.01 M PBS, as an electrolyte, to record the CVs and CAs. The PBS solution was collected afterward. The concentration of CAM in the release medium (*n* = 3) was determined using the absorbance of the release medium at 278 nm and the corresponding plot of absorbance vs CAM concentration in 0.01 M PBS. The percentage of released CAM was defined using Eq V - 5:

$$Released\ CAM\ (\%) = \frac{m_{released}}{m_{loaded}} \times 100 \qquad \text{(V - 5)}$$

where $m_{released}$ indicates the mass of CAM in the release medium after 2 or 4 h and m_{loaded} is the mass of CAM loaded in PEDOT/CAM NPs after synthesis.

V - 2.11. CAM release from ALg-*g*-PAA/PEDOT/CAM

The controlled release of the antibiotic from the Alg-*g*-PAA/PEDOT/CAM hydrogel was performed by applying CA cycles as an electrical stimulus. Assays were conducted using Autolab PGSTAT302N and NOVA software in a three-electrode cell. The electrochemical set-up consisted of a Pt counter electrode, an Ag|AgCl reference electrode, and the Alg-*g*-PAA/PEDOT/CAM hydrogel as the working electrode. The release medium was 5 mL of 0.01 M PBS solution at pH 4, 7 and 10. CA cycles identical to those described for PEDOT/CAM NPs were applied for 2 h to stimulate the release from the hydrogel. The medium was collected right after such time, and 4 h and 24 h after, and analyzed by UV-Vis spectroscopy.

V - 2.12. Bactericidal activity

The bactericidal activity of the loaded CAM was tested with *Escherichia coli* (*E. coli)*, *Streptococcus sanguinis* (*S. sanguinis*) and *Streptococcus mutans (S. mutans*) using the inhibition zone method. First, 1 mL of an overnight culture (grown for 16 h) was added to 5 mL of the Lysogeny broth (LB) medium. Bacteria were seeded on LB agar plates and the samples, which included hydrogel pieces of Alg-*g*-PAA/PEDOT/CAM with two CAM loadings (33 and 66 µg/mL), as well as paper discs impregnated with 20 µL of release solutions, were deposited on top. Negative controls consisted of 20 µL release media from passive diffusion of Alg-*g*-PAA/PEDOT and Alg-*g*-PAA hydrogels. The positive control was a disc impregnated with 20 µL of a CAM solution in water at 66 µg/mL. The effect of CAM on bacterial growth (*i.e.* antibacterial performance) was evaluated after incubation at 37 ^{o}C for 24 h.

V - 2.13. Cell viability assays

Cell viability assays were performed with Vero and HeLa cell lines using the MTT assay. Briefly, cells were seeded at a concentration of 1×10^4 cells/well in 96-well plates and incubated overnight at 37 ^{o}C and 5% CO_2. Cells were then exposed to a dilution series of CAM-containing released media from Alg-*g*-PAA/PEDOT/CAM hydrogels by electrical stimulation (CA), as well as to free CAM (positive control with an initial concentration 33 µg/mL), for 24 h at 37 ^{o}C and 5% CO_2. The negative control was cell culture medium without CAM. After the incubation period, the MTT labeling reagent was added to each well and incubated for 3 h at 37 ^{o}C and 5% CO_2, followed by the addition of 100 µL of solubilizing agent (dimethyl sulfoxide). Finally, absorbance was measured at 570 nm, and the percentage of viable cells relative to untreated control was determined. The results were expressed as average value ± standard deviation (n = 3).

V - 3. Results and discussion

V - 3.1. Preparation and characterization of NPs

PEDOT and PEDOT/CAM NPs were prepared by emulsion polymerization, with the drug being loaded *in situ* during the synthesis (Scheme V - 1).

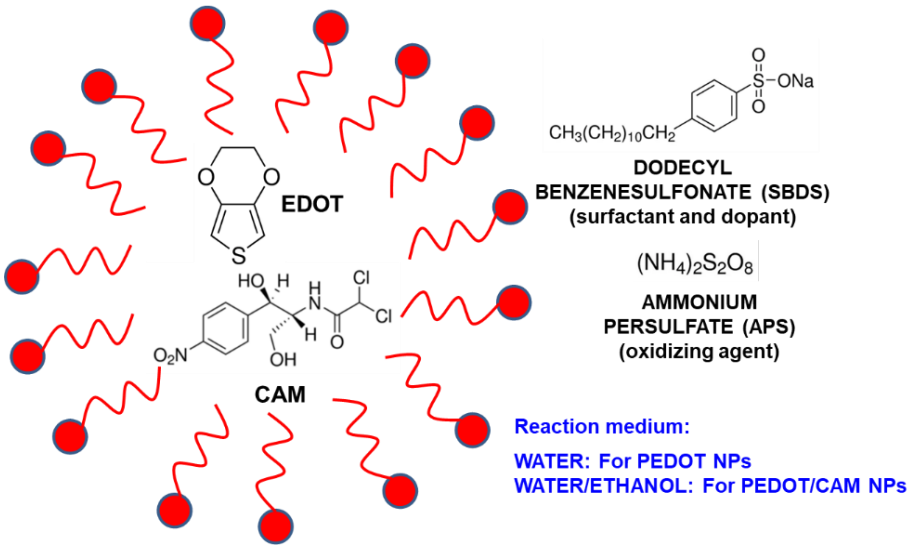

Scheme V - 1. Sketch illustrating the emulsion polymerization of PEDOT and PEDOT/CAM NPs.

The FTIR spectra of PEDOT and PEDOT/CAM NPs, which are shown in Fig. V - 1, display the characteristic peaks of PEDOT that correspond to the C–O–C vibrations (1215 and 1066 cm^{-1}), CH_2 stretching (2924 cm^{-1}), C=C in the thiophene ring (1715 cm^{-1}), C–C inter-ring stretching and C–S–C vibrations (835 and 687 cm^{-1}). The FTIR spectrum of free CAM, which is included in Fig. V - 1, shows many peaks overlapping the characteristic peaks found for unloaded PEDOT, precluding the identification of the antibiotic in PEDOT/CAM NPs. However, the successful loading of CAM was confirmed by UV-Vis spectroscopy. The absorbance vs CAM concentration plot displayed in Fig. V - 2 was used as calibration curve to quantify the LC (%) of PEDOT NPs.

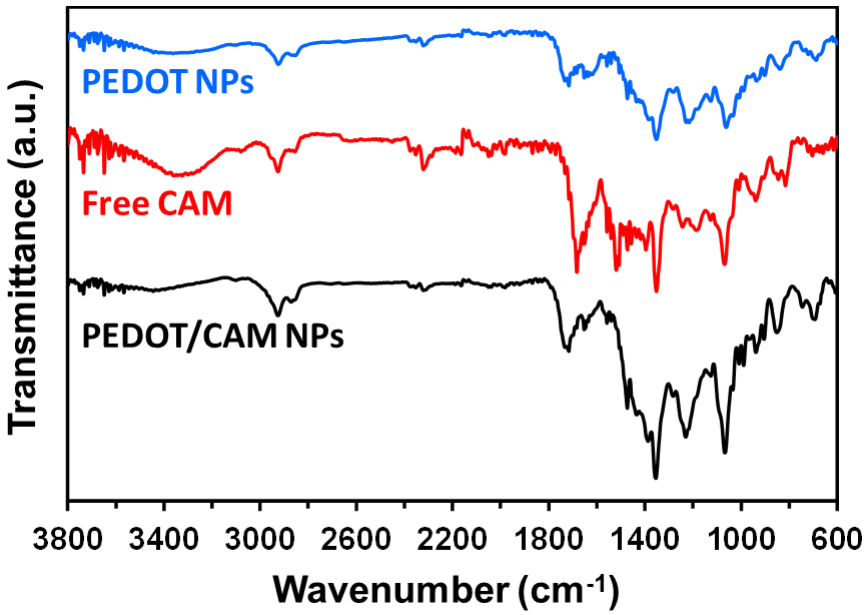

Fig. V - 1. FTIR spectra of free CAM, PEDOT NPs, and PEDOT/CAM NPs.

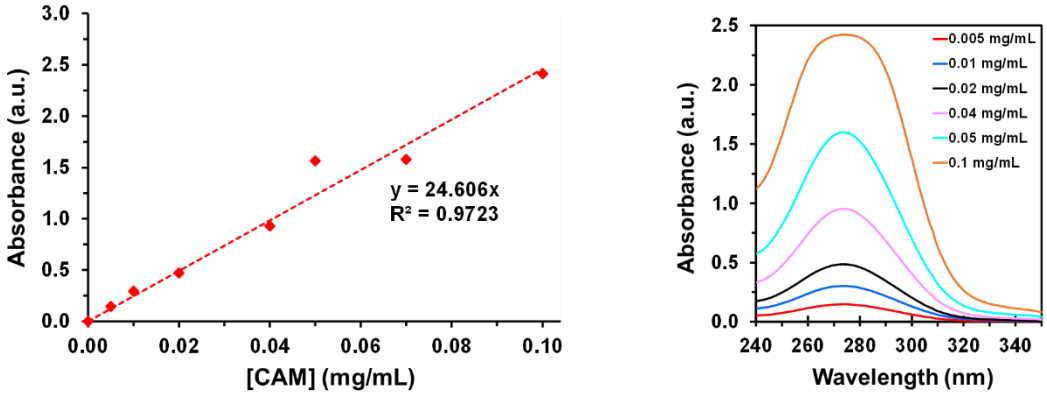

Fig. V - 2. Calibration curve and absorbance vs CAM concentration plot for CAM in ethanol. Error bars are lower than the size of the symbols.

Suspensions of PEDOT/CAM and PEDOT (blank) NPs were incubated in ethanol for 2 weeks to completely extract the antibiotic and then, UV-Vis spectra were recorded for the resulting solutions once the solid residues were eliminated by centrifugation. Fig. V - 3a shows that the solution originated from PEDOT/CAM NPs exhibits the characteristic CAM absorption peak at 278 nm, while this was not observed for the blank solution derived from PEDOT NPs. The LC estimated for the PEDOT/CAM NPs prepared in this work was 14.3 ± 2.5 %, which is slightly higher than the one reported for PEDOT/CAM NPs prepared using dodecylbenzene sulfonic acid (DBSA), rather than SDBS, as stabilizer and dopant agent (LC: 11.9 ± 1.3 %).[14] Furthermore, the LC achieved in this work with SDBS micelles was higher than those obtained for PEDOT/CUR and PEDOT/piperine (PIP) NPs, which were also prepared using DBSA micellar solutions, by 8.4% and 6.0%, respectively.[34] This may be due to

weaker interactions being established between the drugs and PEDOT chains due to a higher charge stabilization of PEDOT by DBSA, thus decreasing charge stabilization effect of PEDOT by the drugs themselves.

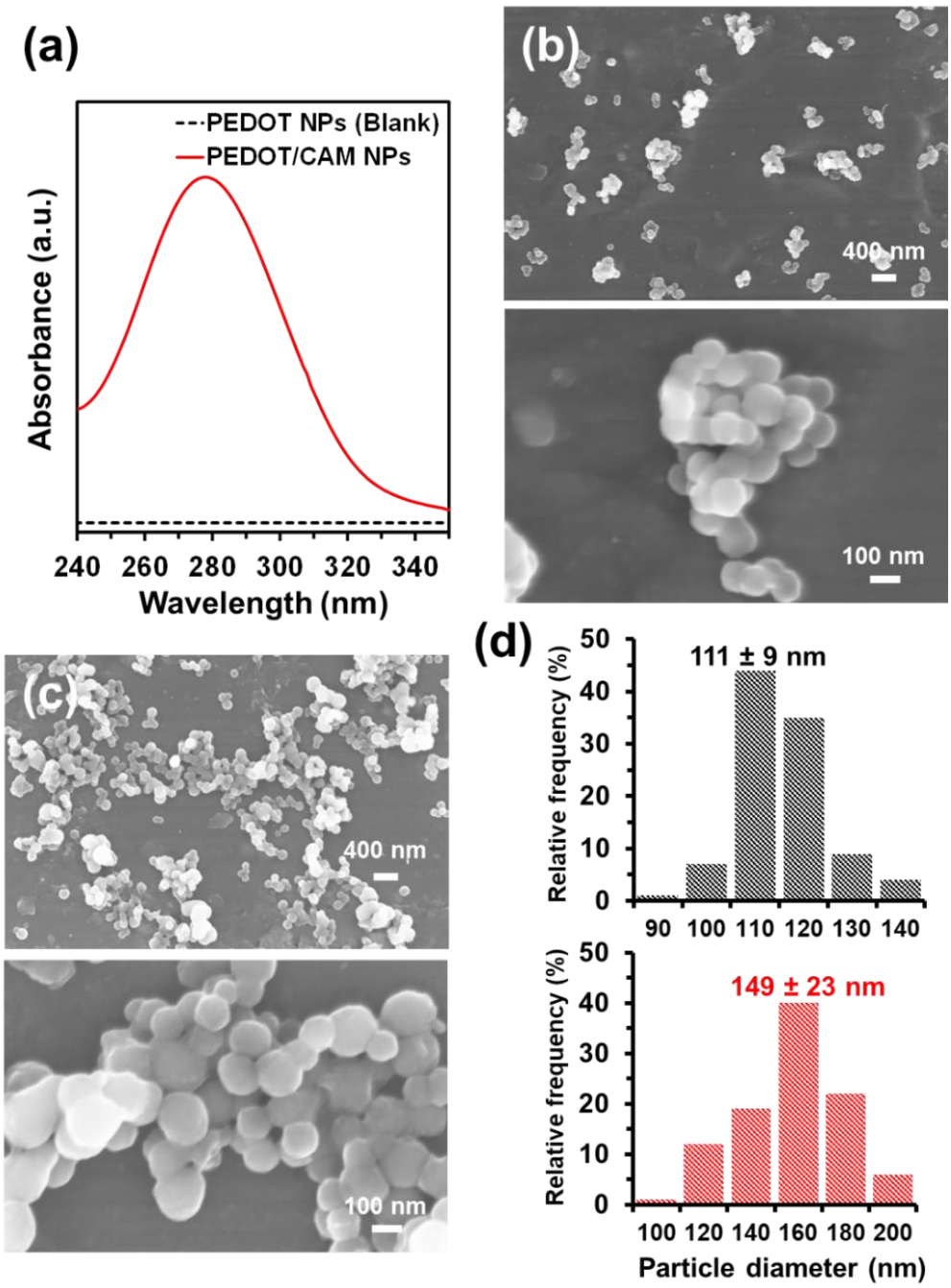

Fig. V - 3. (a) UV-Vis spectra of the supernatants obtained from PEDOT/CAM NPs using ethanol (red line) compared to the blank PEDOT NPs (black dashed line). (b, c) SEM micrographs (top, 16k× magnification; bottom, 80k× magnification) of (b) PEDOT and (c) PEDOT/CAM NPs. (d) Size distribution histograms (*n* = 100) of PEDOT (top) and PEDOT/CAM NPs (bottom).

The morphology of PEDOT and PEDOT/CAM NPs was studied by SEM (Fig. V - 3b-c), with both showing the typical spherical morphology. However, PEDOT NPs presented an effective diameter of 111 ± 9 nm (Fig. V - 3d), which was similar to that obtained for PEDOT NPs synthesized using DBSA (96 ± 16 nm).[34] After CAM loading, the size of the NPs increased to 149 ± 23 nm (Fig. V - 3d), similarly to the increase in diameter also observed for PEDOT NPs loaded with anticancer pentapeptides.[60]

Morphological phenomena were less clear in high resolution TEM micrographs due to aggregation artifacts produced during the preparation of the samples. Nevertheless, TEM results evidenced that the CP chains adopted an amorphous structure in both PEDOT and PEDOT/CAM NPs (Fig. V - 4).

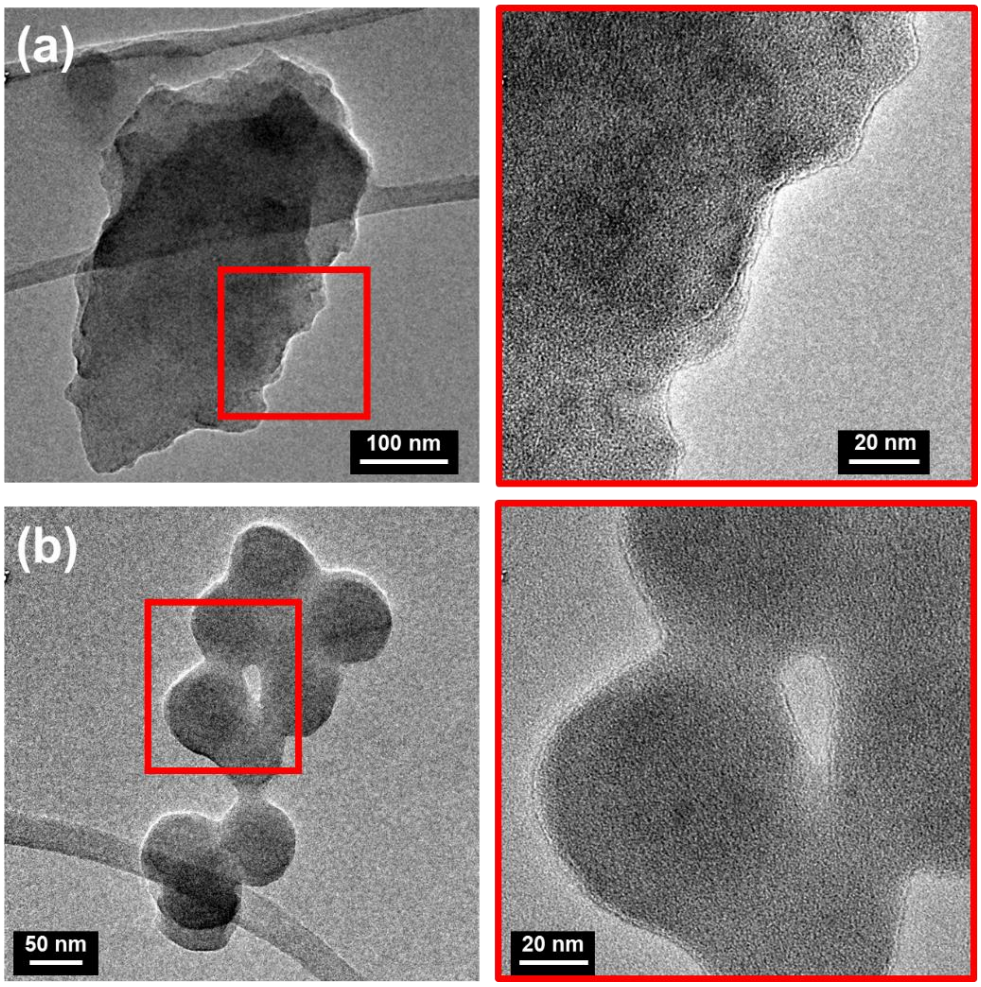

Fig. V - 4. High resolution TEM micrographs of (a) PEDOT and (b) PEDOT/CAM NPs.

DLS measurements confirmed the effect of the antibiotic on the average size of the NPs, with values of 157 ± 27 nm and 268 ± 10 nm for PEDOT and PEDOT/CAM NPs, respectively. The diameters determined by DLS were higher than the ones estimated by SEM, which was attributed to the fact that the former technique provides the hydrodynamic size of the NPs in solution (*i.e.* water and SDBS molecules in the hydrodynamic shell are included), while the latter gives the size of dry NPs. However,

the ratio between the diameters of loaded NPs to unloaded NPs, was very similar for both DLS and SEM measurements (1.7 and 1.6, respectively).

The z-potential, which is a measure of the effective electric charge on the NPs surface, was determined to examine the tendency towards aggregation of PEDOT and PEDOT/CAM NPs. Both unloaded and loaded NPs exhibited negative z-potential values (-30 ± 2 and -29 ± 3 mV, respectively, at 0.01 mg/mL), which are consistent with a high degree of suspension stability and, therefore, a low tendency to agglomerate. As expected, the z-potential increased in suspensions with increasing PEDOT/CAM concentrations (*e.g.* -7 ± 3 mV and -5 ± 3 mV for 0.1 and 0.5 mg/mL suspensions, respectively).

V - 3.2. Electrostimulated release of CAM from PEDOT/CAM NPs

Antibiotic release studies from PEDOT/CAM NPs were conducted in PBS considering two different kinds of electrical stimuli. The released CAM was quantified by measuring the absorbance at 278 nm and using the calibration plot obtained for CAM in PBS (Fig. V - 5).

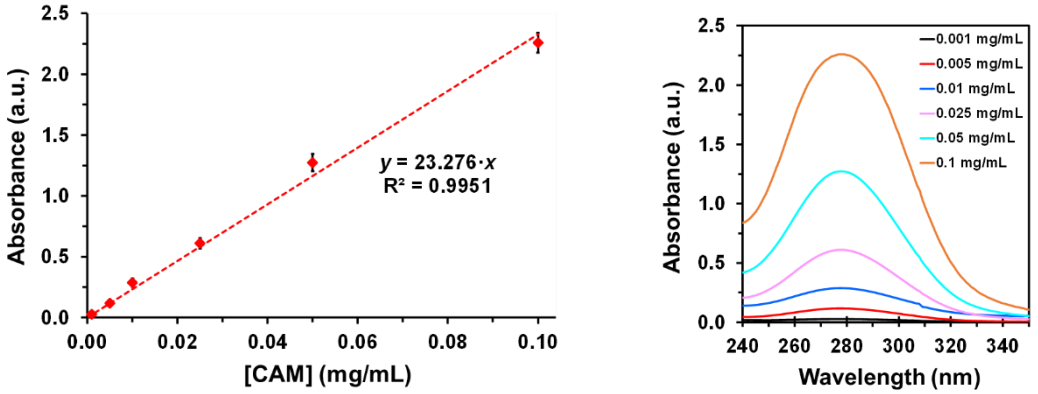

Fig. V - 5. Calibration curve and absorbance vs CAM concentration plot for CAM in PBS.

Fig. V - 6 compares the passive release of CAM from PEDOT/CAM NPs with that induced by electrostimulation using CV or CA for 2 h (*i.e.* 2 h in Fig. V - 6 refers to 280 CV or 9 CA cycles) and 4 h after each electrostimulation regime was finished (*i.e.* 2 h + 4 h in Fig. V - 6 refers to 280 CV or 9 CA cycles + 4 h of passive diffusion). As it can be seen, the passive release, which occurred by the diffusion of CAM molecules across the NPs matrix due to a concentration gradient, was relatively fast, increasing around 14% per hour. Electrostimulation resulted in a faster release rate, with this response being more evident for CA than for CV, especially at the shortest time (*i.e.* 33 ±9 % and 65 ± 6 % for CV and CA after 2h, respectively). Moreover, it should be emphasized that the release achieved after 9 CA cycles plus 4 h of passive diffusion reached 89 ± 5 %, which is much higher than the one observed by simple passive diffusion (55 ± 6 %).

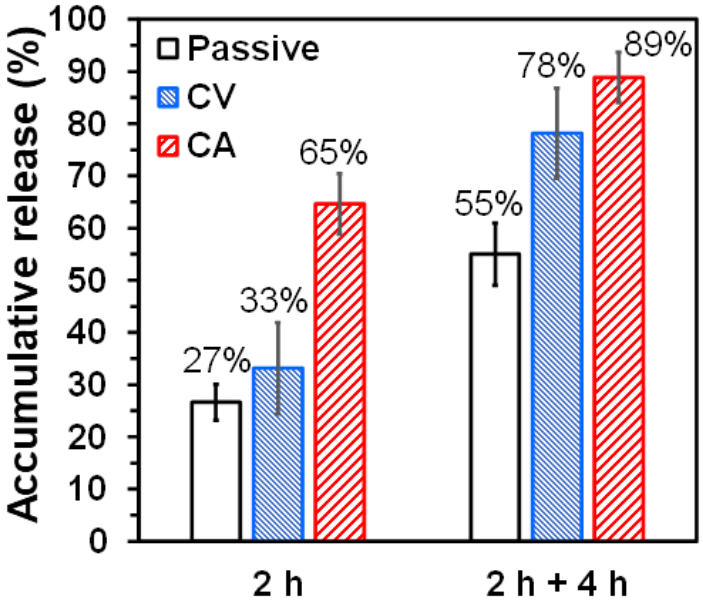

Fig. V - 6. Accumulative release of CAM at different times at pH 7 by passive diffusion and by applying CV and CA electrical stimuli.

The success of the CA stimulus was attributed to the fact that the alternate application of positive and negative potentials favored the swelling and shrinking of the NP matrix through the entrance (positive electrical potential) and escape (negative electrical potential) of solvated counter-anions, thus enhancing CAM release with respect to non-stimulated passive diffusion.

V - 3.3. Preparation and characterization of hydrogels

Alg-*g*-PAA hydrogel was prepared by aqueous polymerization, grafting AA monomer onto Alg, and using MBA and KPS as cross-linker and oxidizing agent, respectively (Scheme V - 2).[59] The incorporation of PEDOT and PEDOT/CAM NPs into Alg-*g*-PAA to produce Alg-*g*-PAA/PEDOT and Alg-*g*-PAA/PEDOT/CAM, respectively, was performed *in situ*, adding the corresponding NPs to the reaction mixture before the introduction of the oxidizing agent.

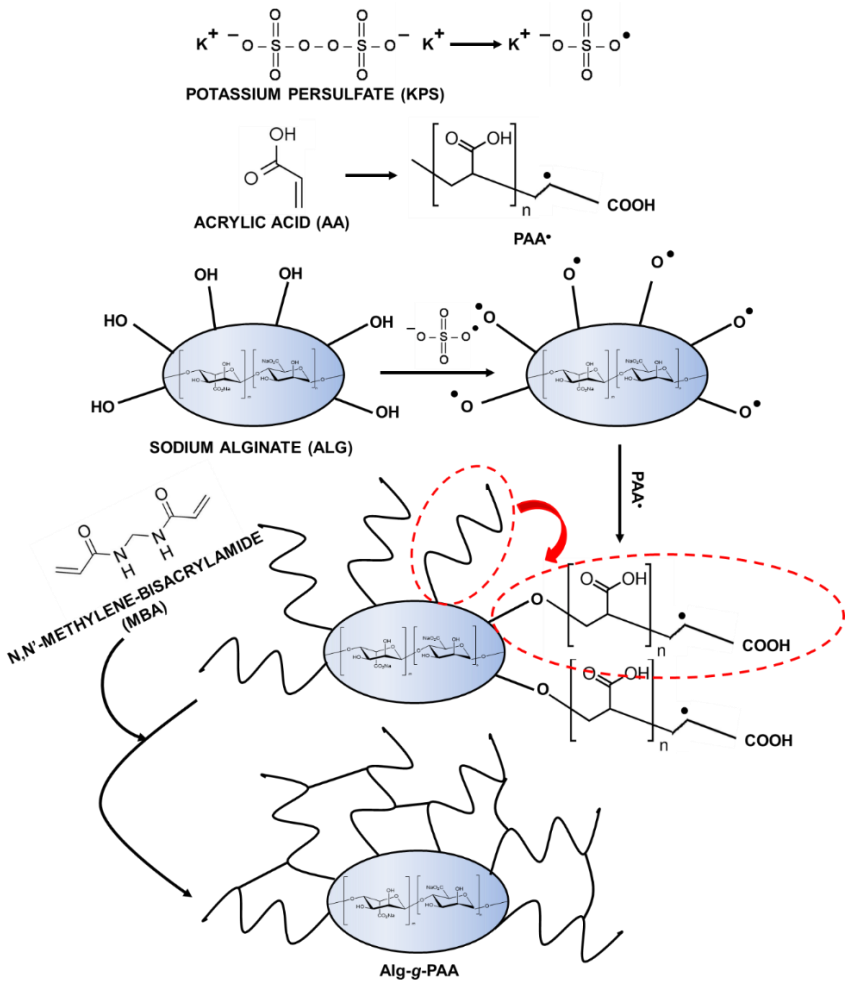

Scheme V - 2. Sketch illustrating the graft polymerization method used to prepare Alg-*g*-PAA.

The FTIR spectrum of Alg-*g*-PAA hydrogel is compared in Fig. V - 7a with those of Alg and AA co-monomer. The spectrum of Alg-*g*-PAA confirms the success of the grafting process, as it contains the characteristic bands of both Alg and AA. More specifically, Alg-*g*-PAA and Alg spectra exhibit the broad band at ~3430 cm^{-1} (O–H stretching), the intense bands at 1595 and 1408 cm^{-1} assigned to carbonyl (C=O asymmetric and symmetric stretching, respectively), and the peak at 1026 cm^{-1} (C–O–C stretching).[61] The Alg-*g*-PAA spectrum also shows an intense peak at 1701 cm^{-1} assigned to the C=O stretching of the AA co-monomer.

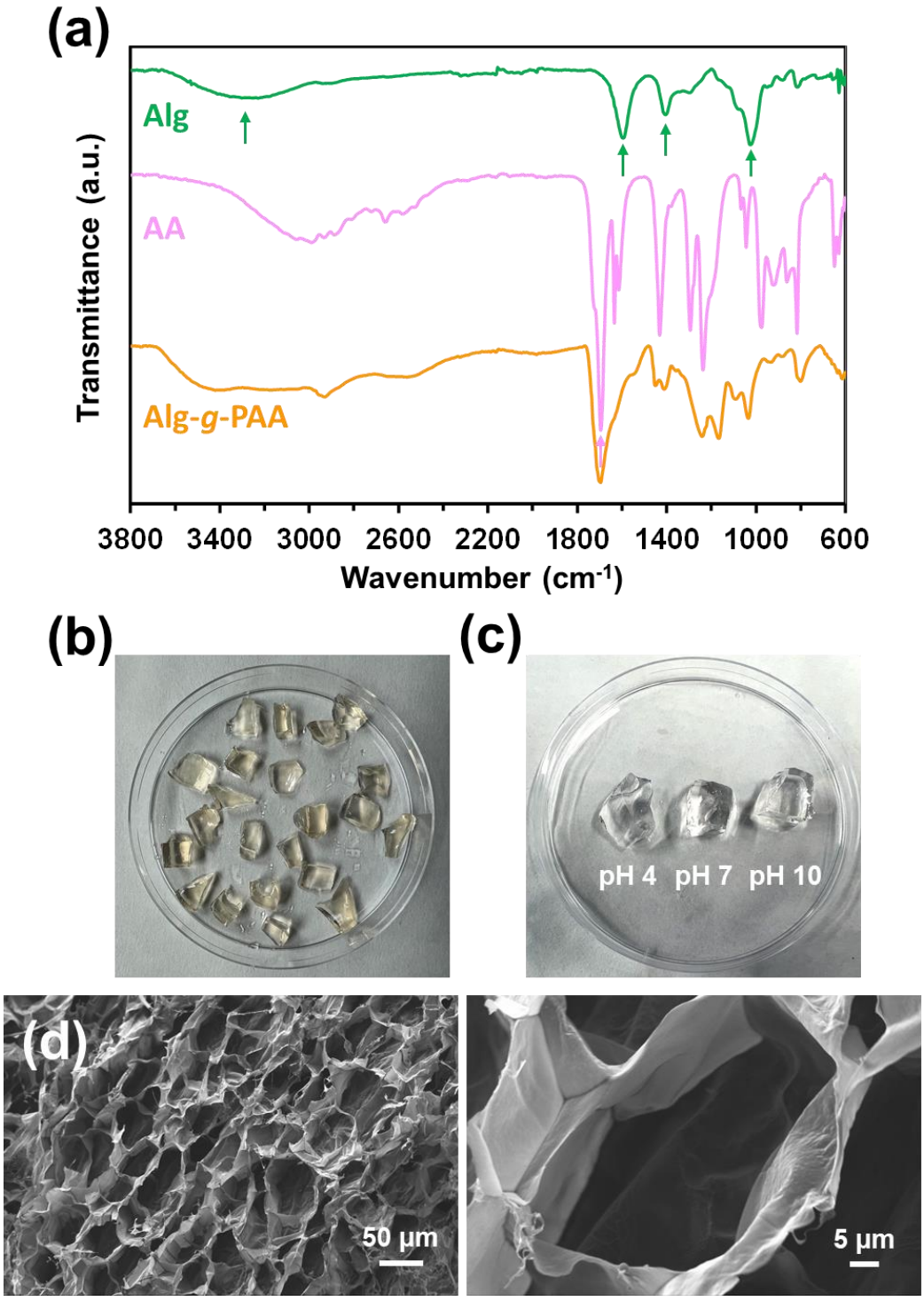

Fig. V - 7. (a) FTIR spectra of Alg, AA and Alg-*g*-PAA hydrogel after lyophilization. (b, c) Photographs of Alg-*g*-PAA (b) as synthesized and (c) after 48 h of hydration in 0.01 M PBS under stirring (80 rpm) at 37 ^{o}C and pH 4, 7 or 10. (d) SEM micrographs of Alg-*g*-PAA (left, 200× magnification; right, 1.5k× magnification).

Although as prepared Alg-*g*-PAA hydrogel displays a semitransparent yellowish color arising from Alg (Fig. V - 7b), its hydration not only induces the expected expansion of volume, but also a change

towards a transparent appearance, independently of the pH (Fig. V - 7c). SEM micrographs of the lyophilized hydrogel present an interconnected porous structure with the typical honeycomb morphology (Fig. V - 7d). The pores exhibit thin walls and distorted round shape, with an average size of 44 ± 9 µm (*n* = 100).

The successful loading of PEDOT NPs on the Alg-*g*-PAA hydrogel was evidenced by the change from the yellowish color to the characteristic dark blue color of PEDOT, as can be seen in Fig. V - 8a. The volume expansion of Alg-*g*-PAA/PEDOT observed upon hydration is very high at the three studied pH values (Fig. V - 8b), as occurred for the hydrogel without PEDOT NPs. SEM micrographs of Alg-*g*-PAA/PEDOT hydrogel (Fig. V - 8c) reflect an inter-connected structure similar to that described for Alg-*g*-PAA, with a similar average pore size (42 ± 9 µm and 44 ± 9 µm for Alg-*g*-PAA/PEDOT and Alg-*g*-PAA, respectively). However, magnified micrographs (Fig. V - 8c, right) show submicrometric clusters of PEDOT NPs spread on the pores of the Alg-*g*-PAA/PEDOT hydrogels and also inside the walls of the pores.

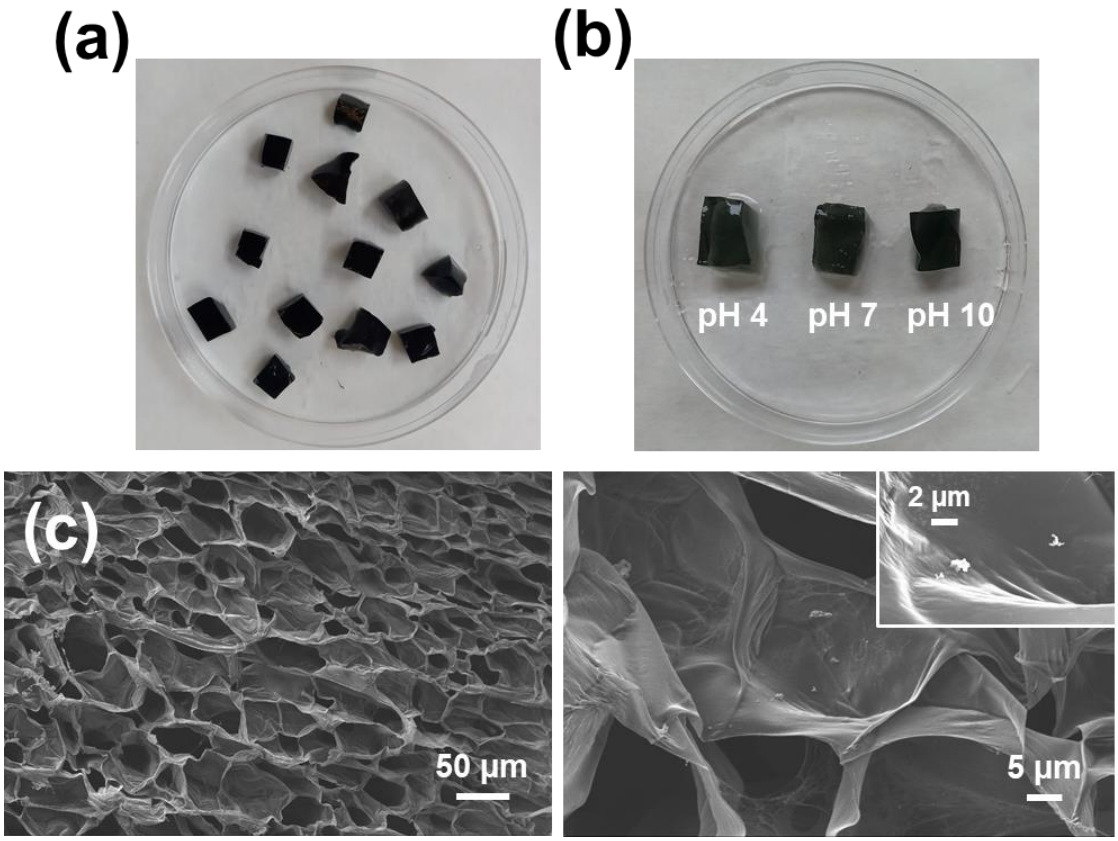

Fig. V - 8. (a, b) Photographs of Alg-*g*-PAA/PEDOT hydrogel (a) as synthesized and (b) after 48 h of hydration in PBS under stirring (80 rpm) at 37 ^{o}C and pH 4, 7 or 10. (d) SEM micrographs of Alg-*g*-PAA/PEDOT hydrogel (left, 200× magnification; right, 1.5k× magnification).

In order to examine the pH response of the prepared hydrogels, both Alg-*g*-PAA and Alg-*g*-PAA/PEDOT dry samples were cut in small pieces and immersed in 5 mL of 0.01 M PBS at pH 4, 7 and 10 under 80 rpm and 37 ^{o}C. Visual inspection (naked eye) of the hydrogel photographs as immersed and after 48 h of hydration (Fig. V - 9) evidenced their high swelling capacity. In order to quantify such observation, the temporal evolution of the swelling ratio (SR) was determined by weighting the swollen hydrogels at different times considering different pH conditions. For Alg-*g*-PAA hydrogel, hydrogen bonding interactions between the protonated carboxylic acid groups (from both Alg and PAA) were expected to be very abundant at the acid pH, thus reducing the swelling capacity of the hydrogel; while at neutral and basic pH values, ionized carboxylate groups were expected to generate repulsive electrostatic interactions within the hydrogel network, allowing very high SRs.[62] Conversely, the Alg-*g*-PAA hydrogel (Fig. V - 9a) revealed a behavior completely different from that expected. More specifically, similar SRs were observed at pH 4 and 7, while the swelling obtained at pH 10 was slightly lower. This has been attributed to the shielding effect of the hydrated Na^{+} ions from the media on the carboxylate groups of the hydrogel, which results in a significant reduction of the repulsive interactions at pH 7 and 10, noticeably affecting the swelling capacity. Thus, due to their higher strength,[63] the interactions of charged ions with water are more stabilizing than hydrogen bonds between the protonated carboxylic acid groups.

For the Alg-*g*-PAA/PEDOT hydrogel, the SR at acid pH was clearly higher than at neutral and basic pH, while the latter two exhibited very similar curves (Fig. V - 9b). Furthermore, the SR of Alg-*g*-PAA/PEDOT at acid pH is significantly higher than that of Alg-*g*-PAA, independently of the time. Similarly, the same trend was detected for Alg-*g*-PAA/PEDOT/CAM hydrogel (Fig. V - 9c). Such enhanced swelling behavior has been attributed to two main aspects: i) the presence of PEDOT NPs disrupt hydrogen bonding interactions, thus allowing the expansion of the hydrogel network at low pH; and ii) the SDBS surfactant molecules contained in the PEDOT NPs increase the negative charge of the network and, hence, the repulsive forces, which further expanded the hydrogel network. The most relevant advantage of this behavior (*i.e.* enhanced expansion of the hydrogel with PEDOT NPs at acid pH) favors the utilization of such system for the controlled delivery of CAM in the acid environment of tumors' sites, while also displaying antibacterial effect to fight infections.

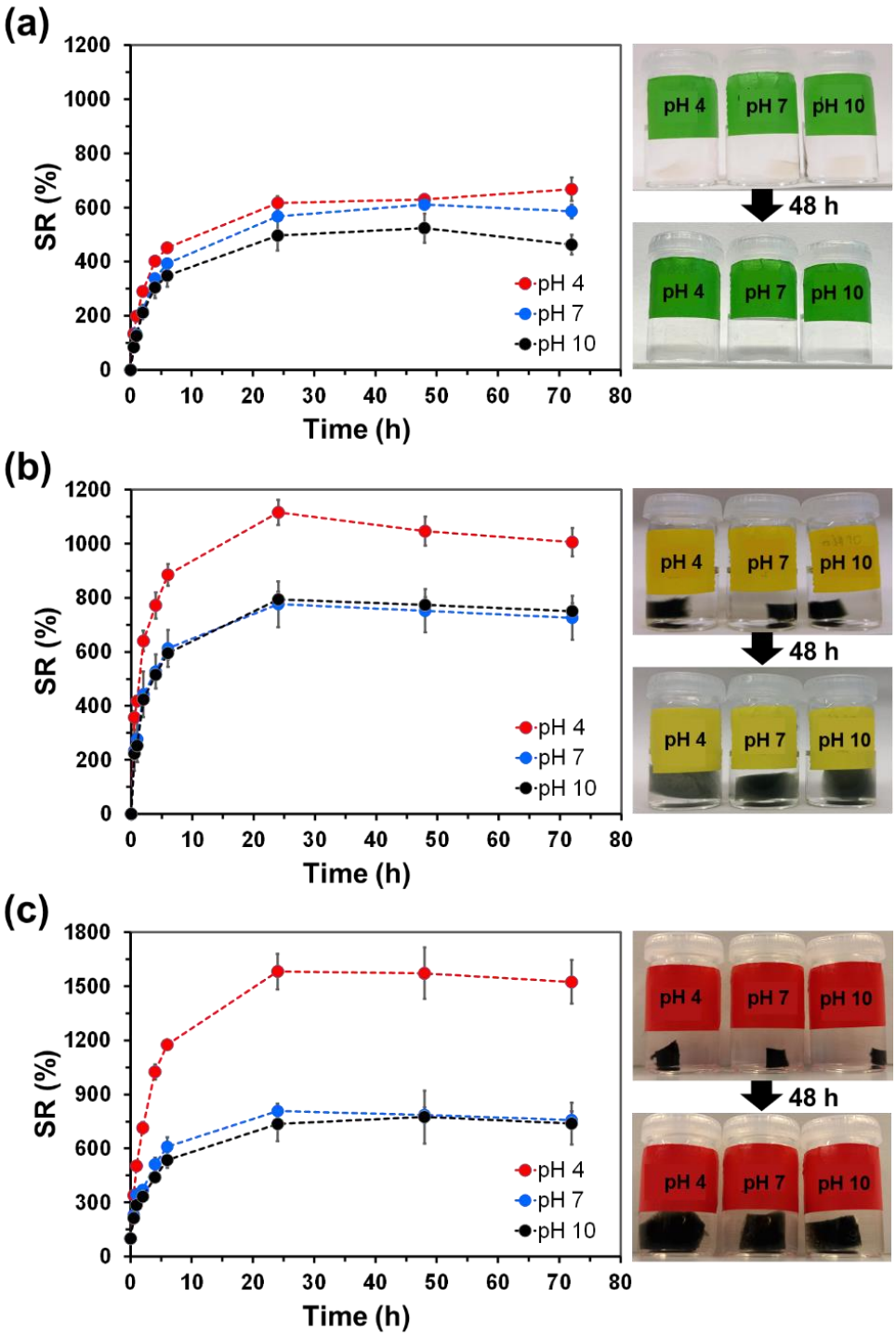

Fig. V - 9. Temporal evolution of the SR (*n* = 3) (left) and photographs of the hydrogels as immersed and after 48 h of immersion in PBS solution (right) for (a) Alg-*g*-PAA; (b) Alg-*g*-PAA/PEDOT and (c) Alg-*g*-PAA/PEDOT/CAM hydrogels.

On the other hand, the EWC of Alg-*g*-PAA hydrogel is practically independent of the pH with 86.3 ± 0.3 %, 85.9 ± 0.3 % and 83.9 ± 1.4 % at pH 4, 7 and 10, respectively. Conversely, not only are the EWC values obtained for Alg-*g*-PAA/PEDOT higher than those for Alg-*g*-PAA, but they also exhibit some pH

dependence with values of 91.3 ± 0.4 %, 88.1 ± 0.3 % and 85.7 ± 0.3b% at pH 4, 7 and 10, respectively. These values, which are consistent with the expansion of the PEDOT-containing hydrogel at acid pH, are similar to those obtained for Alg-*g*-PAA/PEDOT/CAM of 93.5 ± 1.1 %, 87.2 ± 0.7 % and 86.8 ± 2.3 % at pH 4, 7 and 10, respectively. The GF of Alg-*g*-PAA, Alg-*g*-PAA/PEDOT and Alg-g-PAA/PEDOT/CAM is 97 ± 1 %, 96 ± 2 % and 94 ± 1 %, respectively, indicating that the cross-linking efficiency in such hydrogels is very high.

To compare the electrochemical responses of Alg-*g*-PAA and Alg-*g*-PAA/PEDOT/CAM, both hydrogels were studied by CV using the set-up displayed in Fig. V - 10a. As can be seen, the hydrogels were directly used as working electrodes, while the counter and reference electrodes consisting of a Pt wire and an Ag|AgCl electrode. The cyclic voltammograms recorded in 0.01 M PBS at different pHs are compared in Fig. V - 10b-d.

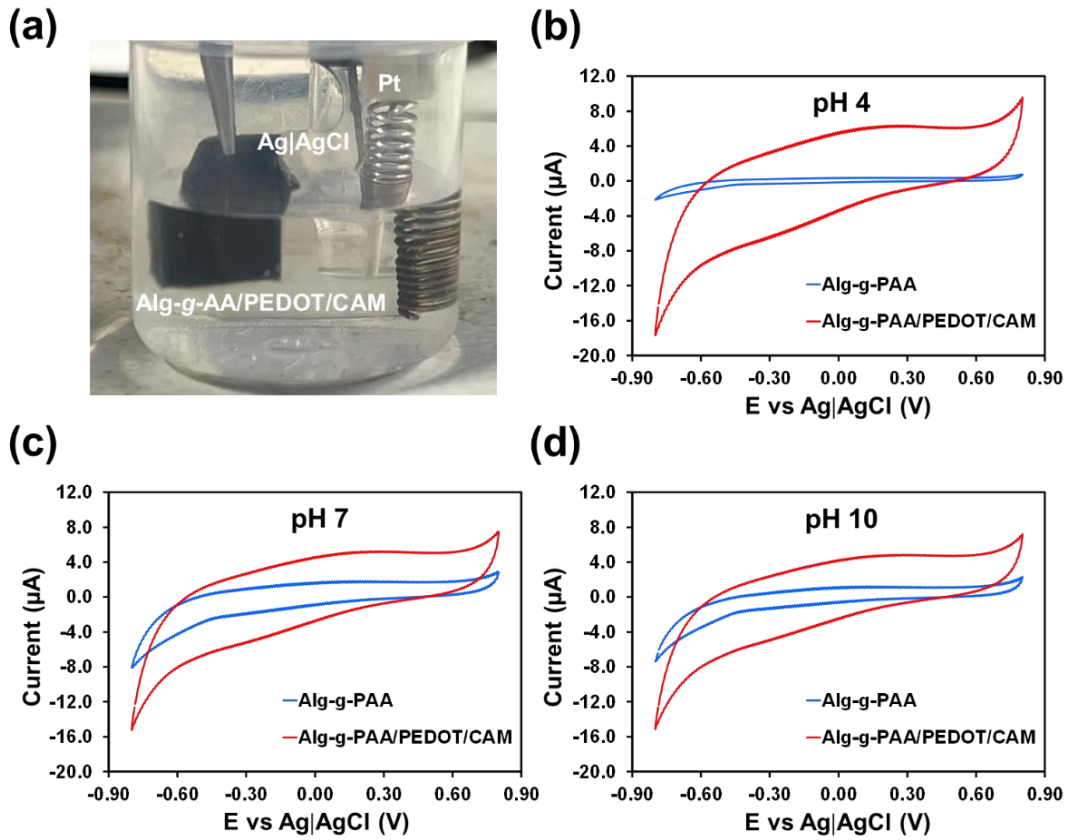

Fig. V - 10. (a) Set-up used for electrochemical measurements. (b-d) Cyclic voltammograms recorded for Alg-*g*-PAA and Alg-*g*-PAA/PEDOT/CAM hydrogels at (b) pH 4, (c) pH 7 and (d) pH 10.

As expected, the electrochemical activity of Alg-*g*-PAA hydrogel, which is proportional to the area of the cyclic voltammogram, is enhanced by loaded electroactive PEDOT NPs. This feature was found to depend on the pH (Fig. V - 10b-d), with the increment of electrochemical activity being higher at

acid pH. Quantitative comparison between Alg-g-PAA and Alg-*g*-PAA/PEDOT/CAM reveals that the electrochemical activity of the CP increases by 1482%, 172% and 277% at pH 4, 7 and 10, respectively. Such behavior correlated well with the swelling response observed earlier: a more open structure (*i.e.* expanded hydrogel network) was obtained at pH 4, which promoted the entrance and escape of ions during the redox process of PEDOT NPs during electrical stimulation.

The viscoelastic properties of as prepared Alg-*g*-PAA/PEDOT/CAM hydrogels were determined by rheological characterization. The storage modulus (*G'*), which accounts for the material's ability to store energy elastically under shear, was monitored by running both amplitude and frequency sweeps (Fig. V - 11).

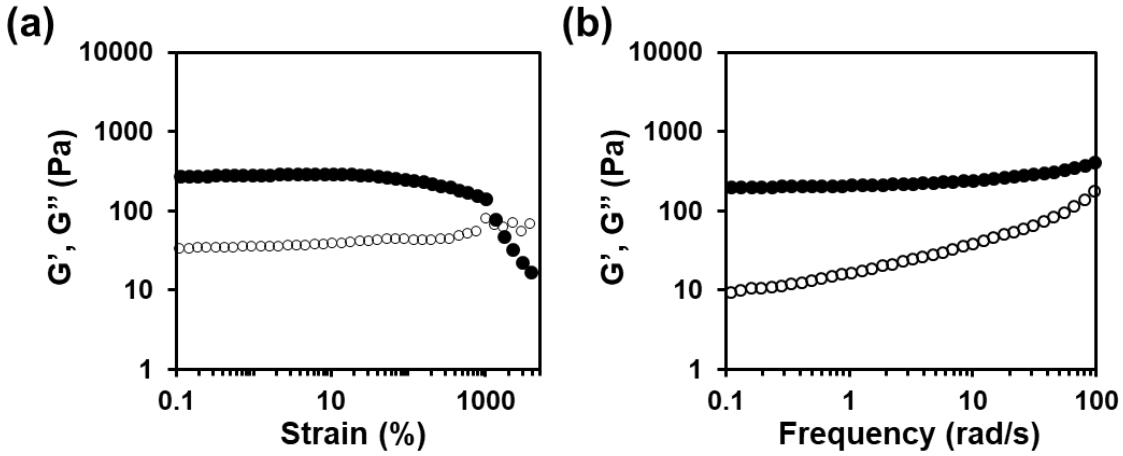

Fig. V - 11. Rheological characterization of as prepared Alg-g-PAA/PEDOT/CAM hydrogels. Representative data recorded under (a) amplitude sweep (at 1 Hz) and (b) frequency sweep (strain at 1%).

Specifically, from the amplitude sweep, *G'* was determined to be 317 ± 75 Pa (at 10% strain). The viscoelastic performance of the hydrogels remained stable up to 100% strain, when *G'* values started to decline and, ultimately, yielded at strain values higher than 100% and reaching *G''* > *G'* at 1300%. After immersion in PBS for 24 h, the *G'* values of the hydrogels determined at 12% strain (amplitude sweep) decreased down to 222 ± 134 Pa, 158 ± 36 Pa, and 120 ± 46 Pa for pH 4, 7, and 10, respectively, on account of the swelling process, which produced a softer material (Fig. V - 12a).

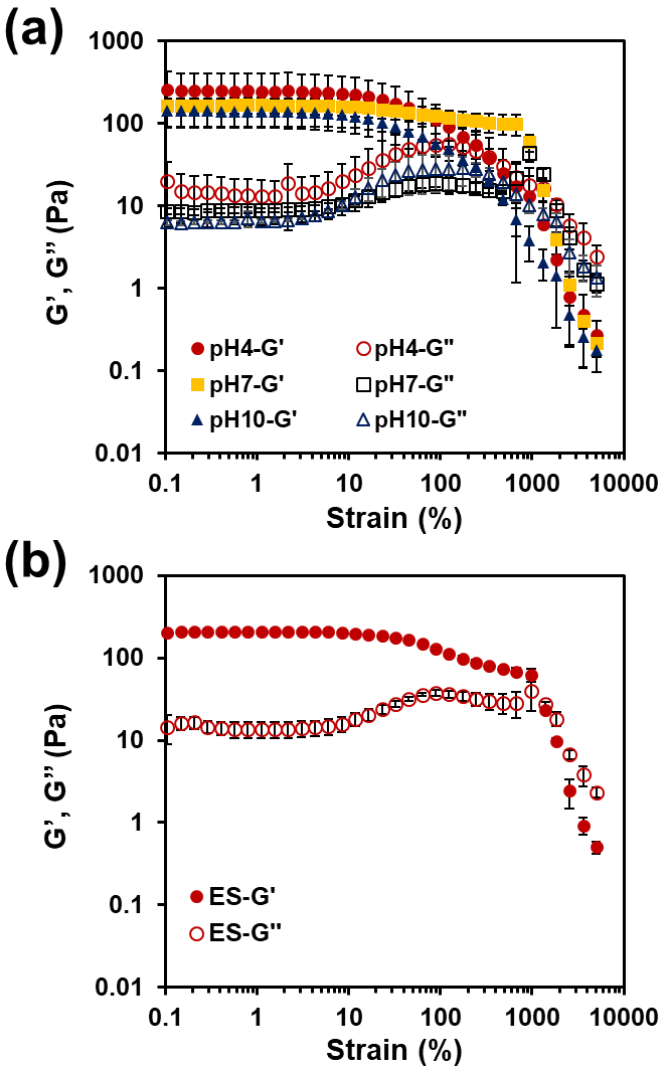

Fig. V - 12. Rheological data for Alg-*g*-PAA/PEDOT/CAM hydrogels recorded under amplitude sweep (at 1 Hz) from 0.1 to 5000% after (a) being immersed in PBS at different pH values for 24 h and (b) after applying the CA electrical stimulus for 2 h (pH 4), followed by 24 h in PBS at pH 4. Error bars: SD with n = 3.

In terms of yielding, *G'* values for samples kept at pH 4 and 10 started to yield at lower strain values, and the crossover between *G'* and *G''* occurred between 300 and 400% strain. In contrast, the response of the samples kept at pH 7 was more similar to that of the as prepared system. Hence, swelling did modify to some extent the viscoelastic performance of Alg-*g*-PAA/PEDOT/CAM hydrogels, being more noticeable for pH 4 and 10. On the other hand, the hydrogel submitted to the electrical stimuli (at pH 4) displayed a *G'* value of 200 ± 10 Pa (at 12% strain), as seen earlier, which indicated that the electrochemical process had little effect on the hydrogel viscoelastic response (Fig. V - 12b).

V - 3.4. CAM release from Alg-*g*-PAA/PEDOT/CAM

The passive and electrostimulated release of CAM from Alg-*g*-PAA/PEDOT/CAM was studied at different pH values. Electrostimulation was performed by applying CA cycles identical to those used for PEDOT NPs for 2 h (*i.e.* a total of 9 CA cycles). Analysis of the drug delivered in absence of stimuli indicated that, after 24 h, most of the drug remains in the carrier, independently of the pH (Fig. V - 13a). Indeed, the amount of CAM passively released, which does not increase with the time of immersion in the medium, is around 1%. This result represents a drastic reduction with respect to PEDOT/CAM NPs (Fig. V - 6), for which the passive release reached a value of around 55% after only 6 h, evidencing that CAM does not only interact with PEDOT chains, but also with water molecules. Conversely, the very slow passive release observed when PEDOT/CAM NPs are loaded into the Alg-*g*-PAA has been attributed to the strength of the interactions formed by the drug and the polar groups of the hydrogel. Thus, such interactions are apparently much stronger than those it could form with water molecules, preventing the diffusion of the CAM molecules through the hydrogel matrix to the medium.

On the other hand, the CAM release from Alg-*g*-PAA/PEDOT/CAM increased significantly upon electrostimulation (Fig. V - 13b). This feature is fully consistent with results obtained for PEDOT/CAM NPs (Fig. V - 6), which confirms that PEDOT/CAM NPs preserve their response to CA cycles when embedded in the hydrogel. Furthermore, the release increased upon decreasing pH, reaching values of 30%, 12% and 2% at pH 4, 7 and 10, respectively, after 6 h (*i.e.* 2 h of electrostimulation + 4 h). Moreover, for pH 4, the release increases to 33% after 26 h (*i.e.* 2 h of electrostimulation + 24 h). Comparison of these results with those obtained by passive diffusion for Alg-*g*-PAA/PEDOT/CAM and by electrostimulation for PEDOT/CAM NPs suggests that the CA-induced CAM release from Alg-*g*-PAA/PEDOT/CAM was driven by the content of water inside the hydrogel (*i.e.* water entropy-driven mechanism). Thus, CA cycles induced the release from the loaded NPs entrapped in the hydrogel, while the competing interactions between the released CAM molecules and either the water molecules and polar groups of the Alg-*g*-PAA matrix were affected by pH. It is worth noting that the hydrogel SR was found to be much higher at acid pH (4) than at neutral pH (7), which in turn was higher than at basic pH (10) (Fig. V - 10b). Accordingly, the abundance of CAM molecules interacting with water increased with decreasing pH, explaining the variation of the released antibiotic with the pH that occurred by diffusion of the CAM molecules that were not interacting with the hydrogel matrix.

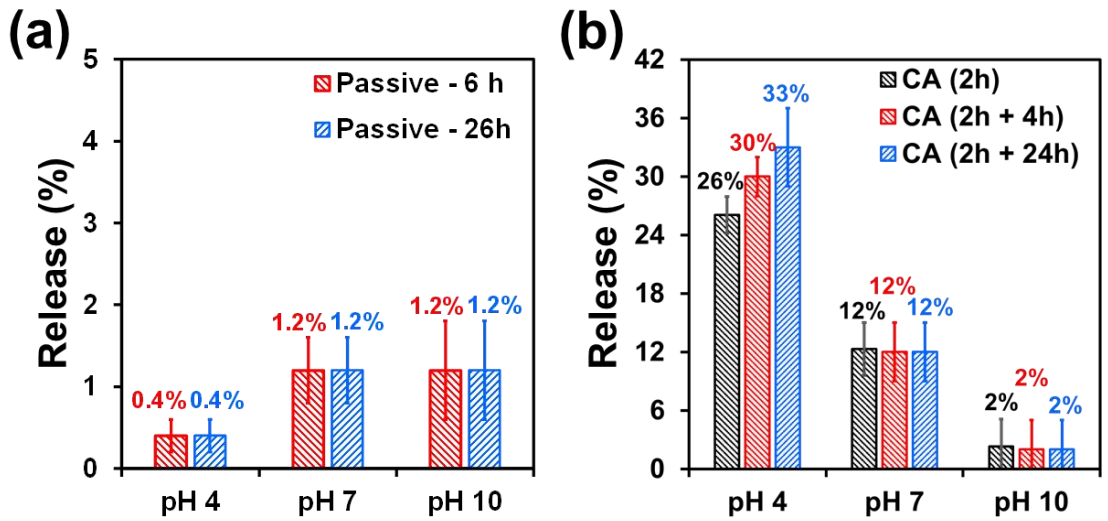

Fig. V - 13. Release of CAM from Alg-*g*-PAA/PEDOT/CAM hydrogel at different pH values (*n* = 3) as observed by (a) passive diffusion after 6 h and 26 h and (b) just after applying the CA electrical stimuli, which took 2 h, and both 4 h and 24 h later.

Comparison of the release profiles displayed in Fig. V - 13 with those reported in the literature for other Alg hydrogels reveals that Alg-*g*-PAA/PEDOT/CAM presents significant advantages in terms of controlled release. For example, the release from CAM-loaded Alg-based hydrogels, which are chemo-responsive to the calcium ion concentration, was recently studied by different authors.[64,65] In deionized water, an initial fast release followed by a sustained rate of release was observed without applying an external stimulus (*i.e.* passive release).[64] Indeed, complete (cumulative release of 100%) release was achieved in around only 3 h. However, this effect was slightly delayed (*i.e.* cumulative release of 40-60% release in 3 h) by enhancing the interactions with the drug through the loading of cellulose nanocrystals into the hydrogel,[64] or by increasing the concentration of calcium ions to increase the cross-linking.[65] Thus, the incorporation of PAA and PEDOT NPs allows to drastically reduce the passive release and, at the same time, to provide pH-selective response to electrical stimuli.

The need for materials with both broad utility and greater application specificity is ever-present. In the case of drug delivery applications, hydrogels with specific, tunable and reversible responses to environmental stimuli are known for decades to be excellent candidates as drug vehicles.[66] Current drug delivery research is evolving from biomimetic materials that are responsive to the host environment to smart materials that respond to multiple stimuli, allowing to better dose and targeting controlled release.[67] This feature is particularly relevant when the released drug an anticancer medication, which usually exhibit a high toxicity profile. Considering the local acidic pH at the microenvironment of tumors, Alg-*g*-PAA/PEDOT/CAM is a sophisticated smart material that fulfils all such requirements. The chemo- and electro-response of Alg-*g*-PAA/PEDOT/CAM, which favors the

release of CAM under electrostimulation in an acid environment, enables a more controlled and efficient release with a hierarchical targeting strategy that was not achieved using single-responsive carriers.[14,21,22] Moreover, the proposed system is expected to work in the same way when drugs similar in size and polarity are used instead of CAM.

V - 3.5. Antibacterial tests

Results from the antibacterial activity of released CAM, which was tested against Gram-negative (*E. coli*) and Gram-positive bacteria (*S. sanguinis* and *S. mutans*), are shown in Fig. V - 14.

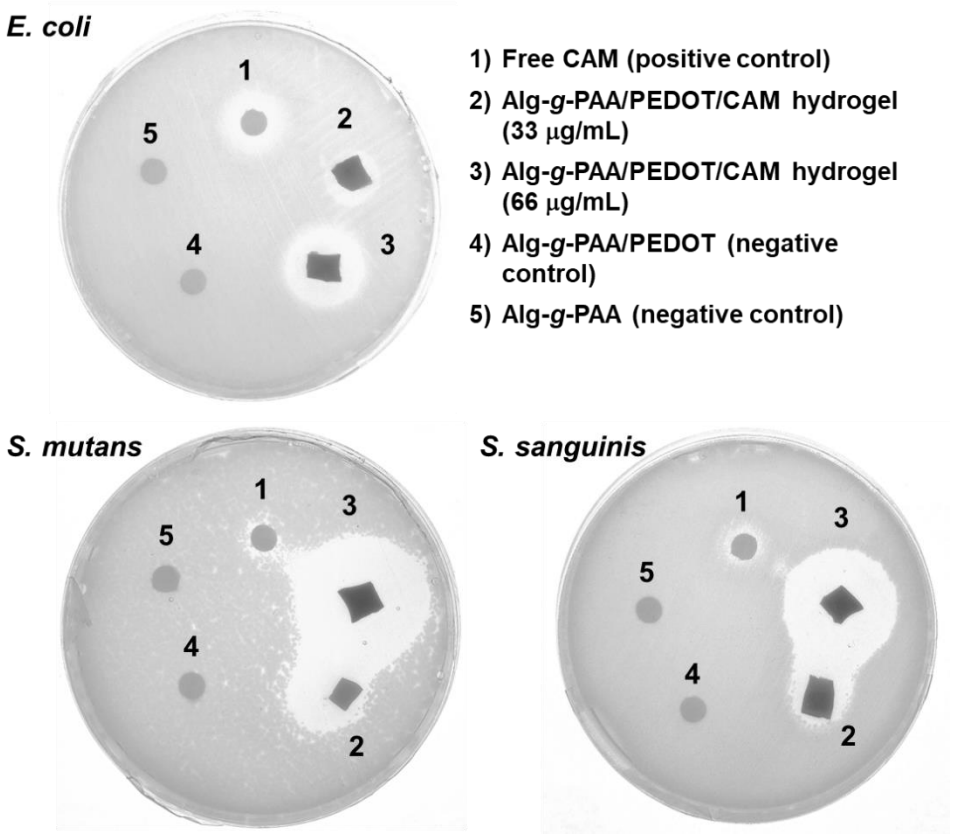

Fig. V - 14. Bactericidal activity against *E. coli*, *S. sanguinis* and *S. mutans* of free CAM (positive control - 1), Alg-*g*-PAA/PEDOT/CAM hydrogels with two drug loading concentrations (33 and 66 μg/mL – 2 and 3), 20 μL of the release medium after passive diffusion from Alg-*g*-PAA/PEDOT hydrogel (without CAM - 4), and 20 μL of the release medium after passive diffusion from Alg-*g*-PAA hydrogels (without CAM nor PEDOT NPs - 5). Inhibition halos observed using the disk diffusion method.

The activity of CAM was not altered after being introduced in the Alg-*g*-PAA/PEDOT/CAM hydrogel. Thus, the release of the drug from Alg-*g*-PAA/PEDOT/CAM by passive diffusion was effective in inhibiting bacterial growth, which is a concentration dependent mechanism. Free CAM (positive control) also hindered bacteria growth, even though, in this case, the inhibition zone was smaller,

probably as a consequence of the lower dose deposited onto the disk (*i.e.* 20 µL at 66 µg/mL). As it was expected, no antibacterial activity was detected for release media samples (20 µL) derived from the passive diffusion of Alg-*g*-PAA/PEDOT and blank Alg-*g*-PAA hydrogels (both without CAM).

V - 3.6. Anticancer activity

The anticancer activity of released CAM was examined using HeLa cancer cells, as well as Vero normal cells. Cell viability was determined for cells after being exposed to CAM released by electrostimulation from Alg-*g*-PAA/PEDOT/CAM hydrogels (Fig. V - 15a), as well as to free CAM (Fig. V - 15b). The dilution series was achieved by successive 1:2 dilutions of the initial concentrations (*i.e.* 33 µg/mL for free CAM). The concentration in Fig. V - 15a is expressed in arbitrary units (a.u.), where a concentration of 1 a.u. refers to the initial CAM concentration in the release media after electrostimulation.

In general, cell viability decreases with increasing drug concentration, independently of the source of CAM (*i.e.* free or released). However, HeLa cells are more sensitive to the presence of CAM (Fig. V - 15b), with Vero cells presenting a higher viability (59%) than the HeLa (31%) cells at 33 µg/mL. For lower drug concentrations, cell viability is higher than 80% regardless of the cell line. This response is also observed for CAM released from Alg-*g*-PAA/PEDOT/CAM hydrogels by electrostimulation (Fig. V - 15a). Interestingly, the initial drug concentration in the release medium might be higher than 33 µg/mL, as initially calculated, thus reducing cell viability for both cell lines. Overall, these features confirm that the potential anticancer activity of CAM was not altered during the encapsulation process or the release by electrostimulation. Next steps in device design should include a careful optimization to further adjust CAM dosage.

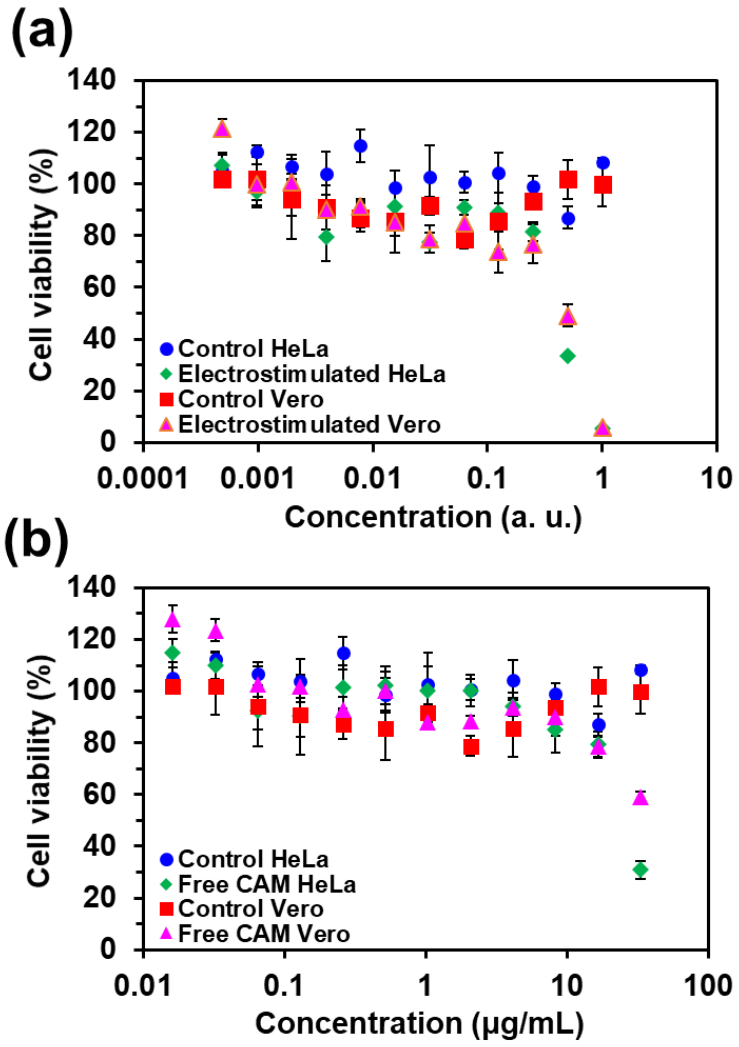

Fig. V - 15. Cell viability for HeLa and Vero cell lines, after being exposed for 24 h to CAM released from Alg-*g*-PAA/PEDOT/CAM hydrogels by applying the CA electrical stimulus, or (b) exposed to free CAM. Error bars indicate the standard deviation (n = 3).

V - 4. Conclusions

Alg-*g*-PAA/PEDOT/CAM hydrogels were prepared by incorporating, during the synthesis, spherical electroresponsive PEDOT/CAM NPs with an average diameter of 149 ± 23 nm. The properties of Alg-*g*-PAA/PEDOT/CAM hydrogel, which were fully characterized using different techniques, evidenced that the SR depends on the pH and that the hydrogel is conductive. CAM-release tests from PEDOT/CAM NPs, which showed an LC of 14.3 ± 2.5 %, revealed a relatively fast passive release rate (*i.e.* around 14% per hour) that increased by applying CV or, especially, CA stimuli. Conversely, CAM-release assays from Alg-*g*-PAA/PEDOT/CAM hydrogel showed that the passive release was negligible, regardless of the pH value. This response has been attributed to the formation of specific interactions between CAM molecules released from the embedded PEDOT/CAM NPs and the polar groups of the

Alg-*g*-PAA matrix. When CA electrostimuli were applied to Alg-*g*-PAA/PEDOT/CAM hydrogel, the amount of CAM molecules released from the NPs to the hydrogel increased and, concomitantly, the diffusion out of the hydrogel increased with the SR (*i.e.* with decreasing pH). Antibacterial tests and cell viability assays proved that the biological activity of CAM was not affected by the loading and release processes.

Considering the bioactivity of CAM, the proposed conducting hydrogel is of particular interest for the treatment of cancer, as well as regulated inhibition of bacterial infections, avoiding the increased antibiotic resistance as patients undergo systemic treatments. Results show that Alg-*g*-PAA/PEDOT/CAM hydrogel allows electro-chemo controlled release of CAM, a broad spectrum antibiotic, which occurs when the pH of the environment is acid and PEDOT/CAM NPs are electrostimulated. Further studies on this bioplatform could lead to an optimization of different variables, including the control of stimulation parameters (*e.g.* duration of the electric stimuli, magnitude of the potential, etc.), as well as a more precise understanding of the pH effect by considering different environments with different acidities (*e.g.* pH 4.5, 5.0, 5.5, 6.0 and 6.5). Additionally, this system presents the potential to be explored for the release of other antibiotics or drugs, or a combination thereof, to environments of specific requirements where the electro-chemo response can be custom exploited.

V - 5. References

(1) Zhao, Z.; Ukidve, A.; Kim, J.; Mitragotri, S. Targeting Strategies for Tissue-Specific Drug Delivery. *Cell* **2020**, *181*, 151-167.

(2) Nazir, F.; Tabish, T. A.; Tariq, F.; Iftikhar, S.; Wasim, R.; Shahnaz, G. Stimuli-Sensitive Drug Delivery Systems for Site-Specific Antibiotic Release. *Drug Discov. Today* **2022**, *27*, 1698-1705.

(3) García-González, C. A.; Sosnik, A.; Kalmár, J.; De Marco, I.; Erkey, C.; Concheiro, A.; Alvarez-Lorenzo, C. Aerogels in Drug Delivery: From Design to Application. *J. Control. Release* **2021**, *332*, 40-63.

(4) Du, W.; Gao, Y.; Liu, L.; Sai, S.; Ding, C. Striking Back Against Fungal Infections: The Utilization of Nanosystems for Antifungal Strategies. *Int. J. Mol. Sci.* **2021**, *22*, 10104.

(5) Frieri, M.; Kumar, K.; Boutin, A. Antibiotic Resistance. *J. Infec. Public Health* **2017**, *10*, 369-378.

(6) Llor, C.; Bjerrum, L. Antimicrobial Resistance: Risk Associated with Antibiotic Overuse and Initiatives to Reduce the Problem. *Ther. Adv. Drug Saf.* **2014**, *5*, 229-241.

(7) Zhang, L.; Wang, Y.; Wang, C.; He, M.; Wan, J.; Wei, Y.; Zhang, J.; Yang, X.; Zhao, Y.; Zhang, Y. Light-Activable on-Demand Release of Nano-Antibiotic Platforms for Precise Synergy of Thermochemotherapy on Periodontitis. *ACS Appl. Mater. Interfaces* **2020**, *12*, 3354-3362.

(8) Atkins, S.; Chueh, A.; Barwell, T.; Nunzi, J. M.; Seroude, L. Capture and Light-Induced Release of Antibiotics by an Azo Dye Polymer. *Sci. Rep.* **2020**, *10*, 3267.

(9) Cai, W.; Weng, X.; Zhang, W.; Chen, Z. Green Magnetic Nanomaterial as Antibiotic Release Vehicle: The Release of Pefloxacin and Ofloxacin. *Mater. Sci. Eng. C* **2021**, *118*, 111439.

(10) Quan, K.; Zhang, Z.; Ren, Y.; Busscher, H. J.; van der Mei, H. C.; Peterson, B. W. Homogeneous Distribution of Magnetic, Antimicrobial-carrying Nanoparticles Through an Infectious Biofilm Enhances Biofilm-Killing Efficacy. *ACS Biomat. Sci. Eng.* **2020**, *6*, 205-212.

(11) Delaney, L. J.; MacDonald, D.; Leung, J.; Fitzgerald, K.; Sevit, A. M.; Eisenbrey, J. R.; Patel, N.; Forsberg, F.; Kepler, C. K.; Fang, T.; Kurtz, S. M.; Hickok, N. J. Ultrasound-Triggered Antibiotic Release from PEEK Clips to Prevent Spinal Fusion Infection: Initial Evaluations. *Acta Biomater.* **2019**, *93*, 12-24.

(12) Zou, M.; Zhao, P.; Huo, S.; Göstl, R.; Herrmann, A. Activation of Antibiotic-Grafted Polymer Brushes by Ultrasound. *ACS Macro Lett.* **2022**, *11*, 15-19.

(13) Puiggalí-Jou, A.; del Valle, L. J.; Alemán, C. Drug Delivery Systems Based on Intrinsically Conducting Polymers. *J. Control. Release* **2019**, *309*, 244-264.

(14) Enshaei, H.; Puiggalí-Jou, A.; del Valle, L. J.; Turon, P.; Saperas, N.; Alemán, C. Nanotheranostic Interface Based on Antibiotic-Loaded Conducting Polymer Nanoparticles for Real-Time Monitoring of Bacterial Growth Inhibition. *Adv. Healthc. Mater.* **2021**, *10*, e2001636.

(15) Sabzi, M.; Afshari, M. J.; Babaahmadi, M.; Shafagh, N. pH-Dependent Swelling and Antibiotic Release from Citric Acid Crosslinked Poly(vinyl alcohol) (PVA)/Nano Silver Hydrogels. *Colloids Surf B Biointerfaces* **2020**, *188*, 110757.

(16) Guo, Y.; Qian, S.; Wang, L.; Zeng, J.; Miao, R.; Meng, Y.; Jin, Y.; Chen, H.; Wang, B. Reversible Antibiotic Loading and pH-Responsive Release from Polymer Brushes on Contact Lenses for Therapy and Prevention of Corneal Infections. **J. Mater. Chem. B 2020**, *8*, 10087-10092.

(17) Lu, M. M.; Ge, Y. R.; Qiu, J.; Shao, D.; Zhang, Y.; Bai, J.; Zheng, X.; Chang, Z. M.; Wang, Z.; Dong, W. F.; Tang C. B. Redox/pH Dual-Controlled Release of Chlorhexidine and Silver Ions from Biodegradable Mesoporous Silica Nanoparticles Against Oral Biofilms. *Int. J. Nanomedicine* **2018**, *13*, 7697-7709.

(18) Ahmed, W.; Zhai, Z.; Gao, C. Adaptive Antibacterial Biomaterial Surfaces and Their Applications. *Mater. Today Bio*. **2019**, *2*, 100017.

(19) Bourgat, Y.; Mikolai, C.; Stiesch, M.; Klahn, P.; Menzel, H. Enzyme-Responsive Nanoparticles and Coatings Made from Alginate/Peptide Ciprofloxacin Conjugates as Drug Release System. *Antibiotics* **2021**, *10*, 653.

(20) Hoque, J.; Bhattacharjee, B.; Prakash, R. G.; Paramanandham, K.; Haldar, J. Dual Function Injectable Hydrogel for Controlled Release of Antibiotic and Local Antibacterial Therapy. *Biomacromolecules* **2018**, *19*, 267-278.

(21) Puiggalí-Jou, A.; Cazorla, E.; Ruano, G.; Babeli, I.; Ginebra, M.-P.; García-Torres, J.; Alemán, C. Electroresponsive Alginate-Based Hydrogels for Controlled Release of Hydrophobic Drugs. *ACS Biomat. Sci. Eng. 2020, 6,* 6228-6240.

(22) Rivas, M.; del Valle, L. J.; Rodríguez-Rivero, A. M.; Turon, P.; Puiggalí, J.; Alemán, C. Loading of Antibiotic into Biocoated Hydroxyapatite Nanoparticles: Smart Antitumor Platforms with Regulated Release. *ACS Biomat. Sci. Eng. 2018, 4,* 3234-3245.

(23) Gao, W.; Chen, Y.; Zhang, Y.; Zhang, Q.; Zhang, L. Nanoparticle-Based Local Antimicrobial Drug Delivery. *Adv. Drug Deliv. Rev.* **2018**, *127*, 46-57.

(24) Maione, S.; Del Valle, L. J.; Pérez-Madrigal, M. M.; Cativiela, C.; Puiggalí, J.; Alemán, C. Antimicrobial Electrospun Fibers of Polyester Loaded with Engineered Cyclic Gramicidin Analogues. *Fibers* **2017**, *5*, 34.

(25) Can Suner, S.; Yildirim, Y.; Yurt, F.; Ozel, D.; Oral, A.; Ozturk, I. Antibiotic Loaded Electrospun Poly(lactic acid) Nanofiber Mats for Drug Delivery System. *J. Drug Deliv. Sci. Technol.* **2022**, *71*, 103263.

(26) Sanchez, M.; Estrany, F.; Borras, N.; Maiti, B.; Díaz-Díaz, D.; del Valle, L. J.; Aleman, C. Antimicrobial Activity of Poly(3,4-ethylenedioxythiophene) n-Doped with a Pyridinium-Containing Polyelectrolyte. *Soft Matter* **2019**, *15*, 7695-7703.

(27) Xu, Q.; Li, X.; Jin, Y.; Sun, L.; Ding, X.; Liang, L.; Wang, L.; Nan, K.; Ji, J.; Chen, H.; Wang, B. Bacterial Self-Defense Antibiotics Release from Organic–Inorganic Hybrid Multilayer Films for Long-Term Anti-Adhesion and Biofilm Inhibition Properties. **Nanoscale 2017**, *9*, 19245-19254.

(28) Donahue, M. J.; Sanchez-Sanchez, A.; Inal, S.; Qu, J.; Owens, R. M.; Mecerreyes, D.; Malliaras, G. G.; Martin, D. C. Tailoring PEDOT Properties for Applications in Bioelectronics. *Mater. Sci. Eng. R Reports* **2020**, *140*, 100546.

(29) Aradilla, D.; Estrany, F.; Alemán, C. Symmetric Supercapacitors Based on Multilayers of Conducting Polymers. *J. Phys. Chem. C* **2011**, *115*, 8430-8438.

(30) Kirchmeyer, S.; Reuter, K. Scientific Importance, Properties and Growing Applications of Poly(3,4-ethylenedioxythiophene). *J. Mater. Chem.* **2005**, *15*, 2077-2088.

(31) Fabregat, G.; Teixeira-Dias, B.; del Valle, L. J.; Armelin, E.; Estrany, F.; Alemán, C. Incorporation of a Clot-Binding Peptide into Polythiophene: Properties of Composites for Biomedical Applications. *ACS Appl. Mater. Interfaces* **2014**, *6*, 11940-11954.

(32) Boehler, C.; Kleber, C.; Martini, N.; Xie, Y.; Dryg, I.; Stieglitz, T.; Hofmann, U. G.; Asplund, M. Actively Controlled Release of Dexamethasone from Neural Microelectrodes in a Chronic in Vivo Study. *Biomaterials* **2017**, *129*, 176-187.

(33) Krukiewicz, K.; Cichy, M.; Ruszkowski, P.; Turczyn, R.; Jarosz, T.; Zak, J. K.; Lapkowski, M.; Bednarczyk-Cwynar, B. Betulin-Loaded PEDOT Films for Regional Chemotherapy. *Mater. Sci. Eng. C* **2017**, *73*, 611-615.

(34) Puiggalí-Jou, A.; Micheletti, P.; Estrany, F.; del Valle, L. J.; Alemán, C. Electrostimulated Release of Neutral Drugs from Polythiophene Nanoparticles: Smart Regulation of Drug-Polymer Interactions. *Adv. Healthc. Mater.* **2017**, *6*, 1700453.

(35) Esrafilzadeh, D.; Razal, J. M.; Moulton, S. E.; Stewart, E. M.; Wallace, G. G. Multifunctional Conducting Fibres with Electrically Controlled Release of Ciprofloxacin. *J. Control. Release* **2013**, *169*, 313-320.

(36) Puiggalí-Jou, A.; Cazorla, E.; Ruano, G.; Babeli, I.; Ginebra, M.-P.; García-Torres, J.; Alemán, C. Electroresponsive Alginate-Based Hydrogels for Controlled Release of Hydrophobic Drugs. *ACS Biomat. Sci. Eng.* **2020**, *6*, 6228-6240.

(37) Adamczak, A.; Ożarowski, M.; Karpiński, T. M. Curcumin, a Natural Antimicrobial Agent with Strain-Specific Activity. *Pharmaceuticals* **2020**, *16*, 153.

(38) Park, J. Y.; Kim, K. A.; Kim, S. L. Chloramphenicol is a Potent Inhibitor of Cytochrome P450 Isoforms CYP2C19 and CYP3A4 in Human Liver Microsomes. *Antimicrob. Agents Chemother.* **2003**, *47*, 3464-3469.

(39) Lamb, R.; Harrison, H.; Hulit, J.; Smith, D. L.; Lisanti, M. P.; Sotgia, F. Mitochondria as New Therapeutic Targets for Eradicating Cancer Stem Cells: Quantitative Proteomics and Functional Validation via MCT1/2 Inhibition. *Oncotarget* **2014**, *5*, 11029.

(40) Kalghatgi, S.; Spina, C. S.; Costello, J. C.; Liesa, M.; Morones-Ramirez, J. R.; Slomovic, S.; Molina, A.; Shirihai, O. S.; Collins, J. J. Bactericidal Antibiotics Induce Mitochondrial Dysfunction and Oxidative Damage in Mammalian Cells. *Sci. Transl. Med.* **2013**, *5*, 192ra85.

(41) Delaunay, Pascual, G.; Feng, B.; Klann, K.; Behm, M.; Hotz-Wagenblatt, A.; Richter, K.; Zaoui, K.; Herpel, E.; Münch, C.; Dietmann, S.; Hess, J.; Aznar Benirtah, S.; Frye, M. Mitochondrial RNA Modifications Shape Metabolic Plasticity in Metastasis. *Nature* **2022**, *607*, 593–603.

(42) Tian, F.; Wang, C.; Tang, M.; Li, J.; Cheng, X.; Zhang, S.; Ji, D.; Huang, Y.; Li, H. The Antibiotic Chloramphenicol May Be an Effective New Agent for Inhibiting the Growth of Multiple Myeloma. *Oncotarget* **2017**, *7*, 51934.

(43) Kostopoulou, O. N.; Kouvela, E. C.; Magoulas, G. E.; Garnelis, T.; Panagoulias, I.; Rodi, M.; Papadopoulos, G.; Mouzaki, A.; Dinos, G. P.; Papaioannou, D.; Kalpaxis, D. L. Conjugation with Polyamines Enhances the Antibacterial and Anticancer Activity of Chloramphenicol. *Nucleic Acids Res.* **2014**, *42*, 8621–8634.

(44) Lamb, R.; Harrison, H.; Hulit, J.; Smith, D. L.; Lisanti, M. P.; Sotgia, F. Mitochondria as New Therapeutic Targets for Eradicating Cancer Stem Cells: Quantitative Proteomics and Functional Validation via MCT1/2 Inhibition. *Oncotarget* **2014**, *5*, 11029–11037.

(45) Killock, D. Drug Therapy: Can the Mitochondrial Adverse Effects of Antibiotics be Exploited to Target Cancer Metabolism?. *Nature Rev. Clin. Onc.* **2015**, *12*, 190–190.

(46) Brown, D. Antibiotic Resistance Breakers: Can Repurposed Drugs Fill the Antibiotic Discovery Void?. *Nat. Rev. Drug Discov.* **2015**, *14*, 821–832.

(47) Esner, M.; Graifer, D.; Lleonart, M. F.; Lyakhovich, A. Targeting Cancer Cells Through Antibiotics-Induced Mitochondrial Dysfunction Requires Autophagy Inhibition. *Cancer Lett.* **2017**, *384*, 60–69.

(48) Nguyen, L. V.; Vanner, R.; Dirks, P.; Eaves, C. J. Cancer Stem Cells: An Evolving Concept. *Nat. Rev. Cancer* **2012**, *12*, 133–143.

(49) Sánchez-Clemente, R.; Igeño, M. I.; Población, A. G.; Guijo, M. I.; Merchán, F.; Blasco, R. Study of pH Changes in Media During Bacterial Growth of Several Environmental Strains. *Proceedings* **2018**, *2*, 1297.

(50) Microbes in Land Use Change Management. Edited by Singh, J. S.; Tiwari, S.; Singh, C.; Singh, A. K. Elsevier Publications, 2021.

(51) Jones, E. M.; Cochrane, C. A.; Percival, S. L. The Effect of pH on the Extracellular Matrix and Biofilms. *Adv. Wound Care* **2015**, *4*, 431–439.

(52) Abedi, E.; Hashemi, S. M. B. Lactic Acid Production - Producing Microorganisms and Substrates Sources-State of Art. *Heliyon* **2020**, *12*, e04974.

(53) Castiñeiras, T. S.; Williams, S. G.; Hitchcock, A. G.; Smith, D. C. *E. Coli* Strain Engineering for the Production of Advanced Biopharmaceutical Products. *FEMS Microbiol. Lett.* **2018**, *365*, fny162.

(54) Valero, A.; Pérez-Rodríguez, F.; Carrasco, E.; Fuentes-Alventosa, J. M.; García-Gimeno, R. M.; Zurera, G. Modelling the Growth Boundaries of Staphylococcus Aureus: Effect of Temperature, pH and Water Activity. *Int. J. Food Micobiol.* **2009**, *133*, 186–194.

(55) Lee, S. H.; Griffiths, J. R. How and Why Are Cancers Acidic? Carbonic Anhydrase IX and the Homeostatic Control of Tumour Extracellular pH. *Cancers* **2020**, *18*, 1616.

(56) Weaver, J. V. M.; Bannister, I.; Robinson, K. L.; Bories-Azeau, X.; Armes, S. P.; Smallridge, M.; McKenna, P. Stimulus-Responsive Water-Soluble Polymers Based on 2-Hydroxyethyl Methacrylate. *Macromolecules* **2004**, *37*, 2395–2403.

(57) Lim, H. L.; Hwang, Y.; Kar, M.; Varghese, S. Smart Hydrogels as Functional Biomimetic Systems. *Biomater. Sci.* **2014**, *2*, 603–618.

(58) Babeli, I.; Ruano, G.; Casanovas, J.; Ginebra, M. P.; García-Torres, J.; Alemán, C. Conductive, Self-Healable and Reusable Poly (3, 4-ethylenedioxythiophene)-Based Hydrogels for Highly Sensitive Pressure Arrays. *J. Mater. Chem. C* **2020**, *8*, 8654–8667

(59) Thakur, S.; Arotiba, O. A. Synthesis, Swelling and Adsorption Studies of a pH-Responsive Sodium Alginate–Poly(acrylic acid) Superabsorbent Hydrogel. *Polym. Bull.* **2018**, *75*, 4587–4606.

(60) Puiggalí-Jou, A.; del Valle, L. J.; Alemán. C. Encapsulation and Storage of Therapeutic Fibrin-Homing Peptides Using Conducting Polymer Nanoparticles for Programmed Release by Electrical Stimulation. *ACS Biomat. Sci. Eng.* **2020**, *6*, 2135–2145.

(61) Hua, S.; Ma, H.; Xun, L.; Yang, H.; Wang, A. pH-Sensitive Sodium Alginate/Poly(vinyl alcohol) Hydrogel Beads Prepared by Combined Ca^{2+} Crosslinking and Freeze-Thawing Cycles for Controlled Release of Diclofenac Sodium. *Int. J. Biol. Macromol.* **2020**, *46*, 517–523.

(62) Mandal, B.; Ray, S. K. Synthesis of Interpenetrating Network Hydrogel from Poly(acrylic acid-co-hydroxyethyl methacrylate) and Sodium Alginate: Modeling and Kinetics study for Removal of Synthetic Dyes from Water. *Carbohydr. Polym.* **2013**, *98*, 257–269.

(63) Zanuy, D.; Alemán, C. Simulation of the Self-Assembly of Poly (α-glutamate) and Dodecyltrimethylammonium: Diffusive Role of the Surfactant Cations. *J. Polym. Sci.: Polym. Phys.* **2008**, *46*, 917–924.

(64) Zhao, J.; Li, S.; Zhao, Y.; Peng, Z. Effects of Cellulose Nanocrystal Polymorphs and Initial State of Hydrogels on Swelling and Drug Release Behavior of Alginate-Based Hydrogels. *Polym. Bull.* **2020**, *77*, 4401-4416.

(65) Xie, L.; Wei, H.; Kou, L.; Ren, L.; Zhou, J. Antibiotic Drug Release Behavior of Poly(vinyl alcohol)/Sodium Slginate Hydrogels. *Materialwiss. Werkstofftech.* **2020**, *51*, 850.

(66) Hoffman A. S. Stimuli-Responsive Plymers: Biomedical Applications and Challenges for Clinical Translation. *Adv. Drug Deliv. Rev.* **2013**, 65, 10–16.

(67) Jo, Y.-J.; Gulfam, M.; Jo, S.-H.; Gal, Y.-S.; Oh, C.-W.; Park, S.-H.; Lim, K. T. Multi-Stimuli Responsive Hydrogels Derived from Hyaluronic Acid for Cancer Therapy Application. *Carbohydr. Polym.* **2022**, *286*, 119303.

Chapter VI – Wireless electrostimulation for cancer treatment: an integrated nanoparticle/coaxial fiber mesh platform

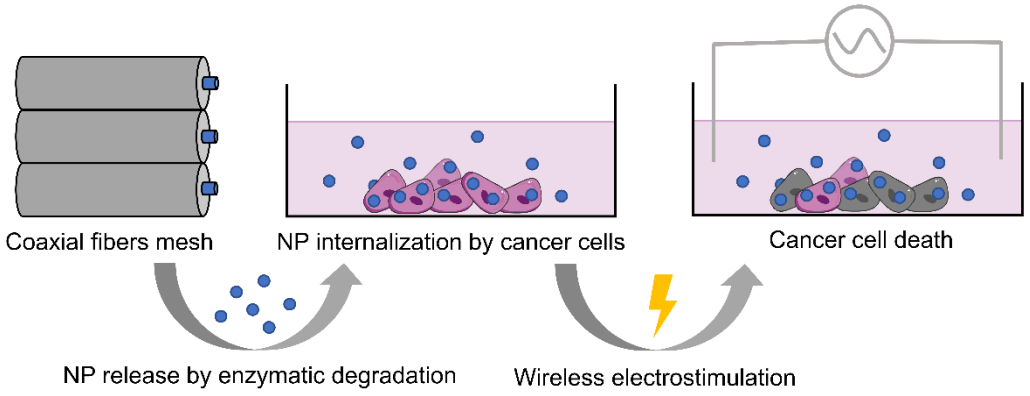

VI - 1. Introduction

Cancer is the leading cause of death in many developed countries. The Global Cancer Observatory (GLOBOCAN database) predicts a steady growth in total diagnostics and deaths related to cancer from the 2018 estimations of 18.1 million new cancer cases and 9.6 million cancer deaths worldwide.[1] In Europe, it was estimated in 2020 that 4 million new cases were diagnosed, and 1.9 million deaths were caused by cancer.[2] In 2019, breast cancer accounted for 30% of cancers diagnosed in women of all ages in the United States of America (USA), while prostate cancer was the most diagnosed in men (20% of new cases).[3] These two types of cancer represented more than 10% of all cancer deaths in the USA.[1]

Although effective, conventional chemotherapy strategies are typically based on systemic treatment, relying on anticancer drug dispersion through the whole body. However, these drugs need high concentrations to be effective, leading to severe secondary effects and toxicity when administered systemically. The use of micro/nanosystems capable of controlled drug delivery, coupled with local administration, avoids the amount of off-target effects, as lower amounts of drug would be required to treat cancer. Some examples include nanofibers,[4] microparticles (MPs),[5] and NPs.[6] Some advantages of these include large surface area/volume ratios, allowing an increase in available reactive surface, potential functionalization for specific tissue-targeting, and the possibility of drug delivery induced by external stimuli.[5–10]

CPs are promising materials for designing smart drug delivery systems. Through the application of electrical current, changes in the redox state of CPS (e.g. PANI,[11] PPy,[12] or poly(3,4-ethylenedioxythiophene):poly(styrene sulfonate) (PEDOT:PSS)) can induce conformational changes that can be harnessed for on-demand immobilization/release of drugs. PEDOT has been extensively studied for biomedical applications due to its physico-chemical stability, high biocompatibility, and high conductivity under physiological conditions.[13,14] The electrochemical properties of PEDOT also render this polymer a good candidate for controlled drug release when assembled as nanotubes (NTs),[15,16] NPs,[17] or hydrogels.[18] Furthermore, polymeric NPs have gained particular interest as nanotechnology-based delivery systems to treat triple-negative breast cancer.[19] Through entrapment of drugs in the polymer chains during synthesis and charge stabilization, drug loading in NPs could be achieved when using PEDOT NPs.

CUR is a bioactive compound extracted from the *Curcuma longa* plant, that has been recently explored as a promising drug due to its disputed antioxidant, anti-inflammatory, anti-diabetic, and antimicrobial properties. Some studies also demonstrate its promising anticarcinogenic properties.[20,21] Therefore, this molecule is a promising drug for cancer treatment. CUR, encapsulated

in NPs, has also been used as a co-adjuvant to improve the effectiveness of radiotherapy and also provide radioprotection of healthy cells.[22]

Wireless electrostimulation has been suggested as a novel strategy for triggering drug release. This approach is based on the principle that electronic transfer takes place without the need for an Ohmic contact. This occurs because of bipolar electrochemistry, when electroconductive materials are placed between two electrodes without direct contact and a sufficiently high potential (critical potential) is applied. When this critical potential is reached, the electric field generated across the solution is enough to obtain an electrical potential difference between the solution and the conducting object able to drive electrochemical reactions to occur at the surface (poles) of such conducting material, termed bipolar electrode (BPE). Considering the length of the BPE (l_{elec}), the distance between the driving electrode ($l_{channel}$), and the driving potential (E_{tot}), the electrical potential at the BPE (ΔE_{elec}) surface is estimated by equation VI - 1:[23,24]

$$\Delta E_{elec} = E_{tot}\left(\frac{l_{elec}}{l_{channel}}\right) \qquad \text{(VI - 1)}$$

Although BPEs are generally on the milli-scale, recent work has shown that BPEs also work on the micro- and nano-scales.[25,26] One limitation to the application of this technique is the requirement of high voltages to reach micro- or nano-scales, as tens of V of applied potential translate into an order of magnitude lower potentials at the surface of the BPE.[26] Studies using *in vitro* wireless neuronal cell stimulation have shown to be safe when applied at potential values of 5.5 V, which have been reported to enhance cell proliferation and differentiation,[27] and at values of 3 V for manipulation of electron transfer on the cell membrane of neurons.[28] Additionally, Hicks *et al.* have demonstrated that carbon NTs, when in clusters can be considered BPE (applied potential of 3 V), but not when presented as single NTs (applied potential of 1.2 kV).[28]

PEDOT NPs are strong candidates for immobilization and controlled release of CUR on cancer cells. However, their storage inside the body targeting a specific organ can be further improved with the use of an appropriate carrier system. Multifunctional bioactive core-shell materials able to promote the controlled release of bioactive agents for biomedical applications (e.g., wound healing) have recently been described in the literature in the form of nanofibrous membranes.[29] Coaxial electrospun fibers are an example of such systems. Several studies show that coaxial fibers can act as reservoirs for the continuous release of active drugs into the bloodstream.[30,31] Ideally, such fibers can also serve as reservoirs for PEDOT NPs and allow their controlled release.

Some examples of suitable coaxial fibers include those developed by Hou *et al*.,[32] Silva *et al*.,[33] and Garrudo *et al*..[34] These fibers are composed of biodegradable polymers such as poly(caprolactone) (PCL) and poly(glycerol sebacate) (PGS). PCL is a Food and Drugs Administration (FDA) approved synthetic aliphatic polyester, easily processable, with good mechanical properties, and extensively

used in tissue engineering applications.[35,36] PGS is also an aliphatic polyester with applications in tissue engineering, wound healing, and drug delivery systems.[37] It can be synthesized from polycondensation of glycerol and sebacic acid, both of which are regarded as safe by the FDA.[38] As proposed in this Chapter, the use of biodegradable and biocompatible polymers to create fiber meshes that can act as reservoirs for NPs is a promising hypothesis. Such a system considers the reported elevated lipase expression in breast[39,40] and prostate[41] cancer and takes advantage of such lipase-rich milieu to catalyze the degradation of polyester meshes and promoting drug-loaded NPs local release.

In this Chapter, we present, for the first time, the development of a wireless electrostimulation system for the treatment of breast and prostate cancer composed of two components: PEDOT NPs loaded with CUR, which are in turn encapsulated in biodegradable coaxial PCL/PGS fibers. The electro-responsive PEDOT NPs allow the controlled delivery of CUR using specific applied potentials on PEDOT NPs, with a negligible release by diffusion. The coaxial fibers, composed of PCL and PGS, were employed to control the systemic release of PEDOT NPs, depending on endogenous enzymatic activity, to be explored as a reservoir for the electro-responsive PEDOT NPs. Thus, having the potential to act as a transdermal implant for postoperative cancer treatment.

The NP/coaxial fiber system proposed has dual-responsiveness stimuli, which have never been described in the literature before. On one hand, the system is responsive to endogenous enzymatic activity at tumor sites, being appropriate for implantation, or as a transdermal device, for long-term release of nanocarriers for therapeutic action in prolonging remission time. On the other hand, the NPs released from the coaxial fibers are responsive to external electric stimulus, allowing for the on-demand delivery of anti-cancer drugs.

VI - 2. Materials and methods

VI - 2.1. Materials

EDOT (97%), CUR, SDBS, APS, Tween® 20, PBS powder pH 7.4, PCL MW 80000, glycerol (>99.5%), sebacic acid (99%), 2,2,2-trifluoroethanol (TFE), 1,1,1,3,3,3-hexafluoropropanol (HFP), ethanol p.a. (99.8%), Pur-A-Lyzer™ Maxi Dialysis Kit MWCO 3.5 kDa, platinum wire (0.25 mm diameter), Lipase (EC 3.1.1.3) from *Aspergillus oryzae* (∼50 U/mg), (-)-riboflavin, Cell Proliferation Kit I (MTT), and Hoechst 33258 were purchased from Sigma-Aldrich (St. Louis, MO, USA). Sodium pyruvate, insulin (human recombinant), Minimum Essential Medium (MEM), fetal bovine serum (FBS), Ham's F-12K (Kaighn's) Medium, Dulbecco's Modified Eagle's Medium (DMEM), trypsin- 2,2',2'',2'''-(ethane-1,2-diyldinitrilo)tetraacetic acid (EDTA) 0.25% phenol red, antibiotic-antimycotic solution and penicillin-streptomycin 10000 U/mL (P/S) were purchased from ThermoFisher Scientific (Waltham, MA, USA).

PC-3 cell line and MCF7 cell line were purchased from the American Type Culture Collection (ATCC, Manassas, VA, USA). A frozen stock of L-929 cell line was used.

VI - 2.2. Synthesis of NPs

The synthesis of PEDOT and CUR/PEDOT NPs was adapted from protocols described elsewhere.[42–44] Firstly, a 9.3 mM SDBS aqueous solution was prepared and kept at 40 °C and 750 rpm for 1h. Then, EDOT was added to the micellar solution to a final concentration of 32.2 mM. In the case of CUR/PEDOT NPs, a 10 mg/mL CUR solution in ethanol was prepared and it was added at the same time as EDOT at 0.1 mL of CUR solution per mL of total final reaction mixture. The mixture was kept at 40 °C and 750 rpm for 1 h, after which, a 0.8 M APS aqueous solution was added at 0.1 mL of solution per mL of total final reaction mixture. The reaction was then kept at 40 °C and 750 rpm, protected from light, for 18 h. Purification of synthesized NPs was achieved by 3 cycles of 40 min centrifugation at 4 °C and 11000 rpm, alternating with 20 min of ultrasounds. The final pellet was then kept at 40 °C in an oven for 3 days to dry.

VI - 2.3. Synthesis of PGS

PGS was prepared following a published protocol.[34] Briefly, sebacic acid and glycerol were mixed in a 1:1 molar ratio, and then heated at 130 °C under a nitrogen atmosphere for 3 h, to ensure complete mixing of the reactants. The reaction mixture was then kept at 120 °C under vacuum for 25 h. PGS was then left to cool down in a desiccator to reduce moisture absorption and used without further processing.

VI - 2.4. Electrospinning

Appropriate core and shell solutions were prepared before electrospinning. The core solutions were: 80% (w/v) PGS in HFP (24 h of agitation); and PGS with PEDOT or CUR/PEDOT NPs (5.4 mg/mL NP pre-dispersed in HFP using ultrasounds for 20 min before PGS addition). The shell solution prepared was a 13% (w/v) PCL solution in TFE (24 h of agitation). Electrospinning was performed using a coaxial spinneret (MECC, Ogori, Fukuoka, Japan) with an outer needle of 2.5 mm of internal diameter and an inner needle of 23G (0.641 mm of outer diameter and 0.337 mm of inner diameter). Electrospinning was conducted at temperature between 18 °C and 21 °C, and relative humidity of (50 – 60) %, a voltage of 20 kV, a distance to the collector of 15 cm, a core solution flow rate of 30 µL/min, and a shell solution flow rate of 180 µL/min.

VI - 2.5. NPs characterization

VI - 2.5.1. NP morphology

PEDOT and CUR/PEDOT NPs were visualized by transmission electron microscopy (TEM, HITACHI H-8100, LaB6 Filament, and an acceleration tension of 200 kV, Tokyo, Japan). NP diameters were measured from 5 images (15 counts each) using NIH ImageJ software (National Institute of Health, MD, USA). The NPs z-potential and hydrodynamic diameter were assessed by DLS, using Malvern Zetasizer Nano ZS, UK.

VI - 2.5.2. Fourier-transform infrared (FTIR)

FTIR spectroscopy was performed using a Spectrum Two FT-IR Spectrometer (PerkinElmer, Waltham, MA, USA), equipped with a Pike Technologies MIRacle Attenuated Total Reflectance (ATR) accessory. Transmittance spectra were obtained over the region (400-4000) cm^{-1} (resolution of 4 cm^{-1}, 8 scans) at room temperature and an automatic baseline correction treatment was applied using the acquisition software PerkinElmer Spectrum IR.

VI - 2.5.3. Cyclic voltammetry (CV)

CV scans were run using carbon screen printed electrodes (SPEs) (Working electrode: C; Counter: Ag; Reference electrode: Ag/AgCl; Metrohm DropSens), connected to a potentiostat (400B Electrochemical Analyzer, CH Instruments). 20 µL of a 10 mg/mL NP solution was drop-cast onto the working electrode area of the carbon SPE and left to air dry overnight. The SPEs were dipped in 2.5 mL of degassed PBS 0.01 M, pH 7.4, with 0.5% (v/v) Tween® 20 as the electrolytic medium. For CUR solution scans, a 0.1 mg/mL CUR solution was prepared in PBS 0.01 M, pH 7.4, with 0.5% (v/v) Tween® 20, where clean SPEs were dipped. Cycles were run in a potential window of -1.5 V to +1.0 V, with scan rates ranging from 0.01 V/s to 0.4 V/s.

VI - 2.5.4. Loading capacity (LC)

A drop of 50 µL of CUR/PEDOT NPs (10 mg/mL) in aqueous suspension was dispersed in 1950 µL of a 70% ethanol solution in PBS (0.01 M, pH 7.4) and incubated for 4 weeks at 4 °C. Afterwards, the NP dispersion was centrifuged at 11000 rpm and 4 °C for 40 min. The concentration of CUR in the medium (n = 3) was determined using the absorbance at 425 nm and the corresponding absorbance vs CUR concentration calibration plot in 70% ethanol solution in PBS (0.01 M, pH 7.4) using a UV-Vis spectrophotometer (Varian Cary 100 Bio). LC was determined using Eq. VI – 2, where m_{loaded} corresponds to the mass of CUR initially incorporated to the solution used for the synthesis of

PEDOT/CUR (0.025 g) minus the mass of CAM remaining free in the solution after the synthesis of PEDOT/CUR.

$$LC\ (\%) = \frac{m_{loaded}}{m_{NPs}} \times 100 \qquad \text{(VI - 2)}$$

VI - 2.6. Fiber characterization

VI - 2.6.1. Fiber morphology

The morphology of coaxial fibers with PGS core and PCL shell (PGS/PCL) was evaluated by SEM, using Hitachi S-2400 SEM (Tokyo, Japan) at 20 kV, after coating with a thin layer of gold/palladium. The morphology of PGS/PCL fibers loaded with PEDOT NPs (PEDOT+PGS/PCL) and loaded with CUR/PEDOT NPs (CUR/PEDOT+PGS/PCL) was evaluated using FEG-SEM JEOL JSM7001F (Jeol, Tokyo, Japan) at 15 kV, after coating with a thin layer of gold/palladium. Fibers' diameters were measured from 5 images (at least 40 counts each) using the software ImageJ (National Institute of Health, MD, USA). FTIR was also performed to characterize the fibers (section VI - 2.5.2.).

VI - 2.6.2. Contact angle

Contact angle measurements of the fiber mats were performed using glycerol in the sessile drop technique by a Krüss DSA25B goniometer (Krüss GmbH, Hamburg, Germany). Drop Shape Analysis 4 Software was instructed to take measurements of the left and right angles every 5 s for 2 min. At least 10 measurements with a deviation of less than 1% per sample were considered for measuring the contact angle of the droplet with the surface of the sample (n≥5).

VI - 2.6.3. Mechanical characterization

Fiber mats' mechanical properties were assessed by a uniaxial tensile test using a texture analyzer TA.XT ExpressC (Stable Micro Systems, Godalming, UK), equipped with 50 N tensile grips, and a constant crosshead speed of 10 mm/min. Samples were cut into rectangular strips (30 mm × 10 mm, n≥5). Young's modulus was calculated from the (0 - 15)% strain linear region in the stress−strain curve and the ultimate tensile strength and maximum extension were measured from the highest peak of the stress-strain curve.

VI - 2.7. CUR and NPs release assays

VI - 2.7.1. CUR unspecific release from CUR/PEDOT NPs using dialysis

A Pur-A-Lyzer™ Maxi 3500 dialysis kit was used to perform dialysis of CUR/PEDOT NPs to assess unstimulated release of CUR from CUR/PEDOT NPs. The membrane was soaked by incubating in MilliQ water at room temperature. Then, 3 mL of 1 mg/mL CUR/PEDOT NPs solution was added to the dialysis tube and immersed in 115 mL of PBS 0.01 M, pH 7.4, with 0.5% (v/v) Tween 20, at 35 ^{o}C. Dialysis medium samples were collected every 24 h, when whole medium was exchanged for fresh medium. At day 6, the dialysis medium was replaced by a PBS solution with 10% (v/v) ethanol and, at day 9 the medium was replaced by PBS with 70% (v/v) ethanol.

VI - 2.7.2. CUR release from CUR/PEDOT NPs using electrostimulation

20 µL of a 10 mg/mL CUR/PEDOT NPs solution was drop-cast unto the working electrode area of the carbon SPE and left to air dry overnight. The SPEs were dipped in 2.5 mL of degassed PBS 0.01 M, pH 7.4, with 0.5% (v/v) Tween® 20 as the electrolytic medium. Electrostimulation was performed in the same setup as CV. Stimulation cycles were run at a fixed time for 180 s at potentials of +0.5 V, -0.5 V, -0.75 V, -1.0 V, -1.25 V, -1.5 V, and -2.0 V, or for fixed potentials (+0.5 V, -1.25 V, -1.5 V, and -2.0 V) for times up to 540 s. The concentration of CUR released to the medium was determined by UV-visible spectroscopy (λ = 425 nm) using a microplate spectrophotometer (Multiskan™ GO, ThermoFisher Scientific).

VI - 2.7.3. Lipolytic activity

The enzymatic activity assays were based on the conversion of *p*-nitrophenyl butyrate (pNPB) to *p*-nitrophenol (pNP) as the result of enzymatic hydrolysis by the lipase. For this, the enzymatic activity assays were performed in 96-well plates over ice, adding to each well 10 µL of supernatants and 90 µL of a 2.63 mM pNPB solution prepared in 50 mM acetate buffer, pH 5.2, and 4% of Triton X-100. The plate was incubated at 37 ^{o}C for 15 min, after which the reaction was stopped by adding 200 µL of acetone to each well. Finally, the absorbance was measured at 405 nm in a microplate spectrophotometer (Multiskan™ GO, ThermoFisher Scientific), and lipolytic activity was calculated defining one unit (U) of enzyme activity as the amount of enzyme releasing 1 µmol of pNP per minute.

VI - 2.7.4. Fiber degradation assay and NP release

Fiber mats were cut in (10 × 10) mm samples and incubated at 37 ^{o}C with a 0.5 mg/mL solution of human lipase expressed in *Aspergillus oryzae* in 0.01 M PBS, pH 7.4, up to 316 h (average 23 ± 6 U/mL).

The concentration of NPs released to the medium was determined by UV-Vis spectroscopy (λ=380 nm) using a microplate spectrophotometer (Multiskan™ GO, ThermoFisher Scientific).

VI - 2.8. Cell culture assays

VI - 2.8.1. Cell culture maintenance

Human prostate cancer cells (PC-3) were cultured in T-flasks (75 cm^2) in Ham's F-12K medium supplemented with 10% FBS and 1% P/S, at 37 ^oC and 5% CO_2, with medium changed every 2 days. Human breast cancer cells (MCF7) were cultured in T-flasks (75 cm^2) in MEM medium supplemented with 0.01 mg/mL human insulin (recombinant), 10 mM sodium pyruvate, 10% FBS and 1% P/S, at 37 ^oC and 5% CO_2, with medium changed every 2 days. Cells were passaged at (80-90)% confluency by incubation with trypsin-EDTA 0.25% phenol red solution for 5 min at 37 ^oC and sub-cultured at a 1:3 split ratio.

Mouse fibroblasts (L-929) were cultured in T-flasks (75 cm^2) in DMEM supplemented with 10% FBS and 1% antibiotic-antimycotic solution, at 37 ^oC and 5% CO_2, with medium changed every 2 days. Cells were passaged at (80-90)% confluency by incubation with trypsin-EDTA 0.1% solution for 5 min at 37 ^oC and sub-cultured at a 1:3 split ratio.

VI - 2.8.2. Cell viability assays

Cell viability after exposure to CUR, PEDOT NPs, and CUR/PEDOT NPs was performed using the MTT assay kit following the protocol recommended by the manufacturer for 96 well plates. Briefly, 100 µL of cells were seeded at a concentration of $1x10^6$ cells/mL of medium and incubated overnight at 37 ^oC and 5% CO_2. The medium was then replaced by fresh medium supplemented with the appropriate concentration of drug or NPs to be tested, and cells were incubated for 24 h at 37 ^oC and 5% CO_2. After the incubation period, the MTT labeling reagent was added to each well to a final concentration of 0.5 mg/mL and incubated for 4 h at 37 ^oC and 5% CO_2. The solubilization buffer (labeling reagent:solubilization buffer, ratio of 1:10) was then added to each well, and the plate was incubated overnight at 37 ^oC and 5% CO_2. Finally, absorbance was measured at 570 nm using a microplate reader (Infinite200 PRO, Tecan, Männedorf, Switzerland).

VI - 2.8.3. Cell uptake of CUR/PEDOT NPs in suspension and immobilized on coaxial fibers

Cells were seeded (1 x 10^6 cells/mL) in a 24-well plate before the addition of CUR, PEDOT NPs, or CUR/PEDOT NPs solutions to the culture medium to a final concentration of 10 or 50 µg/mL and were incubated for 24 h at 37 ^oC and 5% CO_2. Alternatively, cells were incubated with supernatants,

obtained from fiber previously degraded in the presence of the lipase, in a 1:1 supernatant:fresh medium ratio, for 24 h at 37 ^{o}C and 5% CO_2. Additionally, PC-3 cells were incubated with (1x1) cm fiber mat samples and 0.5 mg/mL (average 23 ± 6 U/mL) lipase for 2 weeks at 37 ^{o}C and 5% CO_2. After CUR/PEDOT NPs uptake, cells were fixed with 70% ethanol solution and stained with Hoechst 33258 at a working concentration of 0.5 µg/mL. A fluorescence microscope (LEICA DMI 3000B, Leica camera system, Wetzlar, Germany; Hoechst: λex/em = 340-380/425 nm; CUR/PEDOT NPs: λex/em = 460-500/512-542 nm) was used to assess cellular morphology and the capacity of cells to internalize NPs prepared in a solution and NPs present in supernatants obtained from fiber degradation assays.

VI - 2.8.4. *In vitro* wireless electrostimulation of CUR/PEDOT NPs

The wireless electrostimulation setup used in this study is sketched in Scheme VI - 1. Two platinum wires (0.25 mm diameter) were placed 1 cm apart and attached to each well of a 24-well plate. The plate and wires were sterilized by UV light exposure for 15 min inside a laminar flow hood. Cells were then seeded (1x10^{6} cells/mL) in the 24-well plate and incubated at 37 ^{o}C and 5% CO_2 for 4 h. After this, CUR/PEDOT NPs solution was added to the culture medium (supplemented with 1 mM (-)-riboflavin) to a final concentration of 50 µg/mL and incubated for 24 h at 37 ^{o}C and 5% CO_2. Then, the platinum wires, inserted in the culture medium 1 cm apart to work as electrodes, were connected to a power source and electrostimulation was performed for 24 h using a square wave alternating current (AC, -10 V to 0 V, frequency of 100 Hz). Cell viability was then estimated 24 h after the end of the electrostimulation as described in section VI - 2.8.2.

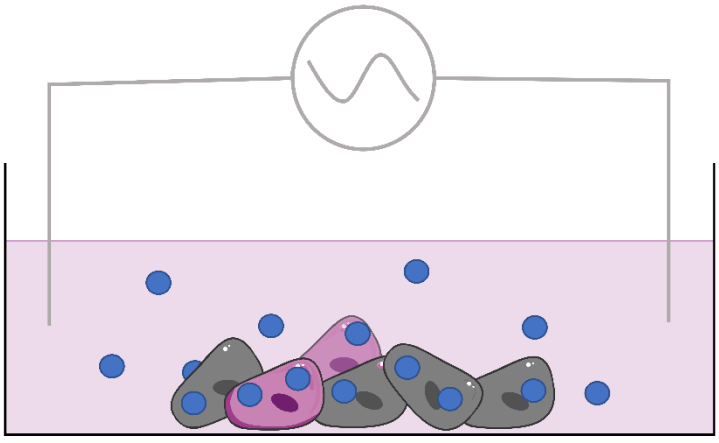

Scheme VI - 1. Schematic representation of the setup used for wireless electrostimulation of CUR/PEDOT NPs with PC-3 cells in culture: Pt wires as driving electrodes (gray lines), CUR/PEDOT NPs as BPEs (blue circles).

VI - 2.9. Statistical analysis

Statistical analysis of the data was performed using Microsoft Excel, with all results being presented as mean values ± standard deviations. Analysis of variance (ANOVA) was performed for the datasets. A *post hoc* Welch's unequal variances *t*-test was used to determine significant differences between independent populations (p-value). (*) means $p < 0.05$ and (**) means $p < 0.01$.

VI - 3. Results and discussion

VI - 3.1. Materials characterization

VI - 3.1.1. PEDOT NPs

PEDOT NPs loaded with CUR (CUR/PEDOT NPs) were obtained to be explored as a component of a controlled drug delivery system, responsive to electrostimulation and further incorporated in a fiber mesh. It was observed that PEDOT NP diameter, estimated by TEM, increases 3.9 times with drug loading (Fig. VI - 1, Table VI - 1). An increase was expected as CUR incorporation in polymer chains would lead to an increase in volume due to stereochemistry (*i.e.* volume occupied by CUR molecules). While the PEDOT NPs synthesized in this work have smaller diameters (25 ± 3 nm) when compared with previously reported (35-100 nm),[42,43,45] the size of the CUR/PEDOT NPs reported here (96 ± 7 nm) and in the literature (96 ± 16) are identical.[43]

For PEDOT NPs, the differences in diameters are possibly due to the differences in synthesis method, such as introducing heating earlier in the synthesis process, scaling up, and longer reaction times (overnight vs 18 h). For SDBS, changes in temperature between 25 ^{o}C and 40 ^{o}C can lead to changes in critical micelle concentration (CMC) and critical micelle transition (CMT),[46] influencing the structure of the micelles, ranging from spherical to rod-like or more complex micellar aggregates. As polymerization occurs inside the micelles, it is important to keep the temperature constant at 40 ^{o}C, allowing the surfactant to have a constant action until the end of the synthesis by maintaining the number of micelles constant, as well as their homogeneity in size and shape. Therefore, the conditions used possibly led to the formation of smaller and/or rounder micelles, and consequentially smaller NPs and more homogeneous NP populations were obtained.

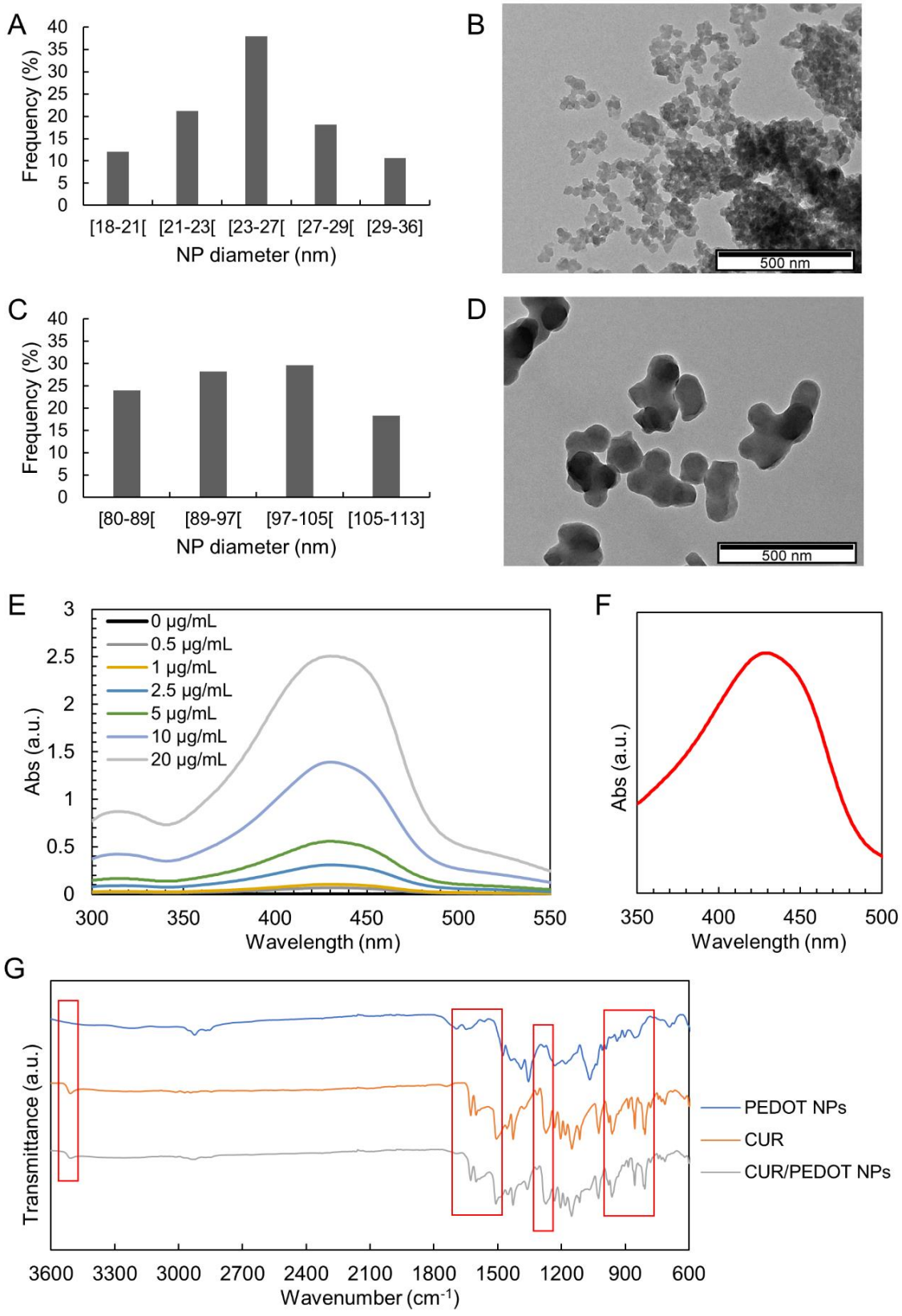

Fig. VI - 1. Size distribution and TEM micrograph of PEDOT NPs (A and B) and CUR/PEDOT NPs (C and D). (E) UV−visible spectra of CUR solutions. (F) UV−Vis spectra of CUR in LC release medium. (G) FTIR spectra of PEDOT NPs, CUR, and CUR/PEDOT NPs.

The LC and, therefore, the successful loading of CUR in PEDOT NPs was assessed by UV-Vis spectroscopy. For this purpose, CUR was extracted from suspensions of CUR/PEDOT NPs by incubating them in 70% ethanol solutions for 4 weeks. Then, UV-Vis spectra were recorded for the medium after centrifugation. The absorbance vs CUR concentration plot, prepared from the characteristic absorption peak of CUR at 425 nm shown in Fig. VI - 1E, was used as a calibration curve to quantify the LC of PEDOT NPs.

The LC calculated for CUR/PEDOT NPs from the CUR absorption peak (Fig. VI - 1F) was 15.3 ± 0.1 %. This is similar to what was reported in our group for PEDOT NPs loaded with the antibiotic CAM,[44] and it is 2.6 times higher than previously reported for CUR-loaded PEDOT NPs (5.9 ± 1.6 %),[47] thus showing the consistency of the results.

Table VI - 1. Average NP diameters (⌀, nm) derived from TEM and DLS, and z-potential values (ζ, mV) for PEDOT and CUR/PEDOT NPs (n≥4).

NPs	$⌀_{TEM}$ (nm)	$⌀_{DLS}$ (nm)	ζ (mV)
PEDOT	25 ± 3	106 ± 17	-55 ± 3
CUR/PEDOT	96 ± 7	245 ± 31	-36 ± 2

Diameters from DLS analysis (Table VI - 1) are 4.3 and 2.5 times larger than those derived from TEM for PEDOT and CUR/PEDOT NPs, respectively. This was expected as polymeric NPs in solution present a higher hydrodynamic diameter that accounts for the relaxation of polymer chains when in solution.[48] The diameter values obtained for both types of NPs by either technique are a good indicator in concerns to accumulation in the tumor and cellular uptake, as the optimum size range is between 20 and 200 nm to prevent clearance by the kidneys and escape macrophages, thus allowing a longer circulation time in the body.[49] A z-potential value of -55 ± 3 mV and -36 ± 2 mV indicates good colloidal stability of PEDOT NPs and CUR/PEDOT NPs, respectively,[48] thus demonstrating the successful role of SDBS in stabilizing the PEDOT NPs in the aqueous solution. However, the presence of CUR reduces the effective surface charge, which is possibly due to the high hydrophobicity of CUR that affects the charge stabilization.

FTIR spectra of CUR, PEDOT NPs, and CUR/PEDOT NPs are shown in Fig. VI - 1G. Characteristic PEDOT peaks were observed for both NP types: C–S bond stretching in the thiophene ring at 691 cm^{-1}, C–C of the thiophene ring at 1360 cm^{-1}, C–O–C vibrations at 1066 cm^{-1}, C=C stretching band at 1475 cm^{-1} and $–CH_2$ stretching vibration at 2921 cm^{-1}.[45,50,51] Importantly, CUR peaks were easily detected in the CUR/PEDOT NPs spectrum: phenolic –OH stretching vibrations at 3508 cm^{-1}, phenolic C–O bending

vibration at 1272 cm^{-1}, C=C stretching vibration at 1508 cm^{-1}, C=O stretching bands at 1624 cm^{-1} and 1599 cm^{-1}, and $–CH_2$ vibrations at 960, 808 and 855 cm^{-1}.[43,52] Thus, these results further confirm the successful loading of CUR into PEDOT NPs by entrapment of the drug in the core of the particles or throughout the polymer chains.

Peak-to-peak separation shifts in the CVs recorded for CUR, PEDOT NPs, and CUR/PEDOT NPs are evident with the increase of the scan rate (Fig. VI - 2), which indicates an electrochemical quasi-reversible process ruled by diffusion of CUR within the PEDOT network.[53] Panels B, D, and F of Fig. VI - 2 show a linear behavior of current density vs square root of the scan rate for CUR/PEDOT NPs, PEDOT NPs, and CUR, respectively. Thus, corroborating the suggestion that a quasi-reversible electron transfer process is taking place. In the voltammograms recorded for CUR/PEDOT NPs, it is noticeable that the increase in the diffusion coefficient of electroactive species leads to an increase in peak current, which is in agreement with the Randles-Sevcik's equation (Eq. VI - 3), where i_p is the current peak in A, n is the number of electrons transferred, A is the electrode area in cm^2, F is the Faraday constant in C/mol, D is the diffusion coefficient in cm^2/s, C is the concentration in mol/cm^3, v is the scan rate in V/s, R is the molar gas constant in J/K/mol and T is the temperature in K.

$$i_p = 0.4463\, nFAC \left(\frac{nFvD}{RT}\right)^{1/2} \qquad \text{(VI - 3)}$$

Cyclic voltammograms presented in Fig. VI - 2 show that the oxidation and reduction peaks of PEDOT NPs (Fig. VI - 2C) and CUR (Fig. VI - 2E) appear at similar potentials (0.1 V and -0.3 V), with the peaks at -0.3 V being more noticeable in CUR/PEDOT NPs (Fig. VI - 2A), suggesting that CUR is present in the NPs.

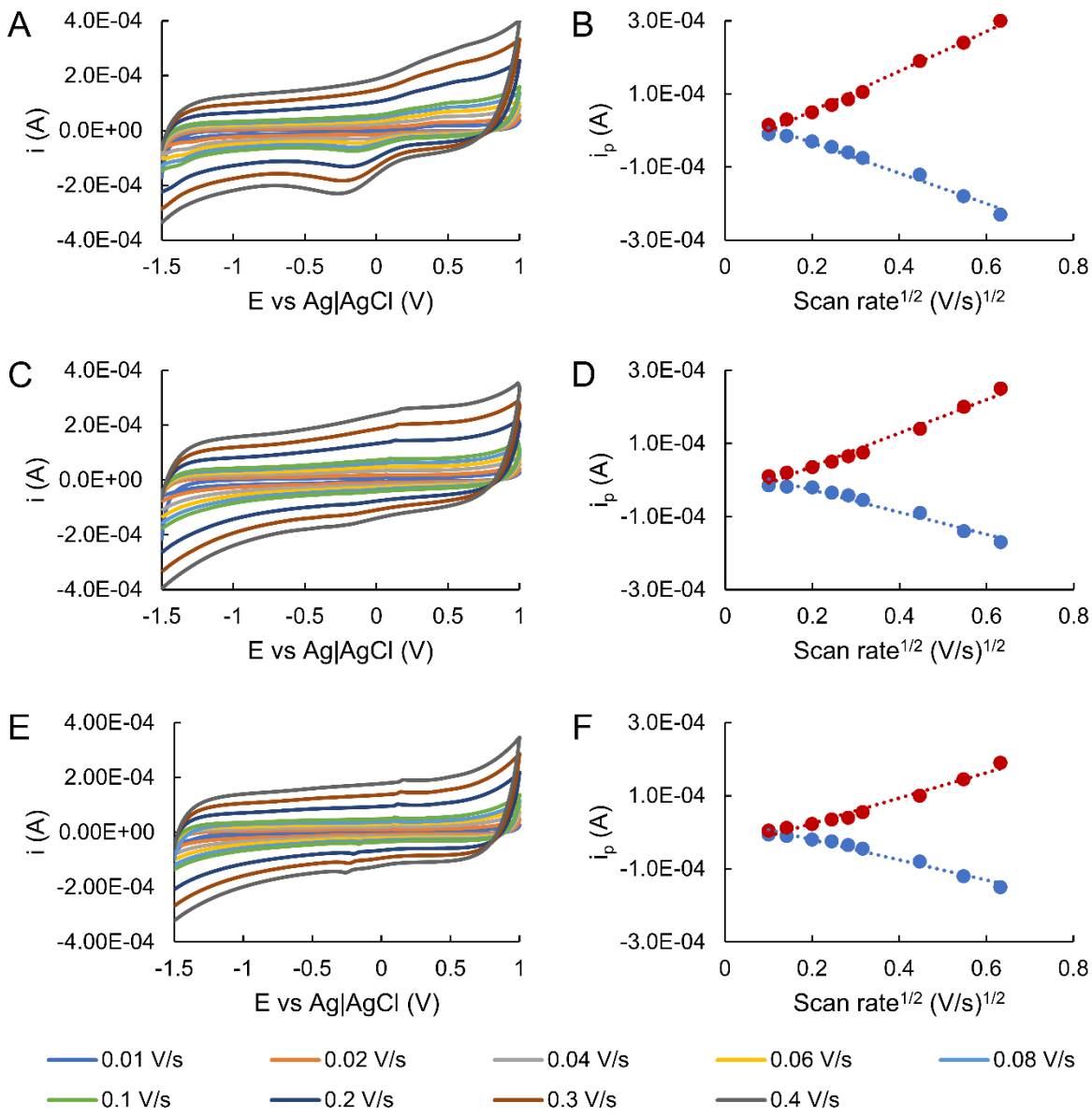

Fig. VI - 2. Cyclic voltammograms of CUR/PEDOT NPs (A), PEDOT NPs (C), and CUR (E) recorded at scan rates varying from 0.01 V/s to 0.4 V/s in 0.01 M PBS, pH 7.4. Variation of the current density (j_p) at the anodic (red) and cathodic (blue) peaks of CUR/PEDOT NPs (B), PEDOT NPs (D), and CUR (F) against the square root of the scan rate.

VI - 3.1.2. Coaxial fibers

PGS/PCL coaxial fibers were electrospun to act as a biocompatible and biodegradable reservoir for NPs. So, CUR/PEDOT NPs were loaded into the core of the fibers and slow release to the medium over time through enzymatic degradation was assessed. Fig. VI - 3 (A and B) shows that PGS/PCL coaxial fibers present a diameter distribution centered around 400 nm, but also a fiber population with a more heterogeneous diameter distribution. In fact, an average diameter of 379 ± 127 nm was found for the population with smaller diameters (< 1 µm), and an average diameter of 2.0 ± 0.8 µm was

found for the population with larger diameters (≥ 1 µm). These values are within the range reported in the literature for these types of fibers, varying from 738 nm to 5.5 µm.[32,33] The presence of two fiber populations with different sizes can be explained by the splitting of the fibers during electrospinning, resulting in the branching of the fibers.[54]

The disparity in fiber diameter is further increased when PEDOT NPs are introduced in the core layer of PGS/PCL fibers, with average diameters of 127±132 nm and 3.8 ± 1.5 µm (Fig. VI - 3 C and D), respectively, for average the smaller and larger diameter populations. On the other hand, the presence of CUR in the PEDOT NPs loaded in the core layer of the fibers appears to decrease the heterogeneity in fiber diameter (Fig. VI - 3 E and F), decreasing the frequency of larger fibers (average diameter of 2.9 ± 1.2 µm) and increasing the frequency of the 200 nm range (average diameter of 136 ± 103 nm).

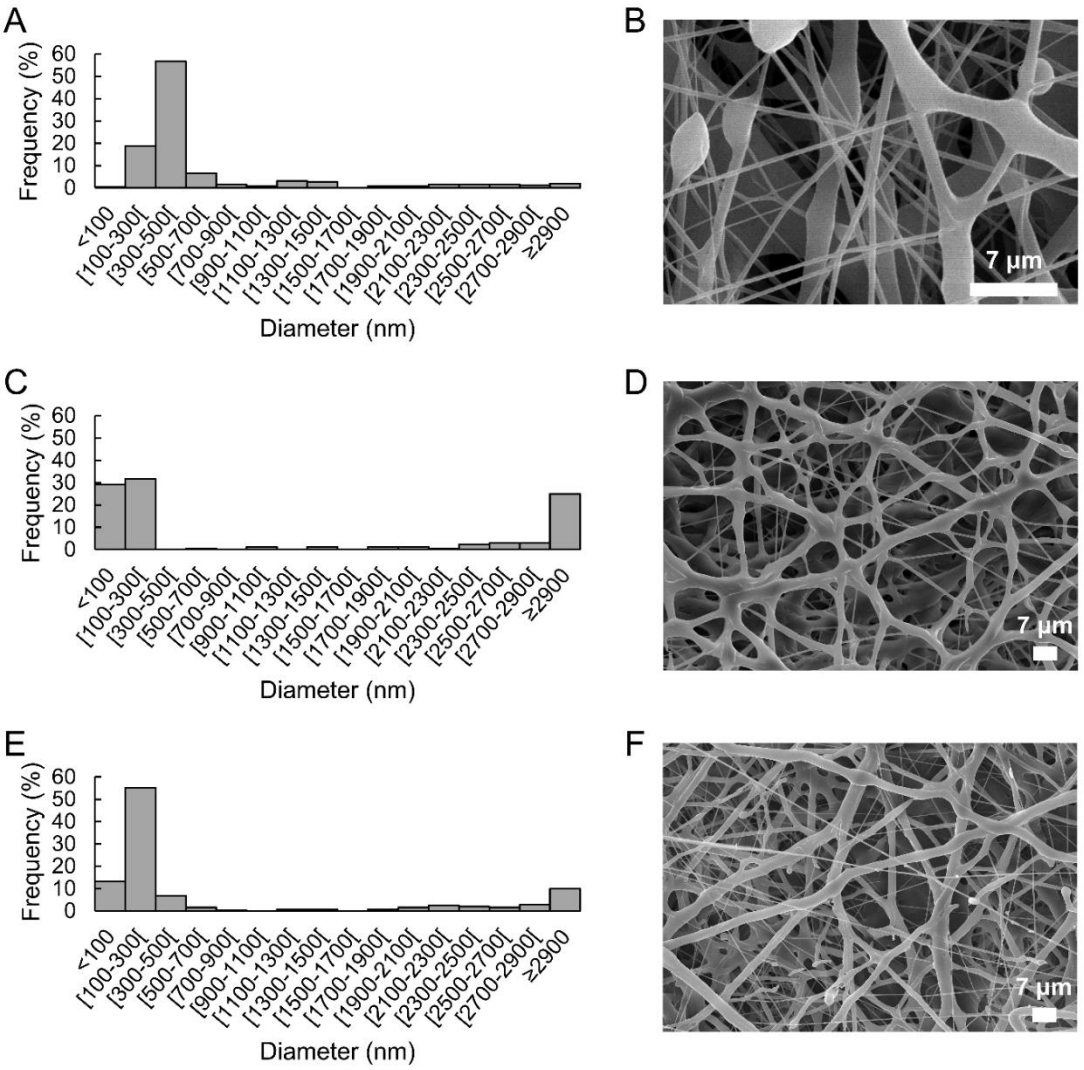

Fig. VI - 3. Diameter distribution and SEM micrograph of PGS/PCL fibers (A and B), PEDOT+PGS/PCL fibers (C and D), and CUR/PEDOT+PGS/PCL fibers (E and F).

The contact angle of the produced fibers was 58º ± 3º for PGS/PCL, 17º ± 3º for PEDOT+PGS/PCL, and 37º ± 3º for CUR/PEDOT+PGS/PCL (Table VI - 2), with a high statistically significant difference between the three fiber types (p-value < 0.01). Contact angle values previously reported for PCL fibers loaded with PEDOT NPs are typically high (120º),[50] and similar to those of plain PCL fibers (110º to 130º).[34,50] A hypothesis is that the influence of PEDOT NPs on fiber diameter distribution might influence the porosity and topology of the fiber mat and promote droplet penetration. On the other hand, the contact angle of CUR/PEDOT NPs loaded fibers present a value between the unloaded PEDOT+PGS/PCL and the pristine PGS/PCL fibers. Again, the fibers morphology and topology of the fiber mat can contribute to this observation. The loading of CUR can increase the affinity of PEDOT NPs towards PGS, as the phenolic hydroxyl groups in the CUR structure could interact with carboxyl groups in PGS,[55] and as such, the interference of CUR/PEDOT NPs with fiber formation is minimized, improving the homogeneity of the fibers in the meshes.

Table VI - 2. Contact angle values and representative pictures of respective measurements of coaxial PGS/PCL fibers, and PGS/PCL fibers loaded with PEDOT or CUR/PEDOT NPs (n≥5).

Sample	Contact angle (º)	Picture
PGS/PCL	58 ± 3	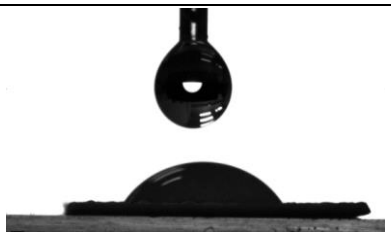
PEDOT+PGS/PCL	17 ± 3	
CUR/PEDOT+PGS/PCL	37 ± 3	

The Young's modulus obtained for PGS/PCL fibers was around 45 MPa (Fig. VI - 4). These fibers had a Young's modulus higher than the ones previously reported in the literature at values of 6 MPa and

16 MPa, respectively for fibers made of 10% and 13% PCL solution.[32,33] Similarly, the value of ultimate tensile strength (5 MPa) is slightly higher than those previously reported (2-3 MPa).[32,33] The elongation of these fibers was 400%, almost half of what was observed by Hou *et al.* for PCL fibers.[32] The differences in fiber production conditions (e.g., higher humidity levels) might have led to a more compact PCL shell layer, which in turn influences the mechanical properties of the fibers. Another hypothesis is that the branching of the fibers during electrospinning might promote a greater entwinement of the fibers, with the thinner fibers providing additional mechanical support.[54]

Encapsulation of both PEDOT NPs and CUR/PEDOT NPs in the fibers changes the mechanical properties of the coaxial fibers (Fig. VI - 4A), leading to a significant decrease in Young's modulus (Fig. VI - 4B), from 45.3 MPa to 38 MPa for PEDOT+PGS/PCL fibers and 39 MPa for CUR/PEDOT+PGS/PCL, suggesting that the presence of NPs increases the capacity of the composite to withstand elastic deformation. These results might be explained by an increase in the conductivity or the viscosity of the electrospinning solutions when the NPs are added, leading to changes in polymer crystallinity, which in turn might lead to changes in the mechanical properties.[56]

We must consider human skin's elastic properties when designing a device suitable for potential subdermal implantation. The reported values for human skin Young's modulus vary from 18 ± 2 MPa to 57 ± 7 MPa, depending on the age and the sex of live subjects.[57] Therefore, we can conclude that Young's moduli of the fibers obtained in this study are within the range of values found for human skin. Additionally, the presence of PEDOT NPs made the fiber mats adaptable to mimic the biomechanical properties of skin at possible implantation sites. Also, these fibers with NPs encapsulated present a shorter plastic regime as corroborated by the significant lowering of the ultimate tensile strength from 5.5 MPa for the plain fibers to around 4.5 MPa in the presence of NPs (Fig. VI - 4C), meaning that the material could break at lower stress-strain values than in the PGS/PCL plain fibers. However, no statistically significant differences were observedin the values of the elongation of the material at the breakpoint (Fig. VI - 4D).

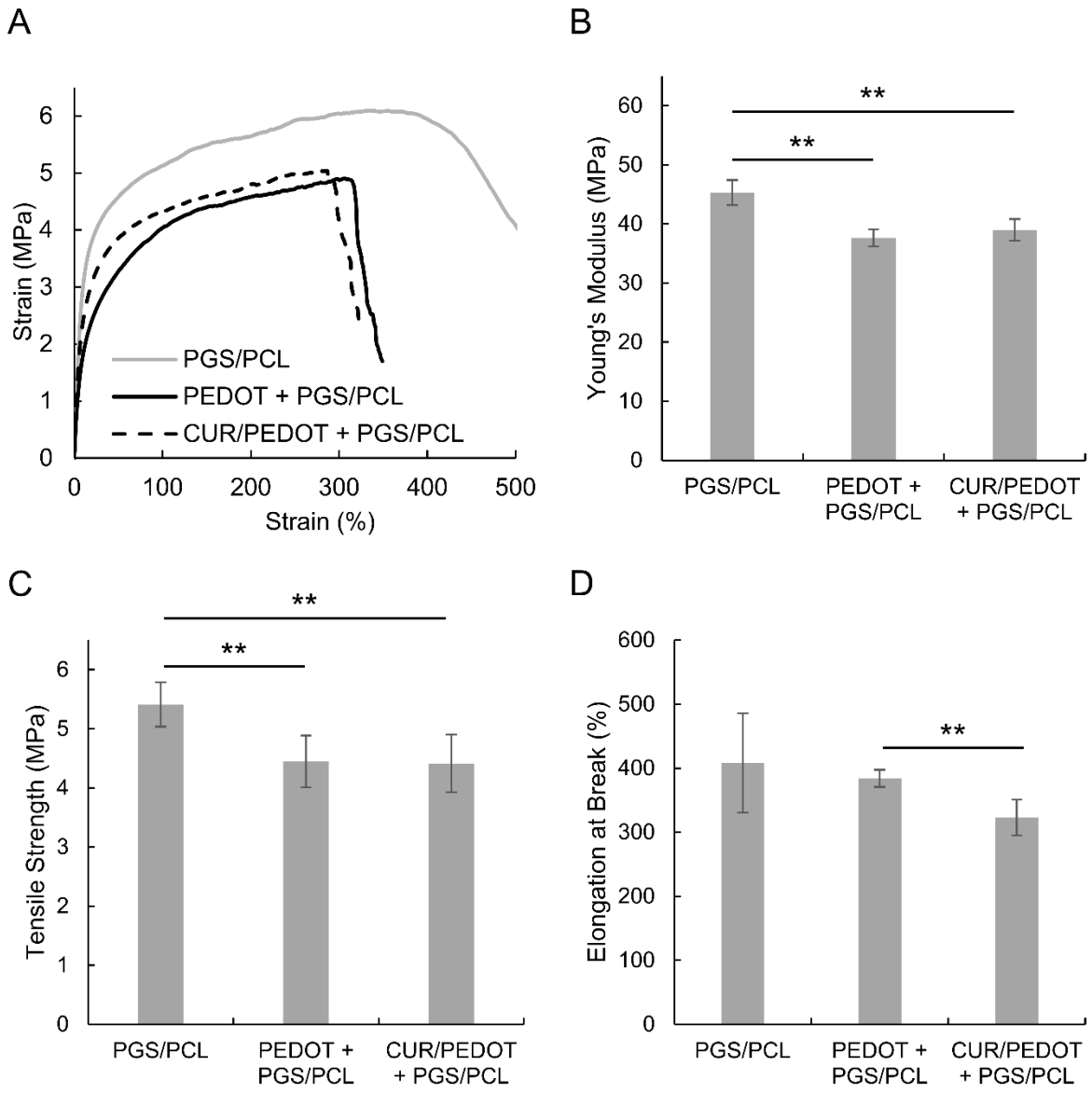

Fig. VI - 4. Representative stress–strain curves obtained via tensile testing of PGS/PCL, PEDOT+PGS/PCL, and CUR/PEDOT+PGS/PCL fibers (A). Change in mechanical properties: (B) Young's modulus, (C) tensile strength, and (D) elongation at break, with the loading of PEDOT NPs or CUR/PEDOT NPs onto PGS/PCL fibers (n≥5). **p-value<0.01.

VI - 3.2. NPs release from PGS/PCL fibers by enzymatic degradation

The biodegradation of the fibers upon the activity of the human lipase expressed in *Aspergillus oryzae* (Fig. VI - 5) was evaluated by mass loss over time (Fig. VI - 6A). The most pronounced mass loss takes place in the first 24 h of incubation with lipase, with around 80% of fiber mass lost for all mesh types at that time point. Biodegradation of PGS and PCL electrospun fibers by the enzymatic activity of lipases has already been shown,[34,35] with a lipase activity of 0.5 U/mL reported to lead to 71.6% mass losses of PGS/PCL and polyaniline (PGS/PCL-PANI) coaxial fibers (diameter of 951 ± 465 nm) over

168 h.[34] This biodegradation is further evidenced by our results for PGS/PCL coaxial fibers, where an average lipase activity of 23 ± 6 U/mL resulted in approximately 80% mass loss for the three types of fibers in only just 24 h. Thus, human endogenous lipase expression at cancer sites could eventually be explored for the biodegradation of an implantable drug delivery system.[39,40]

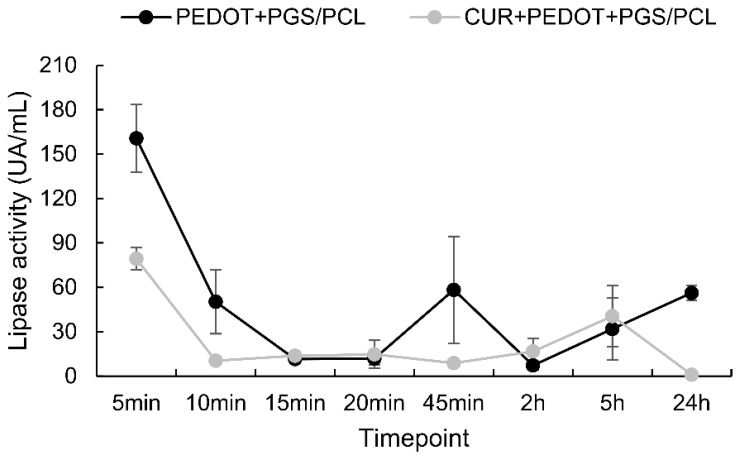

Fig. VI - 5. Lipase activity over fiber degradation time at 37 ^{o}C in 0.01 M PBS, pH 7.4, n=3.

The presence of encapsulated NPs, namely CUR/PEDOT NPs, appears to slow down fiber degradation in the initial mass losses, at 5 h, with values of 55% and 33%, respectively, for unloaded fiber meshes and meshes loaded with CUR/PEDOT NPs. This suggests that the presence of the particles and CUR might impair lipase activity in the medium, which is corroborated by the lipolytic activity results (Fig. VI - 5), where we observed that lipase activity decreased when the NPs were loaded with CUR. One hypothesis to explain this result could be enzyme adsorption to the surface of the electroconductive NPs. This agrees with previous results from our group, where PCL degradation decreased in the presence of a conductive PANI and camphorsulfonic acid (PANI:CSA) layer in PCL-PANI fibers due to direct adsorption of the lipase to the conductive material,[34] as lipase can be adsorbed to PANI fibers to be stabilized.[58] Another hypothesis is an inhibitory effect of CUR in lipolytic activity, as it has been previously reported that this molecule interferes with binding sites in pancreatic lipase.[20,59]

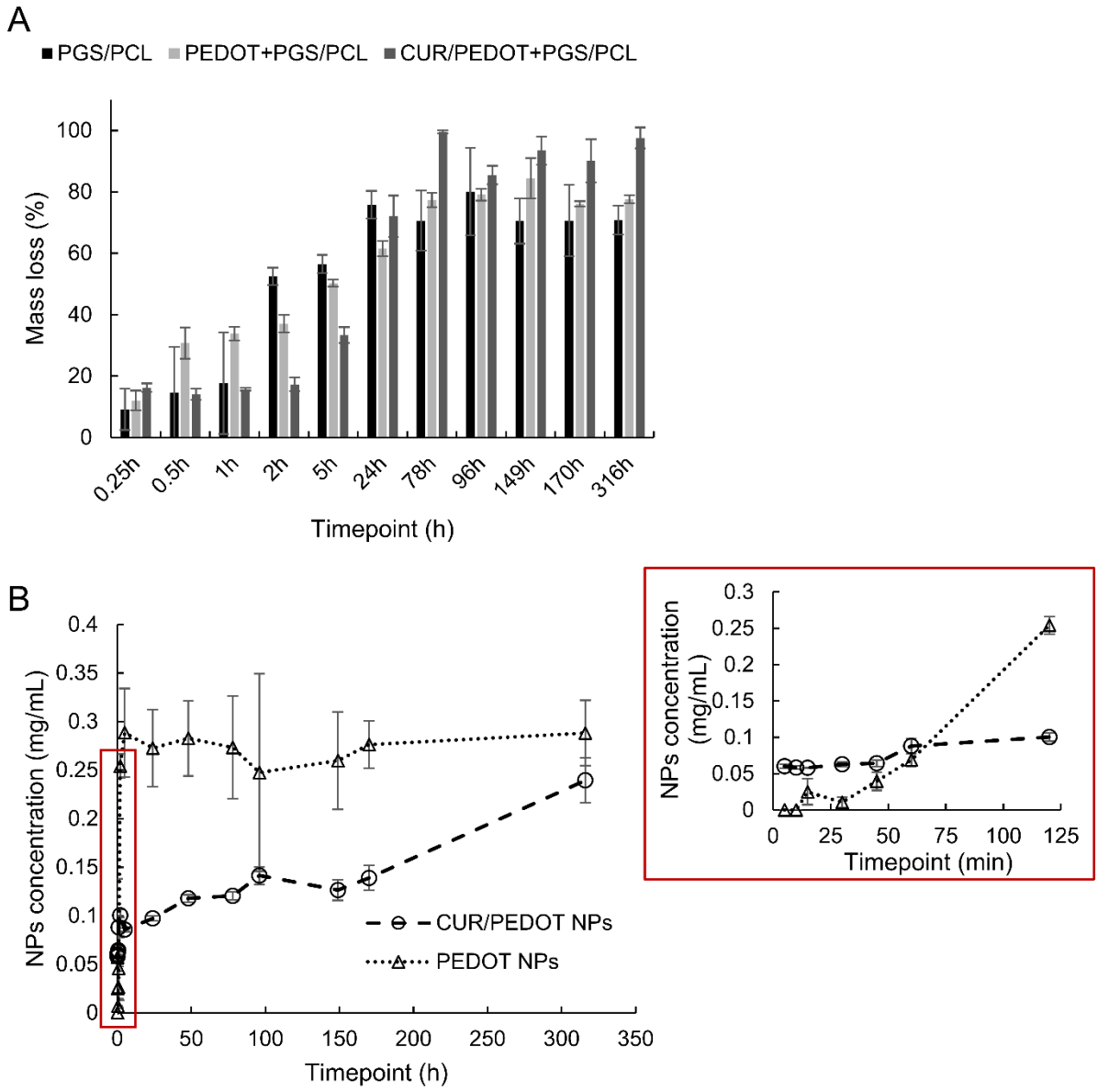

Fig. VI - 6. (A) Mass loss profile of PEDOT+PGS/PCL and CUR/PEDOT+PGS/PCL coaxial fibers, by the enzymatic activity of lipase from Aspergillus oryzae at 37 ^{o}C in 0.01 M PBS, pH 7.4, over time. (B) PEDOT NPs (triangles) and CUR/PEDOT NPs (circles) release profile over time from PGS/PCL coaxial fibers degraded in the presence of lipase at 37 ^{o}C in 0.01 M PBS, pH 7.4. Insert: magnification of release profile for incubation times up to 120 min (n=3).

Regarding NPs release from the coaxial fibers due to lipase activity, the kinetic release profile follows a normal pattern of initial burst release of NPs to the medium for 1 h, followed by a plateau (Fig. VI - 6B). Although similar NP concentrations (approximately 0.25 mg/mL) are achieved in the medium in the final timepoint for both conditions, a higher NPs concentration was achieved after 2 h of incubation for fibers loaded with PEDOT NPs than for CUR/PEDOT NPs. For CUR/PEDOT NPs a first plateau of 0.15 mg/mL NPs in the medium is achieved after 96 h (4 days) which is maintained at least

until timepoint 170 h (around 7 days). Incubation of the fibers for another 6 days (timepoint 316 h) is accompanied by the release of more CUR/PEDOT NPs reaching a total of 0.25 mg/mL. These results evidence the capacity of this material to deliver CUR-loaded NPs steadily and progressively over time in a biologically active environment.

This system evidences the potential for a long-term continuous release of NPs loaded with an anticancer drug at the tumor site in potential *in vivo* applications, when compared to other systems that rely on only one stimulus for the delivery of the drug, like hydrogels and other nanocarriers. The advantage of this NP/coaxial fiber system is the possibility of post-surgery therapy to prolong remission time, as the NPs are slowly released in response to enzymatic activity, and posterior low-voltage electrostimulation can be performed for punctual and controlled release of the anticancer drug.

VI - 3.3. CUR release from CUR/PEDOT NPs

In the initial set of studies, CUR/PEDOT NPs were immobilized on the surface of the working electrode, favoring direct electron transfer from the electrode to the NPs surface, and subjected to varying potentials for a fixed time (180 s) to assess the potential that triggered the release of CUR. The CUR release over time was studied to the potentials that resulted in the most promising release values, to establish kinetic release profiles.

CUR/PEDOT NPs are electroresponsive, as seen by CV, and the redox reactions involved can trigger CUR release, depending on the time and voltage intensity used, being much higher than passive release in PBS (Fig. VI - 7). The amount of CUR released from CUR/PEDOT NPs to the medium under electrotimulation for 180 s depends on the voltages assessed (Fig. VI - 8A). For applied potentials in the range of -1.0 V to +0.5 V, and also for -2.0 V, the release of CUR is similar to the non-stimulated condition (0.0 V), with values below 10% of released drug. The electrical potential that maximizes CUR released (about 65% of loaded drug) was -1.5 V, a value slightly higher than those reported in other studies (-1.25 V).[43] However, the released drug at -1.25 V reported in such studies and in the present study are similar, at values of 39% and 40%, respectively. From these results, we selected 4 voltage values (-2.0 V, -1.5 V, -1.25 V, +0.5 V) to study the drug release profile over time at fixed voltages (Fig. VI - 8B). For +0.5 V and -2.0 V, independently of the electrostimulation time, only around 10% of the drug was released. Release of CUR from PEDOT NPs, in the absence of electrostimulation, was also assessed in a dedicated dialysis experiment, where it took 5 days to reach the same 10% of drug release (Fig. VI - 7) and full release of CUR was only observed at day 10 after addition of 70% ethanol at day 9 to the dialysis medium.

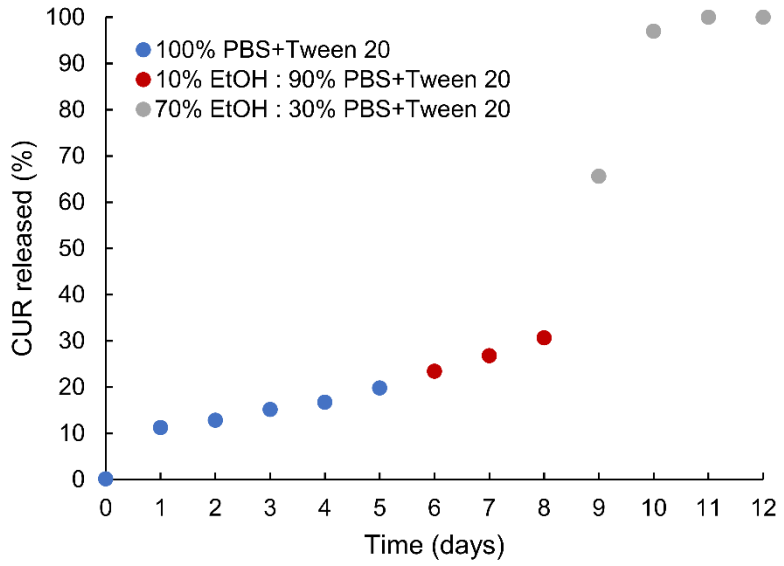

Fig. VI - 7. CUR release profile from PEDOT NPs in aqueous solution by diffusion. Dialysis against 0.01 M PBS + 0.5% Tween 20 (blue), 10% EtOH : 90% 0.01 M PBS + 0.5% Tween 20 (red),and with 70% EtOH : 30% 0.01 M PBS + 0.5% Tween 20 (grey).

When -1.5 V was applied to the CUR/PEDOT NPs, an initial burst of CUR release was observed in the first 60 s, followed by sustained release until the end of the assay, with the best-fit profile being a logarithmic curve (r^2 = 0.992) (Fig. VI - 8B). The final percentages of CUR released at the end of the experiments, after 550 s of electrostimulation, were similar for assays using -1.5 V or -1.25 V, respectively, with values of 79% and 86% CUR released. However, when -1.25 V was applied, the initial burst was significantly smaller and we observed a steady increase in released CUR up to the end of the assay, with a linear correlation appearing to be the best fit (r^2=0.968) (Fig. VI - 8B). The observed differences in the release profile can be explained by a slower electron transfer to PEDOT NPs at -1.25 V, making PEDOT NPs reduction slower and consequently impairing CUR release.

In the work by Puiggali-Jou *et al.*,[43] only around 60% of CUR was released from PEDOT NPs to the medium after applying -1.25 V for 550 s, suggesting that we designed a more efficient system for the release of CUR from PEDOT NPs by electrical stimulation. Some explanations for this include adaptations made to the NP manufacturing, where we introduced heating earlier in the synthesis process, scaled up and prolonged synthesis time, and to the electrical stimulation setup, which was based on carbon screen printed electrodes, instead of a conventional three-electrode system. As discussed in section 3.1.1., keeping a constant reaction temperature, from surfactant solution preparation until the end of the synthesis, helps maintain a constant size and homogeneous shape of micelles, which can lead to the formation of smaller and more homogeneous NPs. A decrease in NP diameter translates into a higher number of NPs available for the same NP suspension concentration,

leading to a higher surface-to-volume ratio. Therefore, the surface area of NPs in contact with the electrode surface will be enhanced and the electron transfer process will be facilitated, triggering CUR release to be more efficient.

Overall, our results show that a controlled release of CUR through electrical stimulation of PEDOT NPs is possible and indicates that voltages applied can be adjusted to match the amount of CUR released, envisaging a possible staged chemotherapy protocol.

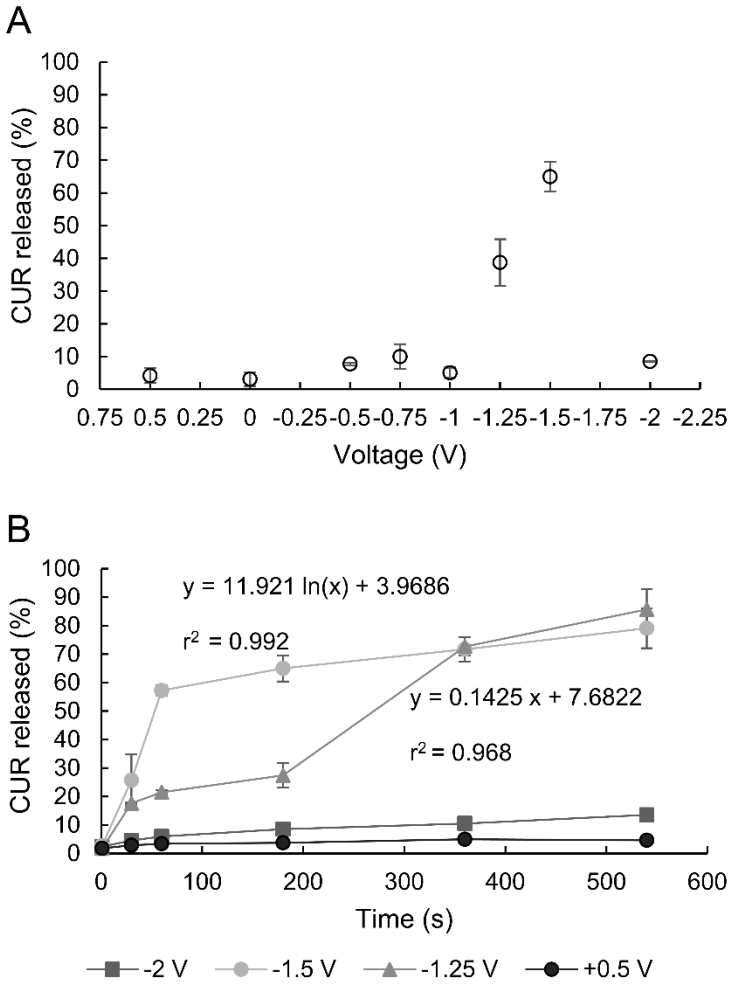

Fig. VI - 8. (A) Effect of voltage (total of 180 s per sample) on CUR release from PEDOT NPs by electrostimulation. The percentage of released drug is expressed by the total amount of loaded drug. (B) Effect of stimulation time under constant voltage values (+0.5 V, -1.25 V, -1.50 V, and -2.0 V) on CUR release from PEDOT NPs by electrostimulation. The percentage of released drug is expressed by the total amount of loaded drug (n=3).

VI - 3.4. Effect of CUR and electrical stimulation of CUR/PEDOT NPs in cancer cells

After determining the release behavior of CUR from PEDOT NPs, with and without electrical stimulation, and the release of CUR/PEDOT NPs from the fibers after enzymatic digestion, the effect of each of these components on cultured cells was assessed. MCF7 and PC-3 cells were used as models for breast and prostate cancers respectively, whereas L-929 cells were used as a somatic cell control.

Firstly, we started by studying the effect of CUR, PEDOT NPs, and CUR/PEDOT NPs on cell viability for the different cell models. CUR greatly reduced the viability of breast cancer cells (MCF7) at concentrations above 10 µg/mL (viability < 20 %), and of prostate cancer cells (PC-3) at concentrations above 25 µg/mL (viability < 35 %) (Fig. VI - 9A). For mouse fibroblasts (L-929), CUR had the same effect only for concentrations above 50 µg/mL (viability < 50 %, Fig. VI - 9A). This suggests that CUR negatively affects cancer cells preferably. PEDOT NPs and CUR/PEDOT NPs proved to be highly biocompatible for MCF7 and L-929 cell lines, with viabilities >80% for all the concentrations studied (Fig. VI - 9B and C), suggesting that NPs loaded with the drug do not have a negative on these cells in the absence of stimulation. For PC-3 cells both PEDOT and CUR/PEDOT NPs presented the lowest cell viability, but still above 60% (Fig. VI - 9B and C) for a concentration of 10 µg/mL, suggesting that these cells are particularly susceptible to both NPs. This slightly cytotoxic effect observed at higher NP concentrations could be related to the synthesis method and trace amounts of surfactant and other reagents. This effect could potentially be overcome by using green nanomaterials (e.g. synthesized using reagents produced by biosynthesis or from plant extracts) such as Ag NPs synthesized using olive leaves extract.[60] Overall, these results further demonstrate that CUR is firmly bound to PEDOT NPs and will not affect MCF7 cultured cells without an electrical trigger, as cell viability is not affected by the presence of CUR/PEDOT NPs. In the case of PC-3 cells, their death can be further increased in the presence of electrical stimulation. This suggests a potential application of the present controlled release system *in vivo*.

Secondly, the effect of CUR, delivered through the NPs on the cancer cell models was studied, using the supernatants enriched with CUR upon electrostimulation of CUR/PEDOT NPs. For this, CUR/PEDOT NPs were immobilized on the surface of SPEs and subjected to electrostimulation for 30 min and -1.5V in the presence of 0.05% Tween® 20 in the cell culture medium. Cancer cells were then incubated for 24 h with the respective mediums containing CUR released from the NPs (approximately 27 µg/mL of CUR). We observed that exposing cancer cells to these supernatants leads to a decrease in cell viability (Fig. VI - 9D), reaching values as low as 32% and 26% for PC-3 and MCF7 cells, respectively, after 24 h, which agrees with what we observed for CUR concentrations above 25 µg/mL in Fig. VI - 9A. A control experiment showed that the presence of 0.05% Tween® 20 alone in cell culture

does not affect cell viability (≥ 90%), and thus one can attribute the decrease in cell viability solely to CUR released by electrostimulation.

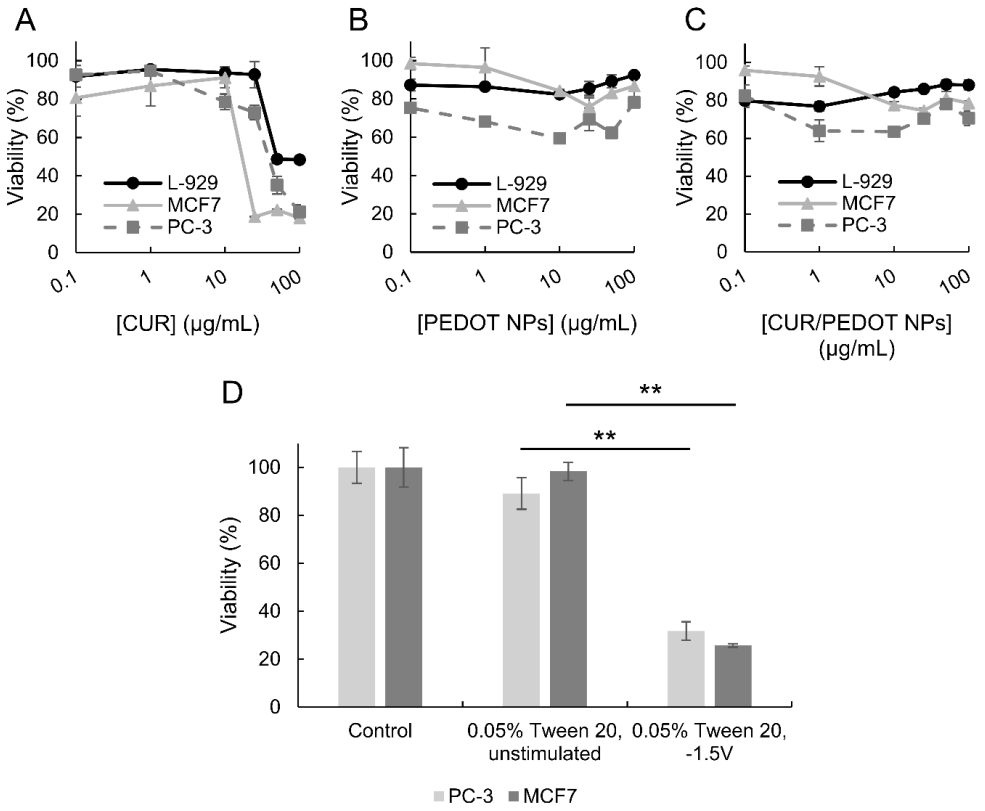

Fig. VI - 9. Cell viability of L-929, MCF7, and PC-3 cells with different concentrations of CUR (A), PEDOT NPs (B), and CUR/PEDOT NPs (C) for 24 h, n=3. (D) Cell viability of PC-3 and MCF7 cells after 24 h exposure to culture mediums containing CUR released from CUR/PEDOT NPs immobilized in SPE surface and subjected to 30 min of electrical stimulation at -1.5V in the presence of 0.05% Tween® 20 (approximately 27 µg/mL of CUR), n = 3. **p-value<0.01.

The third step was to investigate the effect of CUR/PEDOT NPs, released from the coaxial fibers following enzymatic degradation or directly added into the culture media, on the cellular morphology of MCF7 and PC-3 cells. First, we analyzed NP internalization after direct incubation of cells with a NP dispersion. The green fluorescence of CUR/PEDOT NPs staining the intracellular compartment allowed the observation of cellular morphology. Both PC-3 and MCF7 cells (Fig. VI - 10A) can endocyte free CUR/PEDOT NPs (50 µg/mL) throughout 24 h, with considerable green fluorescence being observed (CUR/PEDOT NPs have λex/em = 460-500/512-542 nm). The PC-3 cells presented characteristic elongated morphology and the MCF7 cells presented the characteristic square-like shapes (Fig. VI - 10A). These results suggest that the characteristic morphologies of these cells are not affected by endocytosis of CUR/PEDOT NPs in the absence of electrical stimulation.

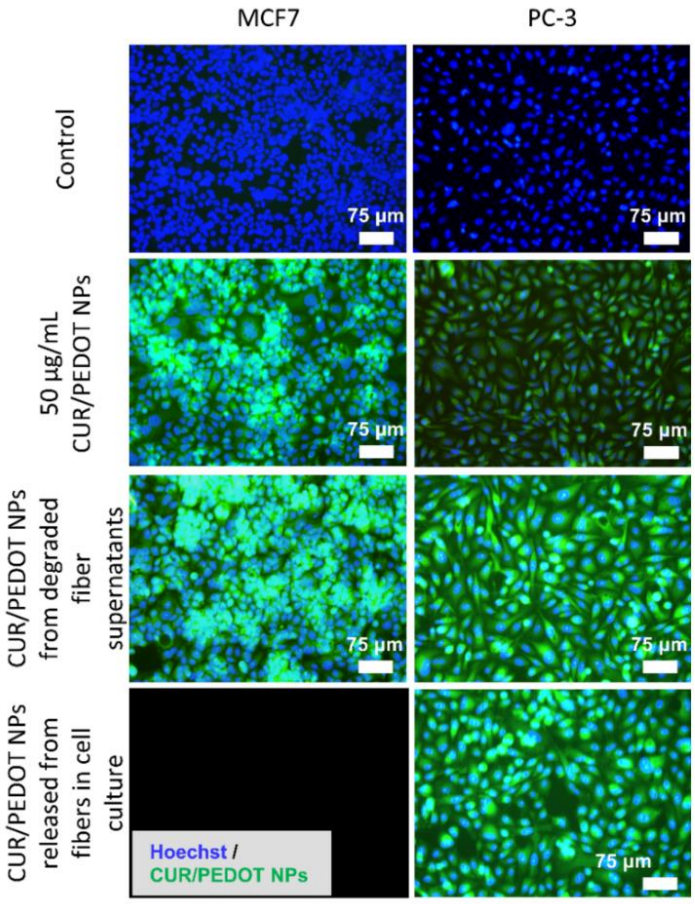

Fig. VI - 10. Fluorescence microscopy images of cultured MCF7 cells (left column) and PC-3 cells (right column) incubated for 24 h in regular culture media (Control, 1st row), with a 50 µg/mL CUR/PEDOT NPs in medium solution (2nd row), with supernatants of previously enzymatically degraded CUR/PEDOT+PGS/PCL fibers (3rd row), and incubated for 2 weeks with CUR/PEDOT+PGS/PCL fibers (≈25 mg/well) and 0.5 mg/mL lipase from *Aspergillus oryzae* (4th row).

Similar results were observed for CUR/PEDOT NPs released from coaxial fibers. In such assays, the cells were also able to internalize the NPs without noticeable morphological changes. The higher green fluorescence intensity observed ((Fig. VI - 10A, 3rd row) is due to the incubation of cells in the presence of a higher concentration of CUR/PEDOT NPs, which after release from the coaxial fibers are present at concentrations of ~0.1 mg/mL (Fig. VI - 6), which corresponds to the double of the concentration used for CUR/PEDOT NPs controls (50 µg/mL, (Fig. VI - 10A, 2nd row). Again, no apparent cytotoxic effect could be detected for both PC-3 and MCF7 cells, which agrees with the high cell viability obtained in assays where cells were incubated with fibers (Fig. VI - 11).

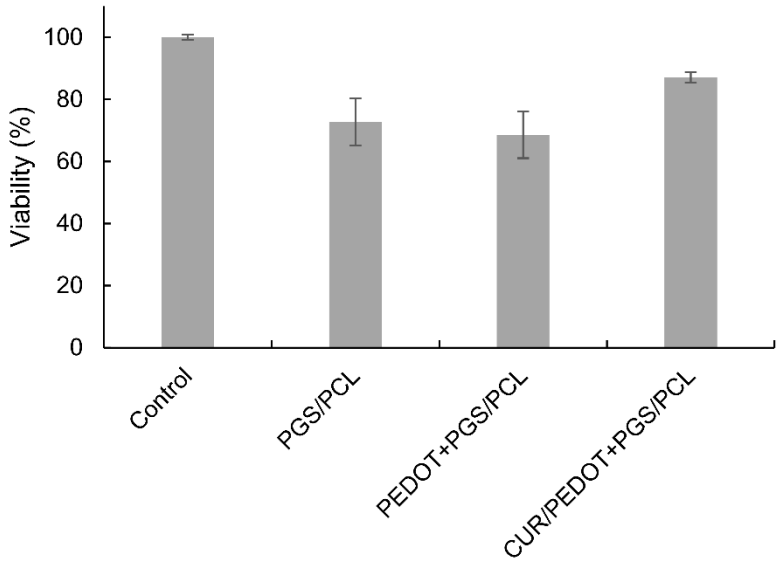

Fig. VI - 11. Viability of PC-3 cells after 24 h incubation with PGS/PCL control fibers and PGS/PCL coaxial fibers containing PEDOT and CUR/PEDOT NPs, n=3.

NPs with a size smaller than 500 nm can be endocytosed by cells, with sizes in the range 200-500 nm requiring clathrin or caveolae mediation.[61–64] The diameters assessed for CUR/PEDOT NPs by TEM (96 ± 7 nm) and DLS (245 ± 31 nm) are a good indicator for accumulation in the tumor and cellular uptake. The optimum size range reported in various kinds of nanocarriers is typically 20-200 nm, to prevent clearance by the kidneys and escape macrophages, thus allowing a longer circulation time in the body.[49] Therefore, CUR/PEDOT NPs, which present a hydrodynamic diameter of 245 nm, still have the potential to be used in *in vivo* applications. The significant green fluorescence (CUR/PEDOT NPs) observed in both cancer cell lines suggests a high efficiency in NP internalization, similar to what has been reported for PEDOT NPs for breast and prostate cancer therapy,[47] and carbon NTs in the monitoring and treatment of liver and pancreatic cancer.[65] Contrary to reported in other works, the CUR/PEDOT NPs in this study have not been modified to improve transport through the cell membrane. Considering *in vivo* applications, it would still be advantageous to functionalize these NPs with specific protein epitopes for each cancer type for specific targeting. This would be highly advantageous, since CUR remains entrapped in CUR/PEDOT NPs during the electrospinning process as CUR in the supernatants obtained from the fibers' enzymatic degradation studies only increases significantly after electrical stimulation (Table VI - 3).

Table VI - 3. CUR concentration in supernatants from fibers degradation by lipase at 37 ^{o}C in 0.01 M PBS, pH 7.4, and after electrical stimulation of CUR/PEDOT+PGS/PCL supernatant after 24 h of electrical stimulation using square wave with potential from -10 V to 0 V, 100 Hz.

Sample	[CUR] (µg/mL)
PGS/PCL	0.13 ± 0.09
PEDOT+PGS/PCL	0.07 ± 0.12
CUR/PEDOT+PGS/PCL	0.70 ± 0.19
CUR/PEDOT+PGS/PCL electrostimulated	4.54 ± 2.03

The fourth study was designed to assess the effect of the fiber meshes and the lipases on the cells. PC-3 cells were directly incubated for 2 weeks with fiber meshes and human lipase expressed in *Aspergillus oryzae*. A strong green fluorescence was also detected inside the cells, indicating CUR/PEDOT NPs endocytosis (Fig. VI - 10A, 4th row). Although some cell detachment was observed, no cytotoxic effect was evidenced by the use of the lipase (Fig. VI - 12). This suggests that enzymatic degradation of the fibers can be achieved in cell culture, with the successful release of CUR/PEDOT NPs and internalization of such NPs by the cells. Although PC-3 cells appear to express enzymes with lipolytic activity (Fig. VI - 13), agreeing with the observed by Nomura *et al*.,[41] effects on fiber degradation in culture could not be observed in a 2-week cell culture experiments, most likely due to frequent medium change that led to decreased lipase activity. Actually, the experimental lipolytic activity, after 4 days of *ex-vivo* culture without medium change, was estimated for breast (MCF7) and prostate (PC-3) cancer cells to be 4.2 ± 1.1 U/mL and 3.8 ± 0.5 U/mL (Fig. VI - 13), respectively.

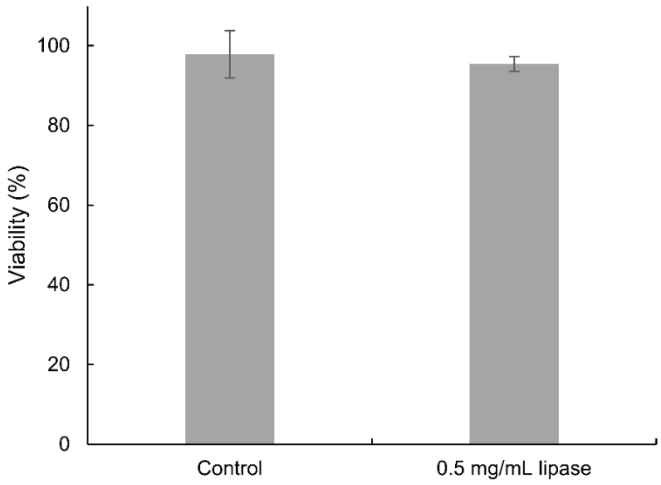

Fig. VI - 12. Viability of PC-3 cells after 24h incubation with 0.05 mg/mL lipase from *Aspergillus oryzae*.

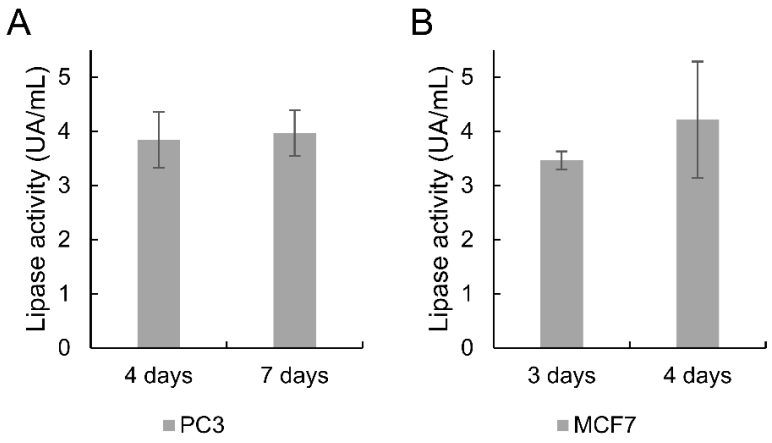

Fig. VI - 13. Lipase activity at 37 ^{o}C throughout varying times of cancer cell culture: (A) PC-3 cells, (B) MCF7 cells.

It is worth noting that no cytotoxic effects were observed resulting from incubation of the cancer cells with fiber meshes or from incubation with biodegraded fibers. One aspect contributing to this result might be because the PGS used to electrospun the coaxial fibers was synthesized using a green method, simply polycondensation of glycerol and sebacic acid without the use of hazardous solvents.[66] The use of green synthesis methods is not only important for the biosafety of future *in vivo* tests but also to guarantee a sustainable production of materials in the biomedical industry. An alternative green route for PGS synthesis could be the use of an enzyme (*Candida antarctica* lipase B, CALB) to catalyze the reaction of glycerol and sebacic acid.[67] Additionally, here we have used commercially available PCL, but this polymer can also be obtained using greener synthetic methods, such as using reactants from sustainable sources, for example using polyol derived from soybean oil to perform ring-opening polymerization,[68] or using L-lactic acid and glycolic acid as organic initiators of the polymerization.[69]

Finally, we decided to assess the performance of CUR/PEDOT NPs, as a drug delivery platform, on PC-3 cell culture to test the anti-tumoral properties in the presence of wireless electrical stimulation. From our results, we expected that CUR/PEDOT NPs will be endocyted by the cells, and CUR release would only take place in the presence of wireless electrical stimulation. For this study, we selected to assess PC-3 cells viability since these cells were more sensitive to CUR. When cells were incubated with PEDOT NPs alone and subjected to electrical stimulation, cell viability decreased to 78% (Fig. VI - 14). However, when CUR/PEDOT NPs were used with electrical stimulation, cell viability significantly decreased to 33%. These results indicate that upon application of an electrical potential, CUR might be released to the culture medium from non-endocyted CUR/PEDOT NPs, or to the cytosol from endocytosed NPs, as a bipolar electrostimulation process is enabled with the use of these NPs as BPEs.

These results suggest that CUR/PEDOT NPs can be used to deliver CUR to cancer cells after the application of wireless electrostimulation.

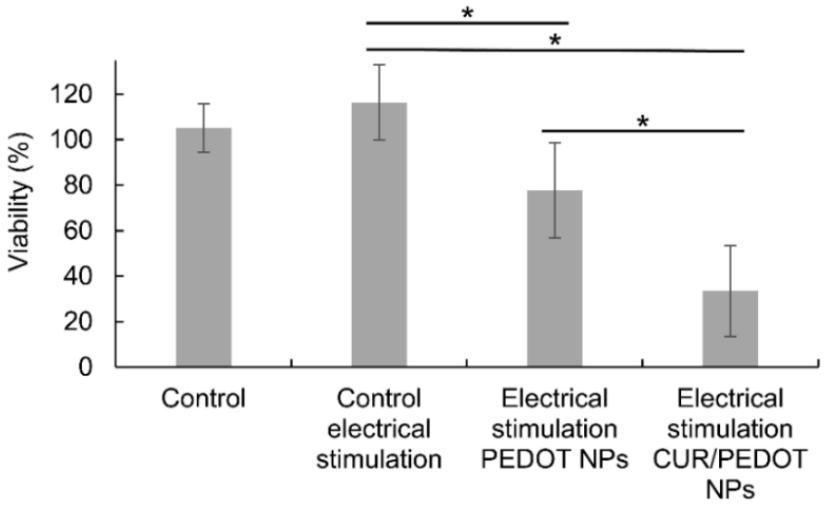

Fig. VI - 14. Viability of PC-3 cells after 24 h incubation in culture medium supplemented with 50 µg/mL of either PEDOT NPs or CUR/PEDOT NPs under wireless electrical stimulation for 24 h using square wave with potential from -10 V to 0 V, 100 Hz, and respective controls: absence of stimulation and wireless electrostimulation under the same conditions without NPs (n = 3, * means p-value < 0.05; ** means p-value < 0.01).

For our last assay, we believe the anti-cancer effect observed in the cells is due to CUR and not to the presence of PEDOT NPs and/or PCL/PGS FIBER debris. The anti-cancer properties of CUR have already been described in the literature,[70,71] and our results are in line with what was expected. First, we demonstrate for three different cell lines (PC-3, prostate cancer model; MCF7, mammary cancer model; and L-929 fibroblasts – Fig. VI - 9A-C) that cell viability is impaired by the presence of soluble curcumin in the culture medium. Lower cell viability is observed for both cancer cell models for higher CUR concentrations when compared to health cells. Next, we demonstrate that CUR released from PEDOT NPs with electrical stimulation (Fig. VI - 8B) can still lead to a substantial reduction in cell viability of both the cancer models used (Fig. VI - 9D). When not electrically stimulated, CUR remains adsorbed to PEDOT NPs. Both pristine and released (ex-culture and in-culture) CUR/PEDOT NPs can be endocytosed by cells without affecting their morphology and only leading to a slight reduction in viability (Fig. VI - 10). Only when electrical stimulation is applied to the cell lines with endocytosed CUR/PEDOT NPs does the cell viability greatly decrease (Fig. VI - 14). Moreover, we demonstrate that the materials used for the design of this wirelessly controlled release system are biocompatible for both healthy and cancer cells. This is important to reduce potential side effects that might arise from its implantation in the body, either locally or as a transdermal patch.

The voltage (-10 V) applied was not harmful to the cells (Fig. VI - 14), most probably because the induced potential at the surface of the BPE, in this case PEDOT NPs (loaded or not with CUR), was lower than the potential applied at the driving electrodes (Pt wires), according with the distance between NPs and the electrodes. Villani and Inagi have reported that the application of a potential of 35 V corresponds to a maximum potential of 3 V at the surface of a single BPE, made of indium tin oxide, in a linear configuration.[72] This occurs when the BPE is placed between the driving electrodes, similar to the setup used in this work (Scheme VI - 1). Abad *et al*. established that the correlation between induced voltage in the BPE and applied electrical potential is mostly linear, for BPEs based on graphite, and for materials with different levels of doping, including PEDOT:PSS.[73] The same study also shows that it is possible to use bipolar electrostimulation to stimulate neural cells using a linear setup configuration. Extrapolating to the wireless setup configuration of the present study, an applied potential of -10 V would roughly translate into -1 V at the surface of the NPs.[26] A voltage value close to the ones previously established as optimal (-1.25 V and -1.5 V) for triggering CUR release from CUR/PEDOT NPs immobilized at the surface of an electrode (Fig. VI - 8A), where electron transfer took place by direct contact. These results suggest that increasing the applied potential to -15 V would perhaps lead to a more pronounced decrease in PC-3 cell viability.

A few studies have recently reported biomedical applications of wireless electrostimulation using different kinds of BPEs, including using gold NPs with applied potentials from around 1V and up to 10 V for applications in electrical intracellular signaling,[74,75] signaling of cancer cell apoptosis,[76] and for cancer treatment.[77] Other studies include applications for cell proliferation and differentiation, such as using soft polymeric materials (e.g. polypyrrole) with an applied potential of 5.5V leads to increased neural cell differentiation,[78] but also applying 2 V while using carbon nanotube porins for transmembrane electron transport had no adverse effects in undifferentiated neurons.[79] Altogether, these studies suggest that the parameters used for wireless electrostimulation in the present work agree with what was found to be compatible with *in vitro* cell culture. Thus, we can conclude that the reduction in cancer cell viability is probably due to the toxic effect of CUR being released from the PEDOT NPs. Nevertheless, a subsequent pharmacodynamic study ought to be conducted to assess the effect of CUR released from this system, which should make use of more suitable analytical techniques for CUR and cell health, and adequate *in vivo* models for a complete pharmacodynamic study of CUR on healthy and cancer cells.

Overall, our results show that wireless electrostimulation using CUR/PEDOT NPs, released from a biodegradable fiber mesh, is a promising controlled drug delivery system to be used in cancer treatment. Although few NP/coaxial fiber systems for drug delivery have previously been reported in the literature, these studies rely on the passive release of the drug from the whole system during *in*

vitro assays[80] or after implantation,[81] similar to other drug-loaded coaxial nanofiber systems,[82–84] but with an added layer for the drug to cross. On the other hand, the NP/coaxial fiber system developed in this work not only has the potential to be implantable at a tumor site,[81] or as a transdermal device[85] due to its biocompatible and FDA-approved materials, but it is biologically responsive to the microenvironment. Unlike other works reported, it also adds another degree of control over the delivery of the drug as the NPs used are wirelessly electroresponsive, thus the release can potentially be triggered on demand.

This NP/coaxial fiber system evidences the potential for long-term anticancer treatment, like post-surgery maintenance therapy, as the NPs could be slowly released at the tumor site in response to enzymatic activity, and posterior low-voltage electrostimulation can be performed for highly controlled release of the anticancer drug. Furthermore, the developed NP/fiber system shows the potential of delivering an anticancer drug in a highly controlled way, thus reducing the side effects of anticancer drugs in long-term treatments and potentially increasing the pool of available drugs for anticancer therapy.

VI - 4. Conclusions

In this Chapter, we have successfully produced PGS/PCL coaxial fibers, with electroresponsive PEDOT NPs embedded in the core of the fibers, which were loaded with the anticancer drug CUR. A biocompatible biodegradation assay using lipases was carried out and the sustained release of NPs from the fibers was achieved. An electric stimulation regime was successfully applied to control the release of CUR from the CUR/PEDOT NPs, achieving 79% of CUR released at an electrical potential of -1.5 V.

CUR, PEDOT NPs, and CUR/PEDOT NPs were shown to be safe for somatic cells, at given concentrations, as shown by high cell viabilities obtained. However, the CUR was shown to be cytotoxicity for PC-3 and MCF7 cancer cell lines, with the viabilities of those cells dropping to <20% and <35%, respectively. Both cancer cell lines were capable of internalizing CUR/PEDOT NPs in 24 h, with no perceived cell death or alterations in cell morphology in the absence of electrical stimulation. Most importantly, wireless electrostimulation of cancer cells using CUR/PEDOT NPs was successfully performed. Indeed, the wireless stimulation assays resulted in a very significant decrease in cancer cell viability (33%), caused by the controlled release of CUR from the electroresponsive CUR/PEDOT NPs.

Overall, our results show the potential of using wireless electrostimulation of drug-loaded NPs for cancer treatment, using safe voltages for the human body, and ensuring the delivery of the anticancer drug in a highly controlled way. Additionally, our results highlight the potential of using FDA-approved

materials to create a transdermal implant that would act as a reservoir for the NPs to be delivered in a sustained manner to the patient.

VI - 5. References

(1) Bray, F.; Ferlay, J.; Soerjomataram, I.; Siegel, R. L.; Torre, L. A.; Jemal, A. Global Cancer Statistics 2018: GLOBOCAN Estimates of Incidence and Mortality Worldwide for 36 Cancers in 185 Countries. *CA Cancer J Clin* **2018**, *68* (6), 394–424. https://doi.org/10.3322/caac.21492.

(2) Dyba, T.; Randi, G.; Bray, F.; Martos, C.; Giusti, F.; Nicholson, N.; Gavin, A.; Flego, M.; Neamtiu, L.; Dimitrova, N.; Negrão Carvalho, R.; Ferlay, J.; Bettio, M. The European Cancer Burden in 2020: Incidence and Mortality Estimates for 40 Countries and 25 Major Cancers. *Eur J Cancer* **2021**, *157*, 308–347. https://doi.org/10.1016/j.ejca.2021.07.039.

(3) Siegel, R. L.; Miller, K. D.; Jemal, A. Cancer Statistics, 2019. *CA Cancer J Clin* **2019**, *69* (1), 7–34. https://doi.org/10.3322/caac.21551.

(4) Feng, X.; Li, J.; Zhang, X.; Liu, T.; Ding, J.; Chen, X. Electrospun Polymer Micro/Nanofibers as Pharmaceutical Repositories for Healthcare. *Journal of Controlled Release* **2019**, *302*, 19–41. https://doi.org/10.1016/j.jconrel.2019.03.020.

(5) Hu, T.; Qahtan, A. S. A.; Lei, L.; Lei, Z.; Zhao, D.; Nie, H. Inhibition of HeLa Cell Growth by Doxorubicin-Loaded and Tuftsin-Conjugated Arginate-PEG Microparticles. *Bioact Mater* **2018**, *3*, 48–54. https://doi.org/10.1016/j.bioactmat.2017.04.007.

(6) Chenthamara, D.; Subramaniam, S.; Ramakrishnan, S. G.; Krishnaswamy, S.; Essa, M. M.; Lin, F. H.; Qoronfleh, M. W. Therapeutic Efficacy of Nanoparticles and Routes of Administration. *Biomater Res* **2019**, *23* (1), 1–29. https://doi.org/10.1186/s40824-019-0166-x.

(7) Woeppel, K. M.; Zheng, X. S.; Schulte, Z. M.; Rosi, N. L.; Cui, X. T. Nanoparticle Doped PEDOT for Enhanced Electrode Coatings and Drug Delivery. *Adv Healthc Mater* **2019**, *8* (21), 1–14. https://doi.org/10.1002/adhm.201900622.

(8) Cervadoro, A.; Palomba, R.; Vergaro, G.; Cecchi, R.; Menichetti, L.; Decuzzi, P.; Emdin, M.; Luin, S. Targeting Inflammation with Nanosized Drug Delivery Platforms in Cardiovascular Diseases: Immune Cell Modulation in Atherosclerosis. *Front Bioeng Biotechnol* **2018**, *6* (NOV). https://doi.org/10.3389/fbioe.2018.00177.

(9) Han, S.; Su, L.; Zhai, M.; Ma, L.; Liu, S.; Teng, Y. A Molecularly Imprinted Composite Based on Graphene Oxide for Targeted Drug Delivery to Tumor Cells. *J Mater Sci* **2019**, *54* (4), 3331–3341. https://doi.org/10.1007/s10853-018-3023-8.

(10) Puiggalí-Jou, A.; Del Valle, L. J.; Alemán, C. Encapsulation and Storage of Therapeutic Fibrin-Homing Peptides Using Conducting Polymer Nanoparticles for Programmed Release by Electrical Stimulation. *ACS Biomater Sci Eng* **2020**, *6* (4), 2135–2145. https://doi.org/10.1021/acsbiomaterials.9b01794.

(11) Li, W.; Zeng, X.; Wang, H.; Wang, Q.; Yang, Y. Polyaniline-Poly(Styrene Sulfonate) Conducting Hydrogels Reinforced by Supramolecular Nanofibers and Used as Drug Carriers with Electric-Driven Release. *Eur Polym J* **2015**, *66*, 513–519. https://doi.org/10.1016/j.eurpolymj.2015.03.020.

(12) Shah, S. A. A.; Firlak, M.; Berrow, S. R.; Halcovitch, N. R.; Baldock, S. J.; Yousafzai, B. M.; Hathout, R. M.; Hardy, J. G. Electrochemically Enhanced Drug Delivery Using Polypyrrole Films. *Materials* **2018**, *11* (7), 1–16. https://doi.org/10.3390/ma11071123.

(13) Xu, C.; Guan, S.; Wang, S.; Gong, W.; Liu, T.; Ma, X.; Sun, C. Biodegradable and Electroconductive Poly(3,4-Ethylenedioxythiophene)/Carboxymethyl Chitosan Hydrogels for Neural Tissue Engineering. *Materials Science and Engineering C* **2018**, *84* (November 2017), 32–43. https://doi.org/10.1016/j.msec.2017.11.032.

(14) da Silva, AC.; de Torresi, SIC. Advances in Conducting, Biodegradable and Biocompatible Copolymers for Biomedical Applications. *Front Mater* **2019**, *6* (98), 1–9. https://doi.org/10.3389/fmats.2019.00098.

(15) Abidian, M. R.; Martin, D. C. Multifunctional Nanobiomaterials for Neural Interfaces. *Adv Funct Mater* **2009**, *19* (4), 573–585. https://doi.org/10.1002/adfm.200801473.

(16) Abidian, M. R.; Kim, D. H.; Martin, D. C. Conducting-Polymer Nanotubes for Controlled Drug Release. *Advanced Materials* **2006**, *18* (4), 405–409. https://doi.org/10.1002/adma.200501726.

(17) Puiggalí-Jou, A.; del Valle, L. J.; Alemán, C. Cell Responses to Electrical Pulse Stimulation for Anticancer Drug Release. *Materials* **2019**, *12* (16), 1–15. https://doi.org/10.3390/ma12162633.

(18) Kleber, C.; Lienkamp, K.; Rühe, J.; Asplund, M. Electrochemically Controlled Drug Release from a Conducting Polymer Hydrogel (PDMAAp/PEDOT) for Local Therapy and Bioelectronics. *Adv Healthc Mater* **2019**, *8* (10), 1–11. https://doi.org/10.1002/adhm.201801488.

(19) Chowdhury, P.; Ghosh, U.; Samanta, K.; Jaggi, M.; Chauhan, S. C.; Yallapu, M. M. Bioactive Nanotherapeutic Trends to Combat Triple Negative Breast Cancer. *Bioact Mater* **2021**, *6*, 3269–3287. https://doi.org/10.1016/j.bioactmat.2021.02.037.

(20) Kim, T. H.; Kim, J. K.; Ito, H.; Jo, C. Enhancement of Pancreatic Lipase Inhibitory Activity of Curcumin by Radiolytic Transformation. *Bioorg Med Chem Lett* **2011**, *21* (5), 1512–1514. https://doi.org/10.1016/j.bmcl.2010.12.122.

(21) Wilken, R.; Veena, M. S.; Wang, M. B.; Srivatsan, E. S. Curcumin: A Review of Anti-Cancer Properties and Therapeutic Activity in Head and Neck Squamous Cell Carcinoma. *Mol Cancer* **2011**, *10*, 1–19. https://doi.org/10.1186/1476-4598-10-12.

(22) Nosrati, H.; Attari, E.; Abhari, F.; Barsbay, M.; Ghaffarlou, M.; Mousazadeh, N.; Vaezi, R.; Kavetskyy, T.; Rezaeejam, H.; Webster, T. J.; Johari, B.; Danafar, H. Complete Ablation of Tumors

Using Synchronous Chemoradiation with Bimetallic Theranostic Nanoparticles. *Bioact Mater* **2022**, *7*, 74–84. https://doi.org/10.1016/j.bioactmat.2021.05.015.

(23) Fosdick, S. E.; Knust, K. N.; Scida, K.; Crooks, R. M. Bipolar Electrochemistry. *Angewandte Chemie - International Edition* **2013**, *52* (40), 10438–10456. https://doi.org/10.1002/anie.201300947.

(24) Loget, G.; Zigah, D.; Bouffier, L.; Sojic, N.; Kuhn, A. Bipolar Electrochemistry: From Materials Science to Motion and Beyond. *Acc. Chem. Res.* **2013**, *46* (11), 2513–2523.

(25) Chow, K. F.; Mavré, F.; Crooks, R. M. Wireless Electrochemical DNA Microarray Sensor. *J Am Chem Soc* **2008**, *130* (24), 7544–7545. https://doi.org/10.1021/ja802013q.

(26) Warakulwit, C.; Nguyen, T.; Majimel, J.; Delville, M. H.; Lapeyre, V.; Garrigue, P.; Ravaine, V.; Limtrakul, J.; Kuhn, A. Dissymmetric Carbon Nanotubes by Bipolar Electrochemistry. *Nano Lett* **2008**, *8* (2), 500–504. https://doi.org/10.1021/nl072652s.

(27) Qin, C.; Yue, Z.; Chao, Y.; Forster, R. J.; Maolmhuaidh, F.; Huang, X. F.; Beirne, S.; Wallace, G. G.; Chen, J. Bipolar Electroactive Conducting Polymers for Wireless Cell Stimulation. *Appl Mater Today* **2020**, *21*, 100804. https://doi.org/10.1016/j.apmt.2020.100804.

(28) Hicks, J. M.; Yao, Y. C.; Barber, S.; Neate, N.; Watts, J. A.; Noy, A.; Rawson, F. J. Electric Field Induced Biomimetic Transmembrane Electron Transport Using Carbon Nanotube Porins. *Small* **2021**, *17* (32). https://doi.org/10.1002/smll.202102517.

(29) Khan, A. ur R.; Huang, K.; Khalaji, M. S.; Yu, F.; Xie, X.; Zhu, T.; Morsi, Y.; Jinzhong, Z.; Mo, X. Multifunctional Bioactive Core-Shell Electrospun Membrane Capable to Terminate Inflammatory Cycle and Promote Angiogenesis in Diabetic Wound. *Bioact Mater* **2021**, *6*, 2783–2800. https://doi.org/10.1016/j.bioactmat.2021.01.040.

(30) Sultanova, Z.; Kaleli, G.; Kabay, G.; Mutlu, M. Controlled Release of a Hydrophilic Drug from Coaxially Electrospun Polycaprolactone Nanofibers. *Int J Pharm* **2016**, *505* (1–2), 133–138. https://doi.org/10.1016/j.ijpharm.2016.03.032.

(31) Laha, A.; Sharma, C. S.; Majumdar, S. Sustained Drug Release from Multi-Layered Sequentially Crosslinked Electrospun Gelatin Nanofiber Mesh. *Materials Science and Engineering C* **2017**, *76*, 782–786. https://doi.org/10.1016/j.msec.2017.03.110.

(32) Hou, L.; Zhang, X.; Mikael, P. E.; Lin, L.; Dong, W.; Zheng, Y.; Simmons, T. J.; Zhang, F.; Linhardt, R. J. Biodegradable and Bioactive PCL-PGS Core-Shell Fibers for Tissue Engineering. *ACS Omega* **2017**, *2* (10), 6321–6328. https://doi.org/10.1021/acsomega.7b00460.

(33) Silva, J. C.; Udangawa, R. N.; Chen, J.; Mancinelli, C. D.; Garrudo, F. F. F.; Mikael, P. E.; Cabral, J. M. S.; Ferreira, F. C.; Linhardt, R. J. Kartogenin-Loaded Coaxial PGS/PCL Aligned Nanofibers for Cartilage Tissue Engineering. *Materials Science and Engineering C* **2020**, *107* (September 2019), 110291. https://doi.org/10.1016/j.msec.2019.110291.

(34) Garrudo, F. F. F.; Nogueira, D. E. S.; Rodrigues, C. A. V.; Ferreira, F. A.; Paradiso, P.; Colaço, R.; Marques, A. C.; Cabral, J. M. S.; Morgado, J.; Linhardt, R. J.; Ferreira, F. C. Electrical Stimulation of Neural-Differentiating IPSCs on Novel Coaxial Electroconductive Nanofibers. *Biomater Sci* **2021**, *9* (15), 5359–5382. https://doi.org/10.1039/d1bm00503k.

(35) Blackwell, C. J.; Haernvall, K.; Guebitz, G. M.; Groombridge, M.; Gonzales, D.; Khosravi, E. Enzymatic Degradation of Star Poly(ε-Caprolactone) with Different Central Units. *Polymers (Basel)* **2018**, *10* (11), 1–15. https://doi.org/10.3390/polym10111266.

(36) Litowczenko, J.; Woźniak-Budych, M. J.; Staszak, K.; Wieszczycka, K.; Jurga, S.; Tylkowski, B. Milestones and Current Achievements in Development of Multifunctional Bioscaffolds for Medical Application. *Bioact Mater* **2021**, *6*, 2412–2438. https://doi.org/10.1016/j.bioactmat.2021.01.007.

(37) Vogt, L.; Ruther, F.; Salehi, S.; Boccaccini, A. R. Poly(Glycerol Sebacate) in Biomedical Applications—A Review of the Recent Literature. *Adv Healthc Mater* **2021**, *10* (2002026). https://doi.org/10.1002/adhm.202002026.

(38) Loh, X. J.; Abdul Karim, A.; Owh, C. Poly(Glycerol Sebacate) Biomaterial: Synthesis and Biomedical Applications. *J Mater Chem B* **2015**, *3* (39), 7641–7652. https://doi.org/10.1039/c5tb01048a.

(39) Kuemmerle, N. B.; Rysman, E.; Lombardo, P. S.; Alison, J.; Lipe, B. C.; Wells, W. A.; Pettus, J. R.; Froehlich, H. M.; Memoli, V. A.; Morganelli, P. M.; Swinnen, J. V; Luika, A.; Chaychi, L.; Fricano, C. J.; Eisenberg, B. L.; William, B.; Kinlaw, W. B. Lipoprotein Lipase Links Dietary Fat to Solid Tumor Cell Proliferation. *Molecular Cancer Theranostics* **2011**, *10* (3), 427–436. https://doi.org/10.1158/1535-7163.MCT-10-0802.Lipoprotein.

(40) Cui, Y.; Jiao, Y.; Wang, K.; He, M.; Yang, Z. A New Prognostic Factor of Breast Cancer: High Carboxyl Ester Lipase Expression Related to Poor Survival. *Cancer Genet* **2019**, *239*, 54–61. https://doi.org/10.1016/j.cancergen.2019.09.005.

(41) Nomura, D. K.; Lombardi, D. P.; Chang, J. W.; Niessen, S.; Anna, M.; Long, J. Z.; Hoover, H. H.; Cravatt, B. F. Monoacylglycerol Lipase Exerts Dual Control over Endocannabinoid and Fatty Acid Pathways to Support Prostate Cancer. *Chem Biol* **2012**, *18* (7), 846–856. https://doi.org/10.1016/j.chembiol.2011.05.009.Monoacylglycerol.

(42) Choi, J. W.; Han, M. G.; Kim, S. Y.; Oh, S. G.; Im, S. S. Poly(3,4-Ethylenedioxythiophene) Nanoparticles Prepared in Aqueous DBSA Solutions. *Synth Met* **2004**, *141* (3), 293–299. https://doi.org/10.1016/S0379-6779(03)00419-3.

(43) Puiggalí-Jou, A.; Micheletti, P.; Estrany, F.; del Valle, L. J.; Alemán, C. Electrostimulated Release of Neutral Drugs from Polythiophene Nanoparticles: Smart Regulation of Drug–Polymer Interactions. *Adv Healthc Mater* **2017**, *6* (18), 1–11. https://doi.org/10.1002/adhm.201700453.

(44) Resina, L.; El Hauadi, K.; Sans, J.; Esteves, T.; Ferreira, F. C.; Pérez-Madrigal, M. M.; Alemán, C. Electroresponsive and PH-Sensitive Hydrogel as Carrier for Controlled Chloramphenicol Release. *Biomacromolecules* **2023**, *24* (3), 1432–1444. https://doi.org/10.1021/acs.biomac.2c01442.

(45) Zhong, X.; Fei, G.; Xia, H. Synthesis and Characterization of Poly(3,4- Ethylenedioxythiophene) Nanoparticles Obtained Through Ultrasonic Irradiation. *J Appl Polym Sci* **2010**, *118*, 2146–2152. https://doi.org/10.1002/app.

(46) Valente, A. J. M.; López Cascales, J. J.; Fernández Romero, A. J. Thermodynamic Analysis of Unimer-Micelle and Sphere-to-Rod Micellar Transitions of Aqueous Solutions of Sodium Dodecylbenzenesulfonate. *Journal of Chemical Thermodynamics* **2014**, *77*, 54–62. https://doi.org/10.1016/j.jct.2014.05.001.

(47) Puiggalí-Jou, A.; Micheletti, P.; Estrany, F.; del Valle, L. J.; Alemán, C. Electrostimulated Release of Neutral Drugs from Polythiophene Nanoparticles: Smart Regulation of Drug–Polymer Interactions. *Adv Healthc Mater* **2017**, *6* (18), 1–11. https://doi.org/10.1002/adhm.201700453.

(48) Jain, K.; Mehandzhiyski, A. Y.; Zozoulenko, I.; Wågberg, L. PEDOT:PSS Nano-Particles in Aqueous Media : A Comparative Experimental and Molecular Dynamics Study of Particle Size , Morphology and z-Potential. *J Colloid Interface Sci* **2021**, *584*, 57–66. https://doi.org/10.1016/j.jcis.2020.09.070.

(49) Eftekhari, A.; Kryschi, C.; Pamies, D.; Gulec, S.; Ahmadian, E.; Janas, D.; Davaran, S.; Khalilov, R. Natural and Synthetic Nanovectors for Cancer Therapy. *Nanotheranostics* **2023**, *7*, 236–257. https://doi.org/10.7150/ntno.77564.

(50) Puiggalí-Jou, A.; Cejudo, A.; Del Valle, L. J.; Alemán, C. Smart Drug Delivery from Electrospun Fibers through Electroresponsive Polymeric Nanoparticles. *ACS Appl Bio Mater* **2018**, *1* (5), 1594–1605. https://doi.org/10.1021/acsabm.8b00459.

(51) Sordini, L.; Silva, J. C.; Garrudo, F. F. F.; Rodrigues, C. A. V.; Marques, A. C.; Linhardt, R. J.; Cabral, J. M. S.; Morgado, J.; Ferreira, F. C. Pedot:Pss-Coated Polybenzimidazole Electroconductive Nanofibers for Biomedical Applications. *Polymers (Basel)* **2021**, *13* (16). https://doi.org/10.3390/polym13162786.

(52) Badria, F. A.; Abdelaziz, A. E.; Hassan, A. H.; Elgazar, A. A.; Mazyed, E. A. Development of Provesicular Nanodelivery System of Curcumin as a Safe and Effective Antiviral Agent: Statistical

Optimization, in Vitro Characterization, and Antiviral Effectiveness. *Molecules* **2020**, *25* (23), 1–27. https://doi.org/10.3390/molecules25235668.

(53) Wang, B.; Aoki, K. J.; Chen, J.; Nishiumi, T. Slow Scan Voltammetry for Diffusion-Controlled Currents in Sodium Alginate Solutions. *Journal of Electroanalytical Chemistry* **2013**, *700*, 60–64. https://doi.org/10.1016/j.jelechem.2013.04.018.

(54) Ahmed, M. K.; Zayed, M. A.; El-dek, S. I.; Hady, M. A.; El Sherbiny, D. H.; Uskoković, V. Nanofibrous ε-Polycaprolactone Scaffolds Containing Ag-Doped Magnetite Nanoparticles: Physicochemical Characterization and Biological Testing for Wound Dressing Applications in Vitro and in Vivo. *Bioact Mater* **2021**, *6*, 2070–2088. https://doi.org/10.1016/j.bioactmat.2020.12.026.

(55) Sun, Z. J.; Sun, B.; Tao, R. Bin; Xie, X.; Lu, X. L.; Dong, D. L. A Poly(Glycerol-Sebacate-Curcumin) Polymer with Potential Use for Brain Gliomas. *J Biomed Mater Res A* **2013**, *101 A* (1), 253–260. https://doi.org/10.1002/jbm.a.34319.

(56) Jin, L.; Wang, T.; Feng, Z. Q.; Leach, M. K.; Wu, J.; Mo, S.; Jiang, Q. A Facile Approach for the Fabrication of Core-Shell PEDOT Nanofiber Mats with Superior Mechanical Properties and Biocompatibility. *J Mater Chem B* **2013**, *1* (13), 1818–1825. https://doi.org/10.1039/c3tb00448a.

(57) Grahame, R.; Holt, P. The Influence of Ageing in the in Vivo Elasticity of Human Skin. *Gerentology* **1969**, *15*, 121–139.

(58) Hong, S. G.; Kim, H. S.; Kim, J. Highly Stabilized Lipase in Polyaniline Nanofibers for Surfactant-Mediated Esterification of Ibuprofen. *Langmuir* **2014**, *30* (3), 911–915. https://doi.org/10.1021/la404189e.

(59) Truong, N. H.; Lee, S.; Shim, S. M. Screening Bioactive Components Affecting the Capacity of Bile Acid Binding and Pancreatic Lipase Inhibitory Activity. *Appl Biol Chem* **2016**, *59* (3), 475–479. https://doi.org/10.1007/s13765-016-0184-5.

(60) Ramazanli, V. N.; Ahmadov, I. S. SYNTHESIS OF SILVER NANOPARTICLES BY USING EXTRACT OF OLIVE LEAVES. *Advances in Biology & Earth Sciences* **2022**, *7* (3), 238–244.

(61) Rejman, J.; Oberle, V.; Zuhorn, I. S.; Hoekstra, D. Size-Dependent Internalization of Particles via the Pathways of Clathrin-and Caveolae-Mediated Endocytosis. *Biochemical Journal* **2004**, *377* (1), 159–169. https://doi.org/10.1042/BJ20031253.

(62) Albanese, A.; Tang, P. S.; Chan, W. C. W. The Effect of Nanoparticle Size, Shape, and Surface Chemistry on Biological Systems. *Annu Rev Biomed Eng* **2012**, *14*, 1–16. https://doi.org/10.1146/annurev-bioeng-071811-150124.

(63) Zhang, S.; Gao, H.; Bao, G. Physical Principles of Nanoparticle Cellular Endocytosis. *ACS Nano* **2015**, *9* (9), 8655–8671. https://doi.org/10.1021/acsnano.5b03184.

(64) Anselmo, A. C.; Zhang, M.; Kumar, S.; Vogus, D. R.; Menegatti, S.; Helgeson, M. E.; Mitragotri, S. Elasticity of Nanoparticles Influences Their Blood Circulation, Phagocytosis, Endocytosis, and Targeting. *ACS Nano* **2015**, *9* (3), 3169–3177.

(65) Ahmadian, E.; Janas, D.; Eftekhari, A.; Zare, N. Application of Carbon Nanotubes in Sensing/Monitoring of Pancreas and Liver Cancer. **2022**. https://doi.org/10.1016/j.chemosphere.2022.134826.

(66) Hou, L.; Zhang, X.; Mikael, P. E.; Lin, L.; Dong, W.; Zheng, Y.; Simmons, T. J.; Zhang, F.; Linhardt, R. J. Biodegradable and Bioactive PCL-PGS Core-Shell Fibers for Tissue Engineering. *ACS Omega* **2017**, *2* (10), 6321–6328. https://doi.org/10.1021/acsomega.7b00460.

(67) Perin, G. B.; Felisberti, M. I. Enzymatic Synthesis of Poly(Glycerol Sebacate): Kinetics, Chain Growth, and Branching Behavior. *Macromolecules* **2020**, *53* (18), 7925–7935. https://doi.org/10.1021/ACS.MACROMOL.0C01709/ASSET/IMAGES/LARGE/MA0C01709_0008.JPEG.

(68) Acik, G. Bio-Based Poly(ε-Caprolactone) from Soybean-Oil Derived Polyol via Ring-Opening Polymerization. *J Polym Environ* **2020**, *28* (2), 668–675. https://doi.org/10.1007/S10924-019-01597-7/METRICS.

(69) Limwanich, W.; Meepowpan, P.; Sriyai, M.; Chaiwon, T.; Punyodom, W. Eco-Friendly Synthesis of Biodegradable Poly(ε-Caprolactone) Using L-Lactic and Glycolic Acids as Organic Initiator. *Polymer Bulletin* **2021**, *78* (12), 7089–7101. https://doi.org/10.1007/S00289-020-03401-2/METRICS.

(70) Tomeh, M. A.; Hadianamrei, R.; Zhao, X. A Review of Curcumin and Its Derivatives as Anticancer Agents. *International Journal of Molecular Sciences 2019, Vol. 20, Page 1033* **2019**, *20* (5), 1033. https://doi.org/10.3390/IJMS20051033.

(71) Tang, H.; Murphy, C. J.; Zhang, B.; Shen, Y.; Van Kirk, E. A.; Murdoch, W. J.; Radosz, M. Curcumin Polymers as Anticancer Conjugates. *Biomaterials* **2010**, *31* (27), 7139–7149. https://doi.org/10.1016/J.BIOMATERIALS.2010.06.007.

(72) Villani, E.; Inagi, S. Mapping the Distribution of Potential Gradient in Bipolar Electrochemical Systems through Luminol Electrochemiluminescence Imaging. *Anal Chem* **2021**, *93* (23), 8152–8160. https://doi.org/10.1021/acs.analchem.0c05397.

(73) Abad, L.; Rajnicek, A. M.; Casañ-Pastor, N. Electric Field Gradients and Bipolar Electrochemistry Effects on Neural Growth: A Finite Element Study on Immersed Electroactive Conducting

Electrode Materials. *Electrochim Acta* **2019**, *317*, 102–111. https://doi.org/10.1016/j.electacta.2019.05.149.

(74) Sanjuan-Alberte, P.; Jain, A.; Shaw, A. J.; Abayzeed, S. A.; Domínguez, R. F.; Alea-Reyes, M. E.; Clark, M.; Alexander, M. R.; Hague, R. J. M.; Pérez-García, L.; Rawson, F. J. Wireless Nanobioelectronics for Electrical Intracellular Sensing. *ACS Appl Nano Mater* **2019**, *2* (10), 6397–6408. https://doi.org/10.1021/ACSANM.9B01374/ASSET/IMAGES/MEDIUM/AN9B01374_M001.GIF.

(75) Robinson, A. J.; Jain, A.; Rahman, R.; Abayzeed, S.; Hague, R. J. M.; Rawson, F. J. Impedimetric Characterization of Bipolar Nanoelectrodes with Cancer Cells. *ACS Omega* **2021**, *6* (44), 29495–29505. https://doi.org/10.1021/ACSOMEGA.1C03547/ASSET/IMAGES/MEDIUM/AO1C03547_M004.GIF.

(76) Jain, A.; Gosling, J.; Liu, S.; Wang, H.; Stone, E. M.; Chakraborty, S.; Jayaraman, P. S.; Smith, S.; Amabilino, D. B.; Fromhold, M.; Long, Y. T.; Pérez-García, L.; Turyanska, L.; Rahman, R.; Rawson, F. J. Wireless Electrical–Molecular Quantum Signalling for Cancer Cell Apoptosis. *Nature Nanotechnology 2023 19:1* **2023**, *19* (1), 106–114. https://doi.org/10.1038/S41565-023-01496-Y.

(77) Jain, A.; Jobson, I.; Griffin, M.; Rahman, R.; Smith, S.; Rawson, F. J. Electric Field Responsive Nanotransducers for Glioblastoma. *Bioelectron Med* **2022**, *8* (1), 1–9. https://doi.org/10.1186/S42234-022-00099-7/FIGURES/3.

(78) Qin, C.; Yue, Z.; Huang, X. F.; Forster, R. J.; Wallace, G. G.; Chen, J. Enhanced Wireless Cell Stimulation Using Soft and Improved Bipolar Electroactive Conducting Polymer Templates. *Appl Mater Today* **2022**, *27*, 101481. https://doi.org/10.1016/J.APMT.2022.101481.

(79) Hicks, J. M.; Yao, Y. C.; Barber, S.; Neate, N.; Watts, J. A.; Noy, A.; Rawson, F. J. Electric Field Induced Biomimetic Transmembrane Electron Transport Using Carbon Nanotube Porins. *Small* **2021**, *17* (32). https://doi.org/10.1002/smll.202102517.

(80) Wen, P.; Zong, M.-H.; Hu, T.-G.; Li, L.; Wu, H. Preparation and Characterization of Electrospun Colon-Specific Delivery System for Quercetin and Its Antiproliferative Effect on Cancer Cells. *J Agric Food Chem* **2018**, *66* (44), 11550–11559. https://doi.org/10.1021/acs.jafc.8b02614.

(81) Yang, G.; Wang, J.; Wang, Y.; Li, L.; Guo, X.; Zhou, S. An Implantable Active-Targeting Micelle-in-Nanofiber Device for Efficient and Safe Cancer Therapy. *ACS Nano* **2015**, *9* (2), 1161–1174. https://doi.org/10.1021/nn504573u.

(82) Li, J.; Liu, Y.; Abdelhakim, H. E. Drug Delivery Applications of Coaxial Electrospun Nanofibres in Cancer Therapy. *Molecules* **2022**, *27* (6). https://doi.org/10.3390/MOLECULES27061803.

(83) Chen, X.; Li, H.; Lu, W.; Guo, Y. Antibacterial Porous Coaxial Drug-Carrying Nanofibers for Sustained Drug-Releasing Applications. *Nanomaterials* **2021**, *11* (5). https://doi.org/10.3390/NANO11051316/S1.

(84) Reise, M.; Kranz, S.; Guellmar, A.; Wyrwa, R.; Rosenbaum, T.; Weisser, J.; Jurke, A.; Schnabelrauch, M.; Heyder, M.; Watts, D. C.; Sigusch, B. W. Coaxial Electrospun Nanofibers as Drug Delivery System for Local Treatment of Periodontitis. *Dental Materials* **2023**, *39* (1), 132–139. https://doi.org/10.1016/J.DENTAL.2022.12.008.

(85) Mehnath, S.; Chitra, K.; Karthikeyan, K.; Jeyaraj, M. Localized Delivery of Active Targeting Micelles from Nanofibers Patch for Effective Breast Cancer Therapy. *Int J Pharm* **2020**, *584*, 119412. https://doi.org/10.1016/J.IJPHARM.2020.119412.

Chapter VII – Harnessing CD44 molecularly imprinted polymers' targeting potential for breast cancer detection

VII - 1. Introduction

Cancer remains one of the most formidable challenges in modern medicine, demanding innovative approaches for both early detection and effective treatment. In this pursuit, MIPs have emerged as a promising avenue, offering unparalleled precision and versatility in cancer management.

Compared to traditional antibody-based approaches, MIPs offer several distinct advantages. Firstly, MIPs can be designed with tailor-made binding sites for specific biomarkers, ensuring selectivity and stability like antibodies.[1,2] This tailored molecular recognition translates to enhanced accuracy in cancer detection and targeted therapy. Additionally, MIPs are highly robust and cost-effective, facilitating large-scale production and deployment in diverse clinical settings. Unlike antibodies, MIPs are not prone to denaturation or degradation, ensuring prolonged shelf life and consistent performance. Furthermore, MIP-based systems exhibit remarkable versatility, accommodating a wide range of biomarkers and therapeutic agents.[3–7] This versatility extends beyond conventional small molecules to complex macromolecules, including proteins and nucleic acids, widening the scope of applications in cancer management.[2,8,9] Whether employed in biosensors for early diagnosis or as drug delivery vehicles for precision therapy, MIPs offer a multifaceted approach for combating cancer with unparalleled efficacy and efficiency.[10] Incorporating cancer biomarkers into MIP-based systems enables sensitive and specific detection of cancer, even at its earlier stages.[11–13] Moreover, MIPs engineered to recognize these biomarkers with high affinity provide a platform for targeted treatment, delivering therapeutic agents directly to malignant cells while sparing healthy tissues.[10,14]

CD44, a transmembrane glycoprotein, has become a pivotal molecule in cancer biology due to its multifaceted roles in cell adhesion, migration, and signalling. Its overexpression and dysregulation have been implicated in various aspects of cancer progression, including tumor growth, metastasis, and resistance to therapy.[15] Exploiting the unique properties of CD44, particularly its overexpression in many cancer types (in particular breast cancer)[16,17] compared to normal tissues, presents an attractive opportunity for targeted cancer therapy.[18] This Chapter delves into the significance of CD44 as a molecular target for breast cancer,[16,17,19] aiming at breast cancer cell targeting to highlight the potential of CD44-targeted approaches in achieving precise and efficient breast cancer treatment strategies.

By imprinting the unique molecular footprint of CD44 onto polymeric matrices, it would be possible to engineer MIPs with exquisite specificity and affinity, enabling precise detection and targeting of cancer cells. Through rational design and molecular imprinting techniques, MIPs could selectively recognize and capture CD44-expressing cancer cells with unparalleled precision. This targeted recognition not only facilitates early detection of cancer but also opens new avenues for

personalized therapy, delivering therapeutic payloads directly to malignant cells while minimizing off-target effects.

In comparison to traditional antibody-based approaches, MIPs offer distinct advantages in CD44 targeting. The customizable nature of MIP synthesis allows for the fine-tuning of binding sites to mimic the molecular architecture of CD44, ensuring superior selectivity and stability.[1,2] Moreover, MIPs exhibit remarkable robustness and cost-effectiveness, making them suitable for widespread adoption in clinical settings.[2] Through the development of a CD44 MIP, an innovative targeting strategy, lies the promise of enhanced selectivity and efficacy in cancer therapy.

In this chapter, we aim to elucidate the potential of MIP-based systems in revolutionizing cancer diagnostics and therapeutics by presenting preliminary results of breast cancer cell targeting using two MIPs synthesized to target the CD44 cancer cell marker. By exploring the synergistic potential of CD44 targeting in MIP-based systems, we aim to contribute to the ongoing efforts to realize the promise of precision medicine for cancer patients worldwide.

VII - 2. Materials and methods

VII - 2.1. Materials

Glass beads (diameter 75 µm) were purchased from Supelco (USA). Toluene (CHROMASOLV, HPLC, 99.9%) was bought from Honeywell (Germany). The epitope for CD44 (sequence: FAGVFHVEKNGRYWC) was purchased from GenScript Biotech (USA).Acetone (99%), (3-aminopropyl) trimethoxysilane (97%), maleic anhydride (≥99%), sodium acetate anhydrous (≥99%), acetic anhydride (≥98%), PBS, polypropylene solid-phase extraction (SPE) tubes (60 ml) and polyethylene (PE) frits (20-µm porosity, for use with 60-ml SPE tubes), NIPAM (>97.0%), TBAm (97%), AAc (99%, 180–200 p.p.m. MEHQ as inhibitor), APMA (>98%), itaconic acid (ItAc, 98%), MBA (99%), and TEMED (99%), APS (98%), Fluorescein O-methacrylate (95%) were purchased from Sigma-Aldrich (USA). All reagents were used as received without further purification.

VII - 2.2. MIP synthesis

Solid-phase synthesis of CD44 epitope imprinted MIPs consists of three significant steps: 1) functionalization of the solid phase with the immobilized peptide (epitope); 2) preparation of the polymerization mixture and addition to the solid phase with the template; and 3) selective removal of the synthesized MIP. For the synthesis of the corresponding non-imprinted polymers (NIPs), step 1 is not performed, as non-functionalized beads are used in step 2 (polymerization).

VII - 2.2.1. Template immobilization

To immobilize the template, 60 g of glass beads were boiled for 15 min in 50 mL of NaOH 1 M inside a closed Schott flask of 100 mL. The beads were then washed and decanted with 500 mL of Milli-Q water, 300 mL of PBS, and 500 mL of Milli-Q water. After the last washing step, the pH of the Milli-Q water was measured to check if it was between 6-7. If the pH exceeded 7, the washing steps were repeated. If the beads had a neutral pH, the reaction proceeded further. In the next step the glass beads were washed with 200 mL of acetone, separate them by decantation and to dry them at 80 °C for 3 h. After drying, the beads were incubated overnight in a solution of 1.26 g of maleic anhydride in 25 mL of acetone. The solution was decanted by gravity, and the beads were washed with eight volumes of 50 mL of acetone using a Buchner funnel and filtration paper. After, the beads were dried in a vacuum oven at 30 °C for 1 h in a Petri dish for increased surface exposure. The beads were transferred to a Schott flask and 300 mg of anhydrous sodium acetate and 25 mL of acetic anhydride were added sequentially. The beads were boiled for 3 h at 95 °C. After cooling, Milli-Q water was added, and the beads were stirred manually. After removing most of the solvent, the beads were transferred to a Buchner funnel and extensively washed with Milli-Q water. After this the beads were again transferred to a Schott flask and a 0.5 mg/mL solution of CD44 peptide was prepared in Milli-Q water, and incubated overnight at room temperature. The beads were transferred from the Schott flask to a Buchner funnel and washed with 200 mL of Milli-Q water until no peptide was present in the washing supernatant. The peptide in each washing volume was measured by UV-Vis spectroscopy absorbance at 280 nm, which allowed the calculation of the amount of peptide covalently bound to the glass beads. After this, the beads were dried at room temperature, and were used immediately or stored at -20 °C until use.

VII - 2.2.2. Polymerization

The preparation of the polymerization mixture started with the dilution of 39 mg of NIPAM (0.34 mmol) and 2 mg of MBA (0.013 mmol) in 98 mL of water inside a Kitasato, with manual agitation. 33 mg of TBAm (0.26 mmol) were dissolved in absolute ethanol and added to the previous mixture. For the MIP synthesized with AAc (MIP AAc), 22 µL of AAc (0.32 mmol) were diluted in 978 µL of Milli-Q water, and 100 µL of this solution (0.032 mmol) were transferred to the Kitasato. For the MIP prepared with ItAc instead (MIP ItAc), 4.16 mg (0.032 mmol) of ItAc were directly added to the Kitasato and manually agitated until dissolved. Next, 5.8 mg of APMA (0.33 mmol) were directly added to the Kitasato, and the volume was completed with Milli-Q water until the total volume was 100 mL. The Kitasato was then sealed with a cap, connected to a vacuum pump, and submerged in an ultrasound bath to be sonicated under vacuum for 10 min, and then the solution was bubbled with a stream of

N_2 for 10 min using a Pasteur pipette and then left aside while degassing. 60 g of beads previously functionalized were transferred to a 250 mL Schott Flask, and the beads were subjected to a cycle of alternate vacuum and N_2 purging for 5 min at room temperature. This alternate cycle was repeated twice. In the case of non-imprinted polymers (NIPs), 60 g of beads were weighed straight from the commercially available package into the 250 mL Schott flask. 30 mg of APS (0.13 mmol) were dissolved in 500 µL of Milli-Q water in an Eppendorf to which 30 µL of TEMED (0.33 mmol) were added. After degassing, the solution of monomers prepared inside the Kitasato was poured into the 250mL flask containing the glass beads while the headspace of the flask was purged with N_2. Sequentially, the solution of APS and TEMED, prepared in the Eppendorf, was added to the glass beads, and the vessel was capped and left to polymerize for 1 h at room temperature. From time to time, gentle manual agitation was performed.

VII - 2.2.3. Template removal

For the selective removal of the template removal from the synthesized MIP, a 20 µm porosity frit was placed inside an SPE cartridge attached to a Kitasato connected to a vacuum pump. The content of the Schott flask was transferred to the cartridge, and the vacuum was turned on. Volumes of 30 mL of room temperature Milli-Q water were poured to wash the beads carefully to avoid the beads getting dry. This step was repeated eight times to wash out unreacted monomers. After, 30 ml of Milli-Q water at 60 °C was added to the SPE cartridge containing the beads. The cartridge was capped and placed in a 60 °C water bath for 15 min. After this time, the MIP solution was collected under vacuum to the Kitasato and transferred to a Schott flask. These steps were repeated until 120 mL of solution were accumulated, and the solution was left to cool down before being stored at 4 °C until use.

VII - 2.3. MIPs and NIPs characterization

DLS studies were performed using Zetasizer Nano (NanoS) Particle Size Analyzer from Malvern Instruments Ltd. (UK). MIP or NIP samples were re-suspended in milli-Q water at a concentration of 0.01 mg/mL and placed into a polystyrene cuvette with a light pass of 1 cm to be analyzed at 25 °C using a scattering angle of 90°.

VII - 2.4. Cell culture

Cell assays were performed using MCF-7 and MDA-MB-231 breast cancer cell lines, which were cultured in RPMI medium, supplemented with 10% FBS, and 1% antibiotic solution (penicillin 100 units/mL, streptomycin 100 µg/mL). Cultures were maintained in a humidified incubator with an atmosphere of 5% CO_2 at 37 °C. Culture media were changed every two days. Cell passaging was

performed in a 1:3 split ratio. When the cells reached 80-90% confluence, they were detached using 1 mL of trypsin (0.25% trypsin/EDTA) for 3 min at 37 °C. Finally, cells were re-suspended in 5 mL of fresh medium and their concentration was determined by counting with a Neubauer camera using 0.4% trypan blue.

VII - 2.5. Immunofluorescence staining and CD44 MIP and NIP fluorescence detection

MCF-7 and MDA-MB-231 cells were seeded at 1 x 10^4 cells/well into a 96-well plate. After 24 h, fixation of cells was performed using 4% paraformaldehyde (PFA) in PBS for 20-30 min prior to 3 washing steps with PBS and subsequent permeabilization, by the addition of 0.1% Triton x100 in PBS for 8 min at room temperature. After washing with PBS, 4% FBS in PBS was added for 1 h at room temperature for the blocking of non-specific binding. Then, after washing again with PBS, Alexa Fluor® 488 anti-mouse/human CD44 Antibody 1:500 in PBS (BioLegend) was added, the plate was stored at 4 °C overnight, and then washed with 0.05% Tween 20 in PBS. The nucleus was stained with Hoescht 5 µL/mL in PBS, for 10 min at 37 °C, followed by washing with PBS. Finally, for actin staining, 1:150 phalloidin in PBS was added for 30 min at room temperature and washed with PBS.

The same procedure was followed, replacing the antibody by the MIPs/NIPs prepared at a concentration of 100 µg/mL in PBS.

VII - 3. Results and discussion

VII - 3.1. MIP characterization

MIPs designed to target the epitope of the cell surface marker CD44 were synthesized using solid-phase synthesis, using NIPAM as a thermoresponsive backbone, MBA and TEMED as initiators, and using TBAm, APMA, and AAc (MIP AAc) or ItAc (MIP ItAc) as monomers.

First, both MIPs and the corresponding NIPs were characterized in terms of size when suspended in solution through DLS (Fig. VII - 1). Both MIP AAc and MIP ItAc presented a diameter of around 50 nm, being in the nano-scale, which is within the ideal size range for cell surface targeting.[20] For the corresponding NIPs, we could observe a slight decrease in diameter, which was to be expected as the non-imprinted counterparts do not present a cavity for the target molecule, therefore reducing the size of the particle.

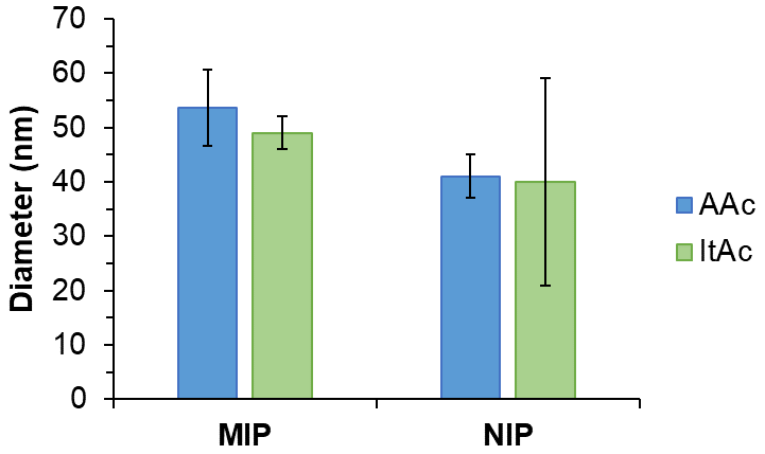

Fig. VII - 1. Average diameters determined by DLS for MIPs and NIPs synthesized for CD44 epitope.

VII - 3.2. Breast cancer cell targeting

CD44 is a cell surface glycoprotein that has been repeatedly reported as being an overexpressed biomarker in breast cancer stem cells,[19,21–23] and it has been especially correlated with breast cancer invasiveness and metastasis.[19,22,24–26] Therefore, two breast cancer cell lines expressing CD44, MCF-7 and MDA-MB-231 cell lines,[19,21,27] were selected to test the selective targeting of the CD44 surface cell marker and compared with the selectivity of the CD44 antibody *in vitro*.

First, the MCF-7 breast cancer cell line was stained with the CD44 antibody to establish the control immunostaining profile of the cancer biomarker (Fig. VII - 2 1st row).[19,27] Then, the MCF-7 cell line was incubated with MIP AAc or MIP ItAc, and the corresponding NIPs (Fig. VII - 2 rows 2 to 5). As expected, none of the NIPs presented a significant fluorescence signal, meaning that the NIPs were not specific towards the CD44 biomarker. However, MCF-7 cells incubated with CD44 MIPs presented fluorescence in both cases, suggesting that MIPs synthesized with AAc and ItAc present affinity towards CD44 expressed by these cells. Such results are in accordance with findings previously reported for fluorescence imaging of other breast cancer cell lines using MIPs targeting CD44, although comparison with CD44 biological antibody is lacking in the literature.[28]

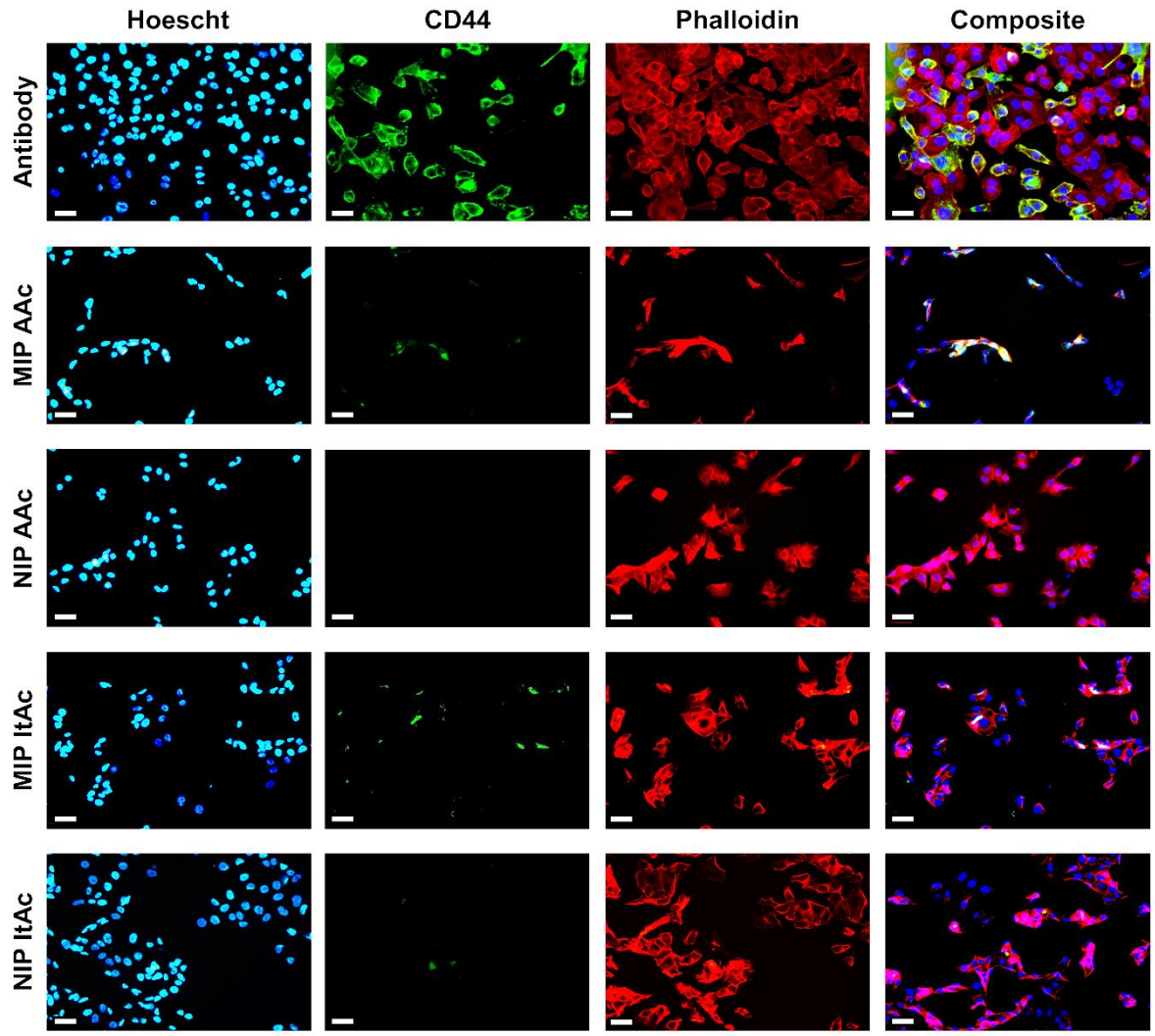

Fig. VII - 2. Fluorescence microscopy images of MCF-7 cells stained with anti-CD44 antibody (green); treated with AAc based MIPs and NIPs (green); and ItAc based MIPs and NIPs (green). Cell nuclei were stained with Hoechst dye (blue) and the actin cytoskeleton with Phalloidin (red). Scale bars = 50 µm.

To allow the analysis of MIPs specificity towards CD44 *in vitro*, the rate of CD44 positive MCF-7 cells was quantified from immunofluorescence with CD44 antibody and detection by AAc and ItAc based MIPs (Fig. VII - 3). Through fluorescence quantification, we could see that a higher rate of MCF-7 cells can be detected with the MIP AAc, as around 18% of MCF-7 cells are CD44 positive (stained by the commercial antibody) and around 15% of MCF-7 cells can be detected with the MIP AAc, while cells detected with MIP ItAc are below 10%; both cases being significantly higher than for the corresponding NIP. These findings suggest that the AAc-based MIP has higher affinity and specificity towards the CD44 biomarker expressed by MCF-7 breast cancer cells.

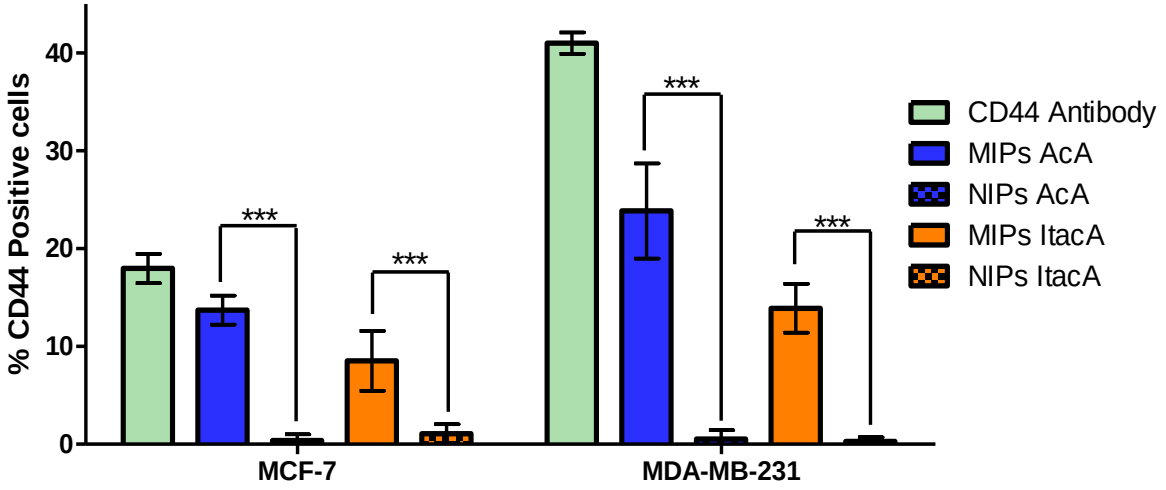

Fig. VII - 3. Rate of CD44 positive MCF-7 and MDA-MB-231 cells quantified from immunofluorescence with CD44 antibody and detection by AAc and ItAc based MIPs and NIPs. Values are expressed as mean ± SD (n=3). *** represent $p \leq 0.001$ between the MIPs and respective NIPs (negative control) (one-way ANOVA with Tukey's multiple comparisons test).

Similarly to the MCF-7 cell line, the MDA-MB-231 breast cancer cell line underwent staining with the CD44 antibody to establish the baseline immunostaining profile of the cancer biomarker (Fig. VII - 4 1st row).[19,27] Subsequently, these cells were exposed to either MIP AAc or MIP ItAc, and to their corresponding NIPs (Fig. VII - 4 rows 2 to 5). As anticipated, neither type of NIP exhibited a significant fluorescence signal, indicating their lack of specificity towards the CD44 biomarker as observed for MCF-7 cells. Conversely, MDA-MB-231 cells treated with the MIPs displayed fluorescence in both cases, showing that the MIPs demonstrate affinity towards CD44 expressed by these breast cancer cells. Such results agree with findings previously reported for fluorescence imaging of breast cancer cell lines, including MDA-MB-231 cells, using MIPs targeting CD44, although comparison with CD44 biological antibody is lacking in the literature.[28]

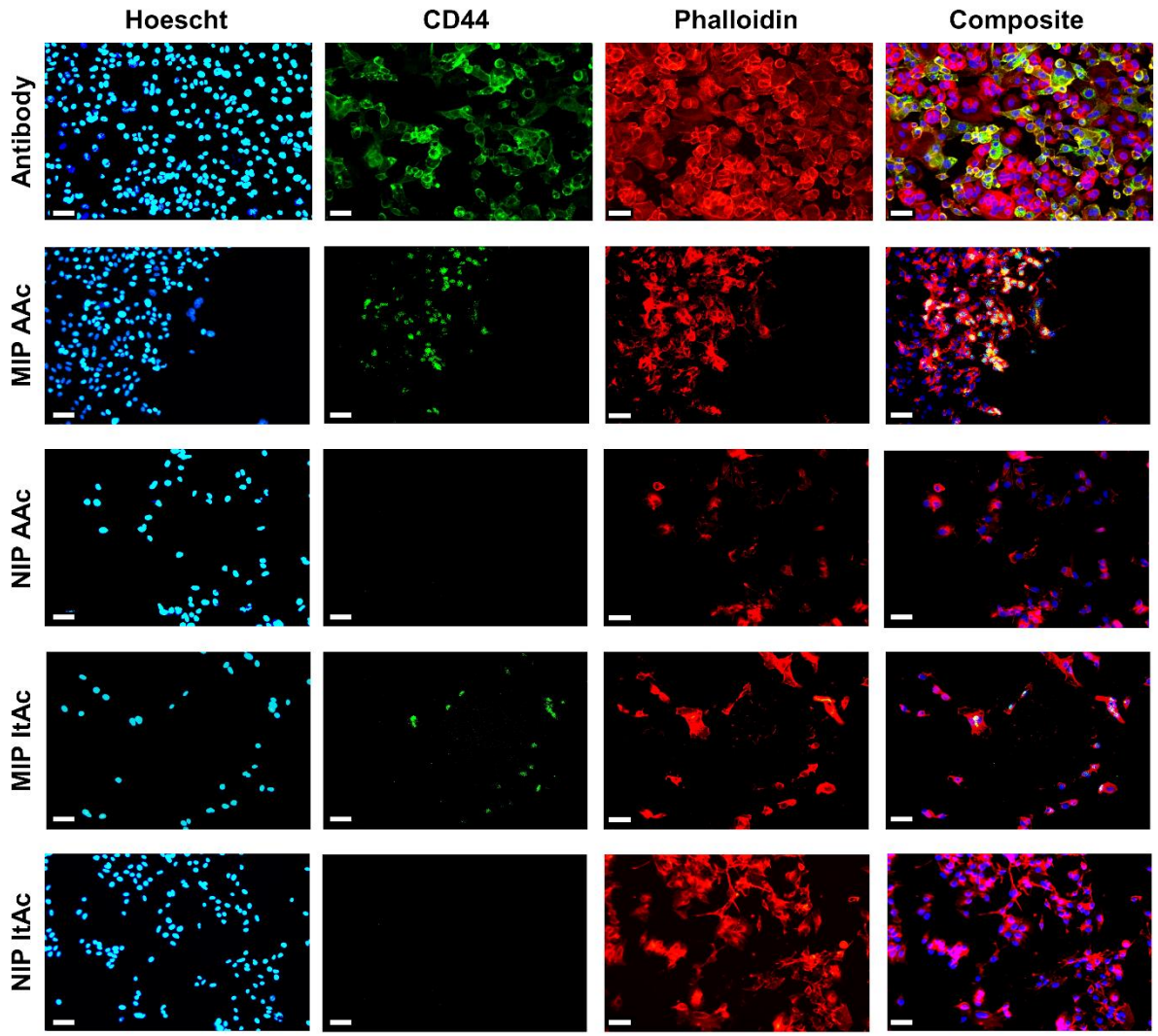

Fig. VII - 4. Fluorescence microscopy images of MDA-MB-231 cells stained with anti-CD44 antibody (green); treated with AAc based MIPs and NIPs (green); and ItAc based MIPs and NIPs (green). Cell nuclei were stained with Hoechst dye (blue) and the actin cytoskeleton with Phalloidin (red). Scale bars = 50 µm.

To enable the assessment of MIP *in vitro* specificity towards CD44, the percentage of CD44-positive MDA-MB-231 cells was measured using immunofluorescence with a CD44 antibody and detection by AAc and ItAc based MIPs and NIPs (Fig. VII - 3). The analysis showed that around 25% of MDA-MB-231 cells were identifiedwith MIP-AAccompared to only around 15% for MIP-ItAc, being these values higher than the ones found for the corresponding NIPs. However, the CD44 commercial antibody detected around 40% of positive cells. Again, these findings suggest that the AAc-based MIP has higher affinity and specificity towards the CD44 biomarker expressed by these cells.

Furthermore, we can observe that in the specific case of MCF-7 cells, there is only a difference of 3% in staining of CD44 positive cells between the MIP-AAc (15%) and the commercial loss of

fluorescence signal of 3% for the MIP AAc (15%) when compared to the CD44 antibody (18%). This leads us to conclude that the affinity and specificity of the AAc-based MIP are very similar to the "natural" antibody, in these assay conditions, suggesting a good performance of this "synthetic antibody". Thus, these MIPs can be designed to have high affinity and selectivity towards CD44, enabling their use in various applications such as imaging, diagnostics, and targeted drug delivery for breast cancer treatment.[29]

VII - 4. Conclusions

CD44 is a cell surface glycoprotein that has been identified as a marker for breast cancer cells. It is crucial to develop MIPs that can specifically bind to CD44, allowing for effective detection and targeting of breast cancer cells. These MIPs can be designed to have high affinity and selectivity towards CD44, enabling their use in various applications such as imaging, diagnostics, and targeted drug delivery for breast cancer treatment. Additionally, MIPs for CD44 can also be utilized in the development of biosensors or microarrays for early detection and monitoring of breast cancer progression.

The MCF-7 and MDA-MB-231 breast cancer cell lines under study showed the expected expression patterns when analyzed using immunofluorescence staining with a monoclonal antibody targeting the CD44 cancer biomarker. As expected, NIPs did not show significant recognition of CD44 biomarker, with detection levels close to baseline under all experimental conditions. Consistent with the differential expression seen in immunostaining, MIPs identified higher levels of CD44 in MDA-MB-231 cells compared to MCF-7 cells. However, when we compared the performance of the two MIP formulations, it was observed that MIPs AAc demonstrated better detection sensitivity for CD44 than MIPs ItAc in both cell lines. This was especially evident in the case of MCF-7 cells, where there was only a 3% difference compared to commercial antibody detection.

Nonetheless, despite their superior performance, quantitative CD44 detection with the best-performing MIPs AAc was still lower than that achieved using the monoclonal CD44 antibody for MDA-MB-231 cells, indicating performance variation based on cell type. This emphasizes the potential challenges in imprinting this CD44 protein with accuracy comparable to biological antibodies.

Overall, incorporation of MIPs for CD44 into diagnostic and therapeutic strategies could potentially improve the accuracy and effectiveness of breast cancer detection, monitoring, and treatment, providing a potential lower cost replacement to antibodies for detection and targeting of breast cancer cells.

VII - 5. References

(1) Pilvenyte, G.; Ratautaite, V.; Boguzaite, R.; Ramanavicius, A.; Viter, R.; Ramanavicius, S. Molecularly Imprinted Polymers for the Determination of Cancer Biomarkers. *Int J Mol Sci* **2023**, *24* (4). https://doi.org/10.3390/ijms24044105.

(2) Resina, L.; Alemán, C.; Ferreira, F. C.; Esteves, T. Protein-Imprinted Polymers: How Far Have "Plastic Antibodies" Come? *Biotechnology Advances*. **2023**, 68. https://doi.org/10.1016/j.biotechadv.2023.108220.

(3) Wang, Y.; Zhang, Z.; Jain, V.; Yi, J.; Mueller, S.; Sokolov, J.; Liu, Z.; Levon, K.; Rigas, B.; Rafailovich, M. H. Potentiometric Sensors Based on Surface Molecular Imprinting: Detection of Cancer Biomarkers and Viruses. *Sens Actuators B Chem* **2010**, *146* (1), 381–387. https://doi.org/10.1016/j.snb.2010.02.032.

(4) Santos, A. R. T.; Moreira, F. T. C.; Helguero, L. A.; Sales, M. G. F. Antibody Biomimetic Material Made of Pyrrole for CA 15-3 and Its Application as Sensing Material in Ion-Selective Electrodes for Potentiometric Detection. *Biosensors (Basel)* **2018**, *8* (8). https://doi.org/10.3390/bios8010008.

(5) Pilvenyte, G.; Ratautaite, V.; Boguzaite, R.; Plausinaitis, D.; Ramanaviciene, A.; Bechelany, M.; Ramanavicius, A. Molecularly Imprinted Polymers for the Recognition of Biomarkers for Some Neurodegenerative Diseases. *J Pharm Biomed Anal* **2023**, *228* (115343).

(6) Zukauskas, S.; Rucinskiene, A.; Ratautaite, V.; Ramanaviciene, A.; Pilvenyte, G.; Bechelany, M.; Ramanavicius, A. Electrochemical Biosensor for the Determination of Specific Antibodies against SARS-CoV-2 Spike Protein. *Int J Mol Sci* **2023**, *24* (1). https://doi.org/10.3390/ijms24010718.

(7) Liustrovaite, V.; Pogorielov, M.; Boguzaite, R.; Ratautaite, V.; Ramanaviciene, A.; Pilvenyte, G.; Holubnycha, V.; Korniienko, V.; Diedkova, K.; Viter, R.; Ramanavicius, A. Towards Electrochemical Sensor Based on Molecularly Imprinted Polypyrrole for the Detection of Bacteria—Listeria Monocytogenes. *Polymers (Basel)* **2023**, *15* (1597). https://doi.org/10.3390/polym15071597.

(8) Piletsky, S.; Canfarotta, F.; Poma, A.; Bossi, A. M.; Piletsky, S. Molecularly Imprinted Polymers for Cell Recognition. *Trends Biotechnol* **2019**, *xxx* (xxx), 1–20. https://doi.org/10.1016/j.tibtech.2019.10.002.

(9) Haupt, K.; Medina Rangel, P. X.; Bui, B. T. S. Molecularly Imprinted Polymers: Antibody Mimics for Bioimaging and Therapy. *Chem Rev* **2020**, *120* (17), 9554–9582. https://doi.org/10.1021/acs.chemrev.0c00428.

(10) Peng, H.; Qin, Y.-T.; He, X.-W.; Li, W.-Y.; Zhang, Y. Epitope Molecularly Imprinted Polymer Nanoparticles for Chemo-/Photodynamic Synergistic Cancer Therapy Guided by Targeted

Fluorescence Imaging. *ACS Appl Mater Interfaces* **2020**. https://doi.org/10.1021/acsami.0c00468.

(11) Yazdani, Z.; Yadegari, H.; Heli, H. A Molecularly Imprinted Electrochemical Nanobiosensor for Prostate Specific Antigen Determination. *Anal Biochem* **2019**, *566*, 116–125.

(12) Tang, P.; Wang, Y.; Huo, J.; Lin, X. Love Wave Sensor for Prostate-Specific Membrane Antigen Detection Based on Hydrophilic Molecularly-Imprinted Polymer. *Polymers (Basel)* **2018**, *10* (5). https://doi.org/10.3390/polym10050563.

(13) Zhang, Y.; Deng, C.; Liu, S.; Wu, J.; Chen, Z.; Li, C.; Lu, W. Active Targeting of Tumors through Conformational Epitope Imprinting. *Angewandte Chemie - International Edition* **2015**, *54* (17), 5157–5160. https://doi.org/10.1002/anie.201412114.

(14) Liu, X.; Zhang, P.; Song, H.; Tang, X.; Hao, Y.; Guan, Y.; Chong, T.; Hussain, S.; Gao, R. Unveiling a PH-Responsive Dual-Androgen-Blocking Magnetic Molecularly Imprinted Polymer for Enhanced Synergistic Therapy of Prostate Cancer. *ACS Appl Mater Interfaces* **2024**, *16*, 4348–4360. https://doi.org/10.1021/acsami.3c13732.

(15) Chen, C.; Zhao, S.; Karnad, A.; Freeman, J. W. The Biology and Role of CD44 in Cancer Progression: Therapeutic Implications. *J Hematol Oncol* **2018**, *11* (1), 1–23. https://doi.org/10.1186/s13045-018-0605-5.

(16) Smith, S. M.; Cai, L. Cell Specific CD44 Expression in Breast Cancer Requires the Interaction of AP-1 and NFκB with a Novel Cis-Element. *PLoS One* **2012**, *7* (11), e50867. https://doi.org/10.1371/JOURNAL.PONE.0050867.

(17) Yan, W.; Chen, Y.; Yao, Y.; Zhang, H.; Wang, T. Increased Invasion and Tumorigenicity Capacity of CD44+/CD24- Breast Cancer MCF7 Cells in Vitro and in Nude Mice. *Cancer Cell Int* **2013**, *13* (1), 62. https://doi.org/10.1186/1475-2867-13-62.

(18) Li, W.; Qian, L.; Lin, J.; Huang, G.; Hao, N.; Wei, X.; Wang, W.; Liang, J. CD44 Regulates Prostate Cancer Proliferation, Invasion and Migration via PDK1 and PFKFB4. *Oncotarget* **2017**, *8* (39), 65143–65151. https://doi.org/10.18632/oncotarget.17821.

(19) Smith, S. M.; Cai, L. Cell Specific CD44 Expression in Breast Cancer Requires the Interaction of AP-1 and NFκB with a Novel Cis-Element. *PLoS One* **2012**, *7* (11), e50867. https://doi.org/10.1371/JOURNAL.PONE.0050867.

(20) Yang, T.; Zhai, J.; Hu, D.; Yang, R.; Wang, G.; Li, Y.; Liang, G. “Targeting Design” of Nanoparticles in Tumor Therapy. *Pharmaceutics* **2022**, *14* (9). https://doi.org/10.3390/PHARMACEUTICS14091919.

(21) Xu, H.; Niu, M.; Yuan, X.; Wu, K.; Liu, A. CD44 as a Tumor Biomarker and Therapeutic Target. *Experimental Hematology & Oncology 2020 9:1* **2020**, *9* (1), 1–14. https://doi.org/10.1186/S40164-020-00192-0.

(22) Wu, K.; Xu, H.; Wu, K.; Tian, Y.; Liu, Q.; Han, N.; Yuan, X.; Zhang, L.; Wu, G. S. CD44 Correlates with Clinicopathological Characteristics and Is Upregulated by EGFR in Breast Cancer. *Int J Oncol* **2016**, *49* (4), 1343–1350. https://doi.org/10.3892/IJO.2016.3639/HTML.

(23) Al-Othman, N.; Alhendi, A.; Ihbaisha, M.; Barahmeh, M.; Alqaraleh, M.; Al-Momany, B. Z. Role of CD44 in Breast Cancer. *Breast Dis* **2020**, *39* (1), 1–13. https://doi.org/10.3233/BD-190409.

(24) Vadhan, A.; Hou, M. F.; Vijayaraghavan, P.; Wu, Y. C.; Hu, S. C. S.; Wang, Y. M.; Cheng, T. L.; Wang, Y. Y.; Yuan, S. S. F. CD44 Promotes Breast Cancer Metastasis through AKT-Mediated Downregulation of Nuclear FOXA2. *Biomedicines* **2022**, *10* (10). https://doi.org/10.3390/BIOMEDICINES10102488/S1.

(25) Louderbough, J. M. V.; Schroeder, J. A. Understanding the Dual Nature of CD44 in Breast Cancer Progression. *Molecular Cancer Research* **2011**, *9* (12), 1573–1586. https://doi.org/10.1158/1541-7786.MCR-11-0156/79451/AM/UNDERSTANDING-THE-DUAL-NATURE-OF-CD44-IN-BREAST.

(26) Hu, S.; Shi, X.; Liu, Y.; He, Y.; Du, Y.; Zhang, G.; Yang, C.; Gao, F. CD44 Cross-Linking Increases Malignancy of Breast Cancer via Upregulation of p-Moesin. *Cancer Cell Int* **2020**, *20* (1), 1–10. https://doi.org/10.1186/S12935-020-01663-4/FIGURES/5.

(27) El-Schich, Z.; Zhang, Y.; Göransson, T.; Dizeyi, N.; Persson, J. L.; Johansson, E.; Caraballo, R.; Elofsson, M.; Shinde, S.; Sellergren, B.; Wingren, A. G. Sialic Acid as a Biomarker Studied in Breast Cancer Cell Lines In Vitro Using Fluorescent Molecularly Imprinted Polymers. *Applied Sciences 2021, Vol. 11, Page 3256* **2021**, *11* (7), 3256. https://doi.org/10.3390/APP11073256.

(28) Wang, H. Y.; Cao, P. P.; He, Z. Y.; He, X. W.; Li, W. Y.; Li, Y. H.; Zhang, Y. K. Targeted Imaging and Targeted Therapy of Breast Cancer Cells via Fluorescent Double Template-Imprinted Polymer Coated Silicon Nanoparticles by an Epitope Approach. *Nanoscale* **2019**, *11* (36), 17018–17030. https://doi.org/10.1039/C9NR04655K.

(29) Cui, M.; Sun, X.; Liu, R.; Du, M.; Song, X.; Wang, S.; Hu, W.; Luo, X. A Dual-Responsive Electrochemical Biosensor Based on Artificial Protein Imprinted Polymers and Natural Hyaluronic Acid for Sensitive Recognition towards Biomarker CD44. *Sens Actuators B Chem* **2022**, *371*, 132554. https://doi.org/10.1016/J.SNB.2022.132554.

Chapter VIII – Self-healable, stretchable and conductive PEDOT:PSS hydrogels based on riboflavin and UV-induced gelatin crosslinking for skin regeneration

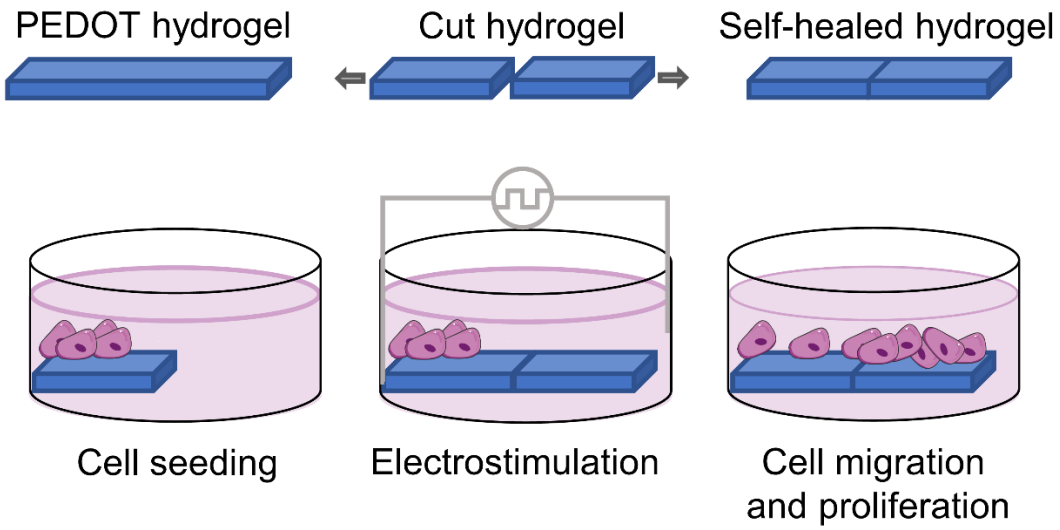

VIII - 1. Introduction

Hydrogels are crosslinked three-dimensional networks of polymer chains that have the ability to absorb water and swell while being water-insoluble. The crosslinking degree of hydrogels dictates their mechanical properties, elasticity, and physical integrity.[1,2] Although the swelling capacity of a hydrogel is related to its crosslinking degree, it can also be related to the functional groups present in the polymer chains, usually highly hydrophilic groups, like hydroxyl and carboxylic acid groups, promoting this property.[3,4] The various applications of hydrogels are determined by their synthetic methodologies and their response to different physicochemical stimuli,[5,6] including applied strain,[7] pH,[8,9] temperature,[10,11] and ionic concentration.[12,13]

Hydrogels are highly biocompatible, presenting properties similar to human tissues that make them suitable to be used in various biomedical applications, including drug delivery,[8,9,14] tissue engineering,[11] bioelectronics,[15] and wound healing.[14,16] The latter can be considered one of the most important biomedical applications of hydrogels nowadays, as innovative solutions for effective wound treatment are needed in the market. This is due to the increasing burden of chronic wounds among patients, with more incidence in a growing geriatric population and the increased prevalence of chronic diseases that cause chronic wounds, such as diabetes, obesity, and cancer.[17–19]

Hydrogels are very promising to be used as wound dressings as they are compatible with exudating and dry wounds.[16] Their mechanical properties, such as low Young's modulus, corresponding to softer materials, and stretchability make hydrogels malleable enough to be applied on top of injured skin.[16,20–23] Other interesting properties may also be imparted in the hydrogels. When compared with conventional dressings, hydrogels can also promote an accelerated healing of the skin, allowing skin regeneration in a humid environment and preventing the formation of large scar tissue, and support antibacterial compounds/polymers to prevent wound infection.[16,20–23]

Several clinical trials have shown that electrical stimulation (ES) using alternating current (AC) can aid in accelerating wound healing and diminishing the formation of scar tissue.[24–26] The use of ES through electroactive wound dressings appears to be very promising, as skin is responsive to electric signals and has an endogenous conductivity varying from 10^{-2} to 260 mS/m depending on testing conditions.[27–30] Applying an external electric field leads to the migration of skin cells, like fibroblasts,[31,32] keratinocytes,[33–35] and endothelial cells,[36,37] to the wound site, therefore, speeding up skin tissue regeneration. Several technologies have been developed using ES to promote skin regeneration, including electrodes coupled to wound dressings or gauzes that were soaked with conducting saline solutions to promote skin tissue recovery.[30] Similar effects could be achieved by introducing CPs in the hydrogel structure.

An interesting class of hydrogels can be achieved through the gelation of a polymer with fixed charges through their chains, leading to intrinsically ion-conducting hydrogels.[38] Electroconductive hydrogels can also be synthesized by incorporating an electronically CP within the hydrogel network, using for example PANI[23] or PEDOT:PSS.[39,40]. While in the swollen state, hydrogels will show ionic conduction of electricity, due to the presence of water and ions, while the presence of a CP may also provide the hydrogels with an electronic conduction contribution.

Gelatin has been explored for the synthesis of hydrogels for skin tissue engineering and wound healing applications, since it is a natural polymer obtained from hydrolysis of collagen, which is the main component of the extracellular matrix of the skin.[41–43] However, gelatin has poor mechanical strength and suffers denaturation at relatively low temperature (around 40 °C), with triple helices transitioning to individual coiled chains.[44] As such, gelatin must be modified to improve its properties to make it suitable for skin tissue engineering. Some strategies include crosslinking using glutaraldehyde, or modifying it with methacrylate to increase the crosslinking degree of the obtained hydrogel.[42,43,45] Another strategy includes blending gelatin with other components to tune the properties of the hydrogel, for example using a mixture of glycerol and citric acid.[44] Gelatin can be processed into an electroconductive hydrogel when blended with an electroconductive polymer, which makes it suitable for ES applications.

In clinical settings, riboflavin (RF) has been used as a catalyst under UV light exposure to promote crosslinking of collagen present in corneal tissue to treat keratoconus, a disease characterized by thinning of the cornea that reduces mechanical strength of the tissue.[46,47] Studies in the literature report that topic application of RF confers collagen fibrils a higher resistance to enzymatic degradation.[47,48] The medical protocol in current use starts with the application of 20 µL of a 2.657 mM RF solution every 2 min for 30 min, followed by 30 min of UV light (360-370 nm) exposure, while continuing the application of the solution. This method has also been recently applied to improve biomechanical properties of decellularized heart valves and to diminish their degradation rate.[49] The RF-induced crosslinking of collagen fibrils consists of a photooxidative crosslinking mechanism mediated by RF, with this molecule acting as a photosensitizer. UV light excites RF to a singlet state that rapidly undergoes an intersystem crossing to the triplet state, which serves as a reactive intermediate for electron transfer to collagen, with the formed radical leading to covalent bond formation. It has also been proposed that singlet oxygen generated by the triplet state of UV-excited RF might react with carbonyl groups in certain amino acids to generate an imidazolone. This intermediate will then react with hydroxyl groups in other amino acids promoting crosslinks between collagen fibrils.[46] The most commonly reported amino acids involved in this type of crosslinking mechanism are tyrosine, histidine, threonine, hydroxyproline, and hydroxylysine,[46] which are all

present in the composition of bovine, porcine, and human skin gelatin derived from collagen hydrolysis.[50]

In this chapter, we describe, for the first time, the development of an electroconductive hydrogel composed of PEDOT:PSS, gelatin (Gel), and RF for UV-induced crosslinking (PEDOT/Gel/RFUV) for skin tissue engineering applications with ES. The use of RF as a UV light-mediated crosslinking allows us to produce our hydrogel with superior mechanical properties, while maintaining typical high biocompatibility. The incorporation of PEDOT:PSS also conferred self-regeneration properties to the PEDOT/Gel/RFUV hydrogel, while maintaining favorable mechanical properties. Finally, the obtained hydrogel was biocompatible and allowed successful fibroblast migration and colonization under ES. Overall, our PEDOT/Gel/RFUV hydrogel has potential clinical applications, including wound healing, skin tissue engineering, and bioelectronics.

VIII - 2. Materials and methods

VIII - 2.1. Materials

Gelatin from porcine skin type A (gel strength 300), (-)-riboflavin (RF, > 98%), and PBS solution, sodium hydroxide pellets (analytical reagent grade), and platinum (Pt) wire (0.25 mm diameter) were purchased from Sigma-Aldrich (St. Louis, MO, USA). PEDOT:PSS, formulation Clevios™ PH1000 (PEDOT:PSS weight ratio of 1:2.5 and dispersion with 1.0-1.3% weight solid content) was purchased from Heraeus (Hanau, Germany). LIVE/DEAD™ Viability/Cytotoxicity Kit, CellTrace™ calcein red-orange AM, DMEM, FBS, trypsin-EDTA, antibiotic-antimycotic solution, and penicillin-streptomycin 10000 U/mL (P/S) were purchased from ThermoFisher Scientific (Waltham, MA, USA). Human umbilical vein endothelial cells (HUVECs) and endothelial growth medium-2 (EGM-2) were purchased from Lonza (Basel, Switzerland). Mouse fibroblasts (L-929) were obtained from frozen stocks of the cell bank available at Stem Cell Engineering Research Group (SCERG), Institute for Bioengineering and Biosciences (iBB) at the Instituto Superior Técnico (IST).

VIII - 2.2. Synthesis of hydrogels

Gelatin and RF (Gel/RF) hydrogels were prepared in MilliQ water at a concentration of 15% (m/v) porcine gelatin type A and varying concentrations of RF at pH 7 or pH 12. Solutions were prepared at 50 °C and stirred for at least 30 min until full dissolution of gelatin. Gel/RF hydrogels were submitted to different UV light exposure times (0, 2, 5, 15, 30, 45 min) to assess the degree of success of UV-catalyzed crosslinking of gelatin (Gel/RFUV).

PEDOT:PSS, gelatin and RF hydrogels were prepared using a 211 mM RF solution, replacing water with PEDOT:PSS dispersion as received (100% PEDOT/Gel/RF hydrogels) or 1:1 water: PEDOT:PSS mixture (50% PEDOT/Gel/RF hydrogels). In both cases the dispersions were basified to pH 12, heated at 60 °C and stirred for at least 30 min until full dissolution of gelatin. PEDOT/Gel/RF hydrogels were submitted to none (PEDOT/Gel/RF) or 45 min UV light (λ_{max} = 367 nm, total power = 2.77 mW/cm^2) exposure time to promote UV-catalyzed crosslinking of gelatin (PEDOT/Gel/RFUV).

VIII - 2.3. Characterization of hydrogels

VIII - 2.3.1. Fourier-transform infrared (FTIR) spectroscopy

FTIR spectroscopy was performed using a Spectrum Two FT-IR Spectrometer (PerkinElmer, Waltham, MA, USA), equipped with a Pike Technologies MIRacle ATR accessory. Transmittance spectra of as prepared hydrogel samples were obtained in the 400 to 4000 cm^{-1} spectral region (resolution of 4 cm^{-1}, 8 scans of data accumulation) at room temperature and an automatic baseline correction treatment was applied using the acquisition software PerkinElmer Spectrum IR.

VIII - 2.3.2. Differential scanning calorimetry (DSC)

DSC analyses were performed for the Gel/RF, Gel/RFUV, 100% PEDOT/Gel/RF and 100% PEDOT/Gel/RFUV hydrogels using a Netzsch DSC-200-F3 Maia® (Netzsch Holding, Selb, Germany), all in the dry form. In all cases, DSC was performed at 5 °C min^{-1} from -30 °C to 150 °C for 1 cycle. For gelatin raw material control sample, 3 cycles were conducted. Data obtained were analyzed with the Software NETZSCH Proteus®.

VIII - 2.3.3. Swelling ratio

Hydrogels were cut into 10 mm x 10 mm samples. Freshly made samples were dried at RT over a week until no mass changes were detectable, weighed, and incubated in 2 mL of MilliQ water at RT. Samples were reweighed after 48 h. Swelling ratios (SR) were calculated through Eq. VIII - 1, where $m_{48\,h}$ represents the weight of the sample after being hydrated for 48h and $m_{0\,h}$ represents the weight of sample freshly prepared.

$$SR\ (\%) = \frac{m_{48\,h} - m_{0\,h}}{m_{0\,h}} \times 100 \qquad \text{(VIII - 1)}$$

VIII - 2.3.4. Self-healing process

Hydrogels were cut into 30 mm × 10 mm samples, and then each sample was cut in two halves with a blade or torn using uniaxial tension. Cut or torn halves were wetted or not with MilliQ water, placed in contact in a plastic Petri dish and incubated at 4, 20, 37, 45 and 70 ^{o}C in a (50-60)% humidified atmosphere.

VIII - 2.3.5. Contact angle

Contact angle measurements of the hydrogels were performed using glycerol in the sessile drop technique by a Krüss DSA25B goniometer (Krüss GmbH, Hamburg, Germany). Drop Shape Analysis 4 Software was instructed to take measurements of the left and right angles every 5 s for 2 min. At least 10 measurements with deviation less than 1% per sample were considered for measuring the contact angle of the droplet with the surface of the sample (n≥5).

VIII - 2.3.6. Cyclic voltammetry (CV)

CV scans were run using working and auxiliary carbon screen printed electrodes (SPEs) and Ag|AgCl reference electrode (Metrohm DropSens), connected to a potentiostat (400B Electrochemical Analyzer, CH Instruments). Hydrogels were cut in 10 mm × 10 mm samples. Samples were dipped in PBS 0.01 M, pH 7.4 and placed on top of the SPE. For RF solution scans, a 5 mM RF solution was prepared and basified at pH 12, and SPEs were dipped in the solution during runs. Cycles were run in a potential window ranging from -1.5 V to +1.0 V, considering different scan rates (from 0.01 V/s to 0.4 V/s).

VIII - 2.3.7. Four-contact electroconductivity measurement

Hydrogels were previously dried and their electroconductivity was evaluated using the 4-contact electroconductivity measurement technique. Four 50 nm thick gold stripes were deposited using a thermal evaporation system Edwards Coating System E 306A (Edwards, Irvine, CA, USA) to improve the electrical contact between the samples (dry hydrogels) and the probes of the measurement equipment. The electroconductivity of three different films was measured by the four-point probe method, using a current source Keithley DC 2400 power source (Keithley Instruments, Cleveland, OH, USA) and an Agilent 34401A multimeter (Agilent Technologies, Santa Clara, CA, USA). Finally, the thickness of the samples was measured using a caliper.

VIII - 2.3.8. Electrochemical impedance spectroscopy (EIS)

Hydrogels were cut into 30 mm × 10 mm samples (*n*=5) and kept in MilliQ water until EIS was performed. Two stainless steel plates were put in contact with the hydrogels forming a sandwich, and the crocodile clips were connected to the plates. The impedance spectra were recorded with the PalmSens4 potentiostat/galvanostat (PalmSens BV, The Netherlands) from 1 MHz to 0.02 Hz with a fixed applied AC potential of 0.01 V with respect to the open circuit potential. EIS data analyses were performed using the software PSTrace 5 (version 5.8.1704, build 29098 f, PalmSens BV, The Netherlands). Equivalent circuit analyses were done by fitting the data using the Levenberg–Marquardt algorithm.

VIII - 2.3.9. Mechanical tests

Mechanical properties of the hydrogels were assessed by a uniaxial tensile test using a texture analyzer TA.XT ExpressC (Stable Micro Systems, Godalming, UK) equipped with 50 N tensile grips, and a constant crosshead speed of 0.25 mm/min. Samples were cut into dog-bone specimens (working length of 20 mm, width of 3.85 mm, and thickness of 3.5 mm, *n*=5). Young's modulus was esteemed from the (0-15)% strain linear region in the nominal stress−strain curve and the ultimate tensile strength and maximum extension were taken from the highest peak of the nominal stress-strain curve.

VIII - 2.3.10. Load bearing capacity

The maximum load sustained by 100% PEDOT/Gel/RFUV hydrogel samples (30 mm × 10 mm) was evaluated. Binder clips were placed at the edges of the sample. One of the binder clips was secured to a spring scale held in a support stand, and a weight was secured to the other binder clip. The weight the sample could withstand without breaking was assessed and pictures were taken.

VIII - 2.4. *In vitro* assays

VIII - 2.4.1. L-929 and HUVEC cell culture

L-929 cells were cultured in T-flasks (75 cm^2) in DMEM supplemented with 10% FBS and 1% antibiotic-antimycotic solution, at 37 ^oC and 5% CO_2, with medium changed every 2 days. Cells were passaged at 80 to 90% confluency by incubation with trypsin-EDTA 0.1% solution for 5 min at 37 ^oC and subcultured at a 1:3 split ratio. HUVECs were expanded in EGM-2 medium and kept at 37 °C, with 5% CO_2 in a humidified atmosphere. The medium was renewed every 3 days.

VIII - 2.4.2. Biocompatibility

To assess the biocompatibility of 100% PEDOT/Gel/RFUV hydrogels, these were sterilized by immersion in antimycotic and antibiotic solution for 3 days. The sterilized materials (discs with top face area of 2 cm^2) were incubated with 2 mL of EGM-2 at 37 ^oC for 1 h. Medium was removed and HUVECs were seeded on the hydrogels at a density of 2.5×10^4 cells/cm^2 and incubated at 37 ^oC for 1 h. Cells were washed twice with PBS and stained for 20 min using the LIVE/DEAD™ Viability/Cytotoxicity Kit, according to the manufacturer protocol for mammalian cells. After washing with PBS, cells were incubated with EGM-2 at 37 ^oC for 3 h. Imaging of the external membrane of living cells with calcein was obtained using a fluorescence microscope (LEICA DMI 3000B, Leica camera system, Wetzlar, Germany).

VIII - 2.4.3. Electrostimulation for skin regeneration

100% PEDOT/Gel/RFUV hydrogels with disc shape (top face area of 2 cm^2) were sterilized, cut in 2 halves and incubated with DMEM/FBS at 37 ^oC overnight. A Pt wire was attached to one half of the material and another Pt wire was glued to the wall of the well plate and submerged in medium. L-929 cells were seeded in one half of the disc that was in contact with the Pt wire, at a cell density of 1 x 10^6 cells/cm^2 and incubated at 37 ^oC for 1 h. Cells were washed twice with PBS and stained for 20 min with 2 µM calcein red-orange AM in DMEM/FBS. After washing with PBS, cells were incubated with DMEM/FBS at 37 ^oC for 1 h, and an empty half disc was placed in contact with the seeded half disc. The Pt wires (1 cm apart) serving as electrodes were connected to a power source and electrostimulation was performed for 1 h using a square wave alternating current (AC, -200 mV to 200 mV, frequency of 100 Hz). After 1.5 h resting, imaging of the external membrane of living cells with calcein red-orange AM was obtained using a fluorescence microscope (LEICA DMI 3000B, Leica camera system, Wetzlar, Germany).

VIII - 2.5. Statistical analysis

Statistical analysis of the data was performed using Microsoft Excel, with all results being presented as mean values ± standard deviations. Analysis of variance (ANOVA) was performed for the datasets. A post hoc Welch's unequal variances t-test was used to determine significant differences between independent populations. *p-value<0.05 indicates a significant result and **p-value<0.01 indicates a very significant result.

VIII - 3. Results and discussion

VIII - 3.1. Synthesis and characterization of hydrogels

VIII - 3.1.1. Optimization of pH, RF and PEDOT:PSS concentration and crosslinking

Gelatin and PEDOT:PSS based hydrogels crosslinked using RF and UV light were fabricated to be used as a smart, wear-and-tear resistant wound dressing for skin tissue regeneration. Firstly, optimization of the fabrication process was performed by varying both the final RF concentration (15 to 316.5 mM) and the pH of the corresponding RF solution in water. Full solubilization of RF could only be achieved at $12 \leq pH < 12.5$ for all the concentrations, otherwise obtaining a suspension. Hydrogel formation took place independently of RF concentration in the investigated concentration range, indicating that gelation properties of gelatin were not affected by the presence of basified RF.

Gel/RF hydrogels, prepared using different concentrations of RF, were exposed to UV light for various times (2 to 45 min) to promote crosslinking of gelatin, with the degree of crosslinking being analyzed by FTIR (Fig. VIII - 1). In Gel/RF hydrogels prepared with 15 and 105.5 mM RF concentrations (Fig. VIII - 1 A-D), no noticeable difference was found in spectra recorded with increasing crosslinking reaction time (up to 45 min). This seems to indicate that no significant crosslinking occurs. However, for the 211 mM RF concentration (Fig. VIII - 1 E- F), some differences in the FTIR spectra are noticeable when the UV exposure time increases from 30 to 45 min in the peaks around the 500-800 cm^{-1} region, suggesting the cleavage of C=C bonds. While the precise molecular mechanism of RF crosslinking is complex and needs to be further studied, the literature agrees that the RF crosslinking reaction can induce the molecular rearrangement of chemical bonds.[46,47] Some of the most known bond rearrangements occur with the imidazole groups of histidine.[51] However, such rearrangement can potentially occur with other amino acids, including hydroxytyrosine and proline.[52] It is possible that the changes observed in the FTIR spectrum of the sample Gel/RFUV 45 min can be a consequence of such rearrangement, indicating successful crosslinking of gelatin. All other peaks remain constant, namely peaks at 1241 cm^{-1} and 1357 cm^{-1} (C–N stretching), 1413 cm^{-1} (S=O stretching), 1476 cm^{-1} (C–H bending), and 1536 cm^{-1} (N–H bending). Therefore, 45 min appears to be the minimum UV exposure time to promote significant chemical changes that we associate to crosslinking. In our next optimization step, we maintained 45 min as the cross-linking time and changed RF concentration to 316.5 mM (Fig. VIII - 1 G – i, j). No differences were noticed between this concentration and the 211 mM concentration. Therefore, these results suggest that the optimum crosslinking reaction conditions appear to be 211 mM RF concentration and 45 min of UV light exposure.

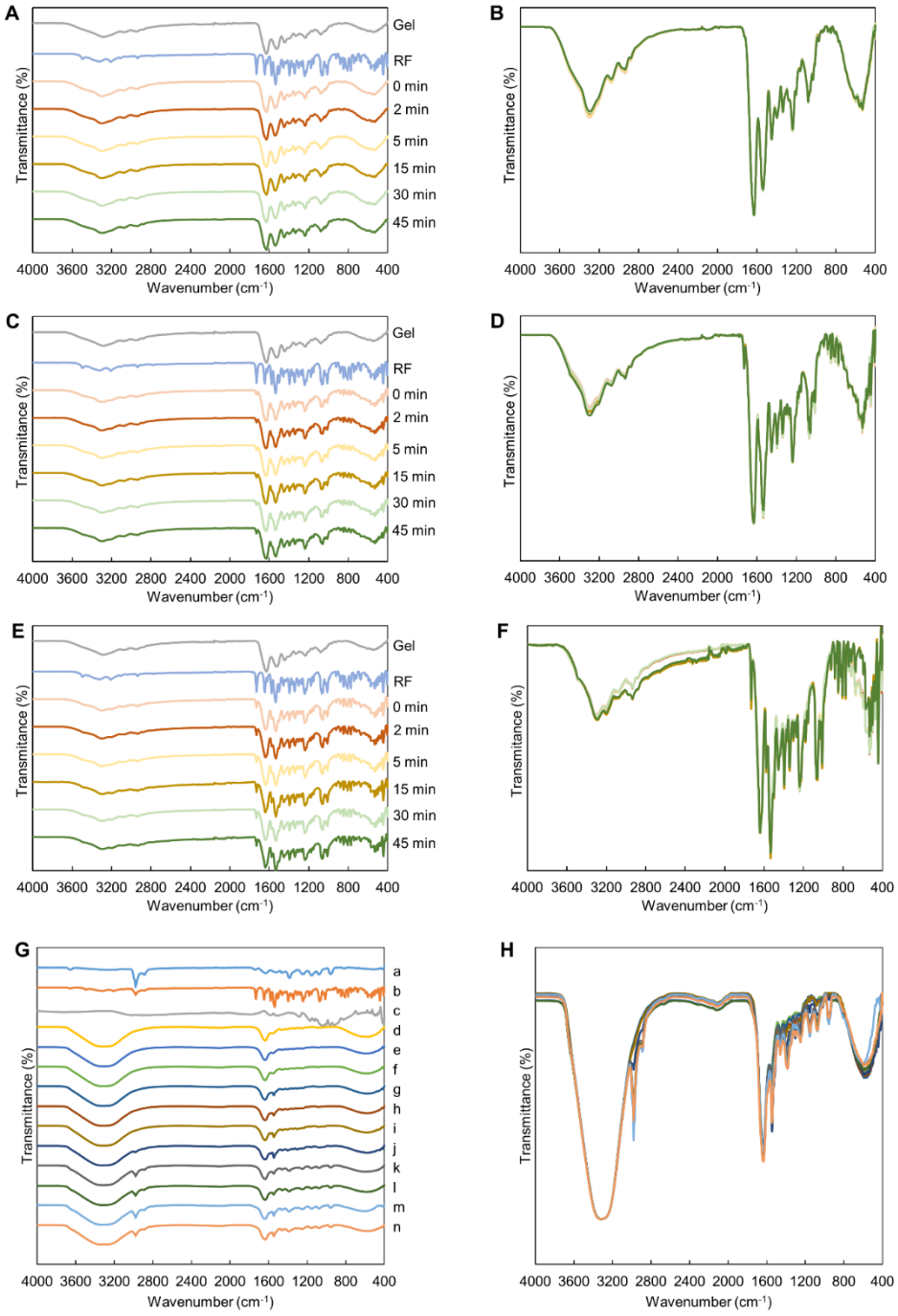

Fig. VIII - 1. FTIR spectra (A – 15 mM; C – 105.5 mM; E – 211 mM) and superposition of dry Gel hydrogels with varying concentrations (B – 15 mM; D – 105.5 mM; F – 211 mM) of RF crosslinked using different exposure times to UV light, and respective controls. FTIR spectra (G) and superposition (H) of Gel/RF hydrogels with varying concentrations of basified RF crosslinked using 45 min exposure time to UV light, Gel/RF/PEDOT hydrogels with 211 mM basified RF crosslinked using 45 min exposure time to UV light varying percentages of PEDOT, and respective controls: a) Gel; b) RF; c) PEDOT; d) Gel 60 ^{o}C; e) Gel/RF 105.5 mM; f) Gel/RFUV 105.5 mM; g) Gel/RF 211 mM; h) Gel/RFUV 211 mM; i) Gel/RF 316.5 mM; j) Gel/RFUV 316.5 mM; k) 50% PEDOT/Gel/RF 211 mM; l) 50% PEDOT/Gel/RFUV 211 mM; m) 100% PEDOT/Gel/RF 211 mM; n) 100% PEDOT/Gel/RFUV 211 mM.

The optimal RF concentration for our study is around 80 times higher than previously reported for corneal treatment, and the UV radiation exposure time is longer than the conventional values reported in clinics.[47] The main reason for this is the corneal treatment is based on the crosslinking of collagen and not gelatin, as it is the case of this work. Therefore, differences in the optimum crosslinking parameters are indeed expected. Second, in corneal tissue treatment, RF is applied every 2 min for 30 min, and then every 5 min during the 30 min UV exposure, most likely leading to a cumulative effect of crosslinking.[46,48]

Changes in crosslinking efficiency were also evaluated through changes in the mechanical properties confirmed by the mechanical characterization of the hydrogels prepared using RF concentrations of 105.5 mM, 211 mM, and 316.5 mM RF solutions (Fig. VIII - 2 A-D). UV application led to significant changes in the mechanical properties of Gel/RF 211 mM hydrogels, where UV application increased the Youngs modulus from 77 ± 8 kPa (Gel/RF) to 114 ± 6 kPa (Gel/RFUV). This indicates the formation of a stiffer material, similar to previously reported studies for crosslinked gelatin hydrogels.[44] This observation supports that the crosslinking was successful for these conditions, as the increase in crosslinking degree should lead to tighter polymeric networks, and also due to a possible increase in triple helix conformation of gelatin chains.[41]

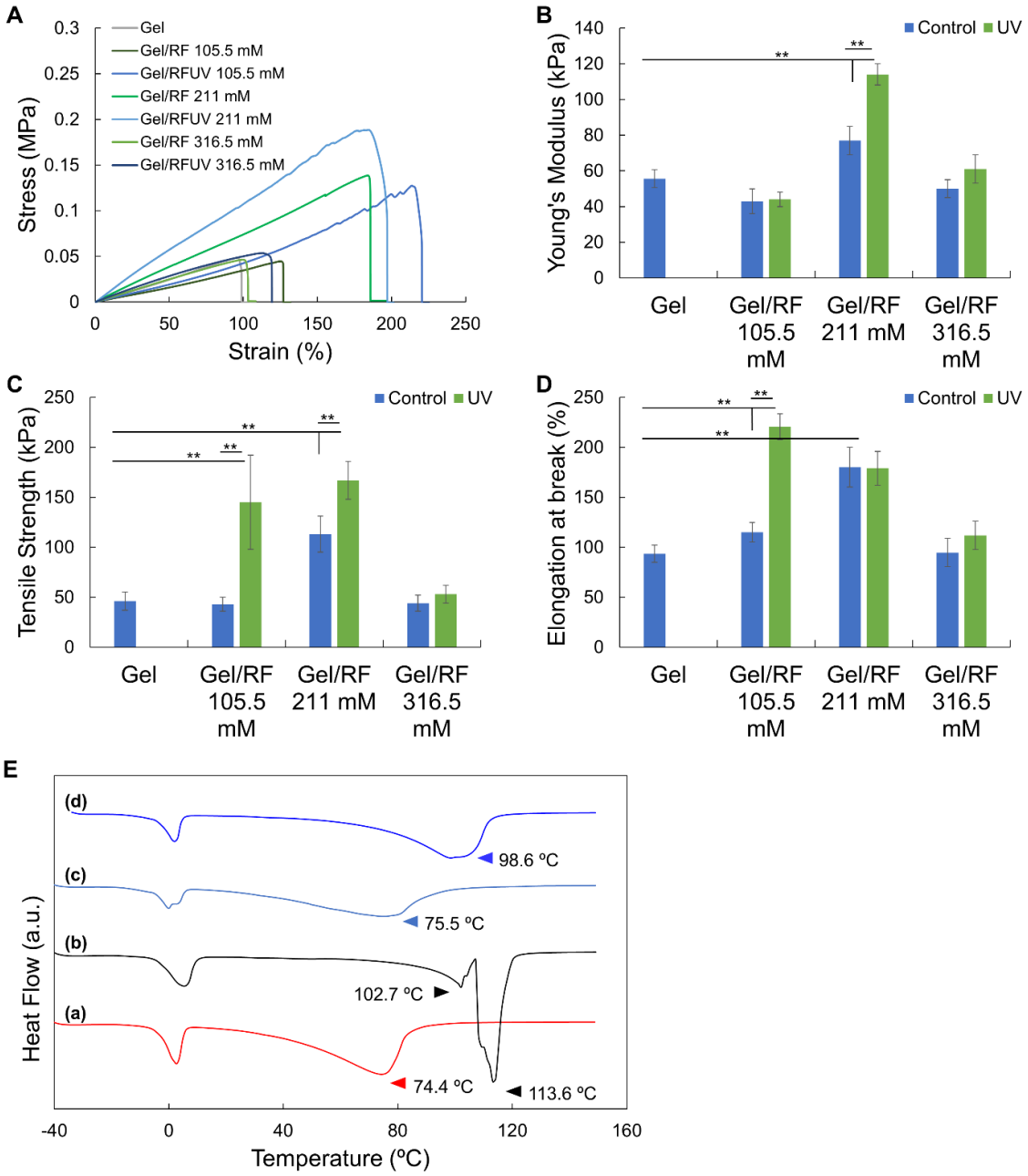

Fig. VIII - 2. Mechanical properties of Gel hydrogels with varying concentrations of RF, as prepared (Control) or crosslinked by UV light exposure (UV): (A) Characteristic stress-strain curves; (B) Young's modulus; (C) tensile strength; (D) elongation at break, n=5. (E) Thermograms of the hydrogels: (a) Gel/RF 211 mM (b) Gel/RFUV 211 mM, (c) 100% PEDOT/Gel/RF 211 mM, (d) 100% PEDOT/Gel/RFUV 211 mM.

A very significant increase was also observed in the respective tensile strength, where the application of UV led to an increase from 113 ± 18 kPa (Gel/RF) to 167 ± 19 kPa (Gel/RFUV), indicating that the hydrogel can withstand a greater tension before breaking. This could mean that the mechanical resistance of the hydrogel is larger, again demonstrating that crosslinking was successful.

Nevertheless, a significant increase in tensile strength from 43 ± 7 kPa to 145 ± 47 kPa was also observed for the 105.5 mM RF condition, even though Young's modulus remains unchanged, showing that this mechanical parameter is less sensible to the crosslinking density. It is also relevant to mention that the further increase of RF concentration to 316.5 mM leads to a decrease of the Young's modulus, tensile strength and elongation at break, of both as-prepared and UV-treated samples, suggesting that RF softens the hydrogel and reduces mechanical resistance and that this effect becomes visible at this concentration.

Although no differences were noticeable for the elongation at break between the crosslinked and not crosslinked gels of the 211 mM and 316.5 mM conditions, the 105.5 mM condition increased from 115 ± 10 % to 221 ± 13 %, thus reaching similar values to the 211 mM conditions (180 ± 20 % and 179 ± 17 % for control and crosslinked hydrogels, respectively).

Further confirmation of crosslinking success of the Gel/RF hydrogels at 211 mM RF and 45 min of UV light exposure was obtained by DSC (Fig. VIII - 2 E). The addition of RF alone leads to an increase of 30 °C in the typical melting point of gelatin gels[53] to 74.4 °C, which agrees with an early study in which the melting temperature increased from 30 °C to 42 °C when carrageenan was added to gelatin.[54] The thermogram of the Gel/RF 211 mM sample has a glass transition at about 5 °C and a melting that peaks at 74.4 °C. The UV exposure increases the glass transition temperature and two melting points appear, the first at 102.7 °C and the second at 113.6 °C. This variation indicates that the amorphous phase becomes more rigid and that the interactions within the crystalline domains (in fact of two types of domains) become stronger, both evidencing the crosslinking modification.

With the optimum crosslinking conditions established (211 mM RF and 45 min of UV exposure), the pristine RF solution was instead prepared in 50% water and 50% PEDOT:PSS (50% PEDOT/Gel/RF), or in 100% PEDOT:PSS (100% PEDOT/Gel/RF). FTIR was again used to assess crosslinking success when incorporating PEDOT in the hydrogels (Fig. VIII - 1 G-H). Apparently, the presence of PEDOT:PSS does not interfere with crosslinking, as the spectra of 50% and 100% PEDOT hydrogels show the peaks associated to the crosslinking of Gel/RFUV 211 mM, (e.g. the peak at 1543 cm^{-1}). Likewise, the crosslinking does not affect PEDOT since the characteristic PEDOT peaks can still be observed for both types of PEDOT hydrogels: C–C of the thiophene ring (C_b-C_b) at 1367 cm^{-1}, C–O–C vibrations at 976 cm^{-1}, C=C stretching band at 1411 cm^{-1} and –CH_2 stretching vibration at 2973 cm^{-1}.[40,55–60]

The effect of UV exposure of the 100% PEDOT/Gel/RFUV hydrogel was also evaluated using DSC (Fig. VIII - 2 E). We chose this sample as the 100% PEDOT/Gel/RFUV hydrogel contains the highest amount of PEDOT:PSS in our selection, and thus any misbehaviour would be promptly detected. The control 100% PEDOT/Gel/RF hydrogel has a glass transition temperature of ca. 0 °C and a melting peak with a maximum at 75.5 °C, which is similar to the melting point of Gel/RF 211 mM (74.4 °C), indicating

that the presence of PEDOT barely affects the structure of the hydrogel, as both the glass transition and melting point of the hydrogel are mostly unaffected. Nevertheless, when exposed to UV light for 45 min the PEDOT hydrogel's melting point increases to 98.6 °C, which is close yet slightly lower than the first melting point of the Gel/RFUV 211 mM hydrogel (102.7 °C), and there is a slight increase of the glass transition temperature. These observations, similar to those that occur with Gel/RF samples, are consistent with increased crosslinking of the hydrogel. A closer analysis to the enthalpy involved in the melting stages reveal that the double peaks found in hydrogels Gel/RFUV (364.9 J g^{-1} and 953.4 J g^{-1}) and 1000% PEDOT/Gel/RFUV (1,471.0 J g^{-1}) require roughly the same amount of heat to occur. As such, the slight decrease in the melting point observed in the 100% PEDOT/Gel/RF hydrogel is likely due to the presence of PEDOT:PSS rather than changes in crosslinking efficiency. From our DSC results, we can conclude that PEDOT:PSS does not significantly interfere with gelatin cross-linking using RF.

Furthermore, we observed that the 100% PEDOT/Gel/RFUV hydrogel could hold different weights as observed in Fig. VIII - 3, of up to 250 g (Fig. VIII - 4), corresponding to 2.45 N, without breaking, indicating an acceptable mechanical resistance of this material.

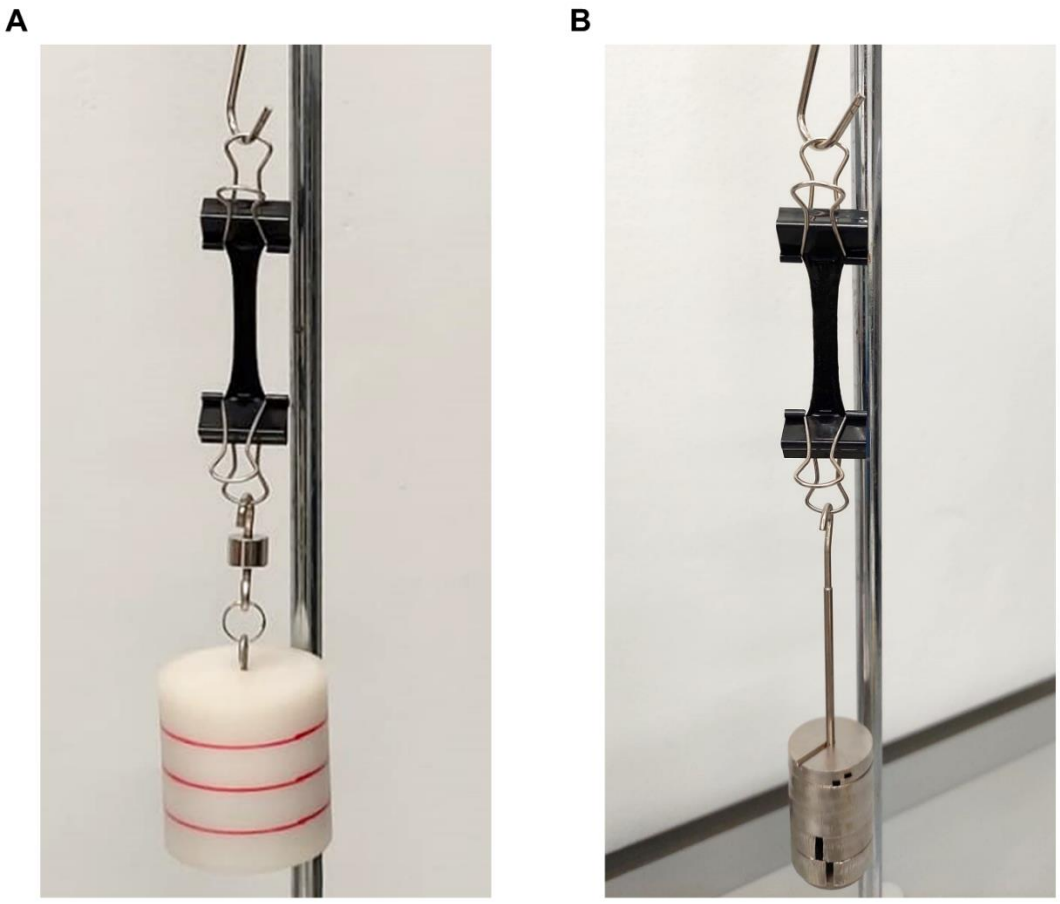

Fig. VIII - 3. Pictures of 100% PEDOT/Gel/RFUV hydrogel samples holding a weight with a mass of 130 g (A) or 250 g (B).

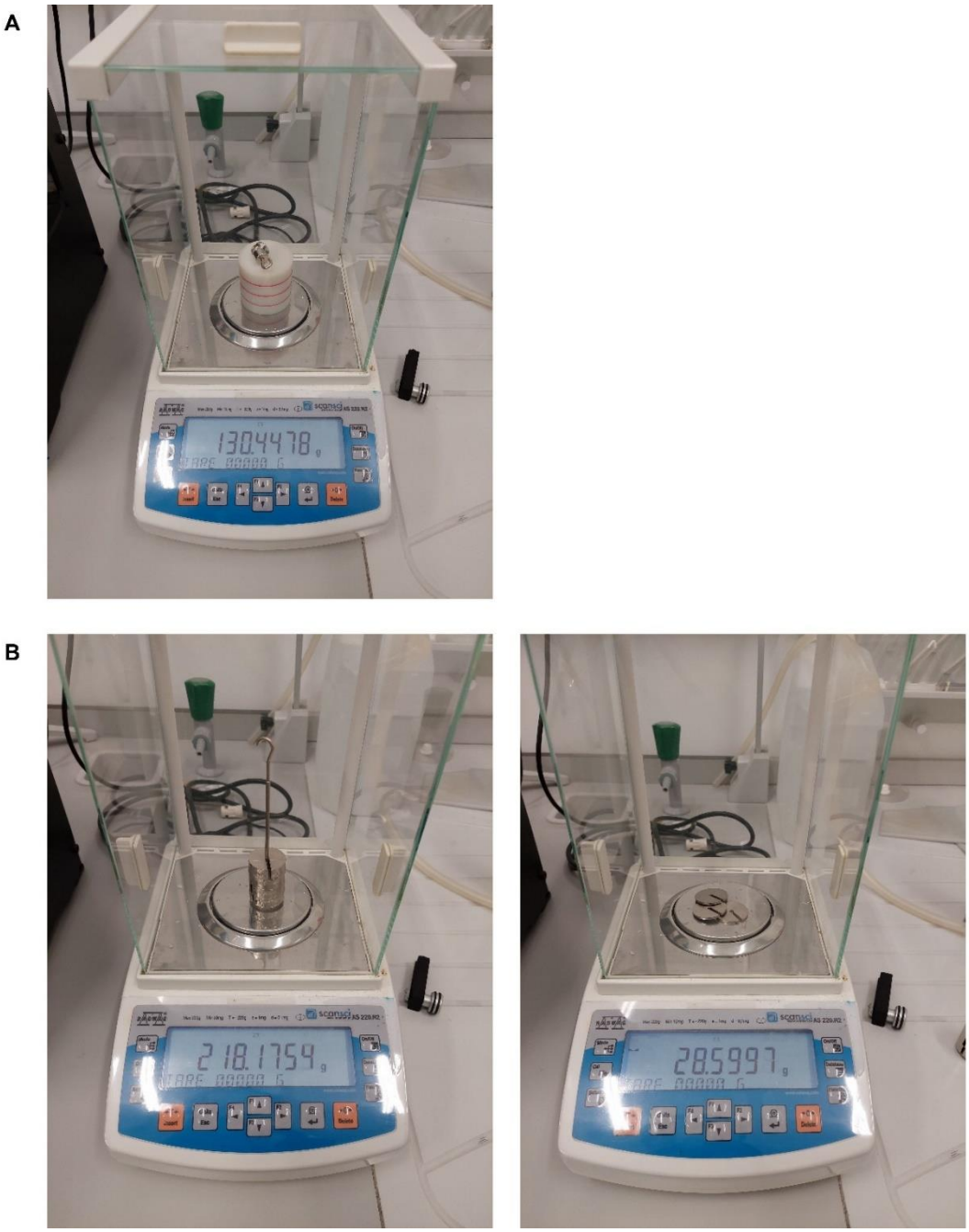

Fig. VIII - 4. Mass of weights used for load bearing experiments, approximately: A) 130 g; B) 250 g (due to scale maximum limit, the pieces used in the experiment were weighed separately).

VIII - 3.1.2. Surface energy and capacity to absorb water

The fabricated hydrogels with varying concentrations of RF and different percentages of PEDOT were characterized in terms of surface energy through contact angle using glycerol (Fig. VIII - 5 A). For the samples without PEDOT, there was no significant difference in contact angle values independently of RF concentration or crosslinking reaction, meaning that all samples are highly hydrophilic. This is

confirmed by the swelling ratios observed, including when PEDOT:PSS is added, with values ranging from 450% to 550% (Fig. VIII - 5 B), which are slightly lower than swelling ratios described in previous work with gelatin methacryloyl-PEDOT:PSS (GelMA-PEDOT:PSS) hydrogels presenting swelling ratios around 600%.[45]

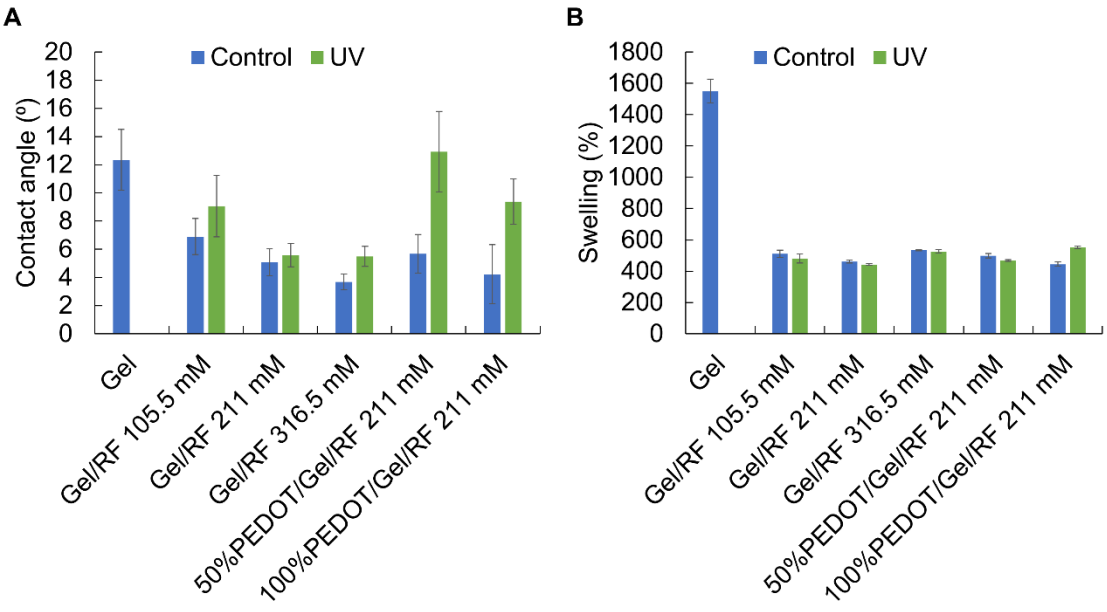

Fig. VIII - 5. (A) Contact angle (°) of glycerol with hydrogels with varying concentrations of RF and PEDOT, with or without exposure to UV light. (B) Swelling ratio of Gel/RFUV hydrogels with varying concentrations of RF and respective controls, and PEDOT/Gel/RFUV with varied composition of PEDOT.

However, when PEDOT is added and the hydrogels are crosslinked with RFUV, the contact angle increases significantly, while, prior to UV exposure, PEDOT/Gel/RF hydrogels have contact angle values that are similar to those of the Gel/RF hydrogels. However, even for the Gel/RF hydrogels a slight increase of the contact angle occurs upon exposure to UV. What is striking is the large increase for the PEDOT hydrogels, with contact angle values that approach that of gelatin. This suggests that with crosslinking reaction, there are significant changes in the polymer network when PEDOT is present. A simpler explanation could rely on the surface segregation of hydrophobic PEDOT at the surface. Should this occur, it is somewhat unexpected, as the UV exposure is carried out at room temperature, and we do not anticipate significant warming of the samples upon exposure to UV. We do not have at present an explanation for this contact angle variation.

Overall, the values of the contact angle for the produced PEDOT:PSS hydrogels (≤ 13°) are much lower than sessile drop advancing angles reported in literature, with angles varying from 75° for PAA-PEDOT hydrogels,[7] 87° for pristine PEDOT:PSS hydrogels and 86° for PEDOT:PSS hydrogels crosslinked

using 3-glycidoxypropyltrimethoxysilane (GOPS),[61] and 50° for PEDOT:PSS coated polyester.[62] Variations in these values might be related to differences in the samples' morphology (considering that PEDOT is an hydrophobic material and will tend to phase separate from the more hydrophilic components), contact angle measurement conditions, like relative humidity and the speed at which the material swells with droplet absorption, leading to drastic changes in contact angle values.[63]

As shown in Fig. VIII - 5 B, the swelling of the various Gel/RF and PEDOT/Gel/RF hydrogels is very similar and lower than that of gelatin. Both RF and PEDOT:PSS have negative effect on the hydrogels swelling, which is not significantly affected by UV exposure.

VIII - 3.2. Mechanical properties of PEDOT hydrogels

The PEDOT hydrogels were characterized in terms of mechanical properties through tensile stress-strain test (Fig. VIII - 6).

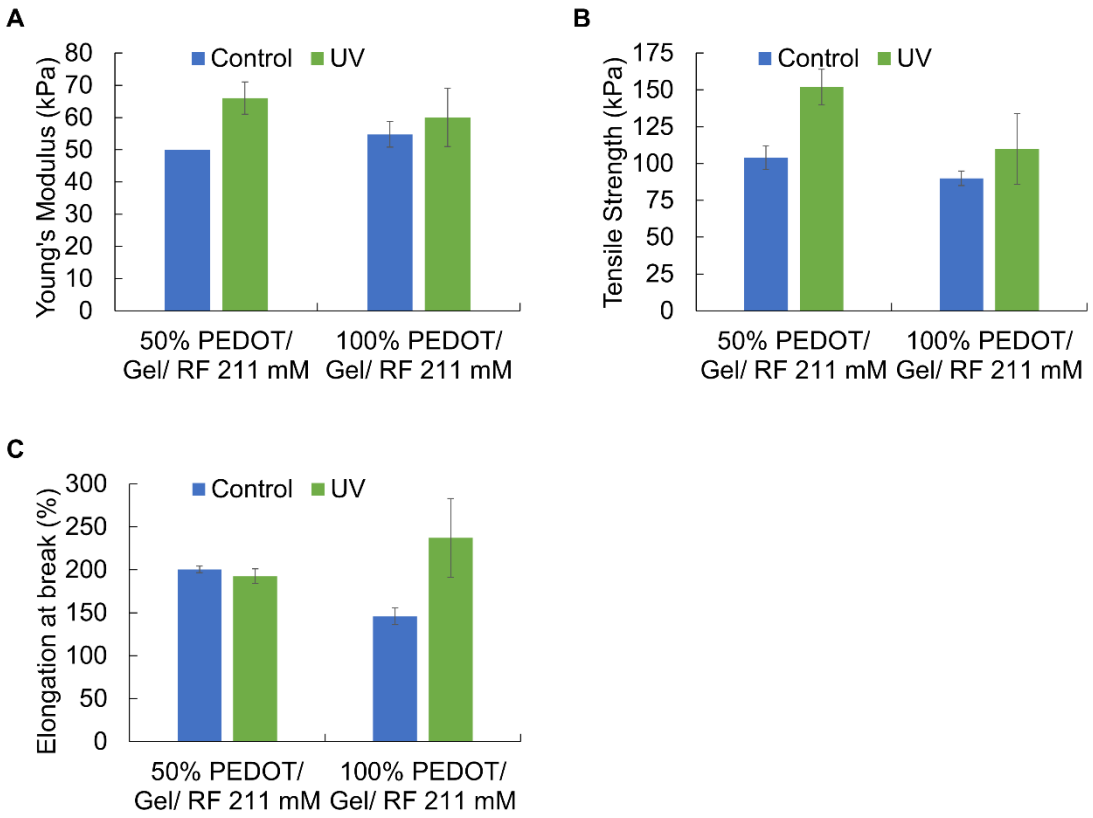

Fig. VIII - 6. Mechanical properties of gelatine-based hydrogels with different amounts of PEDOT:PSS: (A) Young's modulus, (B) ultimate tensile strength and (C) elongation at break, n≥5.

The values of Young's modulus for the 50% PEDOT/Gel/RF and the 100% PEDOT/Gel/RF hydrogels are very similar (Fig. VIII - 6 A). The Young's modulus of the crosslinked hydrogels (66 ± 5 kPa and 60 ± 9 kPa for the 50% and 100%, respectively) is slightly higher than that of the as-prepared, non-

crosslinked, hydrogels (50 ± 4 kPa kPa and 55 ± 8 kPa for the 50% and 100%, respectively. The crosslinking reaction makes the hydrogels stiffer and able to withstand higher elastic deformation. Accordingly, the tensile strength of both 50% and 100% PEDOT crosslinked conditions (Fig. VIII - 6 B) are higher (152 ± 12 kPa and 110 ± 24 kPa, respectively) than those of the non-crosslinked PEDOT hydrogels (104 ± 8 kPa and 90 ± 5 kPa, respectively).

The Young's modulus of our PEDOT:PSS hydrogels are within the range of values reported in the literature. When compared to other types of PEDOT hydrogels, Young's modulus of the 100% PEDOT/Gel/RFUV hydrogel (60 ± 9 kPa) is approximately 20 times lower than the Young's modulus of pristine PEDOT:PSS hydrogels.[64] However, when compared to PEDOT hydrogels functionalized with a carboxylic acid[39] or GelMA-PEDOT:PSS crosslinked hydrogels,[45] the Young's modulus of the 100% PEDOT/Gel/RFUV hydrogel is 2 to 10 times higher. All the conditions are within the 0.5-500 kPa Young's modulus values reported for conducting interpenetrating networks (C-IPN) PEDOT:PSS hydrogels, that mimic elastic modulus of biological tissue.[65] Similarly, the hydrogel presents Young's modulus in the same order of magnitude as crosslinked gelatin hydrogels reported before.[66]

The tensile strength of the 100% PEDOT/Gel/RFUV hydrogel (110 ± 24 kPa) is approximately 10 times lower than PEDOT-alginate hydrogels crosslinked with $CaCl_2$ aqueous solution, as inferred from the stress-strain curves of the hydrogel,[64] and about 30 times lower than pure PEDOT:PSS hydrogels,[40] though it presents slightly higher values than crosslinked gelatin hydrogels.[66] On the other hand, the elongation at break for the 100% PEDOT/Gel/RFUV hydrogel (237 ± 46 %) is approximately 20 times greater than PEDOT-alginate crosslinked hydrogels, including after self-healing,[64] and around 5 times higher than pure PEDOT:PSS hydrogels,[40] but half of the value (approximately 400%) reported for crosslinked gelatin hydrogels.[67] As such, we could conclude that all the PEDOT:PSS hydrogels developed in the present work present mechanical characteristics comparable to those previously reported for PEDOT-based and gelatin-based hydrogels.

Importantly, the values of Young's modulus for these PEDOT:PSS hydrogels, independently of crosslinking or PEDOT:PSS concentration, are within the values of those reported for the first Young's modulus (E1) of human skin in bi-linear elastic skin models (41 kPa to 1.95 MPa), which models the skin as having two linear mechanical behaviors (following Hooke's law), and having two Young's moduli: one below a strain threshold and another above that threshold.[68–72] Thus, we can conclude that the PEDOT hydrogels synthetized in this work are fully compatible with the biomechanical properties of human skin, showcasing their promising application in wound healing.

VIII - 3.3. Self-healing capacity of PEDOT hydrogels

The application of hydrogels in skin tissue engineering will likely expose them to mechanical strain and tension, which may result in their tearing. Therefore, an important property to evaluate is the self-healing capacity of the hydrogels under physiological conditions. This property was evaluated in all cases by cutting hydrogels in half with a blade and then putting the two halves in contact in a humidified atmosphere (50-60% humidity) at 37 ^{o}C. From preliminary results (Table VIII - 1.), the most promising features were achieved for the 100% PEDOT/Gel/RFUV hydrogels, and to a lesser extent for the 50% PEDOT/Gel/RFUV, in self-healing under physiological conditions. We also explored self-healing temperatures from 4 ^{o}C to 70 ^{o}C, with the same 50% PEDOT/Gel/RFUV and the 100% PEDOT/Gel/RFUV conditions presenting self-healing capacity, with the latter composition always being the most successful at self-healing. On the other hand, PEDOT-containing hydrogels that were not crosslinked are not capable of self-healing. It appears that the combination of two factors, crosslinking and presence of PEDOT, is necessary for the hydrogels to undergo this self-healing process.

Table VIII - 1. Preliminary assessment of self-healing properties of hydrogels at 37 ^{o}C, (50-60) % RH, with colors meaning unsuccessful (red), semi-successful (yellow) or successful (green).

Conditions	0% PEDOT	50% PEDOT	100% PEDOT
0 mM RF			
211 mM RF			
0 mM RFUV			
211 mM RFUV			

The self-healing mechanism is likely to combine two processes: a first intimate contact between the two halves and an intermixing process that tends to reestablish the initial structure. The intimate contact might be promoted by the establishment of interactions between PEDOT and PSS moieties with charges of opposing sign, thus promoting the initial bonding of the hydrogel halves for charge stabilization, similarly to ionic coordination reported for other self-healing hydrogels,[73] or even hydrogen bonds.[73,74] Both of these inter-halves interactions are, however, expected to be affected by the existence of an aqueous electrolyte: water will interfere with hydrogen bonding formation between molecules in the neighboring halves and ions will screen the electrostatic interaction between cationic PEDOT and anionic PSS. Another possibility may rely on the exposure of PEDOT hydrophobic domains when the hydrogel is cut into two halves and such domains may promote closer inter-halves contact when these are immersed in a hydrophilic medium. The intermixing process

would rely on the entanglements involving chains or chain segments of the two parts. These stronger interactions may involve the gelatin chains, possibly reestablishing the conformation of gelatin chains in the polymer network structure. This phenomenon could be correlated with optimum healing temperature, as gelatin helixes might be restored due to partial sol-gel transitions at 37 °C, and possibly more efficient transitions due to the presence of PEDOT:PSS.[66,67]

As such, we proceeded to evaluate the self-healing capacity of 100% PEDOT/Gel/RFUV hydrogel, the best sample of our preliminary assessment. The robustness of the hydrogel after healing was also studied using different assays. Tensile strain was applied to 100% PEDOT/Gel/RFUV hydrogel samples healed at 37 ^{o}C, after being torn by tensile strain (Fig. VIII - 7 A), and it was verified that the material breaks at random points, and no apparent tendency to break at the scar point was observed (Fig. VIII - 7 B).

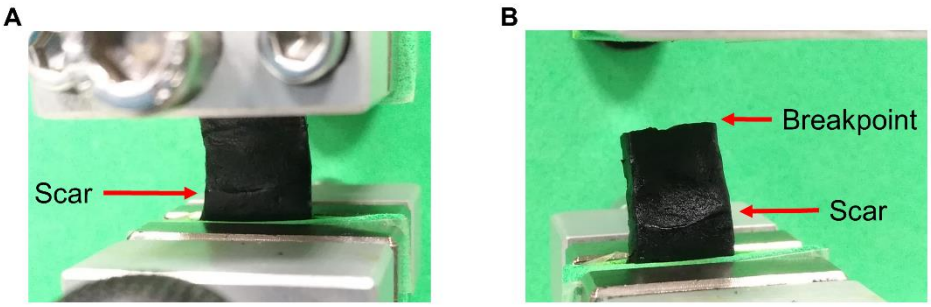

Fig. VIII - 7. (A) Picture of 100% PEDOT/Gel/RFUV hydrogel self-healed at 37^{o}C, and (B) showing scar and breakpoint by application of tensile strength using 50 N load cell.

Self-healing of the 100% PEDOT/Gel/RFUV hydrogel was systematically evaluated at 37 ^{o}C (human body temperature) and 45 ^{o}C (maximum temperature tolerated for local heating). The obtained samples were characterized through a tensile stress-strain assay to study the capacity of the material to recover its original mechanical properties after 1 or 2 cycles of cutting (clean-cut) or rupturing (mechanical cut) of the hydrogel, and healing at a certain temperature (Fig. VIII - 8).

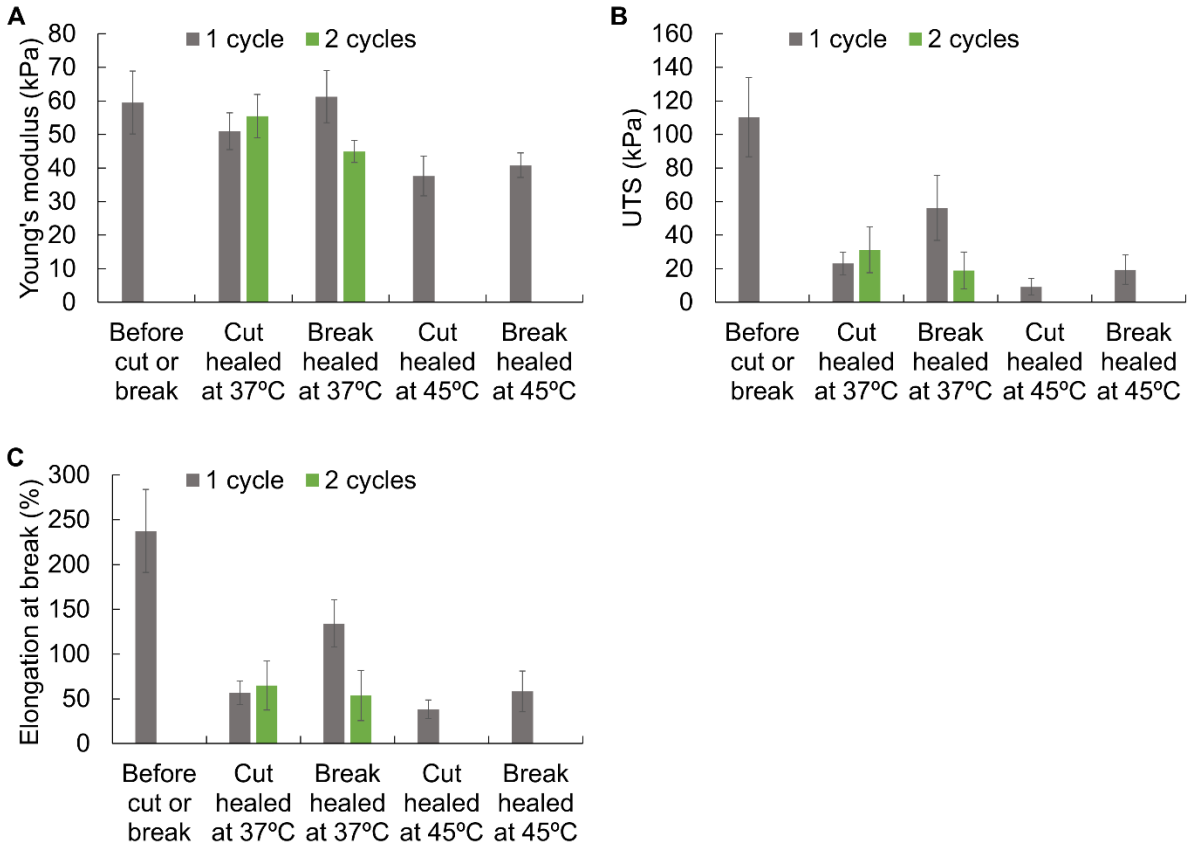

Fig. VIII - 8. Mechanical properties of 100% PEDOT/Gel/RFUV hydrogels with 211 mM RFUV, before and after self-healing under 37 ^{o}C or 45 ^{o}C: (A) Young's modulus, (B) ultimate tensile strength (UTS) and (C) elongation at break, n=5.

The Young's modulus of the hydrogels at 37 ^{o}C is maintained after 2 cycles of cutting (clean-cut) and healing, with the healed hydrogels presenting approximately the same Young's modulus as the one before cutting (60 ± 9 kPa). Similar observations were made to the corresponding hydrogel after mechanical-cut, at 37 ^{o}C and after1 cycle of self-healing. After cycle 2 of self-regeneration at 37 °C, the Young's modulus of the mechanical-cut sample drops to approximately 80% of the initial value.

When the self-healing temperature was changed to 45 °C, dramatic changes in Young's modulus occur. For both the samples healed after clean-cut and mechanical-cut for 1 cycle, the value of the Young's modulus drops to 38 ± 11 kPa and 58 ± 23 kPa, respectively. After 2 cycles of after clean-cut and mechanical-cut, the hydrogels lose consistency and reliable measurements of Young's modulus are not possible. This indicates that the optimal healing temperature for 100% PEDOT/Gel/RFUV hydrogels is 37 ^{o}C, as higher temperatures lead to loss of mechanical strength of the hydrogels.

In terms of ultimate tensile strength and elongation at break, all conditions go through a loss of their properties after cycle 1 or self-regeneration. However, in the samples regenerated after clean-cut and at 37 ^{o}C, the hydrogel maintains their properties after 2 cycles of regeneration.

Overall, considering that Young's modulus values for the 100% PEDOT/Gel/RFUV hydrogels healed at 37 ^{o}C and (50-60) % RH are maintained after 2 cycles of breaking and healing and considering that the remaining mechanical properties are consistent after the first cycle, we conclude that these are the optimum self-healing conditions for these PEDOT hydrogels.

VIII - 3.4. Electrochemical performance and electrical conductivity

The crosslinked hydrogels were characterized in terms of electrochemical performance using CV, electrical conductivity by the 4-contact method and EIS. CV was performed at varying scan rates with the hydrogels hydrated with 0.01 M PBS, pH 7.4, deposited on top of auxiliary and working carbon SPEs. The Ag/AgCl reference electrode was also placed in contact with the hydrogel. Fig. VIII - 9 A-B shows the voltammograms for 50% and 100% PEDOT/Gel/RFUV hydrogels, respectively. Both voltammograms show four peaks corresponding to RF (Fig. VIII - 10 B), and for lower scan rates two PEDOT peaks around -0.7 V and +0.4 V could be observed (Fig. VIII - 10 C). These observations suggest that indeed the crosslinked hydrogels are acting both as electroactive species-containing medium and as solid-like electrolytes, allowing the movement of species between electrodes, without hindering the diffusion phenomena. Furthermore, it was also observed that the addition of PEDOT:PSS to the hydrogels led to a slightly enlarged area (24% and 9% increase for 50% and 100% PEDOT/Gel/RFUV, respectively) when compared to the Gel/RFUV 211 mM sample (Fig. VIII - 10 A), as expected by the addition of an electroconductive polymer.[64,75] Additionally, CV was repeated for 30 consecutive cycles for the PEDOT hydrogels to evaluate the electrochemical performance of the hydrogels (Fig. VIII - 9 C-D). No significant differences were observed between cycles, particularly for the 100% PEDOT/Gel/RFUV hydrogel (Fig. VIII - 9 D), showing the good electrochemical response of the material, as expected.[39,40,75]

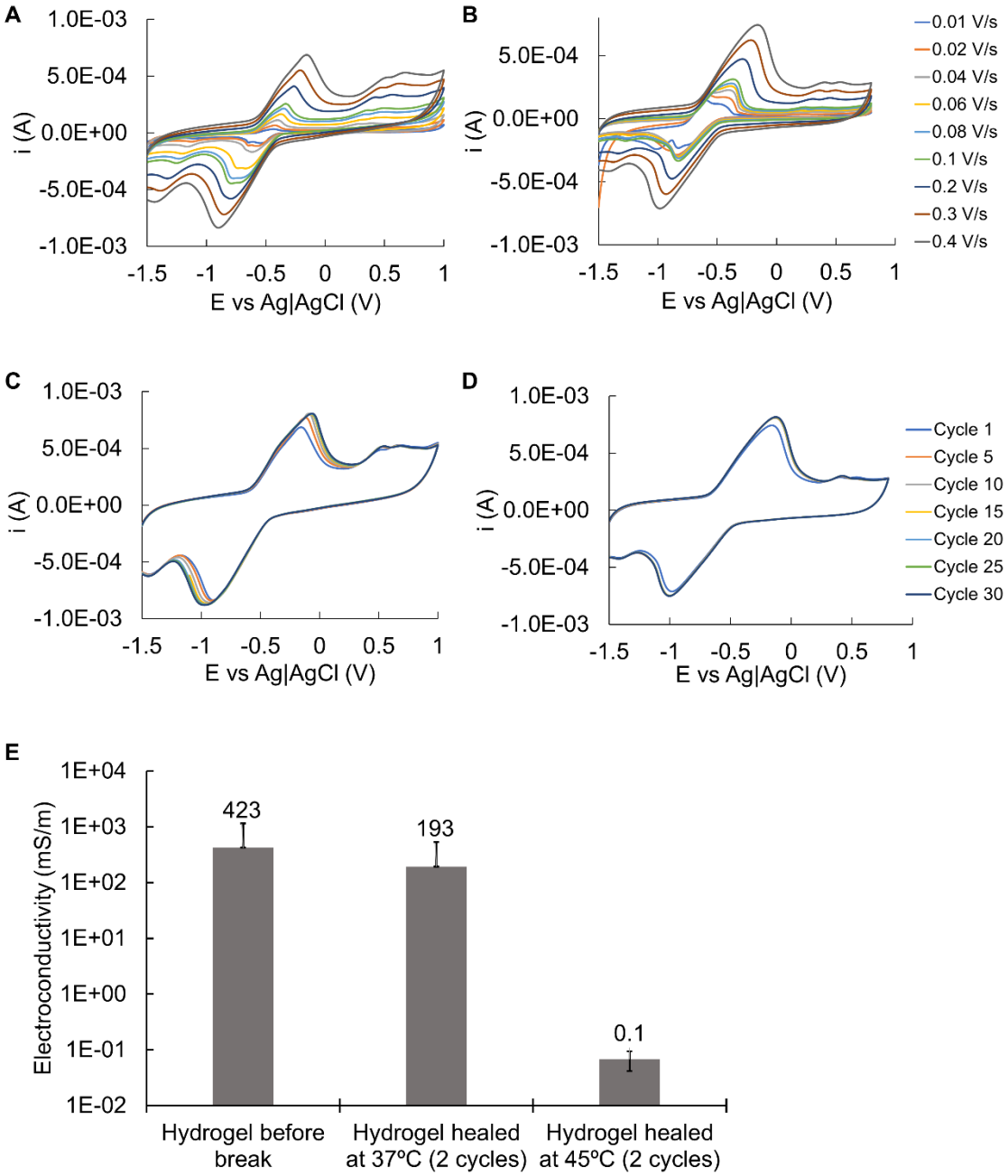

Fig. VIII - 9. CVs recorded for (A) 50% PEDOT/Gel/RFUV and (B) 100% PEDOT/Gel/RFUV hydrogels, at scan rates varying from 0.01 V/s to 0.4 V/s. CVs recorded at a scan rate of 0.4 V/s for 30 repetitive runs for (C) 50% PEDOT/Gel/RFUV and (D) 100% PEDOT/Gel/RFUV hydrogels. (E) Electronic cconductivity values measured by 4-contact method for 100% PEDOT/Gel/RFUV hydrogels.

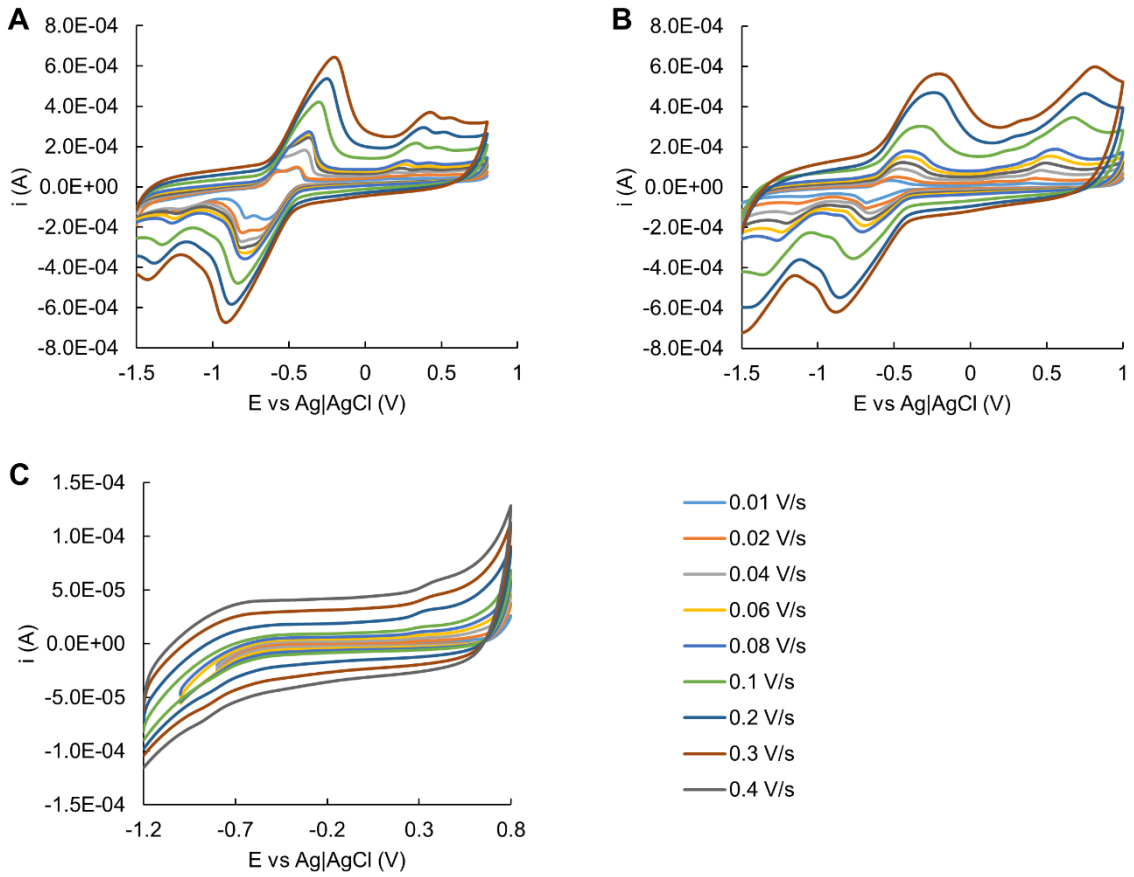

Fig. VIII - 10. Cyclic voltammograms recorded for (A) Gel/RFUV 211 mM hydrogel, (B) 5 mM RF solution and (C) 100% PEDOT/Gel hydrogel, at scan rates varying from 0.01 V/s to 0.4 V/s. Hydrogels dipped in 0.01 M PBS, pH 7.4, solution prepared with the same electrolyte.

Electrical conductivity of PEDOT:PSS hydrogels, before and after self-healing at optimum conditions, was measured for dry samples using the 4-point contact method (Fig. VIII - 9 E). The conductivity of the dry 100% PEDOT/Gel/RFUV hydrogel is of electronic origin and was 423 mS/m, dropping to approximately half of the original value after 2 cycles of breaking and healing the hydrogel at 37 ^{o}C. When regeneration was conducted at 45 ^{o}C, the electroconductivity dropped to 0.1 mS/m. These results evidence the capacity of these hydrogels to partially recover their electrical properties after being cut and self-healed, and further justifies the optimal self-healing temperature at 37 °C.

The conductivity of the 100% PEDOT/Gel/RFUV hydrogel (423 mS/m) is higher than previously reported for conductive PEDOT hydrogels (7.9 mS/m)[64] This suggests that, in addition to the intrinsic electroconductivity of PEDOT, the exposure to UV light might have some effect in the conductivity of the hydrogel, possibly due to a conformation change in the polymer chains, leading to enhancement of carrier transport, thus increasing conductivity.[76,77]

Electrical resistance of the as prepared hydrogels was determined using EIS, with an example of data fitting in a Nyquist plot being given in Fig. VIII - 11, showing a partial semicircle behavior and a

straight line with approximately 45° to the *x*-axis. The fitted equivalent electrical circuit, has two resistances, R1 and R2, a capacitor and a Warburg element (W). R2 represents the charge transfer resistance, which is a polarization resistance at the hydrogel and electrodes interface. The capacitor refers to the charge accumulation at the hydrogel and electrodes contact caused by the electrochemical double layer. The Warburg element (W) corresponds to an impedance increase due to lack of available species near the electrodes, thus decreasing current flow. The Warburg impedance justifies the presence of the straight line in the Nyquist plot in Fig. VIII - 11. R1 represents the electrolyte resistance, meaning the resistance to the passage of charge (which includes both electrons and ions) through the hydrogel. Within the hydrogel we anticipate that the resistance is mostly associated to the ion migration as electrons are unlikey to find a continuous path between the two electrodes and contribute to the hydrogel electrical transport. The ionic resistance R1 is dependent on ion type, concentration of the ions, temperature and hydrogel pore size and mesh structure.[78] From R1, which can be considered the intrinsic resistance of the hydrogel, it was possible to derive (ionic) conductivity values (σ) for the hydrogels (Table VIII - 2), using the equation $\sigma = {}^{L}/_{R_1 A}$, where L corresponds to the thickness of each hydrogel and A corresponds to the area of the electrodes in contact with the hydrogel.

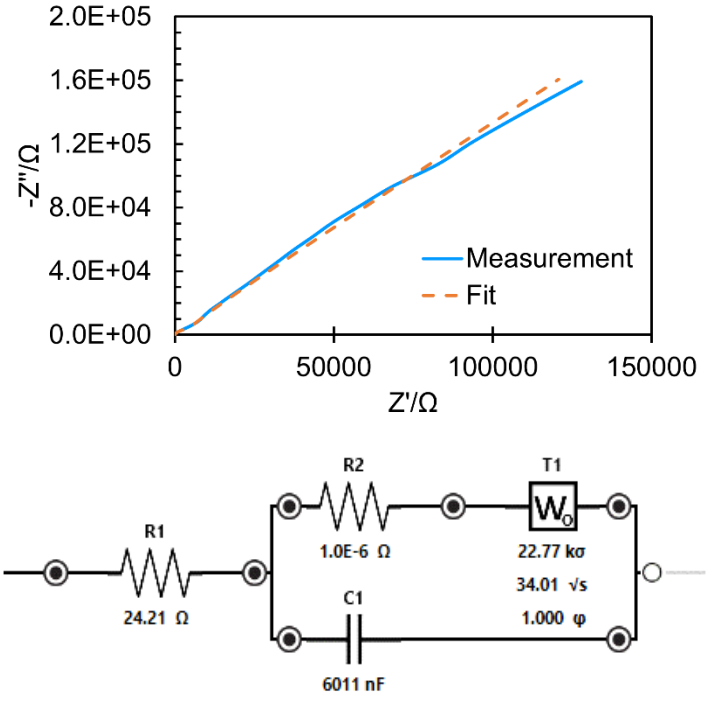

Fig. VIII - 11. Nyquist plot of a measurement and fit for 100% PEDOT/Gel/RFUV hydrogel, and corresponding Randles equivalent circuit.

Table VIII - 2. Conductivity values determined by EIS, fitting using a Randles equivalent circuit, for gelatin and 100% Gel/PEDOT/RFUV hydrogels before and after self-healing at 37 °C and 45 °C after cycle 1 and cycle 2.

Sample	**σ (mS/m)**
Gel	315
100% PEDOT/Gel/RFUV	268
100% PEDOT/Gel/RFUV cycle 1 healing 37 °C	141
100% PEDOT/Gel/RFUV cycle 2 healing 37 °C	190
100% PEDOT/Gel/RFUV cycle 1 healing 45 °C	188
100% PEDOT/Gel/RFUV cycle 2 healing 45 °C	299

Impedance vs frequency plots in Fig. VIII - 12 present a behavior similar to previously reported results for PEDOT:PSS hydrogels.[45,65,75] It is possible to conclude that for lower frequency values the 100% PEDOT/Gel/RFUV hydrogel is less conductive than the pure gelatin hydrogel, in agreement with the conductivity values derived from R1 (Table VIII - 2). Accordingly, as shown in Table VIII - 2, the conductivity of the 100% Gel/PEDOT/RFUV hydrogel (268 mS/m) is slightly lower than that of gelatine (315 mS/m). This is somewhat unexpected in view of the introduction of the electronically conductive PEDOT:PSS. It is also worth to recall the electric conductivity of the dry 100% PEDOT/Gel/RFUV hydrogel, 423 mS/m, mentioned above and which is higher than the value of 268 mS/m for the swollen hydrogel. We conclude that the electrical conductivity of the dry hydrogel is mostly due to electronic transport, while in the swollen state the electrical conductivity is mostly due to ion migration. Considering the impedance of the 100% PEDOT/Gel/RFUV hydrogel shown in Fig. VIII - 12 B, it is hard to predict that its extrapolated impedance at a zero hertz frequency stimulation (that is, DC) would be much lower than that of gelatin. As, under DC bias it will be mostly the electronic transport that is stimulated, the EIS data does not seem to evidence that the presence of PEDOT has a marked positive impact on the electrical conductivity of the swollen 100% PEDOT/Gel/RFUV hydrogel. We may therefore conclude that the electronic conductivity of PEDOT:PSS has no dominant role on the impedance of the PEDOT-based hydrogels. We may even conclude that the addition of PEDOT:PSS to the Gel/RF hydrogel promotes an increase of the impedance. It seems that its presence has a detrimental effect on ion migration (judging from the conductivity data in Table VIII - 2). Considering the self-healed hydrogels, it is possible to observe that the hydrogels did not fully recover their electrical transport properties as impedance vs frequency curves are below that of the 100% Gel/PEDOT/RFUV hydrogel (Fig. VIII - 12), which translates into slightly lower conductivity values.

Nevertheless, for the hydrogel after 1 cycle of healing at 37 °C we can see a partial recovery of the hydrogel's electrical properties, as the curve approaches that of the 100% Gel/PEDOT/RFUV hydrogel.

Altogether, these results evidence the good electrochemical performance and electrical conduction properties of the PEDOT:PSS hydrogels obtained in the present work.

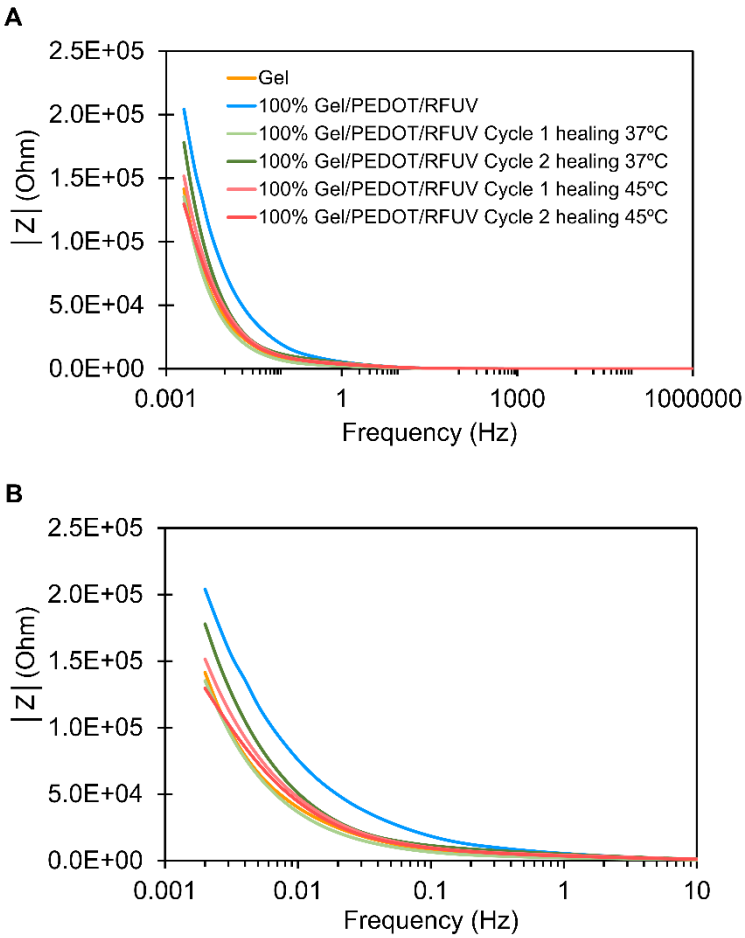

Fig. VIII - 12. (A) Impedance vs frequency plots for gelatin and 100% Gel/PEDOT/RFUV hydrogels before and after self-healing at 37 °C and 45 °C after cycle 1 and cycle 2. (B) Close up of the impedance vs frequency plots at lower frequency values.

VIII - 3.5. Biocompatibility and skin regeneration assay

The tissue engineering and wound healing applications envisioned for the PEDOT:PSS hydrogels described in this work are supported by the described electroconductive and mechanical properties and self-healing capacity of the 100% PEDOT/Gel/RFUV hydrogel. Given these promising properties of the synthesized PEDOT hydrogels, the first step was to assess the biocompatibility of the 100% PEDOT/Gel/RFUV hydrogel by direct observation of calcein staining of HUVECs.

We found that the 100% PEDOT/Gel/RFUV hydrogel was biocompatible as HUVECs presented characteristic green fluorescence of calcein staining after 5 h of incubation on the hydrogel (Fig. VIII -

13). These results are in accordance with previous HUVECs proliferation in gelatin-based hydrogels,[79] and the LIVE/DEAD images of biocompatibility assays reported for C2C12 myoblast cells encapsulated in GelMA-PEDOT:PSS hydrogels.[45] Additionally, it was observed that cell adhesion to the hydrogel was successful without the need of coating the hydrogel surface with cell adhesion proteins, such as laminin. In all, this shows that cells are not negatively affected by the presence of PEDOT in the hydrogel, further demonstrating the potential use of this hydrogel in biomedical applications.

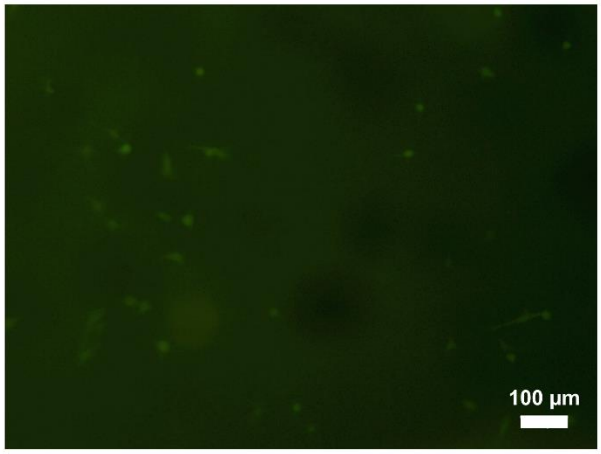

Fig. VIII - 13. Fluorescence imaging of HUVECs incubated on 100% PEDOT/RFUV crosslinked hydrogel after 5 h. Green fluorescence from cells stained with Calcein and background intrinsic PEDOT fluorescence.

After confirming the biocompatibility of the hydrogel, a skin tissue regeneration assay was performed using the L-929 fibroblasts cell line, as an initial model for skin tissue. First, the 100% PEDOT/Gel/RFUV hydrogel was cut in discs to fit in well plates, and then each disc was cut in half using a blade. Fibroblasts were seeded in only one half of the hydrogel to assess the migration of these cells to the other half of the hydrogel in the presence and in the absence of ES (Fig. VIII - 14 A).

In the skin regeneration assay, it was observed that the incubation of L-929 cells in the 100% PEDOT/Gel/RFUV hydrogel in the absence of ES appears to lead to increased cell proliferation after 2.5 h in the area of the hydrogel where cells were initially seeded, as shown by the calcein red-orange staining in Fig. VIII - 14 A, top row. However, some cell migration was also observed after 2.5 h, with 17.6 % of the cells being found in the hydrogel area that was attached after initial cell seeding (Fig. VIII - 14 A - top row, and B). These results suggest that in the absence of ES, the hydrogel is capable of promoting cell proliferation and migration. The increased cell proliferation is in accordance with previous reports of increased expression of Ki-67 protein (a typical marker of cells in a proliferative state) in C2C12 cells seeded on a carboxylic acid functionalized-PEDOT hydrogel,[39] suggesting that the properties of the 100% PEDOT/Gel/RFUV hydrogel help promote cell expansion.

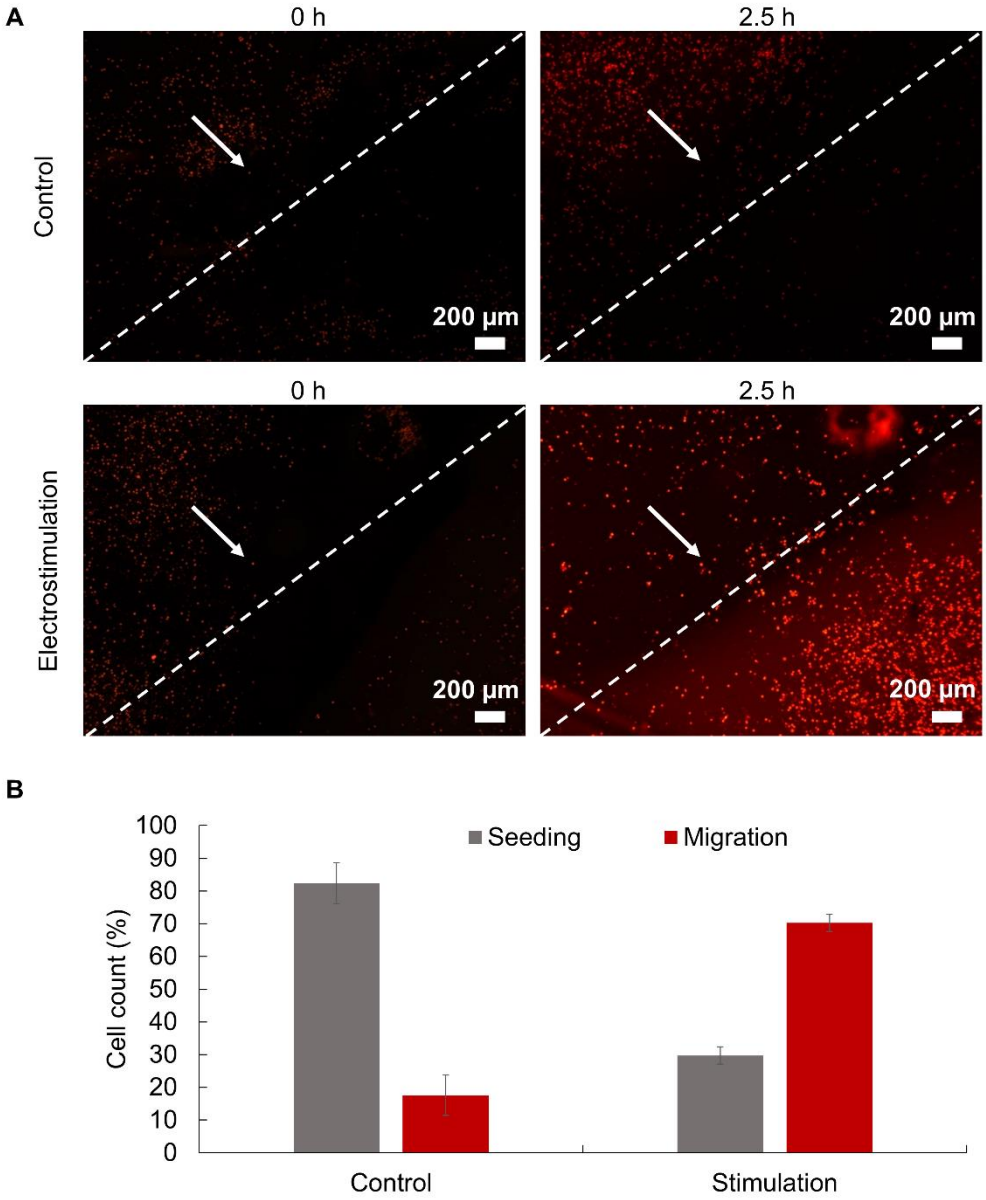

Fig. VIII - 14. (A) Fluorescence imaging of L-929 cells incubated on half of the cut 100% PEDOT/Gel/RFUV hydrogel. After implanting the other half of the hydrogel in the well cells were submitted to 1 h electric stimulation, followed by 1.5 h resting. Red fluorescence from cells stained with calcein red-orange. White dashed lines indicate the cut in the hydrogel. White arrows indicate migration direction of the cells. (B) Cell count (cells/mm^2) in seeding area and migration area at 2.5 h for control and ES condition.

Interestingly, when fibroblasts were electrically stimulated, we observed a significant increase in cell density in the hydrogel area opposed to where the cells were initially seeded (Fig. VIII - 14 A, bottom row). This was further evidenced with cell counting, as 29.8% of the cells were in the seeding area and 70.2% of the cells were in the migration area after 2.5 h (Fig. VIII - 14 B). A hypothesis is that

the electroconductive properties of the hydrogels help to re-establish the endogenous electric field of skin and other epithelial cell layers, like fibroblasts. When wounded, a laterally oriented electric field is formed due to ion imbalance from Na^+, Cl^-, K^+ and Ca^{2+} leakage.[80] As such, the application of low voltage leads to an electric field passing through the hydrogel that lowers the charge imbalance, thus leading to cell migration along the direction of the electric field. Previous reports showed that fibroblasts are responsive to small electric fields and that epithelial skin cells and fibroblasts migrate along directionally applied electric fields, thus validating the present results.[81,82]

Overall, these results show that our PEDOT:PSS hydrogel is highly biocompatible and together with its mechanical and electrical properties makes it a very promising material for biomedical applications for electroresponsive cells and tissues, such as epithelial and skin tissue engineering.

VIII - 4. Conclusions

In this work, we first propose the production of PEDOT/Gel/RFUV hydrogels through a unique strategy. We started by studying the production of gelatin hydrogels using clinically relevant agents, RF and UV light. Optimization of the synthesis parameters was performed, reaching the optimum concentration of 211 mM RF and a UV exposure of 45 min. Additionally, conducting gelatin hydrogels were produced through blending with PEDOT:PSS. Crosslinking of PEDOT/Gel/RF hydrogels was achieved by using the same reaction parameters: 211 mM RF and 45 min of exposure to UV light.

All hydrogels were characterized in terms of their mechanical properties, with the optimal crosslinking conditions leading to very significant increases in Young's modulus, both with and without PEDOT:PSS addition. Crosslinking was successfully achieved by obtaining stiffer materials with superior capacity to withstand elastic deformation. The electrical conductivity of the PEDOT:PSS hydrogels was determined and it was concluded that the dry hydrogels are highly electronically conductive, reaching values up to 423 mS/m, with a better performance than what has been reported for PEDOT:PSS hydrogels. The (ionic) conductivity of the same hydrogel in the swollen state was calculated, from EIS measurements, as 268 mS/m. Combining this result with the impedance of the 100% PEDOT/Gel/RFUV hydrogel at low frequency, which is higher than that of gelatin, we conclude that the presence of PEDOT has a positive impact on the hydrogel electrical conductivity.

It was also shown that 100% PEDOT/Gel/RFUV hydrogels have the capacity to self-heal, with complete healing being observed at (50-60)% RH and 37 °C. This material was characterized before and after healing, with Young's modulus being fully recovered after healing, with the remaining mechanical and electroconductive properties being partially recovered.

Finally, the 100% PEDOT/Gel/RFUV hydrogel was found to be fully biocompatible as shown by calcein staining of live cells. Most importantly, a skin tissue regeneration assay was successfully

established, showing increased cell migration and proliferation when fibroblasts were incubated in the hydrogel and subjected to electrostimulation using squared AC low voltage.

In this work we produced, for the first time, self-healing, stretchable and electroconductive PEDOT:PSS/Gelatin hydrogels crosslinked using RF and UV light. These hydrogels hold great promise in clinical applications, including wound healing, skin tissue engineering and bioelectronics.

VIII - 5. References

(1) Sun, Y.; Nan, D.; Jin, H.; Qu, X. Recent Advances of Injectable Hydrogels for Drug Delivery and Tissue Engineering Applications. *Polym Test* **2020**, *81* (106283). https://doi.org/10.1016/j.polymertesting.2019.106283.

(2) Sekine, Y.; Nankawa, T.; Yunoki, S.; Sugita, T.; Nakagawa, H.; Yamada, T. Eco-Friendly Carboxymethyl Cellulose Nanofiber Hydrogels Prepared via Freeze Cross-Linking and Their Applications. *ACS Appl Polym Mater* **2020**, *2* (12), 5482–5491. https://doi.org/10.1021/ACSAPM.0C00831.

(3) Ćorković, I.; Pichler, A.; Šimunović, J.; Kopjar, M. Hydrogels: Characteristics and Application as Delivery Systems of Phenolic and Aroma Compounds. *Foods* **2021**, *10* (6), 1252. https://doi.org/10.3390/foods10061252.

(4) Grijalvo, S.; Eritja, R.; Díaz Díaz, D. On the Race for More Stretchable and Tough Hydrogels. *Gels* **2019**, *5* (24). https://doi.org/10.3390/gels5020024.

(5) Kesharwani, P.; Bisht, A.; Alexander, A.; Dave, V.; Sharma, S. Biomedical Applications of Hydrogels in Drug Delivery System: An Update. *J Drug Deliv Sci Technol* **2021**, *66*, 102914. https://doi.org/10.1016/J.JDDST.2021.102914.

(6) Alvarez-Lorenzo, C.; Grinberg, V. Y.; Burova, T. v.; Concheiro, A. Stimuli-Sensitive Cross-Linked Hydrogels as Drug Delivery Systems: Impact of the Drug on the Responsiveness. *Int J Pharm* **2020**, *579*, 119157. https://doi.org/10.1016/J.IJPHARM.2020.119157.

(7) Peng, Y.; Tang, S.; Wang, X.; Ran, R. A High Strength Hydrogel with a Core–Shell Structure Simultaneously Serving as Strain Sensor and Solar Water Evaporator. *Macromol Mater Eng* **2021**, *306* (10), 2100309. https://doi.org/10.1002/MAME.202100309.

(8) Xu, L.; Qiu, L.; Sheng, Y.; Sun, Y.; Deng, L.; Li, X.; Bradley, M.; Zhang, R. Biodegradable PH-Responsive Hydrogels for Controlled Dual-Drug Release. *J Mater Chem B* **2018**, *6* (3), 510–517. https://doi.org/10.1039/C7TB01851G.

(9) Shin, Y.; Kim, D.; Hu, Y.; Kim, Y.; Hong, I. K.; Kim, M. S.; Jung, S. PH-Responsive Succinoglycan-Carboxymethyl Cellulose Hydrogels with Highly Improved Mechanical Strength for Controlled Drug Delivery Systems. *Polymers (Basel)* **2021**, *13* (18), 3197. https://doi.org/10.3390/polym13183197.

(10) Zhang, J.; Peppas, N. A. Synthesis and Characterization of PH- and Temperature-Sensitive Poly(Methacrylic Acid)/Poly(N-Isopropylacrylamide) Interpenetrating Polymeric Networks. *Macromolecules* **1999**, *33* (1), 102–107. https://doi.org/10.1021/MA991398Q.

(11) Zhang, Y.; Yu, J.; Ren, K.; Zuo, J.; Ding, J.; Chen, X. Thermosensitive Hydrogels as Scaffolds for Cartilage Tissue Engineering. *Biomacromolecules* **2019**, *20* (4), 1478–1492.

https://doi.org/10.1021/ACS.BIOMAC.9B00043/ASSET/IMAGES/ACS.BIOMAC.9B00043.SOCIAL.JPEG_V03.

(12) Tayel, S. A.; El-Nabarawi, M. A.; Tadros, M. I.; Abd-Elsalam, W. H. Promising Ion-Sensitive in Situ Ocular Nanoemulsion Gels of Terbinafine Hydrochloride: Design, in Vitro Characterization and in Vivo Estimation of the Ocular Irritation and Drug Pharmacokinetics in the Aqueous Humor of Rabbits. *Int J Pharm* **2013**, *443* (1–2), 293–305. https://doi.org/10.1016/J.IJPHARM.2012.12.049.

(13) Salunke, S. R.; Patil, S. B. Ion Activated in Situ Gel of Gellan Gum Containing Salbutamol Sulphate for Nasal Administration. *Int J Biol Macromol* **2016**, *87*, 41–47. https://doi.org/10.1016/J.IJBIOMAC.2016.02.044.

(14) Wang, L.; Li, J.; Xiong, Y.; Wu, Y.; Yang, F.; Guo, Y.; Chen, Z.; Gao, L.; Deng, W. Ultrashort Peptides and Hyaluronic Acid-Based Injectable Composite Hydrogels for Sustained Drug Release and Chronic Diabetic Wound Healing. *ACS Appl Mater Interfaces* **2021**, *13* (49), 58329–58339. https://doi.org/10.1021/ACSAMI.1C16738/SUPPL_FILE/AM1C16738_SI_001.PDF.

(15) Yuk, H.; Lu, B.; Zhao, X. Hydrogel Bioelectronics. *Chem Soc Rev* **2019**, *48* (6), 1642–1667. https://doi.org/10.1039/C8CS00595H.

(16) Ribeiro, M. P.; Morgado, P. I.; Miguel, S. P.; Coutinho, P.; Correia, I. J. Dextran-Based Hydrogel Containing Chitosan Microparticles Loaded with Growth Factors to Be Used in Wound Healing. *Materials Science and Engineering: C* **2013**, *33* (5), 2958–2966. https://doi.org/10.1016/J.MSEC.2013.03.025.

(17) Gupta, A.; Kowalczuk, M.; Heaselgrave, W.; Britland, S. T.; Martin, C.; Radecka, I. The Production and Application of Hydrogels for Wound Management: A Review. *Eur Polym J* **2019**, *111*, 134–151. https://doi.org/10.1016/J.EURPOLYMJ.2018.12.019.

(18) Meaume, S.; Fromantin, I.; Teot, L. Neoplastic Wounds and Degenerescence. *J Tissue Viability* **2013**, *22* (4), 122–130. https://doi.org/10.1016/J.JTV.2013.07.001.

(19) Quattrone, F.; Dini, V.; Barbanera, S.; Zerbinati, N.; Romanelli, M. Cutaneous Ulcers Associated with Hydroxyurea Therapy. *J Tissue Viability* **2013**, *22* (4), 112–121. https://doi.org/10.1016/J.JTV.2013.08.002.

(20) Tummalapalli, M.; Berthet, M.; Verrier, B.; Deopura, B. L.; Alam, M. S.; Gupta, B. Drug Loaded Composite Oxidized Pectin and Gelatin Networks for Accelerated Wound Healing. *Int J Pharm* **2016**, *505* (1–2), 234–245. https://doi.org/10.1016/J.IJPHARM.2016.04.007.

(21) Nacer Khodja, A.; Mahlous, M.; Tahtat, D.; Benamer, S.; Larbi Youcef, S.; Chader, H.; Mouhoub, L.; Sedgelmaci, M.; Ammi, N.; Mansouri, M. B.; Mameri, S. Evaluation of Healing Activity of

PVA/Chitosan Hydrogels on Deep Second Degree Burn: Pharmacological and Toxicological Tests. *Burns* **2013**, *39* (1), 98–104. https://doi.org/10.1016/J.BURNS.2012.05.021.

(22) Anjum, S.; Arora, A.; Alam, M. S.; Gupta, B. Development of Antimicrobial and Scar Preventive Chitosan Hydrogel Wound Dressings. *Int J Pharm* **2016**, *508* (1–2), 92–101. https://doi.org/10.1016/J.IJPHARM.2016.05.013.

(23) Sharma, R.; Kaith, B. S.; Kalia, S.; Pathania, D.; Kumar, A.; Sharma, N.; Street, R. M.; Schauer, C. Biodegradable and Conducting Hydrogels Based on Guar Gum Polysaccharide for Antibacterial and Dye Removal Applications. *J Environ Manage* **2015**, *162*, 37–45. https://doi.org/10.1016/J.JENVMAN.2015.07.044.

(24) Lundeberg, T. C.; Eriksson, S.; Malm, M. Electrical Nerve Stimulation Improves Healing of Diabetic Ulcers. *Ann Plast Surg* **1992**, *29* (4), 328–331. https://doi.org/10.1097/00000637-199210000-00009.

(25) Houghton, P. E.; Kincaid, C. B.; Lovell, M.; Campbell, K. E.; Keast, D. H.; Woodbury, M. G.; Harris, K. A. Effect of Electrical Stimulation on Chronic Leg Ulcer Size and Appearance. *Phys Ther* **2003**, *83* (1), 17–28. https://doi.org/10.1093/PTJ/83.1.17.

(26) Thakral, G.; LaFontaine, J.; Najafi, B.; Talal, T. K.; Kim, P.; Lavery, L. A. Electrical Stimulation to Accelerate Wound Healing. *Diabet Foot Ankle* **2013**, *4* (1). https://doi.org/10.3402/dfa.v4i0.22081.

(27) Korupalli, C.; Li, H.; Nguyen, N.; Mi, F. L.; Chang, Y.; Lin, Y. J.; Sung, H. W. Conductive Materials for Healing Wounds: Their Incorporation in Electroactive Wound Dressings, Characterization, and Perspectives. *Adv Healthc Mater* **2021**, *10* (6), 2001384. https://doi.org/10.1002/ADHM.202001384.

(28) Gharibi, R.; Yeganeh, H.; Rezapour-Lactoee, A.; Hassan, Z. M. Stimulation of Wound Healing by Electroactive, Antibacterial, and Antioxidant Polyurethane/Siloxane Dressing Membranes: In Vitro and in Vivo Evaluations. *ACS Appl Mater Interfaces* **2015**, *7* (43), 24296–24311. https://doi.org/10.1021/ACSAMI.5B08376/ASSET/IMAGES/LARGE/AM-2015-083766_0006.JPEG.

(29) Zhao, X.; Wu, H.; Guo, B.; Dong, R.; Qiu, Y.; Ma, P. X. Antibacterial Anti-Oxidant Electroactive Injectable Hydrogel as Self-Healing Wound Dressing with Hemostasis and Adhesiveness for Cutaneous Wound Healing. *Biomaterials* **2017**, *122*, 34–47. https://doi.org/10.1016/J.BIOMATERIALS.2017.01.011.

(30) Kloth, L. C. Electrical Stimulation Technologies for Wound Healing. *Adv Wound Care (New Rochelle)* **2014**, *3* (2), 81–90. https://doi.org/10.1089/wound.2013.0459.

(31) Brown, M. J.; Loew, L. M. Electric Field-Directed Fibroblast Locomotion Involves Cell Surface Molecular Reorganization and Is Calcium Independent. *Journal of Cell Biology* **1994**, *127* (1), 117–128. https://doi.org/10.1083/JCB.127.1.117.

(32) Wang, Y.; Rouabhia, M.; Lavertu, D.; Zhang, Z. Pulsed Electrical Stimulation Modulates Fibroblasts' Behaviour through the Smad Signalling Pathway. *J Tissue Eng Regen Med* **2017**, *11* (4), 1110–1121. https://doi.org/10.1002/TERM.2014.

(33) Zhao, M.; Song, B.; Pu, J.; Wada, T.; Reid, B.; Tai, G.; Wang, F.; Guo, A.; Walczysko, P.; Gu, Y.; Sasaki, T.; Suzuki, A.; Forrester, J. V.; Bourne, H. R.; Devreotes, P. N.; McCaig, C. D.; Penninger, J. M. Electrical Signals Control Wound Healing through Phosphatidylinositol-3-OH Kinase-γ and PTEN. *Nature* **2006**, *442* (7101), 457–460. https://doi.org/10.1038/nature04925.

(34) Fang, K. S.; Farboud, B.; Nuccitelli, R.; Isseroff, R. R. Migration of Human Keratinocytes in Electric Fields Requires Growth Factors and Extracellular Calcium. *Journal of Investigative Dermatology* **1998**, *111* (5), 751–756. https://doi.org/10.1046/J.1523-1747.1998.00366.X.

(35) Sebastian, A.; Iqbal, S. A.; Colthurst, J.; Volk, S. W.; Bayat, A. Electrical Stimulation Enhances Epidermal Proliferation in Human Cutaneous Wounds by Modulating P53-SIVA1 Interaction. *Journal of Investigative Dermatology* **2015**, *135* (4), 1166–1174. https://doi.org/10.1038/JID.2014.502/ATTACHMENT/9E01A177-85AA-4D02-A5A4-4423A48327E9/MMC1.PDF.

(36) Yen-Patton, G. P. A.; Patton, W. F.; Beer, D. M.; Jacobson, B. S. Endothelial Cell Response to Pulsed Electromagnetic Fields: Stimulation of Growth Rate and Angiogenesis in Vitro. *J Cell Physiol* **1988**, *134* (1), 37–46. https://doi.org/10.1002/JCP.1041340105.

(37) Song, B.; Zhao, M.; Forrester, J. v.; McCaig, C. D. Electrical Cues Regulate the Orientation and Frequency of Cell Division and the Rate of Wound Healing in Vivo. *Proc Natl Acad Sci U S A* **2002**, *99* (21), 13577–13582. https://doi.org/10.1073/PNAS.202235299/ASSET/99E7719B-5E51-4AF8-A48C-535EE80023B5/ASSETS/GRAPHIC/PQ2022352005.JPEG.

(38) Dechiraju, H.; Jia, M.; Luo, L.; Rolandi, M. Ion-Conducting Hydrogels and Their Applications in Bioelectronics. *Adv Sustain Syst* **2022**, *6* (2), 2100173. https://doi.org/10.1002/ADSU.202100173.

(39) Mawad, D.; Artzy-Schnirman, A.; Tonkin, J.; Ramos, J.; Inal, S.; Mahat, M. M.; Darwish, N.; Zwi-Dantsis, L.; Malliaras, G. G.; Gooding, J. J.; Lauto, A.; Stevens, M. M. Electroconductive Hydrogel Based on Functional Poly(Ethylenedioxy Thiophene). *Chemistry of Materials* **2016**, *28* (17), 6080–6088. https://doi.org/10.1021/ACS.CHEMMATER.6B01298/SUPPL_FILE/CM6B01298_SI_001.PDF.

(40) Lu, B.; Yuk, H.; Lin, S.; Jian, N.; Qu, K.; Xu, J.; Zhao, X. Pure PEDOT:PSS Hydrogels. *Nat Commun* **2019**, *10* (1), 1–10. https://doi.org/10.1038/s41467-019-09003-5.

(41) Bigi, A.; Panzavolta, S.; Rubini, K. Relationship between Triple-Helix Content and Mechanical Properties of Gelatin Films. *Biomaterials* **2004**, *25* (25), 5675–5680. https://doi.org/10.1016/J.BIOMATERIALS.2004.01.033.

(42) Campiglio, C. E.; Negrini, N. C.; Farè, S.; Draghi, L. Cross-Linking Strategies for Electrospun Gelatin Scaffolds. *Materials* **2019**, *12* (15), 2476. https://doi.org/10.3390/MA12152476.

(43) Tavakoli, S.; Klar, A. S. Advanced Hydrogels as Wound Dressings. *Biomolecules* **2020**, *10* (8), 1169. https://doi.org/10.3390/BIOM10081169.

(44) Hardman, D.; Thuruthel, T. G.; Iida, F. Self-Healing Ionic Gelatin/Glycerol Hydrogels for Strain Sensing Applications. *NPG Asia Mater* **2022**, *14* (1), 1–13. https://doi.org/10.1038/s41427-022-00357-9.

(45) Spencer, A. R.; Primbetova, A.; Koppes, A. N.; Koppes, R. A.; Fenniri, H.; Annabi, N. Electroconductive Gelatin Methacryloyl-PEDOT:PSS Composite Hydrogels: Design, Synthesis, and Properties. *ACS Biomater Sci Eng* **2018**, *4* (5), 1558–1567. https://doi.org/10.1021/ACSBIOMATERIALS.8B00135/SUPPL_FILE/AB8B00135_SI_002.MOV.

(46) McKay, T. B.; Priyadarsini, S.; Karamichos, D. Mechanisms of Collagen Crosslinking in Diabetes and Keratoconus. *Cells 2019, Vol. 8, Page 1239* **2019**, *8* (10), 1239. https://doi.org/10.3390/CELLS8101239.

(47) McCall, A. S.; Kraft, S.; Edelhauser, H. F.; Kidder, G. W.; Lundquist, R. R.; Bradshaw, H. E.; Dedeic, Z.; Dionne, M. J. C.; Clement, E. M.; Conrad, G. W. Mechanisms of Corneal Tissue Cross-Linking in Response to Treatment with Topical Riboflavin and Long-Wavelength Ultraviolet Radiation (UVA). *Invest Ophthalmol Vis Sci* **2010**, *51* (1), 129. https://doi.org/10.1167/IOVS.09-3738.

(48) Zhang, Y.; Mao, X.; Schwend, T.; Littlechild, S.; Conrad, G. W. Resistance of Corneal RFUVA–Cross-Linked Collagens and Small Leucine-Rich Proteoglycans to Degradation by Matrix Metalloproteinases. *Invest Ophthalmol Vis Sci* **2013**, *54* (2), 1014–1025. https://doi.org/10.1167/IOVS.12-11277.

(49) Liu, C.; Qiao, W.; Cao, H.; Dai, J.; Li, F.; Shi, J.; Dong, N. A Riboflavin–Ultraviolet Light A-Crosslinked Decellularized Heart Valve for Improved Biomechanical Properties, Stability, and Biocompatibility. *Biomater Sci* **2020**, *8* (9), 2549–2563. https://doi.org/10.1039/C9BM01956A.

(50) Hafidz, M.; Yaakob, C. M.; Amin, I.; Noorfaizan, A. Chemical and Functional Properties of Bovine and Porcine Skin Gelatin. *Int Food Res J* **2011**, *18*, 813–817.

(51) Au, V.; Madison, S. A. Effects of Singlet Oxygen on the Extracellular Matrix Protein Collagen: Oxidation of the Collagen Crosslink Histidinohydroxylysinonorleucine and Histidine. *Arch Biochem Biophys* **2000**, *384* (1), 133–142. https://doi.org/10.1006/ABBI.2000.2070.

(52) Gauza-Włodarczyk, M.; Kubisz, L.; Włodarczyk, D. Amino Acid Composition in Determination of Collagen Origin and Assessment of Physical Factors Effects. *Int J Biol Macromol* **2017**, *104*, 987–991. https://doi.org/10.1016/J.IJBIOMAC.2017.07.013.

(53) Tsereteli, G.; Smirnova, O. Calorimetric Study of the Melting of Gelatin Gels. *Polymer Science* **1991**, *33* (10), 2112–2118.

(54) Shimada, R.; Kumeno, K.; Akabane, H.; Nakahama, N. Gelation and Melting of a Mixed Carrageenan-Gelatin Gel. *J. Home Econ. J pn* **1993**, *44*, 999–1005.

(55) Chen, T.; Gu, Y. Green Chemical Process for the Synthesis of Conductive Poly(3,4-Ethylenedioxythiophene) by Nonthermal Plasma-Activated Hydrogen Peroxide. *Plasma Processes and Polymers* **2020**, *17* (1), 1900153. https://doi.org/10.1002/PPAP.201900153.

(56) Jo, E. J.; Male, U.; Huh, D. S. Preparation of Gelatin-Assisted Polypyrrole–Poly(3,4-Ethylenedioxythiophene) Composites. *Bull Korean Chem Soc* **2016**, *37* (11), 1789–1796. https://doi.org/10.1002/BKCS.10977.

(57) Zhong, X.; Fei, G.; Xia, H. Synthesis and Characterization of Poly(3,4- Ethylenedioxythiophene) Nanoparticles Obtained Through Ultrasonic Irradiation. *J Appl Polym Sci* **2010**, *118*, 2146–2152. https://doi.org/10.1002/app.

(58) Puiggalí-Jou, A.; Cejudo, A.; del Valle, L. J.; Alemán, C. Smart Drug Delivery from Electrospun Fibers through Electroresponsive Polymeric Nanoparticles. *ACS Appl Bio Mater* **2018**, *1* (5), 1594–1605. https://doi.org/10.1021/acsabm.8b00459.

(59) Sordini, L.; Silva, J. C.; Garrudo, F. F. F.; Rodrigues, C. A. V.; Marques, A. C.; Linhardt, R. J.; Cabral, J. M. S.; Morgado, J.; Ferreira, F. C. Pedot:Pss-Coated Polybenzimidazole Electroconductive Nanofibers for Biomedical Applications. *Polymers (Basel)* **2021**, *13* (16). https://doi.org/10.3390/polym13162786.

(60) Resina, L.; El Hauadi, K.; Sans, J.; Esteves, T.; Ferreira, F. C.; Pérez-Madrigal, M. M.; Alemán, C. Electroresponsive and PH-Sensitive Hydrogel as Carrier for Controlled Chloramphenicol Release. *Biomacromolecules* **2022**, *24* (3), 1432–1444. https://doi.org/10.1021/acs.biomac.2c01442.

(61) Duc, C.; Vlandas, A.; Malliaras, G. G.; Senez, V. Wettability of PEDOT:PSS Films. *Soft Matter* **2016**, *12* (23), 5146–5153. https://doi.org/10.1039/C6SM00599C.

(62) Boulogne, F.; Ingremeau, F.; Limat, L.; Stone, H. A. Tuning the Receding Contact Angle on Hydrogels by Addition of Particles. *Langmuir* **2016**, *32* (22), 5573–5579. https://doi.org/10.1021/ACS.LANGMUIR.6B01209/SUPPL_FILE/LA6B01209_SI_001.AVI.

(63) Hou, J.; Liu, S.; Lu, X.; -, al; Guo, J.; Wang, X.; Cheng, Y.; Getnet Tadesse, M.; Loghin, C.; Chen, Y.; Wang, L.; Catalin, D.; Nierstrasz, V. Effect of Liquid Immersion of PEDOT: PSS-Coated Polyester Fabric on Surface Resistance and Wettability. *Smart Mater Struct* **2017**, *26* (6), 065016. https://doi.org/10.1088/1361-665X/AA6F25.

(64) Babeli, I.; Ruano, G.; Casanovas, J.; Ginebra, M. P.; García-Torres, J.; Alemán, C. Conductive, Self-Healable and Reusable Poly(3,4-Ethylenedioxythiophene)-Based Hydrogels for Highly Sensitive Pressure Arrays. *J Mater Chem C Mater* **2020**, *8* (25), 8654–8667. https://doi.org/10.1039/D0TC01947J.

(65) Feig, V. R.; Tran, H.; Lee, M.; Bao, Z. Mechanically Tunable Conductive Interpenetrating Network Hydrogels That Mimic the Elastic Moduli of Biological Tissue. *Nat Commun* **2018**, *9* (2740). https://doi.org/10.1038/s41467-018-05222-4.

(66) Yan, X.; Chen, Q.; Zhu, L.; Chen, H.; Wei, D.; Chen, F.; Tang, Z.; Yang, J.; Zheng, J. High Strength and Self-Healable Gelatin/Polyacrylamide Double Network Hydrogels. *J Mater Chem B* **2017**, *5* (37), 7683–7691. https://doi.org/10.1039/C7TB01780D.

(67) Hardman, D.; George Thuruthel, T.; Iida, F. Self-Healing Ionic Gelatin/Glycerol Hydrogels for Strain Sensing Applications. *NPG Asia Materials 2022 14:1* **2022**, *14* (1), 1–13. https://doi.org/10.1038/s41427-022-00357-9.

(68) Joodaki, H.; Panzer, M. B. Skin Mechanical Properties and Modeling: A Review. *Proc Inst Mech Eng H* **2018**, *232* (4), 323–343. https://doi.org/10.1177/0954411918759801.

(69) Ní Annaidh, A.; Bruyère, K.; Destrade, M.; Gilchrist, M. D.; Otténio, M. Characterization of the Anisotropic Mechanical Properties of Excised Human Skin. *J Mech Behav Biomed Mater* **2012**, *5* (1), 139–148. https://doi.org/10.1016/J.JMBBM.2011.08.016.

(70) Dunn, M. G.; Silver, F. H. Viscoelastic Behavior of Human Connective Tissues: Relative Contribution of Viscous and Elastic Components. *Connect Tissue Res* **2009**, *12* (1), 59–70. https://doi.org/10.3109/03008208309005612.

(71) Tonge, T. K.; Atlan, L. S.; Voo, L. M.; Nguyen, T. D. Full-Field Bulge Test for Planar Anisotropic Tissues: Part I – Experimental Methods Applied to Human Skin Tissue. *Acta Biomater* **2013**, *9* (4), 5913–5925. https://doi.org/10.1016/J.ACTBIO.2012.11.035.

(72) Delalleau, A.; Josse, G.; Lagarde, J. M.; Zahouani, H.; Bergheau, J. M. A Nonlinear Elastic Behavior to Identify the Mechanical Parameters of Human Skin in Vivo. *Skin Research and Technology* **2008**, *14* (2), 152–164. https://doi.org/10.1111/J.1600-0846.2007.00269.X.

(73) Zhang, G.; Lv, L.; Deng, Y.; Wang, C. Self-Healing Gelatin Hydrogels Cross-Linked by Combining Multiple Hydrogen Bonding and Ionic Coordination. *Macromol Rapid Commun* **2017**, *38* (12), 1700018. https://doi.org/10.1002/MARC.201700018.

(74) Wang, J.; Tang, F.; Wang, Y.; Lu, Q.; Liu, S.; Li, L. Self-Healing and Highly Stretchable Gelatin Hydrogel for Self-Powered Strain Sensor. *ACS Appl Mater Interfaces* **2020**, *12* (1), 1558–1566. https://doi.org/10.1021/ACSAMI.9B18646/SUPPL_FILE/AM9B18646_SI_003.AVI.

(75) Kleber, C.; Bruns, M.; Lienkamp, K.; Rühe, J.; Asplund, M. An Interpenetrating, Microstructurable and Covalently Attached Conducting Polymer Hydrogel for Neural Interfaces. *Acta Biomater* **2017**, *58*, 365–375. https://doi.org/10.1016/J.ACTBIO.2017.05.056.

(76) Tang, F. C.; Chang, J.; Wu, F. C.; Cheng, H. L.; Hsu, S. L. C.; Chen, J. S.; Chou, W. Y. Alignment of Poly(3,4-Ethylenedioxythiophene) Polymer Chains in Photovoltaic Cells by Ultraviolet Irradiation. *J Mater Chem* **2012**, *22* (42), 22409–22417. https://doi.org/10.1039/C2JM34556K.

(77) Alishah, H. M.; Kazici, M.; Ongül, F.; Bozar, S.; Cantürk Rodop, M.; Kahveci, C.; Arvas, M. B.; Sahin, Y.; Gencten, M.; Kaleli, M.; Akyürekli, S.; Yilmaz, H. U.; Bayram, A. B.; Günes, S. Effect of UV Exposure of ITO/PEDOT:PSS Substrates on the Performance of Inverted-Type Perovskite Solar Cells. *Journal of Materials Science: Materials in Electronics* **2020**, *31* (10), 7968–7980. https://doi.org/10.1007/S10854-020-03336-4/FIGURES/11.

(78) Ruano, G.; Iribarren, J. I.; Pérez-Madrigal, M. M.; Torras, J.; Alemán, C. Electrical and Capacitive Response of Hydrogel Solid-Like Electrolytes for Supercapacitors. *Polymers (Basel)* **2021**, *13* (8), 1337. https://doi.org/10.3390/polym13081337.

(79) Jiang, Y.; Wang, H.; Wang, X.; Yu, X.; Li, H.; Tang, K.; Li, Q. Preparation of Gelatin-Based Hydrogels with Tunable Mechanical Properties and Modulation on Cell–Matrix Interactions. *J Biomater Appl* **2021**, *36* (5), 902–911. https://doi.org/10.1177/08853282211018567.

(80) Tai, G.; Tai, M.; Zhao, M. Electrically Stimulated Cell Migration and Its Contribution to Wound Healing. *Burns Trauma* **2018**, *6* (20). https://doi.org/10.1186/S41038-018-0123-2.

(81) Zhao, M.; Pu, J.; Forrester, J. v.; McCaig, C. D. Membrane Lipids, EGF Receptors, and Intracellular Signals Colocalize and Are Polarized in Epithelial Cells Moving Directionally in a Physiological Electric Field. *The FASEB Journal* **2002**, *16* (8), 857–859. https://doi.org/10.1096/FJ.01-0811FJE.

(82) Simpson, M. J.; Lo, K. Y.; Sun, Y. S. Quantifying the Roles of Random Motility and Directed Motility Using Advection-Diffusion Theory for a 3T3 Fibroblast Cell Migration Assay Stimulated with an Electric Field. *BMC Syst Biol* **2017**, *11* (1), 1–9. https://doi.org/10.1186/S12918-017-0413-5/FIGURES/4.

Chapter IX – Conclusions

IX - 1. Conclusions

1) The restrictions imposed by the (*N*Me)Glu residue drastically reduce the flexibility of CR(*N*Me)EKA in comparison to CREKA, which significantly affects the formation of aggregates with well-defined morphologies. This feature, together with the net molecular charge, which is controlled through the pH, are crucial to explain the significant differences found between the self-assembly behavior of the two peptides.
2) CREKA rarely self-assembles into aggregates with well-defined morphologies, tending to organize in non-shaped structures with no regular organization. Instead, CR(*N*Me)EKA forms abundant and reproducible dendritic microstructures with fractal geometry when the feeding solution presents acid or neutral pH and low peptide concentration.
3) No regular assembly is obtained from solutions with high CR(*N*Me)EKA concentrations, as their dynamics is dominated by strong repulsive peptide-peptide electrostatic interactions, and from solutions at pH 10, in which the total peptide charge is zero. Thus, dendritic structures are only obtained when the molecular charge of CR(*N*Me)EKA, which is controlled through the pH, favors kinetics over thermodynamics during the self-assembly process.
4) CR(*N*Me)EKA dendritic microstructures grow in a two-step process: a) formation of pre-nucleated pseudo-spherical particles and, even, rhombohedral crystals; and b) filling of the inter-particle space following a directional self-assembly process.
5) The assembled PBA-CS/PEDOT carrier successfully combines multiple functions, which can be summarized as follows: a) on-demand controlled release of the anticancer peptide using external electric fields; b) self-regulated pH-controlled delivery in the acidic microenvironment of tumoral tissues; c) peptide protection to maintain its antitumoral activity; and c) mechanical stability and injectability.
6) The release kinetics and dosage from PBA-CS/CR(*N*Me)EKA/PEDOT carrier is controlled through electro-responsive PEDOT NPs, while the dynamic behavior of boronate ester bonds in the PBA-CS hydrogel enhances the peptide release by a factor of 2.6.
7) The bioactivity of the peptide released from PBA-CS/CR(*N*Me)EKA/PEDOT is not affected by the electrostimulation of PEDOT NPs nor by dissociation of the boronate bonds from PBA-CS hydrogel, as has been demonstrated using human prostate cancer cells death assays. Accordingly, the PBA-CS/PEDOT carrier protects the peptide to maintain its antitumoral activity.
8) According to the in lab and *in vitro* studies, the injection of PBA-CS/CR(*N*Me)EKA/PEDOT carrier in acidic tumor environments should allow the controlled delivery of the anticancer peptide by combining the effect of the oxidation and reduction of PEDOT chains on the interactions

between the peptide and the carrier with the effect of the peptide concentration gradient at the interface between the collapsed hydrogel and the release medium.

9) Alg-*g*-PAA/PEDOT/CAM hydrogels have been prepared by incorporating electroresponsive spherical PEDOT/CAM NPs into the pH responsive Alg-*g*-PAA hydrogel during its synthesis. The properties of Alg-*g*-PAA/PEDOT/CAM have been fully characterized, confirming that the swelling ratio depends on the pH and that the hydrogel is conductive.
10) CAM-release tests from PEDOT/CAM NPs, which showed a loading capacity of 14.3% ± 2.5%, have revealed a relatively fast passive delivery rate (*i.e.* around 14% per hour), which can be increased by applying CV and, especially, CA stimuli.
11) CAM-release assays from Alg-*g*-PAA/PEDOT/CAM have shown that the passive delivery is negligible, regardless of the pH. This response has been attributed to the formation of specific interactions between CAM molecules delivered from PEDOT/CAM NPs and the polar groups of the Alg-*g*-PAA matrix.
12) Alg-*g*-PAA/PEDOT/CAM hydrogel allows electro-chemo-controlled release of CAM, which occurs when the pH of the environment is acid and PEDOT/CAM NPs are electrostimulated.
13) Antibacterial tests and cell viability assays have demonstrated that the biological activity of CAM is not altered by Alg-*g*-PAA and PEDOT either during the loading nor the release process.
14) PGS/PCL coaxial fibers with electroresponsive CUR/PEDOT NPs have been successfully prepared. This system allows the sustained release of NPs from the fibers through biodegradation with lipases.
15) The release of CUR from CUR/PEDOT NPs has been controlled through electrical stimulation. Such exogenous stimulus produces a CUR release of around 79% when an electric potential of -1.5 V is applied.
16) CUR, PEDOT NPs, and CUR/PEDOT NPs are safe for somatic cells at given concentrations. However, CUR is cytotoxic for PC-3 and MCF7 cancer cell lines, with the viabilities of those cells dropping to < 20% and < 35%, respectively.
17) Cancer cell lines are capable of internalizing CUR/PEDOT NPs in 24 h, with no perceived cell death or alterations in cell morphology in the absence of electrical stimulation. However, wireless electrostimulation of cancer cells with internalized CUR/PEDOT NPs results in a very significant decrease in cancer cell viability (33%), which is caused by the controlled release of CUR.
18) Two MIP formulations, which are based in AAc and ItAc, have been engineered and prepared for the effective detection and targeting of breast cancer cells. For this purpose, the epitope of

CD44, a cell surface glycoprotein that is overexpressed by cancer cells, has been used as molecular template.

19) Recognition studies with the MIPs prepared in 18) have been performed using MCF-7 and MDA-MB-231 breast cancer cell lines. MIPs identified higher levels of CD44 in MDA-MB-231 cells compared to MCF-7 cells. Furthermore, MIP AAc showed better detection sensitivity for CD44 than MIP ItAc for both cell lines. This is especially prominent in the case of MCF-7 cells.
20) Although there is still room for improvement to achieve results similar to antibodies, results show that the incorporation of MIPs for CD44 into diagnostic and therapeutic strategies could potentially improve the accuracy and effectiveness of breast cancer detection, monitoring, and treatment at a lower cost.
21) The production of conducting PEDOT/Gel/RFUV hydrogels has been optimized using a unique strategy that considers the synthesis parameters of gelatin hydrogels and the blending with PEDOT:PSS.
22) PEDOT/Gel/RFUV hydrogels are stretchable, conducting and self-healing materials.
23) Self-healing has effect on some properties of PEDOT/Gel/RFUV. While the Young's modulus is fully recovered after healing, the remaining mechanical and electroconductive properties are partially recovered.
24) 100% PEDOT/Gel/RFUV hydrogel is fully biocompatible as shown by calcein staining of live HUVEC cells.
25) A successful skin tissue regeneration assay has shown that 100% PEDOT/Gel/RFUV increases cell migration and proliferation when fibroblasts are incubated in the hydrogel and subjected to electrostimulation using squared AC low voltage.

IX - 2. Future work

With this Thesis we have provided significant evidence on the potential of using multiresponsive biomaterials platforms to achieve a highly controlled drug delivey for cancer treatment. Nonetheless, some limitations in the studies could be pinpointed, thus opening up new avenues for research to be performed. As such, in the next paragraphs we synthetize new research oportunities arising from this Thesis:

1) Regarding the bioactivity of the therapeutic agents used throughout this Thesis, all the anticancer activity studies following electrostimulation in Chapters IV, V and VI were performed using *in vitro* 2D cell culture. In the last 10 years, there has been extensive research supporting the favorable characteristics of 3D cell culture systems when compared to 2D for *in vitro* cancer models. A recurrent problem of 2D systems is the false sensitivity of cancer cells to anti-tumor

drugs when 3D models reveal resistance to the same drugs. Explanations for this phenomenon are based on the fact that in 2D systems cells will grow in a monolayer, thus lacking the inherent intricate tumor physiology and the complex architecture of the tumor and its microenvironment. Furthermore, 2D culture systems lose out on cell-to-cell and cell-ECM interactions, whereas hypoxia, pH, ECM, and diffusional struggles are closely reproduced to reality in 3D systems. This is particularly noticeable in sophisticated 3D systems, like those using organoids or co-cultures, although including tumor vascularization could still prove challenging. Keeping this in mind, it would be very beneficial to perform the same bioactivity studies using 3D cell systems that could reproduce the tumor microenvironment more closely.

2) Of course, still regarding drug safety, bioactivity and effectiveness, the logic next step would be to also perform such studies in animal models to show both overall safety of the biomaterials systems to the body, but also the same therapeutic effectiveness that has already been shown *in vitro.*

3) Concerning Chapter VII, positive results showing the potential of using MIPs for breast cancer targeting have been presented. However, the full characterization of the synthesized MIPs needs to be performed. Although size of the MIP NPs has been studied in suspension, microscopy techniques such as SEM should be performed to study morphology of the MIPs. Additionally, functional groups and bonds present in the MIPs should be assessed, thus structural characterization resorting to spectroscopic techniques (*e.g.* FTIR, Raman) should also be performed. Since MIPs are competing with antibodies relating to biding specificity and capacity, binding assays to the target peptide should be performed to establish binding isotherms. Moreover, concerning safety, although *in vitro* cell assays were performed, a full cytotoxicity assessment should be done using normal cells.

4) Still regarding the MIP work, many more avenues could be explored. We have focused on the cancer targeting part. However, a dual-imprinting strategy could be explored. For example, molecular imprinting of an anticancer drug could also be performed. This way, the MIP would provide simultaneous cancer cell targeting and act as a carrier to transport the drug to the cancer site. Furthermore, an electroresponsive MIP could be synthesized by including a monomer of an electroductive polymer to the reaction mixture during synthesis. The EDOT monomer is a strong candidate, as we have already shown that chemical polymerization of PEDOT is possible, under the same reaction conditions used to obtain the MIPs. Assembling the electroconductive MIP component into a bioresponsive (e.g. fibers) or pH-responsive (e.g. hydrogel) layer would further provide a complete multiresponsive biomaterials platform that could provide targeting, drug transport and highly controlled drug delivery to the cancer site.

Annex

List of publications

Articles in international peer-reviewed journals

1) Dias D, Resina L, Ferreira FC, Sanjuan-Alberte P, Esteves T. Synthesis strategies and cancer therapy applications of PEDOT nanoparticles. *Materials Advances* **2024**, 5(19), 7561-7583. https://doi.org/10.1039/D4MA00260A
2) Jones CF, Resina L, Ferreira FC, Sanjuan-Alberte P, Esteves T. Conductive Core−Shell Nanoparticles: Synthesis and Applications. *The Journal of Physical Chemistry C* **2024**, 128(27), 11083–11100. https://doi.org/10.1021/acs.jpcc.4c02012
3) Resina L, Esteves T, Pérez-Rafael S, Hernández-García JI, Ferreira FC, Tzanov T, Bonnard S, Díaz DD, Pérez-Madrigal MM, Alemán C. Dual electro-/pH-responsive nanoparticle/hidrogel system for controlled delivery of anticancer peptide. *Biomaterials Advances* **2024**, 162, 213925. https://doi.org/10.1016/j.bioadv.2024.213925
4) Resina L, Garrudo FFF, Alemán C, Esteves T, Ferreira FC. Wireless electrostimulation for cancer treatment: an integrated nanoparticle/coaxial fiber mesh platform. *Biomaterials Advances* **2024**, 160, 213830. https://doi.org/10.1016/j.bioadv.2024.213830
5) Resina L, Alemán C, Ferreira FC, Esteves T. (Bio)Molecularly Imprinted Polymers: How Far Have "Plastic Antibodies" Come?. *Biotechnology Advances* **2023**, 68(6), 108220. https://doi.org/10.1016/j.biotechadv.2023.108220
6) Frederico B, Garrudo FFF, Alberte P, Resina L, Carvalho M, Jain A, Marques A, Estrany F, Rawson F, Alemán C, Ferreira FC, Silva JC. Hydroxyapatite-Filled Osteoinductive and Piezoelectric Nanofibers for Bone Tissue Engineering. *Science and Technology of Advanced Materials* **2023**, 24(1), 2242242. https://doi.org/ 10.1080/14686996.2023.2242242
7) Garrudo FFF, Filippone G, Resina L, Silva JC, Barbosa F, Ferreira LFV, Esteves T, Marques AC, Morgado J, Ferreira FC. Production of Blended Poly(acrylonitrile): Poly(ethylenedioxythiophene):Poly(styrene sulfonate) Electrospun Fibers for Neural Applications. *Polymers* **2023**, 15(13), 2760. https://doi.org/10.3390/polym15132760
8) Resina L, El Hauadi K, Sans J, Esteves T, Ferreira FC, Pérez-Madrigal MM, Alemán C. Electroresponsive and pH-Sensitive Hydrogel as Carrier for Controlled Chloramphenicol Release. *Biomacromolecules* **2023**, 24, 3, 1432-1444. https://doi.org/10.1021/acs.biomac.2c01442
9) Resina L•, El Hauadi K•, Zanuy D, Esteves T, Ferreira FC, Pérez-Madrigal MM, Alemán C. Dendritic Self-assembled Structures from Therapeutic Charged Pentapeptides. *Langmuir* **2022**, 38, 42, 12905-12914. https://doi.org/10.1021/acs.langmuir.2c02010. •equal contributors

10) Ferreira F, Resina L, Esteves T, Ferreira FC. Comparison and Combination of Organic Solvent Nanofiltration and Adsorption Processes: A Mathematical Approach for Mitigation of Active Pharmaceutical Ingredient Losses during Genotoxin Removal. *Membranes* **2020**; 10(4):73. https://doi.org/10.3390/membranes10040073

Articles prepared to submit to international peer-reviewed journals

1) Resina L, *et al*. Recent advances in smart materials for cancer therapy. Ready to submit.
2) Resina L, *et al*. Self-healable, stretchable and conductive PEDOT:PSS hydrogels based on riboflavin and UV-induced gelatin crosslinking for skin regeneration. Ready to submit.

Patents

1) Ferreira FC, Esteves T, Garrudo FFF, Resina L. Hidrogel Eletrocondutor Autoregenerável, Suas Composições, Usos E Métodos De Obtenção. PT118493. Patent published 2024-07-31.
2) Ferreira FC, Esteves T, Garrudo FFF, Resina L. Self-healing electroconductive hydrogels, their composition, uses, and methods of production. WO2024162863A1. Patent published 2024-08-08.

Oral presentations at conferences

1) Resina L, *et al*. Smart hydrogel/nanoparticle system for controlled chloramphenicol release. ACS Spring 2024, New Orleans, USA.
2) Resina L, *et al*. Dendritic self-assembled structures from therapeutic charged pentapeptides. ACS Spring 2024, New Orleans, USA.
3) Resina L, *et al*. Self-healable, stretchable and conductive hydrogel for skin regeneration. ACS Spring 2024, New Orleans, USA.
4) Resina L, *et al*. Controlled anticancer peptide release using multiresponsive hydrogel/nanoparticle system. ACS Spring 2024, New Orleans, USA.
5) Alemán C, Resina L, *et al.* Controlled therapeutic peptide release using nanoparticles and hydrogels. Peptide Materials 2023, Sorrento, Italy.
6) Resina L, *et al*. Using nanomaterials for cancer treatment: a wireless electrostimulation platform. ACS Fall 2023, San Francisco, USA.
7) Garrudo FFF, Resina L, *et al.* Highly electroconductive PEDOT:PSS platforms for electrical stimulation studies of neural-differentiating iPSCs. ACS Fall 2023, San Francisco, USA.

8) Garrudo FFF, Fillipone G, Resina L, *et al.* Development of electroconductive PAN/PEDOT electrospun fibers for tissue engineering applications. ACS Fall 2023, San Francisco, USA.

9) Resina L, *et al*. Wireless electrostimulation nanomaterials platform for cancer treatment. NanoSpain Conference 2023, Tarragona, Spain.

10) Resina L, *et al*. Wireless electrostimulation for cancer treatment: an integrated nanoparticle/coaxial fiber mesh platform. TERMIS-EU Chapter Meeting 2023, Manchester, UK.

11) Garrudo FFF, Nogueira DES, Resina L, *et al*. Electrical stimulation positively interferes on induced pluripotent stem cell neural differentiation at different stages. TERMIS-EU Chapter Meeting 2023, Manchester, UK.

12) Ferreira FC, Esteves T, Battello S, Mota A, Resina L, Afonso C, Malpei F. Membrane Process for Water Recycle and Lupanine Recovery on Lupin Bean Processing. Engineering with Membranes Conference 2019, Båstad, Sweden.

Poster presentations at conferences

1) Resina L, *et al*. Electro-Responsive and pH-Sensitive Hydrogel as Carrier for Controlled Drug Release. 3rd iBB Workshop at IST Congress Center - Alameda Campus, 2023, Lisbon, Portugal.

2) Miguel F, Resina L, *et al*. Biomimetic conductive hydrogel loaded with Kartogenin-PEDOT nanoparticles for cartilage tissue engineering. European Orthopaedic Research Society EORS 2023, Porto, Portugal.

3) Resina L, *et al*. Multiresponsive hydrogel as carrier for controlled chloramphenicol release. ACS Fall 2023, San Francisco, USA.

4) Resina L, *et al*. Dendritic self-assembled structures from anticancer pentapeptides. ACS Fall 2023, San Francisco, USA.

5) Resina L, Garrudo FFF, Alemán C, Esteves T, Ferreira FC. Wireless electrostimulation for cancer treatment: an integrated nanoparticle/coaxial fiber mesh platform. Ciência 2023, Aveiro, Portugal.

6) Resina L, Garrudo FFF, Alemán C, Esteves T, Ferreira FC. Nanomaterial-based wireless electrostimulation platform for cancer treatment. Advanced Functional Polymers for Medicine 2023, Barcelona, Spain.

7) Resina L, *et al*. Electro-Responsive and pH-Sensitive Hydrogel as Carrier for Controlled Drug Release. Advanced Functional Polymers for Medicine 2023, Barcelona, Spain.
8) Ramirez MD, Molins M, Resina L, *et al.* Multifunctional hydrogels and biopolymer blend scaffolds for skin tissue regeneration. Advanced Functional Polymers for Medicine 2023, Barcelona, Spain.
9) Miguel F, Resina L, *et al*. Electrically conductive hydrogel loaded with PEDOT-Kartogenin nanoparticles for articular cartilage regeneration. TERMIS-EU Chapter Meeting 2023, Manchester, UK.
10) Garrudo FFF, Silva JC, Resina L, *et al*. Development of electroactive composites for the electrical stimulation of stem cells. TERMIS-EU Chapter Meeting 2023, Manchester, UK.
11) Barbosa F, Garrudo FFF, Alberte PS, Resina L, *et al* C. Novel piezoelectric and osteoinductive electrospun nanofibers for bone tissue engineering. TERMIS-EU Chapter Meeting 2023, Manchester, UK.
12) Resina L, *et al*. Wireless electrostimulation for cancer treatment using an integrated nanoparticle/coaxial fiber mesh platform. 2nd iBB Workshop at IST Congress Center - Alameda Campus, 2022, Lisbon, Portugal.
13) Gomes AR, Fernandes TG, Resina L, *et al*. Tauroursodeoxycholic acid increases neural rosette number upon neural induction of human induced pluripotent stem cells. 10th International Meeting of The Portuguese Society for Stem Cells and Cell Therapies, 2019, Covilhã, Portugal.